

Zeitaufgelöste FTIR- und Lumineszenzspektroskopie an Organometallkomplexen und deren Reaktionen

Vom Fachbereich Chemie der Rheinland-Pfälzischen Technischen Universität
Kaiserslautern-Landau zur Verleihung des akademischen Grades "Doktor der
Naturwissenschaften" genehmigte Dissertation

D 386



vorgelegt von

Sophie Theres Steiger

geboren in Neustadt an der Weinstraße

Betreuer:

Prof. Dr. Dr. Gereon Niedner-Schatteburg

Prof. Dr. Markus Gerhardt†

Kaiserslautern, 22.03.2023

Die vorliegende Arbeit wurde im Zeitraum von November 2019 bis Februar 2023 im Fachbereich Chemie der Rheinland-Pfälzischen Technischen Universität Kaiserslautern-Landau (ehemals Technische Universität Kaiserslautern) unter Betreuung vom Prof. Dr. Markus Gerhards† und Prof. Dr. Dr. Gereon Niedner-Schatteburg angefertigt.

Datum des Antrags der Eröffnung des Promotionsverfahrens: 09.02.2023

Datum der wissenschaftlichen Aussprache: 22.03.2023

Promotionskommission

Vorsitzende: Jun.-Prof. Dr. Sabine Becker

1. Berichterstatter: Prof. Dr. Dr. Gereon Niedner-Schatteburg

2. Berichterstatterin: Prof. Dr. Maria Wächtler

Eidesstattliche Erklärung

Erklärung über eigenständige Arbeit

Hiermit erkläre ich, Sophie Theres Steiger, dass ich diese Arbeit gemäß der Promotionsordnung des Fachbereichs Chemie der RPTU in Kaiserslautern eigenständig verfasst und keine anderen als die angegebenen Quellen verwendet habe. Stellen, die sinngemäß oder wörtlich aus anderen Quellen übernommen wurden, sind als solche kenntlich gemacht und im Literaturverzeichnis angegeben.

Kaiserslautern, den _____

(Sophie Theres Steiger)

Danksagung

Ich danke besonders Prof. Dr. Dr. Gereon Niedner-Schatteburg für das Weiterbetreuen meiner Promotion und die Freiheit, an meinem begonnenen Thema uneingeschränkt weiterarbeiten zu können. Danke auch für die zuverlässige Betreuung und Unterstützung nicht nur bei meiner Arbeit, sondern für den ganzen ehemaligen Arbeitskreis Gerhards.

Prof. Dr. Maria Wächtler danke ich für die Übernahme des Zweitgutachtens und die Möglichkeit des Weiterarbeitens an den Apparaturen des ehemaligen Arbeitskreises Gerhards.

Jun.-Prof. Dr. Sabine Becker danke ich für die Übernahme des Vorsitzes der Prüfungskommission.

Mein Dank gilt auch meinem leider verstorbenen Betreuer Prof. Dr. Markus Gerhards für die Aufnahme in seinen Arbeitskreis, die Ausgabe des Themas und die Betreuung des ersten Jahres meiner Promotion.

Ganz besonders bedanken möchte ich mich bei meinem Kollegen Pit Boden für die großartige Zusammenarbeit, die Erklärungen, Unterstützung und Hilfe, wann immer es nötig war, die Motivation, die Geduld und alle Gespräche, ob wissenschaftlich oder nicht. Ohne ihn hätte ich diese Arbeit nach Markus Tod wohl nicht weitergeführt.

Des Weiteren bedanke ich mich bei allen anderen Kollegen des ehemaligen Arbeitskreis Gerhards, insbesondere bei Daniel Marhöfer für die tolle Zusammenarbeit im Labor und die Bereitschaft, jede noch so verrückte Idee in die Tat umzusetzen, bei Pol Boden für seine stete Hilfsbereitschaft und fürs Einspringen, wenn ich mal nicht (rechtzeitig) da sein konnte, und bei Patrick Strebert für seine Unterstützung vor allem im IT-Bereich. Danke an Pit, Pol, Daniel und Patrick für den Zusammenhalt und die schöne gemeinsame Zeit an der Uni und bei diversen Freizeitaktionen.

Ich danke Kirsten Schwing für die gesamte Organisation, was unseren Arbeitskreis betrifft.

Bei meinem ehemaligen Kollegen Patrick Di Martino-Fumo bedanke ich mich auch für die gute Zusammenarbeit und die Hilfestellung bei quantenchemischen Rechnungen.

Bärbel Stemler danke ich für ihre Hilfe bei allen bürokratischen und verwaltungstechnischen Belangen sowie die freundlichen, aufmunternden Gespräche.

Dem gesamten „PC-Flur“ möchte ich für die Gemeinschaft danken.

Mein Dank geht auch an die Arbeitsgruppen von Jun.-Prof. Dr. Sabine Becker, Prof. Dr. Stefan Bräse, Dr. Michael Karnahl, Prof. Dr. Willem Klopper, Prof. Dr. Peter Roesky, Prof. Dr. Biprajit Sarkar, Prof. Dr. Werner Thiel und Prof. Dr. Stefanie Tschierlei für die Bereitstellung der Proben und die erfolgreiche Zusammenarbeit.

Ich danke dem Team der Chemikalienausgabe, Ludvik Napast, Jürgen Rahm und Frank Schröder, insbesondere für das Verwalten der Gasflaschen und für die netten Gespräche.

Herrn Walther Weber, stellvertretend auch für alle anderen Techniker, Handwerker und Helfer von der RPTU in Kaiserslautern, möchte ich für die Hilfe und Hilfsbereitschaft bei technischen Problemen aller Art und zu jeder Tageszeit danken.

Dem evangelischen Studienwerk Villigst danke ich für die Vergabe des Promotionsstipendium einschließlich der schönen Förderungsangebote und den anderen Stipendiaten für den freundlichen und informativen Austausch.

Ich danke auch der Deutschen Forschungsgemeinschaft für die Finanzierung des Abschlusses meiner Promotion im Rahmen des Sonderforschungsbereich TRR88/3MET.

Besonders danke ich meiner Familie und meinem Freund Joachim für die Unterstützung und Geduld mit mir während meiner Promotion.

Kurzzusammenfassung

In dieser Arbeit wurden mittels Lumineszenzspektroskopie und Step-scan-FTIR-Spektroskopie die Leuchteigenschaften sowie die elektronisch angeregten Zustände von Organometallkomplexen im Temperaturbereich von 5 – 290 K untersucht, welche für die Eignung als organische Leuchtdioden (OLEDs) und Photokatalysatoren bzw. -sensibilisatoren relevant sind. Für ein besseres Verständnis der Reaktivität verschiedener Organometallkomplexe wurden die Reaktionen mittels zeitaufgelöster FTIR-Spektroskopie verfolgt. Der Vergleich mit quantenchemischen Rechnungen unterstützt die Charakterisierung der elektronisch angeregten Zustände, Reaktionsprodukte oder Intermediate. Die untersuchten Komplexe erreichen die gewünschten Eigenschaften ohne Seltenerdmetalle und enthalten stattdessen häufiger vorkommende Metalle wie Kupfer.

Daher wurde der Einfluss von Metall-, Halogenid- und Ligandvariationen auf die Leuchteigenschaften und die dafür verantwortlichen elektronisch angeregten Zustände zweikerniger und vierkerniger Kupfer- und Silberkomplexe, die sich potentiell für die Anwendung als OLEDs eignen, untersucht. Auch der elektronisch angeregte Zustand eines weiteren Kupferkomplexes mit interessanten Lumineszenzeigenschaften wurde charakterisiert. Ebenfalls wurden die photophysikalischen Eigenschaften eines Kupfer-Photosensibilisators sowie seine Fähigkeit zum Energieübertrag untersucht. Im Bereich der Reaktivitäten wurden die photochemische Reaktion und ihre ungewöhnliche, dunkle Rückreaktion von Carbonyl-haltigen Chrom-, Molybdän- und Wolframkomplexen verfolgt und der Reaktionsmechanismus aufgeklärt. Auch die thermische Reaktion eines Kupferkomplexes, die sich je nach Lösungsmittel unterscheidet wurde untersucht und mögliche Produkte identifiziert.

Die erlangten Erkenntnisse über den Einfluss verschiedener Ligandmodifikationen, Halogenid- oder Metallzentren auf die gewünschten Eigenschaften der Organometallkomplexe und das Verständnis für die Reaktivität tragen zu der Entwicklung verbesserter Systeme bei, welche ohne Seltenerdelemente gute Eigenschaften für die Verwendung als Leuchtdioden, Katalysatoren oder Photosensibilisatoren aufweisen.

Inhaltsverzeichnis

Kapitel 1:	Einleitung	1
1.1	Besonderheiten der Methoden	2
1.2	Photophysik von Organometallkomplexen	2
1.2.1	<i>Organometallkomplexe als Leuchtdioden</i>	2
1.2.2	<i>Organometallkomplexe als Photosensibilisatoren</i>	6
1.3	Reaktivität von Organometallkomplexen	7
1.3.1	<i>Kooperative Effekte bei thermischer Reaktivität von Kupferkomplexen</i>	7
1.3.2	<i>Photo-induzierte Reaktivität an Carbonyl-Komplexen</i>	7
Kapitel 2:	Spektroskopische Methoden	9
2.1	Infrarot- und Lumineszenzspektroskopie in Forschung und Anwendung	9
2.2	IR-Spektroskopie	11
2.2.1	<i>Fourier-Transformations-IR-Spektroskopie</i>	11
2.3	Zeitaufgelöste FTIR-Spektroskopie	17
2.3.1	<i>Rapid-scan-FTIR-Spektroskopie</i>	17
2.3.2	<i>Step-scan-FTIR-Spektroskopie</i>	18
2.4	UV/Vis-Spektroskopie	22
2.4.1	<i>Elektronische Übergänge</i>	22
2.4.2	<i>Absorptions-/Extinktions-UV/Vis-Spektroskopie</i>	23
2.4.3	<i>Lumineszenzspektroskopie</i>	24
2.4.4	<i>Lumineszenzquantenausbeute</i>	26
2.5	Zeitaufgelöste Lumineszenzspektroskopie	28
2.5.1	<i>Lumineszenzlebensdauern</i>	28
2.5.2	<i>Time-Correlated Single-Photon Counting</i>	28
2.5.3	<i>Time-resolved emission spectroscopy</i>	30
2.6	Quantenchemische Rechnungen	31
2.6.1	<i>Dichtefunktionaltheorie</i>	31
Kapitel 3:	Experimenteller Aufbau und Durchführung	33

3.1	FTIR-Spektroskopie	33
3.1.1	<i>FTIR-Spektrometer Vertex 80v</i>	33
3.2	Laseraufbau	35
3.2.1	<i>Zeitliche Abstimmung zwischen FTIR-Spektrometer und Laser</i>	35
3.2.2	<i>Durchführung zeitaufgelöster FTIR-Messungen</i>	36
3.2.3	<i>Auswertung zeitaufgelöster FTIR-Spektren</i>	37
3.3	UV/Vis-Absorptionsspektroskopie.....	40
3.3.1	<i>UV/Vis/NIR-Spektrometer Lambda 900</i>	40
3.3.2	<i>Durchführung und Auswertung der UV/Vis-Absorptionsspektren</i>	41
3.3.3	<i>Refektionseinheit PrayingMantis</i>	42
3.4	Emissionsspektroskopie	43
3.4.1	<i>Emissionsspektrometer Fluorolog3-22τ</i>	43
3.4.2	<i>Upconversion-Experimente und Singulett-Sauerstoff-Quantenausbeuten</i>	44
3.4.3	<i>Emissionsspektrometer Fluoromax-2</i>	45
3.4.4	<i>Emissionslebensdauerspektrometer DeltaFlex</i>	45
3.5	Probenformen.....	48
3.5.1	<i>Lösungen</i>	48
3.5.2	<i>Feststoffproben</i>	49
3.6	Tieftemperaturmessungen.....	50
3.6.1	<i>„Closed-cycle“-Helium-Kryostat (ARS)</i>	50
3.6.2	<i>„Closed-cycle“-Helium-Kryostat ColdEdge</i>	51
3.6.3	<i>Kombination von Kryostaten und Spektrometern</i>	51
3.7	Quantenchemische Modellierung.....	53
Kapitel 4:	Photophysikalische Eigenschaften von Übergangsmetallkomplexen	55
4.1	Temperature-Dependent Luminescence Studies on Dinuclear Cu(I) 2-(Diphenylphosphino)Pyridine-Based Complexes Show Thermally Activated Delayed Fluorescence but Studies on Analogous Ag(I) Complexes Do Not.....	55
4.1.1	<i>Präambel</i>	55
4.1.2	<i>Entwurf des Manuskripts und ergänzende Informationen</i>	55

4.2	Untersuchung des Einflusses der Halogenide und Ligandenvariationen auf die lumineszenten Zustände vierkerniger Cu ^I -Komplexe	107
4.2.1	<i>Einleitung</i>	107
4.2.2	<i>Aufbau und Synthese</i>	108
4.2.3	<i>Ergebnisse</i>	109
4.2.4	<i>Fazit</i>	144
4.3	Thermally Activated Delayed Fluorescence and Phosphorescence Quenching in Iminophosphonamide Copper and Zinc Complexes.....	146
4.3.1	<i>Präambel</i>	146
4.3.2	<i>Nachdruck und ergänzende Informationen</i>	146
4.4	An Unexpected Boost in Activity of a Cu(I) Photosensitizer by Stabilizing a Transient Excited State.....	212
4.4.1	<i>Präambel</i>	212
4.4.2	<i>Nachdruck und ergänzende Informationen</i>	212
Kapitel 5:	Thermisch induzierte und photoinduzierte Reaktionen von Übergangsmetallkomplexen	277
5.1	Cooperativity-Driven Reactivity of a Dinuclear Copper Dimethylglyoxime Complex 277	
5.1.1	<i>Präambel</i>	277
5.1.2	<i>Nachdruck und ergänzende Informationen</i>	278
5.2	Mechanistic and Kinetic Investigations of ON/OFF (Photo)Switchable Binding of Carbon Monoxide by Chromium(0), Molybdenum(0) and Tungsten(0) Carbonyl Complexes with a Pyridyl-Mesoionic Carbene Ligand	356
5.2.1	<i>Präambel</i>	356
5.2.2	<i>Nachdruck und ergänzende Informationen</i>	356
Kapitel 6:	Zusammenfassung und Ausblick	447
6.1	Photophysik lumineszenter Kupferkomplexe.....	447
6.2	Photophysik und Energieübertragung von Kupfer-Photosensibilisatoren	450
6.3	Thermische Reaktionen eines Kupferkomplexes	450
6.4	Photochemische Reaktivität von Cr(0)-, Mo(0)-, W(0)-Carbonyl -Komplexen.....	451

Kapitel 7: Summary and Outlook	453
7.1 Photophysics of luminescent copper complexes	453
7.2 Photophysics and energy transfer of copper photosensitizers.....	455
7.3 Thermal-induced reactions of a copper complex	456
7.4 Photochemical reactivity of Cr(0)-, Mo(0)-, W(0)-carbonyl complexes.....	457
Kapitel 8: Literaturverzeichnis	459
Kapitel 9: Anhang	469
9.1 Beteiligung an weiteren Veröffentlichungen.....	469
9.1.1 <i>Investigation of Luminescent Triplet States in Tetranuclear Cu(I) Complexes: Thermochromism and Structural Characterization</i>	469
9.1.2 <i>NIR-Emissive Chromium(0), Molybdenum(0), and Tungsten(0) Complexes in the Solid State at Room Temperature</i>	469
9.2 Weitere Projekte in Zusammenarbeit mit Dissertationen aus der anorganischen Chemie an der TU Kaiserslautern	470
9.2.1 <i>Lumineszenz- und FTIR-Untersuchungen an einem dinuklearen Iridium(III)-Komplex und den beiden entsprechenden mononuklearen Komplexen</i>	470
9.2.2 <i>Untersuchung der Lumineszenzeigenschaften eines Platin-Komplexes</i>	484

Kapitel 1: Einleitung

Sparsam mit Energie umgehen ist heutzutage ein wichtiger Aspekt, insbesondere im Hinblick auf Klima- und Umweltschutz.^[1-11] So werden in der Industrie viele Synthesen mit Katalysatoren betrieben, um mildere Prozessbedingungen und höhere Selektivitäten zu erlangen.^[5,12-14] Insbesondere Photokatalysatoren oder Photosensibilisatoren sind auch von Interesse, um die Sonne als kostengünstige Energiequelle nutzen zu können.^[1,15-19] Im Alltag sind energiesparende Lampen und Displays ein Beispiel. Hierbei sind organische Leuchtdioden (engl. Organic Light Emitting Diodes (OLEDs)) zu nennen, die die aktuellen Leuchtdioden (engl. Light Emitting Diodes (LEDs)) und Flüssigkristalldisplays (engl. Liquid Crystal Displays (LCDs)) ablösen.^[4,7,20-25]

Für diese Anwendungszwecke haben sich in den letzten Jahren viele Organometallkomplexe hervor getan. Sie basieren auf einem Metallzentrum, welches von organischen Liganden umgeben ist. Dabei lassen sich verschiedene Eigenschaften über die Wahl von Metall und Ligandenstruktur steuern.^[26-31] Häufig werden dazu Komplexe mit seltenen und teuren Metallen wie Gold, Platin, Iridium oder Ruthenium verwendet.^[12,13,18,28,29,32-38] Ziel der aktuellen Forschung ist es unter anderem, Komplexe zu finden, die ähnlich präferierte Eigenschaften zeigen, wie die bereits bekannten, die jedoch nur auf der Erde häufigere und zugänglichere Metalle wie Kupfer enthalten. Von dieser Art von Komplexen ist bereits eine Vielzahl bekannt^[4,17,21,25,39-41], deren Eigenschaften immer weiter verbessert werden. Dazu ist jedoch ein Verständnis für das Zusammenspiel der Metalle und Liganden und ihre Auswirkungen auf die Funktionalität erforderlich.^[17,39,41-43]

Viele Projekte dieser Arbeit sind im Rahmen des SFB/TRR 88 (3MET) entstanden (Kapitel 4.1, 4.2, 4.3 und 5.1). Bei diesen Projekten wurde ein besonderer Blick auf die Kooperativität mehrerer Metallzentren und deren Einfluss auf die Eigenschaften der Komplexe gelegt. Die Kooperativität bezieht sich hierbei darauf, dass die Lumineszenzeigenschaften oder die Reaktivität nicht mit den entsprechenden monometallischen Komplexen, sondern nur mit den sogenannten „3MET-Komplexen“ erzielt werden können.^[26,44,45] Durch Kooperativität können damit gewünschte Eigenschaften gezielt erzeugt werden, wozu ein Verständnis der „3MET-Komplexe“ erlangt werden muss.^[44,46-49]

Auch das Schwerpunktsprogramm SPP 2102 hat als Ziel das weitergehende Verständnis von Photophysik und Photochemie an Übergangsmetallkomplexen für potentielle Anwendungen als Photokatalysatoren, Photosensibilisatoren oder Leuchtdioden.^[50] Die Kooperationen im Rahmen des SPP 2102 führten zu einer intensiven Betrachtung der elektronisch angeregten

Zustände eines Photosensibilisators (Kapitel 4.4) und der Verfolgung und Aufklärung einer reversiblen photochemischen Reaktion (Kapitel 5.2), welche auch Teil dieser Arbeit sind.

1.1 Besonderheiten der Methoden

Diese Arbeit beschäftigt sich mit den multispektroskopischen Untersuchungen von Organometallkomplexen, die als Leuchtdioden oder Katalysatoren Anwendung finden sollen, sowie deren Reaktionen. Zur Charakterisierung lumineszenter Zustände oder Verfolgung von Reaktionen ist der multispektroskopische Ansatz aus zeitaufgelöster FTIR- und Lumineszenzspektroskopie eine ideale Methode.^[46,51-54] Über Step-scan-FTIR-Spektroskopie lassen sich sowohl lumineszente als auch dunkle angeregte Zustände charakterisieren, während sich mit der zeitaufgelösten Lumineszenzspektroskopie nur strahlende Prozesse untersuchen lassen. Damit ergänzen sich beide Methoden perfekt und lassen eine gegenseitige Kontrolle für die Zuordnung der angeregten Zustände zu. Auch das temperaturabhängige Verhalten kann so sowohl für strahlende als auch nicht-strahlende Zustände untersucht werden. Quantenchemische Rechnungen ergänzen und unterstützen die Charakterisierung.^[49,53,55] Die Zeitauflösung der Methoden im Nano- bis Millisekunden-Bereich ist optimal für die Untersuchung der niedrigsten elektronisch angeregten Zustände der Komplexe für die erwähnten Anwendungsfelder oder die Verfolgung von photochemischen Reaktionen.^[56-59]

1.2 Photophysik von Organometallkomplexen

Der erste Teil der Arbeit beschäftigt sich mit der Untersuchung der Photophysik von Organometallkomplexen. Die Untersuchung der photophysikalischen Eigenschaften ist für die Anwendung der Organometallkomplexe als Leuchtstoffe, Photosensibilisatoren oder -katalysatoren sowie für das grundlegende Verständnis der Komplexeigenschaften wichtig.

1.2.1 Organometallkomplexe als Leuchtdioden

Im Bereich der OLED-Forschung haben sich in den letzten Jahren Kupferkomplexe als geeignete Kandidaten erwiesen.^[20,22,25,42] Anforderungen an diese Komplexe sind eine gute Löslichkeit^[60-63], hohe Quantenausbeuten^[64-67] und Lebensdauern im unteren Mikrosekundenbereich^[64-66]. Alle diese Eigenschaften lassen sich über Metall-, Halogenid- oder Ligandenvariation beeinflussen.^[20,51,66,68,69] Dazu wurden zahlreiche zweikernige Komplexe mit einem Zentrum aus zwei Kupfer und zwei verbrückenden Halogeniden, die eine schmetterlingsartige Form bilden, und einem verbrückenden N-P-Liganden, sowie zwei weiteren endständigen Phosphin-Liganden charakterisiert.^[26,51,60,64-67,70] Die allgemeine Struktur dieser Komplexe ist in Abb. 1.1 gezeigt. Mit diesen Komplexen wurden hohe

Lumineszenzquantenausbeuten von bis zu 99 % mit einer Emission im sichtbaren Bereich erzielt.^[65,66] Die Emissionsfarbe lässt sich dabei über die Variation der Substituenten am verbrückenden N-P-Liganden steuern.^[51,66,71] Für die hohen Quantenausbeuten ist bei diesen Komplexen häufig die thermisch aktivierte verzögerte Fluoreszenz (engl. thermally activated delayed fluorescence (TADF)) verantwortlich.^[20,42,72] Bei diesem Mechanismus wird nach erfolgtem Intersystem Crossing in den T_1 -Zustand thermisch die Barriere zurück in den Singulett-Zustand (S_1) überwunden, was zu einer verzögerten Fluoreszenz mit Lebensdauern im niedrigen Mikrosekundenbereich führt. Dazu muss die Energielücke zwischen dem T_1 - und dem S_1 -Zustand ausreichend klein sein, um bei Raumtemperatur bereits überwunden werden zu können.^[20,42,72] Dies wurde bei den zweikernigen Kupferkomplexen erreicht. Somit landen praktisch alle angeregten Komplexe im S_1 -Zustand und es werden hohe Quantenausbeuten erzielt (Singlet-Harvesting)^[42,60,72]. Mehrere dieser Komplexe aus der Gruppe von Prof. Dr. Stefan Bräse am KIT wurden bereits in der Arbeitsgruppe von Prof. Dr. Markus Gerhards an der TU Kaiserslautern untersucht.^[47,51,63,73] Mit zeitaufgelöster FTIR-Spektroskopie und Lumineszenzspektroskopie wurden die langlebigen lumineszenten Zustände charakterisiert. Nun soll der Einfluss der Metalle und Halogenide auf die Emission und den TADF-Mechanismus untersucht werden. Dazu wird in dieser Arbeit ein Quartett aus vier Komplexen mit den schmetterlingsförmigen Zentren Cu_2Br_2 , Cu_2Cl_2 , Ag_2Br_2 und Ag_2Cl_2 und einem verbrückenden sowie zwei endständige 2-(Diphenylphosphino)pyridin-Liganden (Abb. 1.2), synthetisiert von Dr. Jasmin Busch aus der Gruppe von Prof. Dr. Stefan Bräse, betrachtet. Die angeregten Zustände wurden mit temperaturabhängiger Lumineszenz- und Step-scan-FTIR-Spektroskopie in Kombination mit quantenchemischen Rechnungen aus der Gruppe von Prof. Dr. Willem Klopper vom KIT eingehend charakterisiert (Kapitel 4.1).

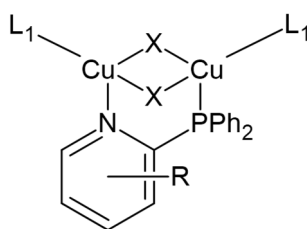


Abb. 1.1: Allgemeine Struktur der zweikernigen Kupferkomplexe der Form $Cu_2X_2L(L_1)_2$ mit den Halogeniden X sowie dem verbrückenden N-P-Liganden L und den beiden endständigen Phosphin-Liganden L_1 . Die endständigen Liganden L_1 können identisch oder unterschiedlich zu L sein.

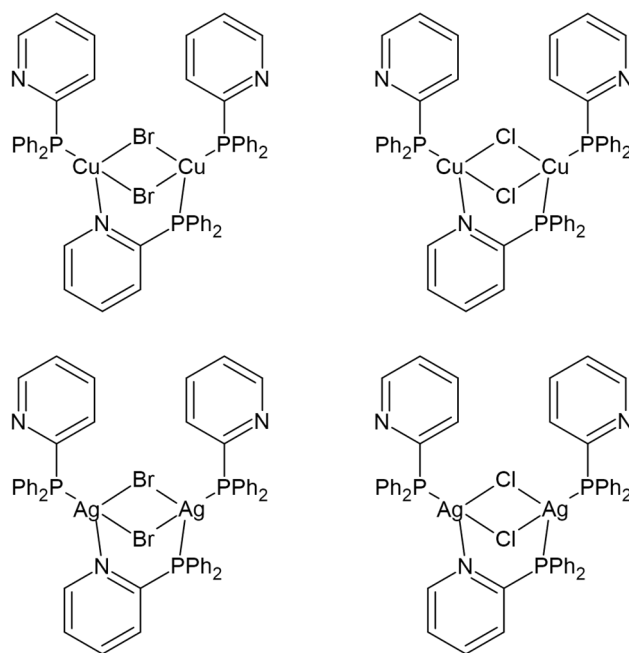


Abb. 1.2: Struktur der zweikernige Komplexe des Quartetts der Form $M_2X_2L_3$ mit den Metallzentren $M = Cu$ (oben) und $M = Ag$ (unten) und den Halogeniden $X = Bromid$ (links) und $X = Chlorid$ (rechts).

Auch zahlreiche vierkernige Kupferkomplexe zeigen für OLEDs geeignete Lumineszenzeigenschaften wie Absorptions- und Emissionbandenlage im sichtbaren Bereich, hohe Quantenausbeuten oder Mikrosekundenlebensdauern für die sichtbare Emission.^[23,53,74–78] Neben den zweikernigen Kupferkomplexen wurden auch vierkernige Komplexe in der Arbeitsgruppe von Prof. Dr. Stefan Bräse synthetisiert. Diese bestehen quasi aus zwei Einheiten der zweikernigen Komplexe ohne die endständigen Liganden.^[53] Für einige vierkernige Kupferkomplexe ist auch ein thermochromes Verhalten mit temperaturabhängiger relativer Besetzung von zwei phosphoreszenten Triplett-Zuständen bekannt.^[79–82] Interessanterweise zeigen auch die vierkernigen Kupferkomplexe aus der Arbeitsgruppe von Prof. Dr. Stefan Bräse mit einem in 6-Position am Pyridinring methylierten Liganden (Abb. 1.3) eine ausgeprägte Thermochromie für Komplexe mit sowohl Iodid als auch Bromid oder Chlorid als Halogenid im Zentrum.^[53] Dieses Lumineszenzverhalten konnte Phosphoreszenz aus verschiedenen Triplett-Zuständen, die sich in der Anordnung des vierkernigen Zentrums unterscheiden, zugeordnet werden. Der zum Vergleich herangezogene Komplex mit der Methylgruppe in 4-Position zeigte dagegen kein solches thermochromes Verhalten.^[53] Der Ligand hat somit einen starken Einfluss auf das Lumineszenzverhalten. Auch das Halogenid beeinflusst die Emission und das thermochrome Verhalten.^[53,75] Daher wurde in dieser Arbeit die Halogenidreihe der vierkernigen Kupferkomplexe mit der Methylgruppe in 4-Position und eine weitere Halogenidreihe mit dem Liganden ohne zusätzliche Methylgruppe (Abb. 1.3) auf Thermochromie oder den TADF-Mechanismus untersucht und der Einfluss der Matrix (KBr-Pressling, reines Pulver, Kristalle)

bestimmt. Die verschiedenen Geometrien und damit unterschiedlichen Triplett-Zustände wurden, wie auch für die in 6-Position methylierten Komplexe^[53], über quantenchemische Rechnungen berechnet und anhand der Step-scan-FTIR-Spektroskopie zugeordnet (Kapitel 4.2).

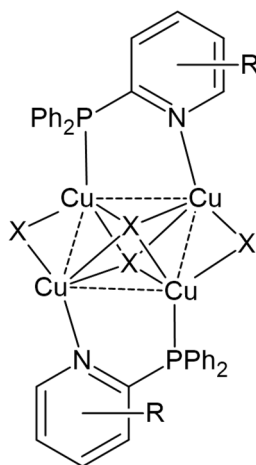


Abb. 1.3: Allgemeine Strukturen der untersuchten vierkernigen Kupferkomplexe mit den Halogeniden X = Iodid, Bromid oder Chlorid und dem verbrückenden Liganden L.

Der TADF-Mechanismus konnte ebenfalls für Alkalimetallkomplexe mit verbrückenden sterisch anspruchsvollen Iminophosphonamid-Liganden aus der Arbeitsgruppe von Prof. Dr. Peter Roesky vom KIT erreicht werden.^[83] Diese Liganden sollen auch in Übergangsmetallkomplexen zu interessanten lumineszenten Eigenschaften führen. Eine Reihe von Kupfer- und Zinkkomplexen wurde in der Arbeitsgruppe von Prof. Dr. Peter Roesky synthetisiert und die Lumineszenz temperaturabhängig von Dr. Sergei Lebedkin aus der Gruppe von Prof. Dr. Manfred Kappes am KIT untersucht. Um den langlebigen angeregten Zustand, welcher für das interessante Lumineszenzverhalten verantwortlich ist, zu charakterisieren, wurde der Kupferkomplex mit 2,6-Diisopropylphenyl-Gruppen (dipp) an dem Iminophosphonimidamin-Liganden (Abb. 1.4) temperaturabhängig mittels Step-scan-FTIR-Spektroskopie im angeregten Zustand untersucht (Kapitel 4.3).

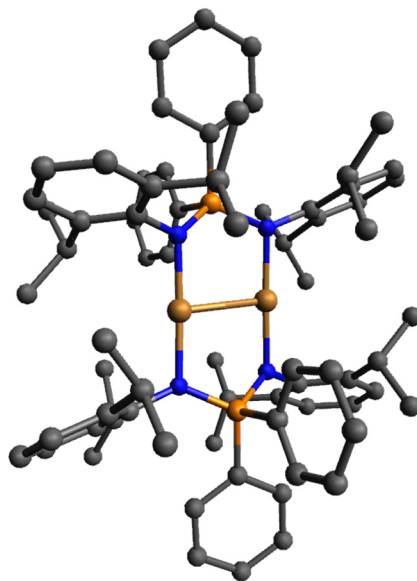


Abb. 1.4: Berechnete Struktur des zweikernigen Kupferkomplexes mit dipp-Iminophosphonimidamin-Liganden. Die Wasserstoffatome und Bindungsordnungen sind der Übersichtlichkeit halber nicht gezeigt.

1.2.2 Organometallkomplexe als Photosensibilisatoren

Neben Leuchtdioden sind Photosensibilisatoren ein wichtiges Anwendungsfeld für Organometallkomplexe.^[21,31,39,41,84] Dabei ist eine Anregung mit Licht aus dem Spektralbereich der Sonne interessant, um diese für katalytische Zwecke nutzen zu können.^[1,11,15,19,85] Langlebige photokatalytisch aktive Zustände sind für einen guten Energieübertrag auf den Photokatalysator wichtig.^[11,15,46,52] Dies kann über Triplett-Zustände erreicht werden, wenn die nicht-strahlenden Kanäle ausreichend gehindert sind. Dabei ist bei Kupferkomplexen insbesondere das „Flattening“^[11,16,46,52] im angeregten Zustand zu verhindern. Erfolgreich wurde von der Arbeitsgruppe von Prof. Dr. Stefanie Tschierlei und Dr. Michael Karnahl (TU Braunschweig) ein heteroleptischer Kupferkomplex mit einerseits dem Xantphos-Liganden und andererseits dem biipo-Liganden (biipo = 16*H*-Benzo-[4',5']-isochinolino-[2',1':1,2]-imidazo-[4,5-*f*]-[1,10]-phenanthrolin-16-on) als Photosensibilisator synthetisiert.^[52] (Abb. 1.5, links) Um das „Flattening“ noch effizienter zu verhindern, wurde der biipo-Ligand um zwei Methylgruppen erweitert (Abb. 1.5, links). Das Lumineszenzverhalten sowie die katalytischen Fähigkeiten dieses neuen Komplexes, sowie des Komplexes mit Bathocuproin-Liganden anstatt des biipo-Liganden (Abb. 1.5, rechts) als Referenz, wurden in Zusammenarbeit mit den Gruppen von Prof. Dr. Stefanie Tschierlei, Dr. Michael Karnahl sowie Prof. Dr. Stefan Lochbrunner von der Universität Rostock untersucht (Kapitel 4.4).

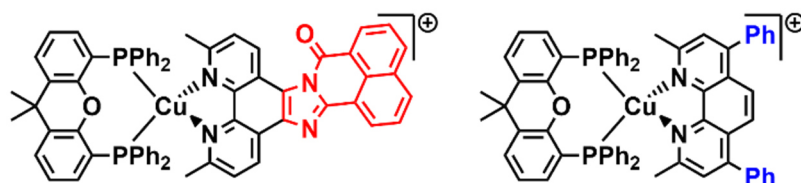


Abb. 1.5: Strukturen des Kupfer-Photosensibilisators mit dem methylierten biipo-Liganden (links) und des Kupfer-Referenzkomplexes mit Bathocuproin-Liganden (rechts).^[86]

1.3 Reaktivität von Organometallkomplexen

Der zweite Teil dieser Arbeit behandelt die Verfolgung von Reaktionen von zwei verschiedenen Organometallkomplexen. Die Reaktivität der Komplexe hängt maßgeblich mit der Wechselwirkung der Metalle mit den Liganden zusammen.^[87,88] So konnte eine reversible Abspaltung eines Kohlenmonoxid-Moleküls von einem Carbonyl-Komplex beobachtet werden und ein dinuklearer Kupferkomplex zeigt deutliche Reaktivität in verschiedenen Lösungsmitteln im Gegensatz zu seinem mononuklearen Pendant.

1.3.1 Kooperative Effekte bei thermischer Reaktivität von Kupferkomplexen

Oft sorgen in Organometallkomplexen kooperative Effekte zwischen mehreren Metallzentren für die gewünschte Reaktivität.^[89-92] Für die Charakterisierung der Kooperativität sind Komplexe nötig, von denen auch einkernige Analoge vorliegen.^[44,91,92] Die untersuchten Kupfer-Dimethylglyoxim-Komplexe wurden sowohl als mononuklearer als auch als dinuklearer Komplex (Abb. 1.6) von Raphael Petrikat aus der Arbeitsgruppe von Jun.-Prof. Dr. Sabine Becker synthetisiert und werden auf ihre Reaktivität hin untersucht. Die Reaktivität der Komplexe wurde mit FTIR-Spektroskopie, Massenspektrometrie, EPR-Spektroskopie und quantenchemischen Rechnungen in einer Kooperation mit den Gruppen von Jun.-Prof. Dr. Sabine Becker, Prof. Dr. Dr. Gereon Niedner-Schatteburg, Prof. Dr. Karin Fink und Dr. Mark Ringenberg untersucht (Kapitel 5.1).

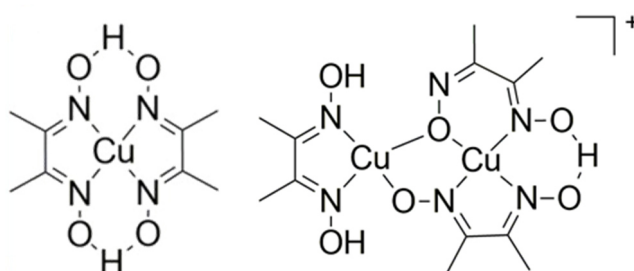


Abb. 1.6: Struktur des mononuklearen (links) und des dinuklearen (rechts) Kupfer-Dimethylglyoxim-Komplexes.^[93]

1.3.2 Photo-induzierte Reaktivität an Carbonyl-Komplexen

Photochemische Reaktionen werden mit Licht initiiert und können häufig selektiver gesteuert werden als thermische.^[84] Daher sind sie wichtig für gezielte Synthese oder

Katalyse. Die photochemische Abspaltung eines Carbonyl-Liganden ist für Carbonylkomplexe mit Metallen der 6. Gruppe in der Oxidationsstufe 0 bekannt^[94–99], jedoch ist diese Reaktion zumeist irreversibel.^[95–97,99] Die Chrom- Molybdän- und Wolfram-Carbonyl-Komplexe mit einem mesoionischen Carbenligand des Typs 1,2,3-Triazol-5-yliden aus der Arbeitsgruppe von Prof. Dr. Biprajit Sarkar von der Universität Stuttgart zeigen interessanterweise eine nahezu vollständige dunkle Rückreaktion in Lösung.^[54](Abb. 1.7) Ihre ungewöhnlichen photophysikalischen und elektrochemischen Eigenschaften wurden bereits untersucht.^[100] Mittels zeitaufgelöster FTIR-Spektroskopie sowohl in Lösung als auch in fester Phase sollen nun der Reaktionsmechanismus, Intermediate und Produkte der photochemischen Hin- und der dunklen Rückreaktion charakterisiert werden (Kapitel 5.2).

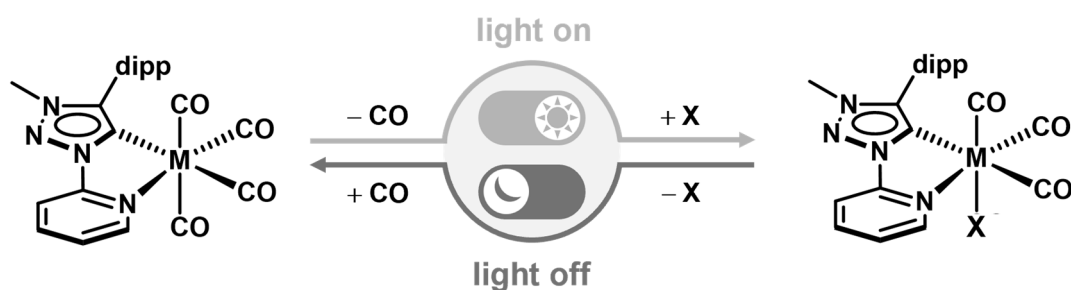


Abb. 1.7: Photochemische CO-Abspaltung und dunkle Rückreaktion der Carbonylkomplexe mit dem Metall M = Chrom, Molybdän oder Wolfram und dem Lösungsmittel X = Acetonitril, Pyridin oder Valeronitril.

Kapitel 2: Spektroskopische Methoden

2.1 Infrarot- und Lumineszenzspektroskopie in Forschung und Anwendung

Absorption und Emission elektromagnetischer Strahlung wird häufig in der chemischen Analytik eingesetzt, da die Spektroskopie schnell und sensitiv Ergebnisse liefern kann.^[101] Sie kann sowohl zur Charakterisierung als auch zur Qualitätskontrolle eingesetzt werden. Ein Vorteil dieser Analytik ist, dass die Probe in den meisten Fällen durch eine Messung nicht beschädigt wird und daher sogar an lebenden Zellen gearbeitet werden kann.^[101,102]

Die Fourier-Transformations-Infrarot-Spektroskopie (FTIR-Spektroskopie) wird in der Forschung häufig zur Strukturaufklärung verwendet, da die Schwingungen direkt mit der Struktur und damit auch der Funktionalität des Moleküls zusammenhängen. Auch in der Analytik nutzt man diese Eigenschaften beispielsweise zur Kontrolle in pharmazeutischen Synthesen^[103], zur Überprüfung in der Schmierstoffherstellung^[104] oder in der Qualitätskontrolle bei Konsumgütern^[105].

Die Charakterisierung kann anhand der spezifischen Schwingungen funktioneller Gruppen wie Carbonyl-Gruppen, Hydroxyl-Gruppen, Amino-Gruppen, aliphatische und aromatische C-H-Schwingungen, Nitrilen oder C-C-Mehrfachbindungen erfolgen.^[106] Diese Gruppen zeigen charakteristische Banden, wodurch ein Vorhandensein dieser Gruppen im untersuchten Molekül gezeigt werden kann. Auch eine Zuordnung über den Fingerprintbereich (etwa ab $\tilde{\nu} < 1500 \text{ cm}^{-1}$)^[106] ist möglich, da die Lage der Banden und das Intensitätsmuster im Fingerprintbereich einzigartig für eine bestimmte Struktur sind^[106], wie ein Fingerabdruck für jeden Menschen einzigartig ist. Hierzu ist ein Vergleich mit Literaturspektren oder quantenchemischen Rechnungen nötig.^[106,107] Literaturspektren finden sich in Datenbanken wie dem National Institute of Standards and Technology Chemistry WebBook^[108] oder der Spectral Database for Organic Compounds SDBS^[109]. Der Literaturvergleich hilft bei der Zuordnung von Substanzen zu einem Spektrum, gleichzeitig lässt sich auch eine quantitative Aussage über die Substanz in der Probe treffen, wenn in der Literatur auch der Extinktionskoeffizient bekannt ist^[110]. Die Dichtefunktionaltheorie liefert heutzutage bereits bei recht kurzen Rechenzeiten gute Vergleiche für die Frequenzen von organischen Molekülen und Übergangsmetallkomplexen.^[107,111,112]

Die Infrarot-Spektroskopie (IR-Spektroskopie) erlangte erst einen Durchbruch mit der Fourier-Transformations-IR-Spektroskopie, da damit Spektren viel schneller aufgenommen (mehrere Spektren pro Sekunde) werden können als mit dispersiven Methoden (3-5 Minuten pro Scan).^[113,114]

Zur Untersuchung dynamischer Prozesse in der Forschung werden zeitaufgelöste Methoden der FTIR-Spektroskopie angewandt. In dieser Arbeit liegt der Fokus hierbei auf der Rapid-scan- und der Step-scan-Methode (siehe Kapitel 2.3). Mit Zeitauflösungen von bis zu 10 ns für die Step-scan-Technik^[115,116] können Proteindynamiken^[117-119] oder photophysikalische Prozesse elektronisch angeregter Zustände von Übergangsmetallkomplexen^[56,57,115] untersucht werden.

Die Luminezenzspektroskopie ist eine starke Methode in der Analytik wie auch in der Forschung, da sie sehr sensitiv ist, wobei sogar einzelne Moleküle detektiert werden können.^[120,121]

In der Analytik wird sie vor allem in biologischen und pharmazeutischen Anwendungen (z.B. Bestimmung von Catecholaminen^[122], biochemische Bildgebung^[121]) sowie Anwendungen der Lebensmittelwissenschaften- und -technologien (z.B. Vitamin B₁₂-Bestimmung^[123]) eingesetzt. Durch die Anwendung von Chemosensoren können über die Lumineszenz auch Anionen^[124], Kationen sowie Übergangsmetallionen^[125] bestimmt werden. Mit ratiometrischen Bio- oder Chemosensoren lässt sich neben der qualitativen auch quantitative Analytik durchführen^[126,127]. Aber auch zur Überprüfung von Materialien beispielsweise in Photovoltaik-Modulen^[128] wird der Vorteil der sensitiven und zerstörungsfreien Spektroskopie genutzt.

In der Forschung wird die Lumineszenz standardmäßig zur Charakterisierung und Untersuchung elektronisch angeregter Zustände organischer^[129,130] oder anorganischer^[21,131] Luminophore verwendet.

Im Folgenden werden die theoretischen Grundlagen der verwendeten Spektroskopiearten erläutert. Der im Rahmen dieser Arbeit betrachtete Wellenlängenbereich ist in Abb. 2.1 dargestellt.

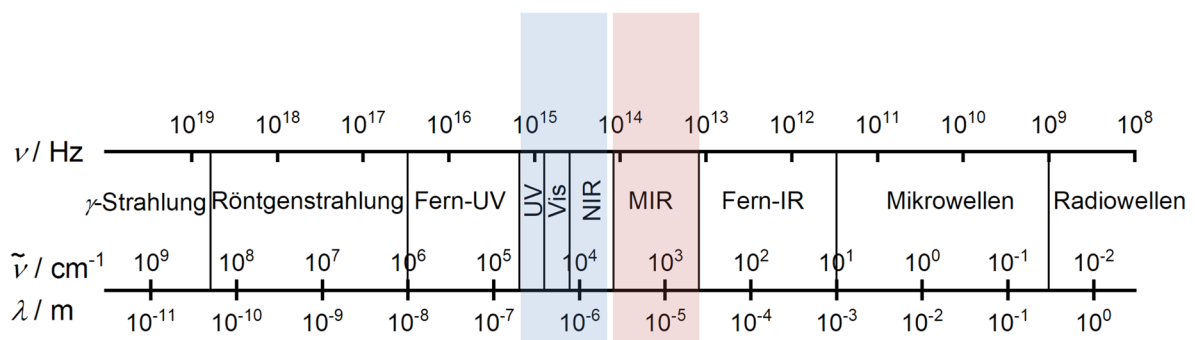


Abb. 2.1: Elektromagnetisches Spektrum mit Kennzeichnung der Bereiche der IR-Spektroskopie (rot) und Lumineszenzspektroskopie (blau), die in dieser Arbeit Anwendung finden.

2.2 IR-Spektroskopie

Mittels der IR-Spektroskopie können Moleküle anhand von Schwingungsanregungen charakterisiert werden. Dabei lassen sich sowohl die Schwingungen charakteristischer Gruppen im Molekül als auch der für jedes Molekül einzigartige „Fingerprintbereich“ zur Analyse heranziehen.^[106]

2.2.1 Fourier-Transformations-IR-Spektroskopie

Im Gegensatz zu dispersiven Methoden hat die FTIR-Spektroskopie den Vorteil, den gesamten zu messenden Spektralbereich auf einmal in einem Interferogramm aufzunehmen. Dieses Messverfahren führt neben dem schnelleren Messen auch zu besseren Signal-zu-Rauschen-Verhältnissen (Multiplex- und Jaquinot-Vorteil) als auch zu einer hohen Wellenzahlengenauigkeit (Connes-Vorteil).^[132]

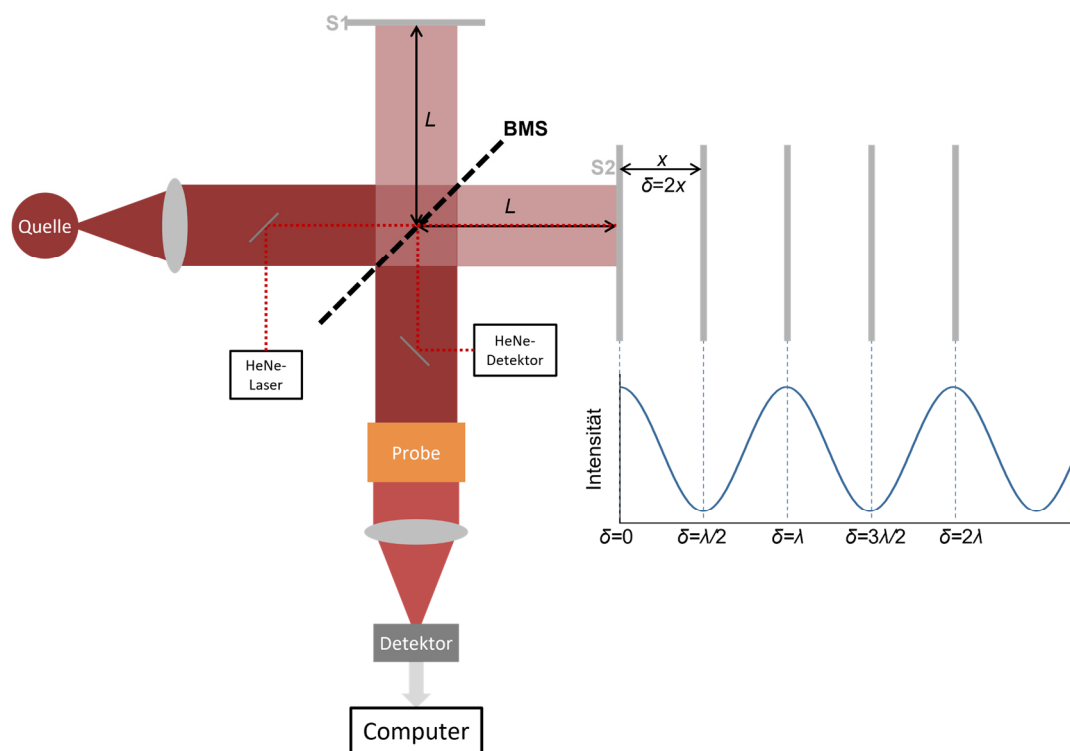


Abb. 2.2: Schematische Darstellung eines Michelson-Interferometers mit Strahlenteiler (BMS), festem Spiegel (S1) und beweglichem Spiegel (S2). Die Interferenz in Abhängigkeit der Spiegelposition ist beispielhaft an einer monochromatischen Welle gezeigt.

Das Herzstück eines FTIR-Spektrometers stellt, neben Infrarot-Strahlungsquelle und Detektor, das Interferometer dar (Abb. 2.2). Meist ist dies ein Michelson-Interferometer.^[133] Die von der Quelle ankommende IR-Strahlung wird auf den Strahlenteiler (BMS) des Interferometers geleitet. Dort wird 50 % der Strahlung reflektiert und die andere Hälfte durchgelassen. Beide Strahlen treffen anschließend jeweils auf einen Spiegel, von denen der Spiegel in Transmissionsstellung (S2) seinen Abstand zum Strahlenteiler variieren kann.

Dadurch verändert sich die vom Licht zurückgelegte Wegstrecke und somit die Phase, mit der es wieder am Strahlenteiler ankommt. Am Strahlenteiler interferieren die beiden Teilstrahlen wieder miteinander. Von dort wird der durch die Interferenz erhaltene Strahl durch die Probe und Richtung Detektor geleitet. Je nach Abstand des beweglichen Spiegels zum Strahlenteiler und je nach Wellenlänge kommt es zu destruktiver, teilweise destruktiver oder konstruktiver Interferenz. Dabei lässt sich die zurückgelegte Weglänge der Strahlen vom Strahlenteiler zum beweglichen Spiegel mit $L + x$ beschreiben, wobei L der Abstand vom Strahlenteiler zum festen Spiegel ist. x ist somit die zusätzliche Wegstrecke. Die optische Wegdifferenz δ zwischen dem zurückgelegten Weg des Lichts auf den festen Spiegel und des Lichts auf den beweglichen Spiegel ist daher $\delta = 2x$. Ist $\delta = 0$ kommt es für alle Wellenlängen zur konstruktiven Interferenz, somit kommt die maximale Intensität am Detektor an. Diese Position des Spiegels wird „centerburst“ genannt.^[133] Für jede einzelne Wellenlänge gilt, ist $\delta = n \cdot \lambda$, mit n als ganze Zahl, also ist δ jeweils ein Vielfaches der Wellenlänge, interferiert diese Welle am Strahlenteiler konstruktiv. Die komplette Auslöschung (destruktive Interferenz) wird bei einer Wegdifferenz von $\delta = \frac{n}{2} \cdot \lambda$ für alle ungeraden n erhalten. Die Intensität $I(\delta)$ des gesamten Wellenlängenbereichs am Detektor gegen die Spiegelpositionen (Gl.(1)) aufgetragen ergibt das Interferogramm. Für eine breitbandige Strahlenquelle stellt es die Summe über alle darin enthaltenen Frequenzen dar (Abb. 2.4).

$$I(\delta) = \int_0^{\infty} B(\nu) \cos(2\pi\delta\nu) d\nu \quad (1)$$

mit $B(\nu)$: Intensität der Frequenz ν

Über Nulldurchgänge des Helium-Neon-Lasers (HeNe-Laser) ($\lambda = 632,8 \text{ nm}$) wird die Spiegelauslenkung des beweglichen Spiegels alle halben Wellenlängen ($\Delta x = \frac{\lambda}{2} = 316,4 \text{ nm}$) des Lasers genau bestimmt. Nach Nyquists Theorem

$$\tilde{\nu}_f \leq \frac{1}{2\Delta x} \quad (2)$$

kann somit ein Bereich von $\tilde{\nu}_f = 15800 \text{ cm}^{-1}$ untersucht werden.^[132] Da meist nur ein kleinerer Messbereich von Nöten ist, kann die Datenmenge über eine Erniedrigung der Anzahl an berücksichtigten Spiegelpositionen, das sogenannte „Undersampling“, reduziert werden.^[132] Wird beispielsweise der Messbereich halbiert, wird nur jede zweite mögliche Spiegelposition angefahren und die Datenmenge sowie die Messzeit einer Step-scan-Messung^[134] halbieren sich. Dabei muss unbedingt verhindert werden, dass IR-Strahlung mit Frequenzen außerhalb des gewählten Messbereichs auf den Detektor trifft. In der Praxis wird dies mit entsprechenden Fenstern oder Bandfiltern gewährleistet.

Die Rayleigh Bedingung

$$\Delta\tilde{\nu} = \frac{1}{\delta_{\max}} = \frac{1}{N \cdot \Delta x} \quad (3)$$

zeigt, dass die spektrale Auflösung $\Delta\tilde{\nu}$ mit größerer maximaler Wegdifferenz δ_{\max} , welche sich aus der Anzahl der Messpunkte N und der Abtastfrequenz Δx berechnet, besser wird.^[106] Ein weiterer Vorteil des HeNe-Lasers ist die genaue Bestimmung der Wegdifferenz, wodurch die Wellenzahlgenauigkeit mit $0,01 \text{ cm}^{-1}$ sehr hoch ist (Connes-Vorteil).^[132]

2.2.1.1 Fourier-Transformation

Um nun von der Intensität im Interferogramm (Gl.(1)) auf ein Spektrum (Intensität bzw. Absorption gegen Wellenzahlen) zu kommen, wird die Fourier-Transformation angewandt. Die Fourier-Analyse zerlegt das Interferogramm in die einzelnen Frequenzen (Abb. 2.3) über folgenden mathematischen Ausdruck:

$$I(\tilde{\nu}) = \int_{-\infty}^{\infty} I(\delta) \cos(2\pi\tilde{\nu}\delta) d\delta \quad (4)$$

mit $I(\tilde{\nu})$: Intensität zur Wellenzahl $\tilde{\nu}$

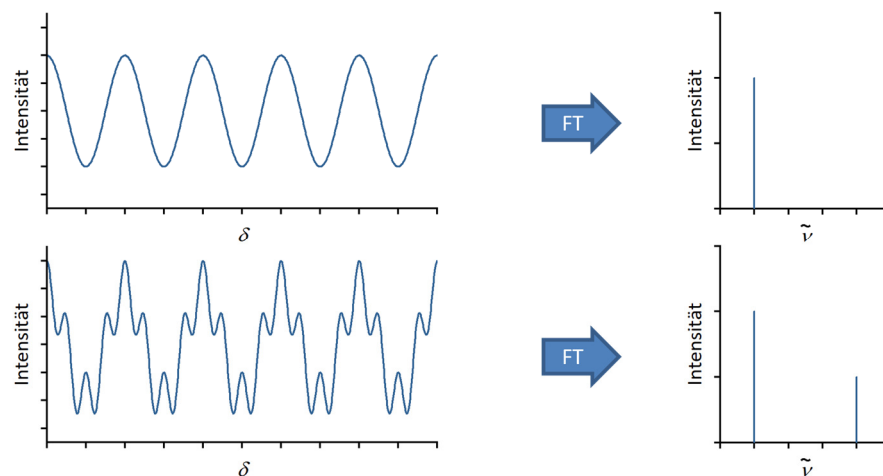


Abb. 2.3: Beispiel der Fourier-Transformation an einer monochromatischen (oben) und einer dichromatischen Welle (unten). Hierbei ist links das Interferogramm und rechts das durch die Fourier-Transformation bestimmte Spektrum zu sehen.

Da das Interferogramm in der Realität nicht exakt symmetrisch um den „centerburst“ ist, erhält man aus der Fourier-Transformation anstelle von Gl.(4) ein komplexes Spektrum $C(\tilde{\nu})$

$$C(\tilde{\nu}) = R(\tilde{\nu}) + iI(\tilde{\nu}) \quad (5)$$

mit $R(\tilde{\nu})$: Realteil des komplexen Spektrums

$I(\tilde{\nu})$: Imaginärteil des komplexen Spektrums

Mit der multiplikativen Phasenkorrektur bzw. Mertz-Methode lässt sich das reale Spektrum $S(\tilde{\nu})$ über die Phasenverschiebung $\phi(\tilde{\nu})$ bestimmen.^[132]

$$S(\tilde{\nu}) = \operatorname{Re}[C(\tilde{\nu}) \exp(-i\phi(\tilde{\nu}))] \quad (6)$$

mit

$$\phi(\tilde{\nu}) = \arctan\left(\frac{R(\tilde{\nu})}{I(\tilde{\nu})}\right) \quad (7)$$

2.2.1.2 Verrechnung der Spektren

Über die Fourier-Transformation erhält man ein Einkanalspektrum der Probe, welches die Intensität am Detektor gegen die Wellenzahl aufträgt. Um daraus ein Absorptionsspektrum zu berechnen, wird ein weiteres Spektrum, das sogenannte Hintergrundspektrum, benötigt. Das Hintergrundspektrum ist ein Spektrum der leeren Probenküvetten bzw. -halterungen und der Matrix um die Probe (KBr-Pressling, Lösungsmittel). Beide Spektren werden miteinander folgendermaßen verrechnet:^[106,135]

$$A = -\log\left(\frac{I}{I_0}\right) \quad (8)$$

mit I_0 : Intensität des Hintergrund-Einkanalspektrums
 I : Intensität des Proben-Einkanalspektrums

Das Prozedere ist in Abb. 2.4 veranschaulicht.

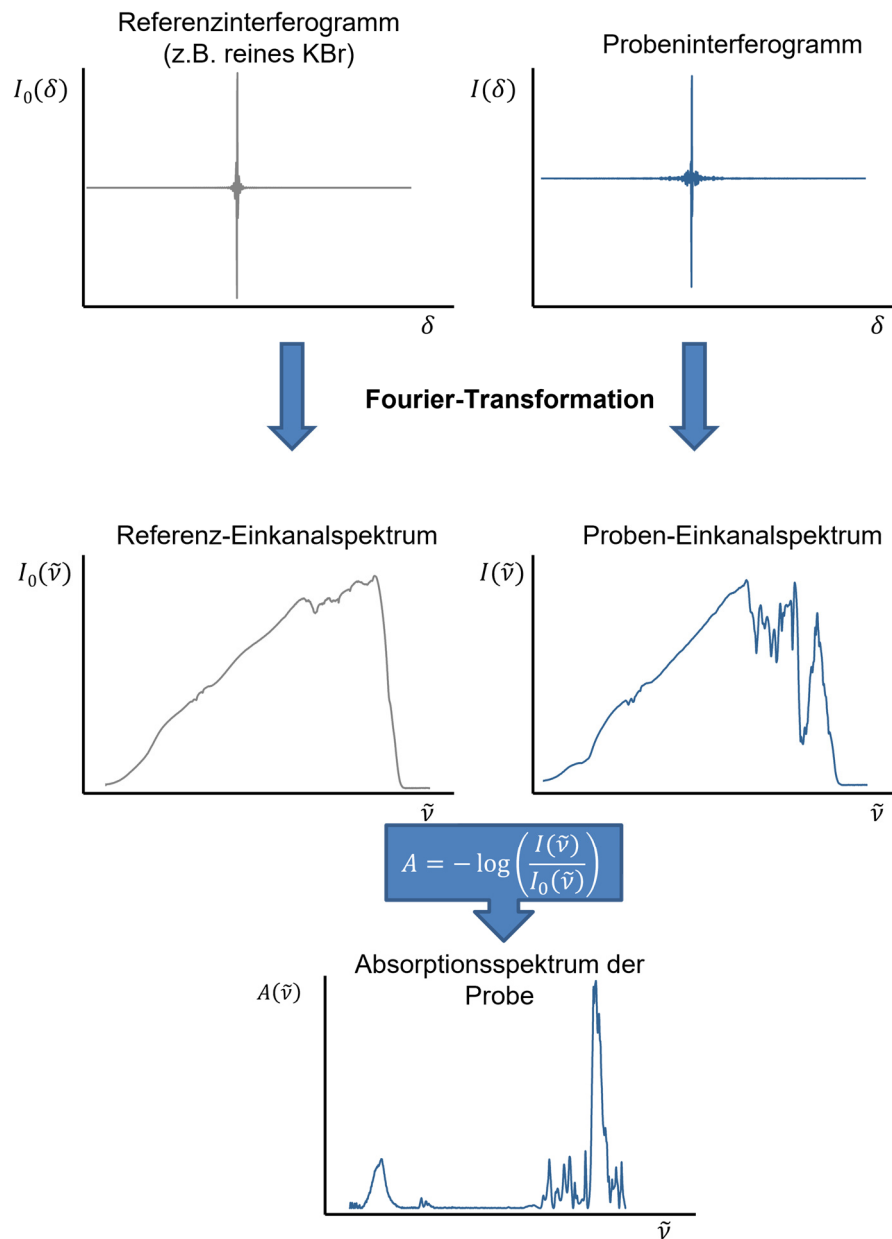


Abb. 2.4: Schaubild zur Berechnung von FTIR-Absorptionsspektren aus Hintergrund- und Probeninterferogrammen bzw. Einkanalspektren.

2.2.1.3 Digitalisierung

Zur Digitalisierung des Interferogramms wird eine Abtastfunktion verwendet, um die Datenverarbeitung zu beschleunigen. Diese Methode wird Fast Fourier-Transformation genannt, üblicherweise wird der Cooley-Tukey-Algorithmus verwendet. Für die Frequenz der Abtastfunktion gilt das Nyquist-Theorem (Gl.(2)).^[113,132]

Dennoch kann es vorkommen, dass im schlechtesten Fall eine Frequenz genau zwischen zwei Abtastpunkten liegt. Damit wäre ein Intensitätsverlust von bis zu 36 % möglich. Da dies dazu führt, dass das Spektrum wie durch einen Lattenzaun (engl. picket fence) betrachtet wirkt,

wird dieser Effekt Picket-Fence-Effekt genannt. Um den Picket-Fence-Effekt zu verringern, wird das Zero-filling angewandt. Dabei werden am Ende des Interferogramm Nullen angehängt, um die Anzahl an Interferogrammpunkten pro Wellenzahl zu erhöhen. Üblicherweise wird ein Zero-filling-Faktor von zwei verwendet; das bedeutet, dass durch das Anhängen von Nullen die Anzahl an Interferogrammpunkten verdoppelt wird.^[132]

2.2.1.4 Apodisation

Die Fourier-Transformation berechnet das Spektrum aus einem theoretisch unendlichen Interferogramm. Das gemessene Interferogramm ist aber endlich. Nun kann ein endliches Interferogramm aus einem unendlichen Interferogramm berechnet werden, indem für alle Wegdifferenzen außerhalb des endlichen Interferogramm mit 0 multipliziert wird und für die innerhalb des Messbereichs mit 1. Diese Funktion wird Boxcar genannt. Allerdings entstehen bei der Fourier-Transformation eines solchen Interferogramms Nebenmaxima um das eigentliche Maximum der sinc-Funktion. Um diese Nebenmaxima zu reduzieren, werden anstelle der Boxcar-Funktion Apodisationsfunktionen angewandt. Sie sorgen für einen weniger scharfen Übergang an den Enden des Interferogramms. Einige Beispiele für die Apodisation sind in Abb. 2.5 gezeigt. Am häufigsten findet die 3-Term-Black-Harris-Funktion^[136] Anwendung, wie auch in dieser Arbeit.^[132,137,138]

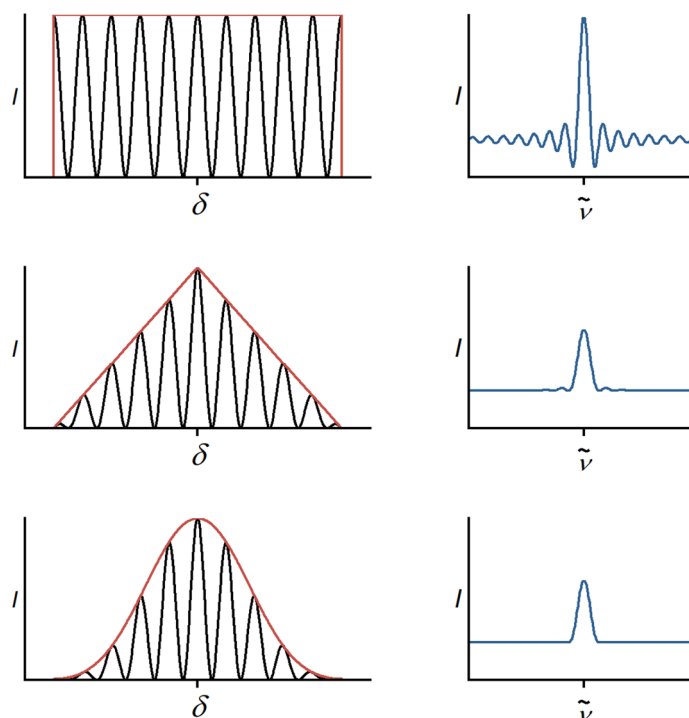


Abb. 2.5: Auswirkung der verschiedenen Apodisationen auf die Fourier-Transformierten Spektren einer monochromatischen Welle. oben: ohne Apodisation (Boxcar), Mitte: triangular, unten: 3-Term-Blackman-Harris.

2.3 Zeitaufgelöste FTIR-Spektroskopie

Da die Aufnahme eines einzelnen FTIR-Spektrums in unter einer Sekunde möglich ist,^[132] sind zeitaufgelöste Betrachtungen von Prozessen im Stunden- oder Minutenmaßstab einfach durch mehrere statische Messungen hintereinander in definierten Zeitabständen möglich. Werden jedoch Prozesse im Mikrosekundenbereich wie schnellere, chemische Reaktionen oder elektronische Anregungen eines Systems untersucht, werden weiterführende Methoden benötigt. Im Folgenden werden die weit verbreitete Rapid-scan- und die Step-scan-Methode genauer vorgestellt, die auch in dieser Arbeit Anwendung finden.

2.3.1 Rapid-scan-FTIR-Spektroskopie

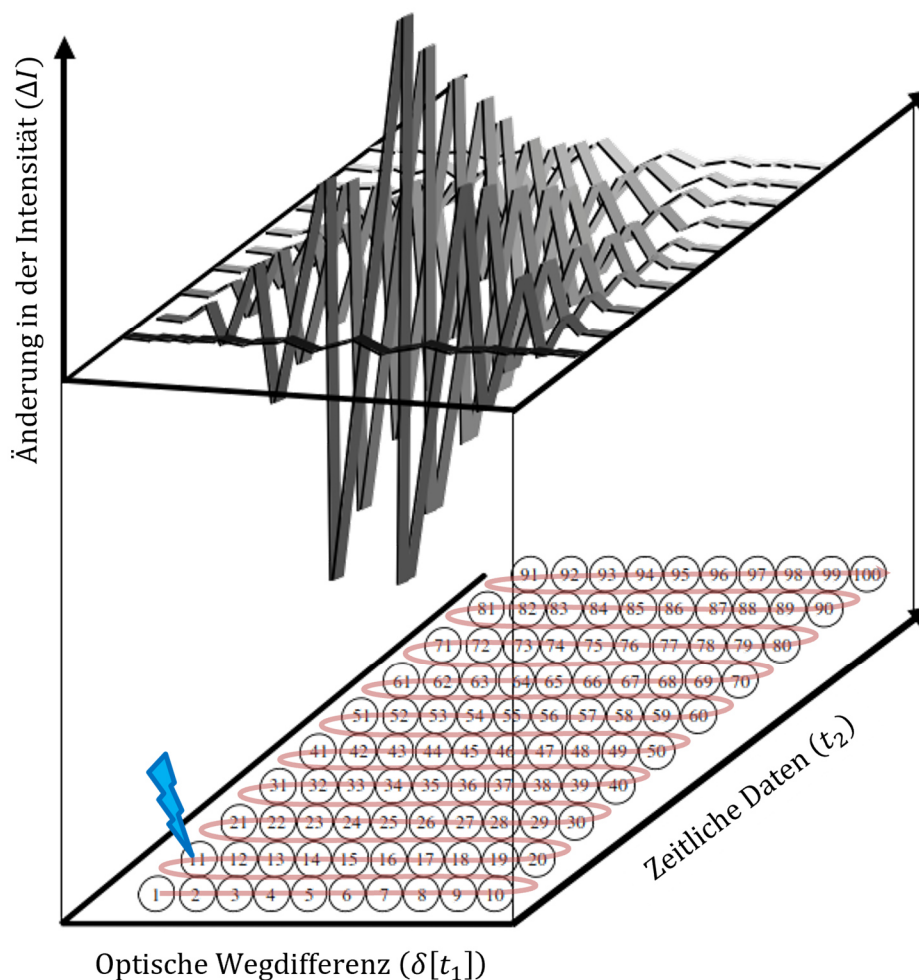


Abb. 2.6: Darstellung des zeitlichen Messablaufs bei der Rapid-scan-Methode (rote Linie). Die Intensitätsmatrix (unten) wird nach einmaliger Initiierung des zu untersuchenden Prozesses (blauer Blitz) sowohl zeilenweise (entlang der Spiegelpositionen δ aufgenommen als auch in zeitaufgelösten Interferogrammen ausgewertet (oben). Abbildung aus ^[139], überarbeitet.

Die Rapid-scan-Methode (Abb. 2.6) hat das gleiche Prinzip wie die statischen Mehrfachmessungen in definierten Zeitabständen. Bei dieser Methode wird der Spiegel sehr schnell mehrfach über alle Spiegelpositionen gefahren und es wird bei jedem Durchlauf ein

Spektrum generiert. Somit ist die maximale Zeitauflösung von der Scangeschwindigkeit abhängig. Generell gilt, dass die Scanzeit etwa eine Größenordnung kleiner sein muss als die Halbwertszeit des untersuchten Prozesses, um eine deutliche Veränderung der IR-Intensität während eines Scan-Durchgangs zu verhindern. Die Scangeschwindigkeit hängt von der Spiegelgeschwindigkeit und der Spiegelauslenkung und damit auch von der spektralen Auflösung ab. Bei einer spektralen Auflösung von 10 cm^{-1} erreichen die besten FTIR-Spektrometer eine Scangeschwindigkeit von ca. 100 Scans pro Sekunde. Mit dieser Scanzeit bzw. Zeitauflösung von 10 ms können also Prozesse mit einer Halbwertszeit von mindestens 100 ms untersucht werden. Da die Rapid-scan-Methode nach einmaliger Initiation den gesamten spektralen und zeitlichen Messbereich scannt, ist diese Methode auch für nicht-reversible Prozesse wie Reaktionen geeignet.^[134,139,140]

2.3.2 Step-scan-FTIR-Spektroskopie

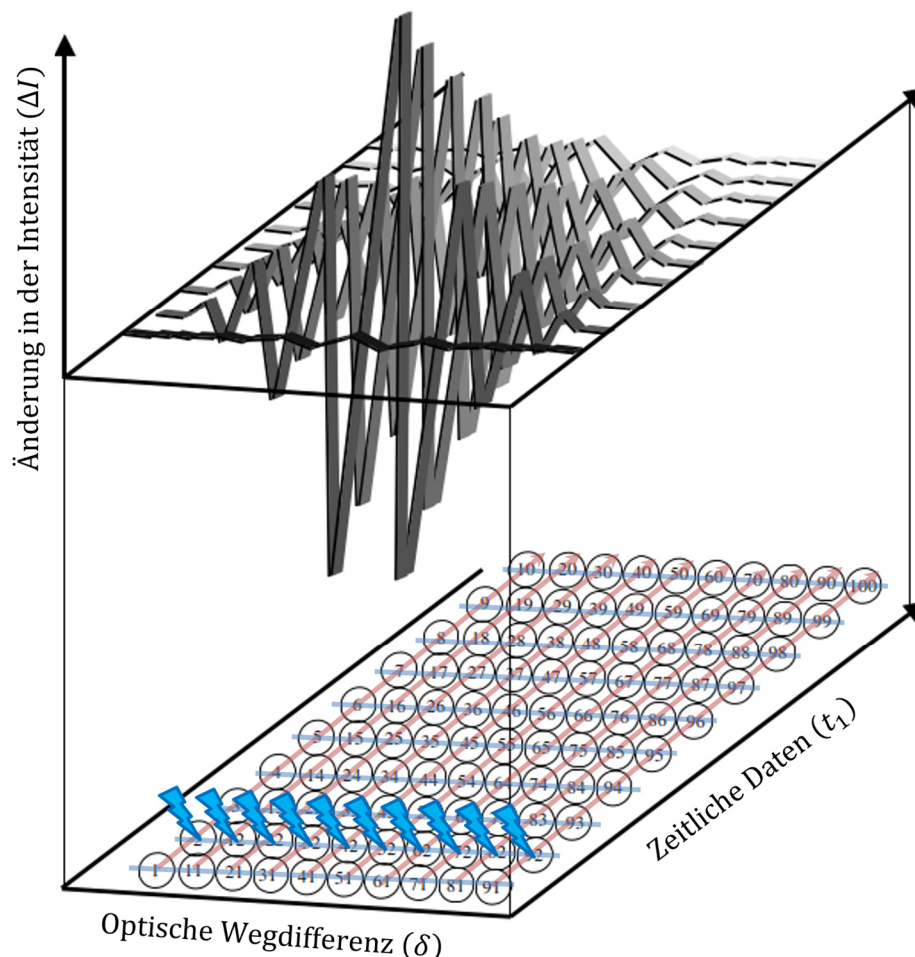


Abb. 2.7: Darstellung des zeitlichen Messablaufs bei der Step-scan-Methode (rote Linien). Die Intensitätsmatrix (unten) wird nach Initiation des zu untersuchenden Prozesses (blaue Blitze) spaltenweise über die Zeit aufgenommen, wobei dieser Prozess für jede Spiegelposition wiederholt wird. Ausgewertet wird die Matrix zeilenweise (entlang der Spiegelpositionen, blaue Linien) und es werden zeitaufgelöste Interferogramme erhalten (oben). Abbildung aus ^[139], überarbeitet.

Für schneller Prozesse, die mit Zeitaufösungen bis in den Nanosekundenbereich untersucht werden sollen, steht die Step-scan-Methode (Abb. 2.7) zur Verfügung. Sie unterscheidet sich von dem statischen Messbetrieb und der Rapid-scan-Methode darin, dass der Spiegel (S2 in Abb. 2.2) hierbei nicht mehr kontinuierlich, sondern schrittweise bewegt wird. An jeder Spiegelposition wird der zu untersuchende Prozess initiiert und die Intensität im Verlauf über die Zeit aufgenommen. Anschließend wird die Messung bei der nächsten Spiegelposition wiederholt. Dies hat den Vorteil, dass die Zeitauflösung unabhängig von der Spiegelgeschwindigkeit gewählt werden kann. Damit ist auch die spektrale Auflösung unabhängig von der zeitlichen. Allerdings können daher nur Prozesse untersucht werden, die innerhalb der Messdauer vollständig reversibel sind, wie im Falle dieser Arbeit beispielsweise elektronisch angeregte Zustände, oder für die sich die Probe zwischen zwei Initiationen komplett austauschen lässt (z.B. Reaktionen in Lösung im Durchflussbetrieb).^[134,139,141]

Für die schrittweise Messung aller Interferogrammpunkte (je nach gewünschter Auflösung und Spektralbereich, Abschnitt 2.2.1) wird der bewegliche Spiegel mit dem HeNe-Laser auf eine Position eingestellt. Nach einer Stabilisierungszeit wird der Prozess und die Messung der Intensität im zeitlichen Verlauf an dieser Position gestartet. Der abgedeckte Zeitbereich ergibt sich dabei aus der Anzahl an Zeitscheiben (Anzahl der Messpunkte) multipliziert mit der gewünschten Zeitauflösung. Die Zeitauflösung wird dabei nur noch von der Elektronik (Detektor und Datendigitalisierung) begrenzt. Beispielsweise decken bei einer Zeitauflösung von 50 ns 10000 Zeitscheiben einen Zeitraum von 500 μ s ab. Der gesamte Prozess wird an jeder Spiegelposition in sogenannten Koadditionen wiederholt, um das Signal-zu-Rauschen-Verhältnis, welches bei höherer Zeitauflösung zunehmend schlechter wird, zu verbessern.^[134] Das Signal-zu-Rauschen-Verhältnis bessert sich um \sqrt{N} mit N der Anzahl an Koadditionen. Anschließend wird die nächste Spiegelposition angefahren und das ganze Prozedere wiederholt. Durch die vielen Wiederholungen und damit vielen elektronischen Anregungen der Proben müssen die Proben, sofern sie nicht kontinuierlich ausgetauscht werden können, über längeren Zeitraum unter Bestrahlung stabil sein.^[134]

Mit der Step-scan-Methode entsteht die Intensitätsmatrix spaltenweise (Abb. 2.7).^[134] Analysiert werden die Daten jedoch zunächst nicht im zeitlichen Verlauf wie ihre Datenaufnahme, sondern entlang der Zeitscheiben (Reihen in der Intensitätsmatrix, Abb. 2.7) als zeitaufgelöste Interferogramme. Dazu wird zunächst ein statisches Signal der Probe ohne Anregung über den DC (direct current)-Ausgang des Spektrometers als Referenz erzeugt. Die zeitaufgelöste Messung erfolgt über den AC (alternative current)-Ausgang des Spektrometers und erfasst nur die Änderungen im Verlauf der Messung. Daher ist die Aufnahme über den

AC-Ausgang sensitiver und kann unabhängig von der statischen Messung stärker verstärkt werden. Zum Verarbeiten der Spektren werden zunächst die zeitaufgelösten Differenzinterferogramme der AC-Messung und das statische Interferogramm der DC-Messung der Fourier-Transformation unterworfen. Die Phasenkorrektur erhält man aus dem DC-Signal. Die erhaltenen Einkanalspektren können wie durch statische Messungen erhaltene Spektren in zeitaufgelöste Absorptionsspektren ΔA_t umgewandelt werden, jedoch muss die unterschiedliche Vorverstärkung von DC- und AC-Messung mit dem Faktor γ berücksichtigt werden. (Abb. 2.8)^[134,141,142]

$$\Delta A_t = -\log\left(\frac{I_t(AC) + \gamma \cdot I(DC)}{\gamma \cdot I(DC)}\right) \quad (9)$$

Die erhaltenen zeitaufgelösten Differenzspektren können zudem noch über mehrere Zeitscheiben gemittelt werden, um das Signal-zu-Rauschen-Verhältnis noch zu verbessern.

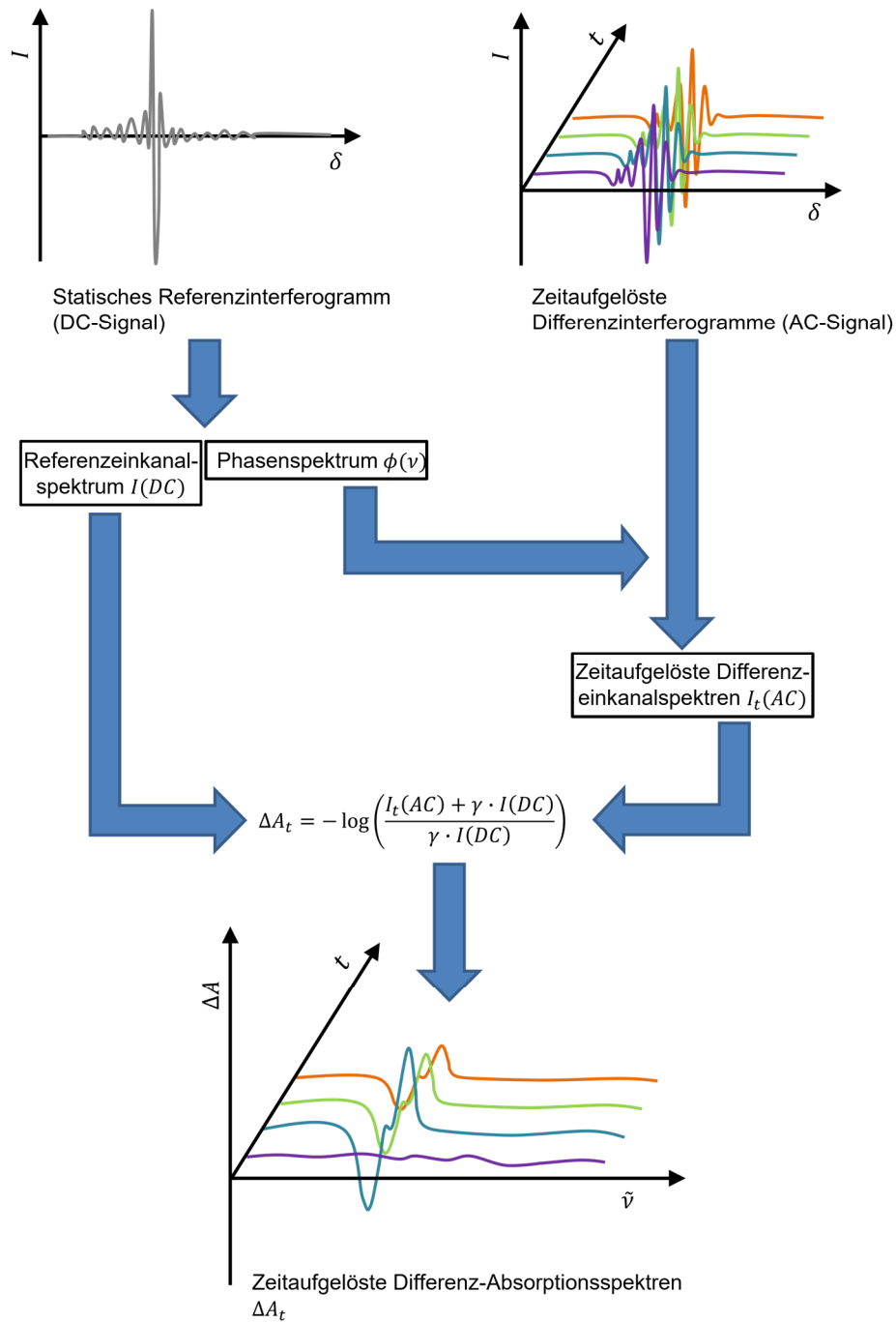


Abb. 2.8: Schaubild zur Berechnung der zeitaufgelösten Differenz-Absorptionsspektren aus einer Step-scan-Messung mit statischem DC- und zeitaufgelöstem AC-Signal. Im ersten Schritt wird die Fourier-Transformation der Interferogramme durchgeführt, anschließend erfolgt die Verrechnung zu den Differenz-Absorptionsspektren.

2.4 UV/Vis-Spektroskopie

2.4.1 Elektronische Übergänge

Im Energiebereich des UV- und sichtbaren Lichts (Abb. 2.1), liegen die elektronischen Übergänge in Molekülen. Es werden normalerweise nicht bloß reine elektronische Übergänge, sondern sogenannte vibronische Übergänge angeregt, da^[143]

$$E_{el} > E_{vib} > E_{rot} \quad (10)$$

mit E_{el} : Energie elektronischer Übergänge
 E_{vib} : Energie der Schwingungsübergänge
 E_{rot} : Energie der Rotationsübergänge

Der vibronische Übergang wird mit dem Übergangsmoment R_{ev}

$$R_{ev} = \int \psi'_{ev}{}^* \boldsymbol{\mu} \psi''_{ev} d\tau \quad (11)$$

mit ψ'_{ev} : Wellenfunktion des vibronischen Zielzustands
 ψ''_{ev} : Wellenfunktion des vibronischen Ausgangszustands
 $\boldsymbol{\mu}$: elektrisches Dipolmoment

beschrieben. Nach der Born-Oppenheimer-Näherung kann die Wellenfunktion als Produkt aus elektronischer Wellenfunktion und Kernwellenfunktion beschrieben werden. Daher lässt sich das vibronische Übergangsmoment aufteilen^[144]

$$R_{ev} = R_e \int \psi'_v{}^* \psi''_v dr \quad (12)$$

in das elektronische Übergangsmoment R_e

$$R_e = \int \psi'_e{}^* \boldsymbol{\mu} \psi''_e d\tau_e \quad (13)$$

und das vibronische Überlappungsintegral, dessen Quadrat auch Franck-Condon-Faktor (FC) genannt wird.

$$FC = \left| \int \psi'_v{}^* \psi''_v dr \right|^2 \quad (14)$$

Daraus ergibt sich anschaulich, dass der Übergang bei einer großen Überlappung der Schwingungsintegrale wahrscheinlicher ist. Da die einzelnen Schwingungswellenfunktionen zueinander orthogonal sind, wäre bei dem gleichen Satz Wellenfunktionen für Grund- und angeregten Zustand der Franck-Condon-Faktor 1 für einen Übergang ins gleiche Schwingungsniveau und 0 für alle anderen. In der Realität sind die Potentialkurven von

Grund- und angeregtem Zustand jedoch meist leicht verschoben zueinander und die Werte der Franck-Condon-Faktoren liegen zwischen 0 und 1 (Abb. 2.9). Die Summe der Franck-Condon-Faktoren bleibt jedoch immer 1.^[101]

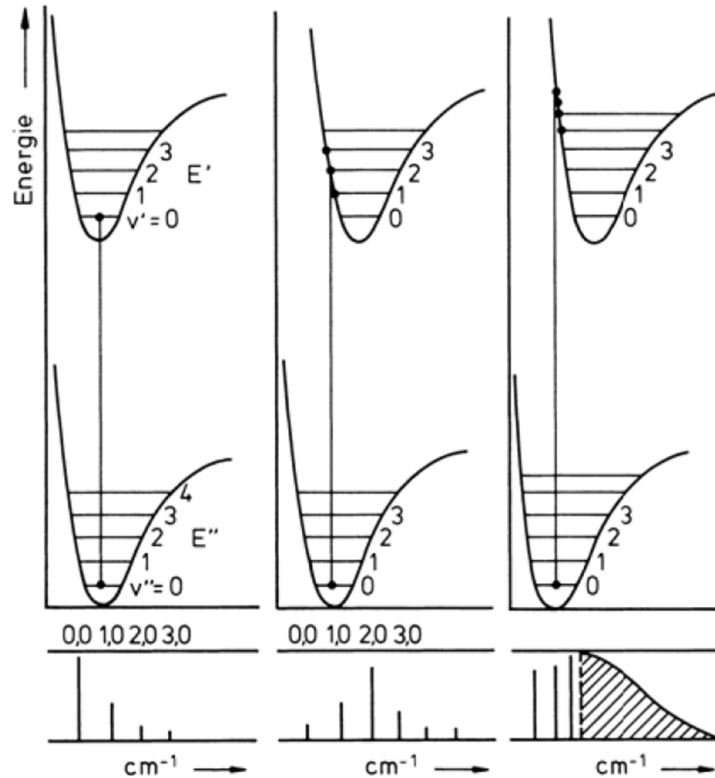


Abb. 2.9: Verschiebung der Potentialkurven von Grund- und angeregtem Zustand mit den vertikalen vibronischen Übergängen (oben) und die Verteilung der Übergänge (unten) ohne Verschiebung (links), mit geringer Verschiebung (Mitte) und großer Verschiebung (rechts) zur Veranschaulichung des Franck-Condon-Prinzips. In der Realität liegt meist der mittlere Fall vor. Abbildung aus ^[143].

2.4.2 Absorptions-/Extinktions-UV/Vis-Spektroskopie

Wechselwirkt nun Energie in Form von Licht der entsprechenden Wellenlänge zur elektronischen Anregung mit dem Molekül, wird diese Energie vom Molekül absorbiert. Dadurch gelangt das Molekül in einen elektronisch angeregten Zustand und die Intensität des Lichts wird geschwächt. Die Absorption A kann über das Lambert-Beer'sche-Gesetz beschrieben werden.^[145]

$$A = \log\left(\frac{I_0}{I}\right) = \varepsilon \cdot c \cdot d \quad (15)$$

mit I_0/I : Intensität vor/nach Probendurchgang
 ε : dekadischer Extinktionskoeffizient
 c : Konzentration
 d : Schichtdicke

2.4.3 Lumineszenzspektroskopie

Wird Energie in Form von Licht von einem Molekül aus einem elektronisch angeregten Zustand emittiert, spricht man von Lumineszenz. Man unterscheidet zwischen Fluoreszenz und Phosphoreszenz, je nach dem, aus welchem angeregten Zustand die Emission erfolgt.^[102,120]

2.4.3.1 Jablonski-Termschema

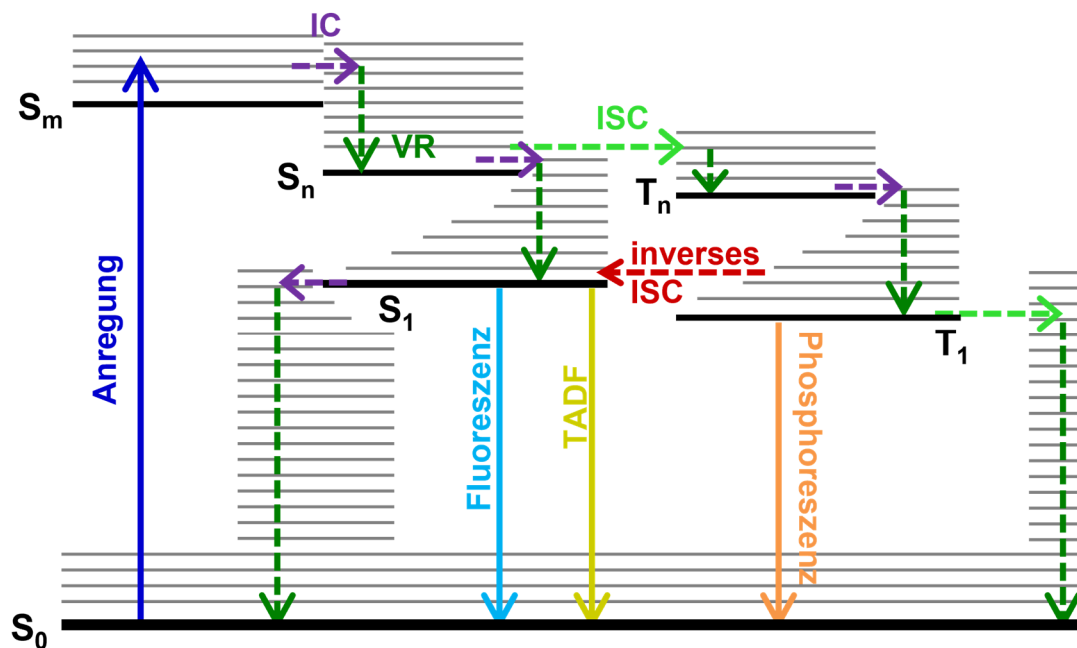


Abb. 2.10: Jablonski-Diagramm eines geschlossenschaligen Systems mit strahlenden (durchgezogene Linien) und nicht-strahlenden (gestrichelte Linien) Übergängen. Nach der Anregung (blau) kommt es zu Internal Conversion (IC, violett) und vibrational relaxation (VR, dunkelgrün). Der Übergang in den Triplettzustand erfolgt über Intersystem Crossing (ISC, hellgrün). Die strahlenden Prozesse aus dem S_1 - bzw. dem T_1 -Zustand sind Fluoreszenz (hellblau), thermisch aktivierte verzögerte Fluoreszenz (TADF, gelb) und Phosphoreszenz (orange).

Die Prozesse, die zwischen Anregung und Emission in einem Molekül ablaufen, können in einem Jablonski-Termschema (Abb. 2.10) dargestellt werden. In vertikalen Strichen werden die Übergänge zwischen verschiedenen Zuständen gezeigt. Die Übergänge selbst sind sehr schnell im Bereich von 10^{-15} s^[120] und damit wesentlich schneller als die Kernbewegungen. Daher gilt die Born-Oppenheimer-Näherung und das Franck-Condon-Prinzip.

In einem geschlossenschaligen System ist der niedrigste Singulett (S_0)-Zustand der Grundzustand. Nach der Anregung gelangt ein Molekül aus dem Grundzustand in ein Schwingungsniveau eines höheren Singulett-Zustands (siehe Kapitel 2.4.1). Durch schnelle nicht-strahlende Prozesse relaxiert das Molekül in den Schwingungsgrundzustand des ersten angeregten Singulett-Zustands. Der Prozess, um in den Schwingungsgrundzustand eines elektronischen Zustands zu gelangen, heißt Schwingungsrelaxation (engl. vibrational

relaxation (VR)). Dabei geht das Molekül durch Energieabgabe in Form von Stößen mit anderen Molekülen aus einem höheren Schwingungszustand in den Schwingungsgrundzustand über. Der Übergang von einem Schwingungsgrundzustand eines höheren elektronischen Zustands in ein hohes Schwingungsniveau eines niedrigeren elektronischen Zustands ist die isoenergetische „internal conversion“ (IC). Zusammen lassen sich diese Prozesse als innere Umwandlung zusammenfassen und spielen sich in einem Zeitrahmen von 10^{-12} s oder weniger ab. Damit sind sie wesentlich schneller als die Fluoreszenz (ca. 10 ns). Somit geht die Emission stets von Grundzustand des ersten elektronisch angeregten Zustands aus (Kasha-Regel^[146]).^[102,120,143]

Neben Fluoreszenz und „internal conversion“ in den S_0 -Zustand können Moleküle im S_1 -Zustand auch ein „Intersystem crossing“ (ISC) in ein schwingungsangeregtes Niveau eines Triplett-Zustands eingehen. Auch dieser Prozess ist isoenergetisch, allerdings spinverboten, weshalb er nur bei ausreichender Spin-Bahn-Kopplung abläuft. Dem ISC folgt dann wieder schnell die VR in den Schwingungsgrundzustand des T_1 -Zustands und das Molekül emittiert aus diesem in den S_0 -Zustand. Diese Emission ist die Phosphoreszenz und durch die spinverbotenen Übergänge wesentlich langsamer (10^{-5} - 10^2 s) als die Fluoreszenz. Durch schwere Atome wird die Spin-Bahn-Kopplung größer und das ISC und die Phosphoreszenz wahrscheinlicher und schneller (Schweratomeffekt). Außerdem ist die Phosphoreszenz gegenüber der Fluoreszenz rotverschoben, da der T_1 -Zustand niedriger liegt als der S_1 -Zustand. Die Emission aus dem S_1 - oder T_1 -Zustand erfolgt in ein Schwingungsniveau des elektronischen Grundzustands, gefolgt von einer schnellen Relaxierung in den Schwingungsgrundzustand durch VR.^[102,120,143]

Dadurch, dass die Absorption vom Schwingungsgrundzustand des S_0 -Zustands in ein Schwingungsniveau eines elektronisch angeregten Zustands übergeht und die Emission vom Schwingungsgrundzustand des S_1 - oder T_1 -Zustands in ein Schwingungsniveau des Grundzustands resultiert eine Spiegelbildlichkeit der Spektren. Die Emission ist dabei immer rotverschoben zur Absorption. Lediglich der 00-Übergang (Übergang aus dem Schwingungsgrundzustand in den Schwingungsgrundzustand) könnte identisch sein. Allerdings ist dieser aufgrund der Lösungsmittelrelaxation im angeregten Zustand auch meist rotverschoben. Diese Rotverschiebung der Emission nennt man Stokes-Shift (Abb. 2.11).^[101,120,147]

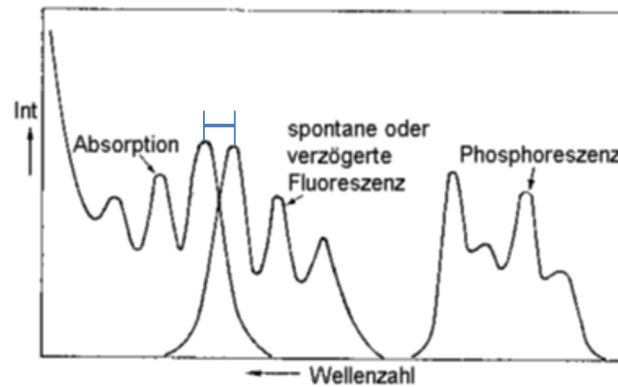


Abb. 2.11: Beispiel für die relative Rotverschiebung von Fluoreszenz und Phosphoreszenz gegenüber der Absorption. Der Stokes-Shift des 00-Übergangs der Fluoreszenz ist mit dem blauen Balken markiert. Abbildung aus ^[148], überarbeitet.

Außer der Fluoreszenz aus dem S_1 -Zustand und der Phosphoreszenz nach ISC ist auch noch der Sonderfall der thermisch aktivierten verzögerten Fluoreszenz (englisch thermally activated delayed fluorescence (TADF)) möglich. TADF wird auch e-Typ-Fluoreszenz genannt. Hierbei erfolgt die Emission aus dem S_1 -Zustand, allerdings befindet sich das Molekül zwischenzeitlich im T_1 -Zustand. Von dort wird die Barriere für das inverse ISC zurück in den S_1 -Zustand thermisch überwunden und es kommt zu Fluoreszenz. Durch die beiden verbotenen Spinwechsel zeigt sich die Fluoreszenz verzögert mit einer erheblich längeren Lebensdauer als reine Fluoreszenz.^[65,101] Für diesen Prozess ist eine sehr kleine energetische Lücke und eine geringe Barriere zwischen T_1 - und S_1 -Zustand von Nöten. Bei tiefen Temperaturen reicht die thermische Energie nicht mehr aus, um über das rISC in den S_1 -Zustand zu gelangen, weshalb statt TADF dann Phosphoreszenz beobachtet werden kann. OLED-Substanzen zeigen häufig TADF, da dadurch hohe Quantenausbeuten und Lebensdauern im μs -Bereich erreicht werden.^[101,149]

Die angeregten Moleküle können mit anderen Molekülen in ihrem Umfeld (z.B. Lösungsmittel, gleiche Moleküle im Grundzustand) interagieren. Dabei können sich komplexe Strukturen bilden, die sogenannten Exciplexe. Entstehen dabei Dimere aus einem angeregten und einem gleichen, nicht angeregten Molekül, nennt man diese Excimere.^[150] Die Emission dieser Komplexe ist rotverschoben zur eigentlichen Emission des Moleküls. Um diese Effekte zu verhindern, werden in der Lumineszenzspektroskopie geringe Konzentrationen verwendet.^[101,120,150]

2.4.4 Lumineszenzquantenausbeute

Die Quantenausbeute ϕ beschreibt, welcher Anteil der absorbierten Photonen n_{abs} auch wieder als Photon emittiert wird n_{em} .^[144]

$$\phi = \frac{n_{\text{em}}}{n_{\text{abs}}} \quad (16)$$

Die Quantenausbeute kann auch über die Ratekonstanten der strahlenden (k_r) und strahlungslosen (k_{nr}) Prozesse definiert werden.^[144]

$$\phi = \frac{k_r}{k_r + k_{nr}} \quad (17)$$

2.5 Zeitaufgelöste Lumineszenzspektroskopie

2.5.1 Lumineszenzlebensdauern

Die Lebensdauer τ eines angeregten Zustands ist das Reziprok der Summe aller Ratekonstanten der Prozesse, die zur Depopulation dieses Zustands führen.^[144]

$$\tau = \frac{1}{k_r + k_{nr}} \quad (18)$$

Die Anzahl an Photonen im emittierenden Zustand ist proportional zur Lumineszenzintensität. Da die Lumineszenzintensität $I(t)$ nach^[151]

$$I(t) = I_0 \exp(-(k_r + k_{nr}) \cdot t) \quad (19)$$

mit der Zeit t abnimmt, ist die Lebensdauer die Zeit, bis die Intensität auf ein e -tel der Ausgangsintensität I_0 zurückgegangen ist. Dies entspricht der mittleren Zeit, die zwischen Anregung und Emission vergeht. Da jedoch die Prozesse bis zum emittierenden Zustand sehr schnell ablaufen, kann diese Zeit mit der Lebensdauer des emittierenden, angeregten Zustands gleichgesetzt werden.^[152]

2.5.2 Time-Correlated Single-Photon Counting

Die Time-correlated single photon counting (TCSPC)-Methode (Abb. 2.12) ist eine besonders empfindliche Methode zum Messen der Lumineszenzabklingkurven zur Bestimmung der Lebensdauern. Am Detektor werden einzelne Photonen detektiert. Um Photonen in der Zeitskala von bis zu Pikosekunden detektieren zu können, wird eine spezielle elektronische Messmethode verwendet. Dabei sendet der Anregungspuls ein Startsignal an die Zeitmessung. Es passiert einen Constant Fraction Discriminator (CFD), der die Startzeit genau bestimmt. Der Time-to-Amplitude Converter (TAC) startet das Ansteigen einer Spannung proportional zur Zeit. Trifft nun ein emittiertes Photon auf den Detektor, wird ein Stoppsignal an den CFD gesendet, welcher das Ansteigen der Spannung stoppt. Der TAC ordnet die Spannung einer Zeit zu, welche in einen Zeitkanal mit der zeitlichen Breite Δt einsortiert wird. Die Zeitauflösung hängt von der Breite der Kanäle ab. Durch mehrfaches Messen entsteht ein Histogramm aus der Anzahl an Photonen gegen die Zeitkanäle. Üblicherweise werden ca. 4000 Kanäle verwendet. Das Histogramm bildet die Abklingkurve des angeregten Zustands ab.^[120,151,152]

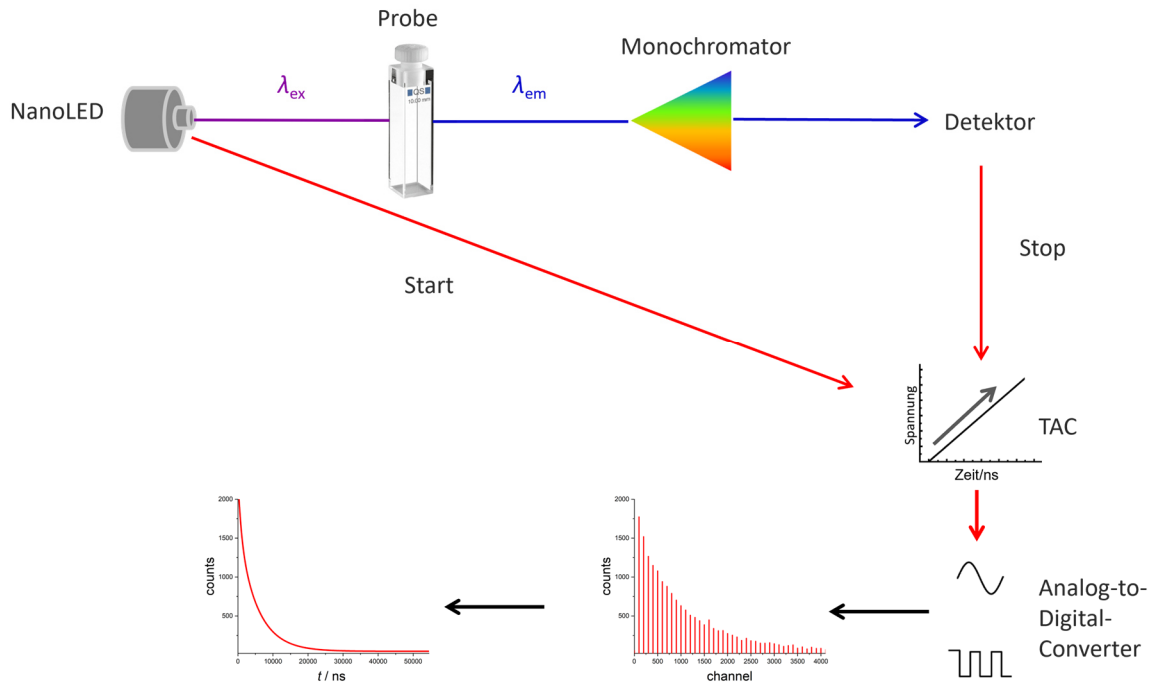


Abb. 2.12: Schematische Darstellung der TCSPC-Methode mit Anregung der Probe durch die NanoLED und Aufladen des Time-to-Amplitude Converter (TAC) bis zum Stop-Signal des Detektors und der Auswertung über den Analog-to-Digital-Converter zu einem Histogramm und schließlich der zeitlichen Abklingkurve.

Nachteil der Methode sind die langen Totzeiten, in denen keine Photonen detektiert werden können, da der TAC sich wieder resetten muss. Da sichergestellt werden muss, dass wirklich pro Anregungspuls nur ein Photon ankommt, kann nämlich lediglich ein Photon auf ca. 100 Anregungspulse detektiert werden. Um diese Rate maximal ausnutzen zu können, wird die reversed-Methode angewandt. Sie funktioniert genauso wie oben beschrieben, nur dass das ankommende Photon am TAC das Startsignal auslöst und der nächste Anregungspuls den TAC stoppt. Dadurch hat der TAC mehr Zeit für ein Reset und es gehen weniger emittierte Photonen in der Reset-Totzeit verloren.^[120,152]

Für lange Lebensdauern bei Phosphoreszenzprozessen ist die TCSPC-Methode wie oben beschrieben nicht geeignet, da nur jede 100. Anregung zur Detektion der Emission führt. Die Totzeit wird somit bei langen Abklingkurven sehr lang. Für diese Lebensdauern wird die multichannel scaling-Methode angewandt. Dabei werden alle, innerhalb eines Zeitkanals zum Zeitpunkt t bis $t + \Delta t$ ankommenden, Photonen gezählt. Damit können höhere Emissionsraten als bei der TCSPC-Methode verarbeitet werden. Nach Ablauf der Kanalbreite Δt werden die Photonen dem nächsten Kanal mit identischer zeitlicher Breite Δt zugeordnet, bis die Range $t_R = i\Delta t$ vollständig gemessen ist. Die entstehende Abklingkurve aus den Zeitkanälen wird „sweep“ genannt.^[151,152]

2.5.3 Time-resolved emission spectroscopy

Zeitaufgelöste Emissionsspektroskopie (englisch Time-resolved emission spectroscopy (TRES)) zeigt den zeitlichen Verlauf eines gesamten Lumineszenzspektrums. TRES-Spektren können ebenfalls mit der TCSPC-Methode (oder multichannel scaling) aufgenommen werden, indem diese in definierten Schritten der Emissionswellenlänge wiederholt wird (Abb. 2.13).^[153]

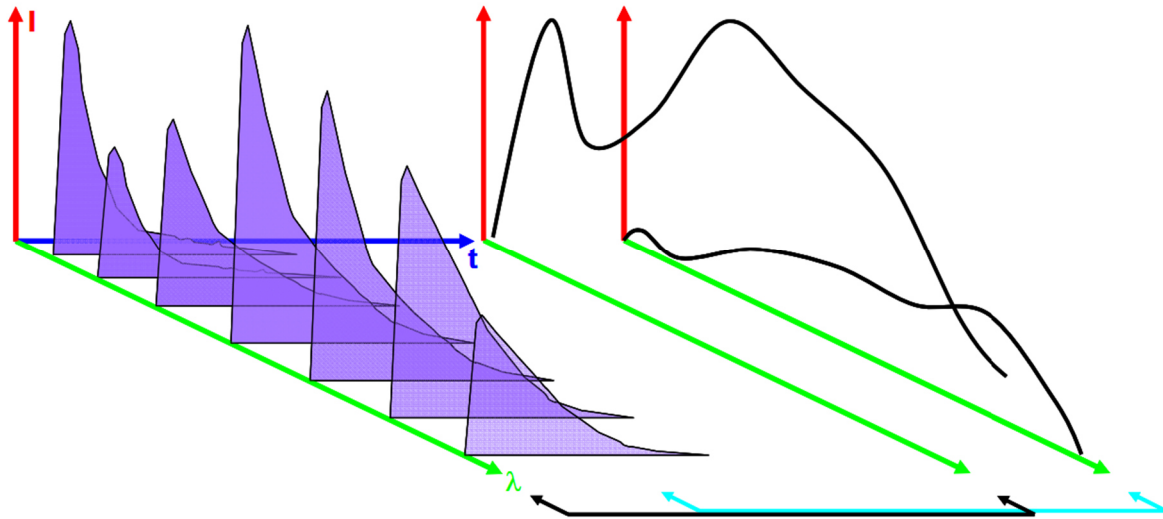


Abb. 2.13: Schematische Darstellung der Aufnahme der einzelnen TCSPC-Kurven einer TRES-Messung (violett) und der Auswertung der Emissionsspektren zu bestimmten Zeitpunkten (schwarzer Pfeil, cyaner Pfeil).^[153]

2.6 Quantenchemische Rechnungen

Quantenchemische Rechnungen bieten die Möglichkeit, Strukturen anhand von IR-Spektren zuzuordnen oder Abschätzungen über die energetische Lage verschiedener (angeregter) Zustände relativ zueinander vornehmen zu können.^[154]

2.6.1 Dichtefunktionaltheorie

Die Dichtefunktionaltheorie (DFT) beschreibt die Energie E eines Systems anhand seiner Elektronendichte $\rho(r)$.^[155,156] Der Zusammenhang zwischen Energie und homogen verteilter Elektronendichte wurde erstmals in den 1920ern von Thomas^[157] und Fermi^[158] beschrieben. Hohenberg und Kohn^[159] bestätigten diese Theorie und zeigten, dass sie auch für inhomogene Dichteverteilungen, und somit für Moleküle, anwendbar ist (1. Hohenberg-Kohn-Theorem). Die Ermittlung der Grundzustandsdichte mit der Energie $E(\rho)$ folgt dem Variationsprinzip (2. Hohenberg-Kohn-Theorem). Dabei lässt sich die Gesamtenergie aus der kinetischen, der potentiellen, der Coulomb- sowie der Austausch- und Korrelationsenergie beschreiben. Die potentielle Energie und die Coulomb-Energie lassen sich einfach über die Elektronendichte ρ berechnen, jedoch ist dies für die kinetische Energie und die Austausch- und Korrelationsenergie nicht möglich. Daher wird die Energie der Dichtefunktionaltheorie folgendermaßen aufgeteilt:

$$E(\rho) = F(\rho) + \int V_{\text{ext}}(\vec{r})\rho(\vec{r})d\vec{r} \quad (20)$$

wobei der zweite Term den systemabhängigen Anteil in Abhängigkeit des externen Potentials $V_{\text{ext}}(\vec{r})$ beschreibt. $F(\rho)$ ist definiert als der Beitrag der kinetischen Energie $T(\rho)$ und der Elektron-Elektron-Wechselwirkungen mit Coulomb-, Austausch- und Korrelationsenergie $V_{ee}(\rho)$.

$$F(\rho) = T(\rho) + V_{ee}(\rho) \quad (21)$$

Dieser Term stellt ein Problem dar, da er für ein System mit inhomogener Elektronendichte nicht bestimmt werden kann.^[155]

2.6.1.1 Kohn-Sham-Formalismus

Kohn und Sham^[160] führen dafür ein Referenzsystem ein, für das sich die kinetische Energie und der Coulomb-Austausch-Term berechnen lassen. Das Referenzsystem besteht anstelle von N wechselwirkenden Elektronen aus N nicht wechselwirkenden Elektronen mit der gleichen Elektronendichte wie das Originalsystem. Dadurch lässt sich die Grundzustandsfunktion über eine einzige Slater-Determinante aus N Einelektronen-Funktionen beschreiben. Diese Einelektronen-Funktionen werden Kohn-Sham-Orbitale

$\psi_i(\vec{r})$ genannt und jedes Kohn-Sham-Orbital ist eine Lösung der eindimensionalen Schrödingergleichung zur jeweils minimalen Orbitalenergie ε_i .^[155]

$$\left(-\frac{\hbar^2}{2m_e} \Delta + V_{\text{eff}}(\vec{r}) \right) \psi_i(\vec{r}) = \varepsilon_i \psi_i(\vec{r}) \quad (22)$$

mit $V_{\text{eff}}(\vec{r})$: Effektives Potential

Die Elektronendichte des Referenzsystems lässt sich aus den Kohn-Sham-Orbitalen berechnen und ist identisch mit der Elektronendichte des Originalsystems.

$$\rho(\vec{r}) = \rho_{\text{KS}}(\vec{r}) = \sum_{i=1}^N e |\psi_i(\vec{r})|^2 \quad (23)$$

Für das Referenzsystem kann die kinetische Energie $T_{\text{KS}}(\rho)$ klassisch aus den Orbitalen, und nicht der Elektronendichte, bestimmt werden. Sie ist jedoch nicht exakt identisch mit der kinetischen Energie des Originalsystems, stellt aber eine gute Näherung dar. Auch der Coulomb-Term $J(\rho)$ der Coulomb-, Austausch- und Korrelationsenergie kann über die Kohn-Sham-Orbitale berechnet werden. Somit ergibt sich für die Gesamtenergie

$$E(\rho) = T_{\text{KS}}(\rho) + J(\rho) + E_{\text{XC}}(\rho) + \int V_{\text{ext}}(\vec{r}) \rho(\vec{r}) d\vec{r} \quad (24)$$

Wobei $E_{\text{XC}}(\rho)$, das Austausch-Korrelationspotential, definiert ist als^[161]

$$E_{\text{XC}}(\rho) = (T(\rho) - T_{\text{KS}}(\rho)) + (V_{ee}(\rho) - J(\rho)) \quad (25)$$

2.6.1.2 Bedeutung der Hybridfunktionale

Ist das Austausch-Korrelationspotential bekannt, kann man die Dichtefunktionaltheorie iterativ lösen.^[155,162] Da dieser Teil allerdings meist zu komplex ist, werden Näherungen verwendet.^[155] Damit hängt die Genauigkeit der Dichtefunktionaltheorie von der Näherung ab.^[163] Gut geeignet sind sogenannte Hybridfunktionale wie PBE0 und B3LYP, die die Local Density Approximation (LDA) und die Generalised Correlation Approximation (GGA) mit Ergebnissen der Hartree-Fock-Methode und speziell entwickelten Korrelationspotentialen verbinden.^[161,164-166]

Durch die Vereinfachung der Berechnung über die Dichte ist die DFT eine, im Hinblick auf die Rechenzeit, billige und gute Methode zur Vorhersage von Strukturen und Frequenzen von Übergangsmetallkomplexen.^[107,167,168]

Kapitel 3: Experimenteller Aufbau und Durchführung

3.1 FTIR-Spektroskopie

3.1.1 FTIR-Spektrometer Vertex 80v

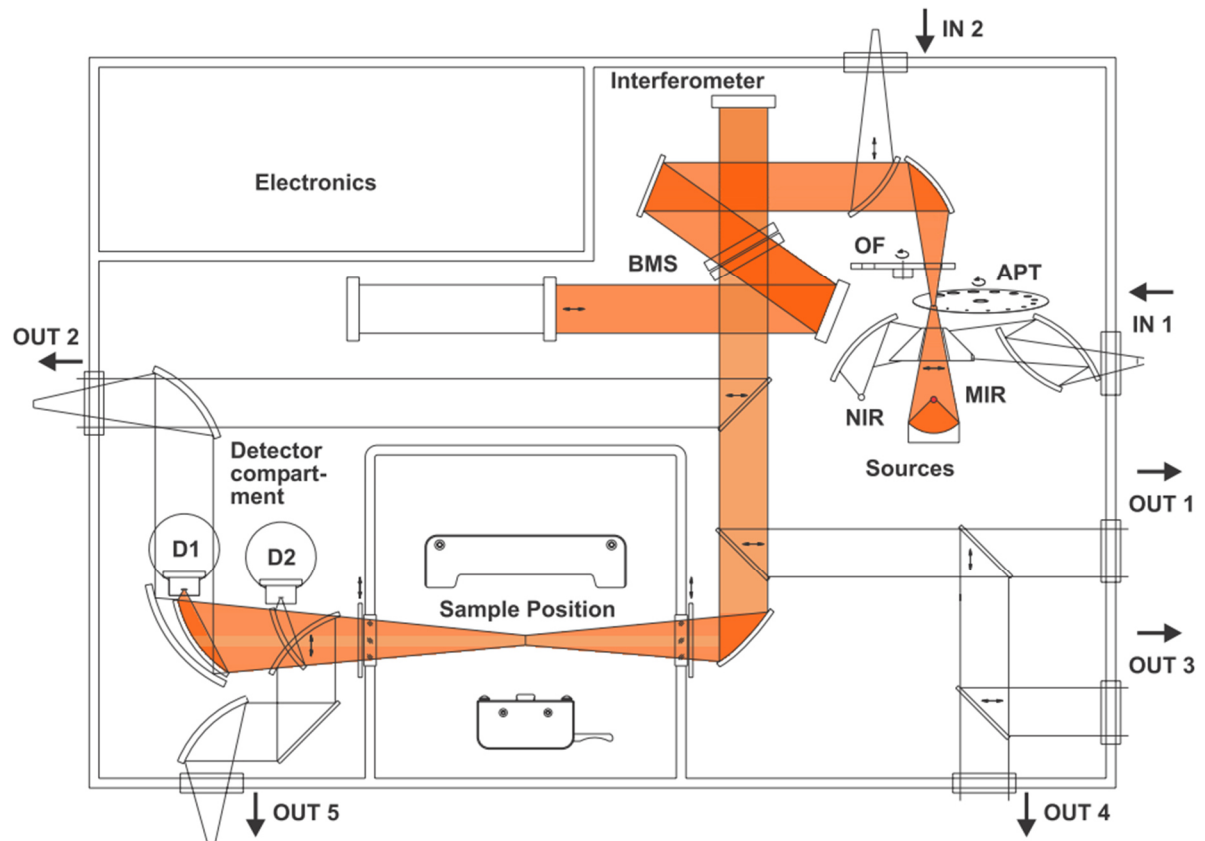


Abb. 3.1: Schematischer Aufbau des FTIR-Spektrometers Vertex 80v der Firma Bruker mit optischen Bauteilen und dem Strahlengang (orange).^[169]

Die FTIR-Messungen wurden am FTIR-Spektrometer Vertex 80v der Firma Bruker (Abb. 3.1) durchgeführt. Als Strahlungsquelle im Mittleren Infrarot (MIR) Bereich dient ein Globar. Die IR-Strahlung wird über eine Apertur (APT) zur Einstellung des Strahldurchmessers zum Interferometer geleitet. Das Interferometer namens UltraScan Interferometer^[170] hat den prinzipiellen Aufbau eines Michelson-Interferometers (Kapitel 2.2.1, Abb. 2.2). Es besteht aus zwei Spiegeln und einem Strahlenteiler (BMS) aus Kaliumbromid. Die IR-Strahlung wird am Strahlenteiler einmal auf den ersten, ortsfesten Spiegel reflektiert und zum anderen zum zweiten, beweglichen Spiegel transmittiert. Der bewegliche Spiegel ist auf einem Luftkissen aus Stickstoff gelagert und bietet zusammen mit dem HeNe-Laser zur Positionsbestimmung die Möglichkeit einer besonders hohen spektralen Auflösung ($<0,2 \text{ cm}^{-1}$)^[170]. Beide Teilstrahlen interferieren wieder am Strahlenteiler und der interferierte Strahl wird durch

den Probenraum gelenkt. Abschließend wird die transmittierte IR-Strahlung an einem Mercury-Cadmium-Tellurid-Detektor (D1) detektiert.

Die Interferometerkammer und die Detektorkammer sind mit KBr-Fenstern vom Probenraum abgegrenzt. Zusätzlich besitzt die Probenkammer seitlich zum IR-Strahlengang ein KBr-Fenster zur Einkopplung von Laserstrahlen. Somit wird im Falle von Messungen elektronisch angeregter Zustände oder photochemischer Reaktionen ein Anregungslaser in die Probenkammer eingekoppelt. Um das Eindringen der Anregungsstrahlung in die Detektor- bzw. Interferometerkammer zu verhindern, sind die Durchgänge zusätzlich mit Germaniumfenstern vor den KBr-Fenstern abgeschirmt. Durch Einbringen verschiedener Breitband- oder Langpass-Filtern in den Strahlengang kann der Messbereich entsprechend angepasst werden (Abb. 3.2). Zur Vermeidung von Signalen durch die Umgebungsluft in den FTIR-Messungen kann die Probenkammer bei Feststoffproben optional evakuiert werden bzw. bei nicht evakuierbaren Probenformen mit Argon gespült werden.

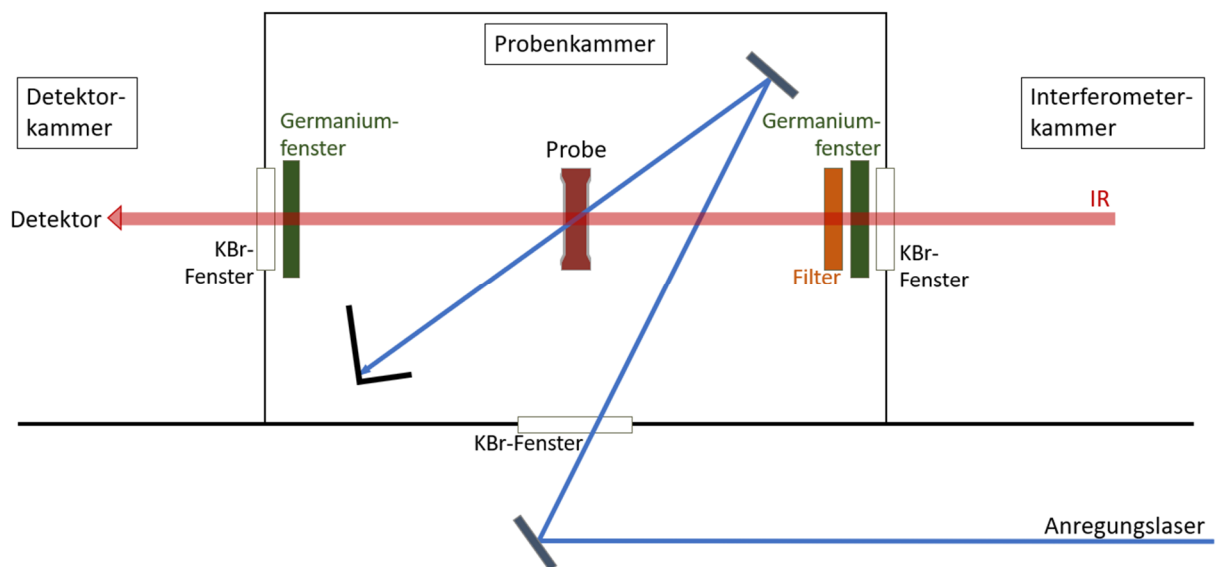


Abb. 3.2: Schematische Darstellung des Probenraums des Vertex 80v mit Fenstern und Strahlengang des IR-Strahls (rot) und des Anregungslasers (blau).

3.2 Laseraufbau

Um FTIR-Messungen angeregter Zustände oder photochemischer Reaktionen durchführen zu können, ist der FTIR-Aufbau um einen 100 Hz NdYAG-Laser Spotlight Evo I der Firma Innolas erweitert (Abb. 3.3). Hierzu wird die Fundamentale des Lasers bei 1064 nm mittels Second Harmonic Generation (SHG) in einem Kaliumdihydrogenphosphat-Kristall auf 532 nm frequenzverdoppelt (zweite Harmonische). Diese kann entweder mittels Third Harmonic Generation (THG) mit der Fundamentalen zu 355 nm (dritte Harmonische) frequenzgemischt werden oder mittels Fourth Harmonic Generation zur vierten Harmonischen bei 266 nm frequenzverdoppelt werden. Je nach Experiment werden die zweite, dritte oder vierte Harmonische verwendet. Über Spiegel wird der Laserstrahl in die Probenkammer eingekoppelt. Mittels Strahlenteilern und Neutralfichtfiltern im Strahlengang wird die Pulsenergie des Lasers auf ca. 1-8 mJ pro Puls eingestellt, je nach Experiment. Bevor die Laserstrahlung in den Probenraum eintritt, wird sie über ein Teleskop aus einer bikonkaven Linse ($f_{\text{bikonkav}} = 10 \text{ cm}$) und einer bikonvexen Linse ($f_{\text{bikonvex}} = 20 \text{ cm}$) aufgeweitet und über eine Blende auf ca. 9 mm Durchmesser begrenzt, was dem Probendurchmesser im Feststoffaufbau entspricht. Im Probenraum wird der Laserstrahl schräg zum Strahlengang des IR-Strahls durch die Probe geleitet, um ein Eindringen des UV- bzw. sichtbaren Anregungslicht in die Detektorkammer zu vermeiden. Die homogene Bestrahlung von Flüssigproben in der abgedichteten Dünnschichtküvette (siehe Abschnitt 3.5.1, Abb. 3.14c) wird sichergestellt, indem diese horizontal ausgerichtet und aus zwei entgegengesetzten Richtungen mit dem Teilstrahlen des Laserstrahl bestrahlt wird.

3.2.1 Zeitliche Abstimmung zwischen FTIR-Spektrometer und Laser

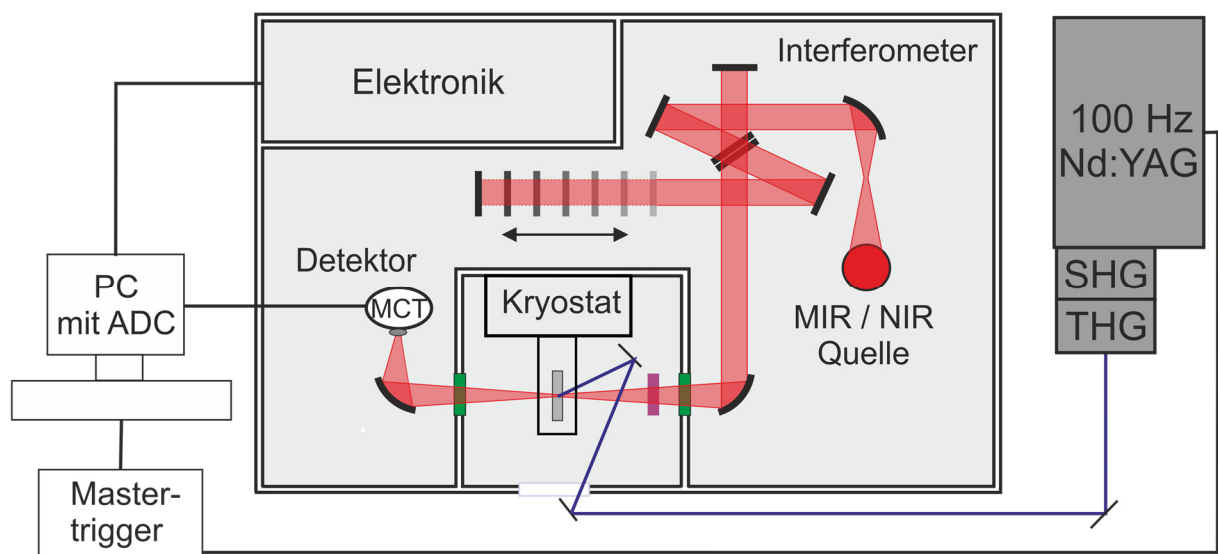


Abb. 3.3: Schematische Darstellung des Step-scan-Aufbaus mit Anregungslaser, Mastertrigger und elektronischer Datenverarbeitung am Vertex 80v.

Für den Step-scan-FTIR-Aufbau sind das Spektrometer, der Laser, die elektronische Datenverarbeitung und der Computer gekoppelt (Abb. 3.3). Das Detektorsignal bei der Messung wird zunächst vorverstärkt und über den DC- bzw. AC-Ausgang an das Transient Recorder Board am Messcomputer zur schnelleren Digitalisierung geleitet. Statische Messungen werden am Spektrometer mit einem Analog-to-Digital-Converter digitalisiert. Die zeitliche Abstimmung des Gesamtaufbaus wird über eine Stanford-Uhr (Stanford Research System DG535) als Mastertrigger gesteuert. Dabei sendet der Mastertrigger ein Trigger-Signal an das Transient Recorder Board, welches die Step-scan-Messung am Spektrometer startet, und an die Blitzlampen sowie die Pockels-Zelle des Lasers. Standardmäßig wird bei Step-scan-Experimenten in dieser Arbeit der Starttrigger für das Spektrometer 800 ns vor dem Puls für die Pockels-Zelle ausgegeben. Der Laserpuls erreicht die Probe somit 1300 ns nach dem Start der Step-scan-Messung.

3.2.2 Durchführung zeitaufgelöster FTIR-Messungen

Je nach gewünschter Zeitauflösung der Messung werden verschiedene Messmodi verwendet. Konventionelle statische Messungen dienen zur Untersuchung des Grundzustands oder der Untersuchung der Edukte oder der Produkte (nahezu) vollständig abgeschlossener Reaktionen, wobei keine zeitaufgelöste Messung benötigt wird. Dabei fährt der bewegliche Spiegel alle Spiegelpositionen ab und man erhält ein Interferogramm. Über die Fourier-Transformation wird dieses in ein Einkanalspektrum umgewandelt. Um ein Transmissions- bzw. Absorptionsspektrum zu erhalten, wird für jede Messung ein Einkanalspektrum des Hintergrunds benötigt. Durch Quotientenbildung aus dem Einkanalspektrum der Probe und des Hintergrunds wird das reine Spektrum der Probe in Transmission bzw. Absorption generiert (Kapitel 2.2.1.2). Für Untersuchungen von Prozessen auf Minuten- und Stundenzeitskala können mehrere statische Messungen in definierten zeitlichen Abständen aufgenommen werden. Höhere Zeitaufösungen (Millisekunden-Sekunden-Bereich) werden mit der Rapid-scan-Methode (Kapitel 2.3.1) erreicht. Die erhaltenen zeitaufgelösten Einkanalspektren werden wie die statischen Messungen ausgewertet. Die Step-scan-Methode (Kapitel 2.3.2) steht für noch schnellerer Prozesse zur Verfügung. Hierbei wird zunächst eine Hintergrundmessung ohne Anregung der zu untersuchenden Probe durchgeführt. Diese Messung ist die sogenannte DC-Messung, da das Signal über den DC-Ausgang des Spektrometers ausgegeben wird. Anschließend wird die zeitaufgelöste Step-scan-Messung des photophysikalischen oder photochemischen Prozesses durchgeführt. Dieses Signal wird über den AC-Ausgang des Geräts ausgegeben und daher AC-Messung genannt.

3.2.3 Auswertung zeitaufgelöster FTIR-Spektren

Aus diesen beiden Messungen erhält man, wie in Kapitel 2.3.2 beschrieben, zeitaufgelöste Differenzspektren (Abb. 3.4), die die zeitaufgelöste Änderung der Probenmessung zur DC-Hintergrundmessung zeigt. Dabei stellen die negativen Banden die Depopulation eines Zustands, während die positiven Banden einem oder mehreren angeregten Zuständen entsprechen. Zum Berechnen des Spektrums eines angeregten Zustands wird auf das Step-scan-Differenzspektrum das statisch gemessene Spektrum des Grundzustands addiert, bis die negativen Banden aufgehoben sind (Abb. 3.4).

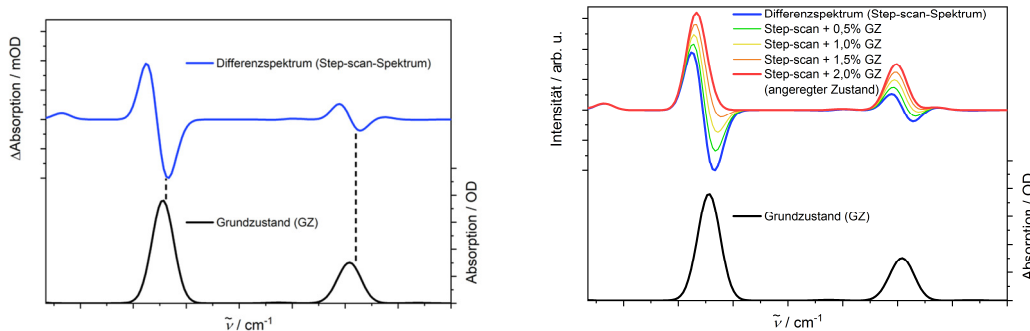


Abb. 3.4: Schematische Darstellung eines Step-scan-Differenzspektrums (blau) im Vergleich mit dem Grundzustandsspektrum (schwarz) (links) und Berechnung des Spektrums des angeregten Zustands durch Addition des Grundzustandsspektrums (hier 2,0 %, rot) (rechts).

Um aus den zeitaufgelösten Messungen Lebensdauern oder Kinetiken von Reaktionen zu erhalten, wird die Intensität am Maximum einer ausgewählten Bande über die Zeit betrachtet. Dazu werden Banden gewählt, die möglichst isoliert sind und ein gutes Signal-zu-Rauschen-Verhältnis aufweisen. Aus dem zeitlichen Verlauf der Bande kann bei Reaktionen die zugrundeliegende Kinetik bestimmt werden oder es ergeben sich die Lebensdauern der angeregten Zustände. Über die Kinetik können die Geschwindigkeitskonstanten aus einem Fit der Daten erhalten werden. Für eine Kinetik erster Ordnung gilt für die Eduktkonzentration $I(t)$ (Abb. 3.5):^[135]

$$I(t) = I_0 \exp(-kt) \quad (26)$$

- I_0 : Ausgangskonzentration
- k : Geschwindigkeitskonstante
- t : Reaktionszeit

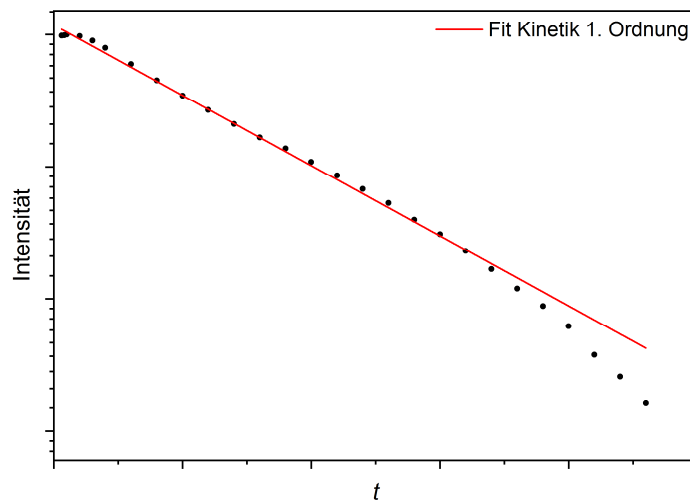


Abb. 3.5: Logarithmische Auftragung der Intensitätsabnahme einer Eduktbande im IR-Spektrum über die Zeit mit einem Kinetik-Fit 1. Ordnung nach Gl. (26).

Lebensdauern werden mit mono- oder polyexponentiellen Gaußfits gefittet (Abb. 3.6). Die Lebensdauerfits sind von folgender Form:

$$I(t) = y_0 + \sum_i \frac{A_i}{\tau_i} \cdot \exp\left(\frac{1}{2} \cdot \left(\frac{w}{\tau_i}\right)^2 - \frac{t - t_c}{\tau_i}\right) \cdot \frac{\operatorname{erf}\left(\frac{z_i}{\sqrt{2}}\right) + 1}{2} \quad (27)$$

y_0 : Offset

A_i : Amplitude der Komponente i

t : Zeit

τ_i : Lebensdauer der Komponente i

t_c : Verschiebung entlang der x-Achse

w : Breite

z_i : $z_i = \frac{t - t_c}{w} - \frac{w}{\tau_i}$

$\operatorname{erf}(x)$: Fehlerfunktion $\operatorname{erf}(x) = \frac{2}{\sqrt{\pi}} \cdot \int_0^x \exp(-u^2) du$

Die Fehlerfunktion dient zum Beschreiben des Anstiegspulses durch die Laserinitiation des Prozesses, der Offset wird zur Anpassung an den realen Offset der Messung benötigt und die modifizierten Exponentialfunktionen beschreiben die Abklingkurve. Diese Fitfunktion wurde bereits von meinen Vorgängern im Arbeitskreis etabliert.^[142,171]

Bei Step-scan-Messungen erhält man unter Berücksichtigung von lediglich einer Wellenzahl am Maximum häufig Lebensdauerkurven mit einem schlechten Signal-zu-Rauschen-Verhältnis. Daher wird zur Bestimmung der Lebensdauern ein breiterer Bereich von

mehreren Wellenzahlen um das Maximum herum gemittelt und diese Intensität gegen die Zeit aufgetragen. Vor dem Fit werden diese Lebensdauerkurven noch geglättet, um den Verlauf der Kurve besser nachvollziehen zu können.

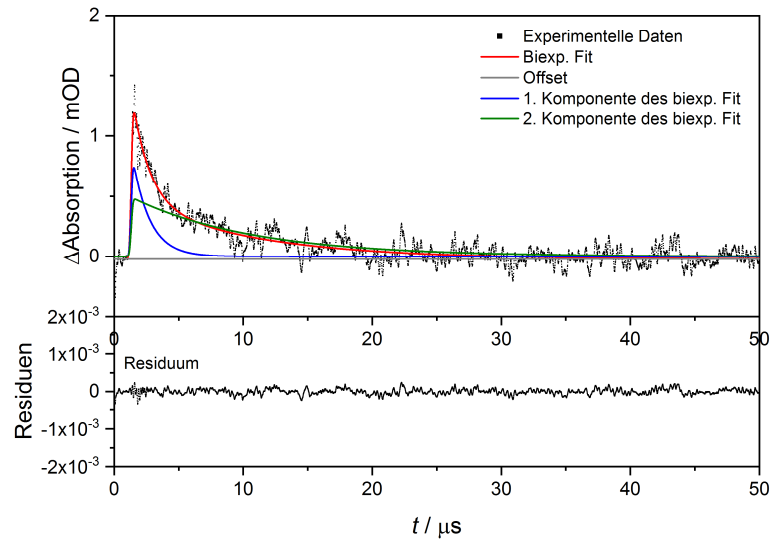


Abb. 3.6: Darstellung der beitragenden Komponenten eines biexponentiellen Fits (Gl. (27)) zur Beschreibung der Abklingkurve einer positiven Bande eines Step-scan-Spektrums zum Ermitteln der Lebensdauern.

3.3 UV/Vis-Absorptionsspektroskopie

3.3.1 UV/Vis/NIR-Spektrometer Lambda 900

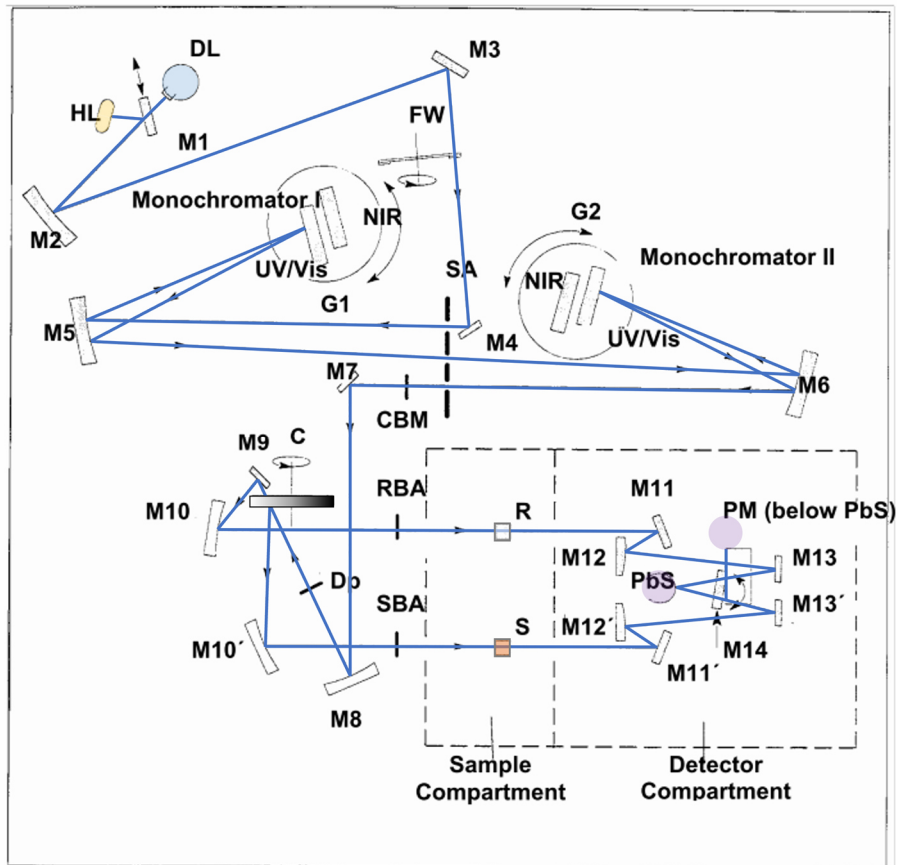


Abb. 3.7: Schematischer Aufbau des Strahlengangs (blaue Linie) des UV/Vis/NIR-Spektrometers Lambda 900 der Firma Perkin Elmer mit Haloganlampe (HL, orange), Deuteriumlampe (DL, hellblau), Spiegeln (M), Monochromator mit Gitter (G), Chopper (C, weiß-schwarz), Probe (S, rot), Referenz (R, weiß) und Detektoren (Photomultiplier (PM) und Bleisulfid (PbS), violett). Abbildung aus [172], überarbeitet.

UV/Vis-Absorptionsmessungen wurden am UV/Vis/NIR-Spektrometer Lambda 900 der Firma Perkin Elmer (Abb. 3.7) durchgeführt. Zur Abdeckung des Spektralbereiches verfügt das Spektrometer über zwei Anregungslampen, eine Wolfram-Halogen-Lampe (UV- und Vis-Bereich, HL) und eine Deuteriumlampe (UV-Bereich, DL). Über einen Spiegel (M1) wird die Strahlung der jeweils benötigten Lampe in den Strahlengang gebracht. Über zwei Monochromatoren mit Gittern (G1 und G2) wird die Wellenlänge eingestellt und während einer Messung durchgestimmt. Anschließend gelangt das Licht auf einen Chopper (C) mit drei Einstellungsmöglichkeiten, von wo es entweder durch die Referenzküvette (R) mit dem Lösungsmittel oder die Probenküvette (S) geleitet wird oder absorbiert wird. Durch diese Doppelstrahltechnik werden Intensitätsschwankungen der Lampe während der Messung berücksichtigt. Nach dem Durchgang der Probe oder der Referenz gelangt die transmittierte Strahlung über Spiegel auf den Detektor. Im sichtbaren und im UV-Bereich wird der

Photomultiplier (PM) verwendet. Für den NIR-Bereich steht ein Bleisulfid-Detektor (PbS) zur Verfügung.

In dem Doppelstrahlspektrometer können Lösungen untersucht werden (Abb. 3.8). Die verwendeten Küvetten haben eine Schichtdicke von 10 mm. Diese sind bei den Messungen auf 25°C mithilfe eines Thermostaten temperiert.



Abb. 3.8: Probenraum des Lambda 900 (von oben fotografiert) mit Referenzstrahlengang (hinten) und Probenstrahlengang (vorne) für die Doppelstrahltechnik (nach rechts Richtung Detektor). Die Küvetten für die Flüssigmessungen enthalten das reine Lösungsmittel (hinten) und die gelöste Probe (vorne).

3.3.2 Durchführung und Auswertung der UV/Vis-Absorptionspektren

Zunächst wird jeweils ein Hintergrundspektrum des reinen Lösungsmittels aufgenommen. Anschließend wird die Probe in die Probenküvette gefüllt und in gleicher Ausrichtung wie beim Hintergrundspektrum wieder in den Strahlengang gestellt. Die erhaltenen Intensitätsspektren werden mit dem Hintergrund verrechnet (Gl. (15)) und als Extinktion gegen die Wellenlänge dargestellt. Bei bekannter Probenkonzentration wird der

Extinktionskoeffizient nach Gleichung (15) berechnet und dieser anstelle der Extinktion aufgetragen.

3.3.3 Reflektionseinheit PrayingMantis

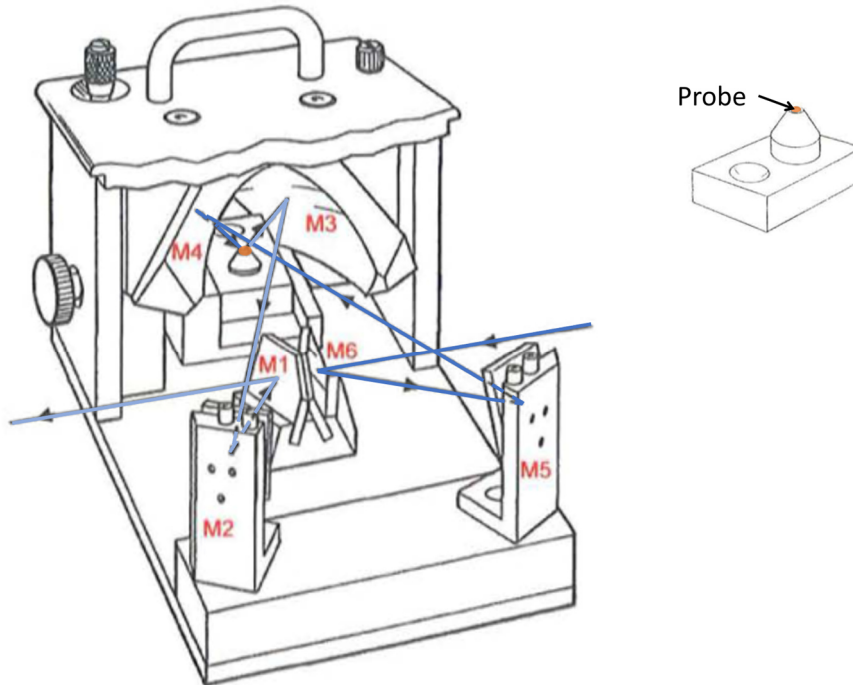


Abb. 3.9: Schematischer Aufbau des Einsatzes der Reflektionseinheit PrayingMantis der Firma Harrick in den Probenstrahlengang des Lambda 900 mit Strahlengang (blau) (links) und Darstellung des Probencups für die pulverförmigen Proben (rechts). Abbildungen aus [173], überarbeitet.

Mittels der Reflektionseinheit PrayingMantis von Harrick (Abb. 3.9) können über die diffuse Reflektion an den Proben auch Absorptionsspektren von Feststoffen aufgenommen werden. Dazu wird die Reflektionseinheit in den Probenstrahlengang eingebaut und der Referenzstrahlengang gegen Umgebungslicht abgeschirmt. Die Probe wird im Verhältnis 1:100 mit Kaliumbromid verdünnt und fein gemörsert. Sie wird in den kleinen Probenbecher der Einheit (Abb. 3.9, rechts) gefüllt und die Oberfläche möglichst gleichmäßig geglättet. Dieses Probengefäß wird in die Reflektionseinheit eingebaut und darin bestrahlt. Durch die gewölbten Spiegel innerhalb der Reflektionseinheit wird die von der Probe nicht-absorbierte, reflektierte Strahlung zurück in den Strahlengang Richtung Detektor geleitet. Auch hier wird das Absorptionsspektrum aus einem Hintergrundspektrum (reines KBr-Pulver) und dem Probenspektrum berechnet.

3.4 Emissionsspektroskopie

Die Emissionsspektroskopie wurde an den Fluorometern Fluorolog3-22 τ (Abb. 3.10) und Fluoromax-2 (Abb. 3.11) der Firma Horiba durchgeführt. An beiden Spektrometern sind die Untersuchung von Proben in Form von Lösungen, KBr-Presslingen und Pulvern sowie Messungen mit dem Kryostaten im Probenraum möglich.

3.4.1 Emissionsspektrometer Fluorolog3-22 τ

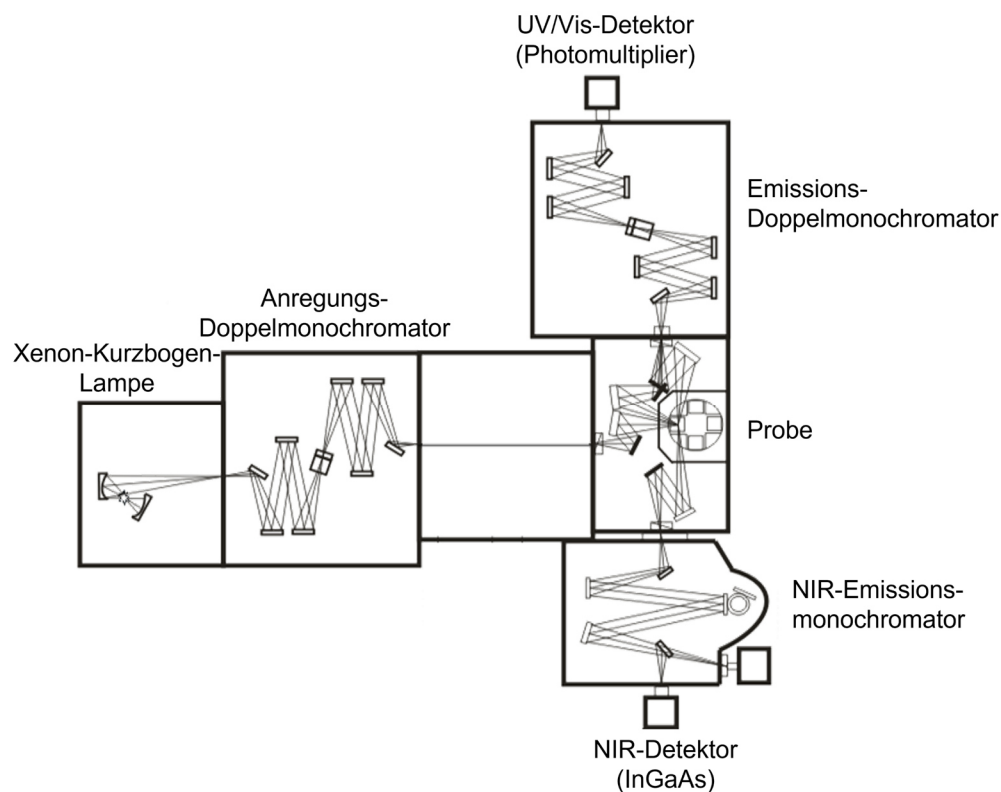


Abb. 3.10: Schematischer Aufbau des Emissionsspektrometers Fluorolog3-22 τ der Firma Horiba mit NIR-Aufbau. Der Strahlengang von der Anregungslampe über den Doppelmonochromator zur Probe, sowie über die jeweiligen Emissionmonochromatoren zu den beiden möglichen Emissionsdetektoren (UV/Vis: Photomultiplier, NIR: Indium-Gallium-Arsenid-Detektor) ist eingezeichnet. Abbildung modifiziert nach [174].

Zur Anregung der Proben besitzt das Fluorolog3-22 τ (Abb. 3.10) eine 450 W-Xenon-Kurzbogen-Lampe. Die breitbandige sichtbare und UV-Strahlung der Lampe wird auf einen Anregungs-Doppel-Monochromator (je 1200 Striche/mm) in Czerny-Turner-Anordnung geleitet. Durch den Doppelmonochromator wird das Streulicht gegenüber einfachen Monochromatoren reduziert. Die gewünschte Anregungswellenlänge strahlt in der Probenkammer auf die Probe. Flüssigproben werden in einer Kuvette im Probenkarussell positioniert und mit einem Thermostaten auf 26°C temperiert. Feststoffproben werden im 45°-Winkel zum Anregungsstrahl und Detektor ausgerichtet. Von dort wird im 90°-Winkel zum Anregungslicht die Emission der Probe im sichtbaren oder UV-Bereich (240-850 nm) über den Emissions-Doppel-Monochromator (je 1200 Striche/mm) in der gewünschten

Wellenlänge an einem Photomultiplier (R928P) detektiert. Emissionen im NIR-Bereich (850-1500 nm) werden 90° in die andere Richtung hinter einem einfachen NIR-Emissionsmonochromator an einem stickstoffgekühlten Indium-Gallium-Arsenid-Detektor (DSS - IGA020L) detektiert. Die 90°-Anordnung sorgt für eine Verringerung von Streueffekten des Anregungslichts am Detektor. Zusätzlich können noch Langpassfilter, entsprechend der Anregungswellenlänge und der Emission angepasst, das Eintreten von Anregungslicht auf der Emissionsseite verhindern. Auf der Seite der NIR-Detektion sind standardmäßig in dieser Arbeit zwei Langpassfilter ($\lambda \geq 500$ nm, $\lambda \geq 850$ nm) verbaut. Die erhaltenen Spektren werden mit einer, von meinem Kollegen Pit Boden aus Referenzmessung erstellten, Korrekturfunktion verrechnet, um die über die Wellenlängen nicht konstante Detektorsensitivität auszugleichen.

3.4.2 Upconversion-Experimente und Singulett-Sauerstoff-Quantenausbeuten

Neben der Emissionsspektroskopie an den Proben wurden auch Untersuchungen von Energieübertragungen durchgeführt. Bei Upconversion-Experimenten wird zur Anregung ein externer HeCd-Laser (KIMMON Series IK5651R-G) von der entgegengesetzten Seite der Anregungslampe des Spektrometers eingekoppelt. Die gewählte Anregungswellenlänge ist 442 nm mit einer Leistung von ~55 mW. Für den Energieübertrag eines Photosensibilisators auf molekularen Sauerstoff in der Probenlösung kann über die NIR-Emission des entstehenden Singulett-Sauerstoffs (1O_2) die Quantenausbeute ϕ des Übertrags bestimmt werden. Diese Methode ist relativ zur bekannten 1O_2 -Quantenausbeute des $[\text{Cr}(\text{ddpd})_2](\text{BF}_4)_3$ -Komplexes ϕ_{ref} bei einer Anregung mit 420 nm angewandt worden.^[86]

$$\phi(^1O_2) = \phi_{\text{ref}}(^1O_2) \cdot \frac{I_s}{I_{\text{ref}}} \cdot \frac{A_{\text{ref}}}{A_s} \quad (28)$$

$I_{(s,\text{ref})}$: integrierte Lumineszenzintensität der Probe (s) bzw. der Referenz (ref)

$A_{s,\text{ref}}$: Absorption der Probe (s) bzw. der Referenz (ref)

3.4.3 Emissionsspektrometer Fluoromax-2

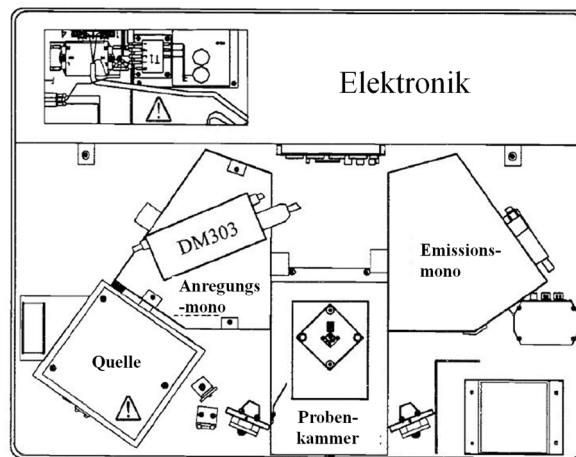


Abb. 3.11: Schematischer Aufbau des Emissionsspektrometers Fluoromax-2 der Firma Horiba.^[175]

Das Fluoromax-2 (Abb. 3.11) ist nahezu analog zum Aufbau des Fluorologs ohne NIR-Aufbau. Es enthält ebenfalls eine Xenon-Kurzbogenlampe, deren Strahlung über einen Anregungsmonochromator in den Probenraum geleitet wird und die Emission der Probe von dort im 90°-Winkel über einen Emissionsmonochromator zu einem Photomultiplier (R928P) gelangt. Der Unterschied zum Fluorolog besteht darin, dass in diesem Spektrometer nur einfache Monochromatoren verbaut sind. Daher ist die Qualität der Spektren durch den größeren Einfluss von Streulichteffekten im Vergleich geringer.

3.4.4 Emissionslebensdauerspektrometer DeltaFlex

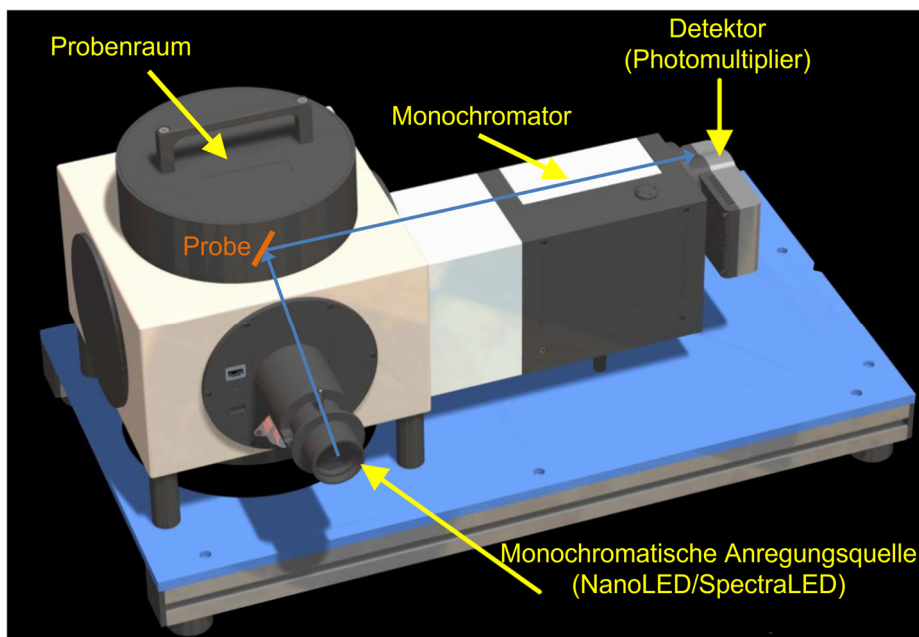


Abb. 3.12: Emissionslebensdauerspektrometer DeltaFlex der Firma Horiba mit Strahlengang (blau). Abbildung aus ^[176], überarbeitet.

Zeitaufgelöste Emissionsdaten wurden am DeltaFlex von Horiba (Abb. 3.12) untersucht. Die Lebensdauern der lumineszenten angeregten Zustände werden mit der Time-Correlated Single Photon Counting (TCSPC)-Methode bestimmt. Zur Anregung der Proben (analog zu Proben beim Fluorolog) werden monochromatische Nano- ($\lambda_{em} = 313, 345, 389 \text{ nm}$) oder Spectra-LEDs ($\lambda_{em} = 341, 390 \text{ nm}$) verwendet. Mit Pulsbreiten von $\sim 1 \text{ ns}$ sind die Nano-LEDs für Messungen im kürzeren Zeitbereich (Range = 100 ns - $100 \mu\text{s}$), während die Spectra-LEDs mit wesentlich längeren Pulsbreiten von $\sim 100 \text{ ns}$ für Phosphoreszenzmessungen mit einem eingestellten Zeitbereich ab $340 \mu\text{s}$ verwendet werden. Die Anregungswellenlänge wird so gewählt, dass die höchste Emissionsintensität erreicht wird. Im 90° -Winkel zur Anregung wird die Emission nach einem Emissionsmonochromator an einem Picosecond-Photon-Detection-Modul (PPD-850), bestehend aus einem schnell-anschlagendem Photomultiplier, einem GHz-Vorverstärker, einem „Constant-Fraction-Discriminator“ und einer festgelegten Hochspannungsversorgung, detektiert. Das Detektionsmodul ist darauf ausgelegt, einzelne Photonen mit Pikosekunden-Genauigkeit zu detektieren. Die detektierten Photonen werden in 4096 Zeitkanälen über den eingestellten Zeitbereich ($100 \text{ ns} - 1,4 \text{ ms}$) zugeordnet. Diese Messungen werden „decay“ genannt. Um den Einfluss von Streulicht des Anregungslichts auf das Experiment gering zu halten, wird bei Flüssigproben eine Kontrollmessung einer Streulösung (Suspension von LUDOX® in Wasser) bei gleichen Einstellungen, aber die Emissionswellenlänge gleich der Anregungswellenlänge, durchgeführt. Diese „prompt“-Messung wird von der „decay“-Messung abgezogen. Da für Feststoffe durch die sehr individuelle Ausrichtung der Probe keine exakte „prompt“-Messung möglich ist, wird hier ein Langpassfilter verwendet, um das Eindringen von Anregungslicht in den Emissionstrahlengang zu verhindern.

Über die Zeitkanäle kann das Histogramm der Abklingkurve in eine zeitabhängige Abklingkurve umgerechnet werden. Diese wird semi-logarithmisch aufgetragen und mit den Lebensdauerfits siehe Gl. (27) gefittet. Da für einen konvergierenden Fit meist mehr Komponenten nötig sind als aus photophysikalischer Sicht sinnvoll, wird letztendlich die gewichtete Lebensdauer aus den Komponenten angegeben.

Im Messmodus für zeitaufgelöste Emissionsspektren (Time-resolved emission spectroscopy, TRES) werden hintereinander schrittweise TCSPC-Messungen über einen Emissionsbereich durchgeführt (Abb. 2.13).

Die Daten einer TRES-Messung werden als Intensitätsmatrix mit der Wellenlänge, der Zeit und der Intensität als Variablen dargestellt. Um die Datenmenge zu reduzieren und übersichtlich zu halten, werden dazu die Counts der Kanäle über einen Zeitbereich von jeweils $1 \mu\text{s}$ gemittelt. Trägt man die Counts zu den einzelnen Mikrosekundenabschnitten

über die Wellenlänge auf, ergeben sich zeitaufgelöste Emissionsspektren (Abb. 3.13). Die Lebensdauern können bei TRES-Experimenten analog zu denen der einfachen TCSPC-Messungen gefittet werden.

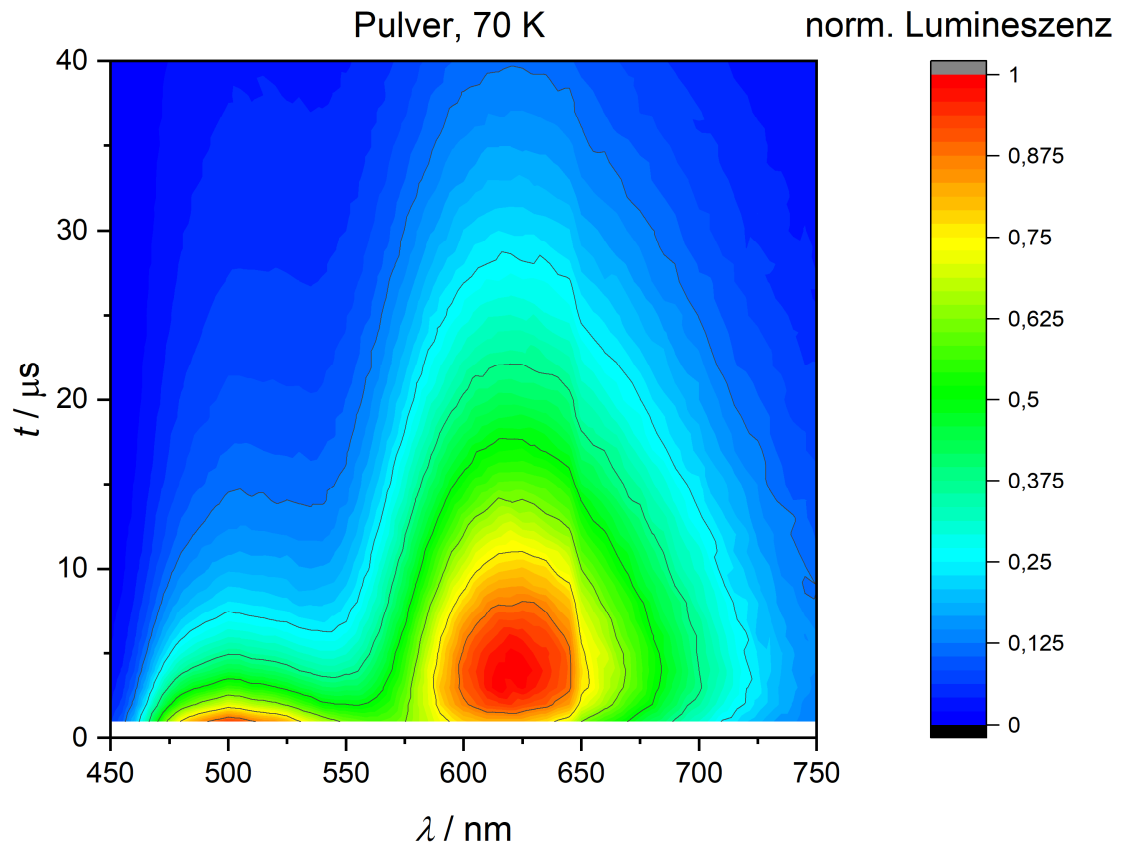


Abb. 3.13: Intensitätsmatrix einer TRES-Messung, woraus man die zeitaufgelösten Spektren zu einem Zeitpunkt t nach der Anregung entlang der Wellenlängen-Achse (waagrecht) erhält und entlang der Zeitachse die TCSPC-Abklingkurven einer Wellenlänge (senkrecht).

3.5 Probenformen

Alle im Rahmen dieser Arbeit untersuchten Proben lagen in kondensierter Phase vor, d.h. als Reinstoffe als Pulver bzw. Kristall, in einer KBr-Matrix (Pressling) oder in Lösung.

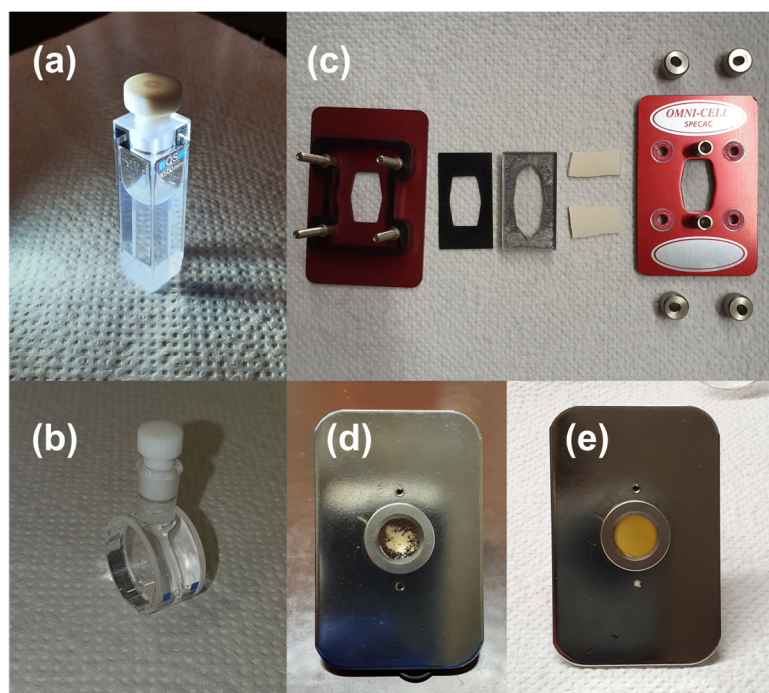


Abb. 3.14: Küvetten für Lösungen: Quarz-Fluoreszenzküvette (a), Quarz-UV/Vis-Transmissionsküvette (b), versiegelte Dünnschichtküvette aus CaF_2 -Platten für den IR-Bereich, bestehend aus Halterung, Gummipuffer, versiegelter CaF_2 -Küvette, Septen zum Abdichten, Abdeckungsplatte mit Muttern (c, von links nach rechts). Probenträger für Feststoffe in der „Bruker“-Halterung: zwei CaF_2 -Fenster für Pulverproben (d), KBr-Pressling (e).

3.5.1 Lösungen

Lösungen für die UV/Vis-Absorptions- und Emissionsspektroskopie werden mit Schlenk-Technik unter Argon als Schutzgas hergestellt. Dazu werden nach der Pump-Freeze-Methode entgaste Lösungsmittel verwendet. Dabei wird das Lösungsmittel in flüssigem Stickstoff eingefroren und 8 min unter Vakuum gesetzt. Anschließend wird es unter Argon 8 min bei Raumtemperatur gerührt. Dieser Vorgang wird je nach Lösungsmittel 4- bis 6-mal wiederholt. Standardmäßig wird die Lösung mit einer Konzentration von $2 \cdot 10^{-5}$ M angesetzt und in die Quarzküvette überführt. Für die Emissionsspektroskopie werden auf allen vier Seiten geschliffene Fluoreszenzküvetten (Abb. 3.14a) verwendet, für die UV/Vis-Absorptionsspektroskopie runde Transmissionsküvetten (Abb. 3.14b), jeweils mit einer Schichtdicke von 10 mm.

Da das Lösungsmittel bei der IR-Spektroskopie einen großen Einfluss hat, muss hierbei die Schichtdicke möglichst gering und die Konzentration verglichen mit der UV/Vis-Spektroskopie sehr hoch gewählt ($> 10^{-3}$ M) werden. Hierbei wird eine versiegelte

Dünnschichtküvette der Firma Specac (Omni-Cell, $d = 200 \mu\text{m}$) mit Calciumfluorid-Fenstern (Abb. 3.14c), welche oberhalb von 1000 cm^{-1} IR-durchlässig sind, verwendet.

3.5.1.1 Gase in Lösung

Um Gase in einem bestimmten Lösungsmittel mit FTIR-Spektroskopie untersuchen zu können, werden diese mit leichtem Überdruck mehrere Minuten durch das entsprechende Lösungsmittel geleitet. Die Lösung wird anschließend schnell in die verschweißte Dünnschichtküvette überführt und gemessen.

3.5.2 Feststoffproben

3.5.2.1 KBr-Presslinge

Für die Herstellung von KBr-Presslingen (Abb. 3.14d) wird Kaliumbromid (je nach Experiment 180-200 mg), welches im Trockenschrank gelagert wird, mit der Probe (je nach Probe 0,2-2,2 mg) fein gemörsert. Das Pulver wird in ein Presswerkzeug mit einem Durchmesser von 13 mm gegeben, welches mit einer ölfreien Membranpumpe evakuiert wird. In einer hydraulischen Presse wird die Probe im evakuierten Presswerkzeug bei 75 GPa für einige Minuten gesintert.

3.5.2.2 Pulver

Reine Pulverproben werden zwischen zwei CaF_2 - oder Quarzplatten mit einer Dicke von 0,5 oder 1 mm und einem Durchmesser von 13 mm gleichmäßig dünn verteilt (Abb. 3.14e). Die Proben werden zusammen mit den Platten als Probe wie ein KBr-Pressling in die jeweiligen Probenräume eingebaut.

3.5.2.3 Gefrorene Lösung (Glas)

Proben im Glas werden aus Lösungen ausgefroren, die, wie in Abschnitt 3.5.1 „Lösungen“ beschrieben, hergestellt wurden. Das Lösungsmittel muss ein glasbildendes Lösungsmittel sein. Küvette und Tieftemperaturmessung werden im folgenden Abschnitt 3.6.1.1 „Herstellung der gefrorenen Lösungen (Gläser)“ beschrieben.

3.6 Tieftemperaturmessungen

Tieftemperaturmessung in der FTIR- und Lumineszenzspektroskopie wurden mithilfe von zwei verschiedenen „Closed-cycle“-Helium-Kryostaten durchgeführt.

3.6.1 „Closed-cycle“-Helium-Kryostat (ARS)

Das erste System ist von Advanced Research Systems (ARS, Model DE-202A) und deckt den Temperaturbereich von 10 – 290 K ab. 10 K ist die minimale, erreichbare Temperatur und die oberere Grenze ist dadurch gegeben, dass die Temperaturstabilität bei 298 K (Raumtemperatur) schlechter ist. Die Temperatur wird über einen Controller mit Heizung (Cryo-Con 32) eingestellt. Der Kaltkopf ist am unteren Ende, wo die Probenhalterung befestigt ist, mit zwei CaF_2 -Fenstern ausgestattet, welche bei FTIR-Messungen gegenüber und bei Lumineszenzmessungen im 90° -Winkel zueinanderstehen. Der Kaltkopf kann mit zwei verschiedenen Probenhalterungen ausgestattet werden. Für KBr-Presslinge oder Pulverproben in der Lumineszenz- oder IR-Spektroskopie steht eine Kupferhalterung aus sauerstofffreiem Kupfer für Platten mit einem Durchmesser von ca. 13 mm zur Verfügung, welche einen Durchgangsdurchmesser von ca. 9 mm hat (Abb. 3.15a). Glasmessungen in der Lumineszenz benötigen einen Kupferhalter für eine kryogene Fluoreszenzküvette mit vier geschliffenen Seiten (Abb. 3.15c). Der Kryostat wird über einen Pumpenstand von Oerlikon Leybold Vacuum mit einer Membranpumpe (DIVAC 0.8T) als Vorpumpe und einer Turbomolekularpumpe (TURBOVAC 80) durchgehend bis zu einem Druck von $< 5 \cdot 10^{-5}$ mbar evakuiert.

3.6.1.1 Herstellung der gefrorenen Lösungen (Gläser)

In der kryogenen Küvette für Lumineszenzmessungen (Abb. 3.15c) wird das glasbildende Lösungsmittel langsam heruntergekühlt, bis es vollständig verglast ist. Anschließend kann die Messung bei tiefer Temperatur oder nach dem Auftauen des Lösungsmittels wieder bei höheren Temperaturen durchgeführt werden. Um die erforderliche geringe Schichtdicke für FTIR-Messungen im Glas zu realisieren, wurde eine Küvette im Eigenbau entwickelt. Diese auseinandernehmbare Küvette besteht aus zwei CaF_2 -Fenstern, welche mit einer Metallscheibe als Spacer mit der Dicke von 1 mm getrennt sind (Abb. 3.15b). Zunächst wird der Spacer gleichmäßig für das spätere Abdichten mit Hochvakuumfett eingestrichen und auf dem ersten CaF_2 -Fenster positioniert. Die Probenlösung kommt in die entstandene Vertiefung. Anschließend wird das zweite CaF_2 -Fenster zum Verschließen auf den Spacer gelegt. Dieser Aufbau wird dann in die vorher beschriebene Feststoffhalterung des Kryostaten eingespannt. Zum Verglasen muss hierbei der Kryostat zunächst mit Argon gespült und befüllt werden. Das Herunterkühlen erfolgt bis zum Verglasen der Probe unter Argon. Dabei muss der Kryostat von außen zusätzlich isoliert werden, da das Argon eine

Wärmebrücke von den Außenwänden zum Kühlfinger bildet. Nach dem Verglasen wird der Kryostat evakuiert und das Glas kann bei tiefer Temperatur gemessen werden.

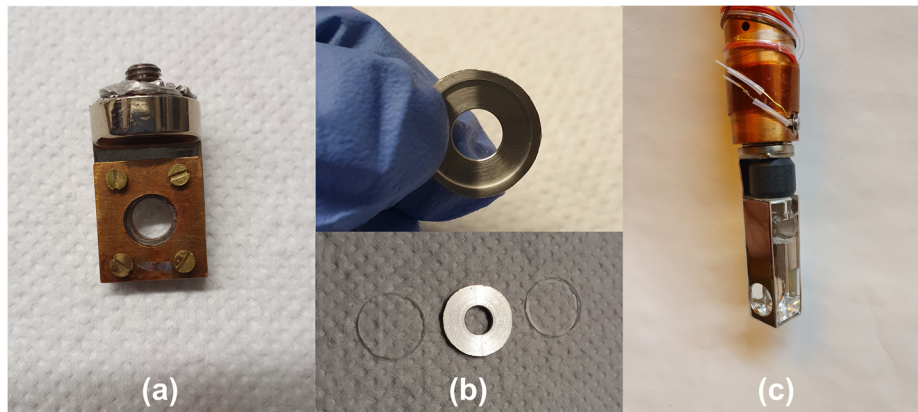


Abb. 3.15: Probenhalterungen im Kryostaten: Kupferhalterung für KBr-Presslinge oder CaF_2 -Fenster (a), CaF_2 -Küvette nach Eigenbau für Glasmessungen im IR-Bereich (b oben: zusammengebaut, b unten: zerlegt) und kryogene Quarzküvette mit Kupferhalterung am Kaltkopf (c).

3.6.2 „Closed-cycle“-Helium-Kryostat ColdEdge

Der zweite Kryostat der Fima ColdEdge ist ähnlich dem von ARS und erreicht einen Temperaturbereich von 5 – 290 K (Controller mit Heizung: Lake Shore Model 335). Er wird ausschließlich für Lumineszenzmessungen an Feststoffproben verwendet. Der würfelförmige Mantel am unteren Ende des Kaltkopfs ist mit drei Quarzfenstern und einem CaF_2 -Fenster ausgestattet, wobei das CaF_2 -Fenster immer in Richtung Detektor ausgerichtet ist. Dieser Kryostat verfügt über einen Feststoffprobenhalter für KBr-Presslinge bzw. CaF_2 -Fenster, analog zum zuvor beschriebenen ARS-Kryostaten. Dieses System wird über einen Pumpenstand von Oerlikon Leybold Vacuum mit einer Membranpumpe als Vorpumpe (DIVAC 3.0) und eine Turbomolekularpumpe (TURBOVAC 90i) bei einem Druck von $< 5 \cdot 10^{-5}$ mbar gehalten.

3.6.3 Kombination von Kryostaten und Spektrometern

Die Kryostaten werden über Gerüste kontaktfrei zum Spektrometer in deren Probenräume eingehängt, um Schwingungsübertragungen des Kompressors auf das Messgerät zu vermeiden. Über zwei kombinierte Verstellische für Höhe und seitliche Verschiebung wird der Kryostat im Probenraum der Spektrometer auf die optimale Position ausgerichtet (Abb. 3.16).

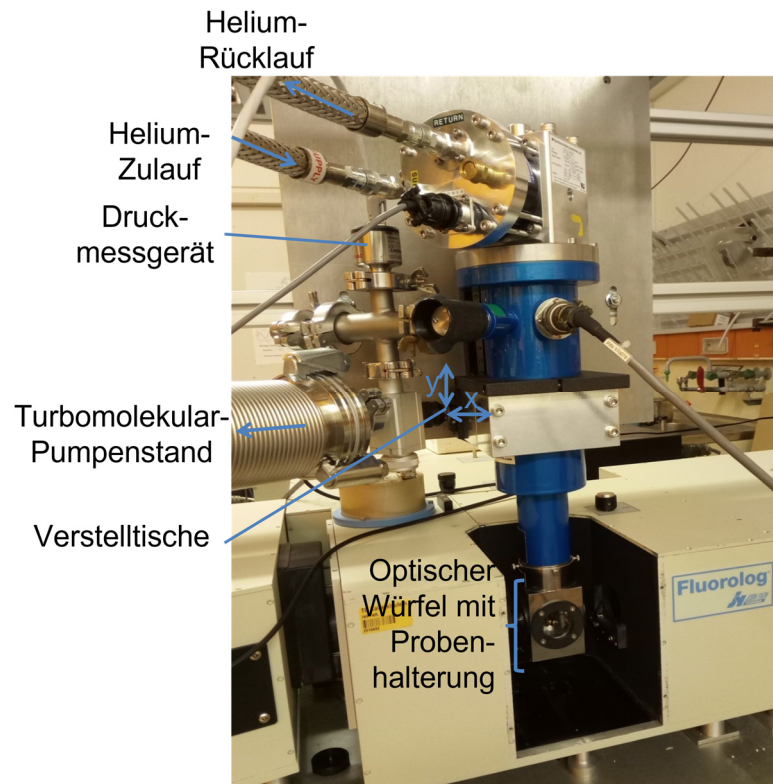


Abb. 3.16: „Closed-cycle“-Helium-Kryostat der Firma ColdEdge im Fluorolog3-22 τ . Der Kryostat ist über ein Gerüst kontaktfrei in das Spektrometer eingehängt und über die Verstelltische justierbar. Abbildung aus ^[171], überarbeitet.

3.7 Quantenchemische Modellierung

Quantenchemische Rechnungen wurden mit der Option GauExternalNewTurbo als Kombination aus den Programmen Gaussian 09 und Turbomole 7.4 durchgeführt. Die Startgeometrien für die Geometrieoptimierungen wurden ausgehend von Kristallstrukturen oder chemischer Intuition angesetzt. Geometrieoptimierungen und harmonische Frequenzrechnungen für die optimierten Geometrien für den ersten Singulett- und den Triplettzustand sowie vertikale Übergänge im Singulettzustand wurden mittels Dichtefunktionaltheorie mit dem Funktional B3LYP und dem Basissatz def2-TZVP mit Dispersionskorrektur D3 mit Becke-Johnson-Damping (BJ) durchgeführt. Der Einfluss eines Lösungsmittels oder der KBr-Matrix wurde mit dem conductor-like screening model COSMO simuliert. Die Energien wurden um die Nullpunktsschwingungsenergie korrigiert. Schwingungsfrequenzen wurden jeweils mit einem Skalierungsfaktor (abhängig vom untersuchten System, siehe Kapitel 4 und 5) korrigiert und mit Gaußkurven mit einer Halbwertsbreite von 8 cm^{-1} gefaltet. Spektren der vertikalen Übergänge wurden ebenfalls mit Gaußkurven gefaltet. Für die Triplettzustände wurde die Spindichte mit einem Isovalue von 0.01 dargestellt.

Kapitel 4: Photophysikalische Eigenschaften von Übergangsmetallkomplexen

Dieses Kapitel behandelt die photophysikalischen Eigenschaften von Übergangsmetallkomplexen mit potentieller Anwendung als OLEDs oder Photosensibilisatoren beziehungsweise zum Verständnis der Komplexeigenschaften. Die Photophysik der Komplexe wird über zeitaufgelöste Step-scan-FTIR-Spektroskopie und Lumineszenzspektroskopie untersucht. Zur Charakterisierung der angeregten Zustände wird der Vergleich mit quantenchemischen Rechnungen herangezogen. Die Messungen werden auch temperaturabhängig durchgeführt, um temperaturabhängiges Verhalten wie TADF zuzuordnen.

4.1 Temperature-Dependent Luminescence Studies on Dinuclear Cu(I) 2-(Diphenylphosphino)Pyridine-Based Complexes Show Thermally Activated Delayed Fluorescence but Studies on Analogous Ag(I) Complexes Do Not

4.1.1 Präambel

In diesem Projekt wurde der Einfluss des Metall- und Halogenidaustauschs innerhalb der zentralen Metall-Halogenideinheit der Komplexe auf die photophysikalischen Eigenschaften untersucht. Die angeregten Zustände und die photophysikalischen Eigenschaften wurden über temperaturabhängige Step-scan-FTIR- und Lumineszenzspektroskopie bestimmt.

Die experimentellen Untersuchungen wurden von Pit Boden und mir durchgeführt. Die Auswertung erfolgte von mir. Wir wurden von Gereon Niedner-Schatteburg betreut.

Florian Rehak hat die quantenchemischen Rechnungen durchgeführt. Er wurde von Wim Klopper betreut. Jasmin Busch hat die Komplexe synthetisiert und wurde von Stefan Bräse betreut. Das Manuskript haben Florian Rehak und Wim Klopper entworfen und der Entwurf wurde von allen Autoren überarbeitet.

4.1.2 Entwurf des Manuskripts und ergänzende Informationen

Im Folgenden ist der erste Entwurf des Manuskripts und die ergänzenden Informationen zu den vom mir erarbeiteten Abschnitten des Projekts aufgeführt.

Temperature-Dependent Luminescence Studies on Dinuclear Cu(I) 2-(Diphenylphosphino)Pyridine-Based Complexes Show Thermally Activated Delayed Fluorescence but Studies on Analogous Ag(I) Complexes Do Not

Florian R. Rehak,^[a] Sophie T. Steiger,^[b] Jasmin M. Busch,^[c] Pit J. Boden,^[b] Martin Nieger,^[d] Marianna Kemell,^[d] Olaf Fuhr,^{[e][f]} Gereon Niedner-Schatteburg,^{*[b]} Stefan Bräse^{*[c][g]}, Wim Klopper^{*[a][e]}

[a] Florian R. Rehak, Wim Klopper

Institute of Physical Chemistry (IPC)
Karlsruhe Institute of Technology (KIT)
Fritz-Haber-Weg 2, 76131 Karlsruhe (Germany)

[b] Sophie T. Steiger, Pit J. Boden, Gereon Niedner-Schatteburg

Chemistry Department and State Research Center Optimas
TU Kaiserslautern
Erwin-Schrödinger-Straße 52, 67663 Kaiserslautern (Germany)

[c] Jasmin M. Busch, Stefan Bräse

Institute of Organic Chemistry (IOC)
Karlsruhe Institute of Technology (KIT)
Fritz-Haber-Weg 6, 76131 Karlsruhe (Germany)

[d] Martin Nieger, Marianna Kemell

Department of Chemistry
University of Helsinki
P.O. Box 55 (A.I. Virtasen aukio 1), FI 00014 University of Helsinki (Finland)

[e] Olaf Fuhr, Wim Klopper

Karlsruhe Institute of Nanotechnology (INT)
Karlsruhe Institute of Technology (KIT)
Hermann-von-Helmholtz-Platz 1, 76344 Eggenstein-Leopoldshafen (Germany)

[f] Olaf Fuhr

Karlsruhe Nano-Micro Facility (KNMF)
Karlsruhe Institute of Technology (KIT)
Hermann-von-Helmholtz-Platz 1, 76344 Eggenstein-Leopoldshafen (Germany)

[g] Stefan Bräse

Institute of Biological and Chemical Systems – Functional Molecular Systems (IBCS-FMS)
Karlsruhe Institute of Technology (KIT)
Hermann-von-Helmholtz-Platz 1, 76344 Eggenstein-Leopoldshafen (Germany)

Dedication: We dedicate this publication to the memory of our late colleague Markus Gerhards in recognition of his long standing devotion for the spectroscopic characterization of molecular complexes with and without involvement of transition-metal centers, which has been pivotal to the present study.

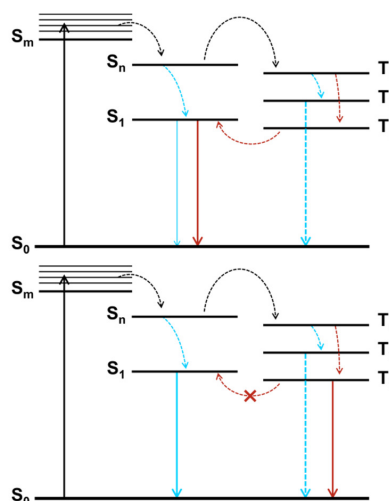
Keywords: Cooperative Effects • Thermally Activated Delayed Fluorescence • Cu(I) Complexes • Ag(I) Complexes • NP-bridging ligand • 2-(Diphenylphosphino)pyridine (PyrPhos) • GW Approximation • Bethe-Salpeter Equation • Photophysical Studies • UV/Vis Spectra • Step-Scan FTIR Spectroscopy

ABSTRACT: The communication between metal atoms can have an impact on several properties of oligonuclear metal complexes such as the absorption and the photoluminescence output. Therefore, the investigation of cooperative effects is of utmost importance for emitter development and its use in, for example, organic light-emitting diodes (OLEDs). In this study, a quartet of dinuclear monometallic Ag(I) and Cu(I) 2-(diphenylphosphino)pyridine (PyrPhos) complexes of the composition $M_2X_2L_3$ (M = coinage metal Cu, Ag; X = halide, Br, Cl; L = PyrPhos ligand) is investigated to determine the impact of the metal halide core on the UV/Vis spectra and photophysical properties. The literature known Cu(I) complexes $Cu_2Br_2L_3$ and $Cu_2Cl_2L_3$ were resynthesized and complemented by their Ag(I) analogues $Ag_2Br_2L_3$ and $Ag_2Cl_2L_3$. Beyond this, also mixed Cu/Ag complexes were synthesized and confirmed via their crystal structures. Single-crystal X-ray diffraction analyses, IR spectroscopy studies, and quantum-chemical calculations gave information on the electronic ground-state structures of the PyrPhos complexes. Spectroscopic signatures of thermally activated delayed fluorescence (TADF) are observed only for the Cu(I) PyrPhos complexes but not for the Ag(I) analogues. The reason for this may be due to a triplet excited-state structure that is unique to the Ag(I) analogues, as revealed by time-resolved FTIR spectroscopic studies and quantum-chemical calculations at the level of time-dependent density functional theory (TDDFT) as well as at the level of a protocol based on the *GW*-approximation and the correlation-augmented Bethe-Salpeter equation (*GW/cBSE*).

Introduction

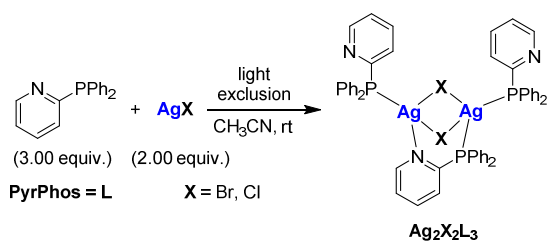
Emission enhancing interactions between metal centers are mostly known and studied of gold complexes.¹⁻⁵ Herein we report on the theoretical and experimental investigation of a set of copper and silver halide complexes to better understand the influence of metal...metal interactions on specific properties of the complexes such as the absorption and the photophysics.

Luminescent complexes based on Cu(I) have gained much attention for their usage in organic light-emitting diodes (OLEDs)⁶⁻¹⁷ besides inter alia their application in light-emitting electrochemical cells (LEECs),¹⁸⁻³⁰ several sensors³¹⁻³⁷ and photoredox catalysis.³⁸⁻⁴⁵ Copper is advantageous compared to the other coinage metals due to its abundance and relatively low costs.^{15, 46} The number of copper atoms varies from mononuclear complexes to clusters depending on the chosen ligand and ratio to copper salt for the synthesis.⁴⁷⁻⁵² Many charged as well as neutral Cu(I) complexes are reported in the literature, whereas for application in OLEDs, non-charged complexes are preferred. During operation, neutral complexes are less likely to migrate through the OLED layers in the direction of the electrodes. Therefore, a blending of the layers as well as losses through non-radiatively decays are minimized and possible shorts are reduced. Dinuclear Cu(I) complexes are relatively stable due to their greater rigidity compared to mononuclear complexes.⁷ The copper atoms can be bridged *via* halides⁵³⁻⁶⁰ and/or an organic ligand.⁶¹⁻⁶² Besides PP-type,⁶³⁻⁶⁴ NN-type⁶⁵⁻⁶⁶ and some NS-type⁶⁷ bridging ligands, NP-type ligands⁶⁸⁻⁷⁰ are commonly used as chelators. A large group of dinuclear Cu(I) complexes based on the NP-type bridging ligand 2-(diphenylphosphino)pyridine (PyrPhos) and derivatives was intensively studied.⁷¹⁻⁷⁹ The luminescence of these complexes as well as of many other Cu(I) complexes is assigned to thermally activated delayed fluorescence (TADF).⁸⁰⁻⁸⁶ By the up-conversion of the triplet excitons to the first excited singlet state (S_1) *via* reverse intersystem crossing (RISC) almost all excitons can be efficiently harvested *via* the S_1 state already at ambient temperature (**Scheme 1**). Therefore, high photoluminescence quantum yields (PLQYs) as well as high electroluminescence efficiencies can be realized. Dinuclear Cu(I) complexes are characterized by their small energy gap between the first two excited states (ΔE_{ST}) and their relatively strong spin-orbit coupling (SOC) in comparison to their mononuclear analogues.⁷ While Cu(I) TADF complexes are widely studied, only few



Scheme 1. Schematic Jablonski diagrams representing the theoretical and experimental findings on the excited state dynamics of the dinuclear Cu(I) and Ag(I) complexes. The upper and lower graphs depict the situation at 290 K and 5 K, respectively. Dashed lines represent non-radiative transitions and solid lines transitions with either absorption or emission of light. Black arrows are valid for all systems, whereas the blue and red arrows are specific for the Ag(I) and Cu(I) complexes, respectively. The thickness of the filled lines reflects the luminescence intensity.

examples of Ag(I) complexes possessing TADF are reported, although Ag(I) is less prone to oxidation and the emission is often blue-shifted.^{11, 87} Mononuclear linear Ag(I) complexes⁸⁸⁻⁹³ as well as complexes with a multiple coordinated Ag(I) atom with halides⁹⁴⁻⁹⁶ or halide-free⁹⁷⁻¹⁰¹ were described as TADF emitters. Regarding dinuclear Ag(I) TADF complexes,¹⁰²⁻¹⁰⁴ only a few examples include halides,¹⁰⁵⁻¹⁰⁶ probably due to the low solubility. In terms of metallophilic interactions between the metal centers, emission enhancing Ag(I)...Ag(I) contacts are stronger compared to Cu(I)...Cu(I) contacts even though Ag(I) and Cu(I) have the same electronic configuration (d^{10}).¹⁰⁷⁻¹⁰⁸ With increasing nuclear charge the relativistic effects



Scheme 2. General synthesis of the dinuclear homometallic Ag(I) PyrPhos complexes $\text{Ag}_2\text{X}_2\text{L}_3$ (X = halide, Br or Cl; L = PyrPhos ligand) in acetonitrile at ambient temperature in the dark.

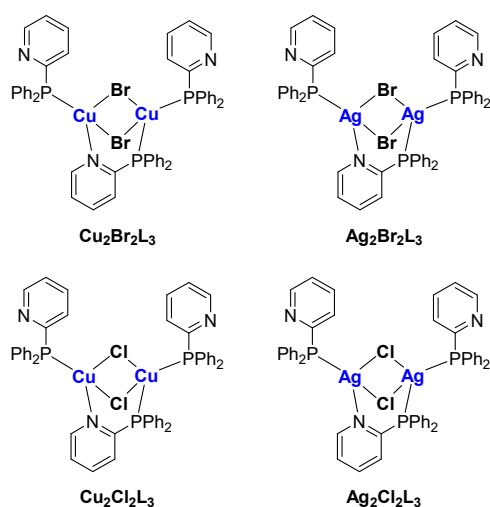


Figure 1. Homoleptic monometallic dinuclear Cu(I) and Ag(I) PyrPhos complexes of the constitution $\text{M}_2\text{X}_2\text{L}_3$ (M = metal, Cu(I) or Ag(I); X = halide, Br or Cl; L = PyrPhos ligand).¹⁰⁹

increase. Therefore, the argentophilic interactions are more pronounced compared to the controversially discussed cuprophilicity, but weaker with respect to aurophilic interactions. An overview of linear arrangements of copper complexes with significant closed-shell $d^{10}\cdots d^{10}$ interactions also in heterometallic combinations with Ag(I) and Au(I) was presented by Stollenz in 2019.¹¹⁰ The first heterometallic Ag(I)/Cu(I) complex was reported by Fackler and co-workers in 1992 based on a Cu_2Ag_2 -core and the bidentate 2-mercaptothiazoline ligand and does not include any halides.¹¹¹ In general, luminescent Ag(I)/Cu(I) complexes presented in the literature so far consist of four or more metal centers in total.¹¹²⁻¹²¹ In this study we focus on PyrPhos based complexes. A dinuclear Ag(I)/Cu(I) complex with a sulfur-containing derivative (diphenyl(1-pyridyl)phosphine sulfide) was reported by Olmos and co-workers in 1997.¹²² While many homometallic Cu(I) complexes of the PyrPhos family are known as stated earlier, homometallic Ag(I) complexes are very rarely described with the PyrPhos ligand.¹²³⁻¹²⁴ To the best of our knowledge, of the dinuclear Ag(I) halide complexes only complex $\text{Ag}_2\text{Cl}_2\text{L}_3$ with the

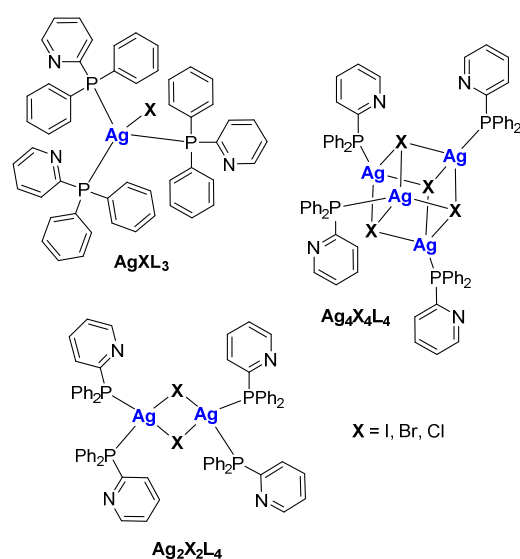


Figure 2. Homoleptic mono-, di- and tetranuclear Ag(I) PyrPhos complexes of the constitution $\text{Ag}_n\text{X}_n\text{L}_n$ (X = halide, Br or Cl; L = PyrPhos ligand) as reference complexes.

PyrPhos ligand (L) is literature known by Alcock and co-workers and was reported already in 1982.¹²⁴ In this work, the quartet of the homoleptic monometallic dinuclear Cu(I) and Ag(I) PyrPhos complexes of the system $\text{M}_2\text{X}_2\text{L}_3$ (with M = Cu(I) and Ag(I), X = Br, Cl, L = PyrPhos ligand)¹²⁵⁻¹²⁶ was used to study the effect of metal exchange (see Figure 1) on the photophysical properties. Additionally, the Cu(I) complex $\text{Cu}_2\text{I}_2\text{L}_3$ was considered to analyse also the influence of halide exchange. From a spectroscopic point of view, the electronic properties were investigated by UV/Vis absorption spectroscopy and temperature-dependent (time-resolved) luminescence spectroscopy in the solid state (KBr matrix) and in solution. Furthermore, transient step-scan FTIR spectroscopy was applied to analyze the structures of the long-lived electronically excited states with lifetimes of nano- and microseconds. This technique has been successfully applied to Cu(I) and Ag(I) complexes in previous works, see for example Wagner *et al.*¹²⁷ and Boden *et al.*¹²⁸ The experimental results were interpreted by comparison to quantum chemical calculations at various levels of theory using density functional theory (DFT), time-dependent DFT (TDDFT) and eigenvalue-only self-consistent *GW* plus correlation-augmented Bethe-Salpeter equation (ev*GW*/cBSE).

Results and Discussion

Complex Synthesis. The syntheses of the dinuclear homometallic PyrPhos Cu(I) complexes $\text{Cu}_2\text{X}_2\text{L}_3$ (with L = PyrPhos ligand, X = I, Br, Cl) were performed according to the literature procedure of Zink and co-workers in dichloromethane (DCM) at ambient temperature.⁶² So far, one synthesis protocol that

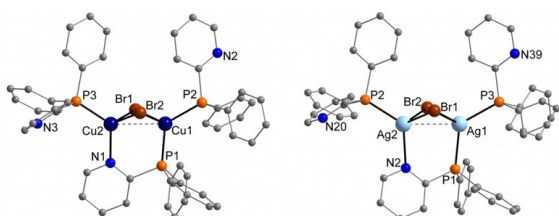


Figure 3. Molecular structures of the dinuclear homometallic bromide PyrPhos complexes with Cu(I), $\text{Cu}_2\text{Br}_2\text{L}_3$ (left) and Ag(I), $\text{Ag}_2\text{Br}_2\text{L}_3$ (right).

lead to a crystal of the Ag(I) complex $\text{Ag}_2\text{Cl}_2\text{L}_3$ (CCDC-1107453) was described in literature by Alcock and co-workers.¹²⁴ The crystal was obtained from a reaction of the PyrPhos ligand with freshly prepared silver chloride (2:1 ratio) in ethanol after heating to reflux for 8 h in the dark, followed by hot filtration and recrystallization of the deposited polycrystalline solid of the filtrate in a 1:1:1 mixture of chloroform, benzene and diethyl ether. Therefore, stoichiometric amounts of the PyrPhos ligand (3.00 equiv.) and commercially available silver chloride (2.00 equiv.) were reacted in ethanol at 80 °C for 8 h under light exclusion. The solid of the suspension was filtered off hot and the clear filtrate was stored at 0 °C. A colorless solid deposited over time. According to the elemental analysis results, the CHN-values found for the precipitate of the filtrate correlate with a 3:1 ratio of the PyrPhos ligand to silver chloride, while the CHN-values found for the filter cake show a 1:1 ratio of ligand to silver salt. In conclusion, complex $\text{Ag}_2\text{Cl}_2\text{L}_3$ is not the favored species in the reaction with the tested conditions. The equivalent reaction in acetonitrile at 90 °C also gave CHN-values of the elemental analysis of the filter cake that fit best with a 1:1 PyrPhos:AgCl ratio. The reaction conditions of acetonitrile, ambient temperature and light exclusion were the expedient parameters for the syntheses of the Ag(I) complexes $\text{Ag}_2\text{Cl}_2\text{L}_3$ and $\text{Ag}_2\text{Br}_2\text{L}_3$ (Scheme 2). The complexes $\text{Ag}_2\text{Br}_2\text{L}_3$ and $\text{Ag}_2\text{Cl}_2\text{L}_3$ were obtained as colorless powders in contrast to their Cu(I) analogues that have pale yellow colors. The iodide analogue $\text{Ag}_2\text{I}_2\text{L}_3$ was not accessible using the same reaction conditions (CH_3CN , rt) as described for the bromide and chloride complexes. The ratios 1:1 and 3:1 for the PyrPhos ligand and the silver halide found in the elemental analysis measurements of the experiments described in the previous section correspond with the composition of the complexes AgClL_3 and $\text{Ag}_4\text{Cl}_4\text{L}_4$, respectively. This assumption could be proved by single crystal X-ray diffraction analyses (compare next chapter and Supplemental Information (SI), Figure S10 and Figure S15).

Mononuclear Ag(I) complexes of this composition are so far only literature known with triphenylphosphine and its methylated analogues instead of the PyrPhos ligand.¹²⁵⁻¹²⁶ The tetranuclear complex $\text{Ag}_4\text{Cl}_4\text{L}_4$ was also reported by Inoguchi and co-workers earlier.¹⁰⁹ These mono- (AgXL_3) and tetranuclear Ag(I) complexes ($\text{Ag}_4\text{X}_4\text{L}_4$) were synthesised directly as reference complexes (Figure 2). Also dinuclear Ag(I) PyrPhos complexes of the composition $\text{Ag}_2\text{X}_2\text{L}_3$ are possible as proved by single-crystal X-ray diffraction analysis for the chloride

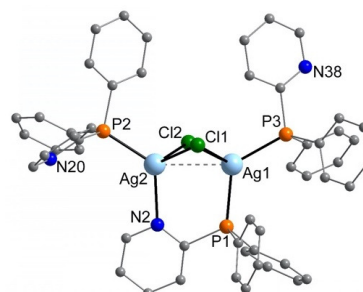


Figure 4. Molecular structure of the homometallic Ag(I) PyrPhos complex $\text{Ag}_2\text{Cl}_2\text{L}_3$, redetermination of BEBGEU at 123 K.¹²⁴ All positions of the nitrogen atoms of the PyrPhos ligands in the dinuclear Ag(I) complex could be assigned.

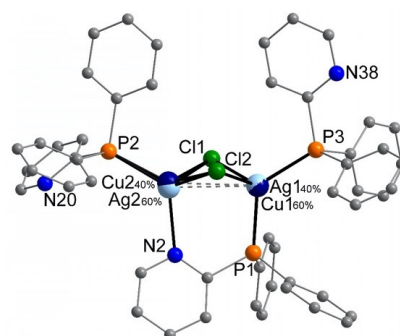


Figure 5. Molecular structure of the heterometallic Ag(I)/Cu(I) PyrPhos complex with chloride, $\text{MM}'\text{Cl}_2\text{L}_3$ (with M, M' = Cu(I) or Ag(I)). The Ag:Cu ratios are given in %.

containing complex $\text{Ag}_2\text{Cl}_2\text{L}_4$ (see Figure S7 and Table S1 in the SI). A similar structural motif, the Ag_2Cl_2 -core coordinated to four phosphorus atoms of two PP-type ligands, was reported by Yersin and co-workers in 2014 and a bromide analogue by Osawa and co-workers in 2017.¹²⁹⁻¹³¹ However, the direct synthesis of the $\text{Ag}_2\text{X}_2\text{L}_4$ complexes with stoichiometric amounts of the starting materials and the reaction conditions used for the synthesis of the other PyrPhos complexes (DCM, rt; CH_3CN , rt and CH_3CN , 90 °C) was not successful. In general, the formation of the tetranuclear Ag(I) PyrPhos complexes was favored at high temperatures. Furthermore, the synthesis of heterometallic Ag(I)/Cu(I) PyrPhos complexes $\text{MM}'\text{X}_2\text{L}_3$ (with M = Cu(I), M' = Ag(I)) was investigated. In DCM at ambient temperature in the dark the reaction of stoichiometric amounts of the PyrPhos ligand with the copper and the silver halide (3:1:1 ratio) resulted in a suspension that consisted of a colorless solid ($\text{Ag}_4\text{X}_4\text{L}_4$) and a yellow solution ($\text{Cu}_2\text{X}_2\text{L}_3$). Therefore, acetonitrile was the solvent of choice for the synthesis of the heterometallic Ag(I)/Cu(I) PyrPhos complexes as well as for the homometallic Ag(I) complexes as described earlier in the text. The reactions were performed at ambient temperature as well as at 90 °C. The obtained CHN-values of the

Table 1. Different types of bi- and/or monometallic structures for position 1 (M(P/N)) and position 2 (M(P/P)) possible in PyrPhos complex $MM'Cl_2L_3$.

Type	M(P/N)	Occupancy M(P/N) [%]	M(P/P)	Occupancy M(P/P) [%]
Type 1	Ag	20 + x	Cu	20 + x
Type 2	Cu	x	Ag	x
Type 3	Ag	40 - x	Ag	40 - x
Type 4	Cu	40 - x	Cu	40 - x

elemental analyses are in agreement with the expected CHN-values for the heterometallic Ag(I)/Cu(I) PyrPhos complexes. Heterometallic structures $MM'X_2L_3$ could be proved by single crystal X-ray diffraction analysis (compare Figure 5, the next chapter as well as SI Figure S16 to Figure S19). However, the Ag:Cu ratio in the crystals of the PyrPhos complexes was not consistent and therefore only the molecular structures of the heterometallic Ag(I)/Cu(I) PyrPhos complexes and corresponding energy-dispersive X-ray (EDX) spectra are presented.

With the complete quartet of the homobimetallic copper complexes $Cu_2Br_2L_3$ and $Cu_2Cl_2L_3$ as well as the analogues silver complexes $Ag_2Br_2L_3$ and $Ag_2Cl_2L_3$ in hand, UV/Vis absorption spectroscopy, (time-resolved) luminescence studies as well as transient step-scan FTIR spectroscopy were performed for comparison with the theoretical findings on the effect of metal exchange. Beyond this, the complex $Cu_2I_2L_3$ was considered for the analysis of halide substitution.

Molecular Structure Determination. The PyrPhos complexes based on Cu(I) and Ag(I) were characterised *via* single crystal X-ray diffraction analyses (see SI for details). For the investigation of the heterometallic Ag(I)/Cu(I) PyrPhos complexes $MM'X_2L_3$ (with $M/M' = Cu(I)/Ag(I)$) additional scanning electron microscopy with energy dispersive X-ray analyses (SEM-EDX) were performed to determine the Ag:Cu ratios of the samples in advance (see Experimental Section and SI).

The pair of the two dinuclear monometallic bromide PyrPhos complexes $Cu_2Br_2L_3$ and $Ag_2Br_2L_3$ is shown in Figure 3. The molecular structure of the copper chloride analogue $Cu_2Cl_2L_3$ is not presented because the structural data were reported in a previous study.⁶² A redetermination of complex $Ag_2Cl_2L_3$ made it possible to assign all positions of the nitrogen atoms of the PyrPhos ligands in the dinuclear Ag(I) complex (Figure 4 and Table S1).¹²⁴ The pyridines of the ancillary PyrPhos ligands coordinated only *via* the phosphorus atom to the metal are pointing in the same directions in all four complexes of this set. In contrast, both pyridines of the ancillary PyrPhos ligands are pointing into the opposite direction of the bridging PyrPhos ligand in the copper iodide complex $Cu_2I_2L_3$ (CCDC-838846) reported in a previous study.⁶² The equal configuration of the PyrPhos ligands is found in the corresponding heterometallic Ag(I)/Cu(I) iodide based complex $MM'I_2L_3$ (with

Table 2. Overview of the metal-metal (MM) and metal-halide (MX) bond lengths in increasing order in the different homometallic $M_2X_2L_3$ PyrPhos complexes with $M = Cu$ or Ag and $X = Br$ or Cl (molecular structures and theory (CAM-B3LYP/def2-TZVP)) and in the pure metal halides as starting materials (start. mat.).¹³²

Complex	MM [Å] X-ray	MX [Å] X-ray	MM [Å] theory	MX [Å] theory	MX [Å] start. mat.
$Cu_2Br_2L_3$	2.896	2.523	2.82	2.52	2.49
		2.532		2.56	
		2.554		2.56	
		2.568		2.57	
		2.544		2.55	
average	2.544	2.55			
$Cu_2Cl_2L_3$	2.878	2.389	2.82	2.38	2.34
		2.395		2.42	
		2.426		2.43	
		2.436		2.44	
		2.412		2.41	
average	2.412	2.41			
$Ag_2Br_2L_3$	3.030	2.722	3.28	2.69	2.89
		2.741		2.70	
		2.745		2.82	
		2.788		2.82	
		2.749		2.75	
average	2.749	2.75			
$Ag_2Cl_2L_3$	3.050	2.615	3.26	2.58	2.77
		2.620		2.60	
		2.652		2.70	
		2.688		2.70	
		2.644		2.64	
average	2.644	2.64			

$M/M' = Cu(I)/Ag(I)$, Figure S16 and Table S1). In the heterometallic PyrPhos complexes with bromide and chloride the same configuration of the PyrPhos ligands as for the quartet is found. Figure 5 shows complex $MM'Cl_2L_3$ (with $M/M' = Cu(I)/Ag(I)$) exemplarily (compare also Figure S19, Table S1 and EDX measurements Figure 15 and Table 4 of the Experimental Section). EDX measurements of PyrPhos complex $MM'Cl_2L_3$ were made from a large area to obtain an average composition and from points to find out compositional variations. The Cu:Ag molar ratio varied from point to point, being between 0.6:1 and 2:1 (see Experimental Section and SI for detailed information). In the selected crystal (representative for the sample, see EDX measurements), used for the single crystal X-ray diffraction analysis, the Ag:Cu ration is determined as 1:1 deviated from the free refinement of the occupancies of Ag and Cu at position 1 (M(N/P)) and position 2 (M(P/P) at the isotropic stage of the refinement and then fixed for the anisotropic refinement (see cif-file for details). The structure is a $MM'Cl_2L_3$ complex (M (position 1) = Ag or Cu and

M' (position 2) = Ag or Cu). Structure and geometrical parameters are in the expected range for $MM'X_2L_3$ structures. Due to the disorder of the Ag(I) and Cu(I) atoms there are four types of bi- and/or monometallic structures for position 1 (M(P/N) and position 2 (M(P/P) possible (type 1: Ag(P/N) / Cu(P/P), type 2: Cu(P/N) / Ag(P/P), type 3: Ag(P/N) / Ag(P/P), type 4: Cu(P/N) / Cu(P/P), compare **Table 1**). All permutation types of complex $MM'Cl_2L_3$ are shown in the SI (**Figure S19**). Our experiments for the formation of $MM'X_2L_3$ complexes show that the monometallic complexation is preferred, formation of the $Ag_2Cl_2L_3$ (type 3) or $Cu_2Cl_2L_3$ (type 4) complexes with a maximum occupancy of 40% each. For the bimetallic complexes the formation of the type 1 complexes $AgCuCl_2L_3$ are preferred (minimum occupancy 20%). This is in good correlation with the results found in the two molecular structures of $MM'Br_2L_3$ (**Figure S17** and **Figure S18**) and the molecular structure of $MM'I_2L_3$ (**Figure S16** and **Table S1**). In complex $MM'Br_2L_3$ (with a general excess of Ag) the occupancy at position 1 is determined as Ag:Ag' 95:5 and as Ag:Cu 75:25 at position 2. In complex $M_2Br_2L_3$ (with a general excess of Cu) the occupancy at position 1 is determined as Ag:Cu 15:85 and at position 2 as Ag:Cu 10:90. The molecular structure and all permutation types of the complexes $MM'Br_2L_3$ are presented in the SI (see **Figure S17**, **Figure S18**, **Table S1** and EDX measurements **Figure S21** to **Figure S35** and **Table S3** to **Table S7**). In the iodide complex $MM'I_2L_3$ the occupancy at position 1 is determined as Ag:Cu 35:65 (see SI **Figure S16**). A bimetallic complex of type 2 is less probable. With increasing occupancy of the type 2 complex also the occupancy of the type 1 is increasing, while the occupancies of type 3 and type 4 complexes are decreasing by the same ratio. In general, the separation of the two bimetallic isomers $AgCuX_2L_3$ and $CuAgX_2L_3$ was not possible. The PyrPhos complexes are hardly soluble in any solvent due to the silver in combination with the halides. In comparison, the chloride PyrPhos complexes have the highest solubility of the halide series $Cl > Br > I$ (compare also next chapter, solubility study). In accordance, PyrPhos complex $MM'Cl_2L_3$ has the highest silver occupancy at position 1 and 2 balanced with copper. The molecular structures of the Ag(I) reference complexes (**Figure 2**) are presented in the SI. The whole set of the mononuclear $AgXL_3$ PyrPhos complexes (with $X = I, Br, Cl$) was obtained (**Figure S8**, **Figure S9**, **Figure S10** and **Table S1**) as well as an iodide containing structure MIL_3 with $M = Cu(I)$ and $Ag(I)$ in a ratio of 1:1 (**Figure S20**, **Table S1** and EDX measurements **Figure S38** to **Figure S43** and **Table S9** to **Table S10**). Also the tetranuclear structures of complex $Ag_4I_4L_4$ (**Figure S13** and **Table S1**), $Ag_4Br_4L_4$ (**Figure S14** and **Table S1**), and complex $Ag_4Cl_4L_4$ (**Figure S15** and **Table S1**), which correspond with a 1:1 ratio of the PyrPhos ligand to silver halide found in the elemental analyses, could be determined including the positions of all nitrogen atoms. In the mononuclear as well as in the tetranuclear Ag(I) complexes, all PyrPhos ligands are coordinated *via* the phosphorus atom to the metal. The silver halide core Ag_4X_4 of the tetranuclear PyrPhos complexes $Ag_4X_4L_4$ has a cubane shape. So far we did not observe any chair-like structures of the tetranuclear Ag(I) PyrPhos complexes as reported for silver halide

Table 3. Solubility of the Cu(I) and Ag(I) PyrPhos (L) complexes in various solvents (*n*-Hex = *n*-hexane, Tol = toluene, EtOH = ethanol, MCB = chlorobenzene, DCM = dichloromethane, CH_3CN = acetonitrile). The classification of the solubility was determined at ambient temperature.

Complex	<i>n</i> -Hex	Tol	EtOH	MCB	DCM	CH_3CN
$Cu_2I_2L_3$	--	--	--	--	-	--
$Cu_2Br_2L_3$	--	--	--	--	-	--
$Cu_2Cl_2L_3$	--	--	--	--	++	--
$Ag_2Br_2L_3$	--	--	--	--	-	--
$Ag_2Cl_2L_3$	--	--	--	-	+	--
$CuBrL_3$	--	--	--	--	++	--
$CuClL_3$	--	-	-	++	++	-
$AgIL_3$	--	--	--	-	+	--
$AgBrL_3$	--	--	--	-	++	--
$AgClL_3$	--	-	-	++	++	-
$Ag_4I_4L_4$	--	--	--	--	--	--
$Ag_4Br_4L_4$	--	--	--	--	--	--
$Ag_4Cl_4L_4$	--	--	--	--	-	--
PyrPhos	-	++	++	++	++	++

complexes with the triphenylphosphine analogue as ligand by Teo and co-workers.¹²⁹⁻¹³¹ The bond lengths of the molecular structures of the dinuclear monometallic PyrPhos complexes with $M = Cu$ or Ag and $X = Br$ or Cl as well as the values found for the calculated structures are given in **Table 2**. The values for the metal-halide (MX) distances of the pure metal halides were taken from the report of Ono and co-workers to complete the data.¹³²

Solubility Study. The solubilities of the different mono-, bi- and tetrametallic Cu(I) and Ag(I) PyrPhos complexes were classified in various solvents (**Table 3**). *n*-Hexane (*n*-Hex), toluene (Tol), ethanol (EtOH), chlorobenzene (MCB), dichloromethane (DCM) and acetonitrile (CH_3CN) were investigated with the metal complex samples at ambient temperature. The solubility of the homoleptic Cu(I) and Ag(I) PyrPhos complexes is relatively low compared to various other homo- and heteroleptic Cu(I) complexes bearing at least one NP-bridging ligand with additional substituents on the pyridine, such as methyl or *tert*-butyl.^{72,77} Almost none of the Cu(I) and Ag(I) complexes in this study showed a solubility higher than 1 mg mL^{-1} in *n*-hexane, toluene, ethanol and acetonitrile. The solubility of the metal complexes in dichloromethane and in chlorobenzene increased in the relation to the size of the corresponding halide, $Cl > Br > I$. Monometallic Cu(I) and Ag(I) complexes MXL_3 are far more soluble in the chlorinated solvents compared to the dimetallic complexes $M_2X_2L_3$, while the tetrametallic complexes $M_4X_4L_4$ are hardly soluble at all. In general, the solubility of the Cu(I) complexes was similar or higher compared to the corresponding Ag(I) complexes.

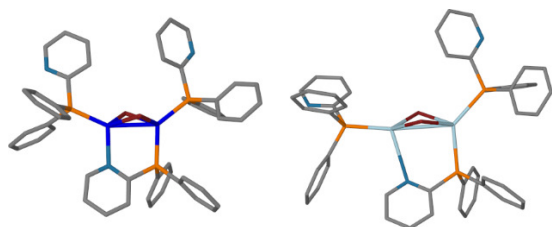


Figure 6. Calculated S_0 structure of $\text{Cu}_2\text{Br}_2\text{L}_3$ (left) and $\text{Ag}_2\text{Br}_2\text{L}_3$ (right) optimized with CAM-B3LYP/def2-TZVP (def2-SV(P) for hydrogen). $\text{Cu}_2\text{Br}_2\text{L}_3$ shows eclipsed conformation with respect to the pyridine groups of the ancillary ligands while $\text{Ag}_2\text{Br}_2\text{L}_3$ shows gauche conformation. Hydrogen atoms omitted for clarity.

Quantum-Chemical Computations. Structure optimizations of the ground state (S_0) of the dinuclear monometallic Cu(I) and Ag(I) complexes at the CAM-B3LYP/def2-TZVP (only def2-SV(P) for hydrogen) level of theory were carried out (Figure 6 and S44). The calculated average metal-halide bond length is in excellent agreement within $\pm 0.01 \text{ \AA}$ for all four complexes. The metal-metal bond lengths of $\text{Cu}_2\text{Br}_2\text{L}_3$ and $\text{Cu}_2\text{Cl}_2\text{L}_3$ show good agreement (within $\pm 0.07 \text{ \AA}$) with the X-ray structures but for $\text{Ag}_2\text{Br}_2\text{L}_3$ and $\text{Ag}_2\text{Cl}_2\text{L}_3$, the metal-metal bond length is overestimated by about 0.2 \AA (Table 2). Furthermore, the left ancillary ligand is rotated along the P-Ag bond when compared to the X-ray structure (see Figure 6 and S44). To verify that the orientation of the left ancillary ligand does not lead to different ground-state structures, structure optimizations of $\text{Ag}_2\text{X}_2\text{L}_3$ starting at the S_0 structure of $\text{Cu}_2\text{X}_2\text{L}_3$ (substituting Cu by Ag therein), and vice versa were carried out, but only the already known structures were obtained (Table S14). For convenience, the orientation of the pyridine group of the left ancillary ligand with respect to the pyridine group of the right ancillary ligand is denoted as “eclipsed” for S_0 of $\text{Cu}_2\text{X}_2\text{L}_3$ and “gauche” for S_0 of $\text{Ag}_2\text{X}_2\text{L}_3$ (Figure 6 and Table S13). For $\text{Cu}_2\text{Br}_2\text{L}_3$ and $\text{Cu}_2\text{Cl}_2\text{L}_3$, two different S_1 and two different T_1 structures with eclipsed conformation of the PyrPhos ligands were located using TDDFT. They were termed “open” and “closed butterfly” with respect to their X-M-M-X dihedral angle, which was found at a 150° and 120° , respectively, see Figure 7 and Table S12. Interestingly, in previous work on tetranuclear Cu(I) complexes,¹²⁸ the motif of closed and open butterfly structures had been found, too. As in this previous work, the closed butterfly T_1 structure is more stable by 10.7 and 10.1 kJ/mol for $\text{Cu}_2\text{Br}_2\text{L}_3$ and $\text{Cu}_2\text{Cl}_2\text{L}_3$, respectively (Figure 8). The reaction paths for the transitions of the open to the closed butterfly structures were roughly estimated by calculating the energy along a path that interpolated linearly between the two minima. These estimates are 128 and 156 kJ/mol for $\text{Cu}_2\text{Br}_2\text{L}_3$ and $\text{Cu}_2\text{Cl}_2\text{L}_3$, respectively. Such high values can be understood in terms of the concerted motion required for this transition. The open butterfly structure starts closing, pushing the pyridine groups of the ancillary PyrPhos ligands outwards (compare Figure 9 top left and right), causing the respective phenyl groups to free up space by pushing on the bridging PyrPhos ligand. Hence, closing the butterfly requires a rather

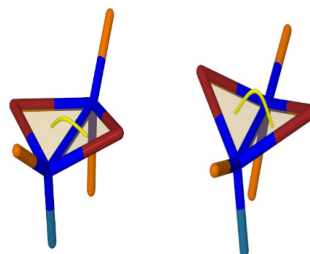


Figure 7. Visualization of open (left) and closed (right) butterfly structure motif of $\text{Cu}_2\text{Br}_2\text{L}_3$.

large amount of energy due to the concerted motion within the molecule and the transition between these two structures becomes unlikely. Using *evGW*/cBSE-CAM-B3LYP the lowest excitation at the open and closed butterfly T_1 and S_1 structures of $\text{Cu}_2\text{Br}_2\text{L}_3$ and $\text{Cu}_2\text{Cl}_2\text{L}_3$ shows M/XLCT character (Figure 9, S45 and S46). The respective singlet-triplet gap ΔE_{ST} for $\text{Cu}_2\text{Br}_2\text{L}_3$ in open and closed butterfly is 193 and 109 meV, respectively, and for $\text{Cu}_2\text{Cl}_2\text{L}_3$ 145 and 195 meV (Table S15). The structural similarity of the open and closed butterfly structures does not allow to distinguish between the two by comparison of their calculated IR spectrum with the experimental excited state spectrum, as shown for $\text{Cu}_2\text{Br}_2\text{L}_3$ in Figure S72. However, both are suitable for TADF due to the M/XLCT character of the lowest excitation and a ΔE_{ST} between 0.1 and 0.2 eV.

The closed butterfly T_1 and S_1 structures in eclipsed conformation with M/XLCT character for the first excitation were also found for $\text{Ag}_2\text{Br}_2\text{L}_3$ and $\text{Ag}_2\text{Cl}_2\text{L}_3$ (Figure 9, S45 and S47). With ΔE_{ST} being even lower than for the Cu analogues with 97 and 96 meV for $\text{Ag}_2\text{Br}_2\text{L}_3$ and $\text{Ag}_2\text{Cl}_2\text{L}_3$, respectively (Table S15). But in contrast to $\text{Cu}_2\text{X}_2\text{L}_3$ the closed butterfly T_1 structures are not the lowest in energy, as the open butterfly with eclipsed conformation is more stable by 5.0 and 2.3 kJ/mol for $\text{Ag}_2\text{Br}_2\text{L}_3$ and $\text{Ag}_2\text{Cl}_2\text{L}_3$, respectively (Figure 8) and shows also M/XLCT character for the first triplet excitation, see Figure 9. In contrast to these T_1 states, the respective M/XLCT* S_1 state shows a charge transfer to the left ancillary ligand instead of a charge transfer to the bridging PyrPhos (Figures 8, 9 and S45). Therefore, due to different S_1 and T_1 characters, TADF will not occur from the open-eclipsed T_1 state. The closed butterfly motifs of $\text{Ag}_2\text{Br}_2\text{L}_3$ and $\text{Ag}_2\text{Cl}_2\text{L}_3$, however, show the required small energy gap ΔE_{ST} and proper M/XLCT character for TADF, but in the spectroscopic experiment, no TADF was observed. This could be rationalized by a third T_1 structure that was found only for $\text{Ag}_2\text{Br}_2\text{L}_3$ and $\text{Ag}_2\text{Cl}_2\text{L}_3$. This structure can be classified as “open butterfly in gauche conformation” and is extremely similar to the respective ground-state S_0 structure. The metal-metal distance, the X-M-M-X dihedral angle and the gauche conformation show only minor changes when going from the open-gauche S_0 to the open-gauche T_1 structure (Table S11, S12 and S13). The open butterfly with gauche conformation is the least stable, being 17.7 and 19.4 kJ/mol higher in energy when compared to the most stable open butterfly structure in eclipsed conformation. A transition between the three different T_1 structures is not

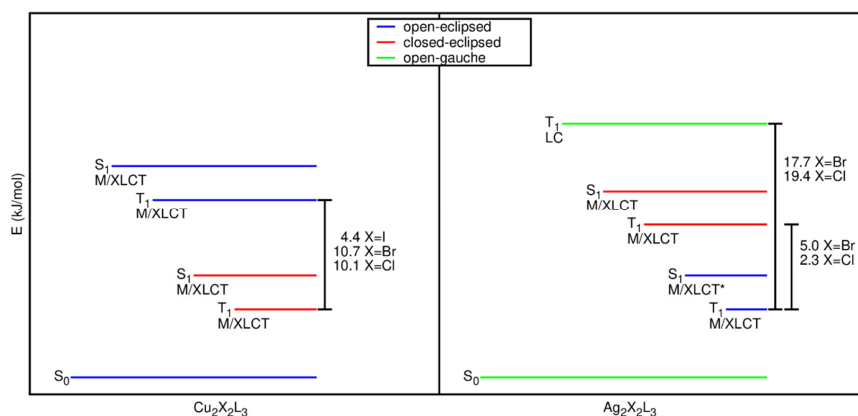


Figure 8. Schematic overview about the various excited states found for $\text{Cu}_2\text{X}_2\text{L}_3$ and $\text{Ag}_2\text{X}_2\text{L}_3$ ($\text{X} = \text{I}, \text{Br}, \text{Cl}$). The term open/closed corresponds to a X-M-M-X dihedral angle of around 150° or 120° while eclipsed/gauche corresponds to the conformation of the pyridine groups of the left and right ancillary ligand. Charge transfer from the metal-halide core to the bridging ligand (M/XLCT), to an ancillary ligand (M/XLCT*) and ligand-centered (LC) excitations are indicated. Energy differences between the different T_1 structures are given.

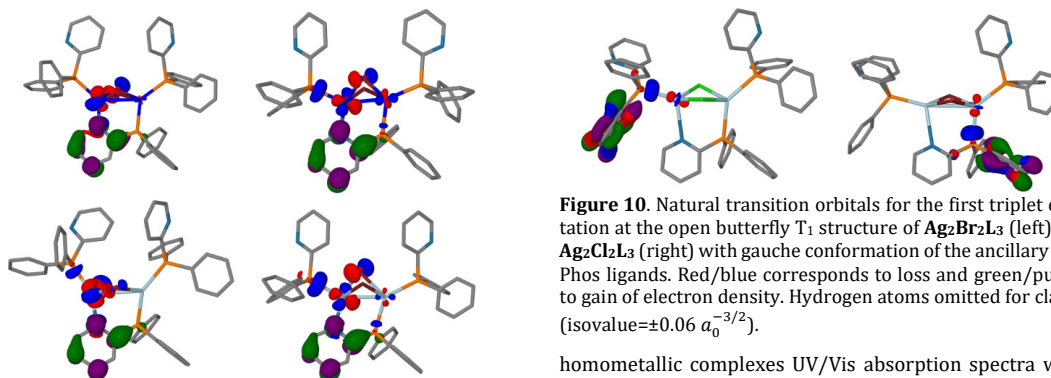


Figure 9. Natural transition orbitals for the first triplet excitation at the T_1 structure of $\text{Cu}_2\text{Br}_2\text{L}_3$ (top) and $\text{Ag}_2\text{Br}_2\text{L}_3$ (bottom) with open (left) and closed (right) butterfly. Red/blue corresponds to loss and green/purple to gain of electron density. Hydrogen atoms omitted for clarity (isovalue = $\pm 0.06 a_0^{-3/2}$).

likely, because the estimates of the theoretical barrier heights are above 167 kJ/mol (Table S15). Additionally, the lowest triplet state at the open butterfly in gauche conformation has LC character, see Figure 10, and shows the best agreement with experimental IR spectra for $\text{Ag}_2\text{Br}_2\text{L}_3$ (Figure S81). All of this leads to the hypothesis that in our experiments, $\text{Ag}_2\text{X}_2\text{L}_3$ gets trapped in a triplet excited-state structure similar to the open butterfly in gauche conformation. This state and structure are unsuitable for TADF and a transition to other excited states is inhibited due to high barriers in between.

UV/Vis Absorption Studies. To gain further insight into the photophysical properties of the dinuclear,

Figure 10. Natural transition orbitals for the first triplet excitation at the open butterfly T_1 structure of $\text{Ag}_2\text{Br}_2\text{L}_3$ (left) and $\text{Ag}_2\text{Cl}_2\text{L}_3$ (right) with gauche conformation of the ancillary PyrPhos ligands. Red/blue corresponds to loss and green/purple to gain of electron density. Hydrogen atoms omitted for clarity (isovalue = $\pm 0.06 a_0^{-3/2}$).

homometallic complexes UV/Vis absorption spectra were recorded in solution (DCM and EtOH) and in the solid state (powder of the complex diluted with KBr, Figure S53). Independent of the medium, the spectra are unstructured and the absorption onsets of the dinuclear monometallic Ag(I) complexes are blue-shifted by approx. 75 nm compared to the Cu(I) homologues. The absorption of the PyrPhos ligand is further blue-shifted by approx. 30 nm relative to the Ag(I) systems. In general, the solid-state spectra are red-shifted by approx. 50 nm compared to the absorption in solution. Furthermore, it should be mentioned that the halide substitution has no significant influence on the UV/Vis absorption. For comparison and interpretation, *evGW/cBSE* calculations using the def2-TZVP basis set were performed in the gas phase for the five abovementioned complexes (Figures 11, S48, S49). The calculated absorption onsets are in good agreement with the experimental findings and in particular the relative shift between the Ag(I) as well as Cu(I) complexes is very well described (Figure 11). The lowest energy vertical excitation is assigned to an M/XLCT transition from the M_2X_2 cluster to the pyridine ring of the

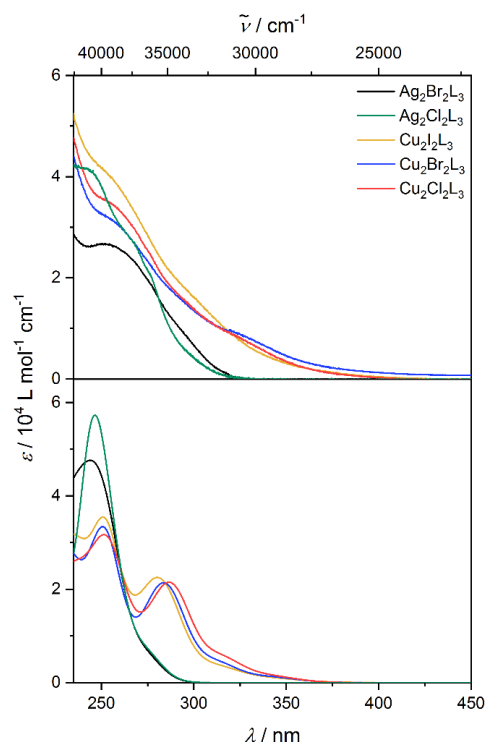


Figure 11. Experimental UV/Vis absorption spectra of $\text{Ag}_2\text{Br}_2\text{L}_3$, $\text{Ag}_2\text{Cl}_2\text{L}_3$, $\text{Cu}_2\text{I}_2\text{L}_3$, $\text{Cu}_2\text{Br}_2\text{L}_3$ and $\text{Cu}_2\text{Cl}_2\text{L}_3$ in DCM (upper trace) and calculated spectra (lower trace, *evGW/cBSE-CAM-B3LYP*). Broadened by Gaussians with full width at half maximum (FWHM) of 2500 cm^{-1} .

bridging ligand and the ancillary ligand, for the Cu(I) and Ag(I) systems, respectively (Figure S50). Ligand-centered transitions strongly contribute to the UV absorption at $\lambda \leq 300\text{ nm}$, which is confirmed by the experimental spectrum of the PyrPhos ligand (Figure S51). As expected, the excitation spectra measured of KBr pellets at 5 K and 290 K under consideration of the respective emission maximum (cf. luminescence studies) show effects that are similar to the solid-state UV/Vis absorption spectra obtained from powder samples (Figures S54 and S55).

Luminescence Studies. Luminescence investigations in different media were performed on the mentioned quartet of monometallic dinuclear Cu(I) and Ag(I) complexes ($\text{Cu}_2\text{Br}_2\text{L}_3$, $\text{Cu}_2\text{Cl}_2\text{L}_3$, $\text{Ag}_2\text{Br}_2\text{L}_3$, $\text{Ag}_2\text{Cl}_2\text{L}_3$) as well as on $\text{Cu}_2\text{I}_2\text{L}_3$ to study the influence of metal and halide substitutions on the luminescence properties.

The luminescence properties of the dinuclear Cu(I) complexes $\text{Cu}_2\text{I}_2\text{L}_3$, $\text{Cu}_2\text{Br}_2\text{L}_3$, and $\text{Cu}_2\text{Cl}_2\text{L}_3$ as neat powder samples at ambient temperature were reported previously.^{62, 71} $\text{Cu}_2\text{I}_2\text{L}_3$ showed the highest PLQY (81%) and the most blue-shifted emission (537 – 539 nm) of this series (36 – 70% PLQY, 545 – 550 nm for $\text{Cu}_2\text{Br}_2\text{L}_3$ and 24 – 37% PLQY, 569 – 577 nm for $\text{Cu}_2\text{Cl}_2\text{L}_3$, slightly depending on the experimental conditions).^{62, 71} However, luminescence data at temperatures down to $\leq 5\text{ K}$ are so far only available for

powder samples of $\text{Cu}_2\text{I}_2\text{L}_3$.⁷¹ For comparative studies under identical experimental conditions on all five mentioned complexes, we conducted static and time-resolved emission spectroscopy at temperatures of 290 – 5 K by preparing the samples as KBr pellets. The KBr matrix has the advantage that all systems show a sufficient photochemical stability and the sample preparation is very well reproducible, which is crucial for the herein presented comparisons that include also quantitative discussion. In the KBr matrix at 290 K, the emission spectra of $\text{Cu}_2\text{I}_2\text{L}_3$ and $\text{Cu}_2\text{Br}_2\text{L}_3$ are almost identical with a luminescence maximum at 533 nm. In contrast, the chloride analogue $\text{Cu}_2\text{Cl}_2\text{L}_3$ has a red-shifted luminescence centered at 556 nm, similar to the literature reports (Figure S56).^{62, 71} Thus, it can be concluded that the luminescence properties of the Cu(I) complexes are slightly influenced by the bridging halides.

The temperature-dependent luminescence investigations in a KBr matrix on the three Cu(I) complexes at 290 – 5 K revealed a red-shift of the emission maximum at low thermal energy (240 cm^{-1} ; 590 cm^{-1} and 550 cm^{-1} for $\text{Cu}_2\text{I}_2\text{L}_3$, $\text{Cu}_2\text{Br}_2\text{L}_3$ and $\text{Cu}_2\text{Cl}_2\text{L}_3$, respectively), similar to the observations on powder samples in previous works (Figures 12, S58 and S59).^{62, 71, 133} The red-shift is characteristic for a TADF mechanism and is accompanied by a slight increase of the luminescence intensity at low temperature, which is explained by the suppression of non-radiative deactivation pathways at low thermal energy. Next to the static emission spectra, the average luminescence lifetimes τ_{av} strongly increase at low temperature with values of 38 μs , 150 μs and 110 μs at 5 K for $\text{Cu}_2\text{I}_2\text{L}_3$, $\text{Cu}_2\text{Br}_2\text{L}_3$ and $\text{Cu}_2\text{Cl}_2\text{L}_3$, respectively (Table S17). These decay constants of over 100 μs are assigned to pure phosphorescence. At the same time, the average time constants at 290 K amount to 5.9 μs , 10.0 μs and 8.6 μs in the same order, which are attributed to TADF. The temperature-dependent behavior of τ_{av} between 290 K and 5 K with a strong increase between approx. 250 K and 100 K is characteristic for a TADF mechanism (Figures S60–S62).^{58, 71} A plateau is reached below 100 K, before the emission again sharply increases below 40 K. This observation is attributed tentatively to a suppression of thermally activated deactivation channels in the KBr matrix at low temperature, closely related to the sharp increase at $\leq 10\text{ K}$ on powder samples in earlier works.⁷¹ At this point it should be mentioned that it is supposed that the triplet sublevels are still in thermal equilibrium at temperatures of $\geq 5\text{ K}$. The temperature-dependent luminescence lifetimes were further evaluated by considering eq. 1⁵⁸ to get an estimation of the energy gap ΔE between the S_1 and T_1 states. This expression is valid under the assumption that these states are in thermal equilibrium.

$$\tau(T) = \frac{3 + \exp(-\frac{\Delta E}{kT})}{\frac{3}{\tau(T_1)} + \frac{1}{\tau(S_1)} \exp(-\frac{\Delta E}{kT})} \quad (\text{eq. 1})$$

The fit (Figures S60–S62) yielded energy gaps of 350 cm^{-1} , 460 cm^{-1} and 455 cm^{-1} for $\text{Cu}_2\text{I}_2\text{L}_3$, $\text{Cu}_2\text{Br}_2\text{L}_3$ and $\text{Cu}_2\text{Cl}_2\text{L}_3$, respectively, similar to the values reported for the powder samples in the literature.^{62, 71}

At the same time, the metal exchange from Cu(I) to Ag(I) turned out to have a much larger impact on the

luminescence properties compared to a halide exchange, as already observed for the UV absorption. Similar to the absorption properties, the emission bands of the Ag(I) systems are clearly blue-shifted with a maximum at 476 nm at 290 K (Figure S56). This is confirmed by the calculated transition energies (Table S16). This blue-shift is explained by the stabilization of the cluster-centered HOMO relative to the LUMO upon exchanging Cu(I) for Ag(I) and is closely related to the observations reported in the literature for $M_2Cl_2(dppb)_2$ ($M = Cu(I), Ag(I)$; dppb = 1,2-bis-(diphenylphosphino)benzene).¹⁰⁶

In contrast to the Cu(I) homologues, the Ag(I) complexes $Ag_2Br_2L_3$ and $Ag_2Cl_2L_3$ do not show a significant red-shift of the emission maximum upon cooling (Figures 12 and S63). Precisely, a small blue-shift of 4 nm from 476 nm to 472 nm was obtained for $Ag_2Br_2L_3$, while no shift was detected for $Ag_2Cl_2L_3$ from 290 K to 5 K. Thus, the static emission spectra give a first indication that there is no significant contribution of TADF. Another important point with respect to the temperature-dependent static emission spectra is that the integrated luminescence remarkably increases by a factor of 45 and 30 from 290 K to 5 K for $Ag_2Br_2L_3$ and $Ag_2Cl_2L_3$, respectively (Figures 12, S64 and S65). This means that, in contrast to the Cu(I) homologues, dark deactivation pathways play a key role for the Ag(I) systems at 290 K. Hereby, it should be noted that the luminescence at 290 K is indeed very weak and close to the detection limit. In contrast to the luminescence intensity, the emission lifetimes are almost completely temperature-independent with decay constants of approx. 1 ns at 290 K and 5 K. These values are much shorter than the microsecond lifetimes of the Cu(I) analogues and are assigned to prompt fluorescence from the S_1 state independent of temperature. However, step-scan FTIR spectroscopy indicates a long-lived dark triplet state for $Ag_2Br_2L_3$ and $Ag_2Cl_2L_3$ (cf. step-scan FTIR studies). In other words, it is possible that in the Ag(I) systems the excited state dynamics after UV excitation include two separate deactivation pathways occurring exclusively within the singlet manifold (prompt fluorescence) and ending up in a dark triplet state, respectively.

The PyrPhos ligand emits at 450 nm at 290 K and red-shifts to 470 nm with an increased luminescence at 5 K, which should rather result from environmental effects than from two distinct luminescent electronically excited states.

At 290 K, the prompt fluorescence in the Ag(I) systems and TADF for the Cu(I) complexes most probably arise from the energetically lowest S_1 state in both cases, which is of closed butterfly structure for the Cu(I) systems. Concerning the electronic character, the emissive transition occurs with a transfer of electron density from a pyridine ring towards the M_2X_2 cluster, independent of the metal exchange.

This situation allows a quantitative comparison of the homometallic bromide and chloride complexes in the sense of two-body cooperativity *via* the following equation:¹³⁴⁻¹³⁶

$$\Delta E_{\text{coop}} = (E(\text{Ag}_2\text{Br}_2\text{L}_3) - E(\text{Cu}_2\text{Br}_2\text{L}_3)) - (E(\text{Ag}_2\text{Cl}_2\text{L}_3) - E(\text{Cu}_2\text{Cl}_2\text{L}_3)) \quad (\text{eq. 2})$$

The expression yields a cooperative effect of $\approx -780 \text{ cm}^{-1}$ at 290 K, meaning that the complexes behave in a way that

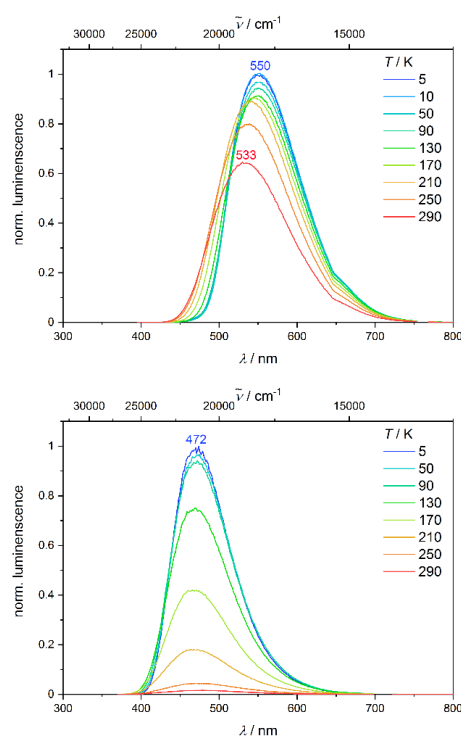


Figure 12. Temperature-dependent emission spectra of $Cu_2Br_2L_3$ ($\lambda_{\text{ex}} = 380 \text{ nm}$) (top) and $Ag_2Br_2L_3$ ($\lambda_{\text{ex}} = 355 \text{ nm}$) (bottom) at 290 – 5 K in a KBr matrix.

their photoluminescence properties cannot be predicted solely by additive contributions of the metal and halide centers (Table S18).

Next to their bright luminescence in the solid state, the Cu(I) complexes $Cu_2I_2L_3$, $Cu_2Br_2L_3$ and $Cu_2Cl_2L_3$ also show emission in organic solution (DCM and/or EtOH) (Figures S67–S68). In DCM, the complex $Cu_2I_2L_3$ shows an emission that is very similar to that in KBr, whereas the luminescence is blue-shifted by ca. 10 nm in EtOH. For $Cu_2Br_2L_3$, the emission in EtOH strongly resembles that in KBr, whereas a low photochemical stability impeded reliable luminescence studies in DCM. The situation is basically inverted for the complex $Cu_2Cl_2L_3$ with a weak emission in EtOH red-shifted by 30 nm relative to that in KBr. The emission of the PyrPhos ligand is very weak in solution and rather similar to that in the solid state (Figures S67–S68). Concerning the Ag(I) complexes, the photochemical stability in solution is not sufficient for a characterization via luminescence spectroscopy despite the applied inert conditions. Overall, the Cu(I) complexes are photochemically more stable, whereby the general trend is that the stability increases from chloride over bromide to iodide.

Subsequent to luminescence spectroscopy, time-resolved step-scan FTIR spectroscopy was applied to yield further information on potential long-lived excited states, in particular for the Ag(I) complexes that rather unexpectedly show no long-lived luminescence.

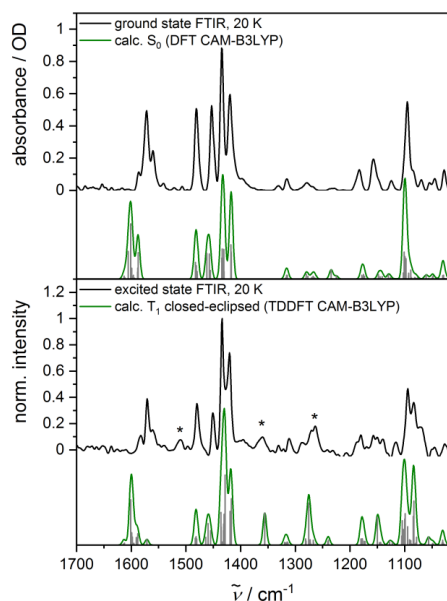


Figure 13. Top: Ground state FTIR spectrum of $\text{Cu}_2\text{Br}_2\text{L}_3$ in a KBr matrix at 20 K in comparison with its calculated S_0 spectrum. Bottom: Excited state IR spectrum (1.4 % of the ground state spectrum added to the step-scan difference spectrum) and calculated spectrum of the closed butterfly T_1 structure in eclipsed conformation (CAM-B3LYP/def2-TZVP).

Step-Scan FTIR Spectroscopy. The ground state FTIR spectra of the dinuclear monometallic Ag(I) and Cu(I) complexes are almost identical, so that neither the metal nor the halide exchange have a significant influence here (Figure S69). This is confirmed by the theoretical spectra that are almost identical and in good agreement with the experiment (Figures 13, 14, S70, S71, S80). Spectral shifts between the experimental and calculated frequencies can be partly explained by the use of a single scaling factor of 0.967 over the considered spectral range of 1700 – 1000 cm^{-1} . The given scaling factor was chosen in a way to obtain overall the best agreement between experiment and theory. An assignment of the most prominent absorption bands is given exemplary in the ESI for $\text{Cu}_2\text{Br}_2\text{L}_3$ and $\text{Ag}_2\text{Br}_2\text{L}_3$ (Tables S19 and S20).

Subsequently, step-scan FTIR spectroscopy was performed by irradiation of the solid state samples at 20 K with 355 nm laser pulses, inducing an M/XLCT excitation from the M_2X_2 core to the pyridine ring of the bridging ligand and of an ancillary ligand for the Cu(I) and Ag(I) complexes, respectively (Figure S50). In the step-scan difference spectra, averaged over the first microsecond after excitation, the negative bands correlate with vibrations in the electronic ground state and result from its depopulation, whereas the positive peaks are assigned to the long-lived electronically excited states (Figures S73–S75, S82–S83). For the systems with a closed-shell ground state studied in this work, the excited state absorption features observed in the step-scan experiments most probably result from the population of one or

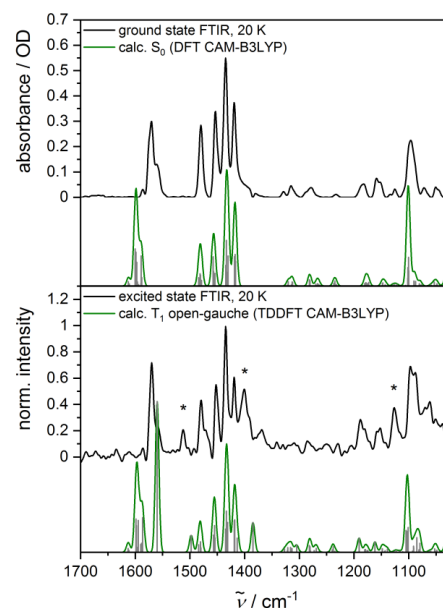


Figure 14. Top: Ground state FTIR spectrum of $\text{Ag}_2\text{Br}_2\text{L}_3$ in a KBr matrix at 20 K in comparison with its calculated S_0 spectrum. Bottom: Excited state IR spectrum (0.8 % of the ground state spectrum added to the step-scan difference spectrum) and calculated spectrum of the open butterfly T_1 structure in gauche conformation (CAM-B3LYP/def2-TZVP).

several long-lived excited triplet states (lifetimes of nanoseconds or microseconds). In contrast to the static ground state IR spectra, the transient IR absorption of the dinuclear Cu(I) complexes is influenced by halide substitution. The pure IR spectra of the excited state were generated by addition of a contribution of 0.75 – 1.40 % of the ground state spectrum to the step-scan difference spectrum to suppress the negative bands (Figures S76–S78). Independent of the halide centers, the excited state IR spectra of the Cu(I) complexes show specific bands at ca. 1505, 1365 and 1270 cm^{-1} (asterisks in Figures 13 and S70–S71) that are not observed in the electronic ground state. Hereby, the frequencies slightly depend on the halide. In the excited state, the bands at 1505, 1365, 1270 and 1160 cm^{-1} are stronger for the complexes $\text{Cu}_2\text{Br}_2\text{L}_3$ and $\text{Cu}_2\text{Cl}_2\text{L}_3$ compared to $\text{Cu}_2\text{I}_2\text{L}_3$, whereas it is the other way around for the peak/shoulder at 1420 cm^{-1} (Figure S79). The measured excited state absorption is in good agreement with the calculated IR spectra of the closed-butterfly triplet states (Figures 13, S70 and S71). As mentioned in the section on theoretical studies, the predicted IR spectra of the open and closed butterfly triplet states are very similar for $\text{Cu}_2\text{Br}_2\text{L}_3$, for example, so that no clear assignment between the open and closed butterfly triplet structures is possible by considering solely the experimental and calculated IR spectra (Figure S72). However, the closed butterfly triplet state is lower in energy by 4.4, 10.7 and 10.1 kJ/mol relative to the open butterfly triplet state for $\text{Cu}_2\text{I}_2\text{L}_3$, $\text{Cu}_2\text{Br}_2\text{L}_3$ and $\text{Cu}_2\text{Cl}_2\text{L}_3$, respectively. Thus, it is conceivable that the most stable triplet state of closed

butterfly geometry is observed spectroscopically. The experimental excited state spectra of the Cu(I) complexes at 290 K are almost identical to those at 20 K, so that the abovementioned assignment should be also valid at higher thermal energy (Figures S76–S78).

The assignment of a triplet state to the step-scan experiment is indeed confirmed by the lifetimes of few microseconds for $\text{Cu}_2\text{Br}_2\text{L}_3$ and $\text{Cu}_2\text{Cl}_2\text{L}_3$ at 290 K (Figures S87–S89), whereby the complete decay of the transient IR signals at 20 K reached beyond the time range of 200 μs covered in the step-scan experiment (see also time-resolved luminescence spectroscopy).

The metal substitution has a larger impact on the excited state IR absorption than the halide exchange. The excited state IR spectra of the $\text{Ag}_2\text{Br}_2\text{L}_3$ and $\text{Ag}_2\text{Cl}_2\text{L}_3$ complexes at 20 K show strong excited state absorption features at ca. 1510, 1400 and 1125 cm^{-1} that are not observed in the corresponding IR ground state spectra and are specific for the excited states (Figures 14 and S80). Interestingly, these peaks are not present or significantly shifted in the excited state spectra of the Cu(I) complexes, so that the metal exchange has a large impact (Figures S85 and S86). However, the halide exchange has a smaller influence than in case of the Cu(I) systems, as the only relevant difference between $\text{Ag}_2\text{Br}_2\text{L}_3$ and $\text{Ag}_2\text{Cl}_2\text{L}_3$ consists of an increased intensity of the band at 1095 cm^{-1} for the bromide analogue (Figure S84).

The bands in the step-scan difference spectra of the Ag(I) complexes show a monoexponential decay with lifetimes of 62 μs and 128 μs at 20 K for $\text{Ag}_2\text{Br}_2\text{L}_3$ and $\text{Ag}_2\text{Cl}_2\text{L}_3$, respectively (Figures S90 and S91). The step-scan investigations on the Ag(I) complexes were limited to low temperature as a result of a very moderate photochemical stability at 290 K. The microsecond lifetimes are a rather surprising result by considering the short fluorescence lifetimes of approx. 1 ns (cf. luminescence studies) and suggest a long-lived dark triplet state. As described in the section on theoretical results, this non-radiative triplet state could result from kinetic trapping within the high-energy triplet state of open gauche geometry. Indeed, the experimental excited state absorption is described best by the calculated spectrum of the open gauche triplet state (Figures 14, S80 and S81). Concretely, the excited state specific vibrations observed experimentally at ca. 1510 and 1400 cm^{-1} are also prominent in the theoretical spectrum of the open butterfly triplet state of gauche configuration, despite deviations between the experimental and theoretical frequencies. At the same time, the calculated IR frequencies assigned to the experimental vibrations at ca. 1510 and 1400 cm^{-1} show very low intensities or are significantly shifted for the open and closed butterfly triplets of eclipsed configuration (Figure S81). Quite similar to the photophysical behavior of $\text{Ag}_2\text{Br}_2\text{L}_3$ and $\text{Ag}_2\text{Cl}_2\text{L}_3$ presented herein, a long-lived non-luminescent MMLCT state with a lifetime of over 1 μs was detected at room temperature for dinuclear Ag(I) complexes containing a naphthyridine diimine ligand.¹³⁷

CONCLUSION

The homoleptic dinuclear Cu(I) PyrPhos complexes (PyrPhos = 2-(diphenylphosphino)pyridine) of the type $\text{Cu}_2\text{X}_2\text{L}_3$

(with X = I, Br, Cl; L = PyrPhos) are known to show an intense luminescence in the solid state at ambient temperature and are therefore excellent candidates for the application in organic light-emitting diodes (OLEDs).⁶² To better understand the influence of the interaction between the metal centers, named as cooperativity, on the absorption and luminescence behavior of the complexes, the dinuclear Cu(I) PyrPhos complexes were resynthesized for this study followed by the synthesis of their Ag(I) analogues ($\text{Ag}_2\text{Br}_2\text{L}_3$ and $\text{Ag}_2\text{Cl}_2\text{L}_3$).¹²⁴ The mono- and tetranuclear Ag(I) PyrPhos complexes AgXL_3 and $\text{Ag}_4\text{X}_4\text{L}_4$ were also synthesized as reference complexes. Reacting stoichiometric amounts of silver halide and PyrPhos ligand in acetonitrile gave the corresponding complexes, while the direct synthesis of $\text{Ag}_2\text{X}_2\text{L}_3$ PyrPhos complexes was not favored. The molecular structures of almost all complexes could be determined by single crystal X-ray diffraction analysis. Also dinuclear heterometallic Ag(I)/Cu(I) PyrPhos complexes could be proved by molecular structures in combination with EDX measurements.

The main aim of this work was to analyse the quartet of the dinuclear PyrPhos complexes $\text{Cu}_2\text{Br}_2\text{L}_3$, $\text{Cu}_2\text{Cl}_2\text{L}_3$, $\text{Ag}_2\text{Br}_2\text{L}_3$ and $\text{Ag}_2\text{Cl}_2\text{L}_3$ theoretically and experimentally; with focus on the impact of metal and halide substitution on the absorption and photophysical properties. The Cu(I) complexes showed strong TADF which can be assigned to singlet and triplet excited states with M/XLCT character for the lowest excitation and small singlet-triplet energy gaps of 0.1 to 0.2 eV. Interestingly, the substitution of halides had only small effects while the metal substitution led to massive changes in the photophysical properties. Step-scan investigations in combination with TDDFT and *evGW*/cBSE calculations suggest the Ag(I) complexes being kinetically trapped in a non-radiative triplet state showing a ligand-centered (LC) excitation, hence, no TADF was observed for $\text{Ag}_2\text{Br}_2\text{L}_3$ and $\text{Ag}_2\text{Cl}_2\text{L}_3$. Additionally, the theoretical investigations found energetically lower lying M/XLCT triplet states and the associated singlet states with singlet-triplet gaps being even lower than their Cu(I) analogues. All of this leads to the assumption that the Ag(I) PyrPhos complexes are in general capable of TADF if the correct triplet state could be populated.

EXPERIMENTAL SECTION

Details of the Chemicals & Solvents used in this Study. The solvents were purchased from *Fisher*, if not stated otherwise. Dichloromethane and acetonitrile for the complex synthesis were dried with the solvent purification system (SPS) from *MBraun* (model MB-SPS-800) and were degassed with argon prior to usage (5 min and 15 min, respectively). The precipitation of the Cu(I) complexes was performed with *n*-pentane sourced from *Merck* (for analysis EMSURE, order no. 1071772500, MDL number MFCD00009498, CAS 109-66-0). The NP-bridging ligand 2-(diphenylphosphino)pyridine (PyrPhos) was commercially available and was purchased from *abcr* (order no. AB426051, MDL number MFCD00192108, CAS 37943-90-1). Copper(I) iodide (99.999% trace metals basis, order no. 215554-100G, MDL number MFCD00010978, CAS 7681-65-4) and copper(I) chloride ($\geq 99.99\%$ trace metals basis, order no. 651745-5G, MDL number MFCD00010971, CAS 7758-89-6) were purchased from *Merck* while copper(I) bromide, silver(I)iodide (99.9%, order no. AB121967, MDL

number MFCD00003412, CAS 7783-96-2) and silver(I) chloride (99.9 %, order no. AB121959, MDL number MFCD00003399, CAS 7783-90-6) were sourced from *abcr* (98%, order no. AB120203, MDL number MFCD00010969, CAS 7787-70-4). Silver(I) bromide (99.9 %, order no. 11301259, MDL number MFCD00003398, CAS 7785-23-1) was purchased from *Fisher*. All chemicals were used without any further purification. The NMR spectra of the Cu(I) and Ag(I) PyrPhos complexes were recorded in degassed deuterated DMSO (DMSO- d_6 , 10 mL glass vials with septum, $\geq 99.80\%$ D, CAS 2206-27-1) and deuterated chloroform ($CDCl_3$, 100 mL brown glass flask, stored at 4 °C, stabilized with silver foils, 99.80% D, CAS 865-49-6). Both deuterated solvents were purchased from *Eurisotop*.

General Remarks. All reactions were carried out under general Schlenk conditions under an argon atmosphere. The PyrPhos ligand was used in stoichiometric amounts with the corresponding copper or silver halides for the synthesis of the Cu(I) and Ag(I) complexes. Dichloromethane as well as acetonitrile served as solvents for the complex synthesis. All reaction mixtures were stirred in the dark.

Copper Complex Syntheses. The synthesis and analytical data of the dinuclear Cu(I) PyrPhos complexes of the constitution $Cu_2X_2L_3$ (with X = I, Br, Cl) were previously reported.⁶² These Cu(I) complexes were reproduced according to the literature procedure. Additionally, a molecular structure of the bromide complex $Cu_2Br_2L_3$ was determined by single crystal X-ray diffraction (see CCDC-2042604). The corresponding crystals were obtained from a dichloromethane solution and *n*-pentane via the layering approach.

$[CuBr(2-(diphenylphosphino)pyridine)_3]$ (**CuBrL₃**) 2-(Diphenylphosphino)pyridine (1.00 g, 3.80 mmol, 3.00 equiv.) and copper(I) bromide (0.182 g, 1.27 mmol, 1.00 equiv.) were suspended in 15 mL dichloromethane. The reaction mixture was degassed with argon for 5 min and was stirred for 24 h at 25 °C. The volume of the clear and yellow solution was reduced to 10 mL under reduced pressure. The solution was added dropwise to 250 mL of *n*-pentane. The precipitate was filtered off, was washed with *n*-pentane (4 × 25 mL) and was dried in vacuo. Complex **CuBrL₃** was obtained as a very pale yellow powder (0.975 g, 0.872 mmol, 83% yield). The product was crystallized from acetonitrile. **¹H NMR** (400 MHz, DMSO- d_6 , ppm) δ = 8.49 (d, $^3J_{HH}$ = 4.3 Hz, 3H, $H_{L(Pyr)}$), 7.60 (tt, $^3J_{HH}$ = 7.7 Hz, $^4J_{HH}$ = 2.3 Hz, 3H, $H_{L(Pyr)}$), 7.38–7.24 (m, 36H, $H_{L(Pyr)}$, $H_{L(Ph)}$). – **¹³C NMR** (101 MHz, DMSO- d_6 , ppm) δ = 159.9 (d, J_{CP} = 28.3 Hz, 3C, $C_{qL(Pyr)}$), 149.9 (d, J_{CP} = 12.4 Hz, 3C, $C_{L(Pyr)}$), 135.9 (d, J_{CP} = 5.7 Hz, 3C, $C_{L(Pyr)}$), 134.0 (d, J_{CP} = 11.9 Hz, 6C, $C_{qL(Ph)}$), 133.9 (d, J_{CP} = 16.1 Hz, 12C, $C_{L(Ph)}$), 129.4 (s, 6C, $C_{L(Ph)}$), 128.7 (d, J_{CP} = 22.7 Hz, 3C, $C_{L(Pyr)}$), 128.3 (d, J_{CP} = 8.2 Hz, 12C, $C_{L(Ph)}$), 123.2 (bs, 3C, $C_{L(Pyr)}$). – **³¹P NMR** (162 MHz, DMSO- d_6 , ppm) δ = –4.60 (bs, 3P). – **MS** (FAB, 3-NBA) *m/z* [%] = 994 (1) [M+Cu]⁺, 852 (1) [M–Br]⁺, 730 (2) [Cu₂BrL₂]⁺, 589 (15) [CuL₂], 460 (7) [3-NBA], 326 (10) [CuL]⁺, 307 (37) [3-NBA]⁺, 264 (9) [L+H]⁺, 185 (3) [PPh₂]⁺, 154 (100) [3-NBA], 137 (77) [3-NBA]. 3-NBA = 3-nitrobenzylalcohol. – **IR** (ATR) $\tilde{\nu}$ [cm⁻¹] = 3043 (vw), 1571 (w), 1481 (w), 1449 (w), 1433 (w), 1418 (w), 1184 (vw), 1152 (vw), 1092 (w), 1048 (vw), 1027 (vw), 987 (w), 766 (w), 741 (m), 694 (m), 619 (vw), 506 (m), 488 (m), 440 (w), 412 (w). – **EA** Anal. calcd. for C₅₁H₄₂BrCuN₃P₃: C 65.63, H 4.54, N 4.50; found: C 63.07, H 4.37, N 4.47. The molecular structure of complex **CuBrL₃** was determined by single crystal X-ray diffraction (CCDC-2086153).

$[CuCl(2-(diphenylphosphino)pyridine)_3]$ (**CuClL₃**) 2-(Diphenylphosphino)pyridine (1.00 g, 3.80 mmol, 3.00 equiv.) and copper(I) chloride (0.125 g, 1.27 mmol, 1.00 equiv.) were suspended in 15 mL dichloromethane. The reaction mixture was degassed with argon for 5 min and was stirred for 24 h at 25 °C. The cloudy and pale yellow solution was filtrated. The volume of the clear yellow filtrate was reduced to 10 mL and added dropwise to 300 mL of *n*-pentane. The precipitate was filtered off, was washed with *n*-pentane (4 × 25 mL) and was dried in vacuo. Complex **CuClL₃** was obtained as an off-white powder (0.775 g, 0.872 mmol, 69% yield). The product was crystallized from acetonitrile. **¹H NMR** (400 MHz, DMSO- d_6 , ppm) δ = 8.61 (bs, 3H, $H_{L(Pyr)}$), 7.69 (t, $^3J_{HH}$ = 7.4 Hz, 3H, $H_{L(Pyr)}$), 7.41–7.28 (m, 36H, $H_{L(Pyr)}$, $H_{L(Ph)}$). – **³¹P NMR** (162 MHz, DMSO- d_6 , ppm) δ = –4.38 (bs, 3P). – **¹H NMR** (400 MHz, $CDCl_3$, ppm) δ = 8.52 (bs, 3H, $H_{L(Pyr)}$), 7.45–7.41 (m, 18H, $H_{L(Pyr)}$, $H_{L(Ph)}$), 7.31–7.27 (m, 6H, $H_{L(Ph)}$), 7.21–7.17 (m, 12H, $H_{L(Ph)}$), 7.12–7.08 (m, 3H, $H_{L(Pyr)}$). – **¹³C NMR** (101 MHz, $CDCl_3$, ppm) δ = 160.0 (d, J_{CP} = 35.1 Hz, 3C, $C_{qL(Pyr)}$), 150.4 (d, J_{CP} = 12.7 Hz, 3C, $C_{L(Pyr)}$), 135.8 (d, J_{CP} = 6.2 Hz, 3C, $C_{L(Pyr)}$), 134.4 (d, J_{CP} = 15.5 Hz, 12C, $C_{L(Ph)}$), 133.7 (d, J_{CP} = 19.0 Hz, 6C, $C_{qL(Ph)}$), 129.8 (d, J_{CP} = 23.0 Hz, 3C, $C_{L(Pyr)}$), 129.5 (s, 6C, $C_{L(Ph)}$), 128.5 (d, J_{CP} = 8.6 Hz, 12C, $C_{L(Ph)}$), 123.1 (s, 3C, $C_{L(Pyr)}$). – **³¹P NMR** (162 MHz, $CDCl_3$, ppm) δ = –3.20 (s, 3P). – **MS** (FAB, 3-NBA) *m/z* [%] = 950 (3) [M+Cu]⁺, 852 (9) [M–Cl]⁺, 687 (7) [Cu₂ClL₂]⁺, 589 (83) [CuL₂], 460 (5) [3-NBA], 423 (5) [Cu₂ClL]⁺, 326 (52) [CuL]⁺, 307 (37) [3-NBA], 264 (40) [L+H]⁺, 185 (13) [PPh₂]⁺, 154 (100) [3-NBA], 137 (63) [3-NBA]. 3-NBA = 3-nitrobenzylalcohol. – **IR** (ATR) $\tilde{\nu}$ [cm⁻¹] = 3043 (vw), 1571 (w), 1481 (w), 1448 (w), 1433 (m), 1419 (w), 1185 (vw), 1153 (vw), 1093 (w), 1047 (vw), 1027 (vw), 987 (w), 766 (w), 740 (m), 692 (m), 618 (w), 505 (m), 444 (w), 409 (w). – **EA** Anal. calcd. for C₅₁H₄₂ClCuN₃P₃: C 68.92, H 4.76, N 4.73; found: C 67.73, H 4.71, N 4.72. The molecular structure of complex **CuClL₃** was determined by single crystal X-ray diffraction (CCDC-2063602).

Silver Complex Syntheses. The syntheses of all Ag(I) complexes were performed in acetonitrile. The reaction conditions as well as details on the filtration and crystallization are given for every complex respectively.

$[Ag_2Br_2(2-(diphenylphosphino)pyridine)_3]$ (**Ag₂Br₂L₃**) 2-(Diphenylphosphino)pyridine (1.84 g, 7.00 mmol, 3.00 equiv.) and silver(I) bromide (0.875 g, 4.66 mmol, 2.00 equiv.) were suspended in 20 mL acetonitrile. The reaction mixture was degassed with argon for 5 min and was stirred for 24 h at 25 °C. The suspension consisted of a colorless and clear solution and a colorless solid. The solid was filtered off, was washed with acetonitrile (2 × 50 mL) and was dried in vacuo in the dark. Complex **Ag₂Br₂L₃** was obtained as a colorless powder (2.51 g, 2.16 mmol, 93% yield). The product was crystallized from the acetonitrile filtrate in the freezer. **¹H NMR** (400 MHz, DMSO- d_6 , ppm) δ = 8.63 (d, $^3J_{HH}$ = 4.7 Hz, 3H, $H_{L(Pyr)}$), 7.75 (tdd, $^3J_{HH}$ = 7.6 Hz, $^4J_{HH}$ = 3.0 Hz, $^5J_{HH}$ = 1.8 Hz, 3H, $H_{L(Pyr)}$), 7.51–7.43 (m, 21H, $H_{L(Pyr)}$, $H_{L(Ph)}$), 7.41–7.35 (m, 15H, $H_{L(Pyr)}$, $H_{L(Ph)}$). – **¹³C NMR** (101 MHz, DMSO- d_6 , ppm) δ = 158.2 (d, J_{CP} = 37.8 Hz, 3C, $C_{qL(Pyr)}$), 150.6 (d, J_{CP} = 13.3 Hz, 3C, $C_{L(Pyr)}$), 136.5 (d, J_{CP} = 7.1 Hz, 3C, $C_{L(Pyr)}$), 134.0 (d, J_{CP} = 17.0 Hz, 12C, $C_{L(Ph)}$), 132.3 (d, J_{CP} = 19.5 Hz, 6C, $C_{qL(Ph)}$), 130.3 (s, 6C, $C_{L(Ph)}$), 129.1 (d, J_{CP} = 26.6 Hz, 3C, $C_{L(Pyr)}$), 128.8 (d, J_{CP} = 9.2 Hz, 12C, $C_{L(Ph)}$), 124.0 (s, 3C, $C_{L(Pyr)}$). – **³¹P NMR** (162 MHz, DMSO- d_6 , ppm) δ = 4.92 (bs, 3P). – **¹H NMR** (400 MHz, $CDCl_3$, ppm) δ = 8.62 (d, $^3J_{HH}$ = 4.7 Hz, 3H, $H_{L(Pyr)}$), 7.81 (t, $^3J_{HH}$ = 6.9 Hz, 3H, $H_{L(Pyr)}$), 7.63–7.59 (m, 12H, $H_{L(Ph)}$), 7.55 (tdd, $^3J_{HH}$ = 7.7 Hz, $^4J_{HH}$ = 3.1 Hz, $^5J_{HH}$ = 1.8 Hz, 3H, $H_{L(Pyr)}$), 7.38–7.34 (m, 6H, $H_{L(Ph)}$), 7.31–7.27 (m, 12H, $H_{L(Ph)}$), 7.21–7.17 (m, 3H, $H_{L(Pyr)}$). Please note that the reference resonance of $CHCl_3$ could not be picked due to an overlap with the

resonances of the compound. – $^{13}\text{C NMR}$ (101 MHz, CDCl_3 , ppm) δ = 158.9 (d, J_{CP} = 36.9 Hz, 3C, $\text{C}_{\text{qL}}(\text{Pyr})$), 150.6 (d, J_{CP} = 12.8 Hz, 3C, $\text{C}_{\text{L}}(\text{Pyr})$), 136.2 (d, J_{CP} = 8.0 Hz, 3C, $\text{C}_{\text{L}}(\text{Pyr})$), 134.5 (d, J_{CP} = 16.8 Hz, 12C, $\text{C}_{\text{L}}(\text{Ph})$), 132.5 (d, J_{CP} = 20.9 Hz, 6C, $\text{C}_{\text{qL}}(\text{Ph})$), 130.3 (d, J_{CP} = 30.0 Hz, 3C, $\text{C}_{\text{L}}(\text{Pyr})$), 130.1 (s, 6C, $\text{C}_{\text{L}}(\text{Ph})$), 128.8 (d, J_{CP} = 9.4 Hz, 12C, $\text{C}_{\text{L}}(\text{Ph})$), 123.6 (s, 3C, $\text{C}_{\text{L}}(\text{Pyr})$). – $^{31}\text{P NMR}$ (162 MHz, CDCl_3 , ppm) δ = 5.94 (s, 3P). – **MS** (FAB, 3-NBA) m/z [%] = 1081 (7) $[\text{M}-\text{Br}]^+$, 1004 (3) $[\text{Ag}_3\text{Br}_2\text{L}_2]^+$, 896 (23) $[\text{AgL}_3]^+$, 822 (100), 818 (37) $[\text{Ag}_2\text{BrL}_2]^+$. – **IR** (ATR) $\tilde{\nu}$ [cm^{-1}] = 3044 (vw), 1569 (w), 1452 (w), 1434 (w), 1418 (w), 1314 (vw), 1182 (vw), 1158 (vw), 1093 (w), 1050 (vw), 1027 (vw), 886 (w), 767 (w), 742 (m), 721 (w), 691 (s), 618 (vw), 501 (s), 488 (m), 431 (w), 416 (w), 395 (w). – **EA** Anal. calcd. for $\text{C}_{51}\text{H}_{42}\text{Ag}_2\text{Br}_2\text{N}_3\text{P}_3$: C 52.56, H 3.63, N 3.61; found: C 52.27, H 3.53, N 3.58. – **mp** = 184 °C. The molecular structure of complex **Ag₂Br₂L₃** was determined by single crystal X-ray diffraction (CCDC-2039552).

$[\text{Ag}_2\text{Cl}_2(2\text{-}(\text{diphenylphosphino})\text{pyridine})_3]$ (**Ag₂Cl₂L₃**) 2-(Diphenylphosphino)pyridine (1.00 g, 3.80 mmol, 3.00 equiv.) and silver(I) chloride (0.363 g, 2.53 mmol, 2.00 equiv.) were suspended in 15 mL acetonitrile. The reaction mixture was degassed with argon for 5 min and was stirred for 24 h at 25 °C. The suspension consisted of a colorless and clear solution and a colorless solid. The solid was filtered off, was washed with acetonitrile (2 × 20 mL) and was dried in vacuo in the dark. Complex **Ag₂Cl₂L₃** was obtained as a colorless powder (1.15 g, 1.07 mmol, 85% yield). The product was crystallized from the acetonitrile filtrate in the freezer. $^1\text{H NMR}$ (400 MHz, $\text{DMSO}-d_6$, ppm) δ = 8.63 (d, $^3J_{\text{HH}}$ = 4.2 Hz, 3H, $\text{H}_{\text{L}}(\text{Pyr})$), 7.73 (tdd, $^3J_{\text{HH}}$ = 7.7 Hz, J_{HH} = 3.2 Hz, $^4J_{\text{HH}}$ = 1.8 Hz, 3H, $\text{H}_{\text{L}}(\text{Pyr})$), 7.57–7.51 (m, 15H, $\text{H}_{\text{L}}(\text{Pyr})$, $\text{H}_{\text{L}}(\text{Ph})$), 7.46–7.42 (m, 6H, $\text{H}_{\text{L}}(\text{Ph})$), 7.40–7.33 (m, 15H, $\text{H}_{\text{L}}(\text{Pyr})$, $\text{H}_{\text{L}}(\text{Ph})$). – $^{13}\text{C NMR}$ (101 MHz, $\text{DMSO}-d_6$, ppm) δ = 157.4 (d, J_{CP} = 43.5 Hz, 3C, $\text{C}_{\text{qL}}(\text{Pyr})$), 150.6 (d, J_{CP} = 13.3 Hz, 3C, $\text{C}_{\text{L}}(\text{Pyr})$), 136.6 (d, J_{CP} = 8.2 Hz, 3C, $\text{C}_{\text{L}}(\text{Pyr})$), 134.1 (d, J_{CP} = 16.6 Hz, 12C, $\text{C}_{\text{L}}(\text{Ph})$), 131.7 (d, J_{CP} = 25.1 Hz, 6C, $\text{C}_{\text{qL}}(\text{Ph})$), 130.4 (s, 6C, $\text{C}_{\text{L}}(\text{Ph})$), 129.5 (d, J_{CP} = 28.8 Hz, 3C, $\text{C}_{\text{L}}(\text{Pyr})$), 128.7 (d, J_{CP} = 9.7 Hz, 12C, $\text{C}_{\text{L}}(\text{Ph})$), 124.2 (s, 3C, $\text{C}_{\text{L}}(\text{Pyr})$). – $^{31}\text{P NMR}$ (162 MHz, $\text{DMSO}-d_6$, ppm) δ = 7.30 (s, 3P). – **MS** (FAB, 3-NBA) m/z [%] = 1179 (1) $[\text{M}+\text{Ag}]^+$, 1038 (3) $[\text{M}-\text{Cl}]^+$, 916 (2) $[\text{Ag}_3\text{Cl}_2\text{L}_2]^+$, 774 (18) $[\text{Ag}_2\text{ClL}_2]^+$, 653 (2) $[\text{Ag}_3\text{ClL}_2]^+$, 633 (72) $[\text{AgL}_2]^+$, 511 (4) $[\text{Ag}_2\text{ClL}]^+$, 369 (100) $[\text{AgL}]^+$, 307 (13) [3-NBA], 264 (15) $[\text{L}+\text{H}]^+$, 185 (20) $[\text{PPh}_2]^+$, 154 (49) [3-NBA], 137 (33) [3-NBA]. 3-NBA = 3-nitrobenzylalcohol. – **IR** (ATR) $\tilde{\nu}$ [cm^{-1}] = 1569 (w), 1479 (w), 1452 (w), 1434 (w), 1419 (w), 1093 (w), 986 (w), 742 (m), 721 (w), 692 (m), 618 (vw), 501 (m), 488 (m), 416 (w). – **EA** Anal. calcd. for $\text{C}_{51}\text{H}_{42}\text{Ag}_2\text{Cl}_2\text{N}_3\text{P}_3$: C 56.90, H 3.93, N 3.90; found: C 56.99, H 3.90, N 3.95. – **mp** = 164 °C. The molecular structure of complex **Ag₂Cl₂L₃** was determined by single crystal X-ray diffraction (CCDC-2042183). The molecular structure is a redetermination of BEBGEU at 123 K.¹²⁴ All positions of the nitrogen atoms of the PyrPhos ligands in the dinuclear Ag(I) complex could be assigned.

$[\text{AgI}(2\text{-}(\text{diphenylphosphino})\text{pyridine})_3]$ (**AgIL₃**) 2-(Diphenylphosphino)pyridine (1.00 g, 3.80 mmol, 3.00 equiv.) and silver(I) iodide (0.297 g, 1.26 mmol, 1.00 equiv.) were suspended in 15 mL acetonitrile. The reaction mixture was degassed with argon for 5 min and was stirred for 24 h at 90 °C. The suspension consisted of a colorless and clear solution and a colorless solid. The solid was filtered off hot, was washed with acetonitrile (25 mL) and was dried in vacuo in the dark. Complex **AgIL₃** was obtained as a colorless powder (0.630 g, 0.615 mmol, 49% yield). The product was crystallized from the acetonitrile filtrate in the freezer. $^1\text{H NMR}$ (400 MHz, $\text{DMSO}-d_6$, ppm) δ = 8.57 (d, $^3J_{\text{HH}}$ = 4.7 Hz, 3H, $\text{H}_{\text{L}}(\text{Pyr})$), 7.68 (tdd, $^3J_{\text{HH}}$ = 7.7 Hz, J_{HH} = 2.7 Hz,

J_{HH} = 1.8 Hz, 3H, $\text{H}_{\text{L}}(\text{Pyr})$), 7.43–7.37 (m, 18H, H_{P}), 7.34–7.28 (m, 18H, $\text{H}_{\text{L}}(\text{Pyr})$, $\text{H}_{\text{L}}(\text{Ph})$). – $^{13}\text{C NMR}$ (101 MHz, $\text{DMSO}-d_6$, ppm) δ = 159.6 (d, J_{CP} = 27.3 Hz, 3C, $\text{C}_{\text{qL}}(\text{Pyr})$), 150.3 (d, J_{CP} = 12.8 Hz, 3C, $\text{C}_{\text{L}}(\text{Pyr})$), 136.3 (d, J_{CP} = 5.7 Hz, 3C, $\text{C}_{\text{L}}(\text{Pyr})$), 133.9 (d, J_{CP} = 14.5 Hz, 12C, $\text{C}_{\text{L}}(\text{Ph})$), 133.4 (d, J_{CP} = 9.8 Hz, 6C, $\text{C}_{\text{qL}}(\text{Ph})$), 129.8 (s, 6C, $\text{C}_{\text{L}}(\text{Ph})$), 128.7 (d, J_{CP} = 25.5 Hz, 3C, $\text{C}_{\text{L}}(\text{Pyr})$), 128.6 (d, J_{CP} = 8.4 Hz, 12C, $\text{C}_{\text{L}}(\text{Ph})$), 123.5 (s, 3C, $\text{C}_{\text{L}}(\text{Pyr})$). – $^{31}\text{P NMR}$ (162 MHz, $\text{DMSO}-d_6$, ppm) δ = 0.20 (s, 3P). – **MS** (FAB, 3-NBA) m/z [%] = 1129 (2) $[\text{M}+\text{Ag}]^+$, 1024 (1) $[\text{M}+\text{H}]^+$, 896 (4) $[\text{M}-\text{I}]^+$, 866 (4) $[\text{Ag}_2\text{IL}_2]^+$, 633 (86) $[\text{AgL}_2]^+$, 460 (5) [3-NBA], 369 (47) $[\text{AgL}]^+$, 307 (32) [3-NBA], 264 (100) $[\text{L}+\text{H}]^+$, 154 (92) [3-NBA], 137 (60) [3-NBA]. 3-NBA = 3-nitrobenzylalcohol. – **IR** (ATR) $\tilde{\nu}$ [cm^{-1}] = 3042 (vw), 1570 (w), 1480 (w), 1447 (w), 1433 (w), 1417 (w), 1149 (w), 1092 (w), 1046 (vw), 1026 (w), 986 (w), 741 (m), 691 (m), 618 (w), 513 (m), 502 (m), 428 (w), 407 (w). – **EA** Anal. calcd. for $\text{C}_{51}\text{H}_{42}\text{AgIN}_3\text{P}_3$: C 59.78, H 4.13, N 4.10; found: C 58.13, H 3.99, N 4.04. – **mp** = 185 °C. The molecular structure of complex **AgIL₃** was determined by single crystal X-ray diffraction (CCDC-2039548).

$[\text{AgBr}(2\text{-}(\text{diphenylphosphino})\text{pyridine})_3]$ (**AgBrL₃**) 2-(Diphenylphosphino)pyridine (1.00 g, 3.80 mmol, 3.00 equiv.) and silver(I) bromide (0.238 g, 1.26 mmol, 1.00 equiv.) were suspended in 15 mL acetonitrile. The reaction mixture was degassed with argon for 5 min and was stirred for 24 h at 25 °C. The suspension consisted of a colorless and clear solution and a colorless solid. The solid was filtered off, was washed with acetonitrile (3 × 20 mL) and was dried in vacuo in the dark. Complex **AgBrL₃** was obtained as a colorless powder (0.860 g, 0.880 mmol, 70% yield). The product was crystallized from deuterated DMSO. $^1\text{H NMR}$ (400 MHz, $\text{DMSO}-d_6$, ppm) δ = 8.52 (d, $^3J_{\text{HH}}$ = 4.0 Hz, 3H, $\text{H}_{\text{L}}(\text{Pyr})$), 7.65 (tt, $^3J_{\text{HH}}$ = 7.7 Hz, J_{HH} = 2.3 Hz, 3H, $\text{H}_{\text{L}}(\text{Pyr})$), 7.41–7.27 (m, 36H, $\text{H}_{\text{L}}(\text{Pyr})$, $\text{H}_{\text{L}}(\text{Ph})$). – $^{13}\text{C NMR}$ (101 MHz, $\text{DMSO}-d_6$, ppm) δ = 159.4 (d, J_{CP} = 29.0 Hz, 3C, $\text{C}_{\text{qL}}(\text{Pyr})$), 150.2 (d, J_{CP} = 12.8 Hz, 3C, $\text{C}_{\text{L}}(\text{Pyr})$), 136.2 (d, J_{CP} = 6.2 Hz, 3C, $\text{C}_{\text{L}}(\text{Pyr})$), 133.9 (d, J_{CP} = 17.3 Hz, 12C, $\text{C}_{\text{L}}(\text{Ph})$), 133.3 (d, J_{CP} = 11.7 Hz, 6C, $\text{C}_{\text{qL}}(\text{Ph})$), 129.8 (s, 6C, $\text{C}_{\text{L}}(\text{Ph})$), 128.8 (d, J_{CP} = 24.8 Hz, 3C, $\text{C}_{\text{L}}(\text{Pyr})$), 128.6 (d, J_{CP} = 8.6 Hz, 12C, $\text{C}_{\text{L}}(\text{Ph})$), 123.5 (s, 3C, $\text{C}_{\text{L}}(\text{Pyr})$). – $^{31}\text{P NMR}$ (162 MHz, $\text{DMSO}-d_6$, ppm) δ = 1.81 (s, 3P). – **MS** (FAB, 3-NBA) m/z [%] = 869 (1) $[\text{M}-\text{Br}]^+$, 818 (2) $[\text{Ag}_2\text{BrL}_2]^+$, 633 (69) $[\text{AgL}_2]^+$, 555 (2) $[\text{Ag}_2\text{BrL}]^+$, 369 (100) $[\text{AgL}]^+$, 264 (12) $[\text{L}+\text{H}]^+$, 185 (29) $[\text{PPh}_2]^+$. – **IR** (ATR) $\tilde{\nu}$ [cm^{-1}] = 3043 (vw), 1570 (w), 1480 (w), 1448 (w), 1434 (m), 1418 (w), 1150 (w), 1093 (w), 1026 (w), 986 (w), 741 (m), 692 (m), 619 (w), 503 (m), 429 (w). – **EA** Anal. calcd. for $\text{C}_{51}\text{H}_{42}\text{AgBrN}_3\text{P}_3$: C 62.66, H 4.33, N 4.30; found: C 60.81, H 4.07, N 4.19. – **mp** = 162 °C. The molecular structure of complex **AgBrL₃** was determined by single crystal X-ray diffraction (CCDC-2042182).

$[\text{AgCl}(2\text{-}(\text{diphenylphosphino})\text{pyridine})_3]$ (**AgCIL₃**) 2-(Diphenylphosphino)pyridine (1.00 g, 3.80 mmol, 3.00 equiv.) and silver(I) chloride (0.181 g, 1.26 mmol, 1.00 equiv.) were suspended in 15 mL acetonitrile. The reaction mixture was degassed with argon for 5 min and was stirred for 24 h at 90 °C. The suspension consisted of a colorless and clear solution and a colorless solid. The solid was filtered off, was washed with acetonitrile (25 mL) and was dried in vacuo in the dark. Complex **AgCIL₃** was obtained as a colorless powder (1.03 g, 1.11 mmol, 88% yield). The product was crystallized from hot ethanol. $^1\text{H NMR}$ (400 MHz, $\text{DMSO}-d_6$, ppm) δ = 8.52 (d, $^3J_{\text{HH}}$ = 4.6 Hz, 3H, $\text{H}_{\text{L}}(\text{Pyr})$), 7.65 (tdd, $^3J_{\text{HH}}$ = 7.8 Hz, J_{HH} = 2.9 Hz, J_{HH} = 1.8 Hz, 3H, $\text{H}_{\text{L}}(\text{Pyr})$), 7.43–7.26 (m, 36H, $\text{H}_{\text{L}}(\text{Pyr})$, $\text{H}_{\text{L}}(\text{Ph})$). – $^{13}\text{C NMR}$ (101 MHz, $\text{DMSO}-d_6$, ppm) δ = 159.0 (d, J_{CP} = 31.8 Hz, 3C, $\text{C}_{\text{qL}}(\text{Pyr})$), 150.3 (d, J_{CP} = 12.8 Hz, 3C, $\text{C}_{\text{L}}(\text{Pyr})$), 136.2 (d, J_{CP} = 6.7 Hz, 3C, $\text{C}_{\text{L}}(\text{Pyr})$), 134.0 (d, J_{CP} = 17.2 Hz, 12C, $\text{C}_{\text{L}}(\text{Ph})$), 133.0 (d, J_{CP} =

14.4 Hz, 6C, C_{qL(Ph)}), 129.9 (s, 6C, C_{L(Ph)}), 128.9 (d, J_{CP} = 25.8 Hz, 3C, C_{L(Pyrr)}), 128.6 (d, J_{CP} = 8.8 Hz, 12C, C_{L(Ph)}), 123.6 (s, 3C, C_{L(Pyrr)}). – ³¹P NMR (162 MHz, DMSO-d₆, ppm) δ = 3.31 (s, 3P). – MS (FAB, 3-NBA) *m/z* [%] = 1038 (1) [M+Ag]⁺, 896 (1) [M-Cl]⁺, 774 (5) [Ag₂ClL₂]⁺, 633 (65) [AgL₂]⁺, 370 (100) [AgL]⁺, 264 (10) [L+H]⁺, 185 (24) [PPh₂]⁺. – IR (ATR) $\tilde{\nu}$ [cm⁻¹] = 3040 (vw), 1569 (w), 1478 (w), 1448 (w), 1432 (w), 1417 (w), 1183 (vw), 1151 (vw), 1092 (w), 1046 (vw), 1028 (w), 986 (w), 769 (w), 742 (m), 691 (m), 617 (w), 512 (m), 487 (m), 441 (w). – EA Anal. calcd. for C₅₁H₄₂AgClN₃P₃: C 65.64, H 4.54, N 4.50; found: C 65.50, H 4.51, N 4.65. – mp = 167 °C. The molecular structure of complex **AgClL₃** was determined by single crystal X-ray diffraction (CCDC-2042603).

[Ag₄L₄(2-(diphenylphosphino)pyridine)₄] (**Ag₄L₄L₄**) 2-(Diphenylphosphino)pyridine (1.00 g, 3.80 mmol, 4.00 equiv.) and silver(I) iodide (0.892 g, 3.80 mmol, 4.00 equiv.) were suspended in 15 mL acetonitrile. The reaction mixture was degassed with argon for 5 min and was stirred for 24 h at 25 °C. The suspension consisted of a colorless and clear solution and a colorless solid. The solid was filtered off, was washed with acetonitrile (3 × 25 mL) and was dried in vacuo in the dark. Complex **Ag₄L₄L₄** was obtained as a colorless powder (1.78 g, 0.891 mmol, 94% yield). The product was crystallized from the acetonitrile filtrate in the freezer. ¹H NMR (400 MHz, DMSO-d₆, ppm) δ = 8.71 (d, ³J_{HH} = 4.6 Hz, 4H, H_{L(Pyrr)}), 7.82–7.77 (m, 4H, H_{L(Pyrr)}), 7.51–7.39 (m, 48H, H_{L(Pyrr)}, H_{L(Ph)}). – ³¹P NMR (162 MHz, DMSO-d₆, ppm) δ = 2.19 (bs, 4P). – ¹H NMR (400 MHz, CDCl₃, ppm) δ = 8.69 (d, ³J_{HH} = 4.7 Hz, 4H, H_{L(Pyrr)}), 7.55–7.50 (m, 24H, H_{L(Pyrr)}, H_{L(Ph)}), 7.39–7.29 (m, 24H, H_{L(Pyrr)}, H_{L(Ph)}), 7.19 (qd, ³J_{HH} = 4.7 Hz, ⁴J_{HH} = 1.7 Hz, 4H, H_{L(Pyrr)}). – ¹³C NMR (101 MHz, CDCl₃, ppm) δ = 150.6 (d, J_{CP} = 12.3 Hz, 4C, C_{L(Pyrr)}), 136.2 (d, J_{CP} = 7.0 Hz, 4C, C_{L(Pyrr)}), 134.5 (d, J_{CP} = 17.5 Hz, 16C, C_{L(Ph)}), 133.7 (d, J_{CP} = 8.9 Hz, 8C, C_{qL(Ph)}), 132.3 (d, J_{CP} = 9.6 Hz, 4C, C_{qL(Pyrr)}), 129.8 (s, 8C, C_{L(Ph)}), 128.8 (d, J_{CP} = 8.7 Hz, 16C, C_{L(Ph)}), 128.5 (d, J_{CP} = 12.0 Hz, 4C, C_{L(Pyrr)}), 123.3 (s, 4C, C_{L(Pyrr)}). – ³¹P NMR (162 MHz, CDCl₃, ppm) δ = -0.21 (bs, 4P). – MS (FAB, 3-NBA) *m/z* [%] = Due to the poor solubility of the complex no mass spectrum could be recorded. – IR (ATR) $\tilde{\nu}$ [cm⁻¹] = 3043 (vw), 1568 (vw), 1477 (vw), 1446 (w), 1434 (w), 1419 (w), 1276 (vw), 1151 (vw), 1094 (w), 1046 (vw), 1027 (vw), 987 (vw), 844 (vw), 766 (w), 742 (w), 722 (vw), 692 (w), 618 (vw), 511 (w), 501 (w), 422 (w), 395 (vw). – EA Anal. calcd. for C₆₈H₅₆Ag₄L₄N₄P₄: C 41.00, H 2.83, N 2.81; found: C 41.00, H 2.70, N 2.85. – mp = 272 °C. The molecular structure of complex **Ag₄L₄L₄** was determined by single crystal X-ray diffraction (CCDC-2039549).

[Ag₄Br₄(2-(diphenylphosphino)pyridine)₄] (**Ag₄Br₄L₄**) 2-(Diphenylphosphino)pyridine (1.00 g, 3.80 mmol, 4.00 equiv.) and silver(I) bromide (0.713 g, 3.80 mmol, 4.00 equiv.) were suspended in 15 mL acetonitrile. The reaction mixture was degassed with argon for 5 min and was stirred for 24 h at 90 °C. The suspension consisted of a colorless and clear solution and a colorless solid. The solid was filtered off hot, was washed with hot acetonitrile (2 × 25 mL) and was dried in vacuo in the dark. Complex **Ag₄Br₄L₄** was obtained as a colorless powder (1.64 g, 0.909 mmol, 96% yield). ¹H NMR (400 MHz, DMSO-d₆, ppm) δ = 8.73 (d, ³J_{HH} = 4.8 Hz, 4H, H_{L(Pyrr)}), 7.85 (tdd, ³J_{HH} = 7.7 Hz, J_{HH} = 3.1 Hz, J_{HH} = 1.8 Hz, 4H, H_{L(Pyrr)}), 7.57–7.42 (m, 48H, H_{L(Pyrr)}, H_{L(Ph)}). – ³¹P NMR (162 MHz, DMSO-d₆, ppm) δ = 8.88 (bs, 4P). – ¹H NMR (400 MHz, CDCl₃, ppm) δ = 8.63 (d, ³J_{HH} = 4.7 Hz, 4H, H_{L(Pyrr)}), 7.66–7.63 (m, 4H, H_{L(Pyrr)}), 7.59–7.52 (m, 20H, H_{L(Pyrr)}, H_{L(Ph)}), 7.39–7.35 (m, 8H, H_{L(Ph)}), 7.32–7.28 (m, 16H, H_{L(Ph)}), 7.21–7.18 (m, 4H, H_{L(Pyrr)}). – ¹³C NMR (101 MHz, CDCl₃, ppm) δ = 158.9 (d, J_{CP} = 62.8 Hz, 4C, C_{qL(Pyrr)}), 150.8 (d, J_{CP} = 52.0 Hz,

4C, C_{L(Pyrr)}), 136.2 (d, J_{CP} = 31.6 Hz, 4C, C_{L(Pyrr)}), 134.5 (d, J_{CP} = 16.8 Hz, 16C, C_{L(Ph)}), 132.4 (d, J_{CP} = 85.2 Hz, 8C, C_{qL(Ph)}), 130.2 (d, J_{CP} = 100.4 Hz, 4C, C_{L(Pyrr)}), 130.2 (s, 8C, C_{L(Ph)}), 128.9 (d, J_{CP} = 9.5 Hz, 16C, C_{L(Ph)}), 123.7 (s, 4C, C_{L(Pyrr)}). – ³¹P NMR (162 MHz, CDCl₃, ppm) δ = 6.47 (s, 4P). – MS (FAB, 3-NBA) *m/z* [%] = Due to the poor solubility of the complex no mass spectrum could be recorded. – IR (ATR) $\tilde{\nu}$ [cm⁻¹] = 1568 (w), 1478 (w), 1446 (w), 1434 (w), 1420 (w), 1275 (vw), 1095 (w), 1028 (vw), 988 (w), 771 (w), 743 (m), 723 (w), 692 (m), 618 (vw), 514 (m), 503 (m), 491 (m), 447 (w), 422 (w). – EA Anal. calcd. for C₆₈H₅₆Ag₄Br₄N₄P₄: C 45.27, H 3.13, N 3.11; found: C 45.32, H 3.07, N 3.15. – mp = 258 °C.

[Ag₄Cl₄(2-(diphenylphosphino)pyridine)₄] (**Ag₄Cl₄L₄**) 2-(Diphenylphosphino)pyridine (1.00 g, 3.80 mmol, 4.00 equiv.) and silver(I) chloride (0.544 g, 3.80 mmol, 4.00 equiv.) were suspended in 15 mL acetonitrile. The reaction mixture was degassed with argon for 5 min and was stirred for 24 h at 90 °C. The suspension consisted of a colorless and clear solution and a colorless solid. The solid was filtered off hot, was washed with hot acetonitrile (2 × 25 mL) and was dried in vacuo in the dark. Complex **Ag₄Cl₄L₄** was obtained as a colorless powder (1.44 g, 0.885 mmol, 93% yield). The product was crystallized from acetonitrile in the freezer. ¹H NMR (400 MHz, DMSO-d₆, ppm) δ = 8.75 (d, ³J_{HH} = 4.7 Hz, 4H, H_{L(Pyrr)}), 7.84 (tdd, ³J_{HH} = 7.7 Hz, J_{HH} = 3.2 Hz, J_{HH} = 1.8 Hz, 4H, H_{L(Pyrr)}), 7.59–7.41 (m, 48H, H_{L(Pyrr)}, H_{L(Ph)}). – ¹³C NMR (101 MHz, DMSO-d₆, ppm) δ = 156.7 (d, J_{CP} = 49.3 Hz, 4C, C_{qL(Pyrr)}), 150.9 (d, J_{CP} = 13.9 Hz, 4C, C_{L(Pyrr)}), 137.0 (d, J_{CP} = 8.3 Hz, 4C, C_{L(Pyrr)}), 134.1 (d, J_{CP} = 16.8 Hz, 16C, C_{L(Ph)}), 131.0 (d, J_{CP} = 29.7 Hz, 8C, C_{qL(Ph)}), 130.8 (d, J_{CP} = 1.9 Hz, 8C, C_{L(Ph)}), 129.6 (d, J_{CP} = 28.6 Hz, 4C, C_{L(Pyrr)}), 129.0 (d, J_{CP} = 10.0 Hz, 16C, C_{L(Ph)}), 124.6 (s, 4C, C_{L(Pyrr)}). – ³¹P NMR (162 MHz, DMSO-d₆, ppm) δ = 10.24 (s, 4P). – ¹H NMR (400 MHz, CDCl₃, ppm) δ = 8.69 (d, ³J_{HH} = 4.7 Hz, 4H, H_{L(Pyrr)}), 7.71–7.68 (m, 4H, H_{L(Pyrr)}), 7.63–7.60 (m, 4H, H_{L(Pyrr)}), 7.59–7.54 (m, 16H, H_{L(Ph)}), 7.41–7.37 (m, 8H, H_{L(Ph)}), 7.34–7.30 (m, 16H, H_{L(Ph)}), 7.25–7.21 (m, 4H, H_{L(Pyrr)}). – ¹³C NMR (101 MHz, CDCl₃, ppm) δ = 157.9 (d, J_{CP} = 160.0 Hz, 4C, C_{qL(Pyrr)}), 151.0 (d, J_{CP} = 13.5 Hz, 4C, C_{L(Pyrr)}), 136.4 (d, J_{CP} = 8.5 Hz, 4C, C_{L(Pyrr)}), 134.5 (d, J_{CP} = 16.5 Hz, 16C, C_{L(Ph)}), 131.6 (d, J_{CP} = 108.0 Hz, 8C, C_{qL(Ph)}), 130.5 (s, 8C, C_{L(Ph)}), 130.4 (d, J_{CP} = 31.3 Hz, 4C, C_{L(Pyrr)}), 129.0 (d, J_{CP} = 9.9 Hz, 16C, C_{L(Ph)}), 124.0 (s, 4C, C_{L(Pyrr)}). – ³¹P NMR (162 MHz, CDCl₃, ppm) δ = 9.88 (s, 4P). – MS (FAB, 3-NBA) *m/z* [%] = 1726 (1) [M+Ag]⁺, 1584 (1) [M-Cl]⁺, 1442 (1) [Ag₃Cl₂L₄]⁺, 1321 (1) [Ag₄Cl₃L₄]⁺, 1179 (2) [Ag₃Cl₂L₃]⁺, 1038 (1) [Ag₂ClL₃]⁺, 896 (1) [AgL₃]⁺, 774 (20) [Ag₂ClL₂]⁺, 633 (63) [AgL₂]⁺, 511 (4) [Ag₂ClL]⁺, 460 (7) [3-NBA], 369 (83) [AgL]⁺, 307 (39) [3-NBA], 264 (24) [L+H]⁺, 186 (17) [L-Ph]⁺, 154 (100) [3-NBA], 137 (69) [3-NBA]. 3-NBA = 3-nitrobenzylalcohol. – IR (ATR) $\tilde{\nu}$ [cm⁻¹] = 2163 (vw), 1570 (vw), 1479 (vw), 1449 (vw), 1435 (vw), 1421 (vw), 1278 (vw), 1096 (vw), 1048 (vw), 987 (vw), 775 (vw), 743 (w), 722 (vw), 691 (w), 618 (vw), 515 (w), 502 (w), 438 (vw), 418 (vw), 401 (vw). – EA Anal. calcd. for C₆₈H₅₆Ag₄Cl₄N₄P₄: C 50.22, H 3.47, N 3.44; found: C 49.96, H 3.40, N 3.47. – mp = 230 °C. The molecular structure of complex **Ag₄Cl₄L₄** was determined by single crystal X-ray diffraction (CCDC-2058468). The analytical data are in accordance with the literature.¹⁰⁹ The molecular structure is a redetermination of BUFL0D at 173 K. All positions of the nitrogen atoms of the PyrPhos ligands in the tetranuclear Ag(I) complex could be assigned.

Data Deposition in Repositories. The details on the chemical synthesis and original analytical data were added to the repository Chemotion (www.chemotion.net/home). The molecular structures can be found on <https://www.ccdc.cam.ac.uk/structures/>. The corresponding codes are given in brackets. **Cu₂L₂L₃**

(CRR-14488, CCDC-838846⁶²), **Cu₂Br₂L₃** (CRR-14474, CCDC-2042604), **Cu₂Cl₂L₃** (CRR-14481, CCDC-876712⁶²), **CuIL₃** (CCDC-979009¹³⁸), **CuBrL₃** (CCDC-2086153), **CuClL₃** (CCDC-2063602), **Ag₂Br₂L₃** (CRR-14494, CCDC-2039552), **Ag₂Cl₂L₃** (CRR-14502, CCDC-2042183, CCDC-1107453¹²⁴), **Ag₂Cl₂L₄** (CCDC-2039550), **AgIL₃** (CRR-14511, CCDC-2039548), **AgBrL₃** (CRR-14521, CCDC-2042182), **AgClL₃** (CRR-14529, CCDC-2042603), **Ag₄I₄L₄** (CRR-14539, CCDC-2039549), **Ag₄Br₄L₄** (CRR-14546, CCDC-2079569), **Ag₄Cl₄L₄** (CRR-14552, CCDC-2058468, CCDC-1116117¹⁰⁹), **MM'I₂L₃** (with **M** = Cu(I) and **M'** = Ag(I), CCDC-2042602), **MM'Cl₂L₃** (with **M** = Cu(I) and **M'** = Ag(I), CCDC-2039551), **MIL₃** (with **M** = Cu(I) and Ag(I) 1:1, CCDC-2062374).

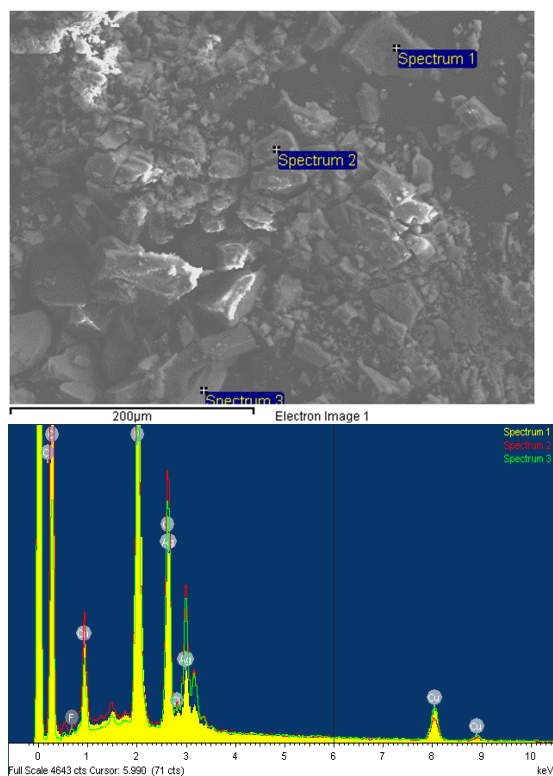


Figure 15. Measurement area and points (top) and corresponding SEM-EDX spectra (bottom) of the chloride containing sample **MM'Cl₂L₃** (**M**, **M'** = Cu(I) or Ag(I)).

EDX Measurements. The metal ratios of the heterometallic samples were measured with with energy dispersive X-ray analysis (EDX). The spectra were measured at 20 keV using an Oxford INCA 350 energy dispersive X-ray spectrometer connected with a Hitachi S-4800 scanning electron microscope (SEM). Measurements were made from a large area to obtain an average composition and from points to find out compositional variations (Figure 15, example of sample **MM'Cl₂L₃** (with **M** = Cu(I) and **M'** = Ag(I)).

The Cu:Ag molar ratio of the sample **MM'Cl₂L₃** indeed varied from point to point, being between 0.6:1 and 2:1 (Table 4). Details of the EDX measurements of the heterometallic samples

M₂Br₂L₃ (with **M** = Cu(I) and Ag(I)) and **MIL₃** (with **M** = Cu(I), Ag(I) 1:1) are given in the SI.

Table 4. Element molar ratios of the sample MM'Cl₂L₃ (with M = Cu(I) and Ag(I)), measured at 20 keV (with Spec. = Spectrum). Processing option: All elements analysed (Normalised). All results are given in atomic%.

Spec.	In stats	C	F	P	Cl	Cu	Ag	Cu:Ag ratio	Cu:A g ratio ^[a]
1	Yes	91.92		5.01	1.63	0.99	0.46	2:1	
2	Yes	92.83		3.37	2.10	0.65	1.06	0.6:1	
3	Yes	86.71	1.40	5.44	3.19	1.63	1.64	1:1	

^[a] in large area

Details of the Quantum-Chemical Computations. The Turbomole program package¹³⁹ and the resolution-of-the-identity (RI) approximation were used for all calculations. The ground and excited state structures were optimized using CAM-B3LYP¹⁴⁰/def2-TZVP (def2-SV(P) for H). Weight derivatives were used for all optimizations. Convergence criteria for the ground state structures were set to 10^{-8} E_h for the energy and 10^{-6} E_h/a₀ for the gradients, all structures were verified to be minima by frequency calculations. The excited states were optimized using the Tamm-Dancoff approximation within TDDFT and the convergence criteria were set to 10^{-7} E_h for the energy and 10^{-5} E_h/a₀ for the gradients. Numerical frequency calculations for all triplet excited states showed no imaginary frequencies. Numerical frequencies were also calculated for the singlet excited states used to calculate the singlet-triplet energy gap, no imaginary frequencies were found. Singlet-triplet energy gaps were calculated as difference in energy of the first singlet and triplet excited state energy using eigenvalue-only self-consistent *GW* with contour deformation for ten occupied and virtual orbitals with the correlation-augmented Bethe-Salpeter Equation and CAM-B3LYP (TDA-evGW(10)/cBSE-CAM-B3LYP).¹⁴¹ The reaction paths to obtain theoretical estimates for the barrier heights were generated using the WOELFLING program with 12 additional structures.

Sample Preparation for Optical Spectroscopy. Spectroscopic grade solvents were purchased from Merck. The solutions were prepared using the common Schlenck technique with concentrations in the range of $2 \cdot 10^{-5}$ M.

KBr pellets were prepared by mixing neat powder of the compound (1.6 – 3.0 mg, depending on the substance and the experiment) with dry KBr (200 mg, stored in a compartment dryer at 80 °C, purchased from Merck) and grinding to a homogenous mixture. This mixture was filled in an evacuable pellet die with a diameter of 13 mm and sintered at a pressure of 0.75 GPa. Please consider the respective sections for more details on the specific pellet preparations.

Experimental Details of the UV/Vis Studies. UV/Vis absorption experiments in solution were performed with a Lambda 900 UV/VIS spectrometer in DCM and EtOH using 10 mm path length quartz cells at 25 °C. The spectra were recorded relative to the pure solvent.

UV/Vis reflectance spectra were recorded with the same spectrometer by incorporation of a diffuse reflectance accessory (Harrick Praying Mantis) into the sample compartment. The powder samples were prepared by mixing neat powder of the compound with dry KBr in a ratio of ca. 1:100 and grinding to a homogenous mixture.

Experimental Details of the Luminescence Studies. Static emission spectroscopy. Steady state luminescence measurements were performed using a Horiba Jobin Yvon Fluorolog 3-22 τ spectrometer equipped with a 450 W xenon lamp and a R928 P photomultiplier detector (240 nm < λ_{em} < 850 nm). Spectral selection was achieved with double grating monochromators in the excitation and emission paths with 1200 grooves/mm (300 nm and 500 nm blaze in the excitation and emission paths, respectively). All the presented emission spectra are shown as obtained from the response of the instrument. Calibration of the excitation monochromator was performed according to the peak at 467 nm in the emission spectrum of the used xenon lamp. The emission monochromator was calibrated according to a water Raman spectrum. Solutions and KBr pellets were prepared as described in the section on the sample preparation (KBr pellets: 1.8 mg for Cu₂L₂L₃; 1.7 mg for Cu₂Br₂L₃; 1.6 mg for Cu₂Cl₂L₃; 1.8 mg for Ag₂Br₂ and 3.0 mg for Ag₂Cl₂). Temperature-dependent experiments between 5 K and 290 K were performed using a closed-cycle helium cryostat (ColdEdge, 101J cryocooler) to cool down the sample. The cryocooler was equipped with a pellet holder (copper) and CaF₂ windows. Emission spectra were recorded by scanning the emission monochromator at a fixed excitation wavelength, whereas excitation spectra were measured by scanning the excitation monochromator and setting the emission monochromator to the maximum of the luminescence band. In the latter case long-pass filters were placed in the emission channel to prevent any contamination of the spectra with scattered excitation light.

Temperature-dependent time-correlated single photon counting (TCSPC). Luminescence lifetimes were determined by time-correlated single photon counting (TCSPC) using a DeltaFlex (Horiba Scientific) spectrometer. The sample was excited with short light pulses of a NanoLED 390 (wavelength: 389 ± 10 nm, pulse duration: 1.3 ns), NanoLED 350 (wavelength: 345 ± 10 ns, pulse duration: < 1 ns), NanoLED 320 (wavelength: 313 ± 10 nm, pulse duration: < 1 ns) or a SpectraLED 390 (wavelength: 390 ± 14 nm, pulse duration: ca. 100 ns). The emission monochromator was set to the respective emission band of the investigated compound. For KBr pellets, a long-pass filter (cut-on wavelengths of 436 nm, 528 nm or 540 nm, depending on the complex) was placed in the emission channel to suppress the influence of scattered excitation light. Precision photon counting was carried out with a PPT (picosecond photon counting) detection module, including a fast-rise photomultiplier with an integral GHz timing preamplifier, a constant fraction discriminator and a regulated HV (high voltage) supply.

For solution samples, the instrumental response function (FWHM = 125 ps) and the influence of excitation light were considered by performing a reference measurement on a LUDOX® solution. The low-temperature measurements were performed using the cryostat presented in the section on static emission spectroscopy.

Decay curves were analyzed by multiexponential fits with the software ORIGIN®. Average lifetimes were calculated using the amplitude-weighted average lifetime, which is defined by

$$\tau_{av} = \sum_i \alpha_i \tau_i \quad (\text{eq. 3})$$

Estimated uncertainties of the lifetimes obtained by TCSPC and step-scan FTIR spectroscopy (see following subchapter) are of the order of 10%.

Experimental Details of Step-Scan FTIR Experiments. All the time-resolved FTIR experiments were performed with the FTIR spectrometer Bruker Vertex 80v, operated in the step-scan mode. A liquid-nitrogen-cooled mercury cadmium telluride (MCT) detector (Kolmar Tech., Model KV100-1-B-7/190) with a rise time of 25 ns, connected to a fast preamplifier and a 14-bit transient recorder board (Spectrum Germany, M314142, 400 MS/s), was used for signal detection and processing. The laser setup used for the measurements includes a Q-switched Nd:YAG laser (Innolas SpitLight Evo I) generating pulses with a duration of about 6 ns at a repetition rate of 100 Hz. The third harmonic (355 nm) of the Nd:YAG laser was used directly for sample excitation. The UV pump beam was attenuated to 1.1 mJ per shot at a diameter of 9 mm. The beam was directed onto the sample and adjusted to have a maximal overlap with the IR beam of the spectrometer. The sample chamber was equipped with anti-reflection-coated germanium filters to prevent the entrance of laser radiation into the detector and interferometer compartments.

The KBr pellets were prepared as described in the section on the sample preparation (2.0 mg for Cu₂L₂L₃; 1.7 mg for Cu₂Br₂L₃; 1.6 mg for Cu₂Cl₂L₃; 1.8 mg for Ag₂Br₂ and 1.7 mg for Ag₂Cl₂). The strongest peak in the ground state spectrum showed an absorption of 0.5 – 0.9 OD with the mentioned concentration. The measurements were performed at temperatures of 20 K (for Cu and Ag complexes) and 290 K (for Cu complexes) using a closed-cycle helium cryostat (ARS Model DE-202A). The cryocooler was equipped with a pellet holder (copper) and CaF₂ windows.

The temporal resolution of the 14-bit transient recorder board was chosen to 10 ns and 20 ns for the Cu and Ag complexes, respectively. Thus, a time range of 100 μ s or 200 μ s was covered with the recorded 10000 time slices. The time when the laser pulse reached the sample was set as zero point in all spectra. The time delay between the start of the experiment and the laser pulse was controlled with a Stanford Research Systems DG535 delay generator and set to 1.3 μ s before the laser excitation of the sample. The spectral region was limited by under-sampling to 988 – 1975 cm⁻¹ or 0 – 1975 cm⁻¹ with a spectral resolution of 4 cm⁻¹, resulting in 555 or 1110 interferogram points, respectively. An IR broad band filter (850 – 1750 cm⁻¹) and the CaF₂ windows (no IR transmission < 1000 cm⁻¹) of the cryostat prevented problems when performing a Fourier transformation (i.e. no IR intensity outside the measured region should be observed). FTIR ground state spectra were recorded systematically to check if there is no sample degradation.

Keywords: Cooperative Effects • Thermally Activated Delayed Fluorescence • Cu(I) Complexes • Ag(I) Complexes • NP-bridging ligand • 2-(Diphenylphosphino)pyridine (PyPhos) • *GW* Approximation • Bethe-Salpeter Equation • Photophysical Studies • UV/Vis Spectra • Step-Scan FTIR Spectroscopy

ASSOCIATED CONTENT

Supporting Information. General information (NMR, mass spectrometry, IR, elemental analysis) and information about

SEM-EDX analysis, single-crystal X-ray analysis, quantum-chemical computations, UV/Vis and luminescence studies, and step-scan FTIR spectroscopy are provided in the Supporting Information (SI). This material is available free of charge via the Internet at <http://pubs.acs.org>.

AUTHOR INFORMATION

Corresponding Authors

Gereon Niedner-Schatteburg – Chemistry Department and State Research Center Optimas, TU Kaiserslautern, Erwin-Schrödinger-Straße 52, 67663 Kaiserslautern, Germany; <https://orcid.org/0000-0001-7240-6673>; Email: gns@chemie.uni-kl.de

Stefan Bräse – Institute of Organic Chemistry and Institute of Biological and Chemical Systems – Functional Molecular Systems, Karlsruhe Institute of Technology (KIT), Kaiserstraße 12, 76131 Karlsruhe, Germany; <https://orcid.org/0000-0003-4845-3191>; Email: braese@kit.edu

Wim Klopper – Institute of Physical Chemistry and Institute of Nanotechnology, Karlsruhe Institute of Technology (KIT), Kaiserstraße 12, 76131 Karlsruhe, Germany; <https://orcid.org/0000-0002-5219-9328>; Email: klopper@kit.edu

Authors

Florian R. Rehak – Institute of Physical Chemistry, Karlsruhe Institute of Technology (KIT), Kaiserstraße 12, 76131 Karlsruhe, Germany; <https://orcid.org/0000-0003-2237-6781>

Sophie T. Steiger – Chemistry Department and State Research Center Optimas, TU Kaiserslautern, Erwin-Schrödinger Straße 52, 67663 Kaiserslautern, Germany

Pit. J. Boden – Chemistry Department and State Research Center Optimas, TU Kaiserslautern, Erwin-Schrödinger-Straße 52, 67663 Kaiserslautern, Germany

Jasmin. M. Busch – Institute of Organic Chemistry, Karlsruhe Institute of Technology (KIT), Kaiserstraße 12, 76131 Karlsruhe, Germany; <https://orcid.org/0000-0002-8020-8893>

Martin Nieger, – Department of Chemistry, University of Helsinki, P.O. Box 55 (A.I. Virtasen aukio 1), FI 00014 University of Helsinki, Finland; <https://orcid.org/0000-0003-1677-0109>

Marianna Kemell – Department of Chemistry, University of Helsinki, P.O. Box 55 (A.I. Virtasen aukio 1), FI 00014 University of Helsinki, Finland; <https://orcid.org/0000-0002-3583-2064>

Olaf Fuhr – Karlsruhe Institute of Nanotechnology and Karlsruhe Nano-Micro Facility (KNMF), Karlsruhe Institute of Technology (KIT), Kaiserstraße 12, 76131 Karlsruhe, Germany; <https://orcid.org/0000-0003-3516-2440>

Author Contributions

The manuscript has been written through contributions of all authors. J.M.B. synthesized and analyzed all presented compounds under the supervision of S.B. The SEM-EDX work was done by M.K., and single-crystal X-ray diffraction analysis was carried out by M.N. and O.F. Spectroscopic studies were conducted by S.T.S. and P.J.B. under the supervision of G.N.-S. Theoretical investigations were done by F.R.R. under the

supervision of W.K. All authors have given approval to the final version of the manuscript.

Notes

The authors declare no competing financial interest.

ACKNOWLEDGMENT

We dedicate this publication to the memory of our late colleague Markus Gerhards in recognition of his long standing devotion for the spectroscopic characterization of molecular complexes with and without involvement of transition-metal centers, which has been pivotal to the present study. We are very grateful for the financial support by the Deutsche Forschungsgemeinschaft (DFG) through the Collaborative Research Center CRC/TRR 88 *3MET – Cooperative Effects in Homo- and Heterometallic Complexes* (Projects C1, C2 and T1). In addition, we wish to thank the Karlsruhe School of Optics and Photonics (KSOP) as well as the DFG for financial support through Germany's Excellence Strategy *3D Matter Made to Order* (3DMM20, Grant No. EXC-2082/1–390761711).

REFERENCES

- Schmidbaur, H.; Schier, A., Auophilic interactions as a subject of current research: an up-date. *Chem. Soc. Rev.* **2012**, *41* (1), 370-412.
- Schmidbaur, H.; Schier, A., A briefing on auophilicity. *Chem. Soc. Rev.* **2008**, *37* (9), 1931-1951.
- Schmidbaur, H.; Cronje, S.; Djordjevic, B.; Schuster, O., Understanding gold chemistry through relativity. *Chem. Phys.* **2005**, *311* (1-2), 151-161.
- Coker, N. L.; Krause Bauer, J. A.; Elder, R. C., Emission Energy Correlates with Inverse of Gold-Gold Distance for Various [Au(SCN)₂]-Salts. *J. Am. Chem. Soc.* **2003**, *126*, 12-13.
- Scherbaum, F.; Grohmann, A.; Huber, B.; Kruger, C.; Schmidbaur, H., "Auophilicity" as a Consequence of Relativistic Effects: The Hexakis(triphenylphosphaneaurio)methane Dication [(Ph₃PAu)₆C]²⁺. *Angew. Chem. Int. Ed.* **1988**, *27* (11), 1544-1546.
- Ravaro, L. P.; Zanon, K. P. S.; de Camargo, A. S. S., Luminescent Copper(I) complexes as promising materials for the next generation of energy-saving OLED devices. *Energy Rep.* **2020**, *6*, 37-45.
- Li, G.; Zhu, D.; Wang, X.; Su, Z.; Bryce, M. R., Dinuclear metal complexes: multifunctional properties and applications. *Chem. Soc. Rev.* **2020**, *49* (3), 765-838.
- Guo, B.-K.; Yang, F.; Wang, Y.-Q.; Wei, Q.; Liu, L.; Zhong, X.-X.; Wang, L.; Gong, J.-K.; Li, F.-B.; Wong, W.-Y.; Alamry, K. A.; Zhao, Y., Efficient TADF-OLEDs with ultra-soluble Copper(I) halide complexes containing non-symmetrically substituted bidentate phosphine and PPh₃ ligands. *J. Lumin.* **2020**, *220*, 116963.
- Liu, Y.; Yiu, S.-C.; Ho, C.-L.; Wong, W.-Y., Recent advances in copper complexes for electrical/light energy conversion. *Coord. Chem. Rev.* **2018**, *375*, 514-557.
- Bizzarri, C.; Spuling, E.; Knoll, D. M.; Volz, D.; Bräse, S., Sustainable metal complexes for organic light-emitting diodes (OLEDs). *Coord. Chem. Rev.* **2018**, *373*, 49-82.
- Bizzarri, C.; Hundemer, F.; Busch, J.; Bräse, S., Triplet emitters versus TADF emitters in OLEDs: A comparative study. *Polyhedron* **2018**, *140*, 51-66.
- Czerwieńiec, R.; Yersin, H.; Shafikov, M. Z.; Suleymanova, A. F., TADF Material Design: Photophysical Background and Case

- Studies Focusing on Cu(I) and Ag(I) Complexes. *ChemPhysChem* **2017**, *18* (24), 3508-3535.
13. Wallesch, M.; Verma, A.; Flechon, C.; Flügge, H.; Zink, D. M.; Seifermann, S. M.; Navarro, J. M.; Vitova, T.; Gottlicher, J.; Steininger, R.; Weinhardt, L.; Zimmer, M.; Gerhards, M.; Heske, C.; Bräse, S.; Baumann, T.; Volz, D., Towards Printed Organic Light-Emitting Devices: A Solution-Stable, Highly Soluble Cu(I)-NHetPHOS. *Chem. Eur. J.* **2016**, *22*, 16400-16405.
 14. Leitl, M. J.; Zink, D. M.; Schinabeck, A.; Baumann, T.; Volz, D.; Yersin, H., Copper(I) Complexes for Thermally Activated Delayed Fluorescence: From Photophysical to Device Properties. *Top. Curr. Chem.* **2016**, *374* (25), 1-34.
 15. Volz, D.; Wallesch, M.; Fléchon, C.; Danz, M.; Verma, A.; Navarro, J. M.; Zink, D. M.; Bräse, S.; Baumann, T., From iridium and platinum to copper and carbon: new avenues for more sustainability in organic light-emitting diodes. *Green Chem.* **2015**, *17* (4), 1988-2011.
 16. Zink, D. M.; Bergmann, L.; Ambrosek, D.; Wallesch, M.; Volz, D.; Mydlak, M., Singlet harvesting copper-based emitters: a modular approach towards next-generation OLED technology. *Translational Materials Research* **2014**, *1* (1), 015003.
 17. Yersin, H.; Rausch, A. F.; Czerwiniak, R.; Hofbeck, T.; Fischer, T., The triplet state of organo-transition metal compounds. Triplet harvesting and singlet harvesting for efficient OLEDs. *Coord. Chem. Rev.* **2011**, *255* (21-22), 2622-2652.
 18. Keller, S.; Prescimone, A.; La Placa, M.-G.; Junquera-Hernández, J. M.; Bolink, H. J.; Constable, E. C.; Sessolo, M.; Ortí, E.; Housecroft, C. E., The shiny side of copper: bringing copper(I) light-emitting electrochemical cells closer to application. *RSC Adv.* **2020**, *10* (38), 22631-22644.
 19. Fresta, E.; Weber, M. D.; Fernandez-Cestau, J.; Costa, R. D., White Light-Emitting Electrochemical Cells Based on Deep-Red Cu(I) Complexes. *Adv. Opt. Mater.* **2019**, *7* (23), 1900830.
 20. Weber, M. D.; Fresta, E.; Elie, M.; Miehlisch, M. E.; Renaud, J.-L.; Meyer, K.; Gaillard, S.; Costa, R. D., Rationalizing Fabrication and Design Toward Highly Efficient and Stable Blue Light-Emitting Electrochemical Cells Based on NHC Copper(I) Complexes. *Adv. Funct. Mater.* **2018**, *28* (17), 1707423.
 21. Fresta, E.; Volpi, G.; Milanesio, M.; Garino, C.; Barolo, C.; Costa, R. D., Novel Ligand and Device Designs for Stable Light-Emitting Electrochemical Cells Based on Heteroleptic Copper(I) Complexes. *Inorg. Chem.* **2018**, *57* (16), 10469-10479.
 22. Elie, M.; Weber, M. D.; Di Meo, F.; Sguerra, F.; Lohier, J. F.; Pansu, R. B.; Renaud, J. L.; Hamel, M.; Linares, M.; Costa, R. D.; Gaillard, S., Role of the Bridging Group in Bis-Pyridyl Ligands: Enhancing Both the Photo- and Electroluminescent Features of Cationic (IPr)Cu(I) Complexes. *Chem. Eur. J.* **2017**, *23* (64), 16328-16337.
 23. Weber, M. D.; Garino, C.; Volpi, G.; Casamassa, E.; Milanesio, M.; Barolo, C.; Costa, R. D., Origin of a counterintuitive yellow light-emitting electrochemical cell based on a blue-emitting heteroleptic copper(I) complex. *Dalton Trans.* **2016**, *45* (21), 8984-8993.
 24. Keller, S.; Pertegás, A.; Longo, G.; Martínez, L.; Cerdá, J.; Junquera-Hernández, J. M.; Prescimone, A.; Constable, E. C.; Housecroft, C. E.; Ortí, E.; Bolink, H. J., Shine bright or live long: substituent effects in [Cu(N[^]N)(P[^]P)]⁺-based light-emitting electrochemical cells where N[^]N is a 6-substituted 2,2'-bipyridine. *J. Mater. Chem. C* **2016**, *4* (17), 3857-3871.
 25. Elie, M.; Sguerra, F.; Di Meo, F.; Weber, M. D.; Marion, R.; Grimault, A.; Lohier, J. F.; Stallivieri, A.; Brosseau, A.; Pansu, R. B.; Renaud, J. L.; Linares, M.; Hamel, M.; Costa, R. D.; Gaillard, S., Designing NHC-Copper(I) Dipyrindylamine Complexes for Blue Light-Emitting Electrochemical Cells. *ACS Appl. Mater. Interfaces* **2016**, *8* (23), 14678-14691.
 26. Brunner, F.; Martínez-Sarti, L.; Keller, S.; Pertegás, A.; Prescimone, A.; Constable, E. C.; Bolink, H. J.; Housecroft, C. E., Peripheral halo-functionalization in [Cu(N[^]N)(P[^]P)]⁺ emitters: influence on the performances of light-emitting electrochemical cells. *Dalton Trans.* **2016**, *45* (38), 15180-15192.
 27. Keller, S.; Constable, E. C.; Housecroft, C. E.; Neuburger, M.; Prescimone, A.; Longo, G.; Pertegas, A.; Sessolo, M.; Bolink, H. J., [Cu(bpy)(P[^]P)]⁺ containing light-emitting electrochemical cells: improving performance through simple substitution. *Dalton Trans.* **2014**, *43* (44), 16593-16596.
 28. Costa, R. D.; Tordera, D.; Ortí, E.; Bolink, H. J.; Schönle, J.; Graber, S.; Housecroft, C. E.; Constable, E. C.; Zampese, J. A., Copper(I) complexes for sustainable light-emitting electrochemical cells. *J. Mater. Chem.* **2011**, *21* (40), 16108.
 29. Armaroli, N.; Accorsi, G.; Holler, M.; Moudam, O.; Nierengarten, J. F.; Zhou, Z.; Wegh, R. T.; Welter, R., Highly Luminescent CuI Complexes for Light-Emitting Electrochemical Cells. *Adv. Mater.* **2006**, *18* (10), 1313-1316.
 30. Wang, Y.-M.; Teng, F.; Hou, Y.-B.; Xu, Z.; Wang, Y.-S.; Fu, W.-F., Copper(I) complex employed in organic light-emitting electrochemical cells: Device and spectra shift. *Appl. Phys. Lett.* **2005**, *87* (23), 233512.
 31. Zhang, J.; Xia, H.; Ren, S.; Jia, W.; Zhang, C., Three AIE-ligand-based Cu(I) coordination polymers: synthesis, structures and luminescence sensing of TNP. *New J. Chem.* **2020**, *44* (14), 5285-5292.
 32. Qian, L.-L.; Wang, Z.-X.; Ding, J.-G.; Tian, H.-X.; Li, K.; Li, B.-L.; Li, H.-Y., A 2D copper(I) metal-organic framework: Synthesis, structure and luminescence sensing for cupric, ferric, chromate and TNP. *Dyes Pigm.* **2020**, *175*, 108159.
 33. Ravaro, L. P.; Mafud, A. C.; Li, Z.; Reinheimer, E.; Simone, C. A.; Mascarenhas, Y. P.; Ford, P. C.; de Camargo, A. S. S., New emissive mononuclear copper (I) complex: Structural and photophysical characterization focusing on solvatochromism, rigidochromism and oxygen sensing in mesoporous solid matrix. *Dyes Pigm.* **2018**, *159*, 464-470.
 34. Smith, C. S.; Mann, K. R., Exceptionally Long-Lived Luminescence from [Cu(I)(isocyanide)₂(phen)]⁺ Complexes in Nanoporous Crystals Enables Remarkable Oxygen Gas Sensing. *J. Am. Chem. Soc.* **2012**, *134* (21), 8786-8789.
 35. Strasser, C. E.; Catalano, V. J., "On-Off" Au(I) ··· Cu(I) Interactions in a Au(NHC)₂ Luminescent Vapochromic Sensor. *J. Am. Chem. Soc.* **2010**, *132*, 10009-10011.
 36. Shi, L.; Li, B.; Yue, S.; Fan, D., Synthesis, photophysical and oxygen-sensing properties of a novel bluish-green emission Cu(I) complex. *Sens. and Actuators B Chem.* **2009**, *137* (1), 386-392.
 37. Shi, L.; Li, B., A Series of Cu(I) Complexes Containing 1,10-Phenanthroline Derivative Ligands: Synthesis, Characterization, Photophysical, and Oxygen-Sensing Properties. *Eur. J. Inorg. Chem.* **2009**, *2009* (15), 2294-2302.
 38. Gracia, L. L.; Luci, L.; Bruschi, C.; Sambri, L.; Weis, P.; Fuhr, O.; Bizzarri, C., New Photosensitizers Based on Heteroleptic Cu(I) Complexes and CO₂ Photocatalytic Reduction with [Ni(II)(cyclam)]Cl₂. *Chem. Eur. J.* **2020**, *26*, 9929 - 9937.
 39. Hockin, B. M.; Li, C.; Robertson, N.; Zysman-Colman, E., Photoredox catalysts based on earth-abundant metal complexes. *Catal. Sci. Technol.* **2019**, *9* (4), 889-915.
 40. Busch, J.; Knoll, D. M.; Zippel, C.; Bräse, S.; Bizzarri, C., Metal-supported and -assisted stereoselective cooperative photoredox catalysis. *Dalton Trans.* **2019**, *48* (41), 15338-15357.

41. Larsen, C. B.; Wenger, O. S., Photoredox Catalysis with Metal Complexes Made from Earth-Abundant Elements. *Chem. Eur. J.* **2018**, *24* (9), 2039-2058.
42. Reiser, O., Shining Light on Copper: Unique Opportunities for Visible-Light-Catalyzed Atom Transfer Radical Addition Reactions and Related Processes. *Acc. Chem. Res.* **2016**, *49* (9), 1990-1996.
43. Paria, S.; Reiser, O., Copper in Photocatalysis. *ChemCatChem* **2014**, *6* (9), 2477-2483.
44. Pirtsch, M.; Paria, S.; Matsuno, T.; Isobe, H.; Reiser, O., [Cu(dap)₂Cl] As an Efficient Visible-Light-Driven Photoredox Catalyst in Carbon-Carbon Bond-Forming Reactions. *Chem. Eur. J.* **2012**, *18* (24), 7336-7340.
45. Kern, J.-M. K.; Sauvage, J.-P., Photoassisted C-C coupling via Electron Transfer to Benzylic Halides by a Bis(di-imine) Copper(I) Complex. *J. Chem. Soc. Chem. Commun.* **1987**, 546-548.
46. Greenwood, N. N.; Earnshaw, A., *Chemistry of the Elements*. 2. Edition, Butterworth, Großbritannien, 1997.
47. Liang, X. Q.; Gupta, R. K.; Li, Y. W.; Ma, H. Y.; Gao, L. N.; Tung, C. H.; Sun, D., Structural Diversity of Copper(I) Cluster-Based Coordination Polymers with Pyrazine-2-thiol Ligand. *Inorg. Chem.* **2020**, *59* (5), 2680-2688.
48. Jazzar, R.; Soleilhavoup, M.; Bertrand, G., Cyclic (Alkyl)- and (Aryl)-(amino)carbene Coinage Metal Complexes and Their Applications. *Chem. Rev.* **2020**, *120* (9), 4141-4168.
49. Ilmi, R.; Juma Al-busaidi, I.; Haque, A.; Khan, M. S., Recent progress in coordination chemistry, photo-physical properties, and applications of pyridine-based Cu(I) complexes. *J. Coord. Chem.* **2018**, *71* (19), 3045-3076.
50. Gneuß, T.; Leitl, M. J.; Finger, L. H.; Yersin, H.; Sundermeyer, J., A new class of deep-blue emitting Cu(I) compounds – effects of counter ions on the emission behavior. *Dalton Trans.* **2015**, *44*, 20045-20055.
51. Bergmann, L.; Friedrichs, J.; Mydlak, M.; Baumann, T.; Nieger, M.; Bräse, S., Outstanding luminescence from neutral copper(I) complexes with pyridyl-tetrazolate and phosphine ligands. *Chem. Commun.* **2013**, *49*, 6501-6503.
52. Zink, D. M.; Grab, T.; Baumann, T.; Nieger, M.; Barnes, E. C.; Klopper, W.; Bräse, S., Experimental and Theoretical Study of Novel Luminescent Di-, Tri-, and Tetranuclear Copper Triazole Complexes. *Organometallics* **2011**, *30*, 3275-3283.
53. Liang, P.; Kobayashi, A.; Sameera, W. M. C.; Yoshida, M.; Kato, M., Solvent-Free Thermal Synthesis of Luminescent Dinuclear Cu(I) Complexes with Triarylphosphines. *Inorg. Chem.* **2018**, *57* (10), 5929-5938.
54. Chen, B.-L.; Liu, L.; Zhong, X.-X.; Asiri, A. M.; Alamry, K. A.; Li, G.-H.; Li, F.-B.; Zhu, N.-Y.; Wong, W.-Y.; Qin, H.-M., Synthesis, characterization and luminescent properties of copper(I) halide complexes containing biphenyl bidentate phosphine ligand. *J. Coord. Chem.* **2017**, *70* (23), 3907-3919.
55. Tsuge, K.; Chishina, Y.; Hashiguchi, H.; Sasaki, Y.; Kato, M.; Ishizaka, S.; Kitamura, N., Luminescent copper(I) complexes with halogenido-bridged dimeric core. *Coord. Chem. Rev.* **2016**, *306*, 636-651.
56. Okano, Y.; Ohara, H.; Kobayashi, A.; Yoshida, M.; Kato, M., Systematic Introduction of Aromatic Rings to Diphosphine Ligands for Emission Color Tuning of Dinuclear Copper(I) Iodide Complexes. *Inorg. Chem.* **2016**, *55* (11), 5227-5236.
57. Hong, X.; Wang, B.; Liu, L.; Zhong, X.-X.; Li, F.-B.; Wang, L.; Wong, W.-Y.; Qin, H.-M.; Lo, Y. H., Highly efficient blue-green neutral dinuclear copper(I) halide complexes containing bidentate phosphine ligands. *J. Lumin.* **2016**, *180*, 64-72.
58. Leitl, M. J.; Kuchle, F. R.; Mayer, H. A.; Wesemann, L.; Yersin, H., Brightly Blue and Green Emitting Cu(I) Dimers for Singlet Harvesting in OLEDs. *J. Phys. Chem. A* **2013**, *117*, 11823-11836.
59. Volz, D.; Nieger, M.; Bräse, S., Di- μ -iodido-bis-([(R)-(+)-2,2'-bis-(diphenyl-phosphanyl)-1,1'-binaphthyl- κ^2 P,P']copper(I)) 0.67-hydrate. *Acta Cryst. E* **2012**, *68* (Pt 4), m466-7.
60. Tsuboyama, A.; Kuge, K.; Furugori, M.; Okada, S.; Hoshino, M.; Ueno, K., Photophysical Properties of Highly Luminescent Copper(I) Halide Complexes Chelated with 1,2-Bis(diphenylphosphino)benzene. *Inorg. Chem.* **2007**, *46*, 1992-2001.
61. Bizzarri, C.; Arndt, A. P.; Kohaut, S.; Fink, K.; Nieger, M., Mononuclear and dinuclear heteroleptic Cu(I) complexes based on pyridyl-triazole and DPEPhos with long-lived excited-state lifetimes. *J. Organomet. Chem.* **2018**, *871*, 140-149.
62. Zink, D. M.; Bächle, M.; Baumann, T.; Nieger, M.; Kuhn, M.; Wang, C.; Klopper, W.; Monkowius, U.; Hofbeck, T.; Yersin, H.; Bräse, S., Synthesis, Structure, and Characterization of Dinuclear Copper(I) Halide Complexes with P[^]N ligands Featuring Exciting Photoluminescence Properties. *Inorg. Chem.* **2013**, *52*, 2292-2305.
63. Bergmann, L.; Braun, C.; Nieger, M.; Bräse, S., The coordination- and photochemistry of copper(I) complexes: variation of N[^]N ligands from imidazole to tetrazole. *Dalton Trans.* **2018**, *47* (2), 608-621.
64. Bizzarri, C.; Strabler, C.; Prock, J.; Trettenbrein, B.; Ruggenthaler, M.; Yang, C. H.; Polo, F.; Iordache, A.; Bruggeller, P.; De Cola, L., Luminescent dinuclear Cu(I) complexes containing rigid tetraphosphine ligands. *Inorg. Chem.* **2014**, *53* (20), 10944-10951.
65. He, L. H.; Luo, Y. S.; Di, B. S.; Chen, J. L.; Ho, C. L.; Wen, H. R.; Liu, S. J.; Wang, J. Y.; Wong, W. Y., Luminescent Three- and Four-Coordinate Dinuclear Copper(I) Complexes Triply Bridged by Bis(diphenylphosphino)methane and Functionalized 3-(2'-Pyridyl)-1,2,4-triazole Ligands. *Inorg. Chem.* **2017**, *56*, 10311-10324.
66. Chen, Y.; Chen, J.-S.; Gan, X.; Fu, W.-F., Dinuclear copper(I) complexes containing diimine and phosphine ligands: Synthesis, copper-copper separation and photophysical properties. *Inorg. Chim. Acta* **2009**, *362* (7), 2492-2498.
67. Nishioka, T.; Mitsui, S.; Kinoshita, I.; Koshiyama, T.; Kato, M., Observation of Halide-Induced Conformational Conversion of Dinuclear Copper Complexes Having a Tetradentate Polypyridine Ligand with a *p*-Xylene Backbone. *B. Chem. Soc. Jpn.* **2007**, *80* (7), 1357-1367.
68. Musina, E. I.; Shamsieva, A. V.; Strel'nik, I. D.; Gerasimova, T. P.; Krivolapov, D. B.; Kolesnikov, I. E.; Grachova, E. V.; Tunik, S. P.; Bannwarth, C.; Grimme, S.; Katsyuba, S. A.; Karasik, A. A.; Sinyashin, O. G., Synthesis of novel pyridyl containing phospholanes and their polynuclear luminescent copper(I) complexes. *Dalton Trans.* **2016**, *45*, 2250-2260.
69. Zink, D. M.; Volz, D.; Baumann, T.; Mydlak, M.; Flügge, H.; Friedrichs, J.; Nieger, M.; Bräse, S., Heteroleptic, Dinuclear Copper(I) Complexes for Application in Organic Light-Emitting Diodes. *Chem. Mater.* **2013**, *25*, 4471-4486.
70. Zink, D. M.; Baumann, T.; Friedrichs, J.; Nieger, M.; Bräse, S., Copper(I) Complexes Based on Five-Membered P[^]N Heterocycles: Structural Diversity Linked to Exciting Luminescence Properties. *Inorg. Chem.* **2013**, *52*, 13509-13520.
71. Hofbeck, T.; Niehaus, T. A.; Fleck, M.; Monkowius, U.; Yersin, H., P[^]N Bridged Cu(I) Dimers Featuring Both TADF and Phosphorescence. From Overview towards Detailed Case Study

- of the Excited Singlet and Triplet States. *Molecules* **2021**, *26* (11).
72. Busch, J. M.; Zink, D. M.; Di Martino-Fumo, P.; Rehak, F. R.; Boden, P.; Steiger, S.; Fuhr, O.; Nieger, M.; Klopper, W.; Gerhards, M.; Bräse, S., Highly soluble fluorine containing Cu(I) AlkylPyrPhos TADF complexes. *Dalton Trans.* **2019**, *48*, 15687-15698.
73. Volz, D.; Chen, Y.; Wallesch, M.; Liu, R.; Flechon, C.; Zink, D. M.; Friedrichs, J.; Flügge, H.; Steininger, R.; Gottlicher, J.; Heske, C.; Weinhardt, L.; Bräse, S.; So, F.; Baumann, T., Bridging the Efficiency Gap: Fully Bridged Dinuclear Cu(I)-Complexes for Singlet Harvesting in High-Efficiency OLEDs. *Adv. Mater.* **2015**, *27* (15), 2538-43.
74. Wallesch, M.; Volz, D.; Zink, D. M.; Schepers, U.; Nieger, M.; Baumann, T.; Bräse, S., Bright copper opportunities: multinuclear Cu(I) complexes with N-P ligands and their applications. *Chem. Eur. J.* **2014**, *20* (22), 6578-90.
75. Volz, D.; Wallesch, M.; Grage, S. L.; Göttlicher, J.; Steininger, R.; Batchelor, D.; Vitova, T.; Ulrich, A. S.; Heske, C.; Weinhardt, L.; Baumann, T.; Bräse, S., Labile or stable: can homoleptic and heteroleptic PyrPHOS-copper complexes be processed from solution? *Inorg. Chem.* **2014**, *53*, 7837-7847.
76. Volz, D.; Hirschbiel, A. F.; Zink, D. M.; Friedrichs, J.; Nieger, M.; Baumann, T.; Bräse, S.; Barner-Kowollik, C., Highly efficient photoluminescent Cu(I)-PyrPHOS-metallopolymers. *J. Mater. Chem. C* **2014**, *2*, 1457-1462.
77. Volz, D.; Zink, D. M.; Bocksrocker, T.; Friedrichs, J.; Nieger, M.; Baumann, T.; Lemmer, U.; Bräse, S., Molecular Construction Kit for Tuning Solubility, Stability and Luminescence Properties: Heteroleptic MePyrPHOS-Copper Iodide-Complexes and their Application in Organic Light-Emitting Diodes. *Chem. Mater.* **2013**, *25*, 3414-3426.
78. Volz, D.; Nieger, M.; Friedrichs, J.; Baumann, T.; Bräse, S., How the Quantum Efficiency of a Highly Emissive Binuclear Copper Complex Is Enhanced by Changing the Processing Solvent. *Langmuir* **2013**, *29*, 3034-3044.
79. Volz, D.; Baumann, T.; Flügge, H.; Mydlak, M.; Grab, T.; Bächle, M.; Barner-Kowollik, C.; Bräse, S., Auto-catalysed crosslinking for next-generation OLED-design. *J. Mater. Chem.* **2012**, *22*, 20786-20790.
80. Klein, M.; Rau, N.; Wende, M.; Sundermeyer, J.; Cheng, G.; Che, C.-M.; Schinabeck, A.; Yersin, H., Cu(I) and Ag(I) Complexes with a New Type of Rigid Tridentate N,P,P-Ligand for Thermally Activated Delayed Fluorescence and OLEDs with High External Quantum Efficiency. *Chem. Mater.* **2020**, *32* (24), 10365-10382.
81. Schinabeck, A.; Chen, J.; Kang, L.; Teng, T.; Homeier, H. H. H.; Suleymanova, A. F.; Shafikov, M. Z.; Yu, R.; Lu, C.-Z.; Yersin, H., Symmetry-Based Design Strategy for Unprecedentedly Fast Decaying Thermally Activated Delayed Fluorescence (TADF). Application to Dinuclear Cu(I) Compounds. *Chem. Mater.* **2019**, *31* (12), 4392-4404.
82. Czerwieńiec, R.; Leitl, M. J.; Homeier, H. H. H.; Yersin, H., Cu(I) complexes - Thermally activated delayed fluorescence. Photophysical approach and material design. *Coord. Chem. Rev.* **2016**, *325*, 2-28.
83. Tao, Y.; Yuan, K.; Chen, T.; Xu, P.; Li, H.; Chen, R.; Zheng, C.; Zhang, L.; Huang, W., Thermally Activated Delayed Fluorescence Materials Towards the Breakthrough of Organoelectronics. *Adv. Mater.* **2014**, *26*, 7931-7958.
84. Linfoot, C. L.; Leitl, M. J.; Richardson, P.; Rausch, A. F.; Chepelin, O.; White, F. J.; Yersin, H.; Robertson, N., Thermally Activated Delayed Fluorescence (TADF) and Enhancing Photoluminescence Quantum Yields of [Cu(I)(diimine)(diphosphine)]⁺ Complexes-Photophysical, Structural, and Computational Studies. *Inorg. Chem.* **2014**, *53*, 10854-10861.
85. Leitl, M. J.; Krylova, V. A.; Djurovich, P. I.; Thompson, M. E.; Yersin, H., Phosphorescence versus Thermally Activated Delayed Fluorescence. Controlling Singlet-Triplet Splitting in Brightly Emitting and Sublimable Cu(I) Compounds. *J. Am. Chem. Soc.* **2014**, *136*, 16032-16038.
86. Czerwieńiec, R.; Yu, J.; Yersin, H., Blue-light Emission of Cu(I) Complexes and Singlet Harvesting. *Inorg. Chem.* **2011**, *50*, 8293-8301.
87. Artem'ev, A. V.; Shafikov, M. Z.; Schinabeck, A.; Antonova, O. V.; Berezin, A. S.; Bagryanskaya, I. Y.; Plusnin, P. E.; Yersin, H., Sky-blue thermally activated delayed fluorescence (TADF) based on Ag(I) complexes: strong solvation-induced emission enhancement. *Inorg. Chem. Front.* **2019**, *6* (11), 3168-3176.
88. Ravinson, D. S. M.; Thompson, M. E., Thermally assisted delayed fluorescence (TADF): fluorescence delayed is fluorescence denied. *Mater. Horiz.* **2020**, *7* (5), 1210-1217.
89. Hamze, R.; Idris, M.; Muthiah Ravinson, D. S.; Jung, M. C.; Haiges, R.; Djurovich, P. I.; Thompson, M. E., Highly Efficient Deep Blue Luminescence of 2-Coordinate Coinage Metal Complexes Bearing Bulky NHC Benzimidazolyl Carbene. *Front. Chem.* **2020**, *8* (401), 1-9.
90. Feng, J.; Reponen, A. P. M.; Romanov, A. S.; Linnolahti, M.; Bochmann, M.; Greenham, N. C.; Penfold, T.; Credgington, D., Influence of Heavy Atom Effect on the Photophysics of Coinage Metal Carbene-Metal-Amide Emitters. *Adv. Funct. Mater.* **2020**, *31* (1), 2005438.
91. Chotard, F.; Sivchik, V.; Linnolahti, M.; Bochmann, M.; Romanov, A. S., Mono- versus Bicyclic Carbene Metal Amide Photoemitters: Which Design Leads to the Best Performance? *Chem. Mater.* **2020**, *32* (14), 6114-6122.
92. Hamze, R.; Shi, S.; Kapper, S. C.; Muthiah Ravinson, D. S.; Estergreen, L.; Jung, M. C.; Tadler, A. C.; Haiges, R.; Djurovich, P. I.; Peltier, J. L.; Jazzar, R.; Bertrand, G.; Bradforth, S. E.; Thompson, M. E., "Quick-Silver" from a Systematic Study of Highly Luminescent, Two-Coordinate, d¹⁰ Coinage Metal Complexes. *J. Am. Chem. Soc.* **2019**, *141* (21), 8616-8626.
93. Romanov, A. S.; Jones, S. T. E.; Yang, L.; Conaghan, P. J.; Di, D.; Linnolahti, M.; Credgington, D.; Bochmann, M., Mononuclear Silver Complexes for Efficient Solution and Vacuum-Processed OLEDs. *Adv. Opt. Mater.* **2018**, *6* (24), 1801347.
94. Calvo, M.; Crespo, O.; Gimeno, M. C.; Laguna, A.; Oliván, M. T.; Polo, V.; Rodriguez, D.; Saez-Rocher, J. M., Tunable from Blue to Red Emissive Composites and Solids of Silver Diphosphane Systems with Higher Quantum Yields than the Diphosphane Ligands. *Inorg. Chem.* **2020**, *59* (19), 14447-14456.
95. Osawa, M.; Hashimoto, M.; Kawata, I.; Hoshino, M., Photoluminescence properties of TADF-emitting three-coordinate silver(I) halide complexes with diphosphine ligands: a comparison study with copper(I) complexes. *Dalton Trans.* **2017**, *46*, 12446-12455.
96. Osawa, M.; Kawata, I.; Ishii, R.; Igawa, S.; Hashimoto, M.; Hoshino, M., Application of neutral d¹⁰ coinage metal complexes with an anionic bidentate ligand in delayed fluorescence-type organic light-emitting diodes. *J. Mater. Chem. C* **2013**, *1* (28), 4375-4383.
97. Teng, T.; Li, K.; Cheng, G.; Wang, Y.; Wang, J.; Li, J.; Zhou, C.; Liu, H.; Zou, T.; Xiong, J.; Wu, C.; Zhang, H. X.; Che, C. M.; Yang, C., Lighting Silver(I) Complexes for Solution-Processed Organic Light-Emitting Diodes and Biological Applications via Thermally Activated Delayed Fluorescence. *Inorg. Chem.* **2020**, *59* (17), 12122-12131.
98. Jia, J.-H.; Liang, D.; Yu, R.; Chen, X.-L.; Meng, L.; Chang, J.-F.; Liao, J.-Z.; Yang, M.; Li, X.-N.; Lu, C.-Z., Coordination-Induced

- Thermally Activated Delayed Fluorescence: From Non-TADF Donor-Acceptor-Type Ligand to TADF-Active Ag-Based Complexes. *Chem. Mater.* **2019**, *32* (1), 620-629.
99. Carbonell-Vilar, J. M.; Fresta, E.; Armentano, D.; Costa, R. D.; Viciano-Chumillas, M.; Cano, J., Photoluminescent Cu(I) vs. Ag(I) complexes: slowing down emission in Cu(I) complexes by pentacoordinate low-lying excited states. *Dalton Trans.* **2019**, *48* (26), 9765-9775.
100. Shafikov, M. Z.; Suleymanova, A. F.; Czerwieńiec, R.; Yersin, H., Design Strategy for Ag(I)-Based Thermally Activated Delayed Fluorescence Reaching an Efficiency Breakthrough. *Chem. Mater.* **2017**, *29* (4), 1708-1715.
101. Shafikov, M. Z.; Suleymanova, A. F.; Czerwieńiec, R.; Yersin, H., Thermally Activated Delayed Fluorescence from Ag(I) Complexes: A Route to 100% Quantum Yield at Unprecedentedly Short Decay Time. *Inorg. Chem.* **2017**, *56* (21), 13274-13285.
102. Artem'ev, A. V.; Davydova, M. P.; Berezin, A. S.; Samsonenko, D. G., Synthesis and Thermochromic Luminescence of Ag(I) Complexes Based on 4,6-Bis(diphenylphosphino)-Pyrimidine. *Inorganics* **2020**, *8* (9), 46.
103. Chakkaradhari, G.; Eskelinen, T.; Degbe, C.; Belyaev, A.; Melnikov, A. S.; Grachova, E. V.; Tunik, S. P.; Hirva, P.; Koshevoy, I. O., Oligophosphine-thiocyanate Copper(I) and Silver(I) Complexes and Their Borane Derivatives Showing Delayed Fluorescence. *Inorg. Chem.* **2019**, *58* (6), 3646-3660.
104. Shafikov, M. Z.; Suleymanova, A. F.; Schinabeck, A.; Yersin, H., Dinuclear Ag(I) Complex Designed for Highly Efficient Thermally Activated Delayed Fluorescence. *J. Phys. Chem. Lett.* **2018**, *9*, 702-709.
105. Chen, J.; Teng, T.; Kang, L.; Chen, X. L.; Wu, X. Y.; Yu, R.; Lu, C. Z., Highly Efficient Thermally Activated Delayed Fluorescence in Dinuclear Ag(I) Complexes with a Bis-Bidentate Tetrakisphosphane Bridging Ligand. *Inorg. Chem.* **2016**, *55* (19), 9528-9536.
106. So, F.; Adachi, C.; Yersin, H.; Leitl, M. J.; Czerwieńiec, R., TADF for singlet harvesting: next generation OLED materials based on brightly green and blue emitting Cu(I) and Ag(I) compounds. *Proc. SPIE* **2014**, *9183*, 91830N.
107. Stollenz, M.; Raymond, J. E.; Perez, L. M.; Wiederkehr, J.; Bhuvanesh, N., Highly Luminescent Linear Complex Arrays of up to Eight Cuprous Centers. *Chem. Eur. J.* **2016**, *22* (7), 2396-2405.
108. Schmidbaur, H.; Schier, A., Argentophilic Interactions. *Angew. Chem. Int. Ed.* **2015**, *54* (3), 746-784.
109. Inoguchi, Y.; Milewski-Mahrla, B.; Neugebauer, D.; Jones, P. G.; Schmidbaur, H., Synthese und eine Röntgenbeugungsanalyse von Kupfer(I)- und Silber(I)-chlorid-Komplexen. *Chem. Ber.* **1983**, *116*, 1487-1493.
110. Stollenz, M., Linear Copper Complex Arrays as Versatile Molecular Strings: Syntheses, Structures, Luminescence, and Magnetism. *Chem. Eur. J.* **2019**, *25* (17), 4274-4298.
111. Fackler, J. P.; Lopez, C. A.; Staples, R. J.; Wang, S.; Wimpenny, R. E. P.; Lattimer, R. P., Self assembly of isostructural copper(I)-silver(I) butterfly clusters with 2-mercaptothiazoline: Syntheses and Structures of $(PPh_3)_2Cu_4(C_3H_4NS_2)_4$, $[(C_5H_5N)Cu_4(C_3H_4NS_2)_4]_n$, $(PPh_3)_2Ag_4(C_3H_4NS_2)_4$ and $(PPh_3)_2Ag_2Cu_2(C_3H_4NS_2)_4$. *J. Chem. Soc. Chem. Commun.* **1992**, 146-148.
112. Polgar, A. M.; Zhang, A.; Mack, F.; Weigend, F.; Lebedkin, S.; Stillman, M. J.; Corrigan, J. F., Tuning the Metal/Chalcogen Composition in Copper(I) - Chalcogenide Clusters with Cyclic (Alkyl)(amino)carbene Ligands. *Inorg. Chem.* **2019**, *58*, 3338-3348.
113. Lu, T.; Wang, J.-Y.; Shi, L.-X.; Chen, Z.-N.; Chen, X.-T.; Xue, Z.-L., Synthesis, structures and luminescence properties of amine-bis(N-heterocyclic carbene) copper(I) and silver(I) complexes. *Dalton Trans.* **2018**, *47*, 6742-6753.
114. Kritchenkov, I. S.; Gitlina, A. Y.; Koshevoy, I. O.; Melnikov, A. S.; Tunik, S. P., Luminescent Silver-Copper "Hourglass" Hepta- and Decanuclear Alkynyl-Phosphine Clusters. *Eur. J. Inorg. Chem.* **2018**, 3822-3828.
115. Zhang, X.; Wang, J.-Y.; Qiao, D.; Chen, Z.-N., Phosphorescent mechanochromism through the contraction of $Ag_{12}Cu_2$ clusters in tetradecanuclear copper-silver acetylide complexes. *J. Mater. Chem. C* **2017**, *5* (34), 8782-8787.
116. Xu, L.-J.; Zhang, X.; Wang, J.-Y.; Chen, Z.-N., High-efficiency solution-processed OLEDs based on cationic Ag_6Cu heteroheptanuclear cluster complexes with aromatic acetylides. *J. Mater. Chem. C* **2016**, *4*, 1787-1794.
117. Hau, S. C. K.; Yeung, M. C.; Yam, V. W.; Mak, T. C. W., Assembly of Heterometallic Silver(I)-Copper(I) Alkyl-1,3-diyne Clusters via Inner-Core Expansion. *J. Am. Chem. Soc.* **2016**, *138* (41), 13732-13739.
118. Jiang, Y.; Guo, W. J.; Kong, D. X.; Wang, Y. T.; Wang, J. Y.; Wei, Q. H., Novel electrochemi-/photo-luminescence of Ag_3Cu_8 heterometallic alkynyl clusters. *Dalton Trans.* **2015**, *44* (9), 3941-3944.
119. Jarzemska, K. N.; Kaminski, R.; Fournier, B.; Trzop, E.; Sokolow, J. D.; Henning, R.; Chen, Y.; Coppens, P., Shedding Light on the Photochemistry of Coinage-Metal Phosphorescent Materials: A Time-Resolved Laue Diffraction Study of an Ag(I)-Cu(I) Tetranuclear Complex. *Inorg. Chem.* **2014**, *53* (19), 10594-10601.
120. Chen, Z.-H.; Zhang, L.-Y.; Chen, Z.-N., Structural Characterization and Luminescence Properties of a Triphosphine-Stabilized $Ag_{16}Cu_9$ Heterometallic Alkynyl Cluster. *Organometallics* **2012**, *31* (1), 256-260.
121. Koshevoy, I. O.; Shakirova, J. R.; Melnikov, A. S.; Haukka, M.; Tunik, S. P.; Pakkanen, T. A., Coinage metal complexes of 2-diphenylphosphino-3-methylindole. *Dalton Trans.* **2011**, *40* (31), 7927-7933.
122. Olmos, M. E.; Schier, A.; Schmidbaur, H., Diphenyl(1-pyridyl)phosphine Sulfide as a Ligand in Mono- and Binuclear Coinage Metal Complexes. *Z. Naturforsch.* **1997**, *52b*, 385-390.
123. Olmos, M. E.; Schier, A.; Schmidbaur, H., 2-(Diphenylphosphino)-pyridine as an Ambidentate Ligand in Homo- and Hetero-binuclear Complexes of Copper, Silver, and Gold. *Z. Naturforsch.* **1997**, *52b*, 203-208.
124. Alcock, N. W.; Moore, P.; Lampe, P. A., Crystal and molecular structures of two complexes of diphenyl(2-pyridyl)phosphine [L]: $[AuClL]$ and $[Ag_2Cl_2L_3]$. *Dalton Trans.* **1982**, *7*, 207-210.
125. Kyros, L.; Kourkoumelis, N.; Kubicki, M.; Male, L.; Hursthouse, M. B.; Verginadis, I.; Gouma, E.; Karkabounas, S.; Charalabopoulos, K.; Hadjikakou, S. K., Structural Properties, Cytotoxicity, and Anti-Inflammatory Activity of Silver(I) Complexes with tris(p-tolyl)phosphine and 5-Chloro-2-Mercaptobenzothiazole. *Bioinorg. Chem. Appl.* **2010**, 386860.
126. Engelhardt, L. M.; Healy, P. C.; Patrick, V. A.; White, A. H., Lewis-Base Adducts of Group-11 Metal(I) Compounds. XXX. 3:1 Complexes of Triphenylphosphine With Silver(I) Halides. *Aust. J. Chem.* **1987**, *40*, 1873-1880.
127. Wagner, H. E.; Di Martino-Fumo, P.; Boden, P.; Zimmer, M.; Klopfer, W.; Breher, F.; Gerhards, M., Structural Characterization and Lifetimes of Triple-Stranded Helical Coinage Metal Complexes: Synthesis, Spectroscopy and

- Quantum Chemical Calculations. *Chemistry* **2020**, *26* (47), 10743.
128. Boden, P.; Di Martino-Fumo, P.; Busch, J. M.; Rehak, F. R.; Steiger, S.; Fuhr, O.; Nieger, M.; Volz, D.; Klopper, W.; Bräse, S., Investigation of Luminescent Triplet States in Tetranuclear CuI Complexes: Thermochromism and Structural Characterization. *Chemistry* **2021**, *27* (17), 5439.
129. Henary, M.; Zink, J. I., Luminescence from the chair and cube isomers of tetrakis[(triphenylphosphine)iodosilver]. *Inorg. Chem.* **1991**, *30*, 3111-3112.
130. Vogler, A.; Kunkely, H., Photoluminescence of tetrameric silver(I) complexes. *Chem. Phys. Lett.* **1989**, *158*, 74-76.
131. Teo, B.-K.; Calabrese, J. C., Stereochemical systematics of metal clusters. Crystallographic evidence for a new cubane .dblharw. chair isomerism in tetrameric triphenylphosphine silver iodide, $(\text{Ph}_3\text{P})_4\text{Ag}_4\text{I}_4$. *Inorg. Chem.* **1976**, *15* (10), 2474-2486.
132. Ono, S.; Kobayashi, M.; Tomoyose, T., Covalency of noble metal halides. *Solid State Ionics* **2005**, *176* (3-4), 363-366.
133. Zhang, Y.; Schulz, M.; Waechtler, M.; Karnahl, M.; Dietzek, B., Heteroleptic diimine-diphosphine Cu(I) complexes as an alternative towards noble-metal based photosensitizers: Design strategies, photophysical properties and perspective applications. *Coord. Chem. Reviews* **2018**, *356*, 127-146.
134. Mueck-Lichtenfeld, C.; Grimme, S., Theoretical analysis of cooperative effects of small molecule activation by frustrated Lewis pairs. *Dalton Trans.* **2012**, *41* (30), 9111-9118.
135. Wall, T.; Leist, M.; Dietrich, F.; Thiel, W. R.; Gerhards, M., Quantification of Cooperativity between Metal Sites in Dinuclear Transition Metal Complexes Containing the (2-Dimethylamino)-4-(2-pyrimidinyl) pyrimidine Ligand. *ChemPlusChem* **2021**, *86* (4), 622-628.
136. Grupe, M.; Boden, P.; Martino-Fumo, D.; Gui, X.; Bruschi, C.; Israil, R.; Schmitt, M.; Nieger, M.; Gerhards, M.; Klopper, W., Time-Resolved Spectroscopy and Electronic Structure of Mono- and Dinuclear Pyridyl-Triazole/DPEPhos-Based Cu(I) Complexes. *Chem. Eur. J.* **2021**.
137. Shields, D. J.; Elkoush, T.; Miura-Stempel, E.; Mak, C. L.; Niu, G.-H.; Gudmundsdottir, A. D.; Campbell, M. G., Visible Light Absorption and Long-Lived Excited States in Dinuclear Silver(I) Complexes with Redox-Active Ligands. *Inorg. Chem.* **2020**, *59* (24), 18338-18344.
138. Maini, L.; Mazzeo, P. P.; Farinella, F.; Fattori, V.; Braga, D., Mechanochemical preparation of copper iodide clusters of interest for luminescent devices. *Faraday Discuss.* **2014**, *170*, 93-107.
139. TURBOMOLE V7.5 2020 a development of University of Karlsruhe and Forschungszentrum Karlsruhe GmbH, Turbomole GmbH, since 2007 available from <https://www.turbomole.org>.
140. Yanai, T.; Tew, D. P.; Handy, N. C., A new hybrid exchange-correlation functional using the Coulomb-attenuating method (CAM-B3LYP). *Chem. Phys. Lett.* **2004**, *393* (1-3), 51-57.
141. Holzer, C.; Klopper, W., Ionized, electron-attached, and excited states of molecular systems with spin-orbit coupling: Two-component *GW* and Bethe-Salpeter implementations. *J. Chem. Phys.* **2019**, *150* (20), 204116.

5. UV/Vis Studies

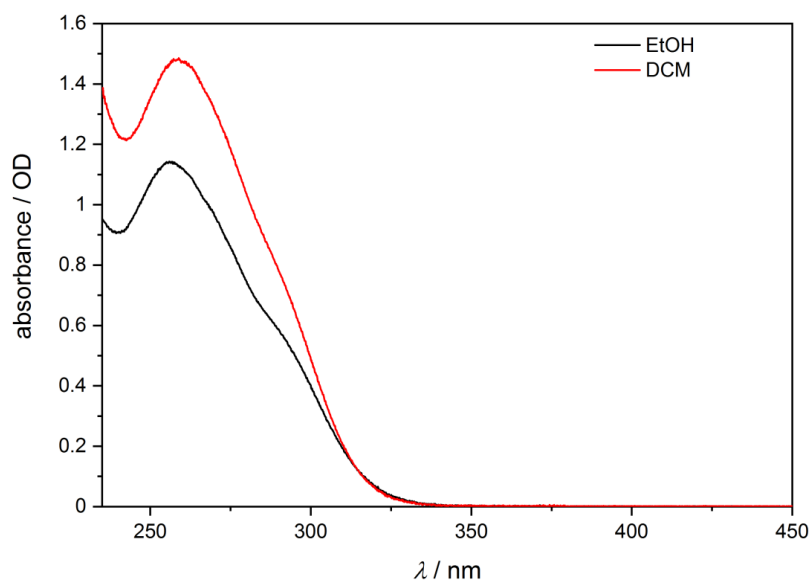


Figure S51. Experimental UV/Vis absorption spectra of **PyrPhos** in DCM and EtOH.

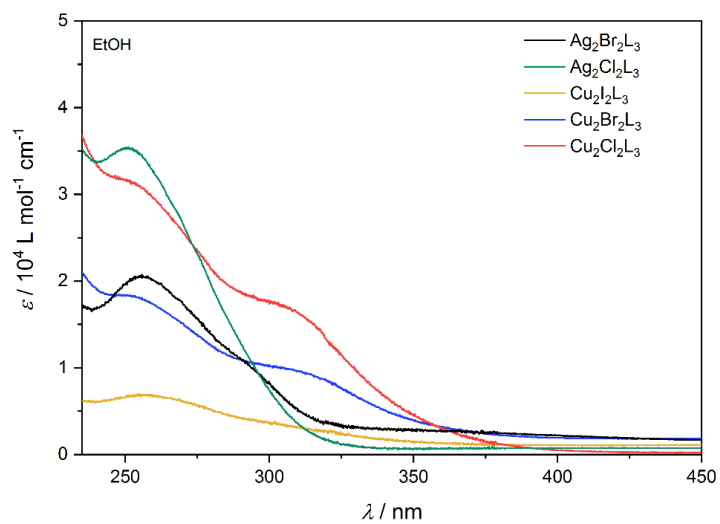


Figure S52. Experimental UV/Vis absorption spectra of **Ag₂Br₂L₃**, **Ag₂Cl₂L₃**, **Cu₂I₂L₃**, **Cu₂Br₂L₃**, **Cu₂Cl₂L₃** in EtOH.

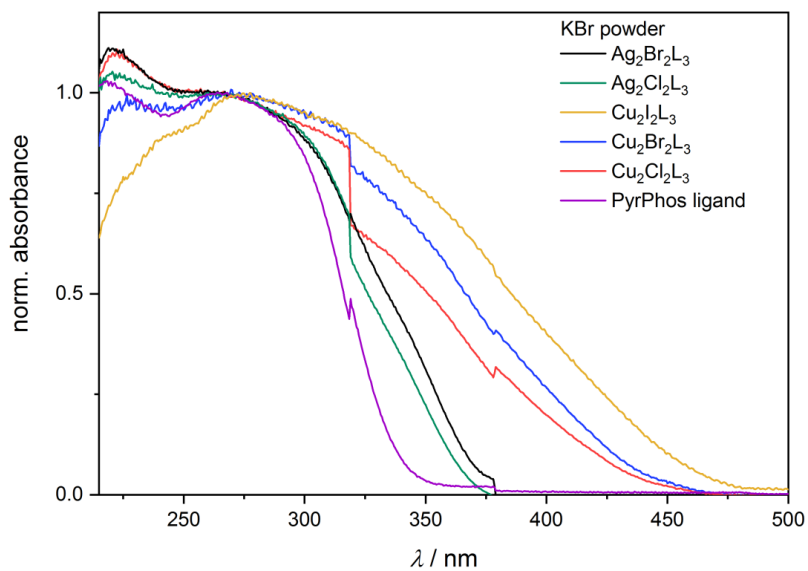


Figure S53. Experimental UV/Vis absorption spectra of $\text{Ag}_2\text{Br}_2\text{L}_3$, $\text{Ag}_2\text{Cl}_2\text{L}_3$, $\text{Cu}_2\text{I}_2\text{L}_3$, $\text{Cu}_2\text{Br}_2\text{L}_3$, $\text{Cu}_2\text{Cl}_2\text{L}_3$ and PyrPhos as powder samples (diluted with KBr powder).

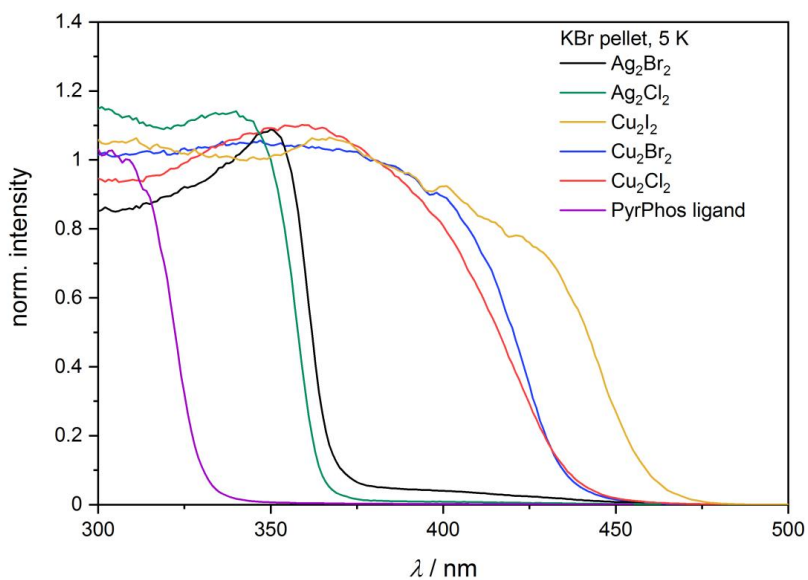


Figure S54. Excitation spectra of $\text{Ag}_2\text{Br}_2\text{L}_3$, $\text{Ag}_2\text{Cl}_2\text{L}_3$, $\text{Cu}_2\text{I}_2\text{L}_3$, $\text{Cu}_2\text{Br}_2\text{L}_3$, $\text{Cu}_2\text{Cl}_2\text{L}_3$ and PyrPhos at 5 K (KBr pellet), measured at the respective emission maximum.

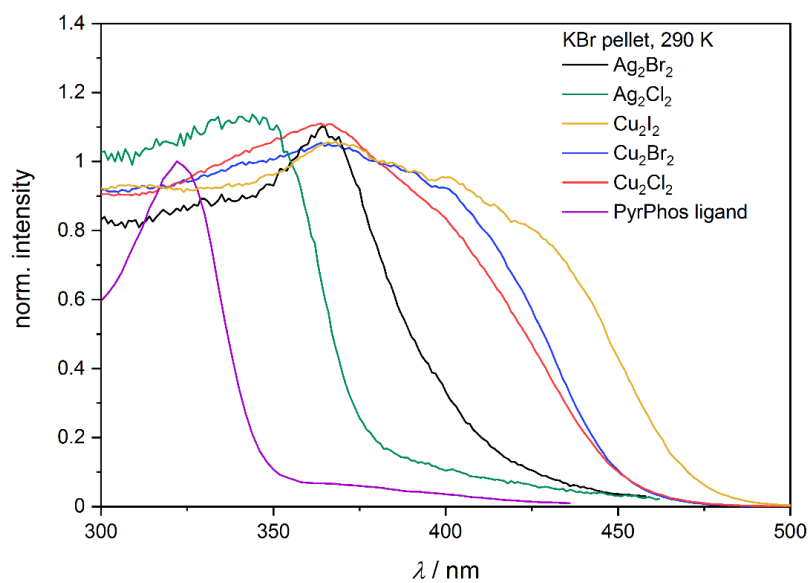


Figure S55. Excitation spectra of $\text{Ag}_2\text{Br}_2\text{L}_3$, $\text{Ag}_2\text{Cl}_2\text{L}_3$, $\text{Cu}_2\text{I}_2\text{L}_3$, $\text{Cu}_2\text{Br}_2\text{L}_3$, $\text{Cu}_2\text{Cl}_2\text{L}_3$ and **PyrPhos** at 290 K (KBr pellet), measured at the respective emission maximum.

6. Luminescence Studies

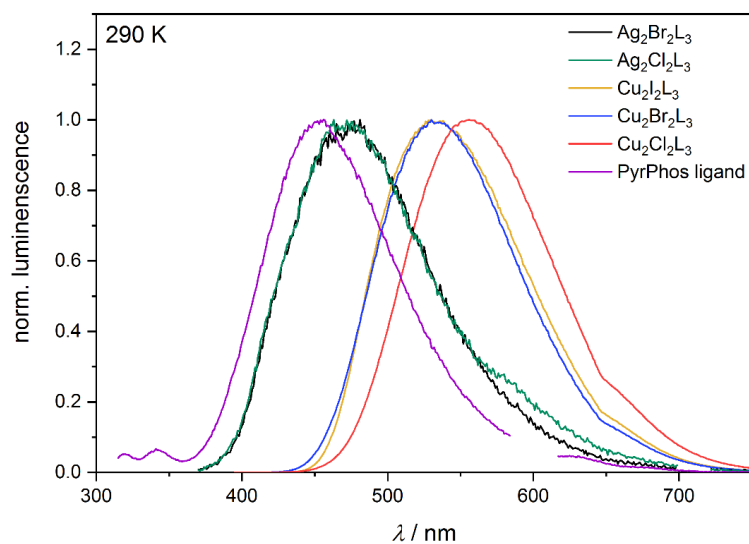


Figure S56. Emission spectra of $\text{Ag}_2\text{Br}_2\text{L}_3$, $\text{Ag}_2\text{Cl}_2\text{L}_3$, $\text{Cu}_2\text{I}_2\text{L}_3$, $\text{Cu}_2\text{Br}_2\text{L}_3$, $\text{Cu}_2\text{Cl}_2\text{L}_3$ and **PyrPhos** at 290 K in a KBr matrix ($\lambda_{\text{ex}} = 355, 355, 420, 380, 380$ and 300 nm, respectively).

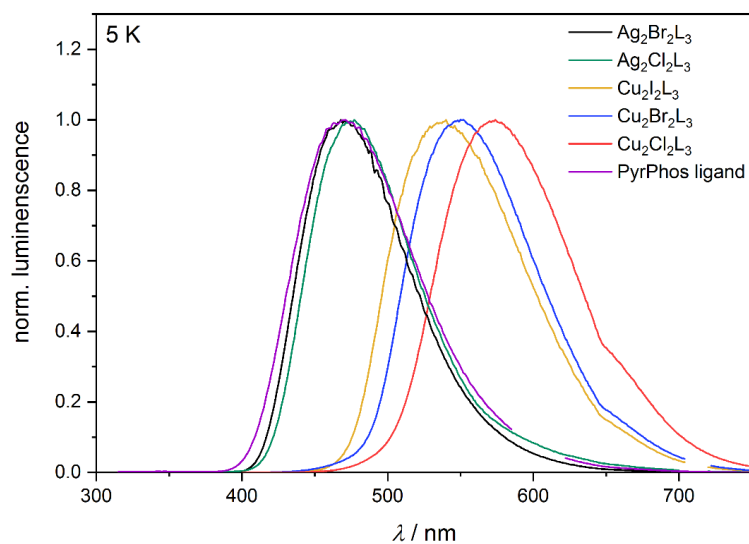


Figure S57. Emission spectra of $\text{Ag}_2\text{Br}_2\text{L}_3$, $\text{Ag}_2\text{Cl}_2\text{L}_3$, $\text{Cu}_2\text{I}_2\text{L}_3$, $\text{Cu}_2\text{Br}_2\text{L}_3$, $\text{Cu}_2\text{Cl}_2\text{L}_3$ and **PyrPhos** at 5 K in a KBr matrix ($\lambda_{\text{ex}} = 355, 355, 420, 380, 380$ and 300 nm, respectively).

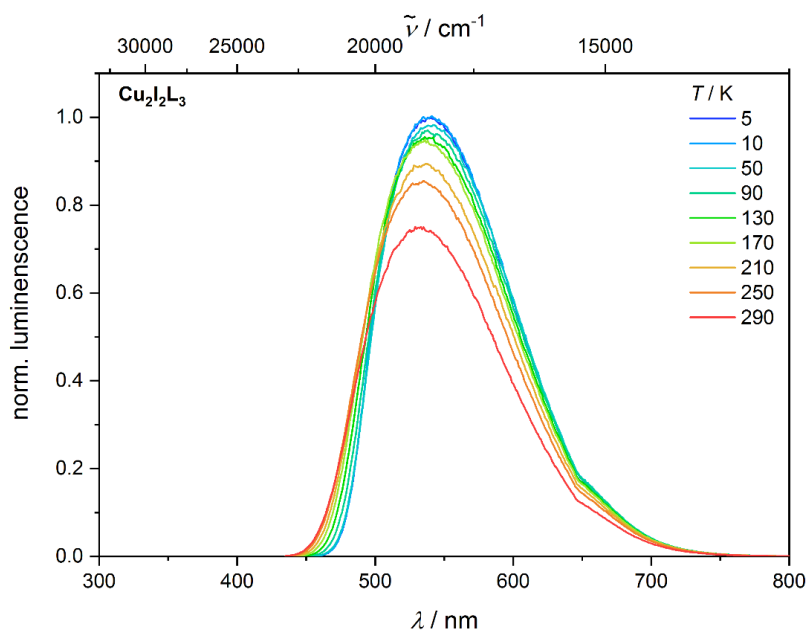


Figure S58. Temperature-dependent emission spectra of $\text{Cu}_2\text{I}_2\text{L}_3$ at 290 – 5 K in a KBr matrix ($\lambda_{\text{ex}} = 420$ nm).

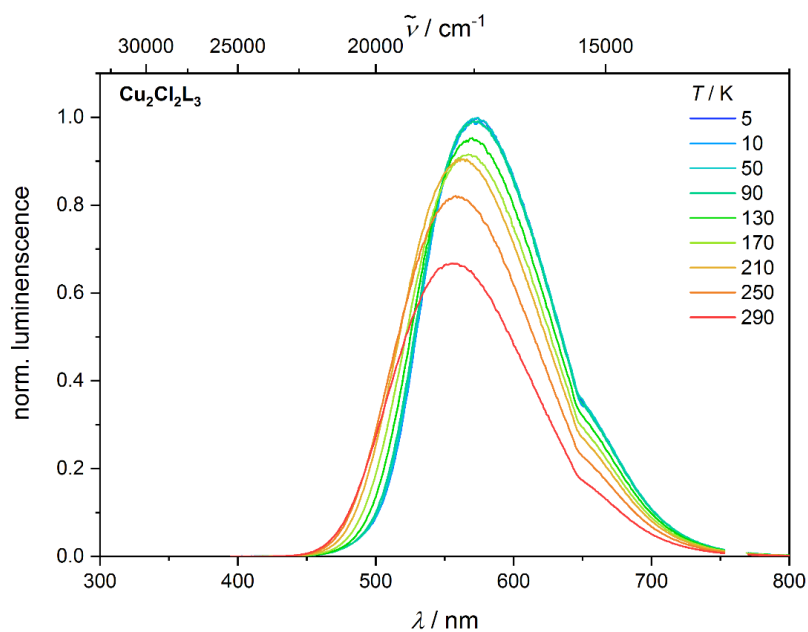
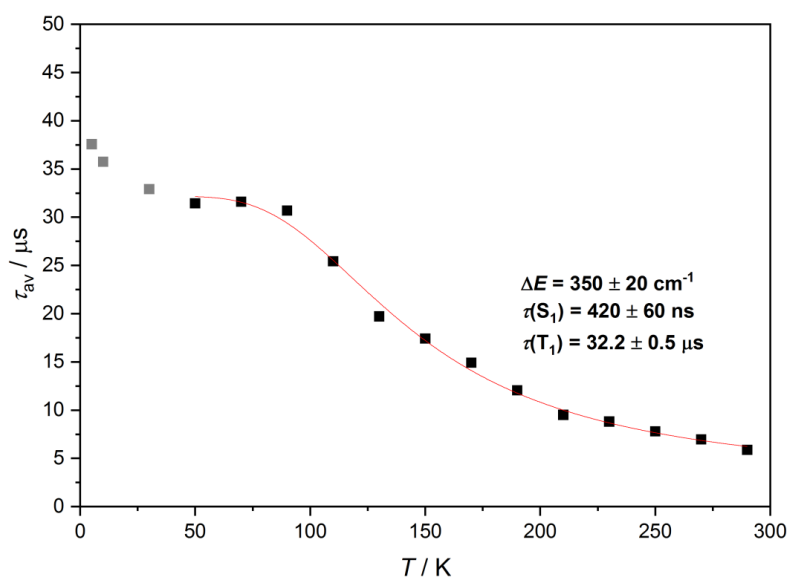


Figure S59. Temperature-dependent emission spectra of $\text{Cu}_2\text{Cl}_2\text{L}_3$ at 290 – 5 K in a KBr matrix ($\lambda_{\text{ex}} = 380$ nm).

Table S17. Luminescence lifetimes of **Ag₂Br₂L₃**, **Ag₂Cl₂L₃**, **Cu₂I₂L₃**, **Cu₂Br₂L₃**, **Cu₂Cl₂L₃** in a KBr matrix at 290 K and 5 K.

	T / K	λ_{ex} / nm	λ_{em} / nm	τ_1	A ₁ / %	τ_2	A ₂ / %	τ_3	A ₃ / %	τ_{av}
Ag₂Br₂L₃	290	345	473	15.7 ns	16	2.0 ns	8	0.3 ns	76	-
	5	345	473	16.4 ns	22	0.4 ns	78	-	-	-
Ag₂Cl₂L₃	290	345	472	15.4 ns	10	1.7 ns	6	0.3 ns	84	-
	5	345	473	4.3 ns	14	0.4 ns	84	-	-	-
Cu₂I₂L₃	290	390	533	7.0 μs	76	2.2 μs	24	-	-	5.9 μs
	5	390	542	60 μs	29	33 μs	45	19 μs	25	38 μs
Cu₂Br₂L₃	290	390	533	11 μs	89	3.1 μs	11			10 μs
	5	390	550	180 μs	75	68 μs	21	14 μs	4	150 μs
Cu₂Cl₂L₃	290	390	556	9.5 μs	84	3.4 μs	16			8.6 μs
	5	390	573	180 μs	48	54 μs	49	9 μs	3	110 μs

**Figure S60.** Plot of the average emission lifetime τ_{av} vs. temperature for **Cu₂I₂L₃** at 290 – 5 K in a KBr matrix ($\lambda_{\text{ex}} = 390$ nm). The red curve represents the fit discussed in the manuscript, where the data points represented in grey were neglected.

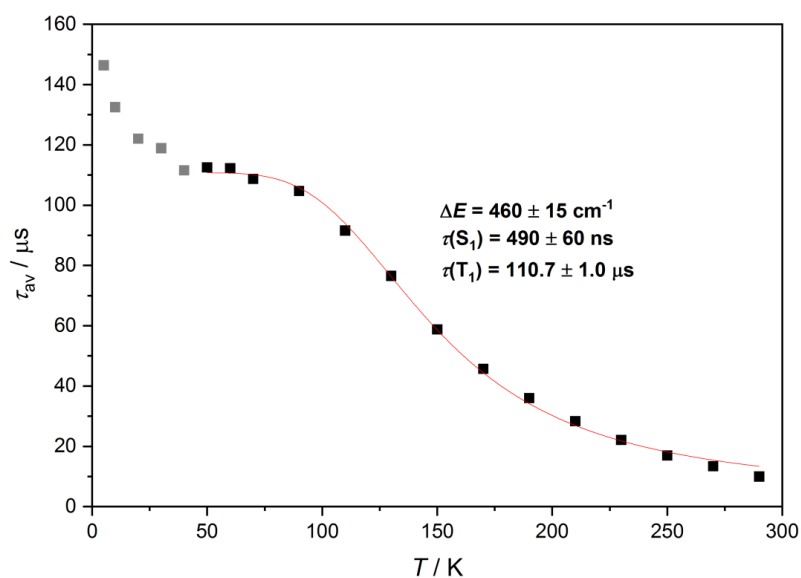


Figure S61. Plot of the average emission lifetime τ_{av} vs. temperature for $\text{Cu}_2\text{Br}_2\text{L}_3$ at 290 – 5 K in a KBr matrix ($\lambda_{ex} = 390$ nm). The red curve represents the fit discussed in the manuscript, where the data points represented in grey were neglected.

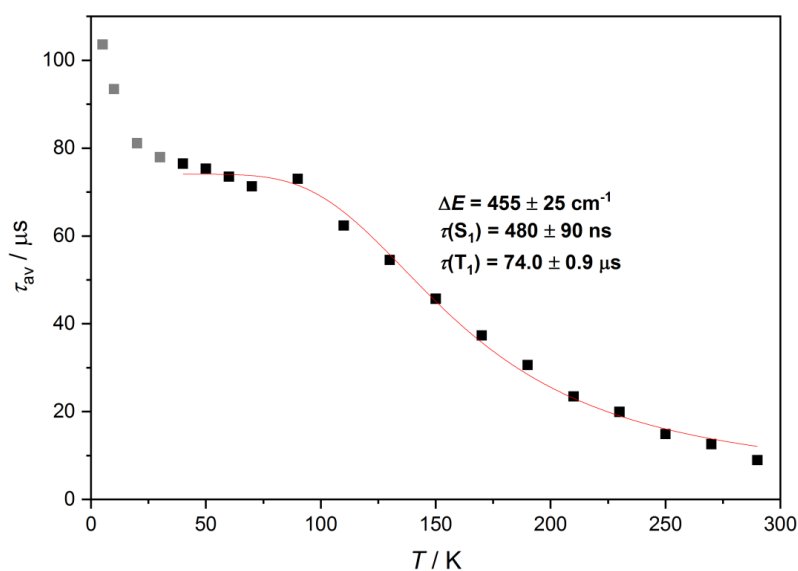


Figure S62. Plot of the average emission lifetime τ_{av} vs. temperature for $\text{Cu}_2\text{Cl}_2\text{L}_3$ at 290 – 5 K in a KBr matrix ($\lambda_{ex} = 390$ nm). The red curve represents the fit discussed in the manuscript, where the data points represented in grey were neglected.

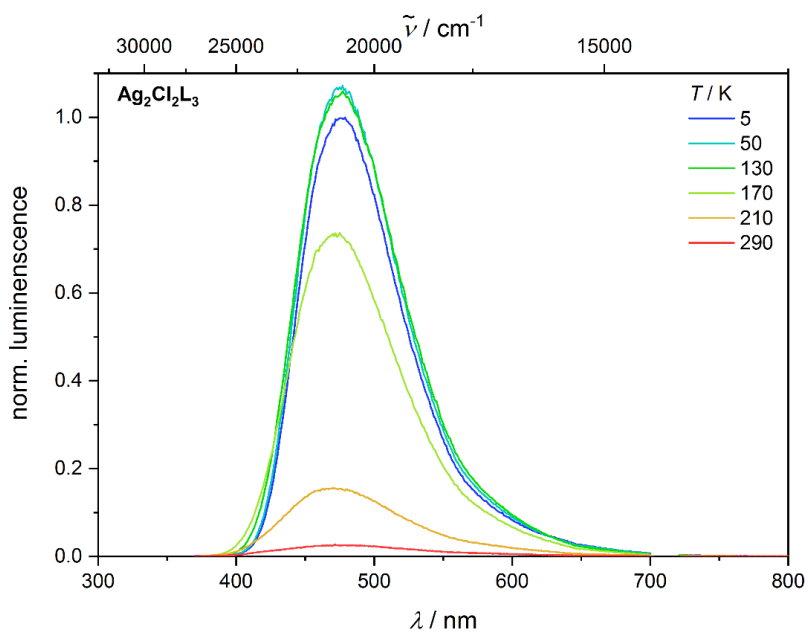


Figure S63. Temperature-dependent emission spectra of $\text{Ag}_2\text{Cl}_2\text{L}_3$ at 290 – 5 K in a KBr matrix ($\lambda_{\text{ex}} = 355$ nm).

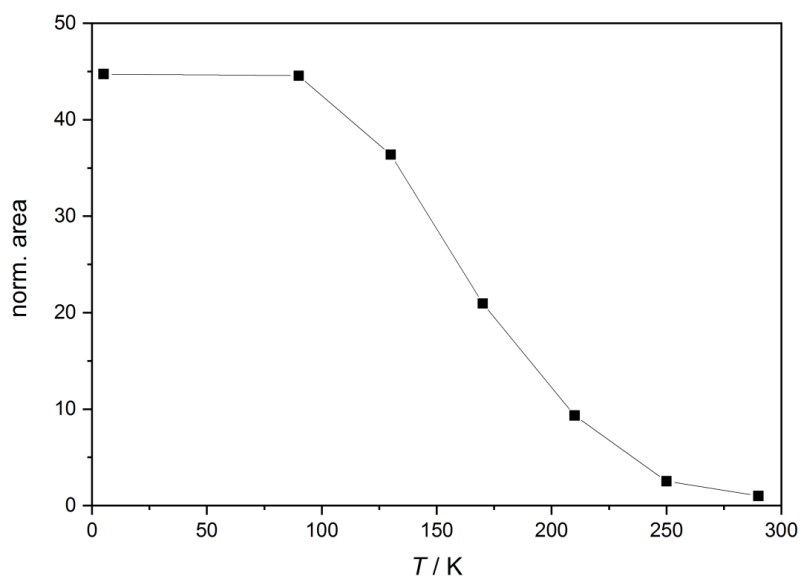


Figure S64. Plot of the integrated emission vs. temperature for $\text{Ag}_2\text{Br}_2\text{L}_3$ at 290 – 5 K in a KBr matrix ($\lambda_{\text{ex}} = 390$ nm). The line is a guide to the eye.

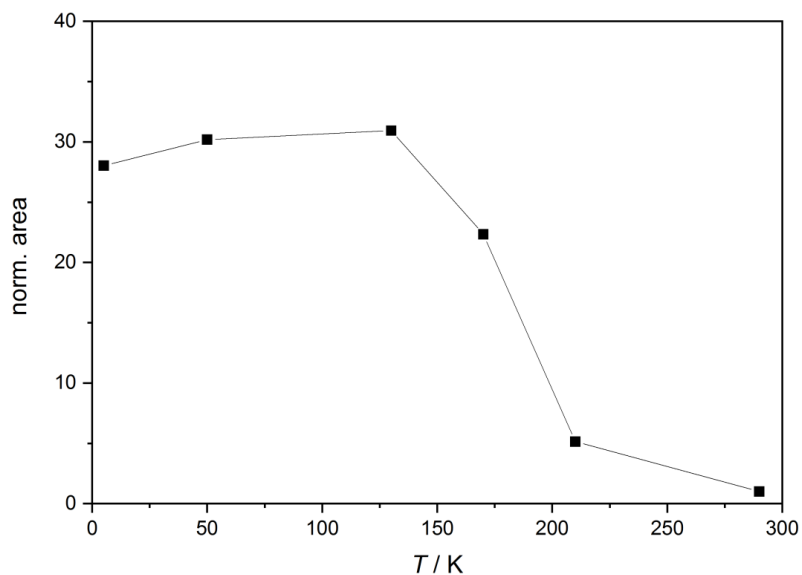


Figure S65. Plot of the integrated emission vs. temperature for $\text{Ag}_2\text{Cl}_2\text{L}_3$ at 290 – 5 K in a KBr matrix ($\lambda_{\text{ex}} = 390$ nm). The line is a guide to the eye.

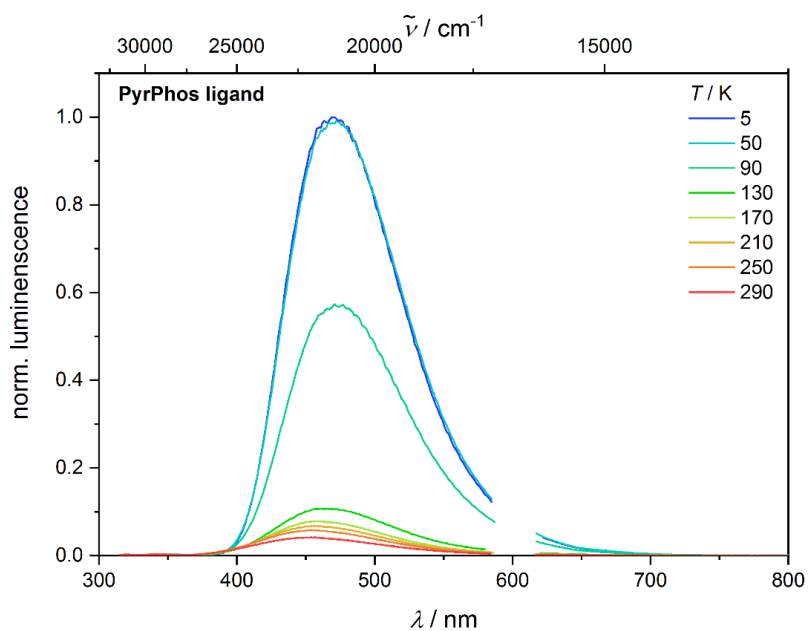
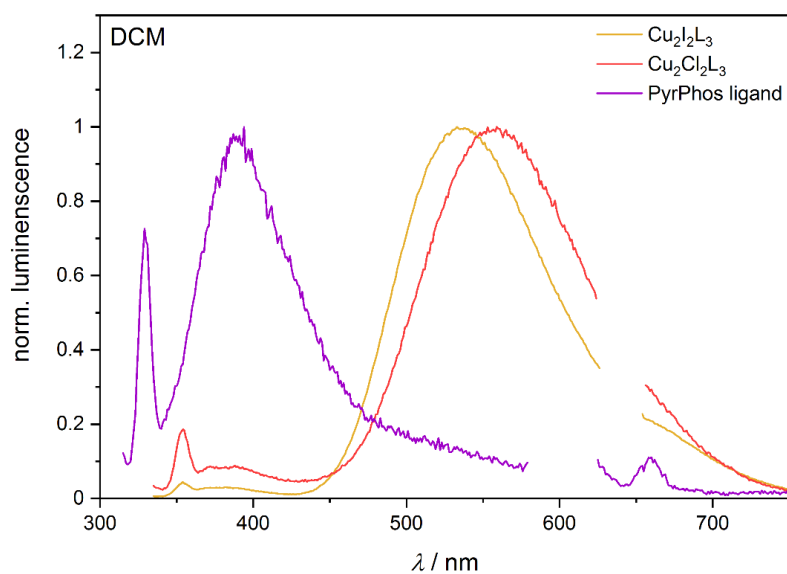


Figure S66. Temperature-dependent emission spectra of **PyrPhos** at 290 – 5 K in a KBr matrix ($\lambda_{\text{ex}} = 300$ nm).

Table S18. Emission maxima of **Ag₂Br₂L₃**, **Ag₂Cl₂L₃**, **Cu₂Br₂L₃** and **Cu₂Cl₂L₃** in a KBr matrix at 290 K and deduced cooperative effect ΔE_{coop} (according to eq. 2 in the manuscript).

	Ag₂Br₂L₃	Ag₂Cl₂L₃	Cu₂Br₂L₃	Cu₂Cl₂L₃	ΔE_{coop}
λ_{em}	473 nm	472 nm	534 nm	556 nm	
$\tilde{\nu}_{\text{em}}$	21142 cm ⁻¹	21186 cm ⁻¹	18727 cm ⁻¹	17986 cm ⁻¹	-785 cm ⁻¹

**Figure S67.** Emission spectra of **Cu₂I₂L₃**, **Cu₂Cl₂L₃** and **PyrPhos** in DCM solution at room temperature (λ_{ex} = 320, 320 and 300 nm, respectively).

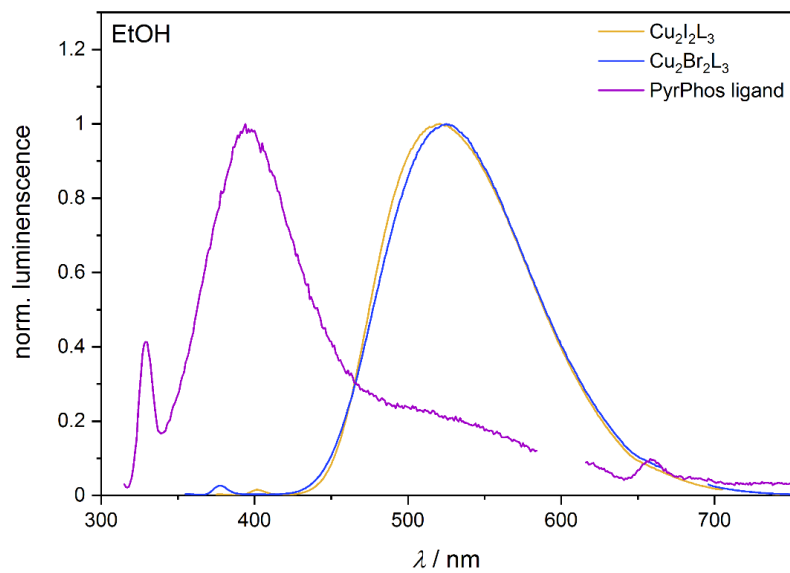


Figure S68. Emission spectra of $\text{Cu}_2\text{I}_2\text{L}_3$, $\text{Cu}_2\text{Br}_2\text{L}_3$ and and **PyrPhos** in EtOH solution at room temperature ($\lambda_{\text{ex}} = 360, 340$ and 300 nm, respectively).

7. Step-scan FTIR Spectroscopy

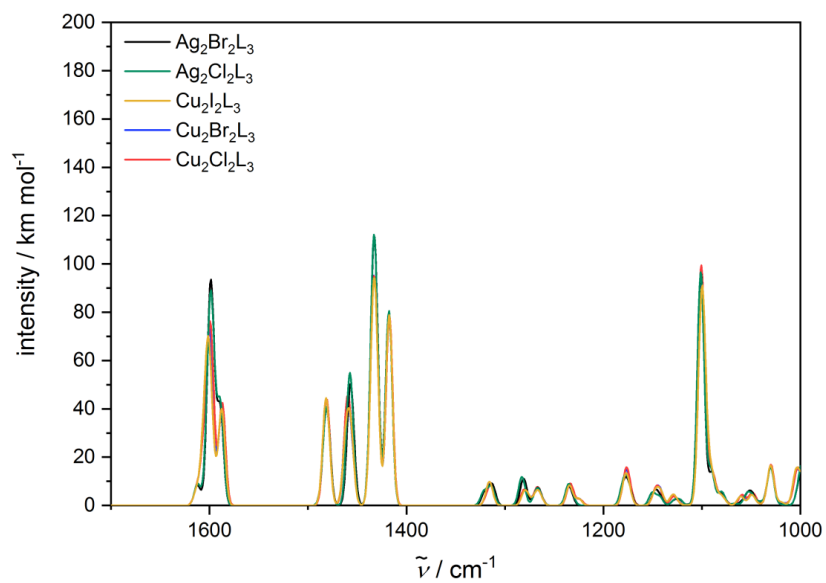


Figure S69. Ground state FTIR spectra of $\text{Ag}_2\text{Br}_2\text{L}_3$, $\text{Ag}_2\text{Cl}_2\text{L}_3$, $\text{Cu}_2\text{I}_2\text{L}_3$, $\text{Cu}_2\text{Br}_2\text{L}_3$ and $\text{Cu}_2\text{Cl}_2\text{L}_3$ in a KBr matrix at 20 K.

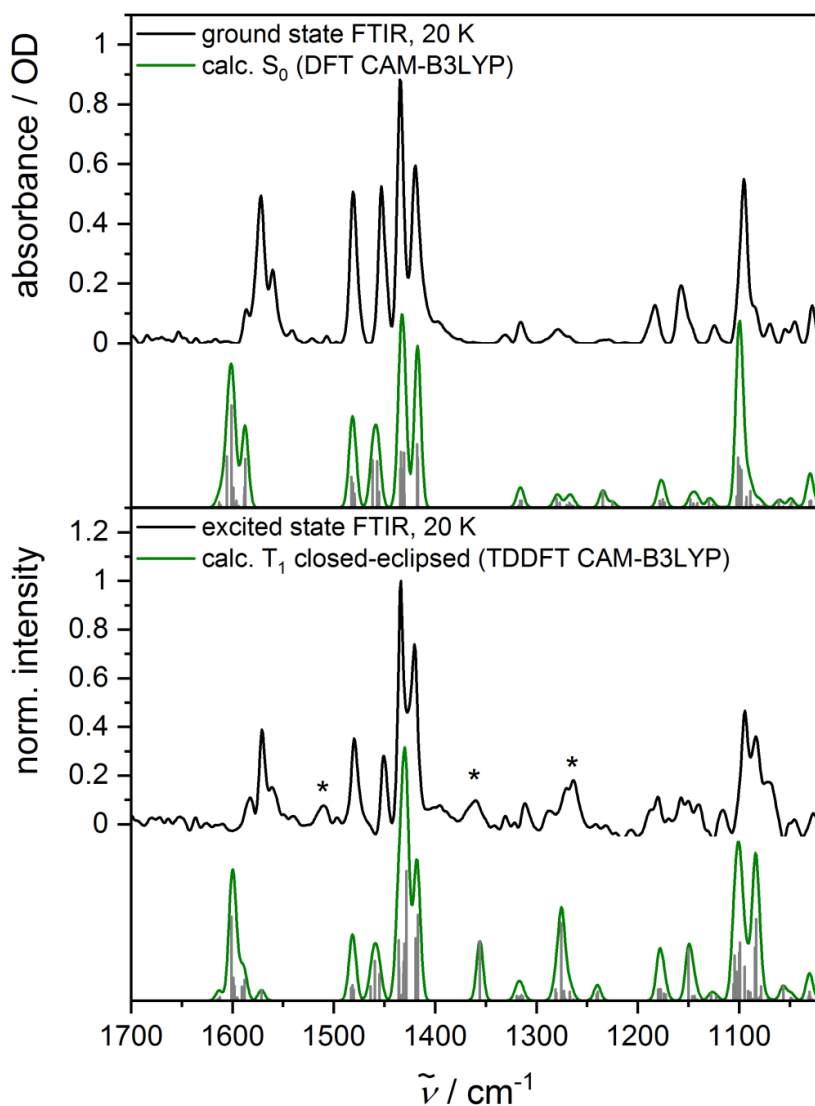


Figure S70. Top: Ground state FTIR spectrum in a KBr matrix at 20 K and calculated S_0 spectrum of $\text{Cu}_2\text{I}_2\text{L}_3$ in a KBr matrix at 20 K. Bottom: Excited state IR spectrum (0.80 % of the ground state spectrum added to the step-scan difference spectrum) and calculated spectrum of the closed butterfly T_1 structure in eclipsed conformation (CAM-B3LYP/def2-TZVP).

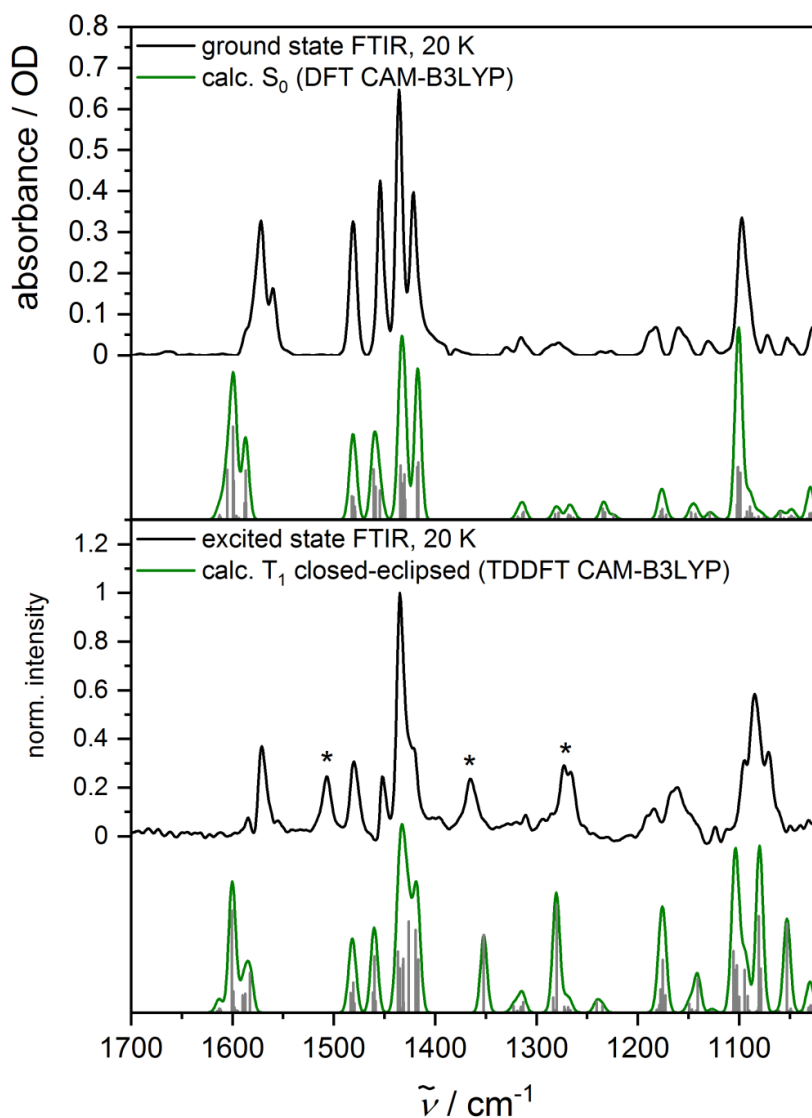


Figure S71. Top: Ground state FTIR spectrum in a KBr matrix at 20 K and calculated S_0 spectrum of $\text{Cu}_2\text{Cl}_2\text{L}_3$ in a KBr matrix at 20 K. Bottom: Excited state IR spectrum (1.40 % of the ground state spectrum added to the step-scan difference spectrum) and calculated spectrum of the closed butterfly T_1 structure in eclipsed conformation (CAM-B3LYP/def2-TZVP).

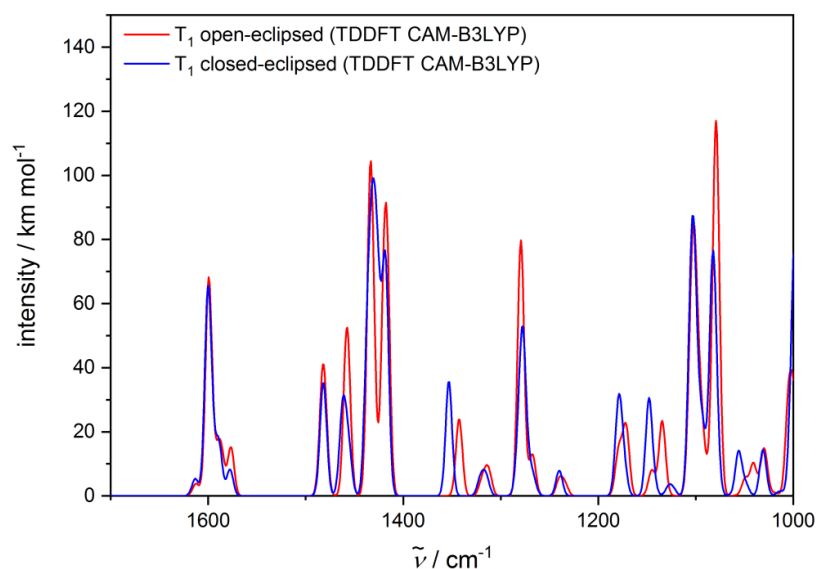


Figure S72. Comparison of calculated numerical frequencies of open and closed butterfly structure of $\text{Cu}_2\text{Br}_2\text{L}_3$ in eclipsed conformation (CAM-B3LYP/def2-TZVP).

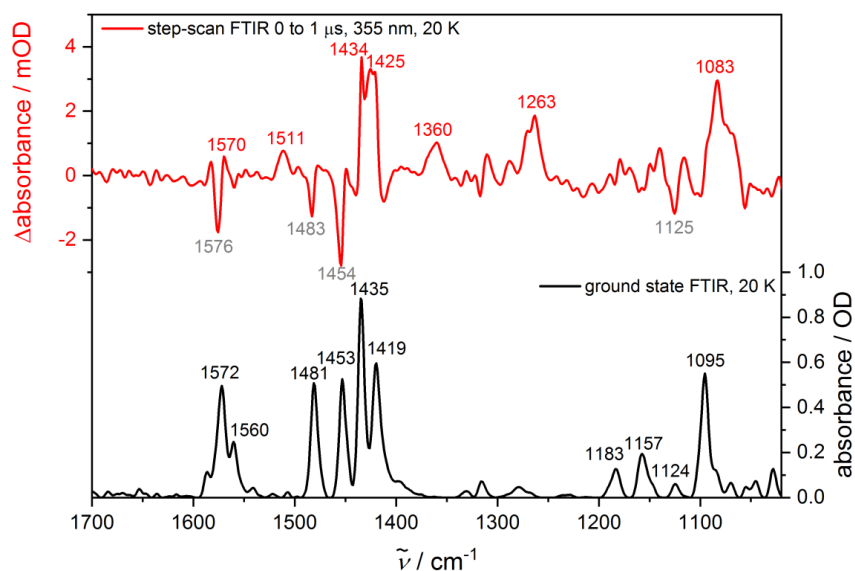


Figure S73. Step-scan difference spectrum at 0 – 1 μs after laser excitation ($\lambda_{\text{ex}} = 355 \text{ nm}$) and ground state FTIR spectrum of $\text{Cu}_2\text{I}_2\text{L}_3$ (KBr, 20 K).

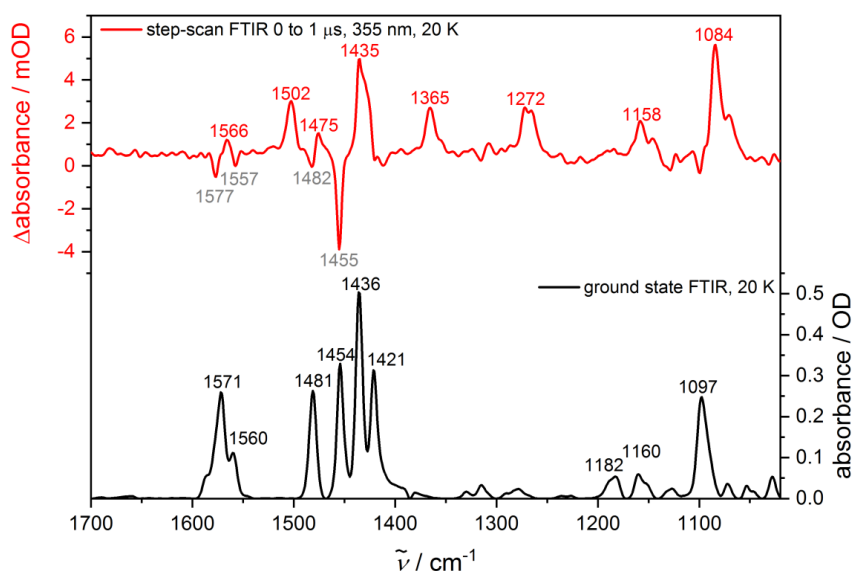


Figure S74. Step-scan difference spectrum at 0 – 1 μs after laser excitation ($\lambda_{\text{ex}} = 355 \text{ nm}$) and ground state FTIR spectrum of $\text{Cu}_2\text{Br}_2\text{L}_3$ (KBr, 20 K).

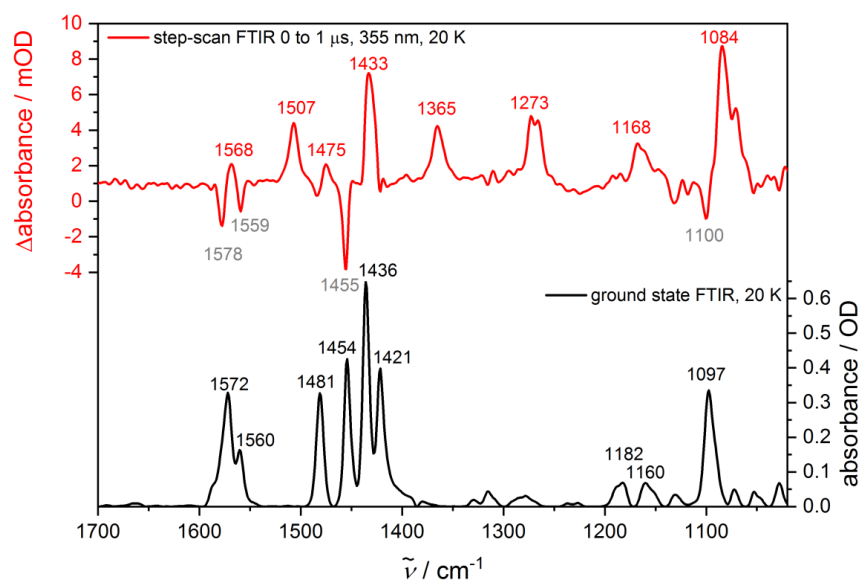


Figure S75. Step-scan difference spectrum at 0 – 1 μs after laser excitation ($\lambda_{\text{ex}} = 355 \text{ nm}$) and ground state FTIR spectrum of $\text{Cu}_2\text{Cl}_2\text{L}_3$ (KBr, 20 K).

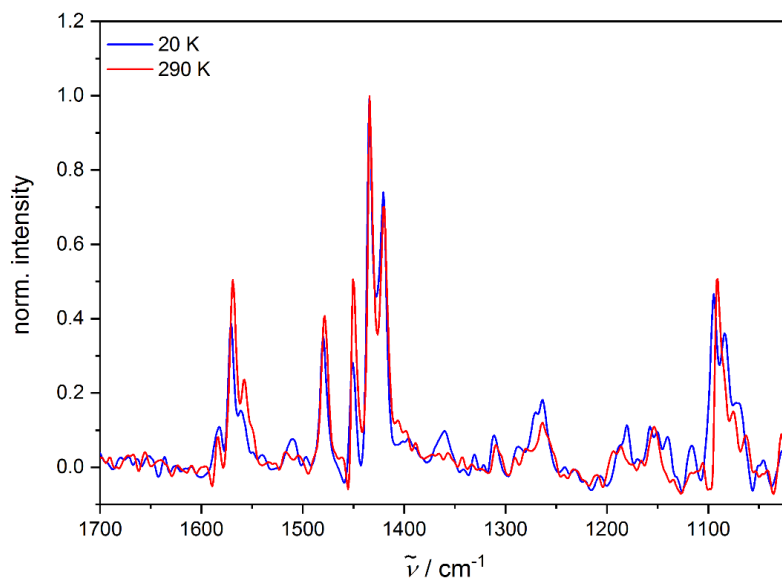


Figure S76. Excited state IR spectra (1.40/0.80 % of the ground state spectrum added to the step-scan difference spectrum) of $\text{Cu}_2\text{I}_2\text{L}_3$ at 20 K and 290 K.

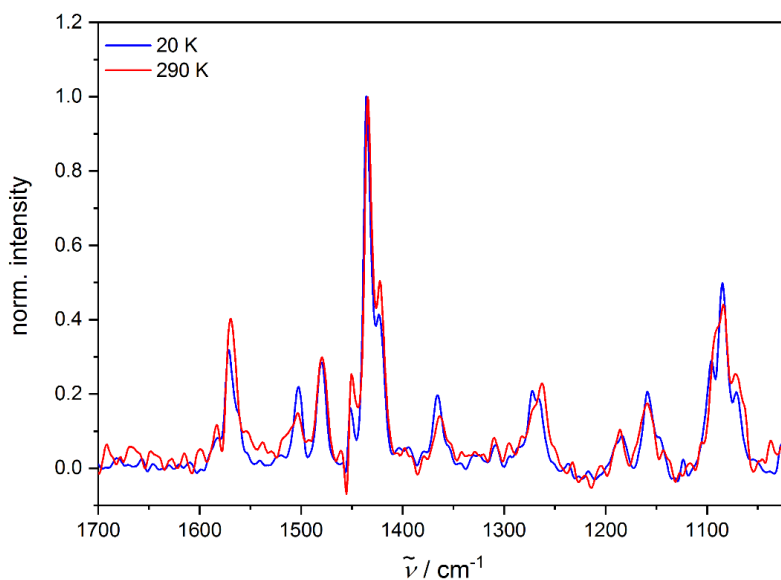


Figure S77. Excited state IR spectra (1.40/1.00 % of the ground state spectrum added to the step-scan difference spectrum) of $\text{Cu}_2\text{Br}_2\text{L}_3$ at 20 K and 290 K.

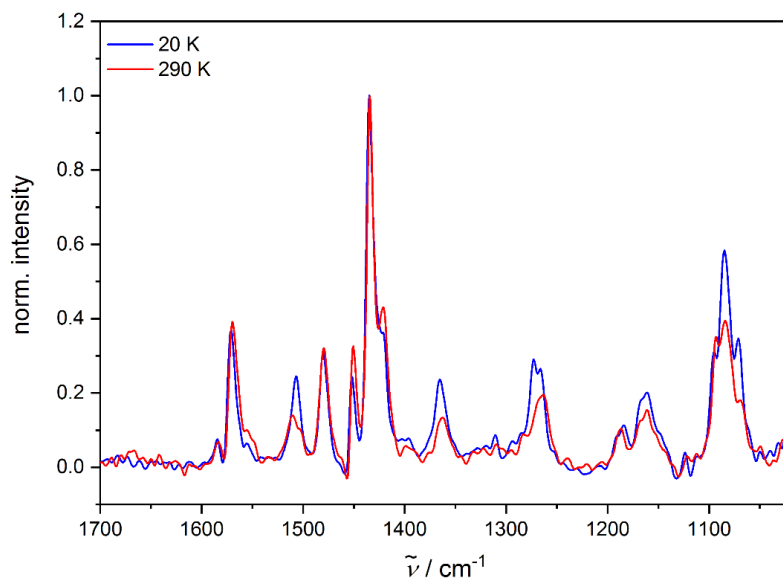


Figure S78. Excited state IR spectra (1.40/1.00 % of the ground state spectrum added to the step-scan difference spectrum) of $\text{Cu}_2\text{Cl}_2\text{L}_3$ at 20 K and 290 K.

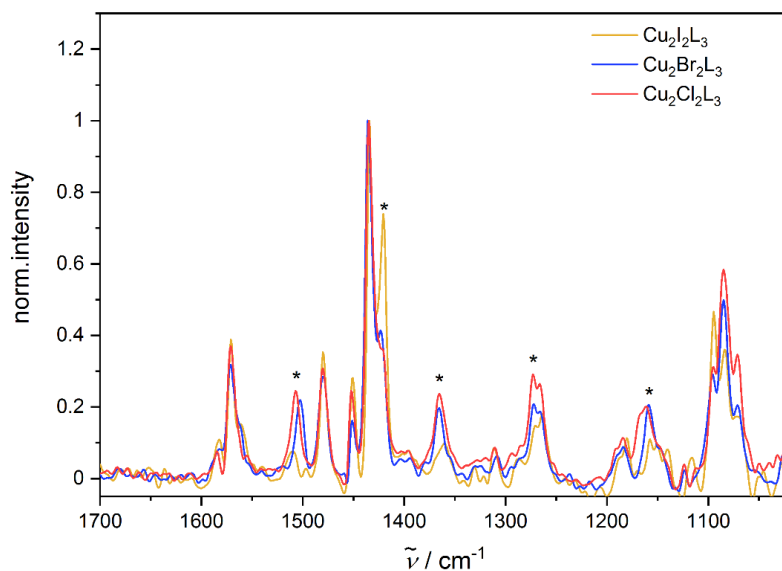


Figure S79. Excited state IR spectra of $\text{Cu}_2\text{I}_2\text{L}_3$, $\text{Cu}_2\text{Br}_2\text{L}_3$ and $\text{Cu}_2\text{Cl}_2\text{L}_3$ at 20 K (0.80/1.40/1.40 % of the ground state spectrum added to the step-scan difference spectrum). The bands marked with asterisks are discussed in the manuscript.

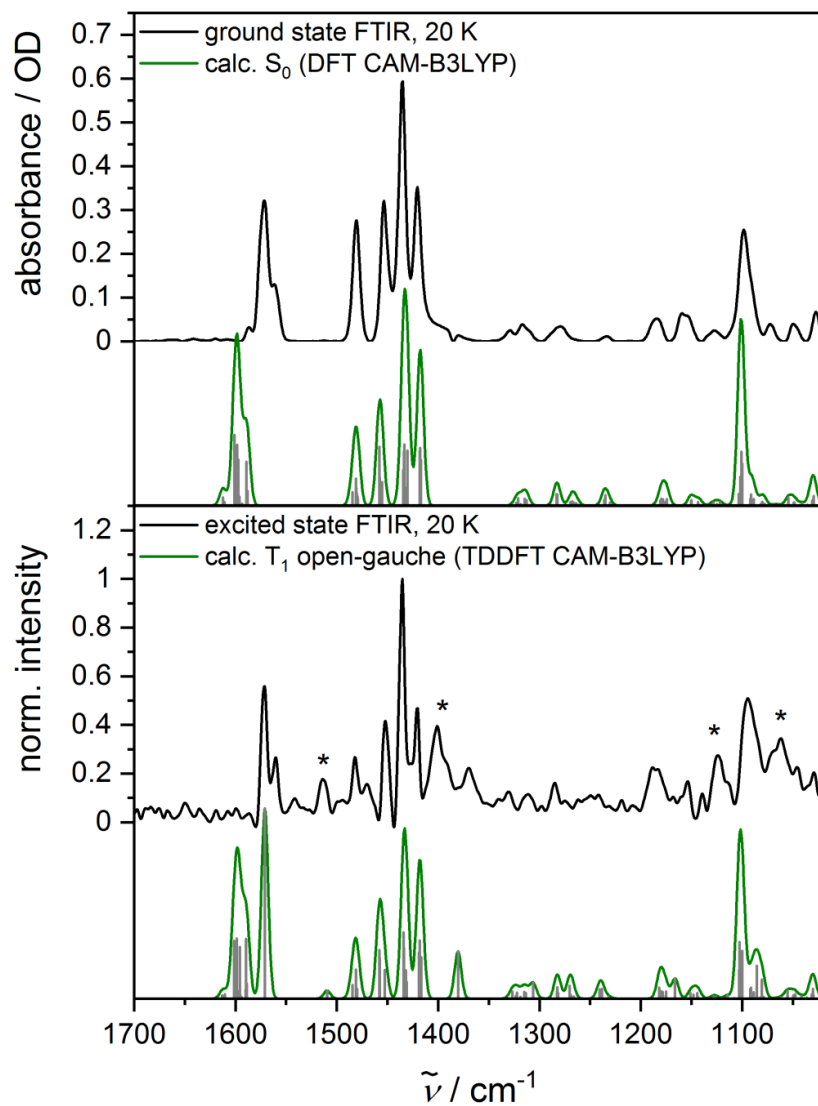


Figure S80. Top: Ground state FTIR spectrum in a KBr matrix at 20 K and calculated S_0 spectrum of $\text{Ag}_2\text{Cl}_2\text{L}_3$ in a KBr matrix at 20 K. Bottom: Excited state IR spectrum (0.75 % of the ground state spectrum added to the step-scan difference spectrum) and calculated spectrum of the open butterfly T_1 structure in gauche conformation (CAM-B3LYP/def2-TZVP).

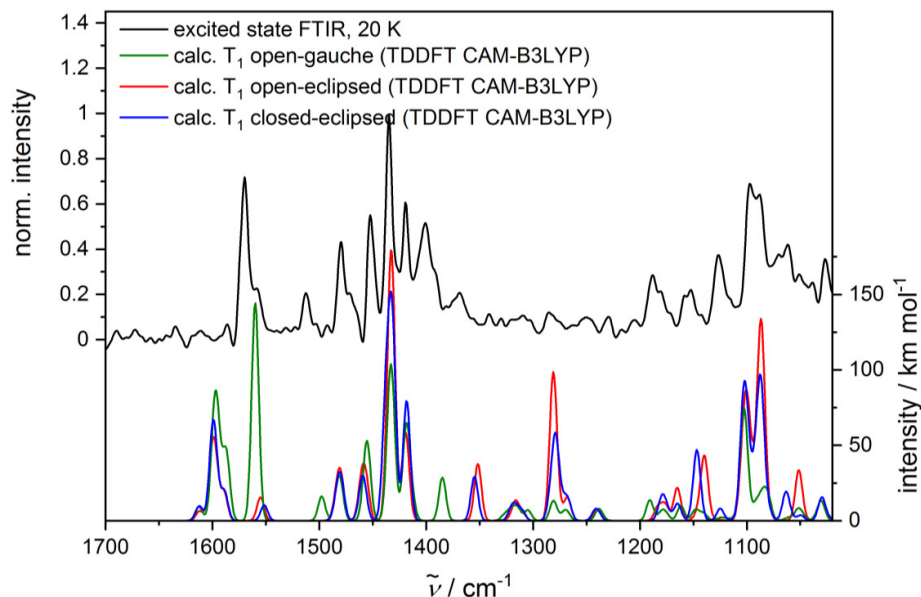


Figure S81. Comparison of calculated numerical frequencies of open and closed butterfly structure in eclipsed conformation, open butterfly in gauche conformation and the experimental excited state IR spectrum of $\text{Ag}_2\text{Br}_2\text{L}_3$ (0.80 % of the ground state spectrum added to the step-scan difference spectrum) in eclipsed conformation (CAM-B3LYP/def2-TZVP).

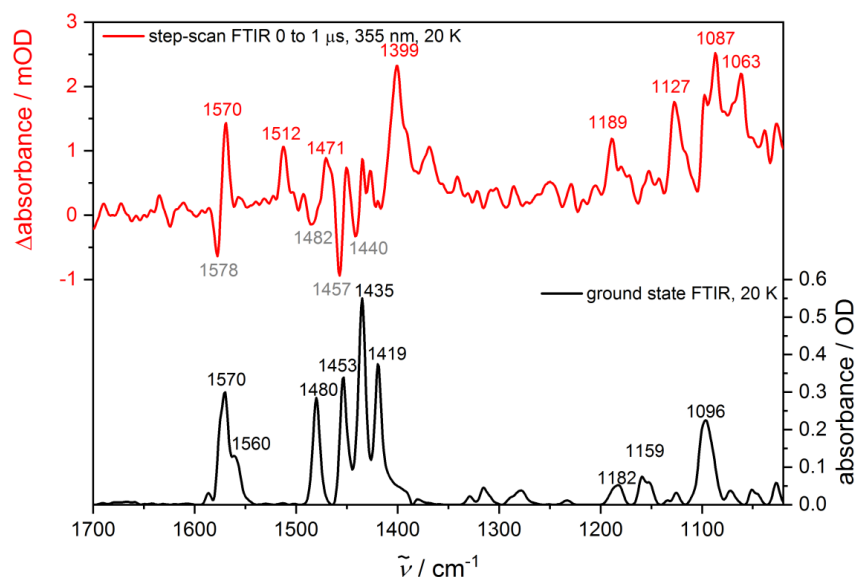


Figure S82. Step-scan difference spectrum at 0 – 1 μs after laser excitation ($\lambda_{\text{ex}} = 355 \text{ nm}$) and ground state FTIR spectrum of $\text{Ag}_2\text{Br}_2\text{L}_3$ (KBr, 20 K).

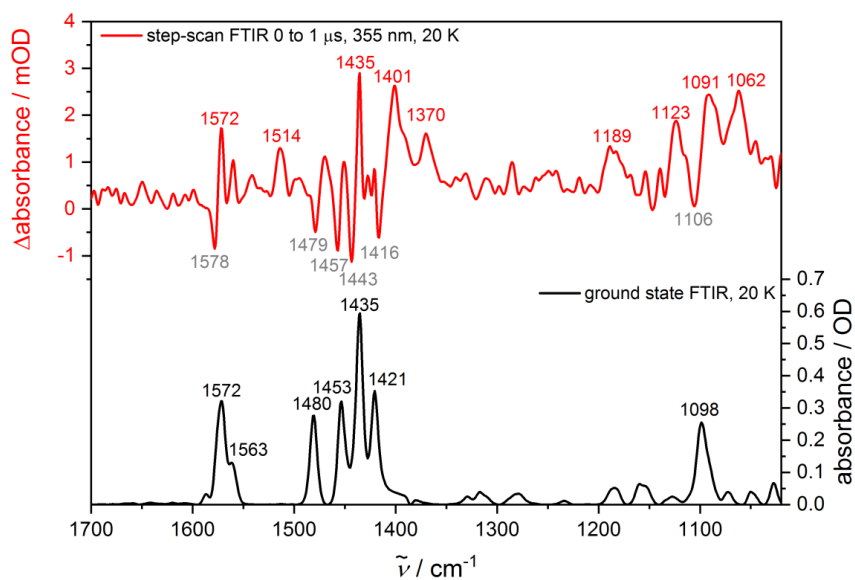


Figure S83. Step-scan difference spectrum at 0 – 1 μ s after laser excitation ($\lambda_{\text{ex}} = 355$ nm) and ground state FTIR spectrum of $\text{Ag}_2\text{Cl}_2\text{L}_3$ (KBr, 20 K).

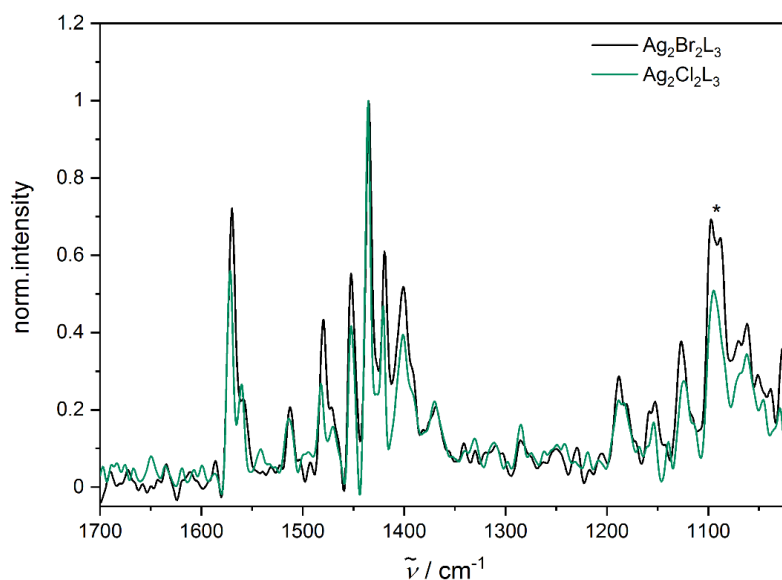


Figure S84. Excited state IR spectra of $\text{Ag}_2\text{Br}_2\text{L}_3$ and $\text{Ag}_2\text{Cl}_2\text{L}_3$ at 20 K (0.80/0.75 % of the ground state spectrum added to the step-scan difference spectrum). The bands marked with asterisks are discussed in the manuscript.

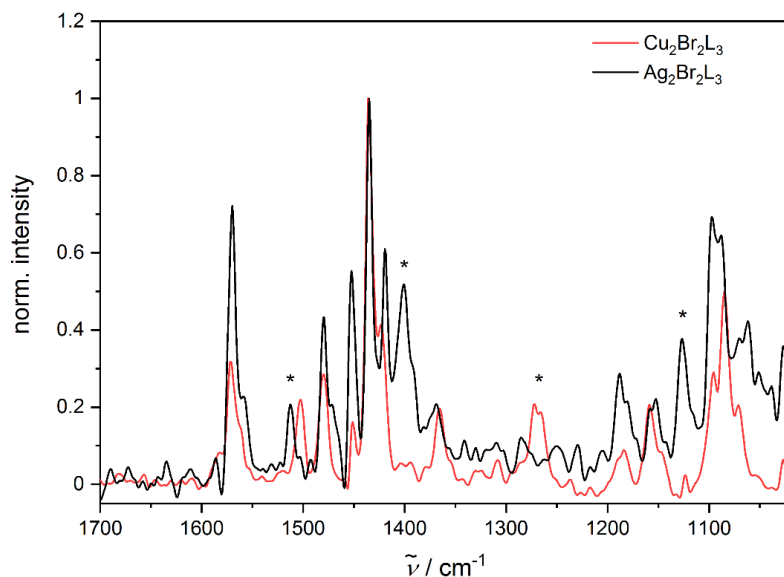


Figure S85. Excited state IR spectra of $\text{Cu}_2\text{Br}_2\text{L}_3$ and $\text{Ag}_2\text{Br}_2\text{L}_3$ at 20 K (1.40/0.80 % of the ground state spectrum added to the step-scan difference spectrum). The bands marked with asterisks are discussed in the manuscript.

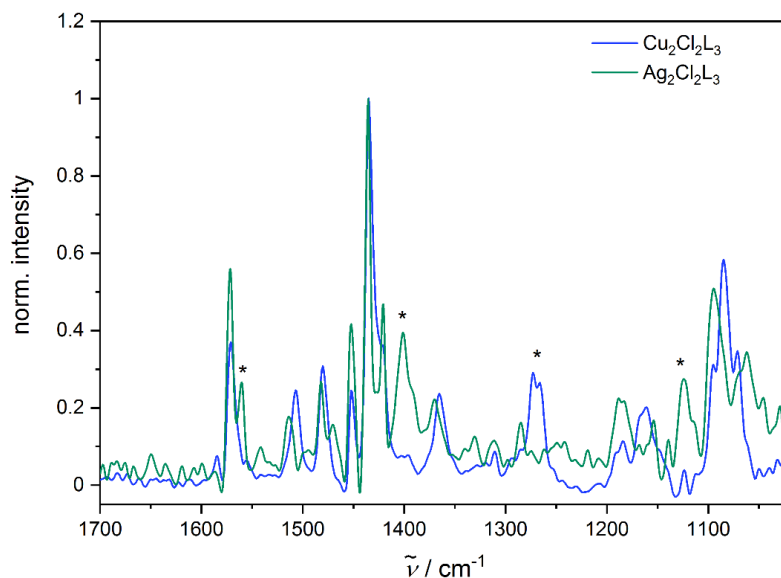


Figure S86. Excited state IR spectra of $\text{Cu}_2\text{Cl}_2\text{L}_3$ and $\text{Ag}_2\text{Cl}_2\text{L}_3$ at 20 K (1.40/0.75 % of the ground state spectrum added to the step-scan difference spectrum). The bands marked with asterisks are discussed in the manuscript.

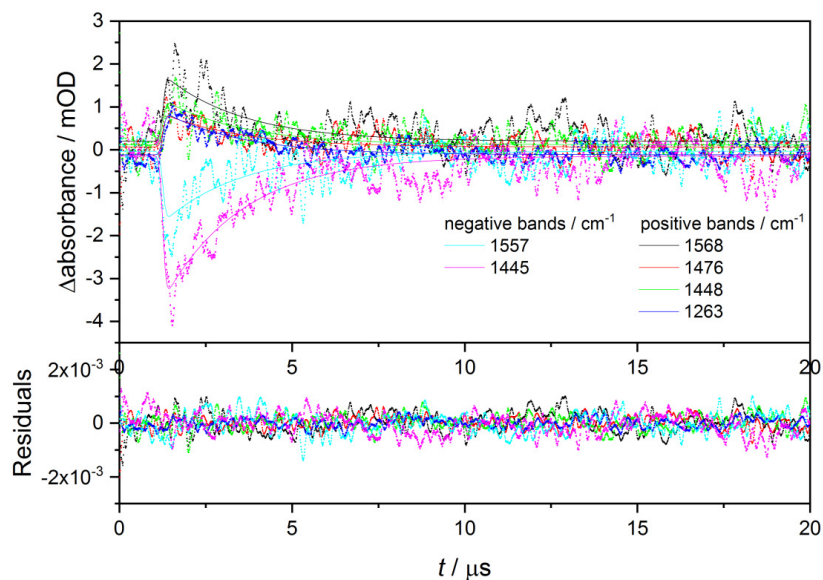


Figure S87. Time traces of the IR signal of positive and negative bands (dots) in the step-scan spectrum of $\text{Cu}_2\text{I}_2\text{L}_3$ at 290 K with a global monoexponential fit, resulting in a decay time of $\tau = 2.3 \mu\text{s}$. The lower trace shows the residuals of the fit.

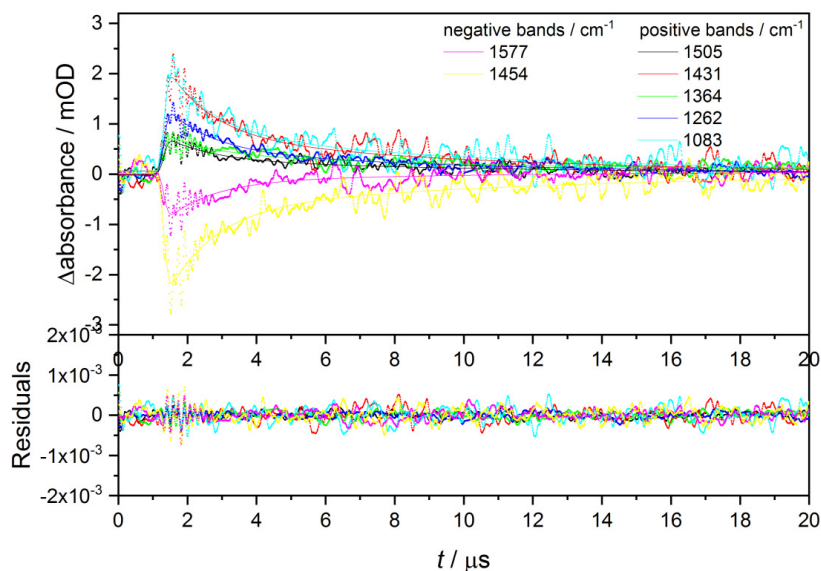


Figure S88. Time traces of the IR signal of positive and negative bands (dots) in the step-scan spectrum of $\text{Cu}_2\text{Br}_2\text{L}_3$ at 290 K with global biexponential fit, resulting in decay times of $\tau_1 = 1.4 \mu\text{s}$ (22 %) and $\tau_2 = 9.4 \mu\text{s}$ (78 %). The lower trace shows the residuals of the fit.

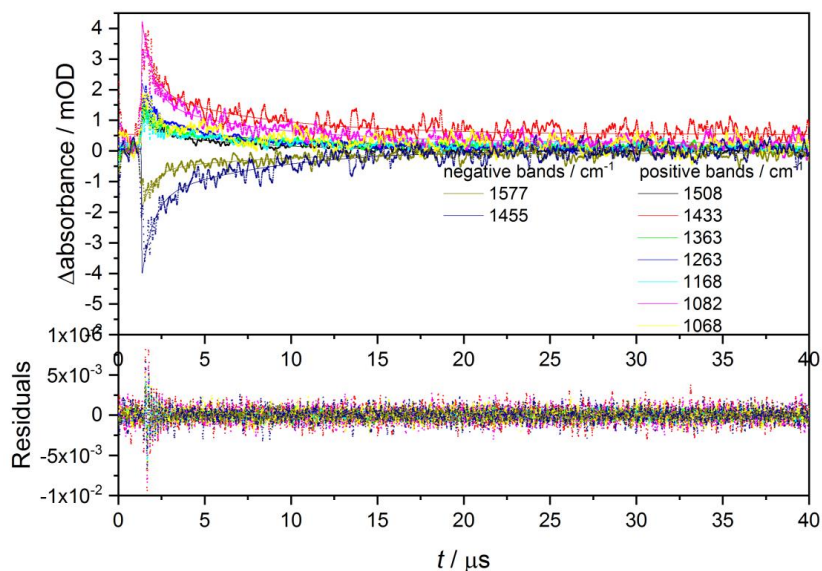


Figure S89. Time traces of the IR signal of positive and negative bands (dots) in the step-scan spectrum of $\text{Cu}_2\text{Cl}_2\text{L}_3$ at 290 K with global biexponential fit, resulting in decay times of $\tau_1 = 0.7 \mu\text{s}$ (14 %) and $\tau_2 = 6.9 \mu\text{s}$ (86 %). The lower trace shows the residuals of the fit.

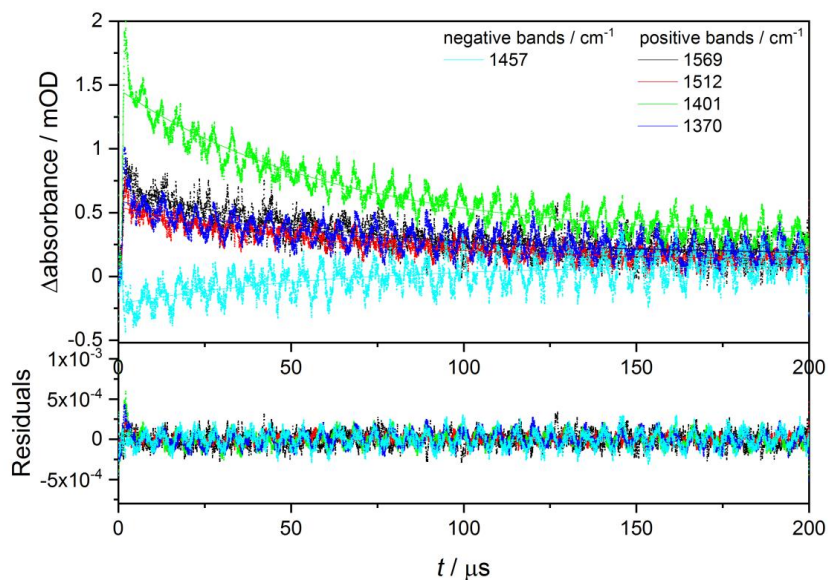


Figure S90. Time traces of the IR signal of positive and negative bands (dots) in the step-scan spectrum of $\text{Ag}_2\text{Br}_2\text{L}_3$ at 20 K with global monoexponential fit, resulting in a decay time of $\tau = 62 \mu\text{s}$. The lower trace shows the residuals of the fit.

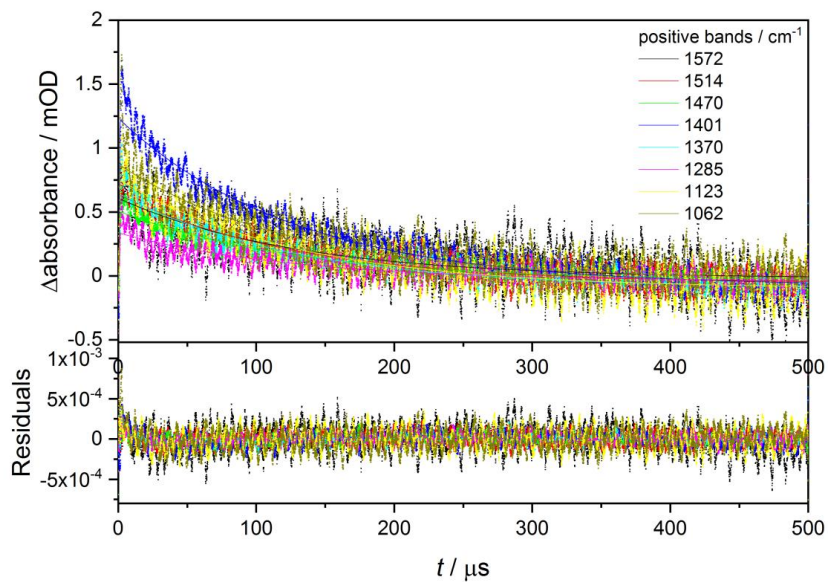


Figure S91. Time traces of the IR signal of positive bands (dots) in the step-scan spectrum of $\text{Ag}_2\text{Cl}_2\text{L}_3$ at 20 K with global monoexponential fit, resulting in a decay time of $\tau = 128 \mu\text{s}$. The lower trace shows the residuals of the fit.

Table S19. Characterization of vibrational modes of **Cu₂Br₂L₃**. The listed frequencies correspond to the experimental values at 20 K.

$\tilde{\nu} / \text{cm}^{-1}$ (ground state)	$\tilde{\nu} / \text{cm}^{-1}$ (excited state)	Character of vibration
1571	1572	C-C and C-N stretching combined with C-H scissoring in the pyridine rings
1560	-	C-C and C-N stretching combined with C-H scissoring in the pyridine rings
-	1502	C-C stretching in the pyridine ring of the bridging ligand
1481	1481	C-H scissoring in the phenyl rings
1454	-	C-P stretching and C-H scissoring combined with C-C and C-N stretching in the pyridine rings
1436	1435	C-H scissoring in the phenyl rings
1421	-	C-H scissoring combined with C-P scissoring in the pyridine rings
-	1366	C-H scissoring in the pyridine ring of the bridging ligand
-	1270	C-N and C-C stretching combined with C-H and N-Cu scissoring in the pyridine ring of the bridging ligand
1182	1184	C-H scissoring in the phenyl rings
1160	1158	aromatic C-H scissoring combined with C-P stretching in the pyridine rings
1097	-	C-P stretching and C-H scissoring in the pyridine rings
-	1085	C-H scissoring in the phenyl rings

Table S20. Characterization of vibrational modes of **Ag₂Br₂L₃**. The listed frequencies correspond to the experimental values at 20 K.

$\tilde{\nu} / \text{cm}^{-1}$ (ground state)	$\tilde{\nu} / \text{cm}^{-1}$ (excited state)	Character of vibration
1570	1570	C-C and C-N stretching combined with C-H scissoring in the pyridine rings
1560	-	C-C and C-N stretching combined with C-H scissoring in the pyridine rings
-	1513	C-C stretching combined with C-H scissoring in the phenyl ring in front of the bridging ligand
1480	1480	C-H scissoring in the phenyl rings
1453	1452	C-P stretching and C-H scissoring combined with C-C and C-N stretching in the pyridine rings
1435	1435	C-H scissoring in the phenyl rings
1419	1419	C-h scissoring combined with C-P scissoring in the pyridine rings
-	1401	C-H scissoring in the phenyl ring in front of the bridging ligand
1182	1188	C-H scissoring in the phenyl rings
1159	-	aromatic C-H scissoring combined with C-P stretching in the pyridine rings
-	1126	aromatic C-H scissoring combined with C-P stretching of the pyridine rings
-	1097	aromatic C-CH scissoring
1096	-	C-P stretching and C-H scissoring in the pyridine rings

8. References

- [1] G. M. Sheldrick, *Acta Cryst. A* **2015**, *A71*, 3-8.
- [2] G. M. Sheldrick, *Acta Cryst. C* **2015**, *C71*, 3–8.
- [3] S. Parsons, H. D. Flack and T. Wagner, *Acta Cryst. B* **2013**, *B69*, 249-259.
- [4] N. W. Alcock, P. Moore and P. A. Lampe, *Dalton Trans.* **1982**, *7*, 207-210.
- [5] a) L. A. Spek, *Acta Cryst.* **2009**, *D65*, 148-155; b) L. A. Spek, *Acta Cryst.* **2015**, *C71*, 9-18.
- [6] Y. Inoguchi, B. Milewski-Mahrta, D. Neugebauer, P. G. Jones and H. Schmidbaur, *Chem. Ber.* **1983**, *116*, 1487-1493.
- [7] O. V. Dolomanov, L. J. Bourhis, R. J. Gildea, J. A. K. Howard and H. Puschmann, *J. Appl. Crystallogr.* **2009**, *42*, 339-341.

4.2 Untersuchung des Einflusses der Halogenide und Ligandenvariationen auf die lumineszenten Zustände vierkerniger Cu^I-Komplexe

4.2.1 Einleitung

Die untersuchten vierkernigen Kupferkomplexe sind eng verwandt mit bereits veröffentlichten zweikernigen^[47,51,65–67,73] und vierkernigen^[53,75] Kupferkomplexen, deren Aufbau sehr ähnlich ist (Abb. 4.1). Diese Komplexe weisen alle eine hohe Quantenausbeute bis zu 99 %^[65,67] auf, wobei diese bei den zweikernigen häufig durch den TADF-Mechanismus^[51,65,66,69] erreicht wird. Damit ist diese Komplexgruppe potentiell auch für die Anwendung als OLED-Substanzen^[51,65–67,72] geeignet.

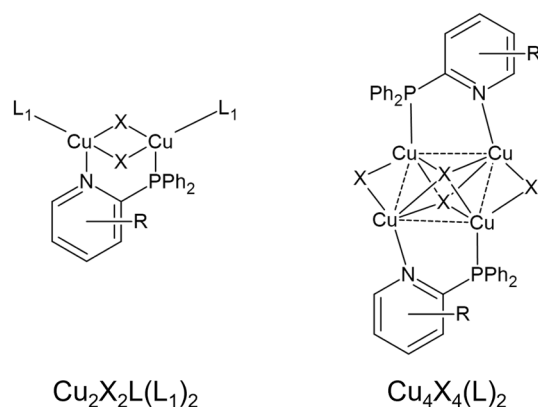


Abb. 4.1: Allgemeine Strukturen der verwandten Zweikerner (links) und Vierkerner (rechts) mit $\text{X}=\text{I}, \text{Br}, \text{Cl}$ und dem verbrückenden Liganden L . Die einfach koordinierten Liganden der Zweikerner (L_1) können identisch oder unterschiedlich zu L sein.

Alle diese Komplexe bestehen aus einem Metall-Halogenid-Zentrum, mit jeweils zwei bzw. vier Kupferzentren und Halogeniden. Zwei Kupferzentren sind jeweils über einen NP-Liganden verbrückt, welcher unterschiedlich substituiert sein kann. Somit bestehen die Vierkerner formal aus zwei Zweikerner-Einheiten ohne die einfach koordinierten Liganden. Die allgemeinen Strukturen sind in Abb. 4.1 dargestellt. Von den bereits bekannten vierkernigen Verbindungen^[53], die eine auffällige Thermochromie zeigen, unterscheiden sich die in diesem Kapitel gezeigten Komplexe lediglich in einer Substitution am Pyridinring des Liganden.

Durch die Kombination aus (zeitaufgelöster) FTIR- und Lumineszenzspektroskopie sowie quantenchemischen Rechnungen können das Verhalten nach der Anregung untersucht und die angeregten Zustände charakterisiert werden. Dabei werden über die temperaturabhängige Lumineszenz sowie die Lumineszenzlebensdauern die lumineszenten Prozesse zugeordnet. Mittels Step-scan-FTIR-Spektroskopie im Vergleich mit quantenchemischen Rechnungen kann dem langlebigen Zustand eine bestimmte Geometrie zugeordnet werden. Bei den vierkernigen Kupferkomplexen finden sich mehrere Geometrien

für den ersten Triplettzustand (angeregter Zustand), welche über die Step-scan-FTIR-Spektroskopie auch temperaturabhängig zugeordnet werden können.

Dies ist insbesondere bei den vierkernigen Komplexen interessant, da die verwandten Kupferkomplexe mit einer Methylgruppe in 6-Stellung am Pyridinring des Liganden L (Vgl. Abb. 4.1 und Abb. 4.2) eine halogenidabhängig unterschiedlich ausgeprägte Thermochromie zeigen^[53]. Im Vergleich zeigte der iodid-haltige Kupferkomplex mit einer Methylgruppe in 4-Position (Abb. 4.2) keine erkennbare Thermochromie in der KBr-Matrix.

4.2.2 Aufbau und Synthese

Die vierkernigen Kupfer-Halogenid-Komplexe sind aus einem Cu_4X_4 -Kern ($\text{X}=\text{I}$, Br oder Cl) und zwei verbrückenden 2-(Diphenylphosphino)pyridine-Derivaten als Liganden aufgebaut. Der 2-(Diphenylphosphino)pyridin-Derivat-Ligand verbrückt dabei je zwei Kupferzentren über das Phosphoratom (P) der Phosphinogruppe und das Stickstoffatom (N) des Pyridinrings. Daher wird er NP-Ligand genannt. Die verwendeten Liganden sind der nicht derivatisierte 2-(Diphenylphosphino)pyridin-Ligand (PyrPhos), der in 4-Stellung am Pyridinring methylierte 4-Methyl-2-(Diphenylphosphino)pyridin-Ligand (4-Me) und die Derivate mit Isochinolineinheit anstelle des Pyridinrings, 1-(Diphenylphosphino)isochinolin (Isochinolin) und 3-Methyl-1-(Diphenylphosphino)isochinolin (Me-Isochinolin) (nur als Kristalle) (Abb. 4.2). Bereits veröffentlicht^[53] ist die Halogenidreihe der Kupfer-Vierkerner mit dem in 6-Stellung am Pyridinring methylierten 6-Methyl-2-(Diphenylphosphino)pyridin-Liganden (6-Me). Allgemein wird der NP-Ligand im Folgenden mit L abgekürzt.

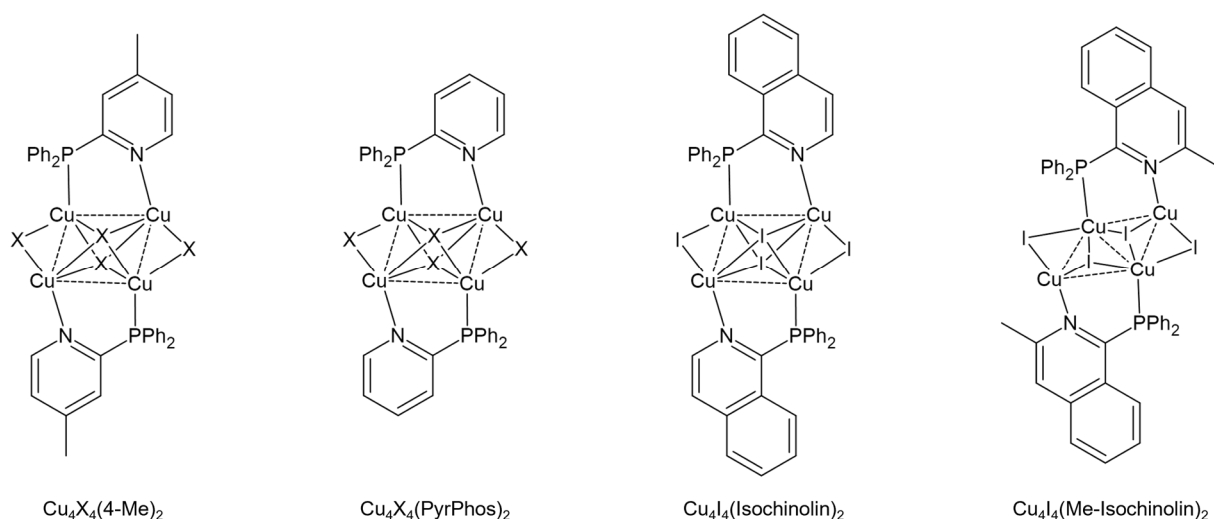


Abb. 4.2: Schematische Darstellung der untersuchten vierkernigen Komplexe mit ihren verschiedenen Liganden (4-Me, PyrPhos, Isochinolin, Me-Isochinolin, von links nach rechts), ($\text{X}=\text{I}$, Br , Cl).

Die vierkernigen Komplexe der Form $\text{Cu}_4\text{X}_4\text{L}_2$ ($\text{X}=\text{I}$, Br , Cl und $\text{L}=\text{Ligand}$) wurden in Dichlormethan (CH_2Cl_2) aus den NP-Liganden und dem Kupferhalogenidsalz (CuX) unter

milden Bedingungen bei Raumtemperatur synthetisiert. Die Synthese wurde von Jasmin Busch im Arbeitskreis von Prof. Stefan Bräse am Karlsruher Institut für Technologie (KIT) durchgeführt.^[177]

4.2.3 Ergebnisse

4.2.3.1 UV/Vis-Absorptionsspektroskopie

Die UV/Vis-Spektren aller untersuchten Komplexe zeigen sehr unstrukturierte Anstiege der Absorption ab ca. 500 nm in gemörsertem KBr-Pulver, gemessen mit einer Reflektionseinheit (Abb. 4.3, links Mitte). In einer Dichlormethan (CH_2Cl_2)-Lösung ist die Absorption im Vergleich mit den Feststoffmessungen aufgrund des solvatochromen Effekts durch das Lösungsmittel blauverschoben. Die Größenordnung der Verschiebung von Pulver zu Lösung ist vergleichbar mit der Verschiebung bei verwandten Kupferkomplexen.^[51,63,65] Eine deutliche solvatochrome Verschiebung spricht für elektronische Übergänge mit einer Ladungsverschiebung vom Metallzentrum auf die Liganden (engl. Metal-to-Ligand-Charge-Transfer (MLCT)).^[100,178,179] Im Spektrum in Lösung zeigen sich schwach ausgeprägte Schultern (ca. 310 nm und 270 nm) für die Komplexe $\text{Cu}_4\text{X}_4(\text{PyrPhos})_2$ und $\text{Cu}_4\text{X}_4(4\text{-Me})_2$ (Abb. 4.3, links oben). Die Spektren sind für die Komplexe mit und ohne Methylgruppe am Pyridinring des Liganden nahezu identisch, wobei der Iodid-Komplex jeweils etwas größere Extinktionskoeffizienten aufweist.

Die Absorption des Komplexes mit Isochinolineinheit ist in CH_2Cl_2 strukturreicher. Eine deutliche Schulter bei ca. 315 nm und ein starker Anstieg der Absorption ab ca. 260 nm ergeben ein strukturiertes Spektrum. Diese ist in der KBr-Matrix wie auch für die Komplexe ohne und mit Methylgruppe rotverschoben zum Spektrum in CH_2Cl_2 mit einem Onset bei ca. 550 nm. Der Anstieg ist flacher als in Lösung und die Schulter ist etwas schwächer ausgeprägt (Abb. 4.3, links), was auf die Skalierung der Pulvermessungen zurückzuführen ist.

Die vertikalen Übergänge wurden für den energetisch niedrigsten elektronischen Grundzustand, einer Struktur mit nahezu tetraedrischer Anordnung der vier Kupferzentren, für die Komplexe $\text{Cu}_4\text{X}_4(4\text{-Me})_2$ und $\text{Cu}_4\text{X}_4(\text{PyrPhos})_2$ berechnet. Die Rechnungen zeigen ebenfalls die vermuteten MLCT-Übergänge. Es wurden die 100 energetisch niedrigsten Übergänge berechnet und mit einer Gaussfaltung ($\text{FWHM} = 1500 \text{ cm}^{-1}$) zu Spektren gefaltet (Abb. 4.3, links unten). Auch die berechneten Spektren zeigen einen unstrukturierten Anstieg ab ca. 500 nm. Der $\text{Cu}_4\text{I}_4(\text{PyrPhos})_2$ -Komplex hat einen früheren Anstieg ab ca. 580 nm, aber bis 450 nm nur eine sehr geringe Oszillatorstärken. Damit beschreibt der Onset des theoretischen Spektrums insbesondere die experimentellen Daten im Feststoff sehr gut. Da die theoretischen Spektren ohne Einfluss der Umgebung berechnet wurden, also in etwa das

Spektrum in der Gasphase wiedergeben, sind solvatochrome Effekte des Lösungsmittels nicht berücksichtigt. Diese erklären jedoch die deutliche Blauverschiebung der Absorption in CH_2Cl_2 -Lösung. Auch die quantenchemischen Rechnungen geben nahezu identische Spektren für die verschiedenen Halogenide der Komplexreihen wieder (Abb. 4.3, links). Die Halogenidvariation und die Methylgruppe am Pyridinring des Liganden haben kaum Einfluss auf die Absorption der Komplexe. Ebenso wird das abweichende Verhalten der Absorption des $\text{Cu}_4\text{I}_4(\text{Isochinolin})_2$ -Komplexes von der quantenchemischen Rechnung mit einer deutlichen Schulter bei ca. 460 nm (Onset ca. 620 nm) und einer größeren Oszillatorstärke gut wiedergegeben. Dieses Verhalten lässt sich über eine bessere Stabilisierung der angeregten MLCT-Zustände auf dem erweiterten π -System des Liganden erklären.

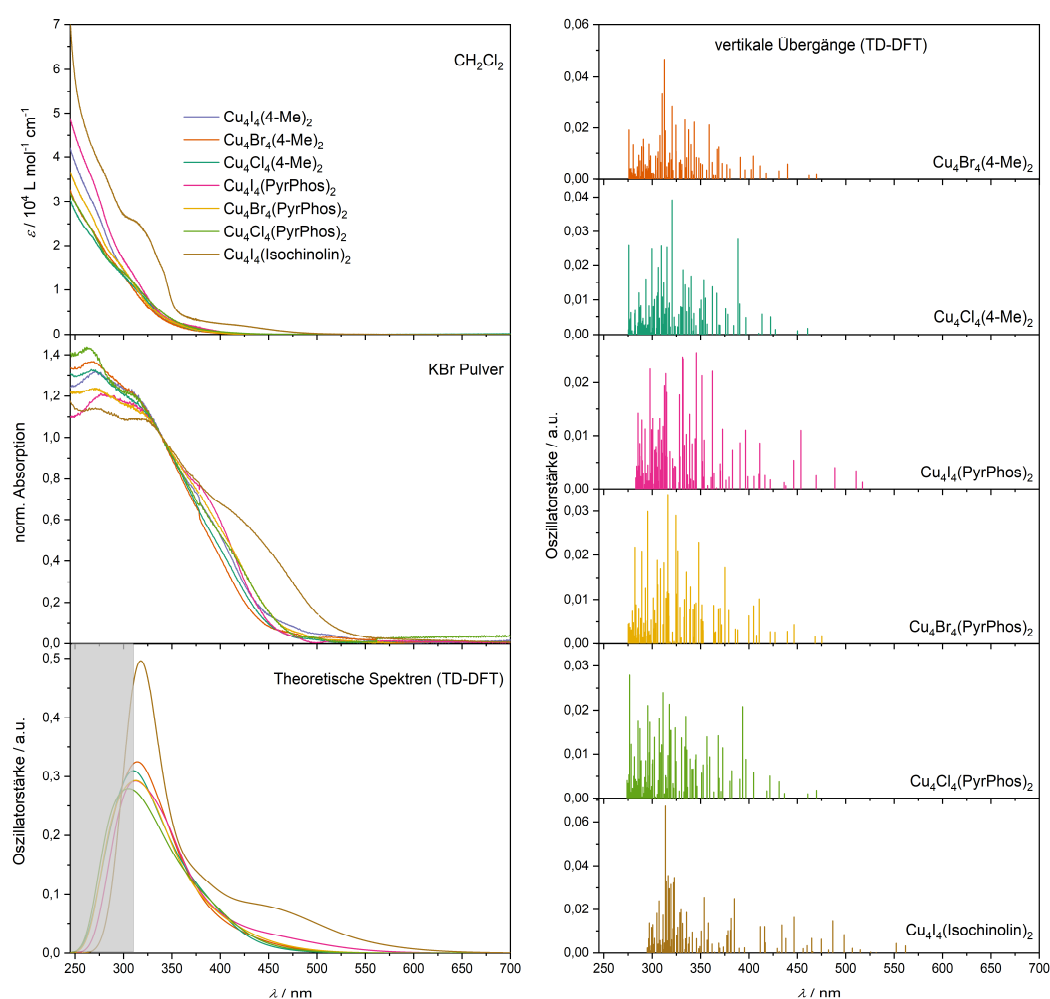


Abb. 4.3: Links: Experimentelle UV/Vis-Absorptionsspektren aller untersuchten Komplexe in Lösung (CH_2Cl_2 , $c = 2 \cdot 10^{-5} \text{ M}$) (oben) und als Feststoff (verdünnt mit gemörsertem KBr-Pulver, 1:100) (Mitte) sowie theoretische UV/Vis-Absorptionsspektren (unten), mit TD-DFT/B3LYP/def2-TZVP berechnet und mit Gaußkurven gefaltet ($\text{FWHM} = 1500 \text{ cm}^{-1}$), für die 100 energetisch niedrigsten Übergänge der closed butterfly-Struktur im Grundzustand aller erstmalig untersuchten Komplexe. Der grau hinterlegte Bereich ist aufgrund der Beschränkung auf die ersten 100 Übergänge nicht mehr aussagekräftig. Rechts: Strichspektren der 100 energetisch niedrigsten vertikalen Übergänge (TD-DFT/B3LYP/def2-TZVP) der untersuchten Komplexe, die den theoretischen Spektren zu Grunde liegen.

4.2.3.2 Lumineszenzspektroskopie im Feststoff

Die Lumineszenzspektroskopie wurde temperaturabhängig an den Proben in Form von KBr-Presslingen, als Pulver und teilweise im Kristall durchgeführt. Darüber kann der Einfluss auf die Lumineszenz von Halogenid, Ligand und Matrix untersucht werden.

Halogenidreihe $\text{Cu}_4\text{X}_4(4\text{-Me})_2$

Die temperaturabhängigen Lumineszenzspektren über den Temperaturbereich von 290 bis auf 10 bzw. 5 K zeigen für die Komplexe mit 4-Methylgruppe am Pyridinring eine leichte Verschiebung von maximal 500 cm^{-1} (Abb. 4.4). In KBr-Matrix weist der Iodid-Komplex eine Blauverschiebung bei tieferen Temperaturen auf, welche vom „Rigidochromismus“^[180,181] stammen könnte. Durch die starrere Umgebung bei tiefer Temperatur kann der elektronisch angeregte Zustand schlechter relaxieren und die Emission ist blauverschoben. Dagegen zeigen der Bromid- und der Chlorid-Komplex eine schwache Rotverschiebung, wobei der Effekt beim Br-Komplex wesentlich deutlicher ausgeprägt ist. Jedoch widerspricht das temperaturabhängige Verhalten der Lumineszenzlebensdauern (siehe Kapitel 4.2.3.3) einem möglichen TADF-Mechanismus. Die Rotverschiebung stammt daher eher von einer Destabilisierung des Grundzustandes oder Stabilisierung des angeregten Zustands bei tiefer Temperatur. Die Intensität der Lumineszenz nimmt mit abnehmender Temperatur zu, was auf eine Unterdrückung der Kanäle zur nicht-strahlenden Deaktivierung des angeregten Zustands zurückzuführen ist. Die integrierte Lumineszenz (Abb. 4.4, Einschübe) steigt für den Iodid-Komplex um das ca. 2,5-fache, während sie für den Chlorid-Komplex nahezu identisch bleibt bei einer Verschmälerung der Emissionsbande. Der Bromid-Komplex liegt mit einer Zunahme der integrierten Lumineszenz um das ca. 1,4-fache dazwischen. Der Temperaturverlauf der integrierten Lumineszenz weist eine, zu tiefen Temperaturen hin abflachende, gerade Steigung auf für $\text{Cu}_4\text{I}_4(4\text{-Me})_2$ und $\text{Cu}_4\text{Br}_4(4\text{-Me})_2$. Der Verlauf für den Chlorid-Komplex zeigt eine nahezu horizontale Gerade ohne signifikante Veränderung der integrierten Lumineszenz über den gesamten Temperaturbereich. Nicht-strahlende Deaktivierungskanäle bzw. ihre Unterdrückung bei tiefer Temperatur zeigen den Trend des abnehmenden Einflusses von Iod über Brom zu Chlor. Anders als die bereits veröffentlichten vierkernigen Kupferkomplexe mit der Methylgruppe in 6-Stellung am Pyridinring zeigt sich bei den 4-Me-Komplexen keine erkennbare Besetzung verschiedener elektronischer Zustände in Abhängigkeit von der Temperatur. Es wird temperaturunabhängig nur ein Triplett-Zustand besetzt. Weitere Zuordnung des beteiligten Zustands erfolgt im Kapitel 4.2.3.7 „Statische und Step-scan-FTIR-Spektroskopie“.

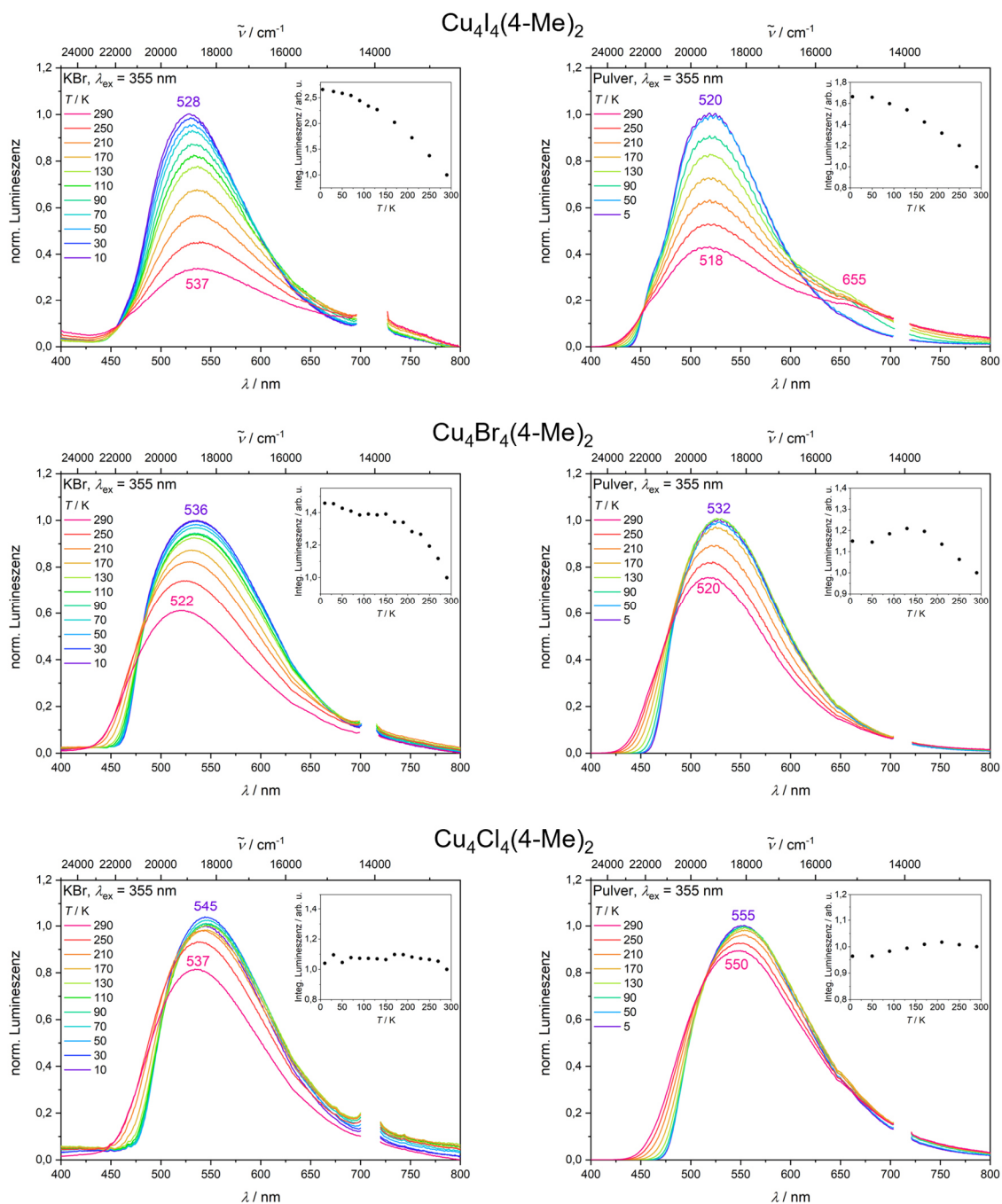


Abb. 4.4: Temperatur-abhängige Lumineszenzspektren der $\text{Cu}_4\text{X}_4(4\text{-Me})_2$ -Komplexe im KBr-Pressling (links) und als Pulver (rechts) mit Verlauf der integrierten Lumineszenzintensität über die Temperatur (Einschübe).

Die temperaturabhängigen Lumineszenzmessungen am reinen Pulver ergaben ähnlich Ergebnisse (Abb. 4.4). Auch hier ist eine Verschiebung um maximal 430 cm^{-1} zu beobachten. Die Verschiebung ist auch im Pulver für den Bromid-Komplex am stärksten ausgeprägt und für den Iodid-Komplex am schwächsten. Die Lumineszenz im Pulver schiebt im Gegensatz zur KBr-Matrix in allen drei Komplexe zu niedrigeren Temperaturen hin zu höheren Wellenlängen. Der Effekt des Rigidochromismus ist schwächer oder nicht mehr vorhanden im Vergleich zu den Beobachtungen in der KBr-Matrix. Dabei ist auch zu bedenken, dass die

Probe im KBr-Pressling einer unflexibleren Umgebung wie in den reinen Pulverproben ausgesetzt ist. Auch im Pulver ist kein Anzeichen in den Lebensdauern für einen TADF-Mechanismus zu erkennen (Kapitel 4.2.3.3). Ebenso ist der Intensitätsverlauf der integrierten Lumineszenz vergleichbar mit dem im KBr-Pressling. Die Intensitätszunahme zu tiefen Temperaturen ist im Pulver für den $\text{Cu}_4\text{I}_4(4\text{-Me})_2$ und den $\text{Cu}_4\text{Br}_4(4\text{-Me})_2$ schwächer. Die Intensität steigt um das ca. 1,7- bzw. 1,1-fache. Die flexiblere Umgebung unterdrückt die nicht-strahlenden Prozesse weniger effizient als in der KBr-Matrix. Die Messungen am Pulver bestätigen für den $\text{Cu}_4\text{Br}_4(4\text{-Me})_2$ und den $\text{Cu}_4\text{Cl}_4(4\text{-Me})_2$, dass keine zwei verschiedenen lumineszenten elektronisch angeregten Zustände temperaturabhängig besetzt werden. Jedoch zeigt der $\text{Cu}_4\text{I}_4(4\text{-Me})_2$ einen verstärkten Ausläufer an der roten Flanke der Emissionsbande bei Temperaturen ab ca. 130 K in Richtung Raumtemperatur, welche auf eine schwache Besetzung eines weiteren Zustands hindeuten könnten. Ein sehr schwacher thermochromer Effekt mit einem zweiten lumineszenten Zustand wie für die verwandten Komplexe mit 6-Methyl-Ligand kann für diesen Komplex damit nicht ganz ausgeschlossen werden.

Vom Bromid- und Chlorid-Komplex mit den 4-Me-Liganden konnten Kristalle in ausreichender Menge zur Aufnahme von Lumineszenzspektren von Jasmin Busch zur Verfügung gestellt werden. Die erhaltenen Daten zeigen ein nahezu identisches Verhalten wie im KBr-Pressling oder als amorphes Pulver (Abb. 4.5). In den temperaturabhängigen Spektren zeigen sich wieder eine Rotverschiebung der Bandenlage zu tiefen Temperaturen um ca. 220 bzw. 270 cm^{-1} für den Bromid- bzw. den Chlorid-Komplex. Das Emissionsmaximum des $\text{Cu}_4\text{Br}_4(4\text{-Me})_2$ -Komplex im Kristall bei Raumtemperatur ist nahezu identisch mit denen im KBr-Pressling oder als Pulver. Die Rotverschiebung beim Herunterkühlen fällt allerdings schwächer aus. Der $\text{Cu}_4\text{Cl}_4(4\text{-Me})_2$ -Komplex hat im Kristall nahezu das gleiche temperaturabhängige Verhalten wie im KBr-Pressling, während die Messung im Pulver eine rotverschobene Emission und eine geringere Verschiebung beim Herunterkühlen aufweist. Die Umgebung hat somit auf den Bromid-Komplex nur einen geringen Einfluss, während sich die Umgebungseffekte auf den Chlorid-Komplex im KBr-Pressling nahezu identisch wie im Kristall auswirken.

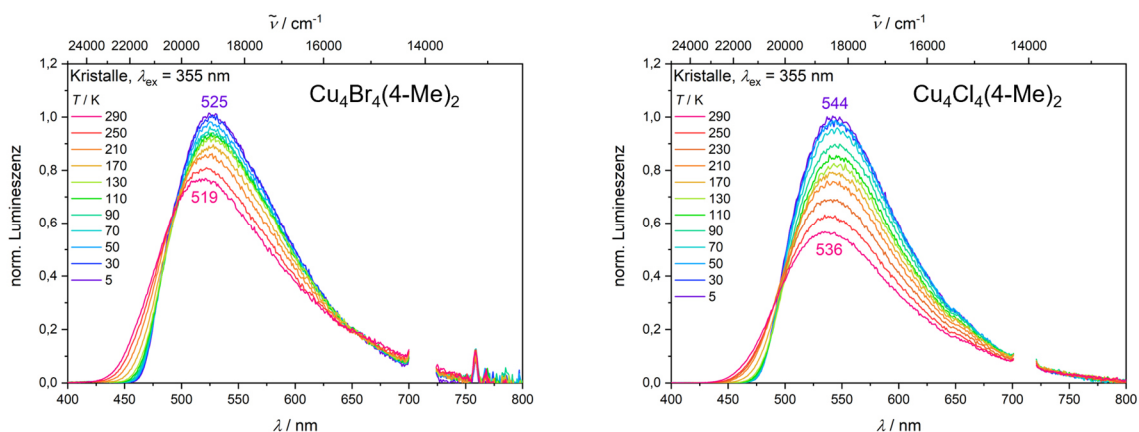


Abb. 4.5: Temperatur-abhängige Lumineszenzspektren der Komplexe $\text{Cu}_4\text{Br}_4(4\text{-Me})_2$ (links) und $\text{Cu}_4\text{Cl}_4(4\text{-Me})_2$ (rechts) in kristalliner Form.

Durch die unterschiedliche Stabilisierung der Zustände beeinflusst die Matrix die Lage der Emission. Auch der rigidochrome Effekt hängt von der Matrix ab und ist in der unflexibleren Umgebung stärker ausgeprägt. Die Unterdrückung nicht-strahlender Deaktivierungskanäle bei tiefen Temperaturen ist im KBr-Pressling effizienter. Unabhängig von der Matrix zeigen die 4-Me-Komplexe keine temperaturabhängige Besetzung verschiedener Zustände.

Halogenidreihe $\text{Cu}_4\text{X}_4(\text{PyrPhos})_2$

Der Iodid-Komplex $\text{Cu}_4\text{I}_4(\text{PyrPhos})_2$ zeigt beim Herunterkühlen in KBr-Matrix zunächst eine Rotverschiebung der Emissionsbande von 570 nm bei 290 K bis 587 nm bei 130 K, was ca. 500 cm^{-1} entspricht (Abb. 4.6, links). Wie auch bei den 4-Me-Komplexen kann diese Rotverschiebung von einer Destabilisierung des Grundzustandes bei tieferer Temperatur stammen. Jedoch beim weiteren Herunterkühlen von 130 K auf 10 K verschiebt sich die Lage der Emissionsbande stark in den blauerem Bereich um ca. 2100 cm^{-1} bis 523 nm. Die integrierte Lumineszenz (Abb. 4.6, Einschübe) steigt bis 130 K schwach auf das ca. 1,2-fache und von 130 K bis 50 K stark auf das doppelte der Intensität bei 290 K an. Dieses unterschiedliche Verhalten deutet auf eine thermisch gehinderte Besetzung eines zweiten lumineszenten Zustands bei tiefer Temperatur hin. Dieses Verhalten ist bereits von den verwandten vierkernigen Komplexen mit dem 6-Me-Ligand bekannt^[53]. Bei den analogen Untersuchungen an Pulverproben sind die Spektren besser aufgelöst als im KBr-Pressling und der Effekt in den temperaturabhängigen Lumineszenzspektren ist deutlich zu sehen (Abb. 4.6, rechts). Hierbei sind die beiden Zustände als deutliche getrennte Banden im Spektrum erkennbar. Die rote Bande (625 nm) bei 290 K verschiebt sich ganz leicht um ca. 25 cm^{-1} weiter in den roten Bereich bis zu einer Temperatur von ca. 90 K (626 nm). Ab dieser Temperatur ist eine zweite, zusätzliche Bande wesentlich blauer bei 509 nm zu sehen, welche vom zweiten besetzten Zustand stammt. Mit abnehmender Temperatur ist die Besetzung des niedrigeren Zustands (rote Bande) immer mehr gehindert bis ab ca. 50 K nur noch die blaue

Bande im Spektrum vorhanden ist. Auch der Verlauf der integrierten Lumineszenz (Abb. 4.6, Einschübe) im Pulver zeigt beim Herunterkühlen zunächst kaum Einfluss der Temperatur. Erst ab dem Erscheinen der zweiten Bande bei ca. 90 K steigt die Intensität mit dem weiteren Herunterkühlen bis 50 K steil auf das 1,2-fache an.

Anders als der Iodid-Komplex zeigen der Bromid- und der Chlorid-Komplex mit dem PyrPhos-Liganden keine thermochromen Effekte mit der Besetzung eines zweiten Zustands. Im Vergleich mit den 6-Me-Komplexen lässt sich annehmen, dass auch im Falle der PyrPhos-Komplexe die Barriere, die zum Erreichen des niedrigeren Zustands überwunden werden muss, vom Iodid- zum Bromid- und Chlorid-Komplex zunimmt. Für die PyrPhos-Komplexe scheint diese bereits beim Bromid-Komplex zu hoch zu sein, um sie bei Raumtemperatur zu überwinden, sodass lediglich ein lumineszenter Zustand im Spektrum zu sehen ist. Sowohl im KBr-Pressling als auch als Pulver zeigen die PyrPhos-Komplexe wie auch die 4-Me-Komplexe eine leichte Rotverschiebung der Bande bei 290 K von 560 nm (Br) und 550 bzw. 562 nm (Cl) nach 565 bzw. 572 (Br) und 562 bzw. 570 nm (Cl) bei 5 K (Abb. 4.6). Die integrierte Lumineszenz (Abb. 4.6, Einschübe) steigt für den Bromid-Komplex um das ca. 1,8-fache im KBr-Pressling und das ca. 1,6-fache als Pulver beim Herunterkühlen von 290 K auf 5 K. Dabei steigt die Intensität zunächst stark bis 250 K (KBr) bzw. 150 K (Pulver) und dann langsam (KBr) an bzw. bleibt nahezu konstant (Pulver). Die integrierte Lumineszenz des Chlorid-Komplexes bleibt wie auch schon für sein Analogon mit den 4-Me-Liganden über den untersuchten Temperaturbereich nahezu konstant.

Die Thermochromie des $\text{Cu}_4\text{I}_4(\text{PyrPhos})_2$ -Komplexes deutet auf ein zu den bereits veröffentlichten 6-Me-Kupferkomplexen^[53] analoges Lumineszenzverhalten hin. Die Barriere zum niedrigeren Triplett-Zustand scheint für die leichteren Halogenide und die 4-Me-Komplexe zu hoch zu sein, um mit thermischer Energie bei Raumtemperatur überwunden zu werden. Die lumineszenten Zustände werden im Kapitel 4.2.3.7 anhand von Step-scan-FTIR-Spektroskopie genauer charakterisiert.

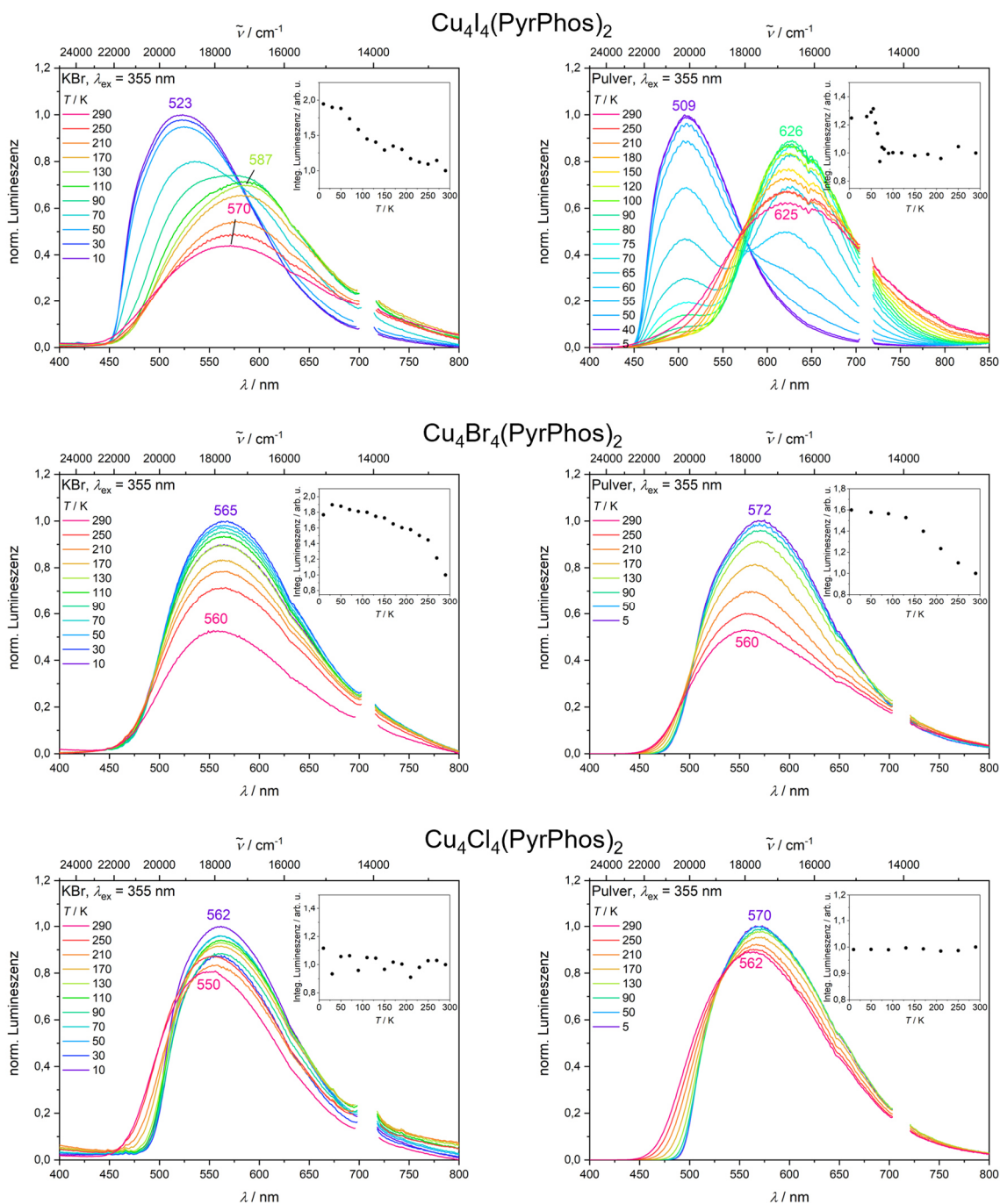


Abb. 4.6: Temperatur-abhängige Lumineszenzspektren der $\text{Cu}_4\text{X}_4(\text{PyPhos})_2$ -Komplexe im KBr-Pressling (links) und als Pulver (rechts) mit Verlauf der integrierten Lumineszenzintensität über die Temperatur (Einschübe).

$\text{Cu}_4\text{I}_4(\text{Isochinolin})_2$

Zum Vergleich wird der Komplex $\text{Cu}_4\text{I}_4(\text{Isochinolin})_2$ mit einem gegenüber Pyridin erweiterten π -System im Liganden untersucht (Abb. 4.7). Dieser zeigt eine starke Blauverschiebung der temperaturabhängigen Lumineszenz beim Herunterkühlen des KBr-Presslings um ca. 1500 cm^{-1} von 667 nm (290 K) auf 604 nm (5 K). Das ist im Einklang mit einem besonders stark ausgeprägten Rigidochromismus für diesen Komplex mit dem

ausgedehnteren Ligandsystem in der KBr-Matrix. Im Pulver dagegen ist zunächst eine schwache Rotverschiebung der Emission von 584 nm (290 K) auf 603 nm (130 K) zu beobachten. Anschließend verschiebt sich die Emission wieder leicht in Richtung des blauen Bereichs auf 592 nm (5 K). Das lässt sich durch gegenläufige Mechanismen erklären, wobei in diesem Fall eine Konkurrenz von TADF und Rigidochromismus denkbar ist. Die Annahme des TADF-Mechanismus beruht auf der kurzen Lebensdauer des Komplexes bei 290 K (siehe Kapitel 4.2.3.3). Der TADF-Prozess kann durchaus auch im KBr-Pressling ablaufen, jedoch wird die Rotverschiebung dabei möglicherweise durch den starken Rigidochromismus überlagert. Der Verlauf der integrierten Lumineszenz zeigt sowohl im KBr-Pressling als auch im Pulver eine leichte S-Form. Die Intensität steigt von 290 K auf 5 K im KBr-Pressling auf das ca. 5-fache und im Pulver auf da 2,2-fache an, was somit einer starken Zunahme entspricht.

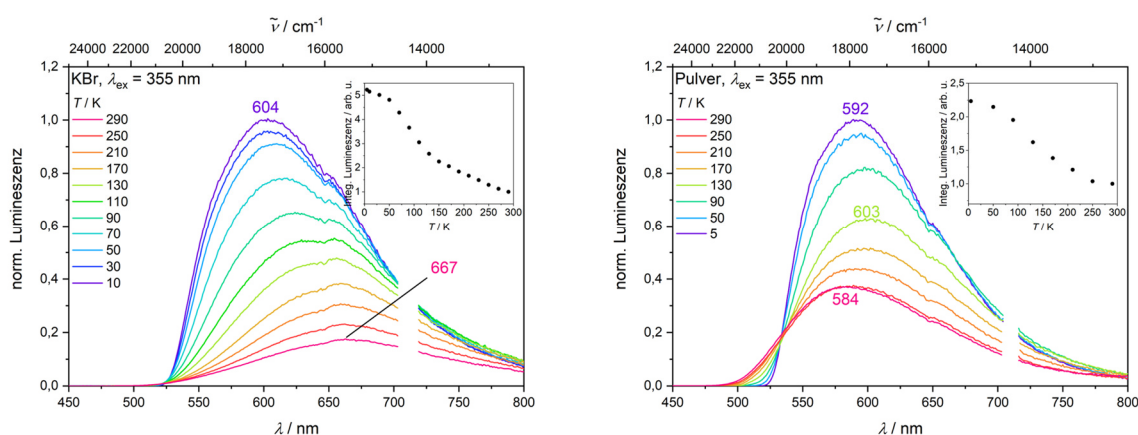


Abb. 4.7: Temperatur-abhängige Lumineszenzspektren des $\text{Cu}_4\text{I}_4(\text{Isochinolin})_2$ -Komplexes im KBr-Pressling (links) und als Pulver (rechts) mit Verlauf der integrierten Lumineszenzintensität über die Temperatur (Einschübe).

Vergleiche

Vergleicht man die Emissionsspektren der Halogenidreihen im Feststoff (Abb. 4.8 (KBr-Pressling), Abb. 4.9 (Pulver)) untereinander, hat bei 10 bzw. 5 K der Iodid-Komplex bei beiden Ligandtypen die jeweils blueste Emission, der lumineszente Zustand liegt energetisch am höchsten. Für die Komplexe ohne Methylgruppe liegen die Emissionen des Bromid- und des Chlorid-Komplexes spektral nahezu identisch, während bei den 4-Me-Komplexen der Chlorid-Komplex die rotteste Emission zeigt. Der lumineszente Zustand des Chlorid-Komplexes liegt somit energetisch am niedrigsten. Der Trend der Halogenide bei tiefer Temperatur ist identisch mit dem der thermochromen 6-Me-Komplexen^[53]. Bei 290 K im Pulver zeigt sich für die 4-Me-Komplexe der gleiche Trend wie bei 5 K. Im KBr-Pressling bei 290 K ist der $\text{Cu}_4\text{I}_4(4\text{-Me})_2$ rotverschoben mit einer identischen Emissionsbandenlage wie $\text{Cu}_4\text{Cl}_4(4\text{-Me})_2$, während der $\text{Cu}_4\text{Br}_4(4\text{-Me})_2$ dazwischen liegt. Bei 290 K liegt bei den $\text{Cu}_4\text{X}_4(\text{PyrPhos})_2$ -Komplexen der Iodid-Komplex nicht im gleichen angeregten Zustand vor

wie der Bromid- und der Chlorid-Komplex. Seine Emission ist daher sowohl im KBr-Pressling als auch im Pulver deutlich rotverschoben zu der der anderen beiden. Im Pulver emittieren der Bromid- und der Chlorid-Komplex nahezu die gleiche Wellenlänge, während im KBr-Pressling die Matrix nur auf den Chlorid-Komplex einen blauschiebenden Einfluss hat und der Bromid-Komplex die gleiche Emissionsbandenlage wie im Pulver hat. Der Isochinolin-Ligand sorgt für eine deutliche Rotverschiebung der Emission.

Die Vergleiche bestätigen die für die Halogenidreihe erwarteten Trends und zeigen den Einfluss der Ligandenvariation. Eine bessere Stabilisierung des $^3\text{MLCT}$ -Zustands auf dem erweiterten π -System der Isochinolin-Liganden, sowie die schwächste Stabilisierung auf dem Liganden mit +I-Effekt der Methylgruppe wurde bestätigt. Die Trends sind unabhängig von der untersuchten Matrix.

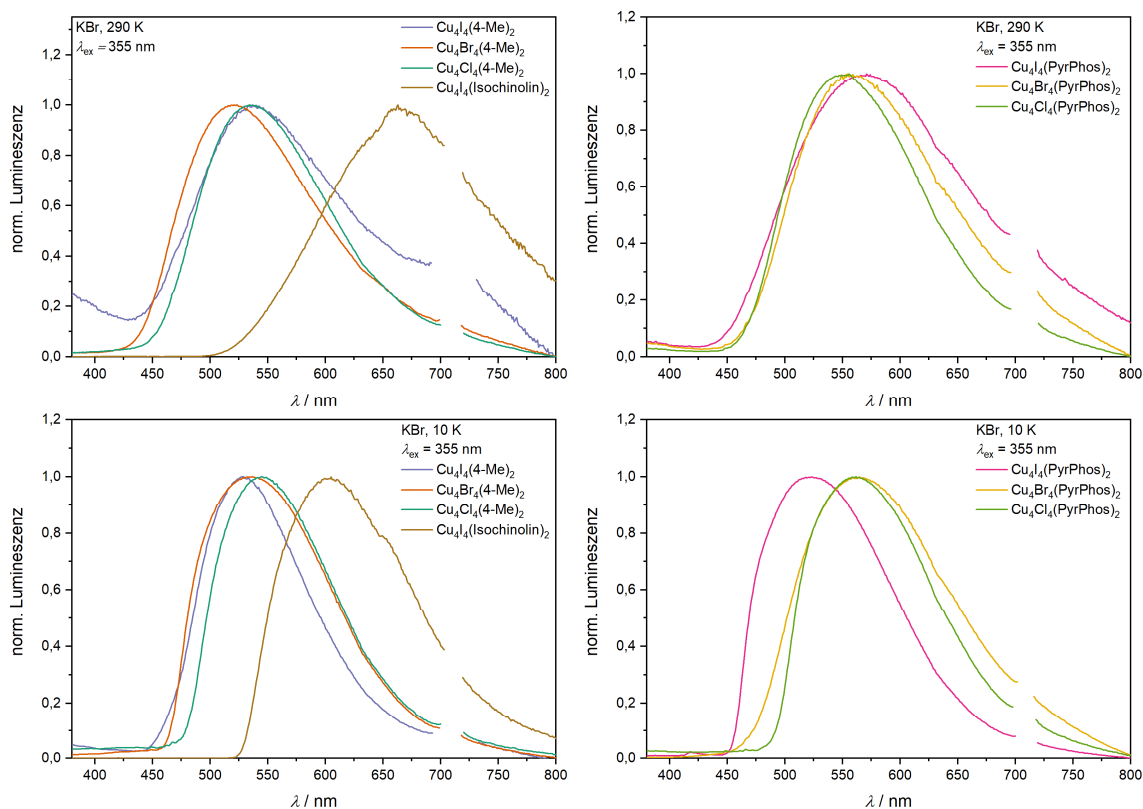


Abb. 4.8: Vergleich der Lumineszenzspektren der Komplexe $\text{Cu}_4\text{I}_4(4\text{-Me})_2$ und $\text{Cu}_4\text{I}_4(\text{Isochinolin})_2$ (links) sowie der Komplexe $\text{Cu}_4\text{X}_4(\text{PyrPhos})_2$ (rechts) im KBr-Pressling bei 290 K (oben) und 10 K (unten).

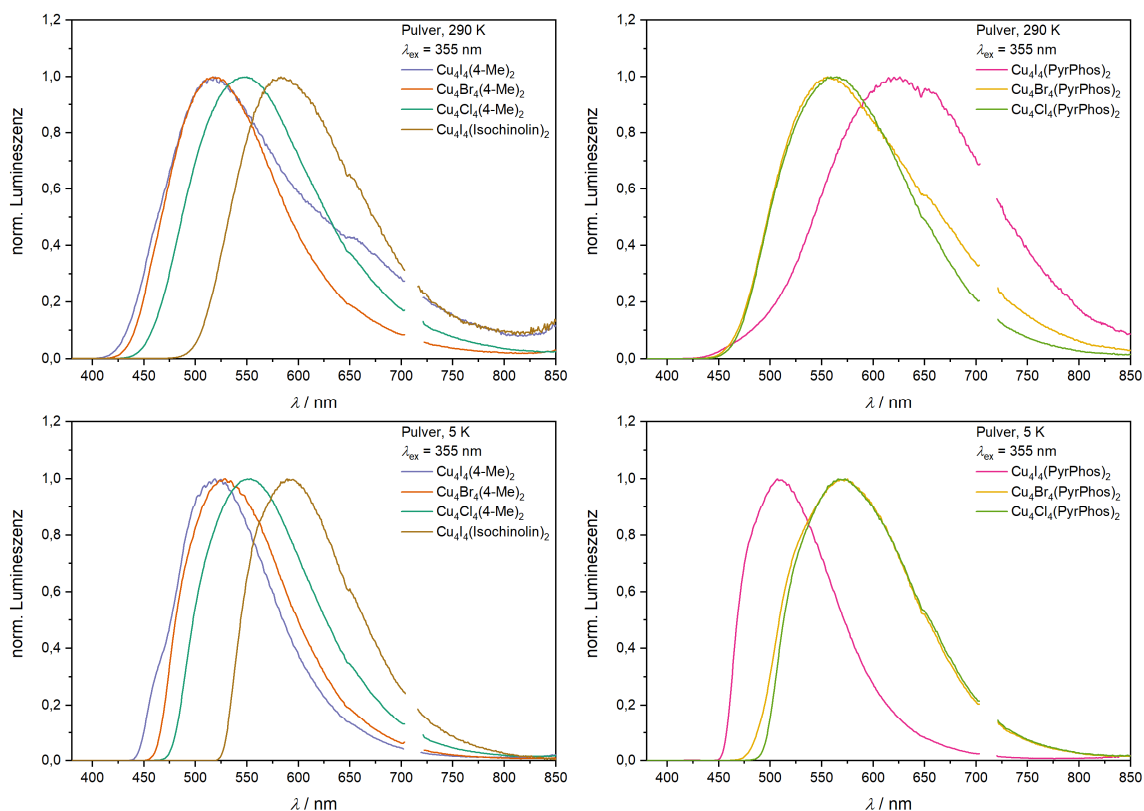


Abb. 4.9: Vergleich der Lumineszenzspektren der Komplexe $\text{Cu}_4\text{X}_4(4\text{-Me})_2$ und $\text{Cu}_4\text{I}_4(\text{Isochinolin})_2$ (links) sowie der Komplexe $\text{Cu}_4\text{X}_4(\text{PyrPhos})_2$ (rechts) im Pulver bei 290 K (oben) und 5 K (unten).

Anregungsspektren

Die Anregungsspektren zeigen die Emissionsintensität am Emissionsmaximum der jeweiligen Temperatur in Abhängigkeit von der Anregungswellenlänge. Alle Anregungsspektren sind an den Pulverproben aufgenommen worden (Abb. 4.10). Die Komplexe der Form $\text{Cu}_4\text{X}_4(4\text{-Me})_2$ haben alle einen ähnlichen Onset (Beginn des Anstiegs der ersten Emissionsintensität) zwischen 435 und 450 nm bei 5 K. Die Komplexe ohne Methylgruppe haben größere Unterschiede im Onset von 430 nm (I) über 455 nm (Br) bis 465 nm (Cl) bei 5 K. Die Unterschiede in den Anregungsspektren bei nahezu identischen Absorptionsspektren (Kapitel 4.2.3.1) sprechen für einen je nach Komplex unterschiedlich effizienten ISC-Prozess aus den verschiedenen angeregten $^1\text{MLCT}$ -Zuständen in die Triplett-Mannigfaltigkeit. Geringe Unterschiede können auch auf Artefakte der Skalierung zurückgeführt werden. Die Anregungsspektren bei 290 K sind rotverschoben zu denen bei 5 K mit Onsets zwischen 450 und 460 nm ($\text{Cu}_4\text{X}_4(4\text{-Me})_2$) bzw. von 455 nm (I) bis 485 nm (Br, Cl) ($\text{Cu}_4\text{X}_4(\text{PyrPhos})_2$). Die Rotverschiebung könnte auf die thermische Besetzung höherer Schwingungsniveaus im elektronischen Grundzustand zurückzuführen sein. Der Trend der Halogenide ist identisch zu dem bei 5 K. Wie auch schon bei den Absorptionsspektren zeigt der Isochinolin-Komplex ein abweichendes Verhalten. Er hat ein

deutlich rotverschobenes Anregungsspektrum verglichen mit den anderen untersuchten Vierkernern mit einem Onset bei ca. 500 nm (5 K) und 530 nm (290 K). Das deutet darauf hin, dass bereits aus den niedrigen angeregten Singulett-Zuständen die Triplett-Zustände bei diesem Komplex sehr effizient besetzt werden.

Für den $\text{Cu}_4\text{I}_4(\text{PyrPhos})_2$ wurden zudem noch die Anregungsspektren beider Zustände bei 60 K untersucht (Abb. 4.11). Der Onset und Verlauf beider Spektren sind identisch. Somit haben beide Zustände ein identisches Anregungsspektrum, was für einen identischen Ursprung beider Emissionsbanden spricht. Es scheint zu einer Besetzung des energetisch niedrigeren Zustands aus dem energetisch höheren Zustand zu kommen.

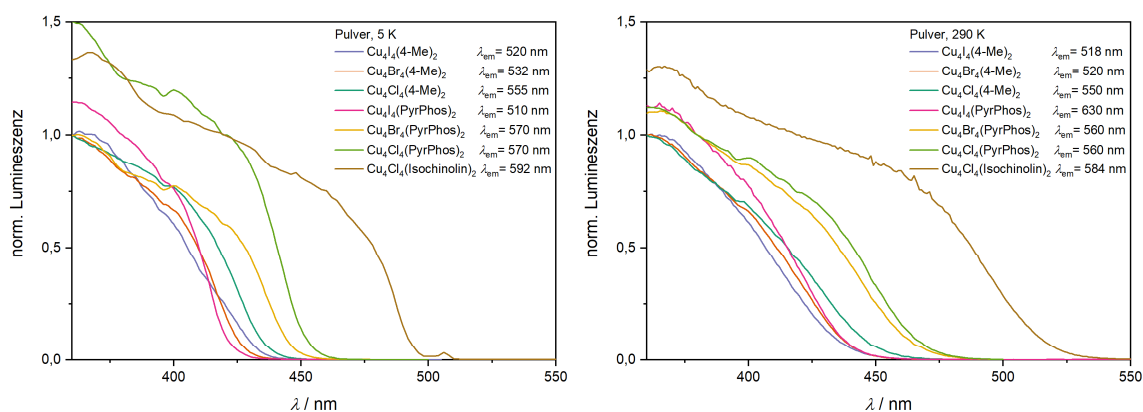


Abb. 4.10: Anregungsspektren aller untersuchten Komplexe an den jeweiligen Emissionmaxima im Pulver bei 5 K (links) und 290 K (rechts).

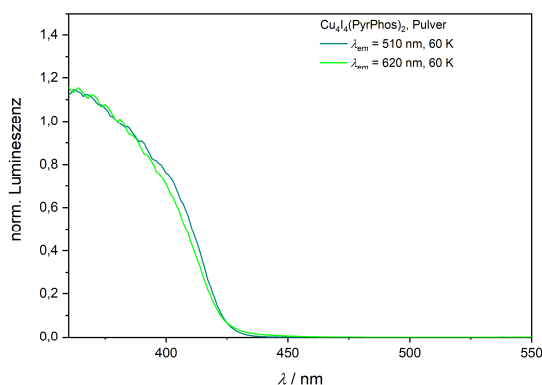


Abb. 4.11: Anregungsspektren beider Emissionsbanden des $\text{Cu}_4\text{I}_4(\text{PyrPhos})_2$ -Komplexes bei 60 K im Pulver an den jeweiligen Emissionmaxima.

4.2.3.3 Lumineszenzlebensdauern im Feststoff

Die Lumineszenzlebensdauern der Feststoffproben (KBr-Presslinge und reines Pulver) wurden mittels TCSPC im Multichannel scaling-Modus temperaturabhängig untersucht. Aus messtechnischen Gründen wurde die Emissionslebensdauer im KBr-Pressling an der

spektralen Emissionswellenlänge mit dem intensivsten Signal am Detektor gemessen und im Pulver am korrigierten Emissionsmaximum. Umgebungsbedingt ergeben sich mehrkomponentige Lebensdauern^[39,182-184], weshalb bei Bedarf auch die amplitudengewichteten mittleren Lebensdauern^[182,183,185] angegeben werden. Die Besetzung verschiedener lumineszenter, elektronischer Zustände mit Mikrosekunden-Lebensdauern und weitgehend deckungsgleichen Emissionsspektren ist unwahrscheinlich und keine überzeugende Erklärung für mehrkomponentige Abklingkurven.

Die Emissionslebensdauern im Feststoff liegen für die vierkernigen Kupferkomplexe mit und ohne Methylgruppe am Pyridinring alle im Mikrosekunden-Bereich (Tabelle 4.1 - Tabelle 4.4) und somit in der Größenordnung der Phosphoreszenz. Dabei hat der Iodid-Komplex in der jeweiligen Liganden-Reihe die kürzeste Lebensdauer. Dies lässt sich mit dem Schweratomeffekt erklären. Schwerere Atome sorgen für eine stärkere Spin-Bahn-Kopplung. Die Phosphoreszenz ist ein spinverbotener Übergang und ist lediglich durch die Spin-Bahn-Kopplung möglich. Je stärker die Spin-Bahn-Kopplung im Komplex vorhanden ist, desto schneller kann die Phosphoreszenz ablaufen. Da der Iodid-Komplex mit den Iod-Atomen vergleichsweise schwerere Elemente enthält, ist die Spin-Bahn-Kopplung stärker und der Phosphoreszenz-Prozess läuft schneller ab, was zu kürzeren Lumineszenzlebensdauern im Vergleich mit dem Br- und dem Cl-Komplex führt. Bei 290 K ergibt sich ebenfalls der Trend $\tau(\text{Cu}_4\text{I}_4\text{L}_2) < \tau(\text{Cu}_4\text{Br}_4\text{L}_2) < \tau(\text{Cu}_4\text{Cl}_4\text{L}_2)$, wobei die Emission des thermochromen $\text{Cu}_4\text{I}_4(\text{PyrPhos})_2$ nicht aus dem gleichen Zustand ausgeht wie für die Br- und Cl-Komplexe mit dem gleichen Liganden. Bei tiefer Temperatur ist der Trend für die Br- und Cl-Komplexe vertauscht (Pulver) bzw. die Lebensdauern der beiden Komplexe sind im Rahmen der Fehlergenauigkeiten gleich (KBr). Wie auch bei der Emissionsbandenlage wirkt sich der Temperatureinfluss auf den Bromid-Komplex stärker aus wie auf den Chlorid-Komplex.

Tabelle 4.1: Lumineszenzlebensdauern der Komplexe $\text{Cu}_4\text{X}_4(4\text{-Me})_2$ im KBr-Pressling bei 10 und 290 K (Fehler $\pm 10\%$).

KBr	T /	$\lambda_{\text{em}} /$	$\lambda_{\text{ex}} /$	$\tau_1 /$	$A_1 /$	$\tau_2 /$	$A_2 /$	$\tau_{\text{av}} /$
4-Me	K	nm	nm	μs	%	μs	%	μs
Cu₄I₄	290	528	390	5,6	86	1,3	14	5,0
	10	522	390	47	52	18	48	33
Cu₄Br₄	290	512	390	13	83	2,8	17	11
	10	522	390	53	94	3,8	4	51
Cu₄Cl₄	290	525	390	15	80	2,8	20	12
	10	535	390	55	90	6,6	10	50

Tabelle 4.2: Lumineszenzlebensdauern der Komplexe $\text{Cu}_4\text{X}_4(4\text{-Me})_2$ im Pulver bei 5 und 290 K (Fehler $\pm 10\%$).

Pulver	T /	$\lambda_{\text{em}} /$	$\lambda_{\text{ex}} /$	$\tau_1 /$	$A_1 /$	$\tau_2 /$	$A_2 /$	$\tau_{\text{av}} /$
4-Me	K	nm	nm	μs	%	μs	%	μs
Cu_4I_4	290	518	390	8,3	92	2,6	8	7,8
	5	520	390	39	72	14	28	32
Cu_4Br_4	290	520	390	15	91	3,8	9	14
	5	532	390	61	81	22	19	54
Cu_4Cl_4	290	550	390	18	95	4,2	5	17
	5	555	390	46	96	10	4	44

 Tabelle 4.3: Lumineszenzlebensdauern der Komplexe $\text{Cu}_4\text{X}_4(\text{PyrPhos})_2$ im KBr-Pressling bei 10 und 290 K (Fehler $\pm 10\%$).

KBr	T /	$\lambda_{\text{em}} /$	$\lambda_{\text{ex}} /$	$\tau_1 /$	$A_1 /$	$\tau_2 /$	$A_2 /$	$\tau_3 /$	$A_3 /$	$\tau_{\text{av}} /$
PyrPhos	K	nm	nm	μs	%	μs	%	μs	%	μs
Cu_4I_4	290	548	390	7,6	76	2,3	24	/	/	6,4
	10	510	390	49	39	23	51	6,3	10	31
Cu_4Br_4	290	545	390	13	60	3,8	40	/	/	9,5
	10	548	390	99	47	38	47	5,0	6	65
Cu_4Cl_4	290	538	390	18	87	3,0	13	/	/	16
	10	547	390	86	45	56	45	11	9	66

Tabelle 4.4: Lumineszenzlebensdauern der Komplexe $\text{Cu}_4\text{X}_4(\text{PyrPhos})_2$ im Pulver bei 5, 60 (nur Cu_4I_4) und 290 K (Fehler $\pm 10\%$).

Pulver	T /	$\lambda_{\text{em}} /$	$\lambda_{\text{ex}} /$	$\tau_1 /$	$A_1 /$	$\tau_2 /$	$A_2 /$	$\tau_{\text{av}} /$
PyrPhos	K	nm	nm	μs	%	μs	%	μs
Cu_4I_4	290	626	390	7,9	84	4,8	16	7,4
	60	620	390	6,5	-38	18	138	/
	60	509	390	26	39	12	61	17
	5	509	390	25	100	0,9	0	25
Cu_4Br_4	290	560	390	16	78	4,4	22	13
	5	572	390	70	94	14	6	66
Cu_4Cl_4	290	562	390	21	99	1,7	1	21
	5	572	390	59	99	2,8	1	58

Die TCSPC-Abklingkurven der roten Emissionsbande des thermochromen $\text{Cu}_4\text{I}_4(\text{PyrPhos})_2$ zeigt im Pulver bei Temperaturen, bei denen beide Banden zu beobachten sind, zunächst einen Anstieg im unteren Mikrosekundenbereich (Abb. 4.12). Die Zeitkomponente des Anstiegs ist kürzer als die Lebensdauer der blauen Bande. Dieser Abstieg deutet auf eine spätere Besetzung des zweiten Zustands aus dem höherenergetischen lumineszenten Zustand hin. Bei höheren Temperaturen wird die Barriere zur Besetzung des niedrigeren Zustands schneller überwunden, sodass in den zeitaufgelösten Lumineszenzmessungen die Besetzung nicht mehr als Anstieg der Lumineszenz detektiert werden kann. Dieses Verhalten wird im Abschnitt „TRES des $\text{Cu}_4\text{I}_4(\text{PyrPhos})_2$ -Komplexes“ weiter diskutiert.

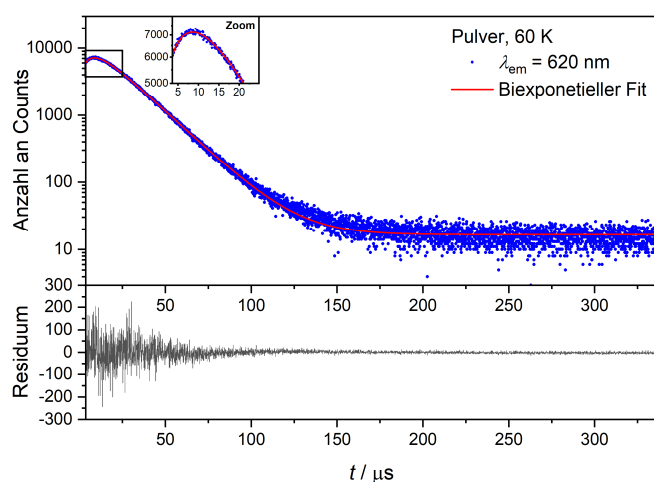


Abb. 4.12: TCSPC-Abklingkurve der roten Emissionbande ($\lambda_{em} = 620 \text{ nm}$) des $\text{Cu}_4\text{I}_4(\text{PyrPhos})_2$ bei 60 K mit biexponentiellem Fit, wobei die Amplitude der ersten Komponente negativ ist und diese den Anstieg innerhalb der ersten 10 μs beschreibt (Zoom).

Die gemittelten Lebensdauern steigen zu tiefen Temperaturen linear auf das 5-6-fache an (Abb. 4.13 und Abb. 4.14), was auf die Unterdrückung nicht-strahlender Deaktivierungskanäle zurückzuführen ist. Für die Komplexe, die keine Thermochromie zeigen, erreicht die Lebensdauer anschließend ein Plateau. Für den thermochromen $\text{Cu}_4\text{I}_4(\text{PyrPhos})_2$ -Komplex lässt sich der Wechsel der Besetzung der beiden lumineszenten Zustände an einem Sprung (Pulver) bzw. einem Bruch (KBr-Pressling) in den Lebensdauer-Temperatur-Verläufen erkennen (Abb. 4.13 und Abb. 4.14 oben links). Die Lebensdauer-Temperatur-Verläufe zeigen für keinen der sechs Komplexe eine S-Form, wie sie für den TADF-Mechanismus üblich wäre^[64,69,185,186]. Daher und mit der langen Lebensdauer bei 290 K lässt sich TADF als Begründung für die Rotverschiebung der Emissionsbanden ausschließen.

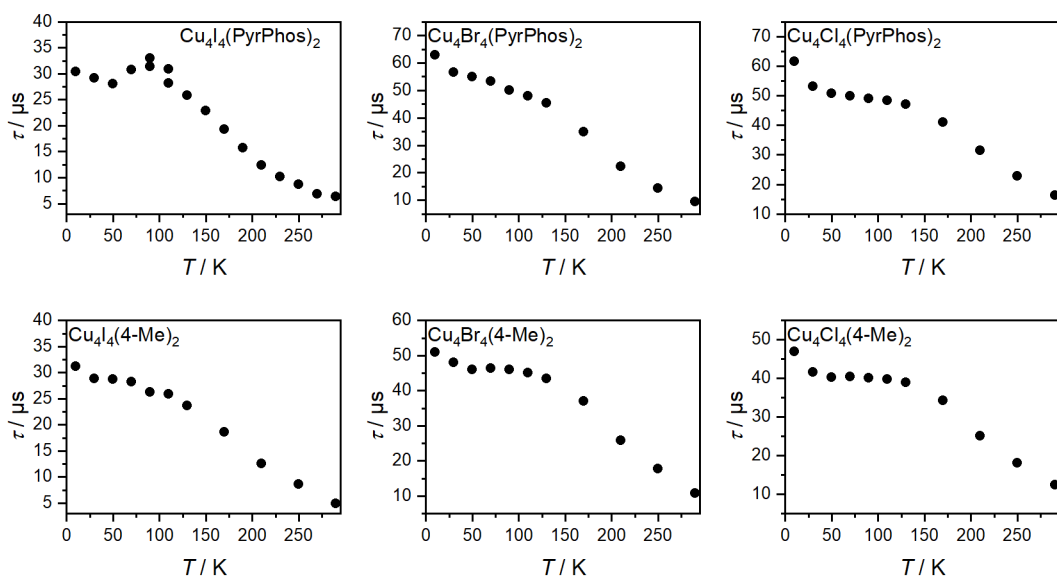


Abb. 4.13: Temperatur-Verlauf der amplitudengewichteten Lebensdauern der Komplexe $\text{Cu}_4\text{X}_4(\text{PyrPhos})_2$ (oben) und $\text{Cu}_4\text{X}_4(4\text{-Me})_2$ (unten) im KBr-Pressling über einen Temperaturbereich von 10 – 290 K (Fehler $\pm 10\%$).

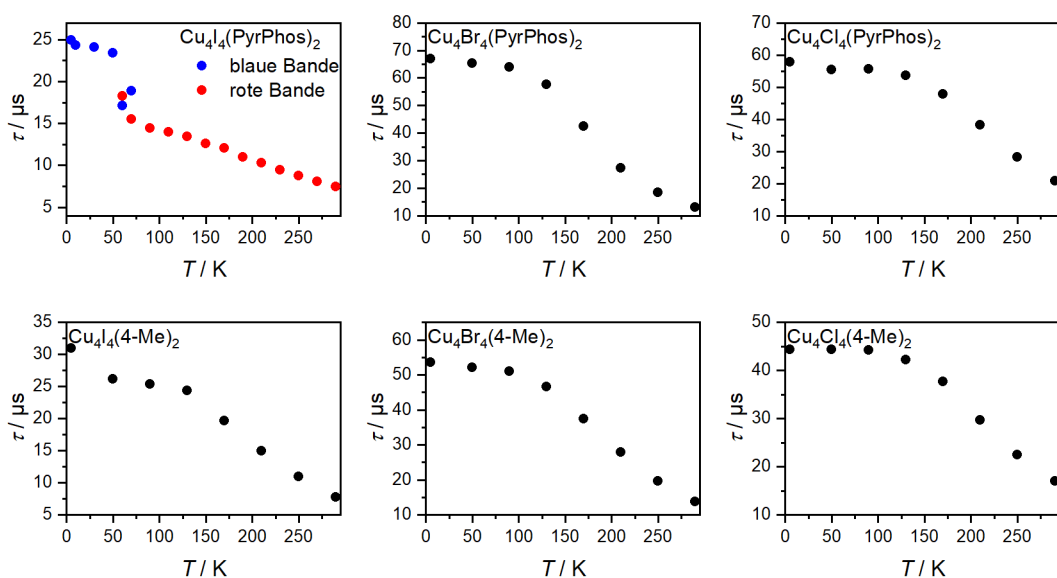


Abb. 4.14: Temperatur-Verlauf der amplitudengewichteten Lebensdauern der Komplexe $\text{Cu}_4\text{X}_4(\text{PyrPhos})_2$ (oben) und $\text{Cu}_4\text{X}_4(4\text{-Me})_2$ (unten) im Pulver über einen Temperaturbereich von 5 – 290 K (Fehler $\pm 10\%$).

Die Emissionslebensdauer des Isochinolin-Komplexes (Tabelle 4.5) ist bei 290 K im KBr-Pressling mit $2,3\ \mu\text{s}$ wesentlich kürzer und im Pulver identisch mit der Lebensdauer der Bromid-Komplexe mit den anderen beiden Liganden. Somit ist auch hier erkennbar, dass die Matrix auf den Isochinolin-Komplex einen größeren Einfluss hat wie auf die Komplexe ohne das erweiterte π -System. Die Lebensdauer bei tiefer Temperatur ist im KBr-Pressling und im Pulver im Rahmen der Fehlergenauigkeit identisch und mit $49\ \mu\text{s}$ bzw. $54\ \mu\text{s}$ wesentlich

länger als bei 290 K. Der Lebensdauer-Temperatur-Verlauf beschreibt eine S-Kurve, was für das Vorliegen eines TADF-Prozesses bei hohen Temperaturen spricht (Abb. 4.15).

Tabelle 4.5: Lumineszenzlebensdauern der Komplexe $\text{Cu}_4\text{I}_4(\text{Isochinolin})_2$ im Pulver bei 5 und 290 K (Fehler $\pm 10\%$).

$\text{Cu}_4\text{I}_4(\text{Isochinolin})_2$	$T /$ K	$\lambda_{\text{em}} /$ nm	$\lambda_{\text{ex}} /$ nm	$\tau_1 /$ μs	$A_1 /$ %	$\tau_2 /$ μs	$A_2 /$ %	$\tau_{\text{av}} /$ μs
KBr	290	613	390	3,5	52	1,1	48	2,3
	5	580	390	53	90	14	10	49
Pulver	290	584	390	15	85	3,5	15	13
	5	592	390	54	100	/	/	54

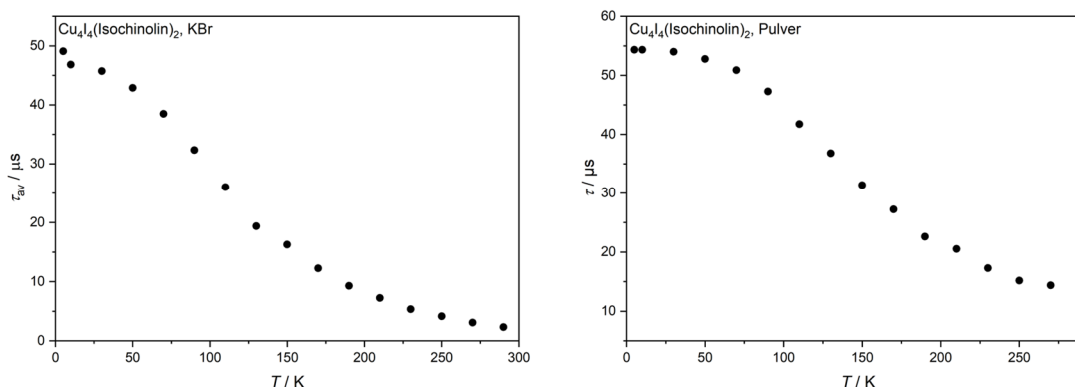


Abb. 4.15: Temperatur-Verlauf der amplitudengewichteten Lebensdauern des Komplexes $\text{Cu}_4\text{I}_4(\text{Isochinolin})_2$ im KBr-Pressling (links) und im Pulver (rechts) über einen Temperaturbereich von 5 – 290 K (Fehler $\pm 10\%$).

Für alle untersuchten Vierkerner hat der Temperatur-Verlauf der Lebensdauern und der integrierten Lumineszenz die gleiche Form. Die Unterdrückung der nicht-strahlenden Deaktivierungskanäle wirkt sich gleichermaßen auf die Zunahme der Intensität und Lebensdauer aus. Die Größenordnung der Lebensdauer liegt im Bereich phosphoreszenter Prozesse (Ausnahme $\text{Cu}_4\text{I}_4(\text{Isochinolin})_2$: TADF bei 290 K). Die Lebensdauer steigt innerhalb einer Halogenidreihe von Iodid zu Bromid und Chlorid aufgrund des Schweratomeffekts. Der Einfluss der Methylgruppe am Liganden zeigt keinen erkennbaren Trend.

4.2.3.4 Lumineszenz in Lösung

Die Messungen in Ethanol bei Raumtemperatur ergeben einen ähnlichen Trend der Emissionsbandenlagen wie im Feststoff bei 290 K (Abb. 4.16). Die niederenergetischste Emissionsbande zeigt der $\text{Cu}_4\text{I}_4(\text{PyrPhos})_2$, wobei auch in Lösung der niedrigere angeregte Zustand nur für diesen Komplex dieser Ligandreihe besetzt wird. Damit hat das

Lösungsmittel Ethanol kaum solvatochromen Einfluss auf die Lumineszenz der Vierkerner. Die erhaltenen Lumineszenzlebensdauern (Tabelle 4.6) sind nahezu identisch mit denen der Pulverproben. Die Abklingkurven lassen sich meist monoexponentiell oder mit lediglich einer weiteren, sehr kleinen (<5 %) und kürzeren Komponente für die Anregungsspitze fiten. Da die Lösung homogen ist, während es die Feststoffproben nicht sein können, wird angenommen, dass die verschiedenen Komponenten der Feststoff-Lumineszenzlebensdauern zumeist von unterschiedlichen Umgebungseffekten stammen^[39,184,187]. Die großen, langen Komponenten in Ethanol stammen daher von unvollständig gelösten Proben wegen der schlechteren Löslichkeit in Ethanol.

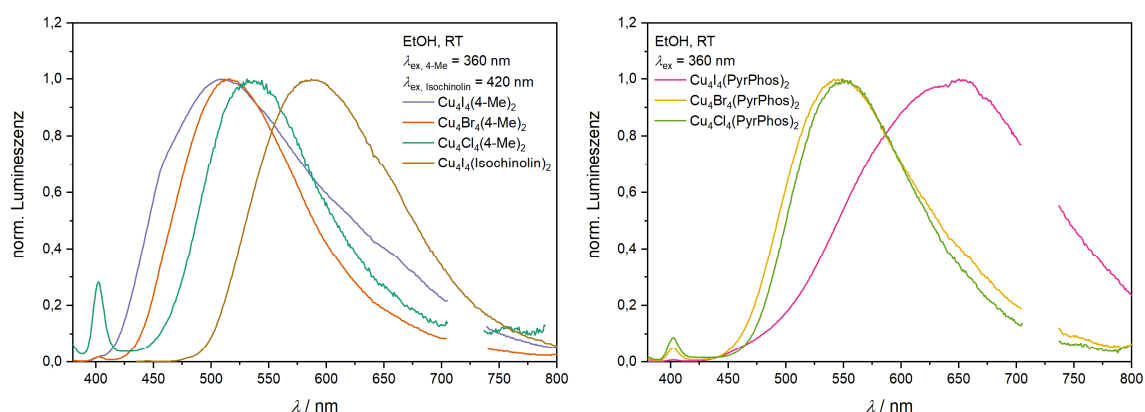


Abb. 4.16: Vergleich der Lumineszenzspektren in Lösung der Komplexe $\text{Cu}_4\text{X}_4(4\text{-Me})_2$ und $\text{Cu}_4\text{I}_4(\text{Isochinolin})_2$ (links) sowie der Komplexe $\text{Cu}_4\text{X}_4(\text{PyrPhos})_2$ (rechts) in Ethanol bei Raumtemperatur.

Die Emission in Dichlormethan (CH_2Cl_2) ist um 1000 bis 3700 cm^{-1} rotverschoben zur Emission im Feststoff und in Ethanol (Abb. 4.17). Dieser starke solvatochrome Effekt deutet auf eine deutliche Stabilisierung des angeregten Zustands durch die Lösungsmittelmoleküle hin. Die Emission in CH_2Cl_2 zeigt im Gegensatz zum Feststoff und Ethanol keine Blauverschiebung der Komplexe mit Methylgruppe im Vergleich zu den PyrPhos-Komplexen. Die Lebensdauer in CH_2Cl_2 (Tabelle 4.7) ist wesentlich kürzer (0.5-5,5 μs) als im Feststoff bzw. in Ethanol für die Iodid- und Chlorid-Komplexe.

Während in Ethanol aufgrund der geringen Löslichkeit vermutlich ungelöste Pulverprobe untersucht wurde, hat das Lösungsmittel CH_2Cl_2 einen starken Einfluss auf die Emission. Eine deutliche Wechselwirkung mit dem Lösungsmittel zeigt sich in der Rotverschiebung der Bande und der Verkürzung der Lebensdauer im Vergleich mit den Daten im Feststoff.

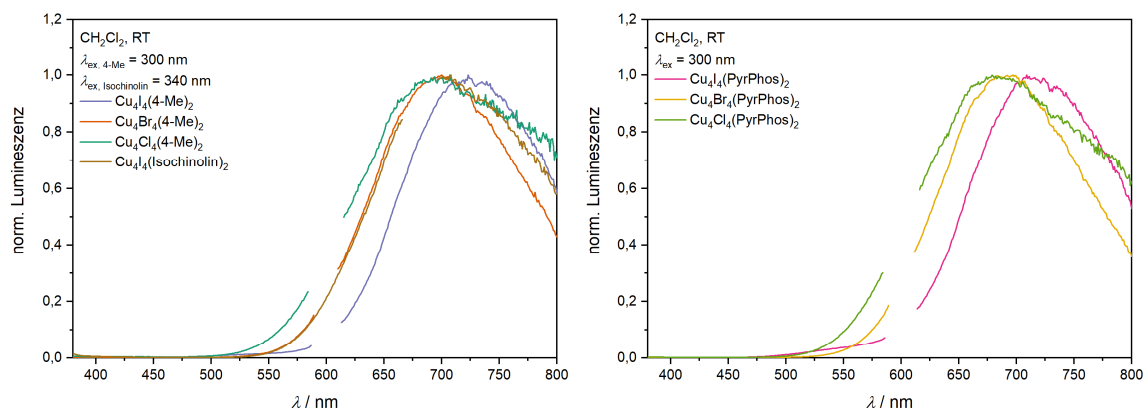


Abb. 4.17: Vergleich der Lumineszenzspektren in Lösung der Komplexe $\text{Cu}_4\text{X}_4(4\text{-Me})_2$ und $\text{Cu}_4\text{I}_4(\text{Isochinolin})_2$ (links) sowie der Komplexe $\text{Cu}_4\text{X}_4(\text{PyrPhos})_2$ (rechts) in Dichlormethan bei Raumtemperatur.

Tabelle 4.6: Lumineszenzlebensdauern aller Komplexe in Lösung (EtOH) bei Raumtemperatur (Fehler $\pm 10\%$).

EtOH	$\lambda_{\text{em}} / \text{nm}$	$\lambda_{\text{ex}} / \text{nm}$	$\tau_1 / \mu\text{s}$	$A_1 / \%$	$\tau_2 / \mu\text{s}$	$A_2 / \%$
$\text{Cu}_4\text{I}_4(4\text{-Me})_2$	484	345	8,3	100	/	/
$\text{Cu}_4\text{Br}_4(4\text{-Me})_2$	498	389	11	100	/	/
$\text{Cu}_4\text{Cl}_4(4\text{-Me})_2$	520	389	6,4	89	0,1	11
$\text{Cu}_4\text{I}_4(\text{PyrPhos})_2$	653	345	6,6	100	/	/
$\text{Cu}_4\text{Br}_4(\text{PyrPhos})_2$	527	345	13	95	2,1	5
$\text{Cu}_4\text{Cl}_4(\text{PyrPhos})_2$	532	389	21	100	/	/
$\text{Cu}_4\text{I}_4(\text{Isochinolin})_2$	562	389	11	91	2,0	9

Tabelle 4.7: Lumineszenzlebensdauern aller Komplexe in Lösung (CH_2Cl_2) bei Raumtemperatur (Fehler $\pm 10\%$).

CH_2Cl_2	$\lambda_{\text{em}} / \text{nm}$	$\lambda_{\text{ex}} / \text{nm}$	$\tau_1 / \mu\text{s}$	$A_1 / \%$	$\tau_2 / \mu\text{s}$	$A_2 / \%$
$\text{Cu}_4\text{I}_4(4\text{-Me})_2$	680	313	3,9	100	/	/
$\text{Cu}_4\text{Br}_4(4\text{-Me})_2$	665	313	12	100	/	/
$\text{Cu}_4\text{Cl}_4(4\text{-Me})_2$	660	313	5,7	96	0,4	4
$\text{Cu}_4\text{I}_4(\text{PyrPhos})_2$	675	313	2,4	100	/	/
$\text{Cu}_4\text{Br}_4(\text{PyrPhos})_2$	663	313	11	100	/	/
$\text{Cu}_4\text{Cl}_4(\text{PyrPhos})_2$	660	345	3,8	97	0,1	3
$\text{Cu}_4\text{I}_4(\text{Isochinolin})_2$	640	345	0,5	100	/	/

4.2.3.5 Lumineszenz der kristallinen Proben von $\text{Cu}_4\text{I}_4(\text{Me-Isochinolin})_2$ und $\text{Cu}_2\text{I}_2(\text{Me-Isochinolin})_2(\text{CH}_3\text{CN})_2$

Ebenfalls mit Lumineszenzspektroskopie untersucht wurde der $\text{Cu}_4\text{I}_4(\text{Me-Isochinolin})_2$. Dieser Komplex lag nur als kristalline Probe in einem Schutzöl vor. Daher ist ein absoluter Vergleich mit dem Isochinolin-Komplex nicht möglich. Um die Kristalle untersuchen zu können, wurden sie wie Pulverproben zwischen zwei CaF_2 -Fenstern eingespannt und in den Kryostaten eingebaut. Die Emission des Komplexes ist bei 5 K sehr breit mit mehreren Maxima zwischen 538 und 631 nm (Abb. 4.18, links). Das Spektrum ist also gut schwingungsaufgelöst. Bei höheren Temperaturen ändert sich das Intensitätsmuster und die Schwingungsauflösung nimmt ab bis bei 290 K nur noch eine breite Emissionsbande zu sehen ist. Kristallisiert man den Komplex nicht in CH_2Cl_2 , sondern in koordinierendem CH_3CN , bildet sich stattdessen ein zweikerniger Komplex der Form $\text{Cu}_2\text{I}_2(\text{Me-Isochinolin})_2(\text{CH}_3\text{CN})_2$ aus. Die Kristallisation wurde wie auch die Synthesen von Jasmin Busch aus dem Arbeitskreis Bräse am KIT durchgeführt. Auch diese Kristalle zeigen eine sehr gute Schwingungsauflösung bei tiefer Temperatur, die zu höheren Temperaturen abnimmt (Abb. 4.18, rechts). Im Vergleich zum vierkernigen Komplex verschiebt sich das Emissionsspektrum von 5 K zu 290 K stärker, aber das temperaturabhängige Verhalten ist ähnlich. Die Lumineszenzlebensdauern beider Komplexe (Tabelle 4.8) sind sehr lang und liegen bei tiefer Temperatur im Millisekundenbereich. Bei 290 K sind sie wesentlich kürzer mit ca. 15 bzw. 10 μs für den Vierkerner und den Zweikerner. Die Lebensdauer nimmt von 290 K an zunächst langsam und ab 130 K schnell zu (Abb. 4.19). Der Me-Isochinolin-Komplex unterscheidet sich daher in seinem temperaturabhängigen Verhalten deutlich von dem der anderen Vierkerner. Jedoch ist ein absoluter Vergleich aufgrund der unterschiedlichen Medien (Kristalle des Me-Isochinolin-Komplexes, KBr-Pressling oder Pulver für die anderen Vierkerner) nicht möglich.

Der vierkernige und der zweikernige Kupferkomplex mit dem methylierten Isochinolin-Liganden zeigen ein sehr ähnliches temperaturabhängiges Luminezenzverhalten. Die Emissionsspektren sind deutlich schwingungsaufgelöst und die Lebensdauern sehr lang im Vergleich mit dem unmethylierten Komplex. Auch zeigen die methylierten Isochinolin-Komplexe im Gegensatz zum unmethylierten Komplex keine Anzeichen für TADF bei 290 K.

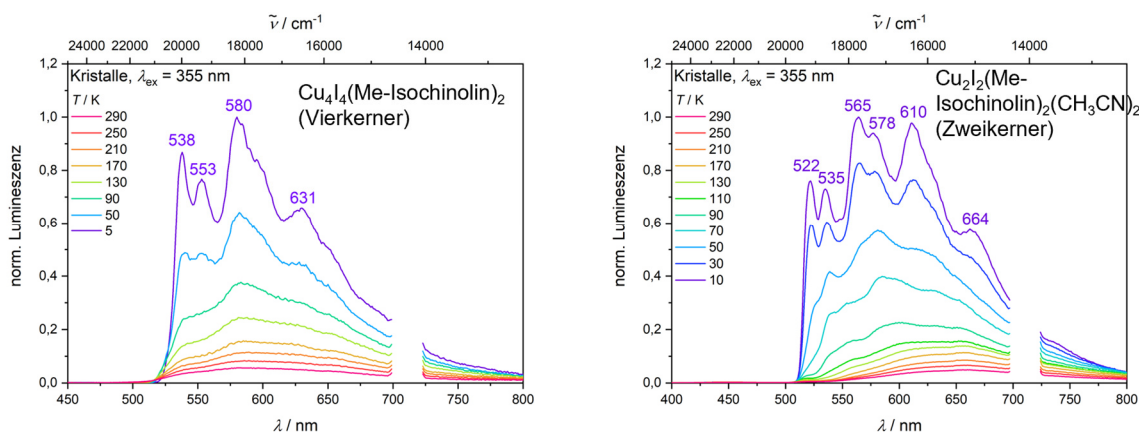
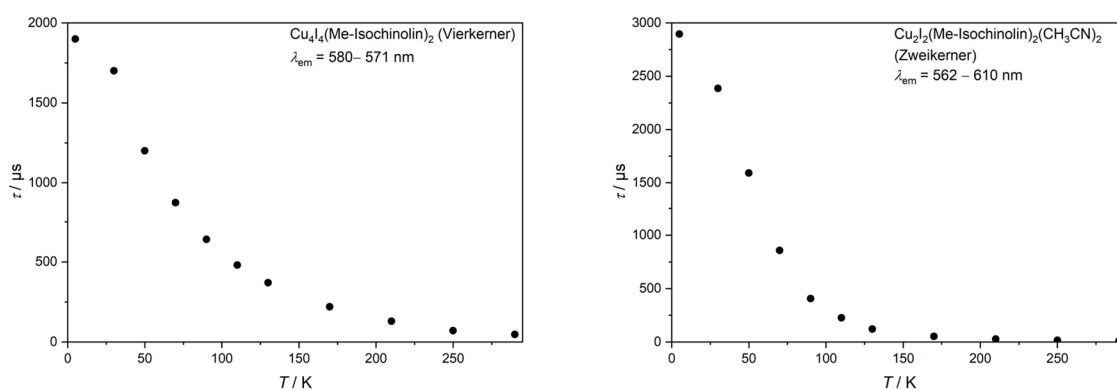


Abb. 4.18: Temperatur-abhängige Lumineszenzspektren des Me-Isochinolin-Vierkerners (links) und des Zweikerners (rechts) in kristalliner Form.

 Tabelle 4.8: Lumineszenzlebensdauern des Me-Isochinolin-Vierkerners und -Zweikerners im Kristall bei 5 und 290 K (Fehler $\pm 10\%$).

Kristalle	T / K	λ_{em} / nm	λ_{ex} / nm	τ_1 / μ s	A_1 / %	τ_2 / μ s	A_2 / %	τ_2 / μ s	A_2 / %	τ_{av} / μ s
Cu₄I₄(Me-Isochinolin)₂	290	571	390	120	31	30	30	5,4	40	48
	5	580	390	2100	92	470	8	/	/	1900
Cu₂I₂(Me-Isochinolin)₂(CH₃CN)₂	290	610	390	40	7	8,9	79	6,0	14	11
	5	562	390	3000	92	1300	8	/	/	2900


 Abb. 4.19: Temperatur-Verlauf der amplitudengewichteten Lebensdauern des Me-Isochinolin-Vierkerners (links) und des Zweikerners (rechts) in kristalliner Form über einen Temperaturbereich von 5 – 290 K (Fehler $\pm 10\%$).

4.2.3.6 Time-resolved Emission Spectroscopy (TRES) des Cu₄I₄(PyrPhos)₂

Die TRES-Daten zeigen den zeitabhängigen Verlauf der Emissionsspektren des Cu₄I₄(PyrPhos)₂-Komplexes. Sie wurden bei 60 und 70 K an der Pulverprobe aufgenommen, da bei diesen Temperaturen beide Emissionsbanden deutlich separiert erkennbar sind und

sich die Intensitätsverhältnisse beider Banden in diesem Temperaturbereich gerade umkehren. Am KBr-Pressling wurden die TRES bei 70 und 90 K aufgenommen, da hierbei die Verbreiterung der Emissionsbande auf die Besetzung beider Zustände schließen lässt.

Die TRES -Spektren im KBr-Pressling (Abb. 4.20, links) zeigen direkt nach der Anregung die gleiche breite, nicht aufgelöste Emissionsbande wie die statische Emissionsspektroskopie. Im zeitlichen Verlauf bei 70 K erkennt man jedoch, dass die Intensität der blauen Schulter (~ 510 nm) der breiten Bande schneller abnimmt als der rotete Teil der Bande. Auch bei 90 K sieht man einen Trend zu kürzeren Lebensdauern der blauen Flanke (~ 550 nm). Die verschiedenen Lebensdauern in einer Bande müssen von zwei verschiedenen lumineszenten Zuständen stammen, deren Emission zu einer Bande überlagert.

Im Pulver zeigen sich wie auch in den statischen Spektren in den TRES-Spektren (Abb. 4.20, rechts) deutlich separierte Banden. Jedoch ändert sich das Intensitätsverhältnis der beiden Banden über die Zeit. Direkt nach der Anregung innerhalb der gewählten Zeitauflösung von $1 \mu\text{s}$ ist die blaue wesentlich intensiver als die rote Bande. Dies ist für sowohl 60 K als auch 70 K gültig, obwohl die Intensitätsverhältnisse bei der statischen Emission von intensiverer roten Bande bei 70 K zu intensiverer blauen Bande bei 60 K tauschen. Betrachtet man die Summe der gemessenen Emission über den gesamten Messbereich von $340 \mu\text{s}$ an den einzelnen Emissionswellenlängen, ergibt sich ein ähnliches Intensitätsmuster wie bei der statischen Emission, da statisch immer der gesamte Zeitbereich aufsummiert im Spektrum zu sehen ist. Der rote Zustand wird erst mit der Zeit besetzt, während die Emission des blauen Zustands schnell abnimmt. Das Intensitätsmaximum der roten Bande wird nach ca. $4,4 \mu\text{s}$ erreicht, wenn die Intensität der blauen Bande schon um die Hälfte abgenommen hat. Mit tieferer Temperatur erfolgt die Besetzung des zweiten Zustands langsamer, sodass das Intensitätsmaximum der roten Bande bei 60 K erst nach etwa $7 \mu\text{s}$ erreicht wird. Somit wird die Barriere für die Besetzung des niedrigeren Zustands mit zunehmender Temperatur schneller überwunden.

Bei 70 K ist die Lebensdauer des höheren Zustands noch etwas länger als die des niedrigeren Zustands, bei 60 K ist auch in der TRES-Matrix die längere Lebensdauer des roten Zustands bereits erkennbar. Aus den TCSPC-Daten ergeben die gemittelten Lebensdauern $18 \mu\text{s}$ für den blauer emittierenden Zustand und 16 bzw. $20 \mu\text{s}$ für den roter emittierenden Zustand bei 70 bzw. 60 K.

Die TRES-Daten zeigen deutlich die thermische, verzögerte Population des energetisch niedrigeren phosphoreszenten Triplett-Zustands. Der elektronisch angeregte Komplex wird

zunächst in einem höherenergetischen Triplett-Zustand gefangen und kann daraus bei ausreichender thermischer Energie die Barriere in den niedrigeren Zustand überwinden.

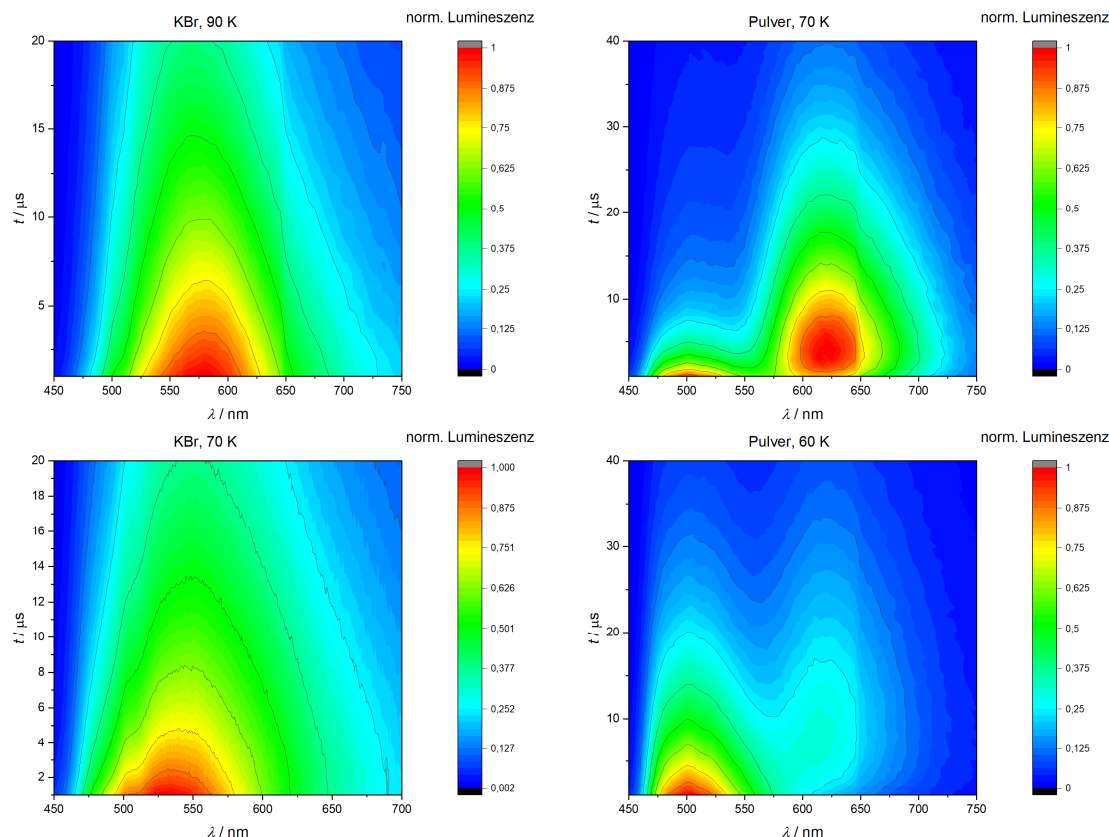


Abb. 4.20: TRES-Spektren des $\text{Cu}_4\text{I}_4(\text{PyrPhos})_2$ im KBr-Pressling bei 90 K (links oben) und 70 K (links unten) sowie im Pulver bei 70 K (rechts oben) und 60 K (rechts unten) nach Anregung mit 390 nm (SpectralLED). Auf der x-Achse ist jeweils die Emissionswellenlänge aufgetragen, auf der y-Achse die Zeit. Die Intensität ist durch die Farbskala normiert angegeben, wobei rot am intensivsten und blau am wenigsten intensiv anzeigt.

4.2.3.7 Statische und Step-scan-FTIR-Spektroskopie

Die FTIR-Untersuchungen sowohl des Grundzustands als auch, mit der Step-scan-Technik, des elektronisch angeregten Zustands wurden an KBr-Presslingen der Proben durchgeführt. Die Proben wurden mit einem Nd:YAG-Laser mit einer Wellenlänge von 355 nm angeregt (siehe Kapitel 3). Zur Zuordnung der Geometrien der Zustände wurden DFT-Rechnungen durchgeführt. Dabei wurden die niedrigsten Triplett-Zustände bei verschiedenen Geometrien berechnet. Singulett-Zustände oder höhere Triplett-Zustände werden aufgrund der Zeitauflösung von 1-2 μs für die Spektren der angeregten Zustände nicht beobachtet, wobei aufgrund der Lumineszenz-Daten auch die Besetzung des S_1 -Zustandes nicht zu erwarten ist. Für die Grund- und Triplett-Zustände lassen sich die gefundenen Minimumstrukturen drei verschiedenen Geometriemotiven zuordnen. Die Geometriemuster richten sich nach der Anordnung der vier Kupferzentren (Abb. 4.21) und gelten daher für alle untersuchten Komplexe gleichermaßen. Die Benennung der Strukturen ist identisch mit den Geometrien in

der Veröffentlichung der 6-Me-Vierkerner^[53]. Die Kristallstrukturen der untersuchten Vierkerner, soweit vorhanden ($\text{Cu}_4\text{Br}_4(4\text{-Me})_2$, $\text{Cu}_4\text{Cl}_4(4\text{-Me})_2$), bilden eine planare Raute der vier Kupferzentren. Diese Struktur wird aufgrund ihrer Geometrie C_2 -Struktur genannt. In Anlehnung an die open und closed butterfly (offener und geschlossener Schmetterling) Strukturen wird die Struktur mit ungefähr tetraedrischer Anordnung der Kupferzentren hier closed butterfly genannt. Die open butterfly Struktur beschreibt eine Struktur zwischen C_2 und closed butterfly, wobei die phosphorgebundenen Kupferzentren den Körper des Schmetterlings darstellen und die stickstoffgebundenen die Flügelspitzen. Bei der Zuordnung von open und closed butterfly wird der Winkel zwischen den Flügelebenen des „Schmetterlings“ betrachtet. Öffnungswinkel von über 90° werden als open butterfly-Strukturen bezeichnet, kleinere, wie bei der Tetraeder-Struktur, als closed butterfly (Abb. 4.21). Die Spindichte des niedrigsten Triplett-Zustands ist je nach Geometrie unterschiedlich lokalisiert (Abb. 4.22). Für die open butterfly Struktur ist die Spindichte auf dem Cu_4X_4 -Zentrum lokalisiert. Damit entspricht dieser einem clusterzentrierten Triplett-Zustand (engl. cluster centred (CC)) (^3CC). Die Spindichte der anderen beiden Geometrien entspricht einem Triplett-MLCT-Zustand ($^3\text{MLCT}$), wobei die Elektronendichte meist nur auf einen Liganden verschoben wird.

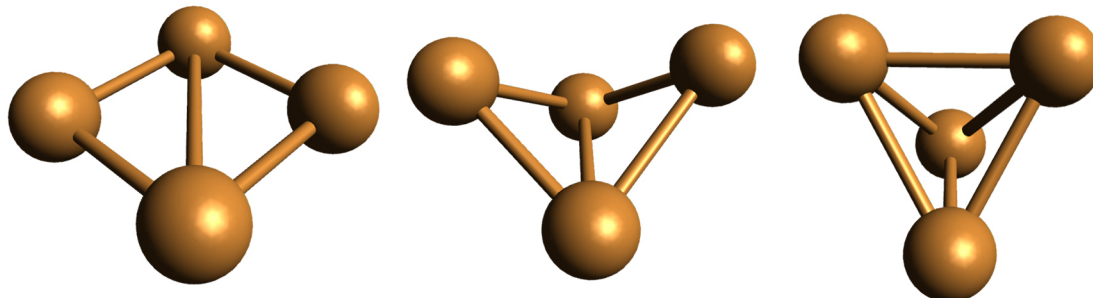


Abb. 4.21: Darstellung der Anordnung der vier Kupferzentren in C_2 (links), open butterfly (Mitte) und closed butterfly (rechts) Struktur am Beispiel des $\text{Cu}_4\text{Br}_4(\text{PyrPhos})_2$.

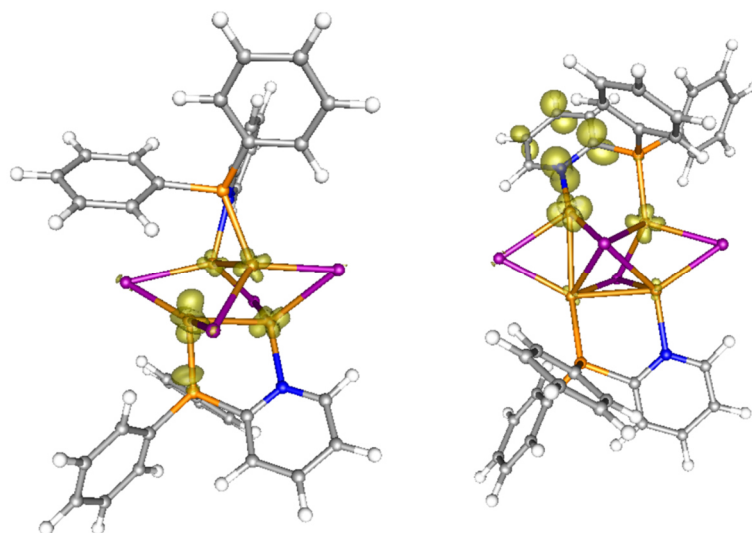


Abb. 4.22: Spindichte des 3CC -Zustands mit closed butterfly Struktur (links) und des 3MLCT -Zustands in der open butterfly Geometrie (rechts) des $Cu_4I_4(PyrPhos)_2$ -Komplexes. Die Spindichte ist für den jeweils niedrigsten Triplett-Zustand mit dieser Geometrie berechnet (UDFT/B3LYP/def2-TZVP, Isovalue 0,01).

Für Lebensdauern konnten aus den Step-scan-Daten für diese Komplexe keine zuverlässigen Daten erhalten werden, da die Spektren starken Offset-Schwankungen in Größenordnung der eigentlichen Banden unterlagen. Jedoch können die Ergebnisse der Lebensdauern aus der Lumineszenzspektroskopie herangezogen werden, da die gleichen Zustände untersucht werden.

Da die Untersuchungen sowohl bei 290 K als auch bei 20 K durchgeführt wurden, können auch thermochrome Komplexe bei den jeweiligen Temperaturen charakterisiert werden.

$Cu_4Br_4(4-Me)_2$ und $Cu_4Cl_4(4-Me)_2$

Die Daten des $Cu_4I_4(4-Me)_2$ sind bereits veröffentlicht und werden hier zum Vergleich innerhalb der Halogenidreihe der Komplexe mit 4-Methylgruppe am Pyridinring herangezogen. Der Grundzustand aller drei Komplexe der Halogenidreihe ist identisch (Abb. 4.23). Außerdem ist der Grundzustand temperaturunabhängig und somit bei 20 K und 290 K identisch (Abb. 4.23).

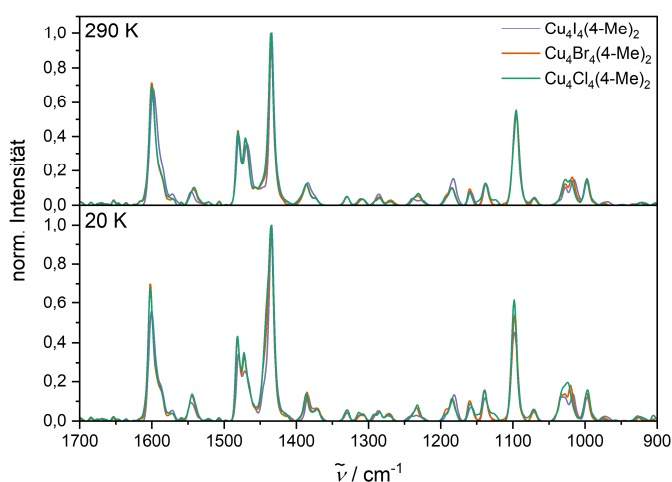


Abb. 4.23: FTIR-Grundzustandsspektren der Komplexe $\text{Cu}_4\text{X}_4(4\text{-Me})_2$ bei 290 (oben) und 20 K (unten).

Im Vergleich zu den quantenchemischen DFT-Rechnungen kann der Grundzustand für $\text{Cu}_4\text{Br}_4(4\text{-Me})_2$ und $\text{Cu}_4\text{Cl}_4(4\text{-Me})_2$ allerdings nicht eindeutig zugeordnet werden, da alle berechneten Geometrien das gleiche Schwingungsspektrum ergeben (Abb. 4.24). Energetisch liegt der Grundzustand in closed butterfly Geometrie um ca. 10 kJ mol^{-1} niedriger als der nächstgünstigste Zustand (open butterfly), und ist somit am wahrscheinlichsten besetzt. Die anderen Geometrien können nicht ausgeschlossen werden, da der Komplex einerseits durch hohe Barrieren zwischen den verschiedenen Grundzuständen in einem der höherliegenden Zustände gefangen sein könnte, andererseits eine Boltzmann-Verteilung der Isomerenbesetzung angenommen werden darf.

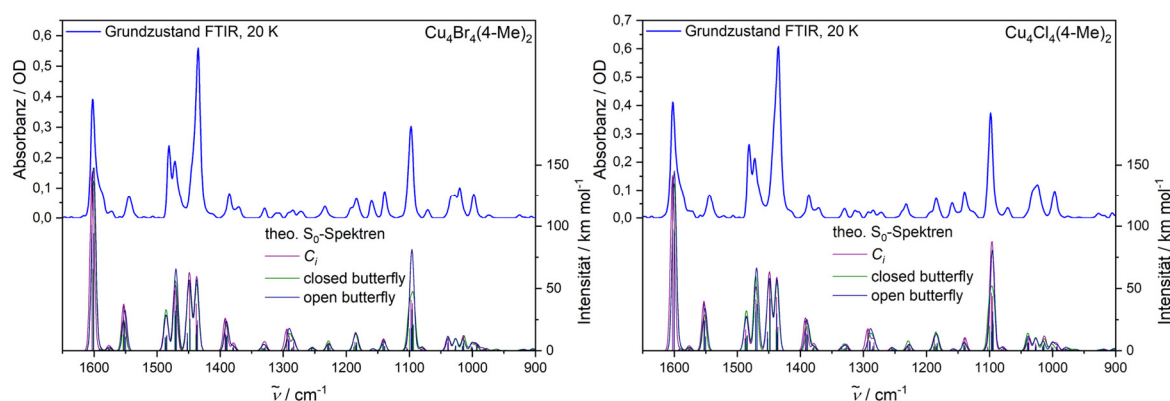


Abb. 4.24: Vergleich des experimentellen Spektrums des Grundzustands bei 20 K mit den theoretischen Spektren des S_0 -Zustands in C_i , closed butterfly und open butterfly Geometrie für die Komplexe $\text{Cu}_4\text{Br}_4(4\text{-Me})_2$ (links) und $\text{Cu}_4\text{Cl}_4(4\text{-Me})_2$ (rechts). (DFT/B3LYP/def2-TZVP, Faltung mit Gaußkurven, FWHM = 8 cm^{-1}).

Erst bei der Anregung treten erkennbare Unterschiede zwischen den drei Komplexen der Halogenid-Reihe auf. Der Bromid- und der Chlorid-Komplex zeigen auch im angeregten

Zustand (Mittlung der ersten 2 μ s nach dem Anregungspuls, Step-scan-Spektrum + 1,5 % Grundzustand (GZ)) bei 20 K und 290 K nahezu identische Spektren. Im Vergleich zu dem Iodid-Komplex zeigt das Spektrum einige Banden (ca. 1525, 1340, 1280, 1220 und 1070 cm^{-1}) mehr oder sie sind wesentlich ausgeprägter (Abb. 4.25). Der Iodid-Komplex wurde aufgrund des Ausbleibens mehrerer Banden im experimentellen Spektrum, welche im theoretischen Spektrum der C_2 -Struktur vorkommen, der closed butterfly Struktur zugeordnet, was einem clusterzentrierten (engl. cluster centred (CC)) Triplett-Zustand entspricht. Umgekehrt stimmen die beiden neu untersuchten Komplexe durch das Vorhandensein zusätzlicher Banden nicht mit der closed butterfly Struktur überein, während die C_2 - und die open butterfly-Strukturen das gemessene Spektrum des angeregten Zustands sehr gut beschreiben (Abb. 4.26 und Abb. 4.27, rechts). Die zusätzlichen Banden können im Vergleich mit den quantenchemischen Rechnungen Schwingungen auf dem am MLCT-Zustand beteiligten Pyridinring zugeordnet werden. Durch die höhere Ladung auf dem Ring werden die Schwingungen gegenüber dem Grundzustand verschoben. Da die Elektronendichte nur auf einem Liganden erhöht wird, bleiben die Schwingungen des anderen Liganden erhalten. Damit verringert sich die Symmetrie und es kommt zu zusätzlichen Banden. Beide möglichen Strukturen im Triplett-Zustand liegen energetisch ca. 40 kJ mol^{-1} höher als der closed butterfly Triplett-Zustand. Eine genaue Zuordnung ist daher für diese Komplexe auch im angeregten Zustand nicht möglich. Die Spektren der angeregten Zustände sind bei 20 K und 290 K (Mittlung über die ersten 1 bzw. 2 μ s nach dem Anregungspuls, Step-scan-Spektrum + 2,0 bzw. 1,5 % Grundzustand (GZ), jeweils Br bzw. Cl) bis auf leichte Rotverschiebungen einiger Banden gleich (Abb. 4.26 und Abb. 4.27, links). Die leichten Verschiebungen kommen von kleinen strukturellen Veränderungen durch die höhere Temperatur und der Kopplung mit thermisch besetzten niederfrequenten Moden zustande. Im Einklang mit den Lumineszenzdaten zeigt sich keine Thermochromie für diese Komplexreihe.

Der Chlorid- und der Bromid-Komplex mit 4-Me-Liganden sind somit in einem $^3\text{MLCT}$ -Zustand mit C_2 - oder open butterfly Struktur gefangen und können den niedrigeren ^3CC -Zustand in closed butterfly Struktur nicht erreichen. Das Halogenid hat keinen Einfluss auf die im untersuchten Frequenzbereich liegenden Schwingungen.

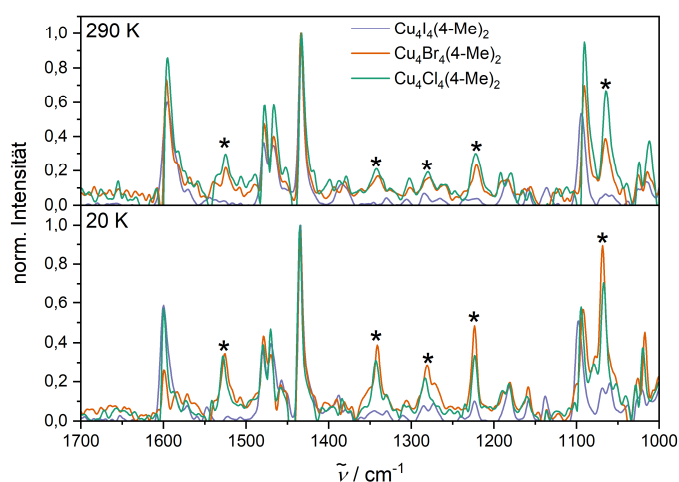


Abb. 4.25: FTIR-Spektren des angeregten Zustands ($\lambda_{\text{ex}} = 355 \text{ nm}$) der Komplexe $\text{Cu}_4\text{X}_4(4\text{-Me})_2$ bei 290 (oben) und 20 K (unten). Die Sternchen markieren Banden, in denen sich die Spektren der Komplexe untereinander unterscheiden.

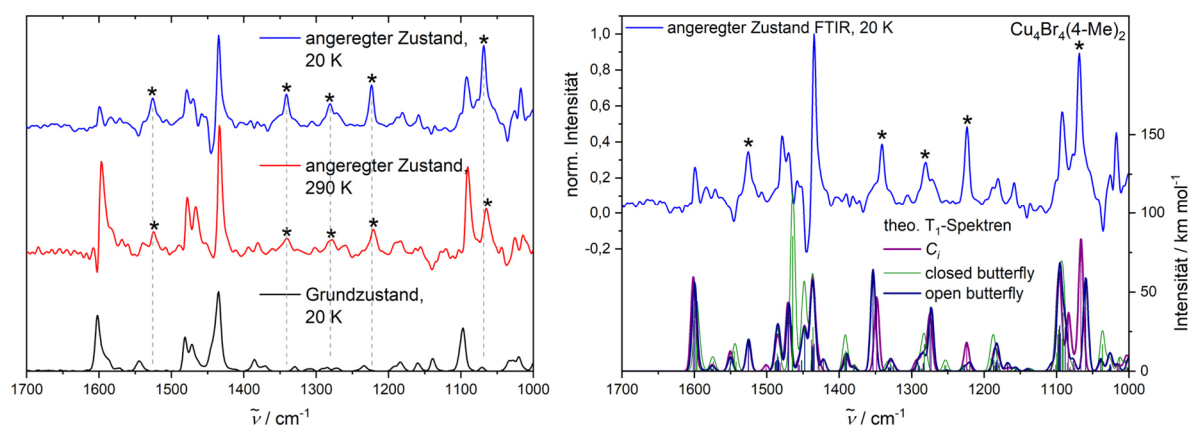


Abb. 4.26: Links: Vergleich des FTIR-Spektrums des Grundzustands mit den Spektren des angeregten Zustands bei 20 K und 290 K des $\text{Cu}_4\text{Br}_4(4\text{-Me})_2$ -Komplexes. Rechts: Vergleich des experimentellen Spektrums des angeregten Zustands bei 20 K mit den theoretischen Spektren des T_1 -Zustands in C_i , closed butterfly und open butterfly Geometrie. (UDFT/B3LYP/def2-TZVP, Faltung mit Gaußkurven, FWHM = 8 cm^{-1}). Mit Sternchen markierte Banden sind spezifisch für den jeweiligen angeregten Zustand.

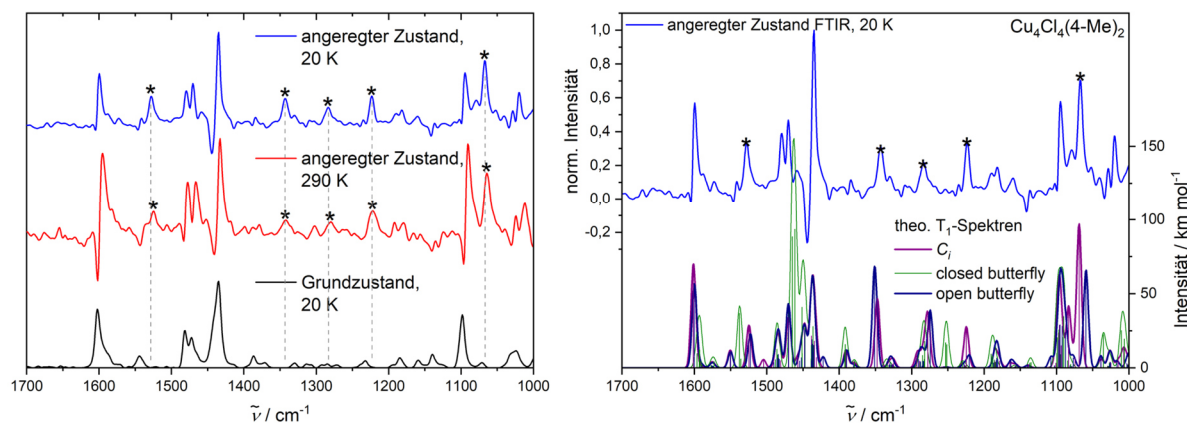


Abb. 4.27: Links: Vergleich des FTIR-Spektrums des Grundzustands mit den Spektren des angeregten Zustands bei 20 K und 290 K des $\text{Cu}_4\text{Cl}_4(4\text{-Me})_2$ -Komplexes. Rechts: Vergleich des experimentellen Spektrums des angeregten Zustands bei 20 K mit den theoretischen Spektren des T_1 -Zustands in C_1 , closed butterfly und open butterfly Geometrie. (UDFT/B3LYP/def2-TZVP, Faltung mit Gaußkurven, FWHM = 8 cm^{-1}). Mit Sternchen markierte Banden sind spezifisch für den jeweiligen angeregten Zustand.

Halogenidreihe $\text{Cu}_4\text{X}_4(\text{PyrPhos})_2$

Die Halogenidreihe der vierkernigen Komplexe mit dem PyrPhos-Liganden wurde ebenfalls mittels FTIR-Spektroskopie untersucht. Das Grundzustandsspektrum ist auch für diese Komplexreihe temperaturunabhängig (Abb. 4.28, links oben). Untereinander verglichen zeigt sich, dass die Grundzustandsspektren der drei Komplexe nur sehr kleine Abweichungen voneinander in der Intensität der Banden aufweisen. Die Halogenide haben also auch hier keinen signifikanten Einfluss auf die Schwingungen im Fingerprintbereich. Der Vergleich der theoretischen Spektren zeigt, dass die verschiedenen Geometrien (C_i , open und closed butterfly) keine Unterschiede im Fingerprintbereich erkennen lassen, sodass eine Zuordnung einer bestimmten Geometrie im Grundzustand nicht möglich ist (Abb. 4.28). Wie auch bei den 4-Me-Komplexen ist energetisch die closed butterfly Struktur für den Bromid- und den Chlorid-Komplex um ca. 10 kJ mol^{-1} bevorzugt. Für den Iodid-Komplex liegen alle drei Grundzustände energetisch im Bereich der Fehlergenauigkeit der DFT-Rechnungen. Alle theoretischen Spektren haben eine gute Übereinstimmung mit den experimentellen Daten.

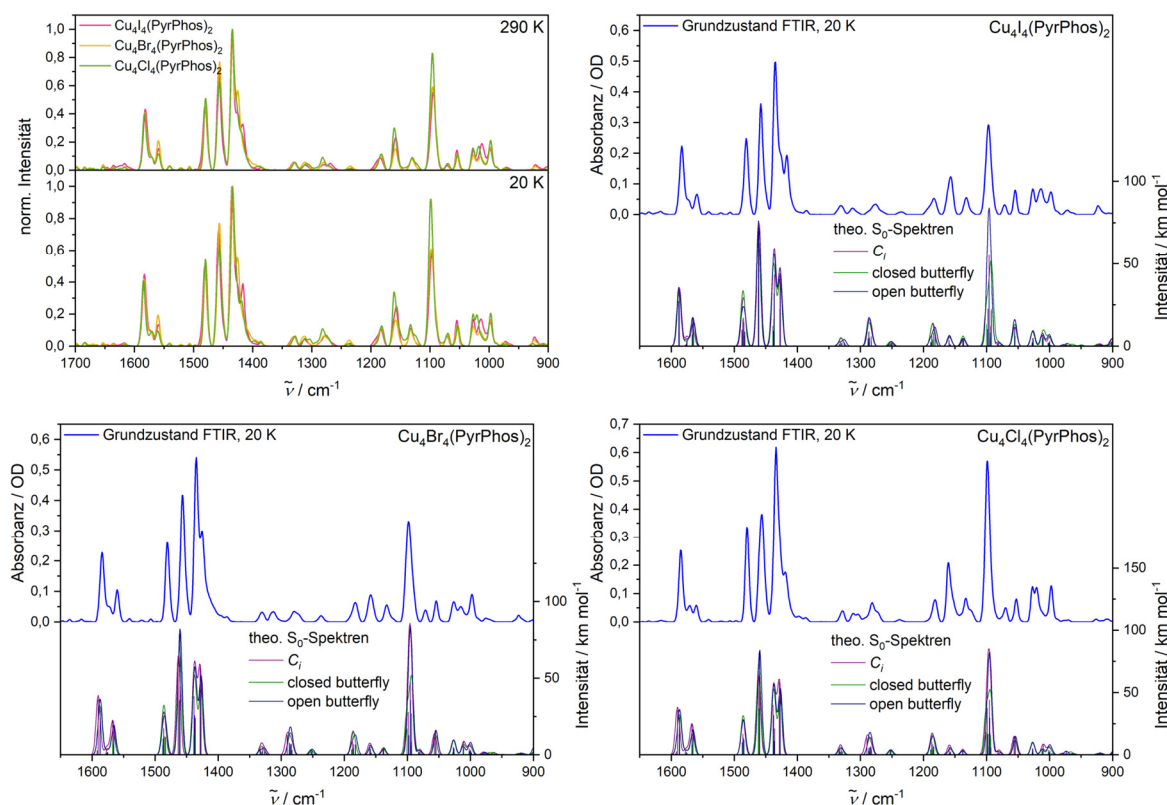


Abb. 4.28: FTIR-Grundzustandsspektren aller $\text{Cu}_4\text{X}_4(\text{PyrPhos})_2$ -Komplexe bei 290 und 20 K (oben links) und Vergleich des experimentellen Spektrums des Grundzustands bei 20 K mit den theoretischen Spektren des S_0 -Zustands in C_7 , closed butterfly und open butterfly Geometrie für die Komplexe $\text{Cu}_4\text{I}_4(\text{PyrPhos})_2$ (oben rechts), $\text{Cu}_4\text{Br}_4(\text{PyrPhos})_2$ (unten links) und $\text{Cu}_4\text{Cl}_4(\text{PyrPhos})_2$ (unten rechts). (DFT/B3LYP/def2-TZVP, Faltung mit Gaußkurven, FWHM = 8 cm^{-1}).

Die Spektren des angeregten Zustands bei 20 K wurden aus den Step-scan-Spektren, über die ersten 2 μs nach der Laseranregung gemittelt, mit Addition von 2,0 (I), 1,0 (Br) und 0,8 % (Cl) des Grundzustands berechnet. Im Vergleich mit dem Grundzustand sind drei zusätzlich Banden im Spektrum der angeregten Zustände zu erkennen (Abb. 4.29 und Abb. 4.31, links). Die drei Banden liegen bei ca. 1280, 1355 und 1525 cm^{-1} , wobei letztere für den Iodid-Komplex nicht aufgelöst ist. Der Vergleich mit den theoretischen Spektren ergibt eine sehr gute Übereinstimmung mit dem MLCT-Triplett-Zustand der open butterfly Geometrie (Abb. 4.29 und Abb. 4.31, rechts). Das Spektrum des angeregten Zustands des Chlorid-Komplexes wird ebenfalls von der berechneten C_7 -Struktur eines $^3\text{MLCT}$ -Zustands gut beschrieben (Abb. 4.31). Alle für den angeregten Zustand spezifischen Banden stammen von C-C-Streck- und C-H-Biegeschwingungen im Pyridinring des Liganden, welcher am MLCT-Übergang beteiligt ist, und sind daher gegenüber dem Grundzustand stark verschoben.

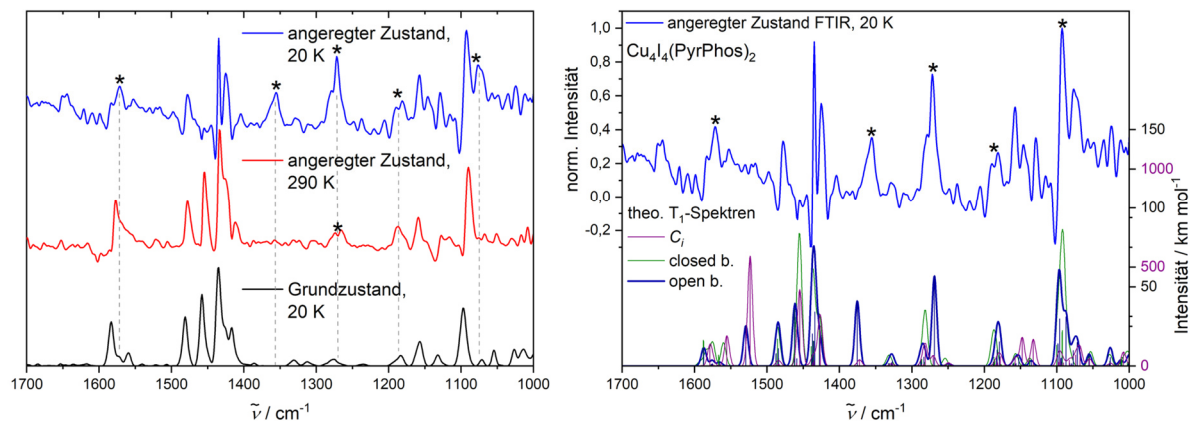


Abb. 4.29: Links: Vergleich des FTIR-Spektrums des Grundzustands mit den Spektren des angeregten Zustands bei 20 K und 290 K des $\text{Cu}_4\text{I}_4(\text{PyrPhos})_2$. Rechts: Vergleich des experimentellen Spektrums des angeregten Zustands bei 20 K mit den theoretischen Spektren des T_1 -Zustands in C_2 , closed butterfly und open butterfly Geometrie. (UDFT/B3LYP/def2-TZVP, Faltung mit Gaußkurven, FWHM = 8 cm^{-1}). Mit Sternchen markierte Banden sind spezifisch für den jeweiligen angeregten Zustand.

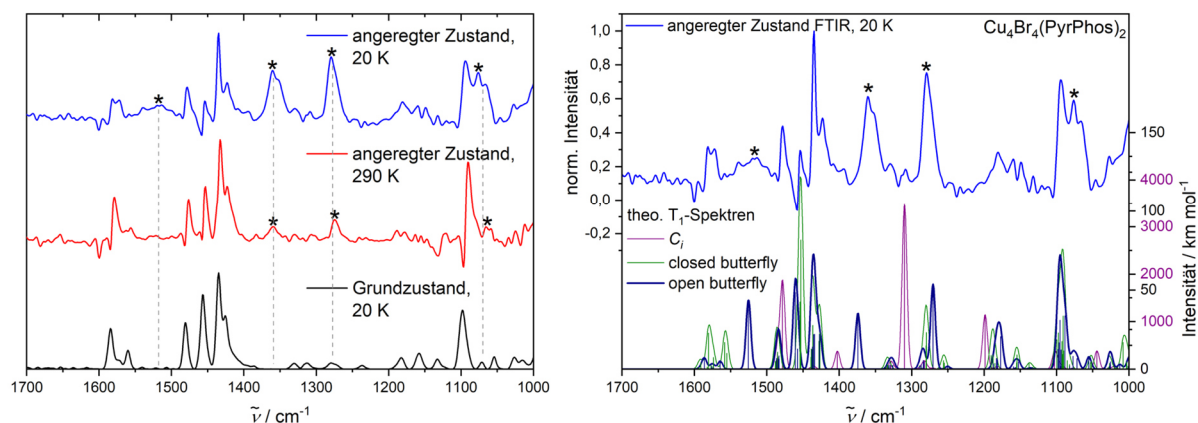


Abb. 4.30: Links: Vergleich des FTIR-Spektrums des Grundzustands mit den Spektren des angeregten Zustands bei 20 K und 290 K des $\text{Cu}_4\text{Br}_4(\text{PyrPhos})_2$. Rechts: Vergleich des experimentellen Spektrums des angeregten Zustands bei 20 K mit den theoretischen Spektren des T_1 -Zustands in C_2 , closed butterfly und open butterfly Geometrie. (UDFT/B3LYP/def2-TZVP, Faltung mit Gaußkurven, FWHM = 8 cm^{-1}). Mit Sternchen markierte Banden sind spezifisch für den jeweiligen angeregten Zustand.

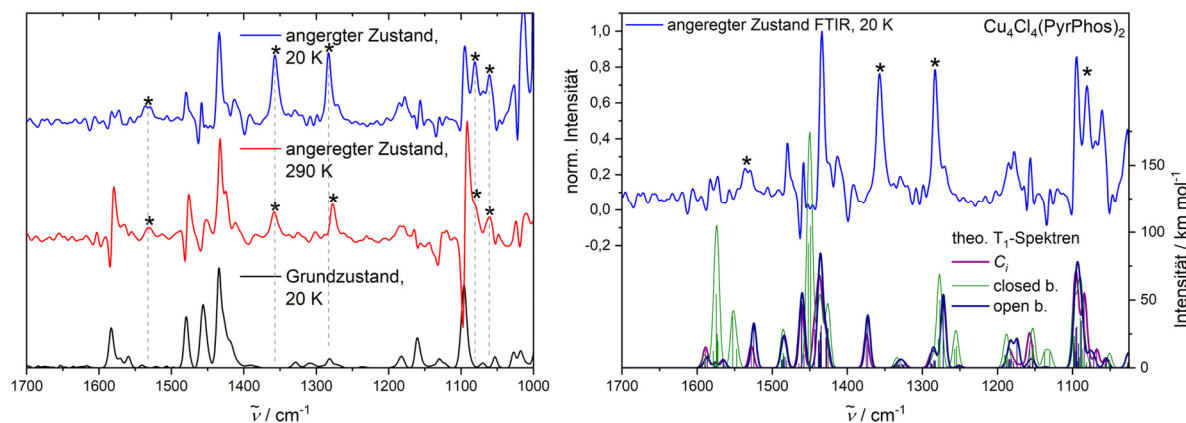


Abb. 4.31: Links: Vergleich des FTIR-Spektrums des Grundzustands mit den Spektren des angeregten Zustands bei 20 K und 290 K des $\text{Cu}_4\text{Cl}_4(\text{PyrPhos})_2$. Rechts: Vergleich des experimentellen Spektrums des angeregten Zustands bei 20 K mit den theoretischen Spektren des T_1 -Zustands in C_1 , closed butterfly und open butterfly Geometrie. (UDFT/B3LYP/def2-TZVP, Faltung mit Gaußkurven, FWHM = 8 cm^{-1}). Mit Sternchen markierte Banden sind spezifisch für den jeweiligen angeregten Zustand.

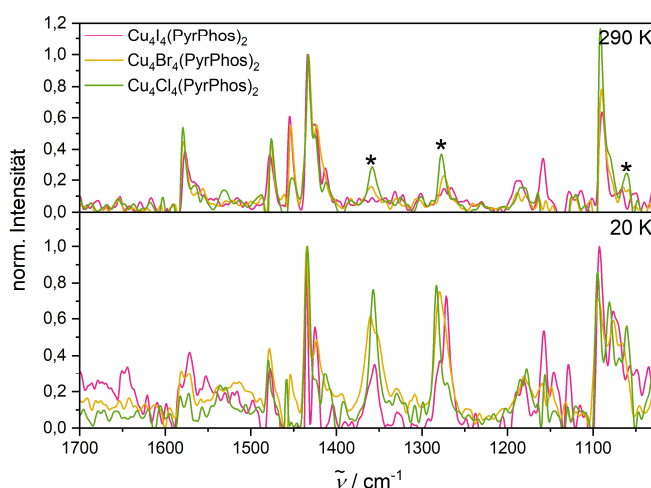


Abb. 4.32: FTIR-Spektren des angeregten Zustands ($\lambda_{\text{ex}} = 355 \text{ nm}$) der Komplexe $\text{Cu}_4\text{X}_4(\text{PyrPhos})_2$ bei 290 (oben) und 20 K (unten). Die Sternchen markieren Banden, in denen sich die Spektren der Komplexe untereinander unterscheiden.

Die Spektren des angeregten Zustands bei 290 K (Mittlung der ersten 2 μs nach Anregung, Step-scan + 1,0 (Br) bzw. 1,5 % (Cl)) unterscheiden sich für die Komplexe $\text{Cu}_4\text{Br}_4(\text{PyrPhos})_2$ und $\text{Cu}_4\text{Cl}_4(\text{PyrPhos})_2$ gegenüber denen bei 20 K lediglich durch schwache Rotverschiebung einiger Banden und eine etwas schwächere Ausprägung der spezifischen Banden (Abb. 4.30 und Abb. 4.31, links). Somit ist anzunehmen, dass der gleiche Zustand wie auch bei 20 K besetzt wird. Diese Ergebnisse decken sich mit denen der Lumineszenzspektroskopie.

Das Spektrum des angeregten Zustands des $\text{Cu}_4\text{I}_4(\text{PyrPhos})_2$ bei 290 K unterscheidet sich dagegen deutlich von dem bei 20 K und gleichzeitig von denen der anderen beiden Komplexe (Abb. 4.32). Die charakteristischen Banden für den angeregten Zustand bei 20 K sind nicht zu

finden, stattdessen ähnelt das Spektrum des angeregten Zustands dem Grundzustandsspektrum. Das theoretische Spektrum des closed butterfly 3CC -Zustands beschreibt das Spektrum des angeregten Zustands bei 290 K am besten (Abb. 4.33). Da sich die Elektronendichte nur auf dem vierkernigen Zentrum verschiebt, unterscheiden sich die Schwingungen dieses angeregten Zustands im Fingerprintbereich kaum von denen des Grundzustands. Charakteristisch ist neben der Abwesenheit der charakteristischen Banden bei 20 K vor allem die im Vergleich zum Grundzustand ausgeprägtere Bande bei ca. 1275 cm^{-1} , welche C-H-Biegeschwingungen der H-Atome im Pyridinring, welche dem Cluster am nächsten liegen, zuzuordnen ist. Die Spindichte auf dem Cluster ist nicht symmetrisch verteilt (Abb. 4.22), sondern mehr an zwei Kupferzentren, welche von einem Liganden verbrückt sind, als auf den anderen beiden mit dem zweiten Liganden, lokalisiert. Das sorgt für eine Verschiebung der Intensität dieser CH-Biegeschwingung.

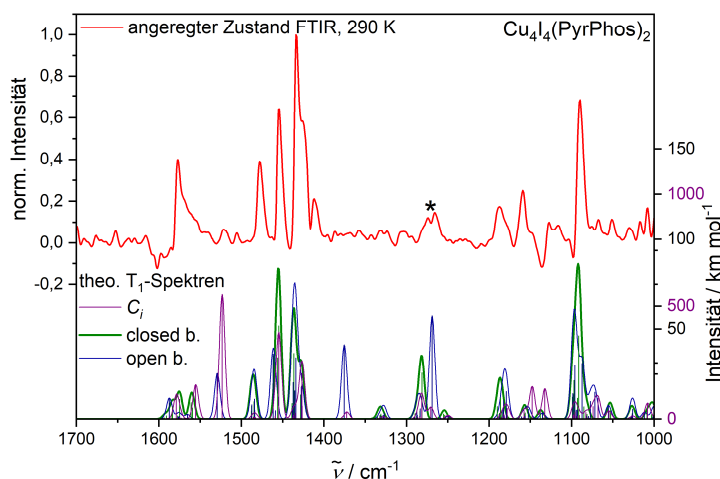


Abb. 4.33: Vergleich des experimentellen Spektrums des angeregten Zustands bei 290 K mit den theoretischen Spektren des T_1 -Zustands in C_i , closed butterfly und open butterfly Geometrie für den Komplex $\text{Cu}_4\text{I}_4(\text{PyrPhos})_2$. (UDFT/B3LYP/def2-TZVP, Faltung mit Gaußkurven, FWHM = 8 cm^{-1}). Die mit Sternchen markierte Bande ist spezifisch für den angeregten Zustand.

Damit lassen sich durch Step-scan-FTIR-Spektroskopie bei 20 K und 290 K zwei verschiedene Triplet-Zustände dem angeregten Zustand des $\text{Cu}_4\text{I}_4(\text{PyrPhos})_2$ zuordnen. Dies bestätigt die in den Lumineszenz-Daten bereits identifizierte Thermochromie.

$\text{Cu}_4\text{I}_4(\text{Isochinolin})_2$

Auch der $\text{Cu}_4\text{I}_4(\text{Isochinolin})_2$ -Komplex wurde mittels zeitaufgelöster FTIR-Spektroskopie untersucht. Der Grundzustand ist bei 20 K und 290 K identisch und kann aufgrund der starken Ähnlichkeit der theoretischen Grundzustandsspektren aller drei Geometrien nicht zugeordnet werden (Abb. 4.34). Der closed butterfly Grundzustand ist um ca. 10 kJ mol^{-1} am energetisch günstigsten.

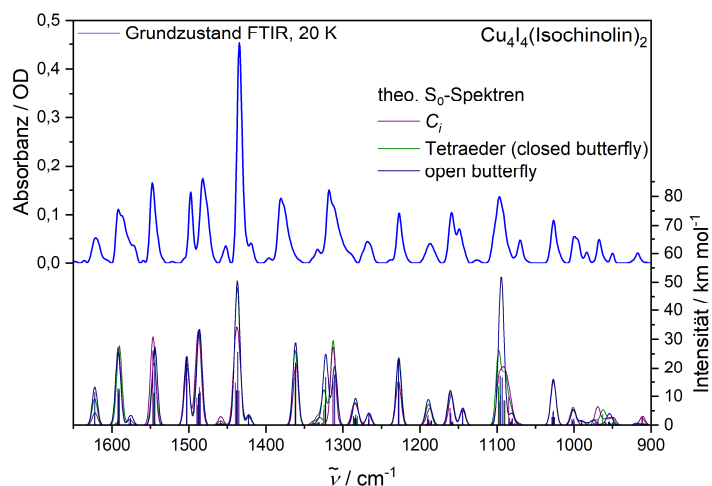


Abb. 4.34: Vergleich des experimentellen Spektrums des Grundzustands bei 20 K mit den theoretischen Spektren des S_0 -Zustands in C_i , Tetraeder- (closed butterfly) und open butterfly Geometrie für den $\text{Cu}_4\text{I}_4(\text{Isochinolin})_2$ -Komplex. (DFT/B3LYP/def2-TZVP, Faltung mit Gaußkurven, FWHM = 8 cm^{-1}).

Im angeregten Zustand bei 290 K ist das Spektrum (Step-scan + 1 % Grundzustand) dem Grundzustand sehr ähnlich (Abb. 4.35). Aufgrund der rotverschobenen UV/Vis-Spektren wurde dieser Komplex auch mit einer Anregung bei 532 nm untersucht. Diese Messungen zeigen das gleiche Ergebnis für die IR-Absorption im elektronisch angeregten Zustand. Kein theoretisches Spektrum der optimierten Triplett-Strukturen beschreibt das experimentelle Spektrum wirklich gut. Das deutet darauf hin, dass das Spektrum des angeregten Zustands bei 290 K zu schwach ist und es somit bei der Aufaddierung mit dem Grundzustand zu Artefakten kommt. Das Spektrum bei 20 K bei einer Anregung mit 355 nm unterscheidet sich deutlich vom Grundzustand, ist aber teilweise sehr unstrukturiert. Auch hier ist eine eindeutige Zuordnung der Triplett-Geometrien schwierig (Abb. 4.36, links). Allerdings liegen die drei berechneten Strukturen im Triplettzustand energetisch nahezu identisch innerhalb von $3,3 \text{ kJ mol}^{-1}$. Durch eine gleichzeitige Besetzung der open und der closed butterfly Strukturen lässt sich das Spektrum annähernd beschreiben. Bei einer Anregung mit 532 nm ist das Spektrum aufgelöster als mit 355 nm Anregung. Es unterscheidet sich deutlich vom Grundzustand und lässt sich in etwa mit dem theoretischen Triplett-Spektrum der open butterfly Geometrie beschreiben (Abb. 4.35 und Abb. 4.36, rechts).

Damit scheint für den Isochinolin-Komplex die Anregungswellenlänge entscheidend für die Besetzung der Triplett-Zustände zu sein. Mit höherer Anregungsenergie (355 nm) wird vermutlich auch die Barriere zum closed butterfly Triplett-Zustand überwunden, während bei niedrigerer Anregungsenergie (532 nm) nur der open butterfly Triplett-Zustand erreicht wird.

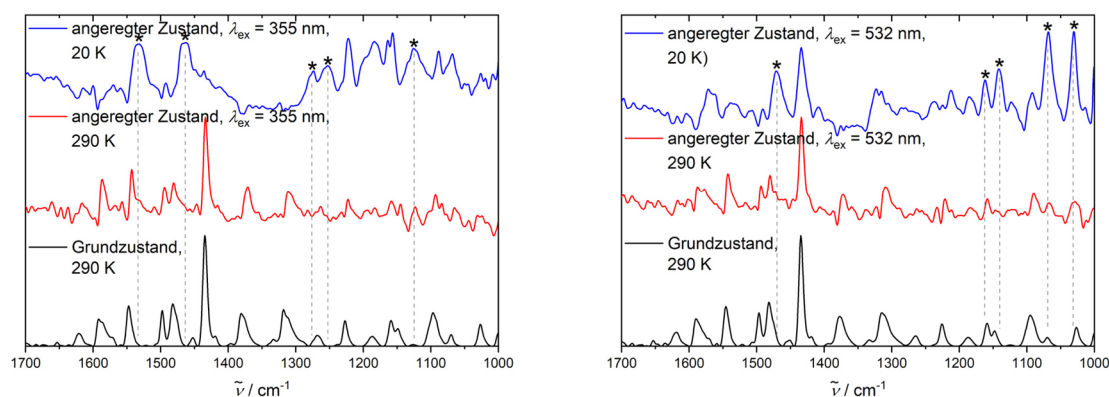


Abb. 4.35: Vergleich des FTIR-Spektrums des Grundzustands mit den Spektren des angeregten Zustands bei 20 K und 290 K des $\text{Cu}_4\text{I}_4(\text{Isochinolin})_2$ -Komplexes bei einer Anregungswellenlänge von 355 nm (links) und 532 nm (rechts). Mit Sternchen markierte Banden sind spezifisch für den angeregten Zustand bei 20 K.

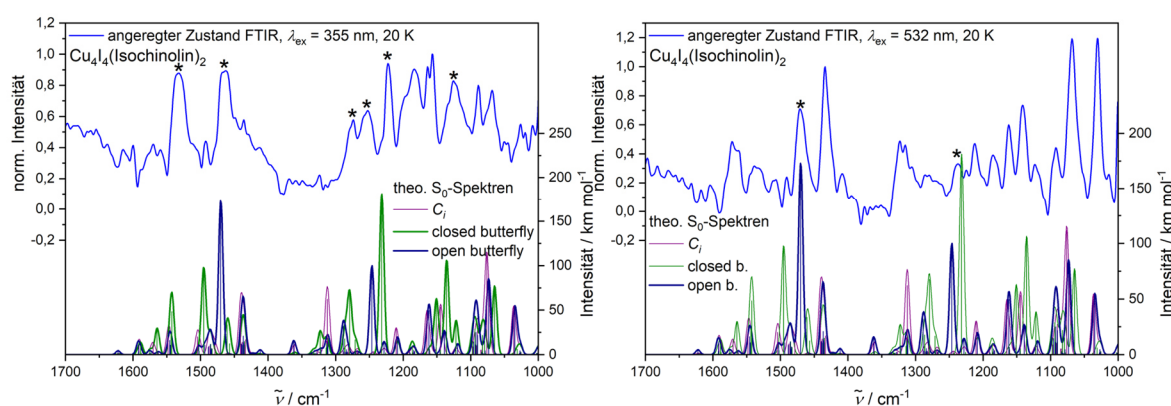


Abb. 4.36: Vergleich des experimentellen Spektrums des angeregten Zustands bei 20 K mit den theoretischen Spektren des T_1 -Zustands in C_i -, closed butterfly und open butterfly Geometrie für den Komplex $\text{Cu}_4\text{I}_4(\text{Isochinolin})_2$ bei einer Anregungswellenlänge von 355 nm (links) und 532 nm (rechts). (UDFT/B3LYP/def2-TZVP, Faltung mit Gaußkurven, FWHM = 8 cm^{-1}). Die mit Sternchen markierte Bande ist spezifisch für den angeregten Zustand.

4.2.4 Fazit

Die Komplexreihen der vierkernigen Kupferkomplexe der Form $\text{Cu}_4\text{X}_4(\text{L})_2$ wurden sowohl mit (zeitaufgelöster) Lumineszenz- als auch zeitaufgelöster Step-scan-FTIR-Spektroskopie im Vergleich mit DFT-Rechnungen charakterisiert. Sie zeigen alle eine deutliche Emission im Bereich von 720 – 505 nm, abhängig vom Komplex und vom Medium.

Das Medium beeinflusst dabei neben der Lage der Emissionbanden auch die Auflösung der Spektren und das temperaturabhängige Verhalten der Emission. Der rigidochrome Effekt ist in der KBr-Matrix deutlich ausgeprägter als in reinem Probenpulver. Daher lassen sich bei Untersuchungen im Pulver andere Effekte wie die temperaturabhängige Destabilisierung des Grundzustands bzw. Stabilisierung des elektronisch angeregten Zustands oder TADF besser beobachten, da sie nicht signifikant vom Rigidochromismus überlagert werden. Während die

Komplexe mit Methylgruppe in 4-Stellung am Pyridinring des Liganden keine Thermochromie zeigen, lässt sich am $\text{Cu}_4\text{I}_4(\text{PyrPhos})_2$ insbesondere im Pulver ein deutliches thermochromes Verhalten beobachten. Die PyrPhos-Komplexe mit den Halogeniden Bromid und Chlorid weisen dagegen keine Thermochromie auf. Wie auch bei den 6-Me-Komplexen ist somit die Barriere für die leichteren Halogenide höher und kann bei Raumtemperatur nicht mehr thermisch überwunden werden. Mit Lumineszenzlebensdauern im Mikrosekundenbereich für alle untersuchten Komplexe lässt sich die Emission Phosphoreszenz zuordnen.

Die Bestimmung der Triplett-Strukturen mit Step-scan-FTIR-Spektroskopie zeigt für die 4-Me-Komplexe $\text{Cu}_4\text{Br}_4(4\text{-Me})_2$ und $\text{Cu}_4\text{Cl}_4(4\text{-Me})_2$ eine temperaturunabhängige Besetzung eines MLCT-Triplett-Zustands mit open butterfly- oder C_7 -Struktur. Bei den PyrPhos-Komplexen konnte bei tiefer Temperatur für alle eine open butterfly Struktur im MLCT-Triplett-Zustand zugeordnet werden. Während dies für den Bromid- und den Chlorid-Komplex auch bei 290 K der Fall ist und sie somit ebenfalls keine Thermochromie aufweisen, unterscheidet sich das Spektrum des angeregten Zustands des $\text{Cu}_4\text{I}_4(4\text{-Me})_2$ bei 290 K von dem bei 20 K. Der besetzte Triplett-Zustand hat nach Zuordnung der theoretischen Spektren bei 290 K eine closed butterfly Struktur eines clusterzentrierten Triplett-Zustands. Damit ließen sich die beiden an der Thermochromie beteiligten Zustände des $\text{Cu}_4\text{I}_4(4\text{-Me})_2$ charakterisieren.

Nicht mit den anderen Ligandtypen vergleichbar verhält sich der $\text{Cu}_4\text{I}_4(\text{Isochinolin})_2$. In der Emission ist im KBr-Pressling ein starker rigidochromer Effekt zu beobachten, während der Komplex im Pulver Anzeichen für TADF aufweist. Die Step-scan-Untersuchungen des angeregten Zustands ergeben eine Abhängigkeit der Besetzung der Triplett-Zustände von der Anregungswellenlänge. Der Ligand mit erweitertem π -System hat somit bei diesem Komplextyp einen starken Einfluss auf die Art der angeregten Zustände und die (temperaturabhängigen) Lumineszenzeigenschaften.

4.3 Thermally Activated Delayed Fluorescence and Phosphorescence Quenching in Iminophosphonamide Copper and Zinc Complexes

4.3.1 Präambel

In diesem Projekt wurden die photophysikalischen Eigenschaften von Iminophosphonamid-Kupfer und Zinkkomplexen betrachtet. Mittels temperaturabhängiger Step-scan-FTIR-Spektroskopie und DFT-Rechnungen konnte der angeregte Zustand eines Kupferkomplexes bestimmt werden.

Pit Boden und ich haben die temperaturabhängigen Step-scan-FTIR-Messungen durchgeführt. Ich habe die DFT-Rechnungen umgesetzt. Pit Boden und ich wurden von Markus Gerhards und Gereon Niedner-Schatteburg betreut.

Bhupendra Goswami, Thomas J. Feuerstein und Ravi Yadav haben die Komplexe synthetisiert und analytisch charakterisiert. Sie wurden von Peter Roesky betreut. Die temperaturabhängigen Lumineszenzuntersuchungen wurden von Sergei Lebedkin durchgeführt. Er wurde von Manfred Kappes betreut. Zur Ausarbeitung des Manuskripts haben alle Autoren beigetragen.

4.3.2 Nachdruck und ergänzende Informationen

JOHN WILEY AND SONS LICENSE
TERMS AND CONDITIONS

Dec 07, 2022

This Agreement between Sophie Steiger ("You") and John Wiley and Sons ("John Wiley and Sons") consists of your license details and the terms and conditions provided by John Wiley and Sons and Copyright Clearance Center.

License Number	5443830655830	Requestor type	Author of this Wiley article
License date	Dec 07, 2022	Format	Print and electronic
Licensed Content Publisher	John Wiley and Sons	Portion	Full article
Licensed Content Publication	Chemistry - A European Journal	Will you be translating?	No
Licensed Content Title	Thermally Activated Delayed Fluorescence and Phosphorescence Quenching in Iminophosphonamide Copper and Zinc Complexes	Title	Zeitaufgelöste FTIR- und Lumineszenzspektroskopie an Organometallkomplexen und deren Reaktionen
Licensed Content Author	Peter W. Roesky, Manfred M. Kappes, Markus Gerhards, et al	Institution name	Technische Universität Kaiserslautern
Licensed Content Date	Jun 1, 2021	Expected presentation date	Feb 2023
Licensed Content Volume	27	Requestor Location	Sophie Steiger Erwin-Schrodinger-Straße 52
Licensed Content Issue	61		Kaiserslautern, 67655 Germany Attn: Sophie Steiger
Licensed Content Pages	10	Publisher Tax ID	EU826007151
Type of use	Dissertation/Thesis	Total	0.00 EUR



Thermally Activated Delayed Fluorescence and Phosphorescence Quenching in Iminophosphonamide Copper and Zinc Complexes

Bhupendra Goswami⁺⁺,^[a] Thomas J. Feuerstein⁺⁺,^[a] Ravi Yadav,^[a] Sergei Lebedkin,^[b] Pit J. Boden,^[c] Sophie T. Steiger,^[c] Gereon Niedner-Schatteburg,^[c] Markus Gerhards⁺,^[c] Manfred M. Kappes,^[b, d] and Peter W. Roesky^{*[a]}

Abstract: The synthesis of copper and zinc complexes of four variably substituted iminophosphonamide ligands is presented. While the copper complexes form ligand-bridged dimers, the zinc compounds are monomeric. Due to different steric demand of the ligand the arrangement of the ligands within the dimeric complexes varies. Similar to the structurally related iminophosphonamide complexes of alkali metals and calcium, the steady-state and time-resolved photoluminescence (PL) of four of the seven compounds studied here as solids in a temperature range of 5–295 K can be described within the scheme of thermally activated delayed fluorescence (TADF). Accordingly, they exhibit bright blue-green phosphorescence at low temperatures (< 100 K), which turns into delayed fluorescence by increasing the temper-

ature. However, unusually, the fluorescence is practically absent in two copper complexes which otherwise still conform to the TADF scheme. In these cases, the excited singlet states decay essentially non-radiatively and their thermal population from the corresponding low-lying triplet states efficiently quenches PL (phosphorescence). Three other copper and zinc complexes only exhibit prompt fluorescence, evidencing a wide variation of photophysical properties in this class of compounds. The excited states of the copper complex with especially pronounced phosphorescence quenching were also investigated by low-temperature time-resolved infrared spectroscopy and quantum chemical calculations.

Introduction

The term imino-aza-phosphorus(V)-ligand covers a wide variety of ligands containing both nitrogen and phosphorus atoms. The common feature of these ligands is the presence of one or more terminal R–N=P units.^[1] Amongst this class are the monoanionic diiminophosphinates of the general formula $[R_2P-(NR')_2]^-$, which are alternatively termed iminophosphonamides. In analogy to amidinates which are often compared with carboxylates, they can be regarded as the nitrogen analogues of phosphinate anions $[R_2PO_2]^-$.^[2] Like amidinates, iminophosphonamides are chelating ligands, forming four-membered

metallacycles upon metal coordination. Therefore, these compounds also belong to a general class of NXN donor ligands. Among these ligands, iminophosphonamides deserve special interest due to several features: (i) Due to the zwitterionic nature of the $R_2P^+(NR')_2$ (NPN) ligand the σ -donor properties of the nitrogen atoms are enhanced.^[3] For instance, recently, Nakata et al. found both experimentally and theoretically that iminophosphonamide-chlorosilylene is a stronger σ -donor in comparison with the common non-heterocyclic carbenes (NHCs) and silylenes (NHSis).^[4] (ii) Due to a rather long P–N bond of approx. 1.60 Å iminophosphonamides exhibit a wider bite angle than amidinates or, more generally, other NXN

[a] Dr. B. Goswami,⁺⁺ Dr. T. J. Feuerstein,⁺⁺ Dr. R. Yadav, Prof. Dr. P. W. Roesky
Institute of Inorganic Chemistry
Karlsruhe Institute of Technology (KIT)
Engesserstrasse 15, 76131 Karlsruhe (Germany)
E-mail: roesky@kit.edu

[b] Dr. S. Lebedkin, Prof. Dr. M. M. Kappes
Institute of Nanotechnology
Karlsruhe Institute of Technology (KIT)
Hermann-von-Helmholtz-Platz 1, 76344 Eggenstein-Leopoldshafen (Germany)

[c] P. J. Boden, S. T. Steiger, Prof. Dr. G. Niedner-Schatteburg,
Prof. Dr. M. Gerhards⁺
Fachbereich Chemie und Forschungszentrum OPTIMAS
TU Kaiserslautern
67663 Kaiserslautern (Germany)

[d] Prof. Dr. M. M. Kappes
Institute of Physical Chemistry
Karlsruhe Institute of Technology (KIT)
Fritz-Haber Weg 2, 76131 Karlsruhe (Germany)

[⁺⁺] These authors contributed equally to this work.

[⁺] Deceased December 28, 2020.

Supporting information for this article is available on the WWW under
<https://doi.org/10.1002/chem.202101247>

This manuscript is part of a Special Issue "Cooperative effects in heterometallic complexes".

© 2021 The Authors. Chemistry - A European Journal published by Wiley-VCH GmbH. This is an open access article under the terms of the Creative Commons Attribution Non-Commercial License, which permits use, distribution and reproduction in any medium, provided the original work is properly cited and is not used for commercial purposes.

bidentate chelating ligands like boraamidates ($X=BR$),^[5] triazenides ($X=N$)^[6] and sulfamidates ($X=SR$).^[7,8] (iii) Besides the σ -donor strength, the high steric demand of the pentavalent phosphorous atom further contributes to the stabilization of metal centers. (iv) Finally, yet importantly, a ^{31}P nucleus in the ligand backbone may beneficially serve as a spectroscopic marker for monitoring chemical transformations.^[9]

Moreover, metal complexes of iminophosphonamides are attractive from the photophysical point of view. Indeed, metal coordination of ligands containing both phosphorous and nitrogen sites has frequently resulted in compounds demonstrating interesting photoluminescence (PL) properties.^[10] This holds true also for iminophosphonamides. Recently, we reported on the alkali metal complexes of a chiral iminophosphonamine ligand.^[11] In the solid state, in contrast to the fluorescent ligand, these complexes show efficient blue-green long-lived phosphorescence at low temperatures ($< 100\text{ K}$) and thermally activated delayed fluorescence (TADF)^[12] above $\approx 150\text{ K}$ with quantum yields of up to 36% at room temperature. This surprising difference has been attributed to the dimeric ligand arrangement in the alkali metal complexes, enabling symmetry-breaking intramolecular charge transfer between the 'monomeric' ligand units, which can strongly enhance intersystem crossing (ISC) and triplet formation.^[13]

The TADF is then facilitated by a small energy gap ($\approx 400\text{--}700\text{ cm}^{-1}$) between the relaxed excited singlet (S_1) and first triplet (T_1) states of the iminophosphonamine ligand and its complexes. This results in thermal population of the S_1 state from the lower-lying triplet state and in S_1 fluorescence dominating at elevated temperatures. Similar observations were made for the related calcium complexes.^[14]

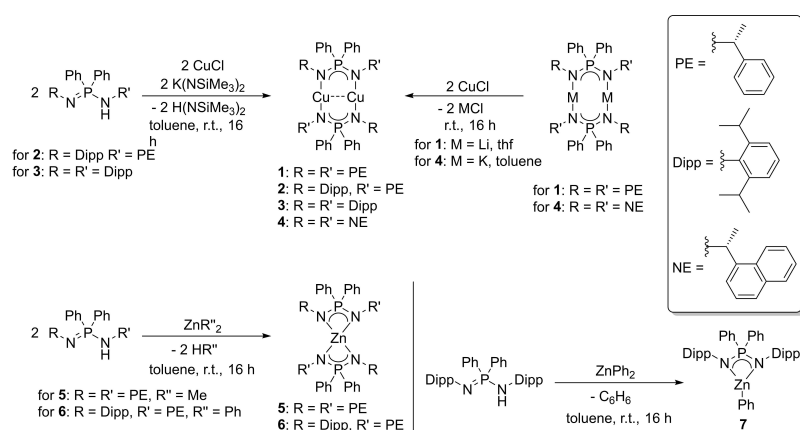
These findings encouraged us to investigate coordination of the iminophosphonamine ligands with other metals, including transition metals. Herein we report on the synthesis of copper(I) and zinc(II) iminophosphonamide complexes. Copper(I) complexes are generally characterized by a large impact of the metal centers on the PL properties as well as a high number of

reported TADF emitting compounds.^[15] Copper(I) complexes of NXN ligands are known to adopt dinuclear forms with two closely arranged metal centers, which may result in metal-philic interactions.^[16] Additionally, linear structures are usually observed with parallel-aligned ligands. In contrast, zinc(II)-NXN complexes, due to a central tetrahedral coordination sphere, generally form monometallic structures with orthogonally arranged ligands.

Depending on the metal and ligand substituents, a very different PL behavior was observed for the copper(I) and zinc(II) iminophosphonamide complexes studied as solids in a temperature interval of 5–295 K, ranging from prompt fluorescence to TADF and long-lived phosphorescence. We moreover utilized step-scan FTIR analysis to characterize the excited triplet state of a selected copper complex and its dynamics on the microsecond time scale. The spectroscopic experiments were supported by density functional theory (DFT) modelling.

Results and Discussion

At first the synthesis was focused on copper(I) complexes of the four differently substituted, previously described iminophosphonamide ligands. As a starting point the lithiated ligand $[\text{Li}_2\{(\text{R})\text{-PEPIA}\}_2]$ ((R)-PEPIA = *P,P*-diphenyl-*N,N'*-bis((*R*)-1-phenylethyl)phosphinimidic amide) was reacted with copper(I) chloride in a metathesis reaction to yield the dinuclear copper(I) complex $[\text{Cu}_2\{(\text{R})\text{-PEPIA}\}_2]$ (**1**) (Scheme 1). The ^1H NMR spectrum of **1** is quite similar to that of the lithiated ligand. The most pronounced difference is the $^3J_{\text{PH}}$ constant for the coupling between the $^i\text{Pr-CH}$ protons and the phosphorous atom, which amounts to $^3J_{\text{PH}} = 18.8\text{ Hz}$ for **1** and $^3J_{\text{PH}} = 21.6\text{ Hz}$ for $[\text{Li}_2\{(\text{R})\text{-PEPIA}\}_2]$. The $^{13}\text{C}\{^1\text{H}\}$ NMR spectrum is comparable to the spectrum of the parent compound as well. However, a notably larger chemical shift of $\delta = 39.6\text{ ppm}$ is observed in the $^{31}\text{P}\{^1\text{H}\}$ NMR spectrum of **1** ($\delta = 20.6\text{ ppm}$ for $[\text{Li}_2\{(\text{R})\text{-PEPIA}\}_2]$). Furthermore, whereas a *pseudo*-quartet resonance due to $^2J_{\text{PLi}}$ coupling



Scheme 1. Synthesis of compounds 1–7.

is observed for the lithium complex, a singlet resonance is detected for the copper compound **1** (Figure S3.3). In the IR spectrum of **1** (Figure S4.1) the lack of any vibration modes above 3054 cm^{-1} indicates the absence of N–H groups. Single crystals suitable for X-ray crystallography were grown by recrystallization from *n*-hexane, whereby complex **1** crystallizes in the chiral orthorhombic space group $P2_12_12_1$. As expected, the molecular structure of compound **1** in the solid state represents a dinuclear molecule in which two copper(I) ions, in close contact, bridge two ligands. The Cu1...Cu2 distance of $2.534(2)\text{ \AA}$ is in the usual range for cuprophilic interactions.^[17] The NPN angles ($\text{N1-P1-N2 } 110.1(5)^\circ$ and $\text{N4-P2-N3 } 110.3(5)^\circ$) are slightly widened in comparison with the X-ray data for the starting compound ($\text{N1-P1-N2 } 108.52(14)^\circ$ and $\text{N3-P2-N4 } 99.7(2)^\circ$ in $[\text{Li}_2\{(\text{R})\text{-PEPIA}\}_2]$). Moreover, the N1-P1-P2-N3 torsion angle between the two ligands of $140.223(2)^\circ$ in **1** is not far from 180° , which is ascribed to the affinity of copper(I) ions for the linear coordination geometry as well as to the reduction of steric restraints between the nitrogen substituents. Accordingly, the phenyl moieties on the nitrogen atoms N1 and N3 protrude below the paper plane in Figure 1, while the respective moieties on N2 and N4 emerge from it.

Next, we moved on to the synthesis of the Cu(I) complex of the bulkier asymmetric ligand (*R*)-HPE^{Dipp}PIA ((*R*)-HPE^{Dipp}PIA = *P,P*-diphenyl-*N*-(*R*)-1-phenylethyl)-*N'*-(2',6'-diisopropylaniline)-phosphinimidic amide). The protonated ligand was straightforwardly reacted in a one-pot synthesis with equivalent amounts of potassium bis(trimethylsilyl)amide (KHMDs) and CuCl. After workup $[\text{Cu}_2\{(\text{R})\text{-PE}^{\text{Dipp}}\text{PIA}\}_2]$ (**2**) was obtained as a white crystalline solid. All resonances in the ^1H and $^{13}\text{C}\{^1\text{H}\}$ NMR spectra (Figures S3.4 and S3.5) can be assigned to the respective Dipp and PE substituents as well as to the aromatic protons. Furthermore, a similar chemical shift of the singlet resonance in the $^{31}\text{P}\{^1\text{H}\}$ NMR ($\delta = 38.0\text{ ppm}$) is observed for complex **2** in comparison to **1**.

This signal is significantly shifted downfield as compared to the phosphorous resonance at $\delta = -10.9\text{ ppm}$ for (*R*)-HPE^{Dipp}PIA. Single crystals of **2** were obtained after recrystallization from hot toluene. The compound crystallizes in the tetragonal chiral space group $P4_32_12$. The molecular structure shows that two copper centers are bridged by the iminophosphonamide

ligands, in a structure similar to that of **1** and the related structure $[\{\text{Ph}_2\text{P}(\text{NSiMe}_3)_2\}_2\text{Cu}_2]$.^[16a] The two flanking Dipp groups in complex **2** are trans positioned, probably to minimize the steric repulsion. The NPN angles ($\text{N1-P1-N2 } 109.5(2)^\circ$) in the molecular structure of complex **2** (Figure 1) are nearly identical to the NPN angles for **1**. However, the ligands in **2** are aligned nearly coplanar with a N1-P1-P2-N4 torsion angle of $179.66(2)^\circ$. This is attributed to the higher steric demand of the two Dipp substituents. The Cu–N bond lengths are almost identical and lie in the range of previously reported complexes. The Cu1...Cu2 distance of $2.5324(7)\text{ \AA}$ is nearly the same as observed for **1**.

The next step in the systematic study of the influence of the ligand steric demand on the structure and photophysical properties of the copper(I) complexes was the synthesis of complex **3** with four Dipp substituents incorporating the achiral symmetric ligand *P,P*-diphenyl-*N,N'*-bis(2,6-diisopropylphenyl)phosphinimidic amine (H-DippPIA).^[9] The desired product $[\text{Cu}_2\{\text{DippPIA}\}_2]$ (**3**) was obtained by a similar one-pot procedure as described for **2** (Scheme 1) in form of colorless crystals. In the ^1H NMR and $^{13}\text{C}\{^1\text{H}\}$ NMR spectra of **3** all signals can be ascribed to the Dipp substituted iminophosphonamide ligand. The multiplicity is also in full agreement with the deprotonated symmetrically substituted ligand. However, the singlet resonance in the $^{31}\text{P}\{^1\text{H}\}$ NMR spectrum of **3** ($\delta = 8.4\text{ ppm}$) is significantly shifted to lower ppm in comparison with **1** and **2**. Complex **3** crystallizes in the monoclinic space group $P2_1/n$ with half of a molecule in the asymmetric unit. Like complex **2**, compound **3** has an inversion center in the middle of the molecule. The structural features of **3** are almost similar to those observed for **1** and **2**. The intermetallic Cu1...Cu1' interaction in **3** is $2.5292(10)\text{ \AA}$, which is consistent with that observed in the related compounds $[\{(2,6\text{-Me}_2\text{C}_6\text{H}_3\text{N}_2\text{C}(\text{H})\}_2\text{Cu}_2]$ ^[18] and $[\{\text{PrNC}(\text{Me})\text{N}^{\text{Pr}}\}_2\text{Cu}_2]$.^[19] The N1-Cu1-N2' bond angle amounts to $176.82(12)^\circ$ which is close to linearity and in consistency with the arrangements in complexes **1** and **2**. The respective Cu1-N1 and Cu1'-N2 bond lengths of $1.895(3)$ and $1.886(3)\text{ \AA}$ in **3** are slightly longer than those observed for $[\{(2,6\text{-Me}_2\text{C}_6\text{H}_3\text{N}_2\text{C}(\text{H})\}_2\text{Cu}_2]$ ($1.869(1)\text{ \AA}$). Furthermore, the N1-P1-P1'-N1' torsion angle of $180.00(2)^\circ$ in **3** is the highest of compounds **1-3**, presumably because of the higher steric demand induced by the Dipp-groups.

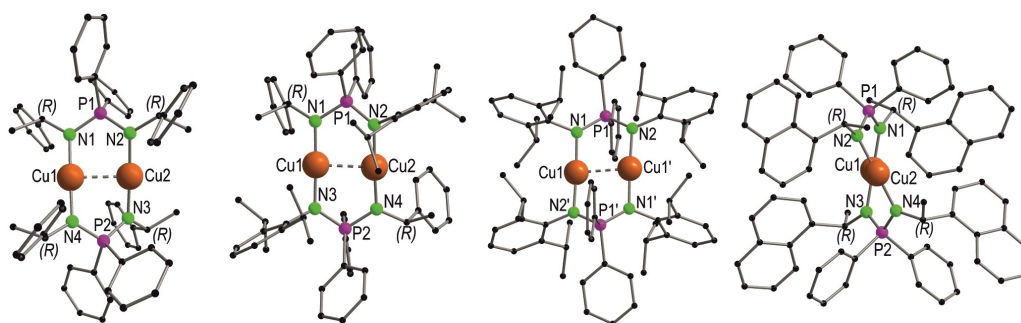


Figure 1. Molecular structure of compounds **1–4** (from left to right) in the solid state. Structural parameters are given in the supporting information.

After the successful isolation of the binuclear copper complexes 1–3, the substituent groups were altered to increase the π -character of the ligand. It is well known that, functionalized extended π -conjugated systems may strongly influence photophysical properties, for example due to intermolecular π - π interactions.^[20] In this regard, the [(*R*)-NEPIA][−] ligand ((*R*)-NEPIA = *P,P*-diphenyl-*N,N'*-bis((*R*)-1-naphthylethyl)phosphinimidic amide) was prepared, featuring naphthyl groups at the nitrogen centers. [Cu₂{(*R*)-NEPIA}₂] (4) was obtained from the salt metathesis reaction of CuCl and the potassium salt of [(*R*)-NEPIA][−] (Scheme 1). After extraction and standard workup procedure, it was isolated as a colorless solid. The ¹H NMR spectrum of complex 4 (Figure S3.10) is consistent with a symmetric arrangement in solution. More precisely, the characteristic doublet of quartets at $\delta = 5.12$ (³*J*_{PH} = 16.3 Hz, ³*J*_{HH} = 6.4 Hz) is assigned to the naph(CH)CH₃ protons, whereas the doublet at $\delta = 1.9$ ppm (³*J*_{HH} = 6.5 Hz) is attributed to the naph(CH)CH₃ protons. In the ¹³C{¹H} NMR spectrum (Figure S3.11), the methine and methyl moieties can be assigned to the resonances at $\delta = 50.6$ ppm (naph(CH)CH₃) and $\delta = 31.3$ ppm (naph(CH)CH₃), respectively.

The purity of the complex can be assessed by the detection of a single resonance at $\delta = 40.2$ ppm in the ³¹P{¹H} NMR spectrum, which is significantly shifted upfield as compared to $\delta = 38.0$ ppm in the dicopper(I) complex 2. Complex 4 crystallizes in the orthorhombic chiral space group *P*2₁2₁2₁ with one molecule in the asymmetric unit. The Cu1...Cu2 distance in complex 4 amounts 2.5054(8) Å, which is within the typical range of cuprophilic interactions.^[17] The N1-Cu1-N4 (175.6(2)°) and N2-Cu2-N3 (174.7(2)°) bond angles are close to linearity. Furthermore, the P-N contact lengths in 4 are almost equal (P1-N1 1.611(4), P1-N2 1.608(4), P2-N3 1.611(4) and P2-N4 1.612(4)), suggesting delocalization of the anionic charge over the NPN backbone.

Next, we focused on the synthesis of zinc(II) complexes. As a starting point, two equivalents of the protonated iminophosphonamide (*R*)-HPEPIA were reacted in a base elimination reaction with dimethyl zinc to yield the Zn(II) complex [Zn{(*R*)-PEPIA}₂] (5) (Scheme 1). The ¹H and ¹³C{¹H} NMR spectra of 5 (Figures S3.13 and S3.14) appear quite similar to the corresponding spectra for the Cu(I) complex 1. In consistency in the ³¹P{¹H} NMR spectrum a single resonance is

observed at $\delta = 35.7$ ppm which is located in a comparable range as for 1–4. Furthermore, the complex can be clearly detected via EI mass spectrometry as a molecular peak [M⁺] at *m/z* = 910.3507 (Figure S5.2). Single crystals of compound 5 were obtained from *n*-pentane. The complex crystallizes in the triclinic space group *P*1 with two molecules in the asymmetric unit. The Zn–N bond lengths are all in a narrow range of 2.025(3)–2.054(3) Å. Besides the iminophosphonamide bite angles (N1–Zn–N2 74.34(12)° and N3–Zn–N4 74.48(12)°), all N–Zn–N angles are in the range of 128.19(13)–130.83(13)°. Therefore, the Zn(II) core is coordinated distorted tetrahedrally by the four nitrogen atoms, which is in agreement with the calculated distortion parameters with the program SHAPE 2.1 (Table S6.2).^[21] Furthermore, the two ligands are aligned nearly perfectly opposite towards each other, with a nearly rectangular torsion angle of N1–P1–P2–N3 of 92.92(2)° (Figure 2).

Furthermore, in order to vary the ligand in the coordination sphere of a Zn(II) complex, the (*R*)-HPE^{Dipp}PIA ligand was reacted with ZnPh₂ in a molar ratio of 2:1 (Scheme 1), which resulted in the formation of the homoleptic zinc complex [Zn{(*R*)-PE^{Dipp}PIA}₂] (6). The disappearance of the NH resonance in the ¹H NMR spectrum indicated the successful formation of complex 6. Furthermore, the ¹H NMR spectrum of 6 exhibits a single set of resonances suggesting a certain degree of symmetry in solution. The Ph(CH)CH₃ signal appears as a doublet of quartets in the aliphatic region at $\delta = 3.79$ ppm (²*J*_{PH} = 18.57, ³*J*_{HH} = 6.53 Hz). A doublet at $\delta = 1.37$ ppm (²*J*_{HH} = 6.52 Hz) is assigned to the Ph(CH)CH₃ protons. The purity of complex 6 was further confirmed by the detection of only one peak at $\delta = 37.5$ ppm in the ³¹P{¹H} NMR spectrum, which is significantly shifted downfield compared to $\delta = -10.9$ ppm for (*R*)-HPE^{Dipp}PIA. Complex 6 crystallizes in the orthorhombic space group *P*2₁2₁2₁ with one molecule in the asymmetric unit. The central zinc atom is coordinated by four nitrogen atoms of two [(*R*)-PE^{Dipp}PIA][−] ligands. However, in contrast to compound 5 the central zinc atom is closer to a square planar coordination geometry with nearly parallel aligned NPN backbones, as indicated by the calculated distortion parameters (Figure S6.8 and Table S6.2). In order to minimize the steric repulsion, the Dipp groups adopt *trans* positions with respect to the central metal core. Furthermore, due to the unsymmetrical nature of the ligand the Zn–N bonds are not identical and are in the

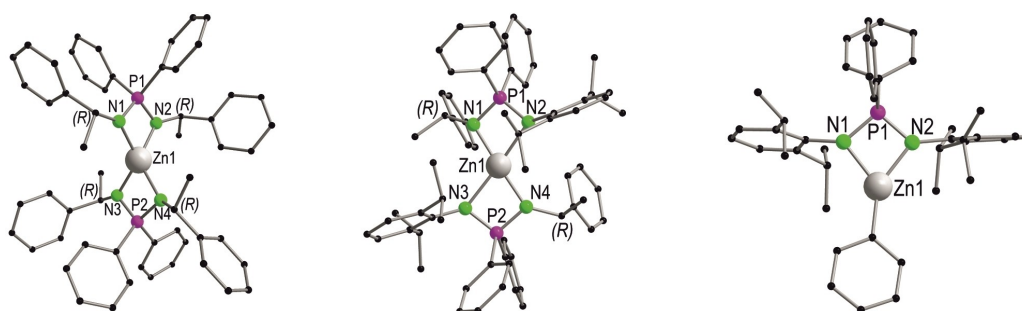


Figure 2. Molecular structure of compounds 5, 6 and 7 (from left to right) in the solid state. Structural parameters are given in the supporting information.

range of 1.994(3)–2.197(3) Å. The bite angles of the iminophosphonamides in complex **6** (N1–Zn–N2 72.06(11)° and N3–Zn–N4 71.94(10)°) are slightly narrower than the corresponding bite angles in **5**.

In order to synthesize a zinc analogue of complex **3**, ZnPh₂ was reacted with HDippPIA in a 1:2 molar ratio. However, formation of the heteroleptic complex [(DippPIA)ZnPh] (**7**) was observed in contrast to the homoleptic complexes **5** and **6**. This might be due to the sterically hindered nature of HDippPIA which prevents the coordination of two ligands on the same Zn(II) metal center. Complex **7** could be reproduced with a 1:1 molar ratio of the reagents (Scheme 1) and exhibits good solubility in common organic solvents such as thf, diethylether and toluene and is even slightly soluble in *n*-pentane. The heteroleptic nature of complex **7** was confirmed by ¹H NMR spectroscopy and no signs of ligand redistribution to a homoleptic complex were observed. The aromatic resonances appear in the range of δ = 7.63–6.77 ppm. The characteristic septet of the CH(CH₃)₂ moiety appears at δ = 3.88 ppm (³J_{HH} = 6.81 Hz), whereas the CH(CH₃)₂ resonance appears as doublet at δ = 1.03 ppm (³J_{PH} = 6.87 Hz). In the ¹³C{¹H} NMR spectrum, the resonances at δ = 29.4 ppm and δ = 24.1 ppm can be attributed to CH(CH₃)₂ and CH(CH₃)₂, respectively. In the ³¹P{¹H} NMR spectrum, the appearance of a single peak at δ = 17.2 ppm further indicates the purity of the product. The molecular structure of **7** is similar to that of the related [(DippPIA)ZnMe] and [(DippPIA)ZnEt] complexes reported by Stasch.¹⁹

The Zn–N (Zn–N1 2.027(2) Å and Zn–N2 1.996(2) Å) and Zn–C (Zn–C37 1.931(3) Å) bond lengths in **7** are consistent with those in related complexes. The N1–Zn–N2 acute bite angle of 74.50(8)° in complex **7** is wider than that of 65.9(2)° in the related amidinate complex [(MeC(NDipp)₂)₂Zn].

Photoluminescence properties

The structures and dimeric ligand arrangements of the bimetallic copper complexes **2**, **3** and especially **1** are close to those of the previously reported iminophosphonamide alkali metal complexes [M₂{(R)-PEPIA}₂] (M = Li, Na, K, Rb and Cs, see Scheme 1).¹¹ The monometallic zinc complexes **5** and **6** coordinating two iminophosphonamide ligands are analogous to the calcium complexes [Ca{(R)-PEPIA}₂].¹⁴ In view of the bright phosphorescence and thermally activated delayed fluorescence (TADF) observed for the alkali metal and calcium derivatives,^{11,14} a comparison with PL properties of the copper and zinc complexes **1–7** appears particularly interesting. Figures 3 and 4 show PL excitation (PLE) and emission spectra of the solid (polycrystalline) samples of **1–4** and **5–7**, respectively, at selected temperatures between 5 and 295 K, together with the emission intensity as a function of temperature. The spectra at further intermediate temperatures are presented in Figures S7.1–7 in the supporting information. Below T ≈ 50 K all complexes intensely emit at 450–530 nm under UV photoexcitation. The onset of absorption (PLE) at 360–400 nm (shifted to ca. 330 and 450 nm in **7** and **6**, respectively) is consistent with the white to pale yellow appearance of the powder

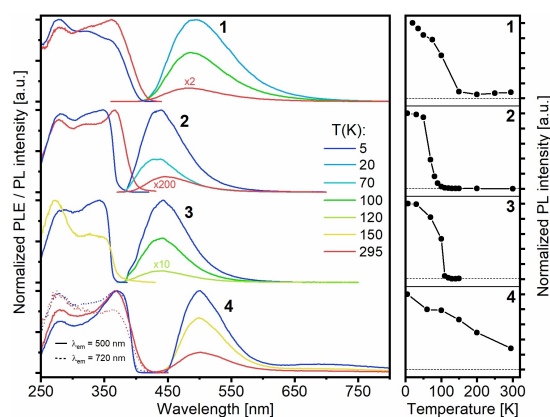


Figure 3. Left: Normalized photoluminescence excitation (PLE) and emission (PL) spectra of the solid bimetallic copper compounds **1–4** at temperatures between 5 and 295 K. The PL/ PLE spectra were excited at 350 (1), 340 (2), 340 (3) and 350 nm (4) and recorded at 480 (1), 450 (2), 460 (3) and 500 nm (4), if not indicated otherwise. Right: Integral PL intensities versus temperature in the range of 5–295 K (also shown on the logarithmic scale for **2** and **3** in Figures S7.2 and S7.3).

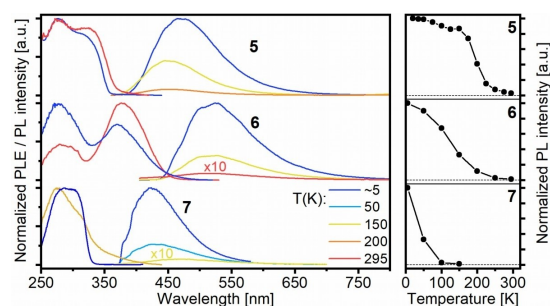


Figure 4. Left: Normalized photoluminescence excitation (PLE) and emission (PL) spectra of the solid monometallic zinc complexes **5–7** at temperatures between 5 and 295 K. The PL/ PLE spectra were excited at 330 (5), 380 (6), and 300 nm (7) and recorded at 480 (5), 520 (6) and 450 nm (7). Right: Integral PL intensities versus temperature in the range of 5–295 K.

samples. Similar spectra were observed for the alkali metal and calcium complexes, indicating related structures.^{11,14} The low-temperature emission of the latter and dimeric complexes **1–3** and **5** shares the same origin: it is phosphorescence with a lifetime from tens of microseconds to a few milliseconds. The phosphorescence is a major relaxation channel at low temperatures, referring, for instance, to the quantum efficiency, Φ_{PL} , of ≈ 100% for **1** and **5** at T = 5 K, as estimated from the PL temperature dependences and Φ_{PL} values measured at room temperature using an integrating sphere (see the supporting information). Furthermore, similar to the alkali metal and calcium complexes, **1–3** and **5** show a TADF-characteristic temperature dependence of the PL decay time, τ , as illustrated in Figure 5 for **5**. Here a strong decrease of τ in the temperature interval from 100 to 200 K reflects a transition from phosphor-

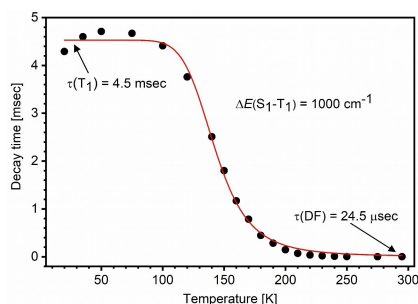


Figure 5. PL decay time of Zn complex **5** versus temperature. PL was excited at 337 nm with a nsec-pulsed laser, recorded at 470 nm and approximated with monoexponential decay curves (Figure S7.9). The red line is a fit to the TADF model of equilibrated states (Eq. (S1) in the supporting information). This estimates the S_1 - T_1 energy separation in **5** to be about 1000 cm^{-1} .

escence ($\tau = 4.5\text{ msec}$) to delayed fluorescence (with an effective decay time of $24\text{ }\mu\text{sec}$ at 295 K). The red curve in Figure 5 represents a fit of the experimental data to the simple TADF model of the thermally equilibrated singlet (S_1) and triplet (T_1) states (for details see the supporting information).^[12a,c-e,17] According to this model, the energy separation ΔE between these states is about 1000 cm^{-1} in **5** and 500 cm^{-1} in **1** (Figure S7.10). These values compare well to those determined for the alkali metal and calcium complexes.^[11,14] However, delayed fluorescence in **1** and **5** has a relatively low quantum efficiency (9 and 3%, respectively, at 295 K). The S_1 state in these compounds apparently decays to the ground state mostly nonradiatively. Accordingly, the PL intensity rapidly drops over the phosphorescence-to-TADF crossover temperature interval (Figures 3, 4). Similarly moderate delayed fluorescence efficiencies were found for the related lithium, cesium and calcium compounds.^[11,14] Remarkably, this trend towards lower fluorescence quantum efficiency becomes dramatic in the copper complexes **2** and **3**, which emit practically no fluorescence at all. On the other hand, as mentioned above, they show the TADF-characteristic temperature dependence of the PL (phosphorescence) decay time, correlating with a strong, thermally activated decrease of the emission intensity. These parameters vary especially spectacularly in **3**: over the narrow temperature interval of $75\text{--}130\text{ K}$, τ decreases from ca. 280 to $1\text{ }\mu\text{sec}$ (Figure S7.12), while the PL intensity falls by more than 1000 -fold (Figure S7.3). By further increasing the temperature above 150 K , the emission vanishes completely. Such photophysical behavior can still be described within the TADF framework, assuming that the excited singlet state S_1 relaxes to the ground state S_0 virtually completely via internal conversion, i.e. nonradiatively (Figure 6). Thermally activated population of S_1 via reversed intersystem crossing (rISC) from the lower but energetically close-lying, triplet state T_1 can thus effectively deplete T_1 .

By analogy with TADF, one can designate the last process as “thermally activated phosphorescence quenching”. To the best of our knowledge, such behavior has not yet been described in

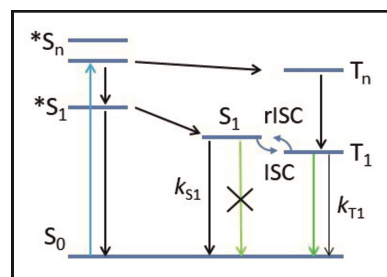


Figure 6. Scheme of photophysical processes suggested for copper complexes **2** and **3** (colored arrows: photoexcitation and emission transitions). It is similar to the standard TADF scheme valid for energetically close-lying relaxed excited singlet state S_1 and triplet state T_1 , facilitating thermally activated reverse intersystem crossing (rISC) from T_1 to S_1 . However, in difference to TADF, S_1 in **2** and **3** efficiently relaxes to the ground state S_0 nonradiatively as practically no fluorescence from S_1 is observed (crossed green arrow). It is assumed that the triplet manifold is mainly populated via intersystem crossing from the vertically excited singlet states $*S_{1,n}$.

literature - likely not due to its rarity, but rather due to a still limited number of detailed low-temperature photophysical studies of metal complexes, particularly those without any PL at room temperature. Indeed, it is well established that a small energy gap $\Delta E(S_1-T_1)$ generally correlates with a low oscillator strength/ radiative rate (k_{S1r}) of the $S_1 \rightarrow S_0$ fluorescence.^[12c] This is mirrored in long S_1 lifetimes defined for efficient TADF emitters, typically up to hundreds of nanoseconds ($k_{S1r} \leq 10^7\text{ s}^{-1}$). For instance, the S_1 intrinsic lifetime of 230 nsec was estimated for the sodium iminophosphonamide complex.¹¹ Apparently, the efficiency of such ‘slow’ fluorescence critically depends on suppression of the nonradiative decay, i.e. internal conversion $S_1 \rightarrow S_0$ (typical rate $k_{S1n} \approx 10^9\text{--}10^{10}\text{ s}^{-1}$ in organic and metallorganic luminophores).^[22] This is one of the reasons why the design of efficient TADF emitters is challenging. In this context, the copper complexes **2** and **3** just exemplify the case of a highly dominating nonradiative decay of S_1 ($k_{S1n} \gg k_{S1r}$).

Applying the model of equilibrated S_1 and T_1 states (Eq. (S1) to **2** and **3** yields $\Delta E(S_1-T_1) \approx 250$ and 950 cm^{-1} , respectively (Figures S7.11 and S7.12). However, the assumption of thermal equilibrium between S_1 and T_1 is likely not valid, considering the efficient nonradiative decay of S_1 and a high ratio of ΔE to the thermal energy, kT , at the crossover temperature (≈ 10 for **3**). If the nonradiative decay of S_1 is much faster than the ISC channel $S_1 \rightarrow T_1$, the expression for the temperature-dependent phosphorescence decay time, $\tau(T)$, reduces to (Eq. (1))

$$\tau(T) = \frac{\tau(T_1)}{1 + \tau(T_1) A \exp\left(-\frac{\Delta E}{kT}\right)} \quad (1)$$

where $\tau(T_1)$ is the intrinsic phosphorescence lifetime and $A \exp(-\Delta E/kT)$ represents the rate of thermally activated reversed intersystem crossing (rISC) between the T_1 and S_1 states. Note, however, that both Equations (1) and (S1) yield practically the same estimates for the energy separation ΔE , as a result of a

strong variation of $\tau(T)$ (over three orders of magnitude in **3**), which is described by the exponential factor $\exp(-\Delta E/kT)$. The experimental estimate of ΔE for the complex **3** was supported by calculations (see below).

In contrast to the compounds discussed above, the PL of **6**, **7** and the major emission of **4** at 500 nm represent prompt fluorescence, also at cryogenic temperatures, with a lifetime < 5 nsec (time resolution of the apparatus used). Such different behavior can be explained by their particular ligand structure and crystal packing. [(*R*)-NEPIA] ligands of **4** possess phenyl and naphthyl groups. In solid **4**, these groups of neighboring molecules arrange themselves roughly in parallel, at inter- and intramolecular separation distances of 4.1 Å (Figure S6.5). Such arrangement can enable weak π -stacking interactions. In addition to the fluorescence, **4** shows a minor broad emission at 700 nm, which decays within microseconds (Figure 3). Both bands only moderately depend on the temperature. We tentatively ascribe these emissions to, respectively, singlet and triplet excimers or excitons generated in the stacked phenyl-naphthyl units.

The poor triplet formation (absence of phosphorescence / TADF) in **6** might be related to the nearly planar coordination of the NPN backbones of two iminophosphonamide ligands around the zinc atom. In contrast, a strongly bent or twisted geometry is observed in the zinc complex **5** as well as in the dimeric iminophosphonamide complexes of alkali metals and calcium. As mentioned in the introduction, we have attributed the origin of phosphorescence / TADF in the latter compounds to intramolecular charge transfer between the 'monomeric' ligand units, resulting in enhanced intersystem crossing (ISC) and triplet formation.^[13] This process is expected to strongly depend on the mutual ligand configuration. For instance, the efficient triplet formation in dimers of BODIPY fluorescent dye molecules - also attributed to intramolecular charge transfer - has only been observed for the orthogonally arranged monomeric units and ceased in their planar configuration.^[23] A similar effect may occur in **6**. Somewhat in contradiction to this rationalization, the phosphorescent copper complexes **1–3** also demonstrate a planar arrangement of the two NPN backbones (see above). However, the efficient triplet formation in these complexes can be attributed to the heavy atom effect of the two copper atoms. According to the calculated frontier molecular orbitals of **3** (Figure S9.1), the copper centers are directly involved in the electronic transitions. The highest and lowest molecular orbitals are largely localized on the copper centers and the iminophosphonamide ligands, respectively. Correspondingly, the lowest energy excitation is of mainly metal-to-ligand charge transfer character, similar to many copper(I) d^{10} systems reported in the literature.^[15d]

Finally, the zinc complex **7** is the only example among the studied compounds of a single iminophosphonamide ligand coordination. Accordingly, this complex does not match the above scheme suggested for the dimeric iminophosphonamide metal complexes and does not demonstrate efficient triplet formation (a significant effect of zinc on ISC in **7** can be safely ruled out). Instead **7** only shows prompt fluorescence. It is intense at low temperatures, decreases strongly upon increas-

ing the temperature, and likely results from a solely ligand-localized excitation.

Step-scan FTIR spectroscopy and DFT modelling

Time-resolved step-scan FTIR investigations were performed for the copper complex **3** containing the bulky ligands DippPIA⁻ in particular to further characterize its long-lived excited triplet state. **3** was chosen as it shows the most surprising temperature-dependent PL behavior (see above). The samples for transient FTIR experiments were prepared as KBr pellets, a technique which was introduced by Palmer et al.^[24] and has been established in the Gerhards group over the last few years.^[25] For instance, a series of bi- and tetranuclear OLED (organic light emitting diode) - relevant Cu(I) complexes has recently been investigated with this technique.^[25a,c,26]

The measured steady-state (ground state) FTIR spectrum of **3** is in perfect agreement with the IR spectrum calculated within density functional theory (DFT) (Figure 7). Hence, the experimental absorption bands could be assigned to specific vibrations which are listed in the supporting information (Table S8.1). Practically no change in the ground state IR

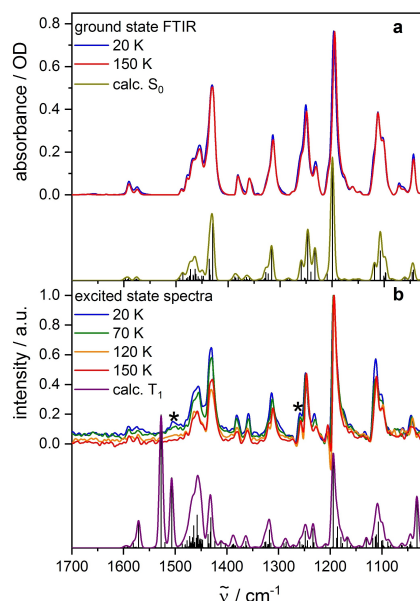


Figure 7. a) Upper trace: FTIR steady-state (ground state, S_0) spectra of **3** at 20 and 150 K. Lower trace: Calculated IR transitions and simulated IR spectrum of the S_0 state. b) Upper trace: experimental excited state IR spectra of **3** at 20, 70, 120 and 150 K obtained from the step-scan difference spectra (averaged over 2 μ s after laser pulse). The asterisks indicate distinct bands characteristic for the excited state. Lower trace: Calculated IR transitions and simulated IR spectrum of the T_1 state. Calculations: DFT/B3LYP-D3(BJ)/def2-TZVP, IR absorption frequencies scaled by 0.975, convolution with Gaussian profiles, FWHM = 8 cm^{-1} .

spectrum was observed between 20 K and room temperature, indicating the persistent crystal structure. The sample was then excited at 20–150 K with 355 nm laser pulses and time-resolved difference IR spectra were recorded. The spectrum shown in Figure S8.1 was averaged over the first 2 μs after the laser pulse (see supporting information for further details).

For a better direct comparison of the measured IR absorption in the electronic ground (S_0) and excited states (Figure 7), the IR absorption spectrum of the latter was generated by addition of 3.5% of the ground state spectrum to the step-scan difference spectrum in order to suppress the negative bands resulting from depopulation of S_0 . Interestingly, a new band is observed at 1505 cm^{-1} , where the S_0 state does not absorb, so that this feature is specific for the excited state. Additionally, a distinct peak is observed at 1259 cm^{-1} in the excited state, instead of a shoulder in the S_0 spectrum. The described impact of UV excitation on the IR absorption indicates structural changes. The corresponding excited state can be assigned to the triplet state of **3**.

Indeed, the experimental excited state spectrum is in good agreement with the calculated spectrum of the lowest triplet state T_1 (calculated by unrestricted DFT (UDFT)) with respect to the spectral positions (Figure 7b). The observed specific absorption band slightly above 1500 cm^{-1} most likely corresponds to the prominent doublet of peaks in the calculated spectrum at 1528 and 1507 cm^{-1} . This doublet is an aromatic C–C-stretching vibration in the phenyl substituents on the phosphorous atom of the ligand, whereas the band at 1259 cm^{-1} corresponds to a combined mode involving C–N stretching motion.

Step-scan FTIR investigations were then performed additionally at 70 K, 120 K and 150 K for comparison with the PL data (Figures 7 and S8.2). The corresponding excited state spectra and the underlying step-scan difference spectra are similar to that at 20 K. The absorption around 1505 cm^{-1} diminishes with the temperature, but is recognizable till at least 120 K. Even at 150 K there might be a very weak excited state absorption around 1500 cm^{-1} . This assertion is supported when comparing the step-scan spectra averaged over 0–0.5 μs and 3.0–3.5 μs after laser excitation, where a decay over time is visible to some extent in this spectral region (Figure S8.3). At the same time, the peak at 1259 cm^{-1} is visible in all four spectra. This difference might be due to broadening of the former band at higher temperatures, for example, via coupling to low-energy modes, thus making it difficult to probe spectroscopically. The significant similarities between the excited state spectra at different temperatures are consistent with the same (major) excited state being involved.

Its lifetime was determined from the step-scan data by considering the decay of the most prominent positive and negative bands in the difference IR spectrum over time after laser excitation. These bands were first fitted separately (see, for example, Figure S8.4 for the bleach band at 1199 cm^{-1} at 20 K), yielding input values for a global fit over all chosen bands. A biexponential decay was determined at all probed temperatures (Figures S8.5–8) with strongly temperature-dependent time constants. The time constants of the main component of

about 140 and 83 μs (contribution of 95 and 86%) at 20 and 70 K, respectively, are in reasonable agreement with the PL data (taking into account the different sample preparations and excitation laser intensities in these experiments). On the other hand, the step-scan IR spectroscopy still detects the excited state with an effective lifetime of about 11 μs at 150 K (Table S8.2), whereas the steady-state PL signal is very weak and decays on the sub-microsecond time scale at this temperature (see above). This discrepancy might indicate that the photophysical scheme in Figure 6 – primarily focused on the emissive excited states – is oversimplified for **3** and some other non-emissive long-lived (triplet) state might be involved. It may be minor below 100 K, but dominant over microseconds after laser pulse excitation at higher temperatures. This issue requires further investigation. In addition to the frontier molecular orbitals (Figure S9.1), we illustrate the electronic character of the T_1 state of **3** by a spin density plot (Figure 8).

It clearly indicates spin localization on the phenyl groups, nitrogen atoms and, to a minor extent, on the copper atoms. This correlates with the structural changes in the excited state: for instance, asymmetric NPN bite angles of 98.4° and 108.1° were calculated for the two iminophosphonamide units of **3** in the T_1 state, compared to the equal angles of 108.5° in the S_0 state. The structural parameters of the S_0 and T_1 states are listed in the supporting information (Table S9.1).

Conclusions

We described the synthesis of a series of binuclear Cu(I) and mononuclear Zn(II) iminophosphonamide complexes. Four differently substituted iminophosphonamide ligands were employed. Except the Zn complex **7** with a single iminophosphonamide ligand, they all adopt coordination of two ligands to the metal centers, similar to the structurally related alkali metal and calcium complexes.^[11,14] Due to the different steric demand of the substituents the arrangement of the complexes in the solid-state varies slightly, which influences the photophysical proper-

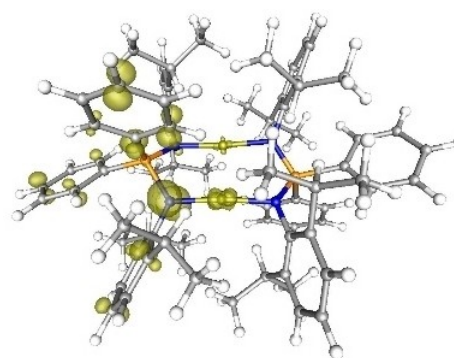


Figure 8. Spin density of **3** in its T_1 state (isovalue: 0.01 a.u.) (DFT/B3LYP-D3(BJ)/def2-TZVP). It localizes mainly at the phenyl rings and the N atoms of the iminophosphonamide ligand.

ties. Some of the Cu(I) and Zn(II) complexes show bright long-lived phosphorescence in the solid state at low temperatures (< 100 K), which transforms into thermally activated delayed fluorescence (TADF) at elevated temperatures - similar to their alkali metal and calcium analogues. While the PL of two Cu complexes (2, 3) can also be described within the TADF scheme, there is a qualitative difference insofar as these complexes, involve the *non-emissive* relaxed singlet excited state S_1 coupled by intersystem crossing (ISC) to the low-lying *emissive* triplet state T_1 . Accordingly, 2 and 3 show bright phosphorescence below ≈ 80 K, its thermally activated quenching in the narrow temperature interval above ≈ 80 K, and practically no PL above ≈ 150 K. Transient step-scan FTIR spectroscopy on the Cu complex 3 allowed further probing of the T_1 state. The step-scan FTIR spectra revealed a characteristic T_1 state vibration assigned to the phenyl stretching mode on the basis of DFT calculations. This mode in turn fingerprints the structural relaxation of 3 upon population of the T_1 state. In contrast, two Zn complexes (6, 7) were found to exhibit solely prompt fluorescence. The poor triplet formation in these compounds was attributed to their particular ligand coordination. The present work thus further illustrates the very diverse PL properties of metal complexes based on iminophosphonamide ligands.

Remarkably, the energy levels of the S_1 and T_1 states appear rather similar (and energetically close to each other) in most of iminophosphonamide metal complexes studied so far.^[11,14] In this regard, the specific ligand structure and coordination arrangement primarily affect the rates of transitions within a common framework of ground and excited states. Of particular interest is the possibility to strongly influence ISC efficiency and corresponding triplet formation (as well as TADF output) via subtle changes in ligand design and choice of the metal centers/ coordination.

From application point of view, the iminophosphonamide metal complexes studied so far cannot compete in terms of quantum efficiency and, very importantly, processing with well-established TADF emitters like purely organic 2,4,5,6-tetra(9H-carbazol-9-yl)isophthalonitrile.^[12b] However, we believe that both synthetic and photophysical potential of this class of luminescent metal complexes is by far not fully explored and may promise further examples with interesting (and perhaps also practically relevant) photophysical properties.

Experimental Section

Experimental details are given in the supporting information. The supporting information also compiles crystallographic and spectroscopic data for all new compounds (^1H , $^{13}\text{C}\{^1\text{H}\}$, $^{31}\text{P}\{^1\text{H}\}$ NMR, IR, Raman and PL spectra), as well as additional data from step-scan FTIR experiments and DFT calculations.

Deposition numbers 2075954 (1), 2075955 (2), 2075956 (3), 2075957 (4), 2075958 (5), 2075959 (6), and 2075960 (7) contain the supplementary crystallographic data for this paper. These data are provided free of charge by the joint Cambridge Crystallographic Data Centre and Fachinformationszentrum Karlsruhe Access Structures service.

Acknowledgements

Financial support by the DFG-funded transregional collaborative research center SFB/TRR 88 "Cooperative Effects in Homo and Heterometallic Complexes (3MET)" is gratefully acknowledged (projects C2, C3 and C7). Open Access funding enabled and organized by Projekt DEAL.

Conflict of Interest

The authors declare no conflict of interest.

Keywords: copper · iminophosphonamides · photoluminescence · step-scan FTIR · TADF · zinc

- [1] A. Steiner, S. Zacchini, P. I. Richards, *Coord. Chem. Rev.* **2002**, *227*, 193–216.
- [2] F. T. Edelmann, *Chem. Soc. Rev.* **2012**, *41*, 7657–7672.
- [3] A. M. Kalsin, T. A. Peganova, I. S. Sinopalnikova, I. V. Fedyanin, N. V. Belkova, E. Deydier, R. Poli, *Dalton Trans.* **2020**, *49*, 1473–1484.
- [4] S. Takahashi, J. Sekiguchi, A. Ishii, N. Nakata, *Angew. Chem. Int. Ed.* **2021**, *60*, 4055–4059; *Angew. Chem.* **2021**, *8*, 4101–4105.
- [5] a) C. Fedorchuk, M. Copey, T. Chivers, *Coord. Chem. Rev.* **2007**, *251*, 897–924; b) D.-Y. Lu, T.-S. Kuo, Y.-C. Tsai, *Angew. Chem. Int. Ed.* **2016**, *55*, 11614–11618; *Angew. Chem.* **2016**, *38*, 11786–11790.
- [6] a) S.-O. Hauber, F. Lissner, G. B. Deacon, M. Niemeyer, *Angew. Chem. Int. Ed.* **2005**, *44*, 5871–5875; *Angew. Chem.* **2005**, *36*, 6021–6025; b) C. GuhaRoy, R. J. Butcher, S. Bhattacharya, *J. Organomet. Chem.* **2008**, *693*, 3923–3931; c) M. R. Gyton, A. R. Leverett, M. L. Cole, A. I. McKay, *Dalton Trans.* **2020**, *49*, 5653–5661.
- [7] a) F. Pauer, J. Rocha, D. Stalke, *J. Chem. Soc. Chem. Commun.* **1991**, 1477–1479; b) R. Fleischer, B. Walfort, A. Gbureck, P. Scholz, W. Kiefer, D. Stalke, *Chem. Eur. J.* **1998**, *4*, 2266–2274; c) M. M. Meinholz, S. K. Pandey, S. M. Deuerlein, D. Stalke, *Dalton Trans.* **2011**, *40*, 1662–1671.
- [8] B. Prashanth, S. Singh, *J. Chem. Sci.* **2015**, *127*, 315–325.
- [9] A. Stasch, *Chem. Eur. J.* **2012**, *18*, 15105–15112.
- [10] a) S. Bestgen, C. Schoo, B. L. Neumeier, T. J. Feuerstein, C. Zovko, R. Köppe, C. Feldmann, P. W. Roesky, *Angew. Chem. Int. Ed.* **2018**, *57*, 14265–14269; *Angew. Chem.* **2018**, *43*, 14461–14465; b) M. K. Rong, F. Holtrup, J. C. Sloopweg, K. Lammertsma, *Coord. Chem. Rev.* **2019**, *382*, 57–68; c) C. Zovko, S. Bestgen, C. Schoo, A. Görner, J. M. Goicoechea, P. W. Roesky, *Chem. Eur. J.* **2020**, *26*, 13191–13202.
- [11] T. J. Feuerstein, B. Goswami, P. Rauthe, R. Köppe, S. Lebedkin, M. M. Kappes, P. W. Roesky, *Chem. Sci.* **2019**, *10*, 4742–4749.
- [12] a) A. Endo, M. Ogasawara, A. Takahashi, D. Yokoyama, Y. Kato, C. Adachi, *Adv. Mater.* **2009**, *21*, 4802–4806; b) H. Uoyama, K. Goushi, K. Shizu, H. Nomura, C. Adachi, *Nature* **2012**, *492*, 234–238; c) Y. Tao, K. Yuan, T. Chen, P. Xu, H. Li, R. Chen, C. Zheng, L. Zhang, W. Huang, *Adv. Mater.* **2014**, *26*, 7931–7958; d) H. Yersin, R. Czerwieniec, M. Z. Shafikov, A. F. Suleymanova, *Highly Efficient OLEDs: Materials Based on Thermally Activated Delayed Fluorescence*, Wiley Periodicals, Weinheim, **2018**, p. 1; e) T. J. Penfold, F. B. Dias, A. P. Monkman, *Chem. Commun.* **2018**, *54*, 3926–3935.
- [13] H. Khandelwal, A. R. Mallia, R. T. Cheriya, M. Hariharan, *Phys. Chem. Chem. Phys.* **2012**, *14*, 15282–15285.
- [14] B. Goswami, T. J. Feuerstein, R. Yadav, R. Köppe, S. Lebedkin, M. M. Kappes, P. W. Roesky, *Chem. Eur. J.* **2021**, *27*, 4401–4411.
- [15] a) D. M. Zink, M. Bächle, T. Baumann, M. Nieger, M. Kühn, C. Wang, W. Klöpper, U. Monkowius, T. Hofbeck, H. Yersin, S. Bräse, *Inorg. Chem.* **2013**, *52*, 2292–2305; b) D. M. Zink, T. Baumann, J. Friedrichs, M. Nieger, S. Bräse, *Inorg. Chem.* **2013**, *52*, 13509–13520; c) M. J. Leiti, V. A. Krylova, P. I. Djurovich, M. E. Thompson, H. Yersin, *J. Am. Chem. Soc.* **2014**, *136*, 16032–16038; d) R. Czerwieniec, M. J. Leiti, H. H. H. Homeier, H. Yersin, *Coord. Chem. Rev.* **2016**, *325*, 2–28; e) M. Klein, N. Demirel, A. Schinabeck, H. Yersin, J. Sundermeyer, *Molecules* **2020**, *25*, 3990; f) G. U. Mahoro, J. Fernandez-Cestau, J.-L. Renaud, P. B. Coto, R. D. Costa, S. Gaillard, *Adv. Opt. Mater.* **2020**, *8*, 2000260.

- [16] a) H. Ackermann, O. Bock, U. Müller, K. Dehnicke, *Z. Anorg. Allg. Chem.* **2000**, *626*, 1854–1856; b) T. J. Feuerstein, *Synthese photolumineszenter Metallkomplexe, UV-LED NMR-Charakterisierung eines photolabilen Komplexes sowie photolithographische Immobilisierung von Metallopolymere*, PhD Thesis, Karlsruhe Institute of Technology (KIT), Karlsruhe, Germany, **2019**; c) B. Goswami, *Enantiopure Iminophosphonamide Complexes: Synthesis, Photoluminescence and Catalysis*, PhD Thesis, Karlsruhe Institute of Technology (KIT), Karlsruhe, Germany, **2020**.
- [17] M. J. Leitl, F.-R. Küchle, H. A. Mayer, L. Wesemann, H. Yersin, *J. Phys. Chem. A* **2013**, *117*, 11823–11836.
- [18] A. C. Lane, C. L. Barnes, W. E. Antholine, D. Wang, A. T. Fiedler, J. R. Walensky, *Inorg. Chem.* **2015**, *54*, 8509–8517.
- [19] B. S. Lim, A. Rahtu, J.-S. Park, R. G. Gordon, *Inorg. Chem.* **2003**, *42*, 7951–7958.
- [20] Z. Chen, A. Lohr, C. R. Saha-Möller, F. Würthner, *Chem. Soc. Rev.* **2009**, *38*, 564–584.
- [21] M. Llunell, P. Alemany, S. Alvarez, Shape 2.1 for Windows (32 bit). Available from: http://www.ee.ub.edu/index.php?option=com_jdownloads&view=viewcategories&Itemid=529. Accessed: 09/03/2021.
- [22] J. R. Lakowicz, *Principles of Fluorescence Spectroscopy* (Ed.: J. R. Lakowicz), Springer US, Boston, MA, **2006**, p. 1.
- [23] a) Y. Cakmak, S. Kolemen, S. Duman, Y. Dede, Y. Dolen, B. Kilic, Z. Kostereli, L. T. Yildirim, A. L. Dogan, D. Guc, E. U. Akkaya, *Angew. Chem. Int. Ed.* **2011**, *50*, 11937–11941; *Angew. Chem.* **2011**, *50*, 12143–12147; b) N. Epelde-Elezcano, E. Palao, H. Manzano, A. Prieto-Castañeda, A. R. Agarrabeitia, A. Tabero, A. Villanueva, S. de la Moya, Í. López-Arbeloa, V. Martínez-Martínez, M. J. Ortiz, *Chem. Eur. J.* **2017**, *23*, 4837–4848.
- [24] G. D. Smith, M. S. Hutson, Y. Lu, M. T. Tierney, M. W. Grinstaff, R. A. Palmer, *Appl. Spectrosc.* **2001**, *55*, 637–642.
- [25] a) M. Zimmer, F. Dietrich, D. Volz, S. Bräse, M. Gerhards, *ChemPhysChem* **2017**, *18*, 3023–3029; b) M. Dorn, J. Kalmbach, P. Boden, A. Pöpcke, S. Gómez, C. Förster, F. Kuczelinis, L. M. Carrella, L. A. Büldt, N. H. Bings, E. Rentschler, S. Lochbrunner, L. González, M. Gerhards, M. Seitz, K. Heinze, *J. Am. Chem. Soc.* **2020**, *142*, 7947–7955; c) P. Boden, P. Di Martino-Fumo, J. M. Busch, F. R. Rehak, S. Steiger, O. Fuhr, M. Nieger, D. Volz, W. Klopfer, S. Bräse, M. Gerhards, *Chem. Eur. J.* **2021**, *27*, 5439–5452.
- [26] J. M. Busch, D. M. Zink, P. Di Martino-Fumo, F. R. Rehak, P. Boden, S. Steiger, O. Fuhr, M. Nieger, W. Klopfer, M. Gerhards, S. Bräse, *Dalton Trans.* **2019**, *48*, 15687–15698.

Manuscript received: April 7, 2021
Accepted manuscript online: April 26, 2021
Version of record online: June 1, 2021

Chemistry–A European Journal

Supporting Information

Thermally Activated Delayed Fluorescence and Phosphorescence Quenching in Iminophosphonamide Copper and Zinc Complexes

Bhupendra Goswami, Thomas J. Feuerstein, Ravi Yadav, Sergei Lebedkin, Pit J. Boden, Sophie T. Steiger, Gereon Niedner-Schatteburg, Markus Gerhards, Manfred M. Kappes, and Peter W. Roesky*

Table of Contents

1. Experimental section	S1
1.1 General Procedures.....	S1
1.2 Nuclear Magnetic Resonance (NMR) Spectroscopy	S1
1.3 Elemental Analysis (EA)	S1
1.4 Infrared (IR) Spectroscopy.....	S2
1.5 Electron Ionization (EI) Mass Spectrometry.....	S2
1.6 Single Crystal X-ray Diffraction.....	S2
1.7 Photoluminescence (PL) Measurements	S2
1.8 Step-scan Fourier-Transform Infrared (FTIR) Spectroscopy	S3
1.9 Theoretical Methods	S4
2. Synthesis	S5
[Cu ₂ {(R)-PEPIA} ₂] (1).....	S5
[Cu ₂ {(R)-PE ^{Dipp} PIA} ₂] (2).....	S6
[Cu ₂ {DippPIA} ₂] (3).....	S7
[Cu ₂ {(R)-NEPIA} ₂] (4)	S8
[Zn{(R)-PEPIA} ₂] (5)	S9
[Zn{(R)-PE ^{Dipp} PIA} ₂] (6)	S10
[Zn{DippPIA}Ph] (7).....	S11
3. NMR spectra.....	S12
4. IR spectra.....	S23
5. EI-MS spectra	S27
6. Crystallographic data	S28
7. Photoluminescence data.....	S34
8. Step-scan FTIR spectroscopy.....	S43
9. Additional calculated data	S49
10. References.....	S53

Supporting Information

1. Experimental section

1.1 General Procedures

All manipulations of air-sensitive materials were performed under the rigorous exclusion of oxygen and moisture in flame-dried Schlenk-type glassware either on a dual manifold Schlenk line, interfaced to a high vacuum (10^{-3} torr) line, or in an argon-filled MBraun glove box. Hydrocarbon solvents (toluene, *n*-pentane) were dried by using an MBraun solvent purification system (SPS-800), degassed and stored under vacuum. *n*-hexane and thf were predried over CaCl_2 before decantation, distillation from potassium benzophenoneketyl and storage over 4 Å molecular sieves. MeOH was predried over CaCl_2 before decantation, distillation from magnesium turnings and storage over 3 Å molecular sieves. Dichloromethane (dcm) was distilled from phosphorus pentoxide and stored over 4 Å molecular sieves. Copper(I)chloride was obtained from abcr, Potassium bis(trimethylsilyl)amide 95% and Diphenylzinc were obtained from Sigma Aldrich, the 1.2 molar dimethylzinc solution in toluene was obtained from Acros Organics. All purchased chemicals were used without further purification.

{{(R)-HPEPIA, (R)-LiPEPIA}^[1], (R)-HPE^{Dipp}PIA,^[2] (R)-HNEPIA,^[2] and H-DippPIA^[3] were synthesised according to their respective literature.

1.2 Nuclear Magnetic Resonance (NMR) Spectroscopy

NMR spectra were recorded on a Bruker Avance II 300 MHz or Avance III 400 MHz. Chemical shifts were measured relative to the characteristic solvent resonances as internal standards [7.16 ppm (^1H) and 128.06 ppm (^{13}C)]. They are expressed in parts per million (ppm) and reported relative to tetramethylsilane. 85% phosphoric acid was used as external reference for ^{31}P - and $^{31}\text{P}\{^1\text{H}\}$ -NMR. ^1H -NMR spectra are reported as follows: chemical shift (δ in ppm), multiplicity (br for broad singlet, s for singlet, d for doublet, q for quartet, m for multiplet), coupling constant(s) (Hz), number of protons (concluded from the integrals), specific assignment. $^{13}\text{C}\{^1\text{H}\}$ NMR spectra are reported in terms of the chemical shift and specific assignment. If necessary, NMR assignments were made using a combination of 1D and 2D techniques [^1H - ^1H COSY, ^1H - ^{13}C HMQC, and ^1H - ^{13}C HMBC].

All compounds were thoroughly dried before examination of the NMR spectra to remove any disturbing solvent signals if possible.

1.3 Elemental Analysis (EA)

Elemental analyses were carried out with a Vario Micro Cube (Elementar Analysensysteme GmbH).

Supporting Information

1.4 Infrared (IR) Spectroscopy

IR spectra were obtained on a Bruker Tensor 37 FTIR spectrometer equipped with a room temperature DLaTGS detector, a diamond ATR (attenuated total reflection) unit, and a nitrogen flushed chamber. In terms of their intensity, the signals were classified into the categories vs = very strong, s = strong, m = medium, w = weak and vw = very weak.

1.5 Electron Ionization (EI) Mass Spectrometry

EI mass spectra were recorded at 70 eV on a Finnigan MAT 8200 instrument.

1.6 Single Crystal X-ray Diffraction

A suitable crystal was covered in mineral oil (Aldrich) and mounted on a glass fiber. The crystal was transferred directly to the cold stream of a STOE IPDS 2 or a STOE StadiVari diffractometer. All structures were solved by using the programs SHELXS/T^[4] and Olex2^[5]. The remaining non-hydrogen atoms were located from successive difference Fourier map calculations. The refinements were carried out by using full-matrix least-squares techniques on F2 by using the program SHELXL.^[4a] In each case, the locations of the largest peaks in the final difference Fourier map calculations, as well as the magnitude of the residual electron densities, were of no chemical significance.

Crystallographic data for the structures reported in this paper have been deposited at the Cambridge Crystallographic Data Centre as a supplementary publication no. 2075954-2075960. Copies of the data can be obtained free of charge on application to CCDC, 12 Union Road, Cambridge CB21EZ, UK (fax: +(44)1223-336-033; email: deposit@ccdc.cam.ac.uk).

1.7 Photoluminescence (PL) Measurements

PL measurements were performed with a Horiba Jobin Yvon Fluorolog-322 spectrometer equipped with a closed-cycle optical cryostat operating within a temperature range of ca. 5-300 K. A Hamamatsu R9910 photomultiplier was used as detector for the emission spectral range of about 300-830 nm. The solid samples (crystalline powders) were measured as dispersions in a thin layer of viscous polyfluoroester oil (ABCR) placed between two 1 mm quartz (Spectrosil® 2000) plates. The latter were mounted on the cold finger of the cryostat. All emission spectra were corrected for the wavelength-dependent response of the spectrometer and detector (in relative photon flux units). Emission decay traces were recorded by connecting a photomultiplier to a 500 MHz LeCroy LT322 oscilloscope (via a 50, 500, 2.500 or 10.000-Ohm load depending

Supporting Information

on the decay time scale) and using a nitrogen laser (~2 nsec, ~5 μ J per pulse) for pulsed photoexcitation. For compound **7** a quadrupled Nd:YAG laser at 266 nm excitation wavelength was applied. PL efficiencies of solid complexes at ambient temperature were determined using an integrating sphere out of optical PTFE, which was installed into the sample chamber of the spectrometer, according to the method of de Mello *et al.*^[6] The uncertainty of this measurement was estimated to be $\pm 10\%$.

For TADF, the energy separation ΔE between S_1 and T_1 states can be estimated from the temperature dependence of PL decay time, $\tau(T)$, within the simple model of the thermally equilibrated S_1 and T_1 states, according to equation S1:^[7]

$$\tau(T) = \frac{3 + \exp\left(-\frac{\Delta E}{kT}\right)}{\frac{3}{\tau(T_1)} + \frac{1}{\tau(S_1)} \exp\left(-\frac{\Delta E}{kT}\right)} \quad (\text{S1})$$

where kT is the thermal energy, $\tau(S_1)$ and $\tau(T_1)$ are the intrinsic fluorescence and phosphorescence lifetimes, and statistical factor 3 takes into account three T_1 substates. Note that this model does not account for temperature dependences of both radiative and nonradiative relaxation processes. The assumption of the thermally equilibrated S_1 and T_1 states implies that the forward and reversed intersystem crossing which couples S_1 and T_1 is much faster than any other (non)radiative relaxation process involving these states.

1.8 Step-scan Fourier-Transform Infrared (FTIR) Spectroscopy

All the time-resolved FTIR experiments were performed with the FTIR spectrometer Bruker Vertex 80v, operated in the step-scan mode. A liquid-nitrogen-cooled mercury cadmium telluride (MCT) detector (Kolmar Tech., Model KV100-1-B-7/190) with a rise time of 25 ns, connected to a fast preamplifier and a 14-bit transient recorder board (Spectrum Germany, M3I4142, 400 MS/s), was used for signal detection and processing. The laser setup used for the measurements includes a Q-switched Nd:YAG laser (Innolas SpitLight Evo I) generating pulses with a duration of about 6 ns at a repetition rate of 100 Hz. The third harmonic (355 nm) of the Nd:YAG laser was used directly for sample excitation. The UV pump beam was attenuated to about 1.5 mJ per shot at a diameter of 9 mm. The beam was directed onto the sample and adjusted to have a maximal overlap with the IR beam of the spectrometer. The sample chamber was equipped with anti-reflection-coated germanium filters to prevent the entrance of laser radiation into the detector and interferometer compartments.

For the preparation of a KBr pellet, compound **3** (1.2 mg) was mixed with dry KBr (180 mg, stored in a compartment dryer at 80 °C, purchased from Merck) and ground to a homogenous mixture. This mixture was filled in an evacuable pellet die with a diameter of 13 mm and sintered at a pressure of 0.75 GPa. Experiments at temperatures between 20 K and 150 K at the pellet were performed using a closed-cycle helium cryostat

Supporting Information

(ARS Model DE-202A) to cool down the sample held at a background pressure of $p \leq 5 \cdot 10^{-5}$ mbar. The cryocooler was equipped with a pellet holder (copper) and CaF_2 windows.

The temporal resolution of the 14-bit transient recorder board was chosen according to the excited state lifetime of the system and set to 100 ns at 20 K/70 K and 20 ns at 120 K/150 K. The time at which the laser pulse reached the sample was set as zero point in all spectra. The time delay between the start of the experiment and the laser pulse was set to 1.3 μs and controlled with a Stanford Research Systems DG535 delay generator. The spectral region was limited by undersampling to 988 – 1975 cm^{-1} with a spectral resolution of 4 cm^{-1} resulting in 555 interferogram points. An IR broadband filter (850 – 1750 cm^{-1}) and CaF_2 windows (no IR transmission < 1000 cm^{-1}) prevented problems when performing a Fourier transformation (i.e. no IR intensity outside the measured region should be observed). FTIR ground state spectra were recorded systematically to check if there is no sample degradation.

1.9 Theoretical Methods

The molecular structure of compound **3** from X-ray crystallography was used as input structure and geometry optimizations were performed with the Bery algorithm of Gaussian 09^[8] by using energies and gradients computed by Turbomole 7.4.^{[9][10]} All calculations were performed with the DFT functional B3LYP with dispersion correction (no three-body interaction) (D3(BJ))^[11] as implemented in Turbomole using the resolution of identity (RI) approximation and the def2-TZVP basis set. The lowest triplet state was optimized as a ground state by unrestricted DFT (UDFT). Harmonic frequency calculations were performed for the optimized minimum structures. The vibrational frequencies are scaled by a factor of 0.975 to minimize the differences between the experimental and calculated frequencies. A Gaussian convolution with a full-width at half-maximum of 8 cm^{-1} was applied to the calculated vibrational transitions.

Additionally, the energetically lowest excited singlet and triplet states were optimized by time-dependent DFT with the same functional and basis set as in the ground state. All the indicated relative energies are corrected by the zero-point vibrational energy.

Supporting Information

2. Synthesis

[Cu₂{(R)-PEPIA}₂] (1)

The lithium iminophosphonamide [Li₂{(R)-PEPIA}₂] (200 mg, 0.23 mmol, 1.00 eq.) and 46 mg copper(I)chloride (0.46 mmol, 2.00 eq.) were dissolved in thf (10 mL). The reaction mixture was stirred for 20 h at room temperature. The solvent was evaporated under reduced pressure, the residue was extracted with dcm (15 mL) and filtered through a syringe filter. The solvent was evaporated under reduced pressure and the residue washed with *n*-pentane (3 x 20 mL). After drying under vacuum, the product was obtained as a white solid. Single crystals suitable for X-ray structure analysis were obtained in form of colourless needles after recrystallization from hot *n*-hexane.

Yield: 122 mg (54 %). **Elemental analysis** calc. (%) for [C₅₆H₅₆Cu₂N₄P₂] (974.13): C 69.05, H 5.79, N 5.75; found: C 67.66, H 5.54, N 5.52.

¹H-NMR (300 MHz, C₆D₆): δ [ppm] = 7.82-7.75 (m, 8 H, Ar-CH), 7.52-7.50 (m, 8 H, Ar-CH), 7.19-7.07 (m, 24 H, Ar-CH), 4.13 (dq, ³J_{PH} = 18.8 Hz, ³J_{HH} = 6.5 Hz, 4 H, CH), 1.58 (d, ³J_{HH} = 6.5 Hz, 12 H, CH₃). – ¹³C{¹H}-NMR (75 MHz, C₆D₆): δ [ppm] = 149.7 (³J_{PC} = 6.5 Hz, *i*-Ar-C), 133.9 (d, ¹J_{PC} = 96.9 Hz, *i*-Ar_{phos}-C), 133.2 (d, ²J_{PC} = 8.8 Hz, *o*-Ar_{phos}-CH), 130.6 (d, ⁴J_{PC} = 2.7 Hz, *p*-Ar_{phos}-CH), 127.9 (d, ³J_{PC} = 11.3 Hz, *m*-Ar_{phos}-CH), 127.0 (*o*-Ar-CH), 125.8 (*p*-Ar-CH), 54.2 (d, ²J_{PC} = 5.0 Hz, CH), 30.4 (d, ³J_{PC} = 10.7 Hz, CH₃), the resonance for *m*-Ar-CH overlaps with the solvent signal. – ³¹P{¹H}-NMR (121 MHz, C₆D₆): δ [ppm] = 39.6. – IR (ATR): $\tilde{\nu}$ = 3054 (vw), 3022 (vw), 2957 (vw), 2917 (vw), 2857 (vw), 1599 (vw), 1488 (vw), 1435 (w), 1362 (vw), 1323 (vw), 1309 (vw), 1271 (vw), 1194 (vw), 1107 (s), 1067 (m), 1027 (m), 1008 (m), 996 (m), 976 (m), 884 (m), 745 (s), 715 (m), 693 (vs), 627 (w), 607 (w), 567 (w), 533 (m), 506 (s), 448 (vw) cm⁻¹. **EI-MS** *m/z* (fragment, calc., %) = 974.2430 ([M]⁺, 974.2567, 25); 959.2390 ([M-CH₃]⁺, 959.2332, 8). –

Supporting Information

[Cu₂{(R)-PE^{Dipp}PIA}₂] (2)

CuCl (38.0 mg, 0.38 mmol, 1.00 eq.), (R)-HDippPEPIA (183.0 mg, 0.38 mmol, 1.00 eq.) and KBTSA (76.0 mg, 0.38 mmol, 1.00 eq.) were dissolved in toluene (30 mL) and were stirred at room temperature for 16 h. After filtration the filtrate was concentrated under reduced pressure, which yielded a crystalline solid. The resulting colorless solid was washed with *n*-pentane (5 mL). Single crystals suitable for X-ray analysis were obtained from hot toluene. The solvent was decanted, and the product was washed with cold *n*-pentane (5 mL) before drying under vacuum and isolation as colorless solid.

Yield (based on crystals): 150 mg (34 %). **Elemental analysis** calcd. (%) for [C₇₁H₈₀Cu₂N₄P₂] (2·Toluene) (1178.46): C 72.36, H 6.84, N 4.75; found: C 72.99, H 7.07, N 4.99.

¹H-NMR (C₆D₆, 400 MHz): δ [ppm] = 7.97 (br, 4 H, Ar-CH), 7.46-7.44 (m, 4 H, Ar-CH), 7.32-7.28 (m, 4 H, Ar-CH), 7.14-7.09 (m, 9 H, Ar-CH), 7.01-6.76 (m, 15 H, Ar-CH), 4.18-4.11 (m, 2 H, Ph(CH)CH₃), 3.90-3.74 (m, 4 H, CH(CH₃)₂), 1.47 (d, ³J_{HH} = 6.42 Hz, 6 H, CH(CH₃)₂), 1.44 (d, ³J_{HH} = 6.76 Hz, 6 H, CH(CH₃)₂), 1.31 (d, ³J_{HH} = 6.70 Hz, 6 H, Ph(CH)CH₃), 0.65 (d, ³J_{HH} = 6.78 Hz, 6 H, CH(CH₃)₂), 0.43 (d, ³J_{HH} = 6.82 Hz, 6 H, CH(CH₃)₂). – ¹³C{¹H}-NMR (C₆D₆, 100 MHz): δ [ppm] = 148.5 (d, ³J_{PC} = 8.4 Hz, Ar-C_q), 147.5 (d, ¹J_{PC} = 5.0 Hz, Ar_{phos}-C_q), 146.7 (d, J_{PC} = 5.3 Hz, Ar-C), 141.2 (Ar-C), 133.7 (d, ³J_{PC} = 9.2 Hz, Ar-CH), 132.9 (d, ³J_{PC} = 8.6 Hz, Ar-CH), 130.6 (Ar-CH), 128.2 (Ar-CH), 128.0 (d, J_{PC} = 2.7 Hz, Ar-CH), 127.5 (Ar-CH), 127.4 (Ar-CH), 127.2 (Ar-CH), 126.4 (Ar-CH), 124.2 (Ar-CH), 124.02 (Ar-CH), 123.93 (Ar-CH), 56.2 (d, ²J_{PC} = 4.8 Hz, Ph(CH)CH₃), 30.9 (d, J_{PC} = 8.9 Hz, CH(CH₃)₂), 28.5 (d, ³J_{PC} = 23.1 Hz, Ph(CH)CH₃), 26.0 (d, ³J_{PC} = 24.2 Hz, Ph(CH)CH₃), 23.3 (CH(CH₃)₂), 22.4 (CH(CH₃)₂). – ³¹P{¹H}-NMR (C₆D₆, 121 MHz): δ [ppm] = 38.0. – IR (ATR): $\tilde{\nu}$ [cm⁻¹] = 3075 (vw), 3051 (vw), 2966 (m), 2947 (w), 2864 (w), 1587 (vw), 1489 (w), 1461 (w), 1450 (m), 1433 (s), 1381 (m), 1363 (m), 1309 (m), 1270 (m), 1191 (s), 1174 (s), 1119 (s), 1107 (s), 1090 (m), 1067 (s), 1052 (m), 1027 (s), 1005 (s), 997 (m), 975 (s), 931 (m), 887 (s), 833 (m), 796 (m), 763 (m), 754 (m), 746 (s), 730 (m), 716 (m), 692 (vs), 623 (w), 605 (m), 577 (s), 545 (m), 529 (vs), 512 (m), 503 (vs), 494 (m), 464 (m), 450 (m), 414 (vw).

Supporting Information

[Cu₂{DippPIA}₂] (3)

Following a similar procedure as described above for **2** the reaction of CuCl (74.0 mg, 0.74 mmol, 1.00 eq.), H-DippPIA (400.0 mg, 0.74 mmol, 1.00 eq.) and KBTSA (149.0 mg, 0.74 mmol, 1.00 eq.) afforded single crystals from toluene suitable for X-ray analysis. The solvent was decanted, and the product was washed with cold *n*-pentane (5 mL) before drying under vacuum and isolation as colorless solid.

Yield (based on crystals): 225 mg (25 %). **Elemental analysis** calcd. (%) for [C₇₂H₈₈Cu₂N₄P₂] (1198.56): C 72.15, H 7.40, N 4.67; found: C 72.65, H 6.70, N 4.67.

¹H-NMR (C₆D₆, 300 MHz): δ [ppm] = 9.94-9.89 (m, 2 H, Ar-CH), 7.73-7.68 (m, 2 H, Ar-CH), 7.36 (m, 2 H, Ar-CH), 7.13-7.02 (m, 12 H, Ar-CH), 6.96-6.92 (m, 4 H, Ar-CH), 6.80-6.77 (m, 2 H, Ar-CH), 6.66-6.62 (m, 6 H, Ar-CH), 6.34-6.29 (m, 2 H, Ar-CH), 4.45-4.37 (m, 4 H, CH(CH₃)₂), 3.66-3.59 (m, 4 H, CH(CH₃)₂), 1.82 (d, ³J_{HH} = 6.75, 12 H, CH(CH₃)₂), 1.12 (d, ³J_{HH} = 6.86, 12 H, CH(CH₃)₂), 0.47 (d, ³J_{HH} = 6.82, 12 H, CH(CH₃)₂), 0.35 (d, ³J_{HH} = 6.70, 12 H, CH(CH₃)₂). ¹³C{¹H}-NMR (C₆D₆, 75 MHz): δ [ppm] = 146.1 (Ar-C_q), 145.6 (d, J_{PC} = 5.7 Hz, Ar-C_q), 141.9 (Ar-C_q), 133.2 (d, J_{PC} = 6.9 Hz, Ar-C_q), 127.1 (d, ³J_{PC} = 10.6 Hz, Ar-CH), 124.4 (Ar-CH), 123.5 (d, ³J_{PC} = 42.0 Hz, Ar-CH), 100.1 (Ar-C), 68.1 (CH(CH₃)₂), 25.8 (CH(CH₃)₂). ³¹P{¹H}-NMR (C₆D₆, 121 MHz): δ [ppm] = 8.4 **IR** (ATR): $\tilde{\nu}$ [cm⁻¹] = 3055 (w), 2959 (s), 2921 (s), 2861 (m), 1589 (w), 1479 (m), 1456 (m), 1428 (m), 1381 (m), 1358 (m), 1311 (m), 1258 (s), 1246 (vs), 1230 (s), 1190 (vs), 1158 (m), 1111 (m), 1099 (m), 1070 (m), 1044 (s), 998 (m), 964 (m), 932 (m), 918 (s), 883 (m), 827 (m), 791 (m), 744 (vs), 712 (m), 696 (m), 621 (m), 609 (s), 600 (m), 581 (m), 539 (m), 518 (s), 507 (s), 482 (m), 453 (m), 427 (m).

Supporting Information

[Cu₂{(R)-NEPIA}₂] (4)

Following a similar procedure as described above for **1**, the reaction of CuCl (71.0 mg, 0.71 mmol, 1.00 eq.) with [K₂{(R)-NEPIA}₂] (400.0 mg, 0.74 mmol, 1.00 eq.) afforded single crystals from toluene suitable for X-ray analysis. The solvent was decanted, and the product was washed with cold *n*-pentane (5 mL) before drying under vacuum and isolation as colorless solid.

Yield (based on crystals): 250 mg (30 %). **Elemental analysis** calcd. (%) for [C₇₂H₆₄Cu₂N₄P₂] (1174.34): C 73.64, H 5.49, N 4.77; found: C 74.07, H 5.85, N 4.86.

¹H-NMR (C₆D₆, 300 MHz): δ [ppm] = 9.01 (d, ³J_{HH} = 6.7 Hz, 4 H, *o*-Ar_{phos}-CH), 7.91-7.86 (m, 8 H, Ar_{phos}-CH), 7.68-7.66 (m, 4 H, Ar-CH), 7.61-7.59 (m, 4 H, Ar-CH), 7.53-7.48 (m, 8 H, Ar-CH), 7.27-7.23 (m, 4 H, Ar-CH), 7.14-7.09 (m, 5 H, Ar-CH), 6.81-6.72 (m, 11 H, Ar-CH), 5.12 (dq, ³J_{HH} = 6.4 Hz, ³J_{PH} = 16.3 Hz, 4 H, naph(CH)CH₃), 1.9 (d, ³J_{PH} = 6.5 Hz, ³J_{HH} = 1.7 Hz, 12 H, naph(CH)CH₃). **¹³C{¹H}**-NMR (C₆D₆, 75 MHz): δ [ppm] = 145.6 (d, ³J_{PC} = 3.6 Hz, Ar-C_q), 134.0 (Ar-C), 133.7 (Ar-C), 132.9 (d, ³J_{PC} = 8.9 Hz, Ar-CH), 132.7 (Ar-CH), 131.2 (Ar-CH), 130.4 (Ar-CH), 128.9 (Ar-CH), 127.9 (Ar-CH), 127.7 (Ar-CH), 126.4 (d, J_{PC} = 20.5 Hz, Ar-CH), 125.1 (d, J_{PC} = 40.9 Hz Ar-C), 124.0 (Ar-CH), 123.3 (Ar-C), 50.6 (d, J_{PC} = 5.3 Hz, naph(CH)CH₃), 31.3 (d, ³J_{PC} = 13.8 Hz, naph(CH)CH₃). **³¹P{¹H}**-NMR (C₆D₆, 121 MHz): δ [ppm] = 40.2. **IR** (ATR): $\tilde{\nu}$ [cm⁻¹] = 3050 (m), 2963 (m), 2949 (vw), 1595 (m), 1510 (m), 1479 (vw), 1435 (m), 1393 (m), 1378 (m), 1363 (m), 1317 (m), 1302 (m), 1255 (m), 1226 (m), 1166 (m), 1141 (vs), 1117 (m), 1106 (s), 1100 (m), 1075 (s), 997 (s), 968 (m), 947 (m), 884 (m), 856 (vs), 839 (s), 796 (m), 776 (m), 746 (s), 715 (m), 694 (s), 653 (vs), 631 (s), 621 (s), 609 (vs), 579 (s), 554 (m), 521 (m), 508 (m), 496 (m), 480 (vs), 467 (s), 453 (m), 425 (m).

Supporting Information

[Zn{(R)-PEPIA}₂] (5)

The iminophosphoramidate (R)-HPEPIA (200 mg, 0.47 mmol, 1.00 eq.) was dissolved in toluene (10 ml) and cooled to -78°C. 0.42 ml of a 1.2 molar dimethylzinc solution in toluene (0.50 mmol, 1.07 eq.) was added. The reaction mixture was warmed to room temperature overnight. The solvent was evaporated under reduced pressure and the residue was redissolved in *n*-pentane (10 mL), whereas a clear colourless solution was obtained. During 16 h the product crystallized in form of colourless block-shaped single crystals suitable for X-ray crystallography. The Product was isolated as colourless solid after decantation of the mother liquor and drying under vacuum.

Yield (based on crystals): 132 mg (55 %). **Elemental analysis** calc. (%) for [C₅₆H₅₆N₄P₂Zn] (912.42): C 73.72, H 6.19, N 6.14; found: C 73.17, H 5.73, N 6.26.

¹H-NMR (300 MHz, C₆D₆): δ [ppm] = 7.67-7.56 (m, 14 H, Ar-H), 7.24-7.19 (m, 8 H, Ar-H), 7.11-7.00 (m, 18 H, Ar-H), 4.30 (dq, ³J_{PH} = 14.9 Hz, ³J_{HH} = 6.5 Hz, 4 H, CH), 1.65 (dd, ³J_{HH} = 6.6 Hz, ⁴J_{PH} = 1.7 Hz, 12 H, CH₃). – ¹³C{¹H}-NMR (75 MHz, C₆D₆): δ [ppm] = 149.9 (d, ³J_{PC} = 4.8 Hz, *i*-Ar-C), 132.9 (d, ²J_{PC} = 9.5 Hz, *o*-Ar_{phos}-CH), 132.8 (d, ¹J_{PC} = 91.7 Hz, *i*-Ar_{phos}-C), 130.7 (d, ⁴J_{PC} = 2.8 Hz, *p*-Ar_{phos}-CH), 128.3 (*m*-Ar-CH), 127.9 (d, ³J_{PC} = 11.3 Hz, *m*-Ar_{phos}-CH), 127.3 (*o*-Ar-CH), 126.3 (*p*-Ar-CH), 54.6 (d, ²J_{PC} = 1.5 Hz, CH), 30.6 (d, ³J_{PC} = 15.1 Hz, CH₃). – ³¹P{¹H}-NMR (121 MHz, C₆D₆): δ [ppm] = 35.7. – IR (ATR): $\tilde{\nu}$ = 3215 (w), 3055 (w), 3023 (w), 2960 (vw), 2918 (w), 2855 (w), 1595 (vw), 1486 (w), 1435 (w), 1347 (vw), 1304 (vw), 1274 (w), 1195 (w), 1142 (m), 1107 (s), 1067 (w), 1048 (w), 1025 (w), 976 (w), 837 (m), 745 (s), 719 (m), 693 (vs), 605 (m), 562 (m), 509 (vs). – EI-MS *m/z* (fragment, calc., %) = 910.3507 ([M]⁺, 910.3272, 34); 895.3166 ([M-CH₃]⁺, 895.3037, 71.5).

Supporting Information

[Zn{(R)-PE^{Dipp}PIA}]₂ (6)

ZnPh₂ (220.0 mg, 1.0 mmol, 1.00 eq.) and (R)-HPE^{Dipp}PIA (481.0 mg, 2.0 mmol, 2.00 eq.) was dissolved in toluene (30mL) and stirred afforded for 16 h. The solvent was removed under reduced pressure and product was washed with *n*-Pentane. The single crystals suitable for X-ray analysis was obtained from *n*-Pentane. The solvent was decanted, and the product was washed with cold *n*-pentane (5 mL) before drying under vacuum and isolation as colorless solid.

Yield (based on crystals): 410 mg (40 %). **Elemental analysis** calcd. (%) for [C₆₄H₇₂ZnN₄P₂] (1024.62): C 75.02, H 7.08, N 5.47; found: C 74.87, H 6.68, N 5.32.

¹H-NMR (C₆D₆, 400 MHz): δ [ppm] = 7.68-7.66 (m, 4 H, *o*-Ar_{phos}-CH), 7.40-7.35 (m, 4 H, Ar-CH), 7.14-7.07 (m, 10 H, Ar-CH), 6.94-6.84 (m, 12 H, Ar-CH), 6.76-6.72 (m, 2 H, Ar-CH), 6.65-6.61 (m, 4 H, Ar-CH), 3.79 (dq, ³J_{HH} = 6.53 Hz, ³J_{PH} = 18.57 Hz, 2 H, Ph(CH)CH₃), 3.42 (br, 4 H, CH(CH₃)₂), 1.37 (d, ³J_{HH} = 6.52 Hz, 6 H, Ph(CH)CH₃), 0.75 (br, 24 H, CH(CH₃)₂). ¹³C{¹H}-NMR (C₆D₆, 100 MHz): δ [ppm] = 149.2 (d, ³J_{PC} = 6.1 Hz, Ar-C_q), 148.1 (Ar-C_q), 146.0 (d, J_{PC} = 5.7 Hz, Ar-C_q), 140.5 (d, J_{PC} = 3.1 Hz, Ar-C), 139.4 (Ar-CH), 133.6 (Ar-CH), 132.5 (d, J_{PC} = 9.2 Hz, Ar-CH), 132.2 (d, J_{PC} = 9.4 Hz, Ar-CH), 131.5 (d, J_{PC} = 2.7 Hz, Ar-CH), 131.1 (Ar-CH), 130.2 (Ar-CH), 129.0 (Ar-CH), 126.9 (Ar-CH), 126.7 (Ar-CH), 123.9 (d, J_{PC} = 3.5 Hz, Ar-CH), 123.5 (d, J_{PC} = 3.0 Hz, Ar-CH), 54.2 (Ph(CH)CH₃), 30.4 (d, ³J_{PC} = 11.8 Hz, Ph(CH)CH₃), 28.9 (CH(CH₃)₂), 23.7 (CH(CH₃)₂). ³¹P{¹H}-NMR (C₆D₆, 162 MHz): δ [ppm] = 37.5 **IR** (ATR): $\tilde{\nu}$ [cm⁻¹] = 3347 (m), 3055 (m), 3024 (s), 2960 (m), 2864 (m), 1587 (w), 1482 (w), 1433 (vs), 1363 (s), 1316 (s), 1264 (m), 1203 (s), 1144 (s), 1113 (vs), 1049 (m), 1027 (m), 984 (m), 950 (m), 864 (m), 771 (m), 749 (m), 717 (m), 696 (vs), 574 (m), 512 (m).

Supporting Information

[Zn{DippPIA}Ph] (7)

ZnPh₂ (147.0 mg, 0.28 mmol, 1.00 eq.) and H-DippPIA (150.0 mg, 0.28 mmol, 1.00 eq.) were dissolved in toluene (30mL) and stirred for 16 h. The solvent was removed under reduced pressure and the product was washed with *n*-pentane. Single crystals suitable for X-ray analysis were obtained from *n*-pentane. The solvent was decanted, and the product was washed with cold *n*-pentane (5 mL) before drying under vacuum and isolation as colorless solid.

Yield (based on crystals): 120 mg (63 %). **Elemental analysis** calcd. (%) for [C₄₂H₄₉ZnN₂P] (678.22): C 74.38, H 7.28, N 4.13; found: C 73.68, H 6.78, N 4.16.

¹H-NMR (C₆D₆, 400 MHz): δ [ppm] = 7.63-7.61 (m, 2 H, Ar-CH), 7.33-7.28 (m, 4 H, Ar-CH), 7.14-7.12 (m, 9 H, Ar-CH), 6.92-6.77 (m, 6 H, Ar-CH), 3.88 (sept, ³J_{HH} = 6.81 Hz, 4 H, CH(CH₃)₂), 1.03 (d, 24 H, CH(CH₃)₂). ¹³C{¹H}-NMR (C₆D₆, 100 MHz): δ [ppm] = 146.9 (d, J_{PC} = 1.4 Hz, Ar-C_q), 146.3 (d, J_{PC} = 5.1 Hz, Ar-C_q), 140.9 (Ar-C_q), 139.5 (Ar-CH), 135.2 (Ar-CH), 134.3 (Ar-CH), 131.9 (d, J_{PC} = 8.7 Hz, Ar-CH), 131.2 (d, J_{PC} = 2.8 Hz, Ar-CH), 128.2 (Ar-CH), 127.8 (Ar-CH), 124.4 (d, J_{PC} = 2.8 Hz, Ar-CH), 124.0 (d, J_{PC} = 2.3 Hz, Ar-CH), 29.4 (CH(CH₃)₂), 24.1 (CH(CH₃)₂). ³¹P{¹H}-NMR (C₆D₆, 162 MHz): δ [ppm] = 17.2. **IR** (ATR): $\tilde{\nu}$ [cm⁻¹] = 3058 (w), 2962 (m), 2948 (m), 2922 (m), 2866 (m), 1588 (vw), 1457 (m), 1432 (s), 1382 (m), 1359 (m), 1335 (m), 1316 (s), 1285 (vs), 1256 (s), 1237 (s), 1210 (s), 1188 (s), 1116 (m), 1098 (m), 1078 (m), 1057 (m), 1043 (s), 996 (s), 988 (s), 932 (s), 815 (m), 786 (s), 755 (m), 744 (vs), 725 (m), 715 (m), 698 (vs), 670 (vs), 599 (m), 548 (m), 519 (m), 500 (s), 477 (s), 440 (m).

Supporting Information

3. NMR spectra

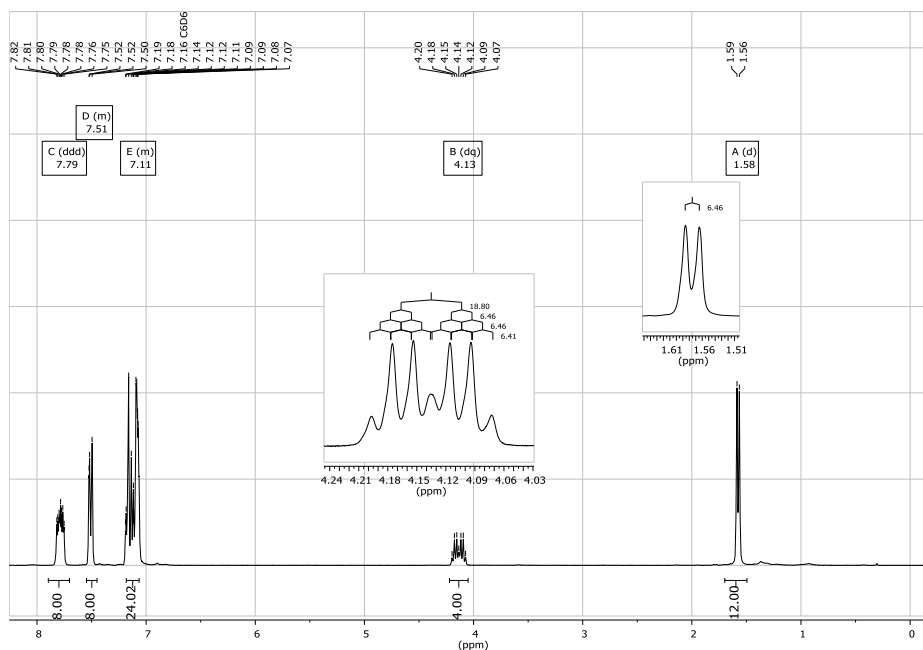


Figure S3.1. $^1\text{H-NMR}$ (300 MHz, C_6D_6 , 298 K) spectrum of **1**.

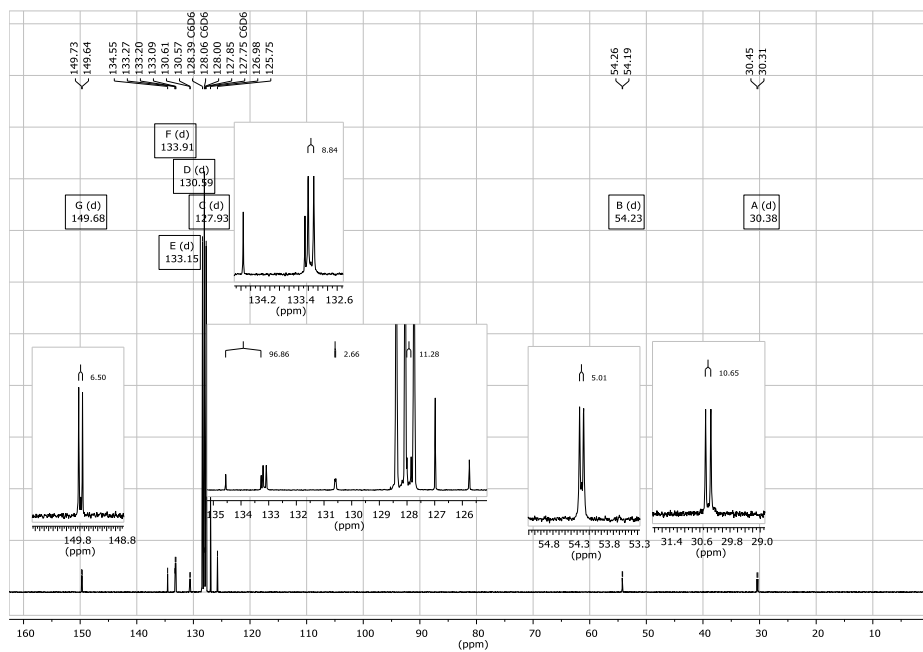
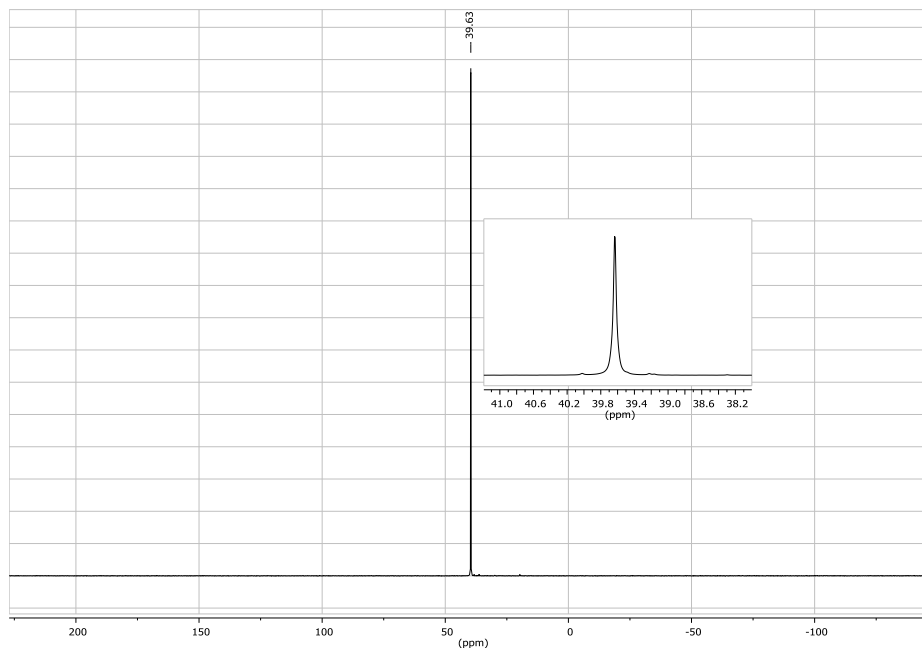
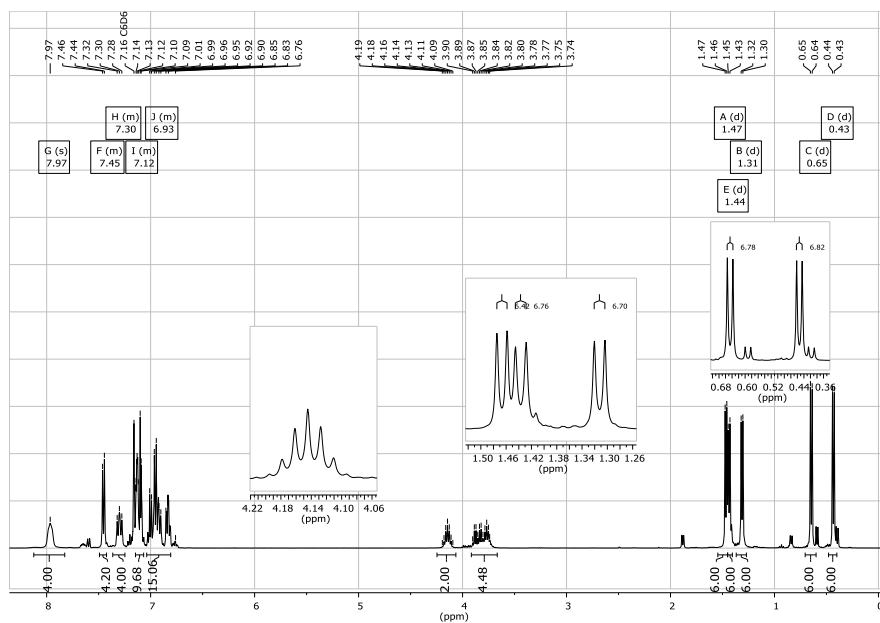
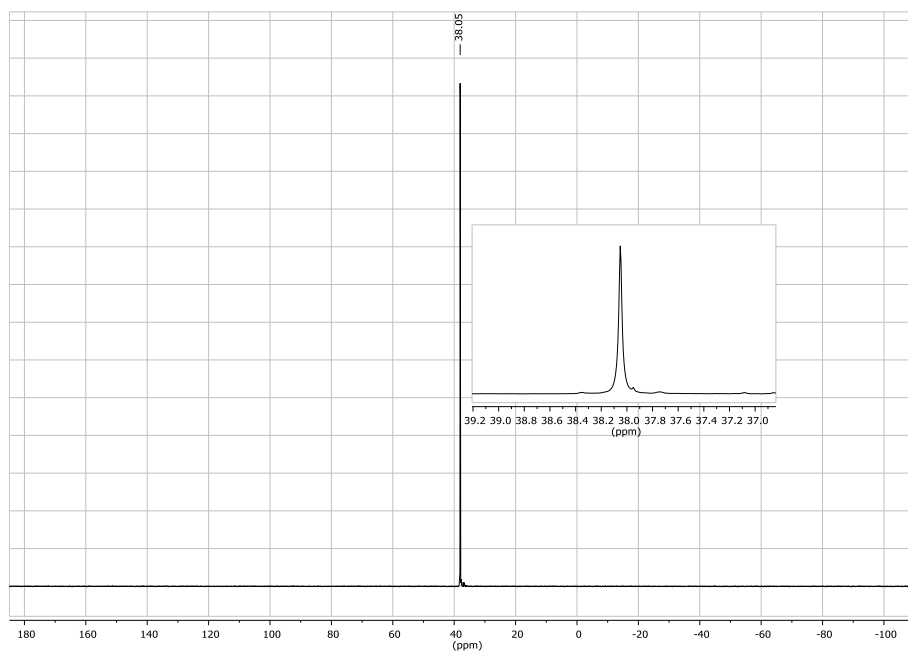
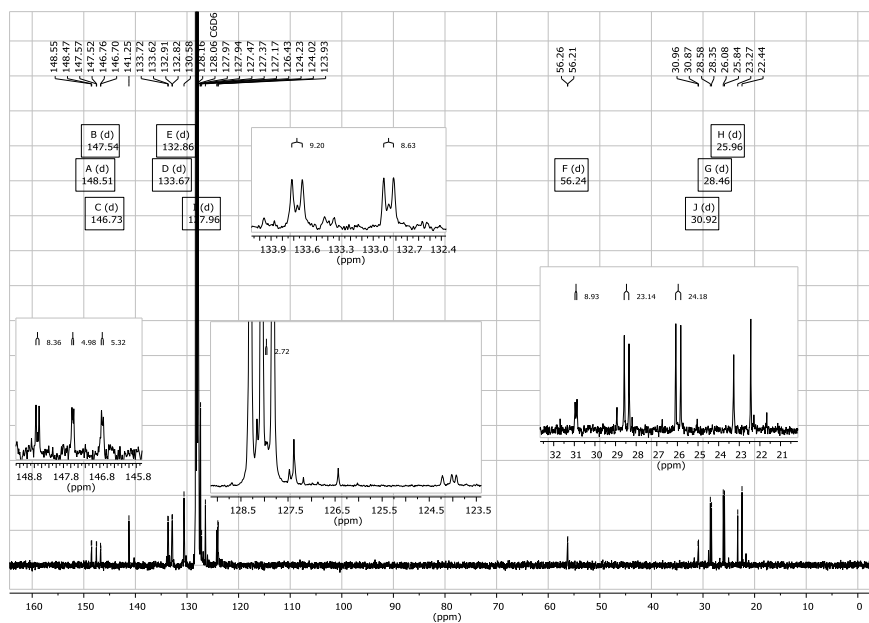


Figure S3.2. $^{13}\text{C}\{^1\text{H}\}$ -NMR (75 MHz, C_6D_6 , 298 K) NMR spectrum of **1**.

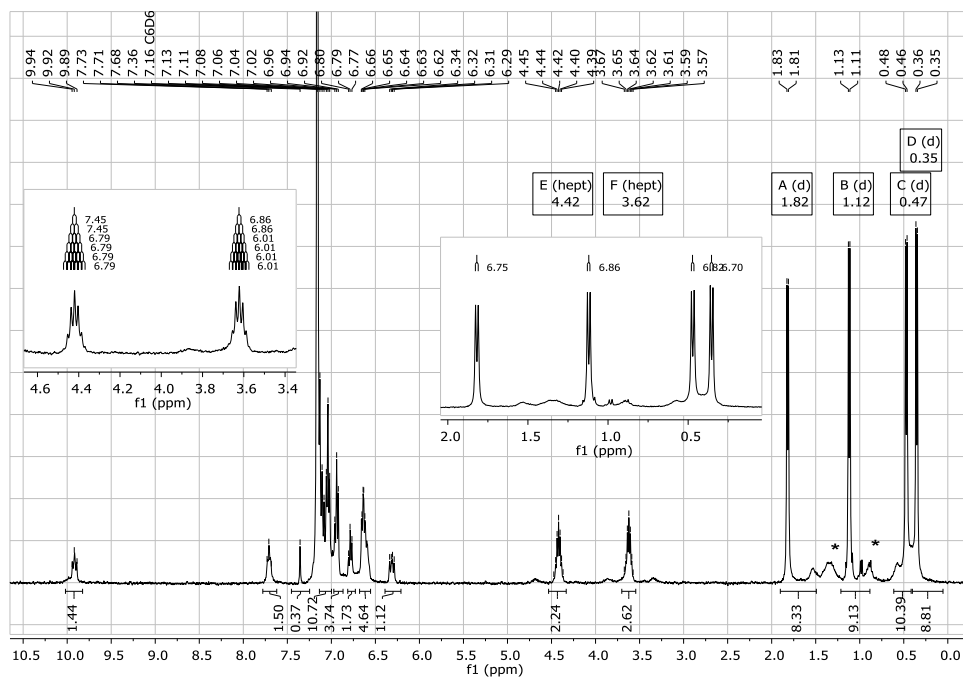
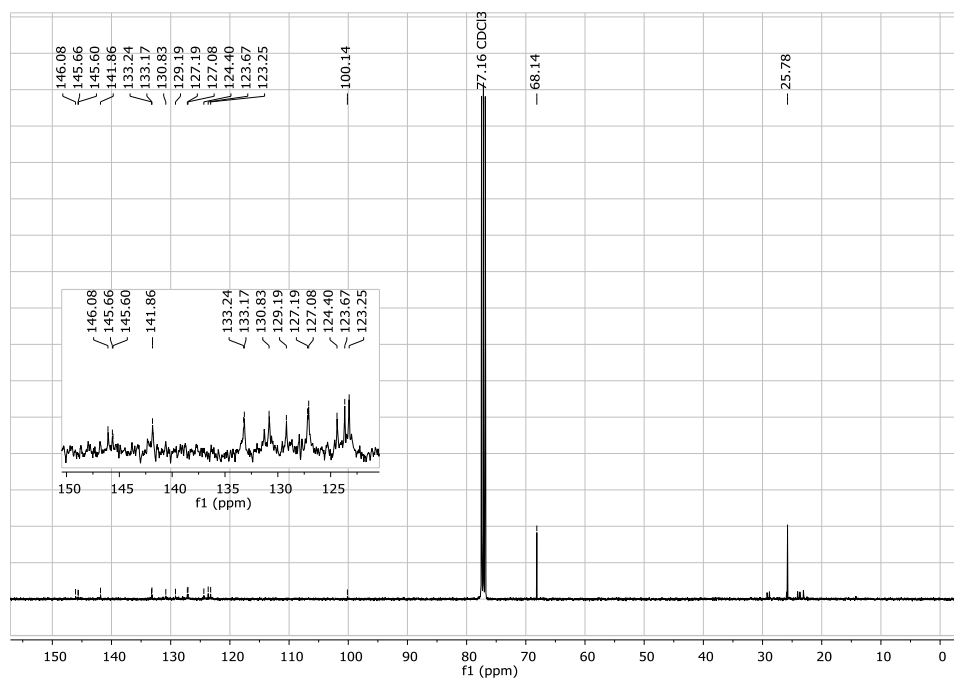
Supporting Information


 Figure S3.3. $^{31}\text{P}\{^1\text{H}\}$ -NMR (121 MHz, C_6D_6 , 298 K) spectrum of complex 1.

 Figure S3.4. ^1H (400 MHz, C_6D_6 , 298 K) NMR spectrum of complex 2.

Supporting Information



Supporting Information


 Figure S3.7. ¹H (400 MHz, C₆D₆, 298 K) NMR spectrum of complex 3. * = grease.

 Figure S3.8. ¹³C{¹H} (100 MHz, C₆D₆, 298 K) NMR spectrum of complex 3.

Supporting Information

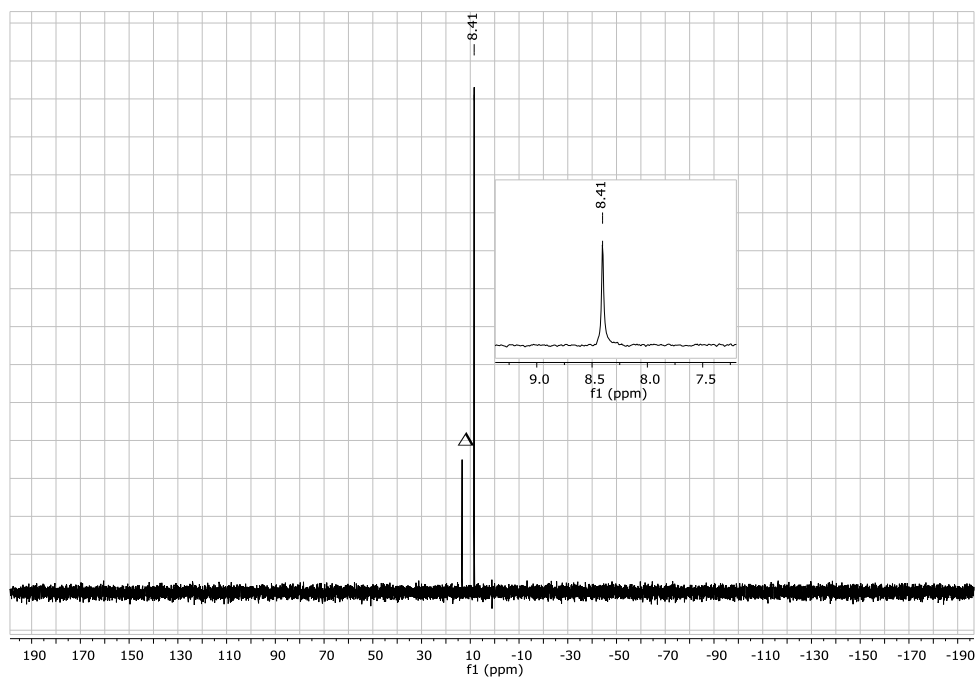


Figure S3.9. $^{31}\text{P}\{^1\text{H}\}$ (162 MHz, C_6D_6 , 298 K) NMR spectrum of complex 3 (Δ = unidentified impurity).

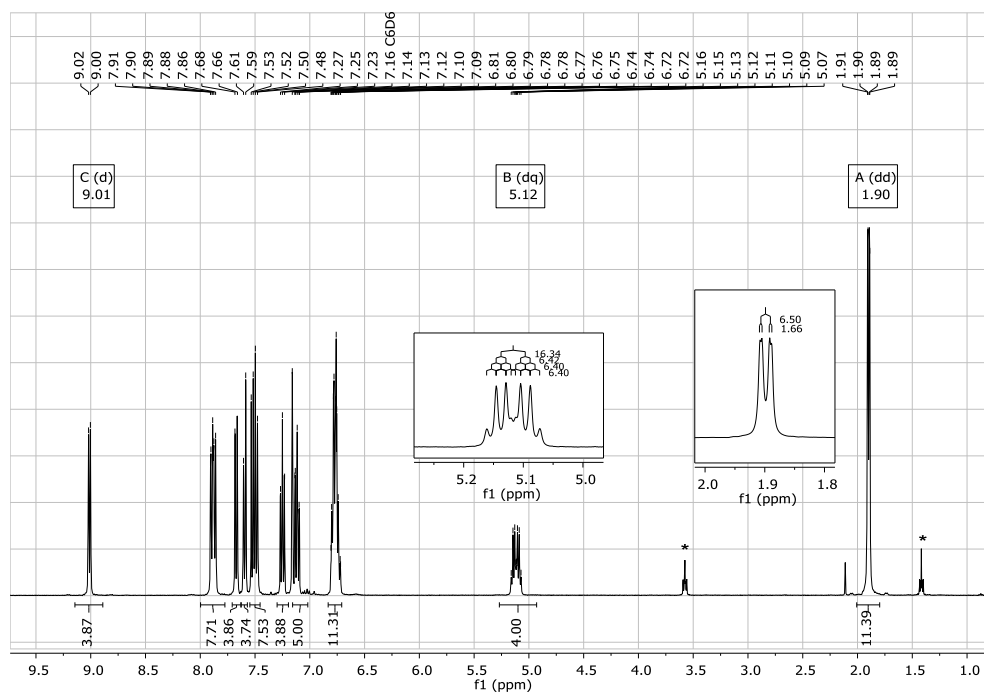
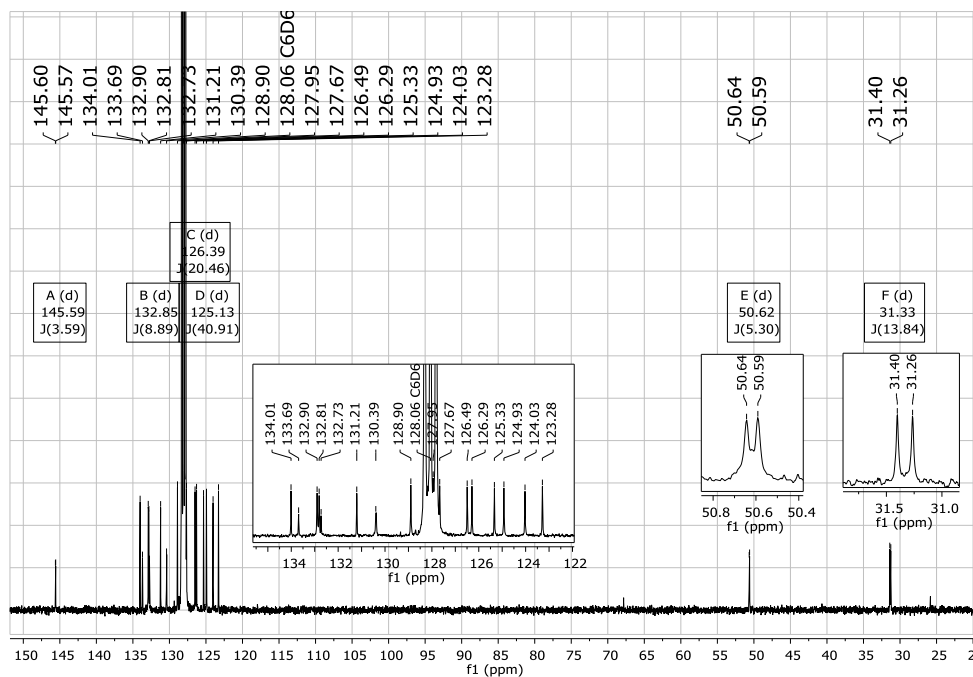
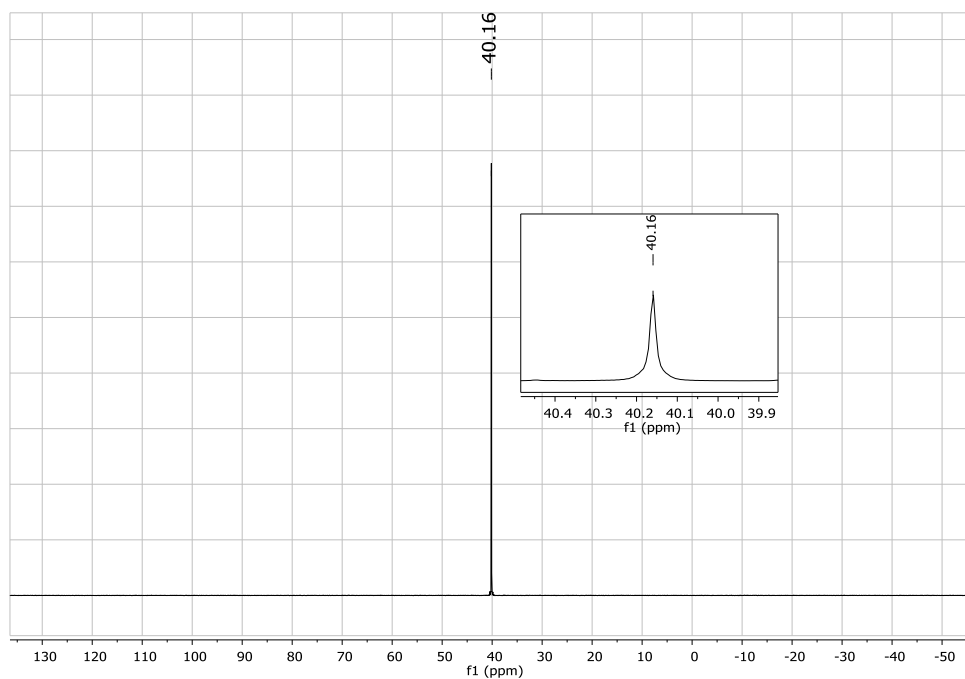
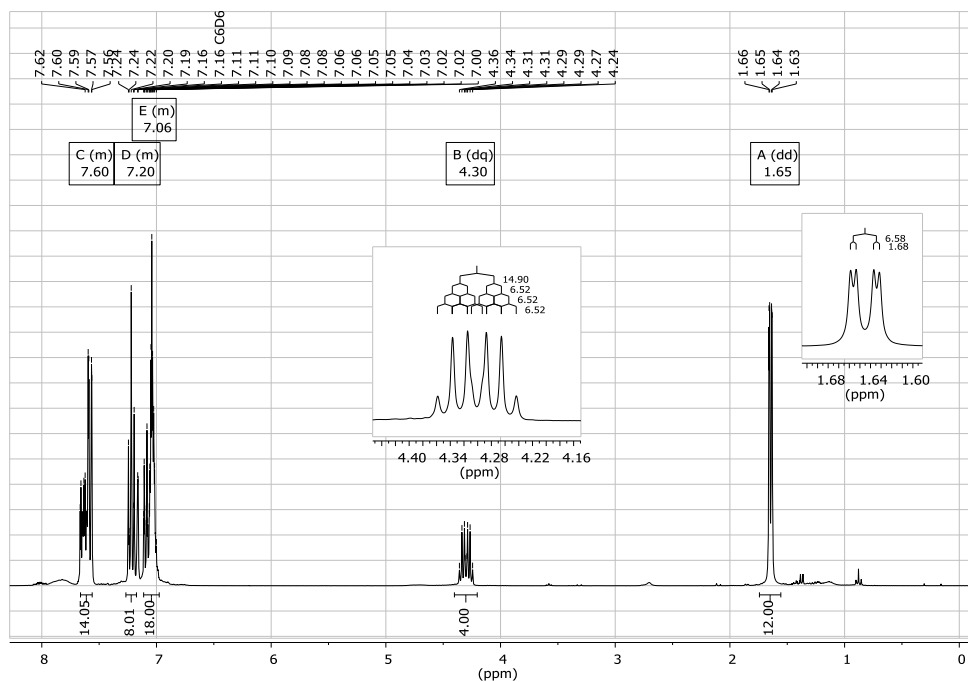
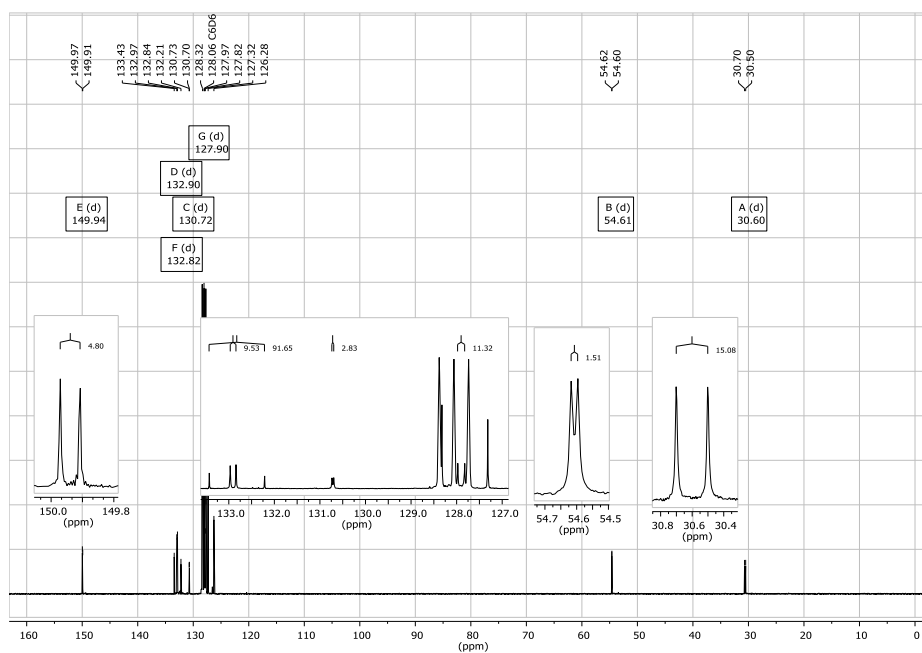


Figure S3.10. ^1H (400 MHz, C_6D_6 , 298 K) NMR spectrum of complex 4. * = thf.

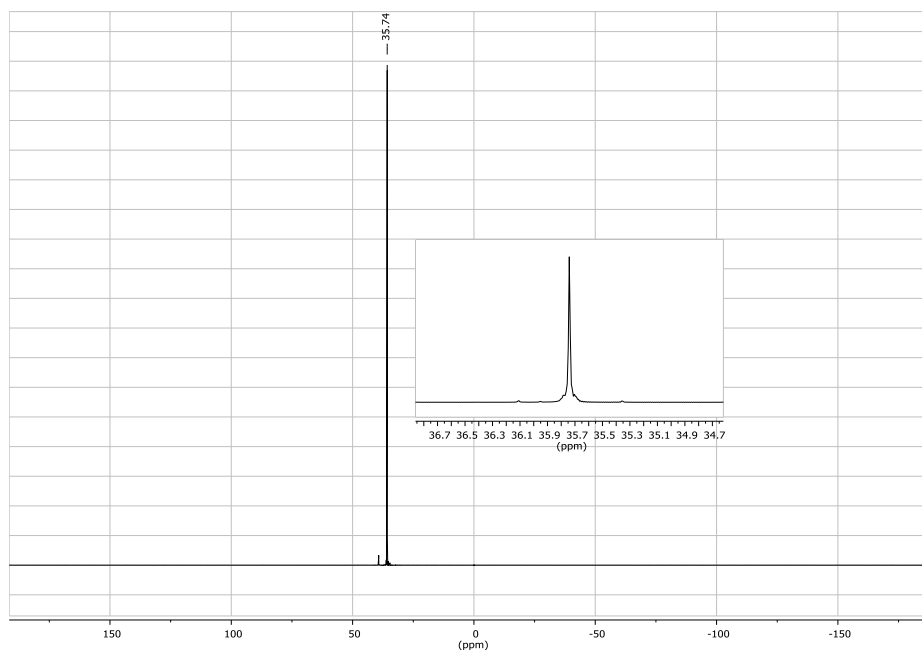
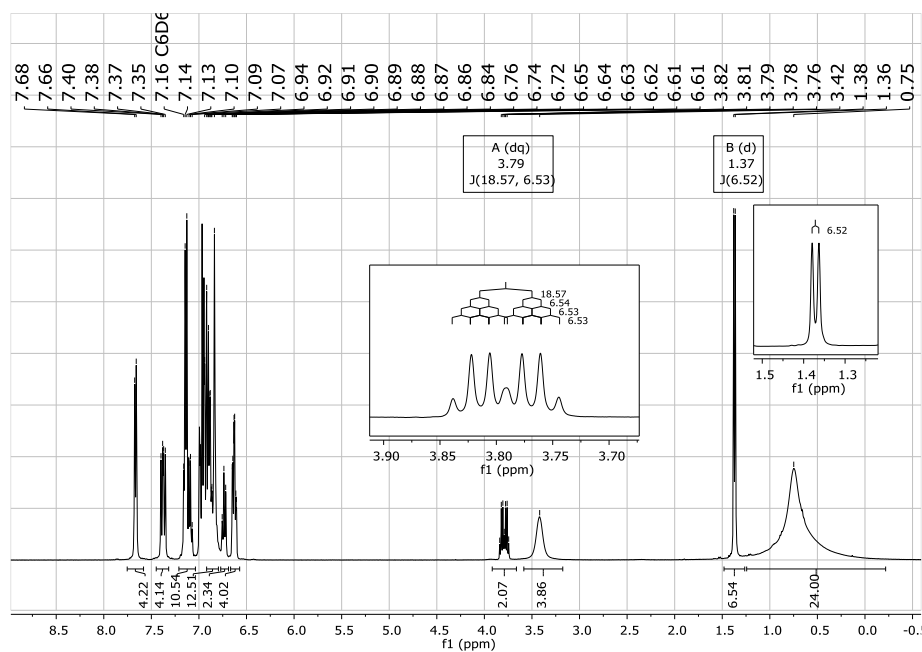
Supporting Information


 Figure S3.11. $^{13}\text{C}\{^1\text{H}\}$ (100 MHz, C_6D_6 , 298 K) NMR spectrum of complex 4.

 Figure S3.12. $^{31}\text{P}\{^1\text{H}\}$ (162 MHz, C_6D_6 , 298 K) NMR spectrum of complex 4.

Supporting Information


 Figure S3.13. $^1\text{H-NMR}$ (300 MHz, C_6D_6 , 298 K) spectrum of complex 5.

 Figure S3.14. $^{13}\text{C}\{^1\text{H}\}$ -NMR (75 MHz, C_6D_6 , 298 K) spectrum of complex 5.

Supporting Information


 Figure S3.15. $^{31}\text{P}\{^1\text{H}\}$ -NMR (121 MHz, C_6D_6 , 298 K) spectrum of complex 5.

 Figure S3.16. ^1H (400 MHz, C_6D_6 , 298 K) NMR spectrum of complex 6.

Supporting Information

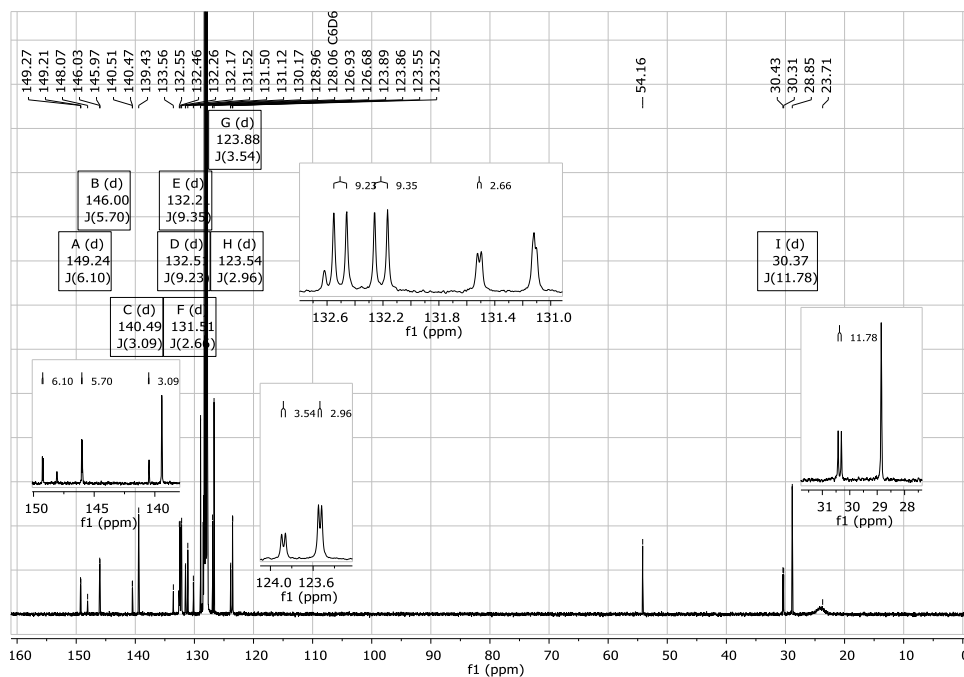


Figure S3.17. $^{13}\text{C}\{^1\text{H}\}$ (100 MHz, C_6D_6 , 298 K) NMR spectrum of complex 6.

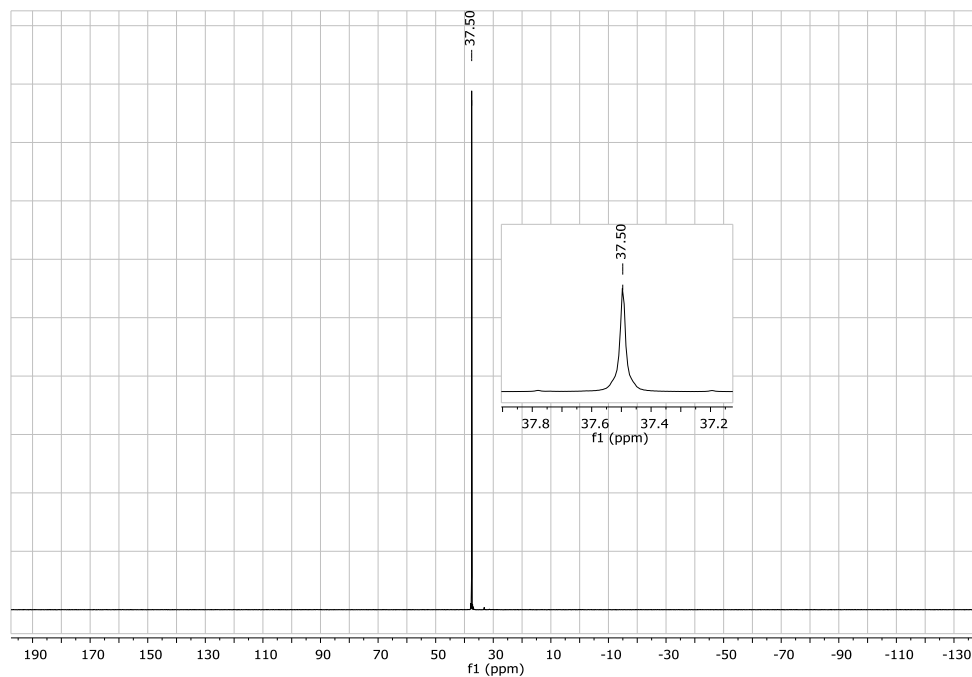
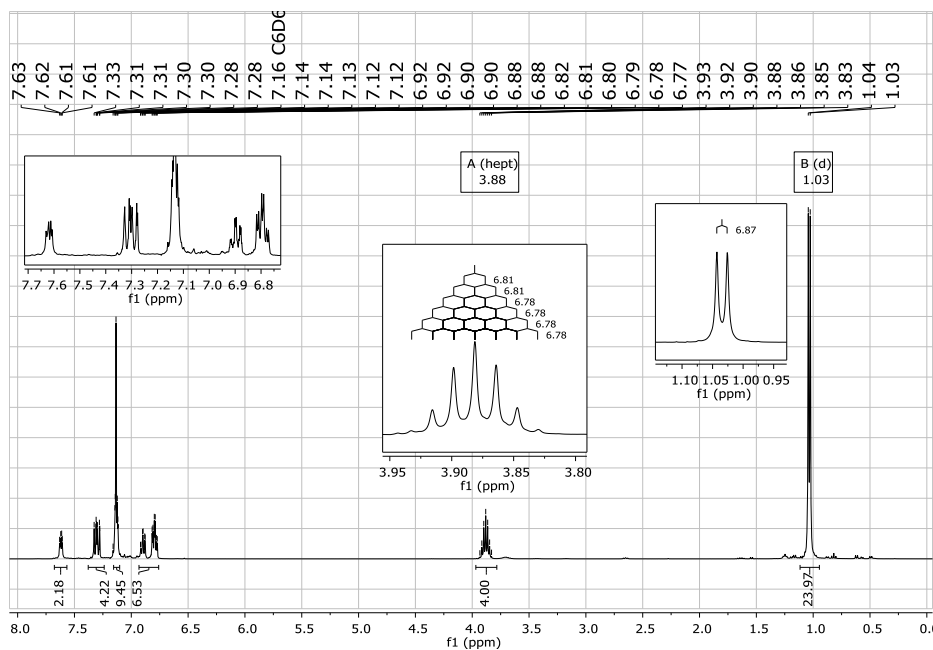
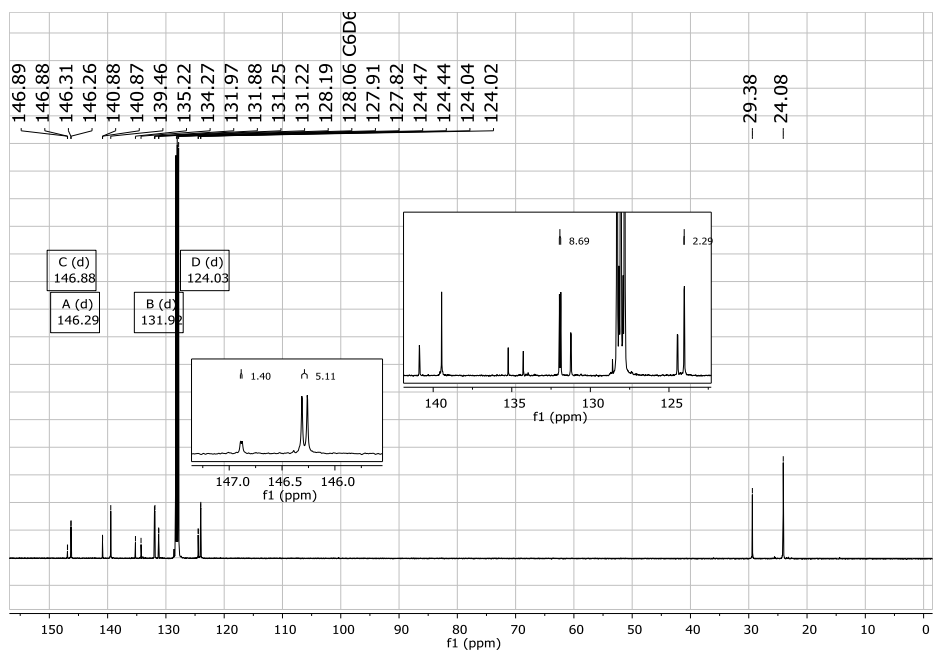


Figure S3.18. $^{31}\text{P}\{^1\text{H}\}$ (162 MHz, C_6D_6 , 298 K) NMR spectrum of complex 6.

Supporting Information


 Figure S3.19. ^1H (400 MHz, C_6D_6 , 298 K) NMR spectrum of complex **7**.

 Figure S3.20. $^{13}\text{C}\{^1\text{H}\}$ (100 MHz, C_6D_6 , 298 K) NMR spectrum of complex **7**.

Supporting Information

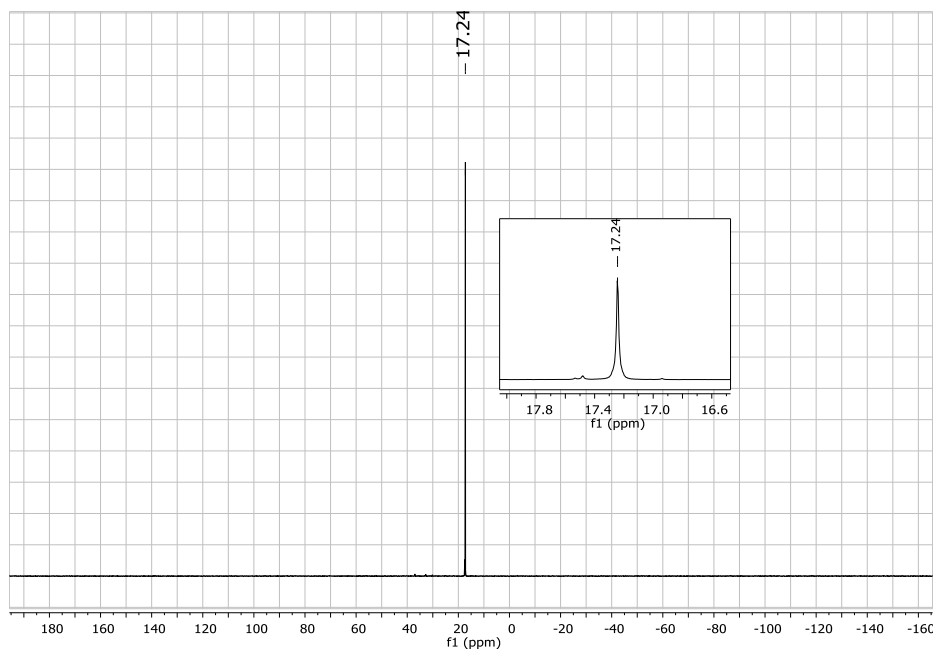


Figure S3.21. $^{31}\text{P}\{^1\text{H}\}$ (162 MHz, C_6D_6 , 298 K) NMR spectrum of complex 7.

Supporting Information

4. IR spectra

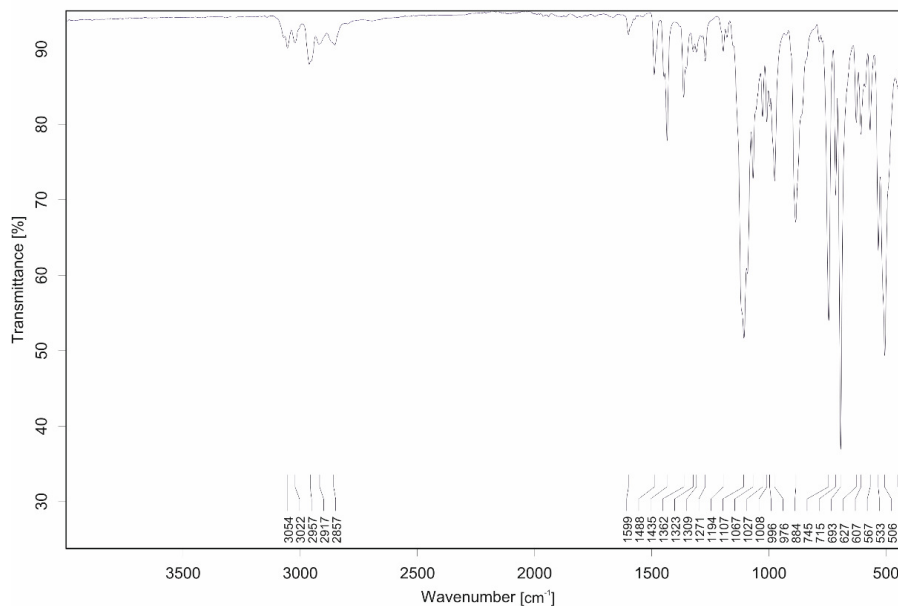


Figure S4.1. IR spectrum of complex 1

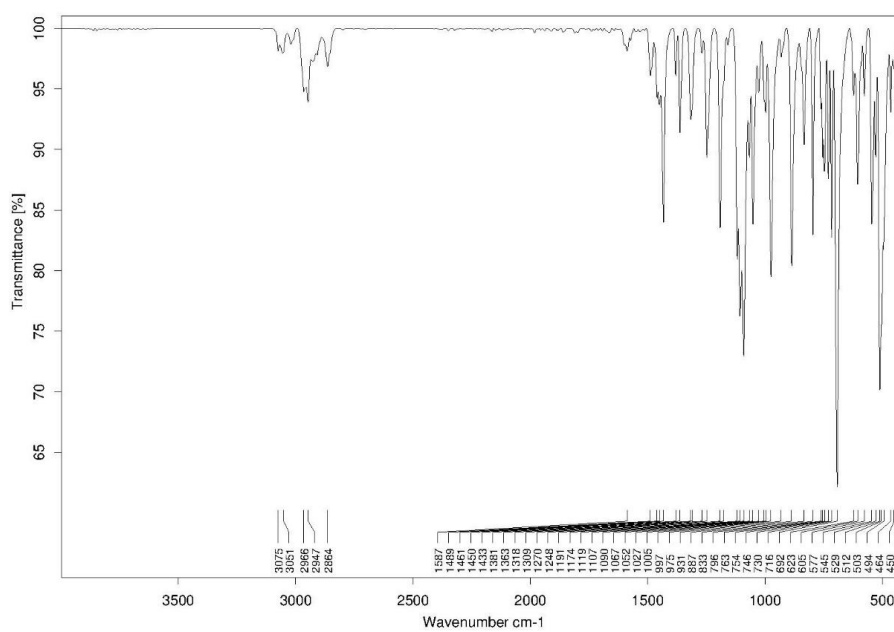


Figure S4.2. IR spectrum of complex 2.

Supporting Information

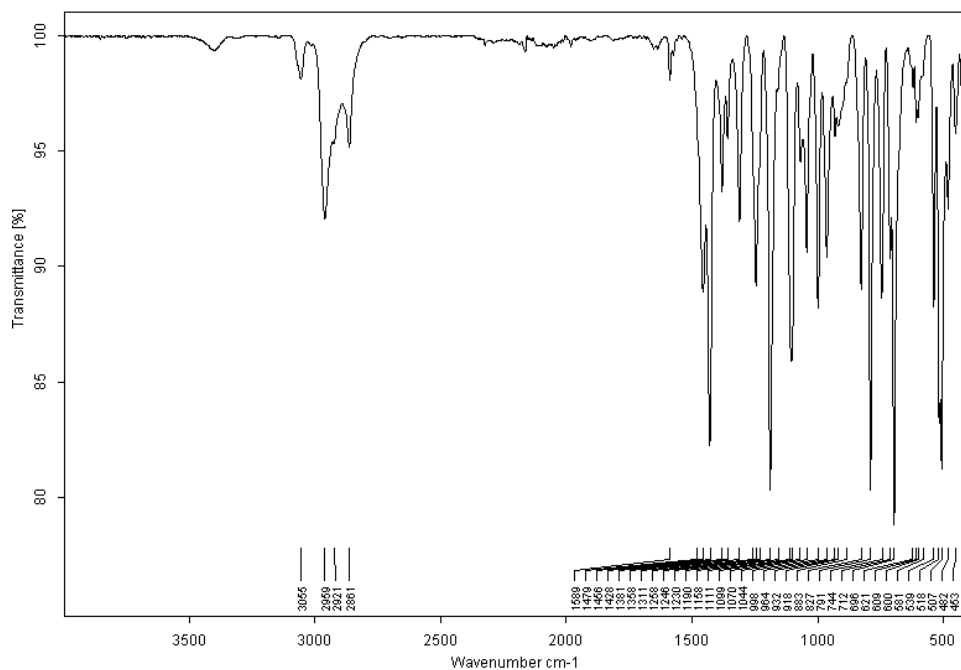


Figure S4.3. IR spectrum of complex 3.

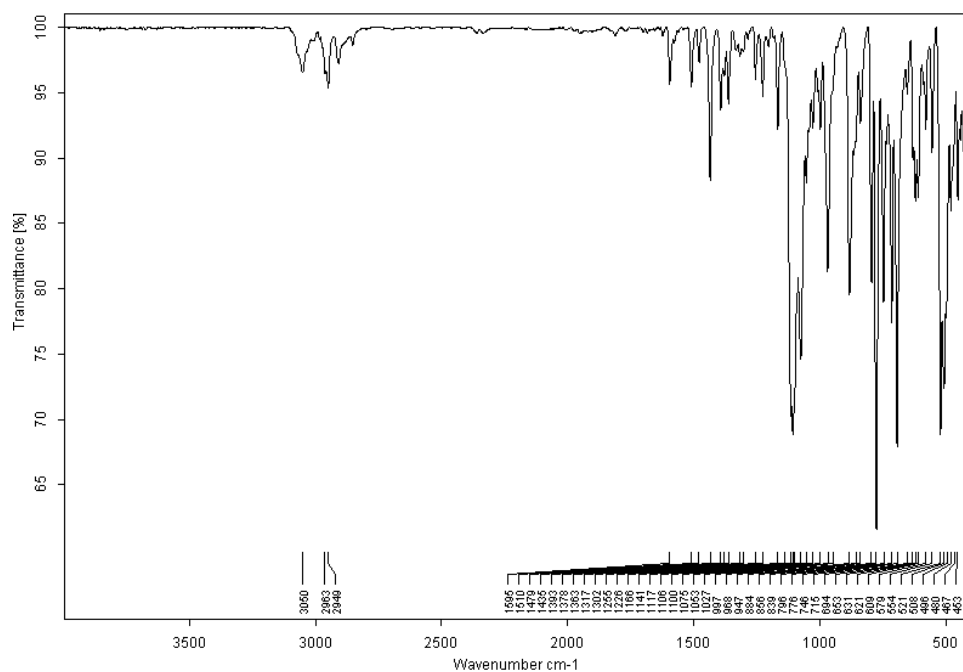


Figure S4.4. IR spectrum of complex 4.

Supporting Information

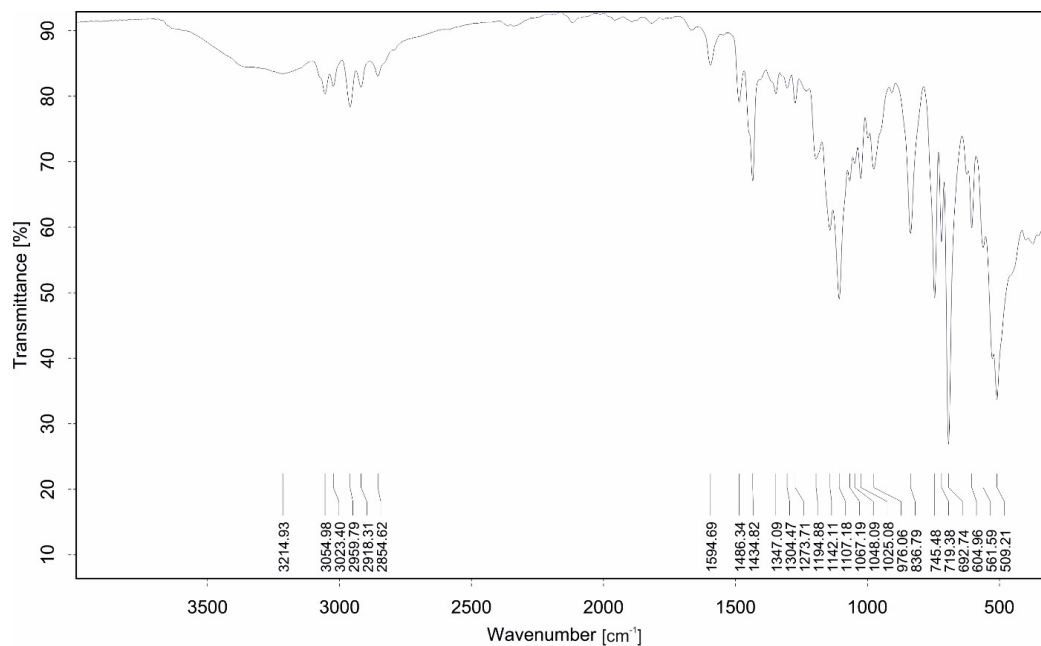


Figure S4.5. IR spectrum of complex 5.

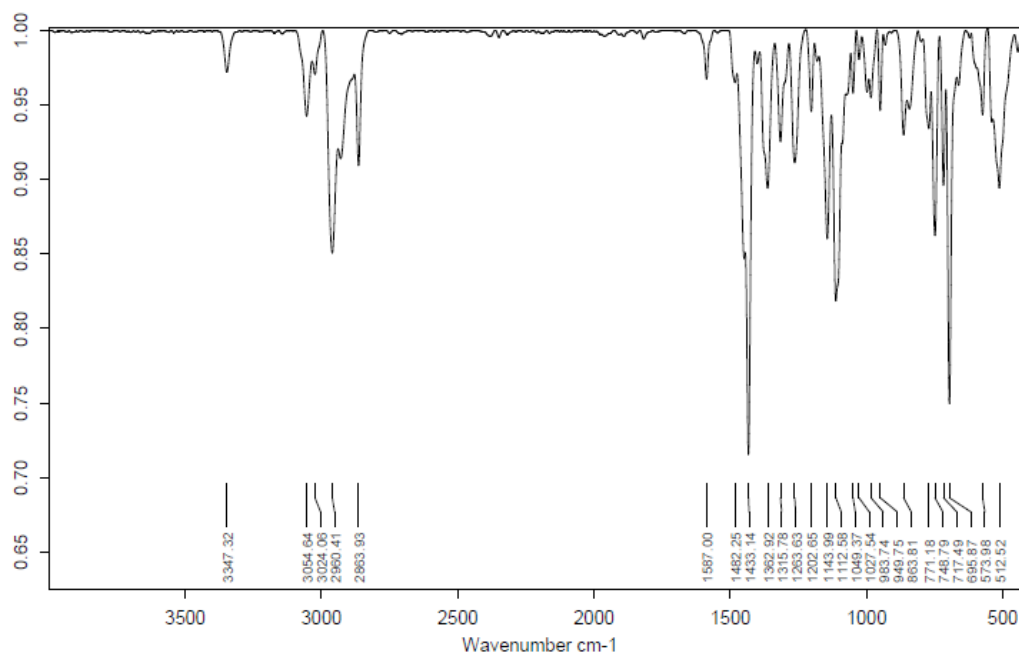


Figure S4.6. IR spectrum of complex 6.

Supporting Information

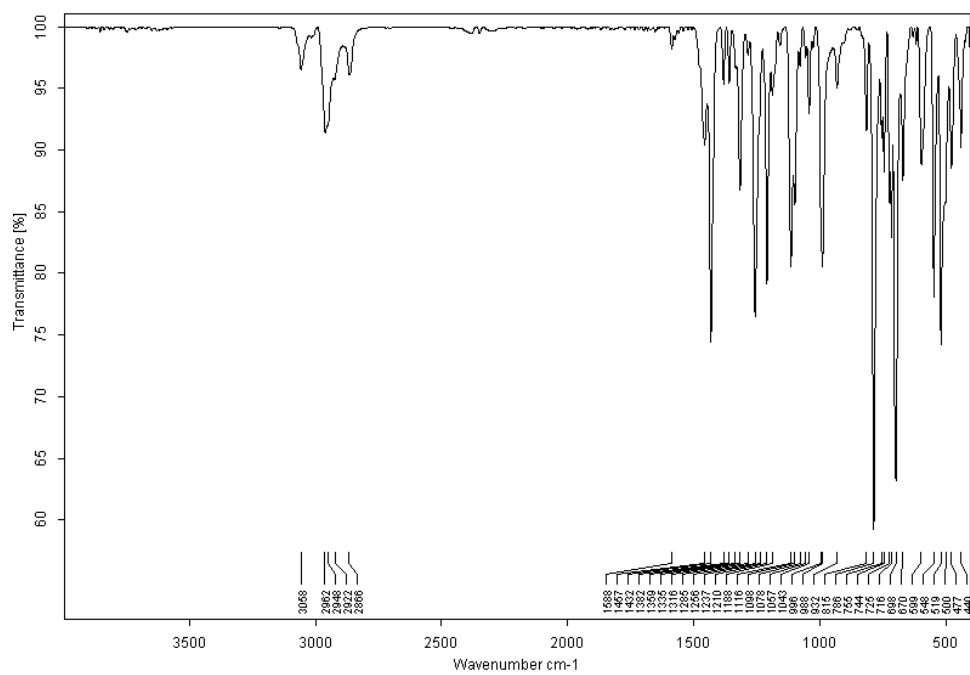


Figure S4.7. IR spectrum of complex 7.

Supporting Information

5. EI-MS spectra

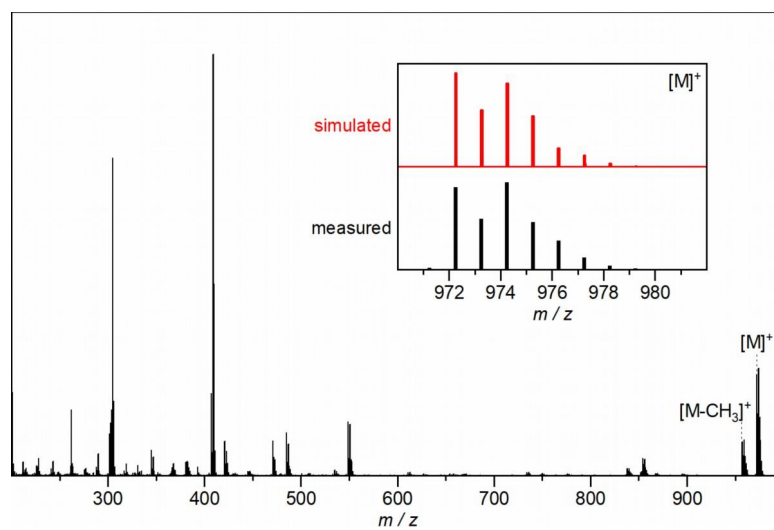


Figure S5.1. EI-MS spectrum of 1.

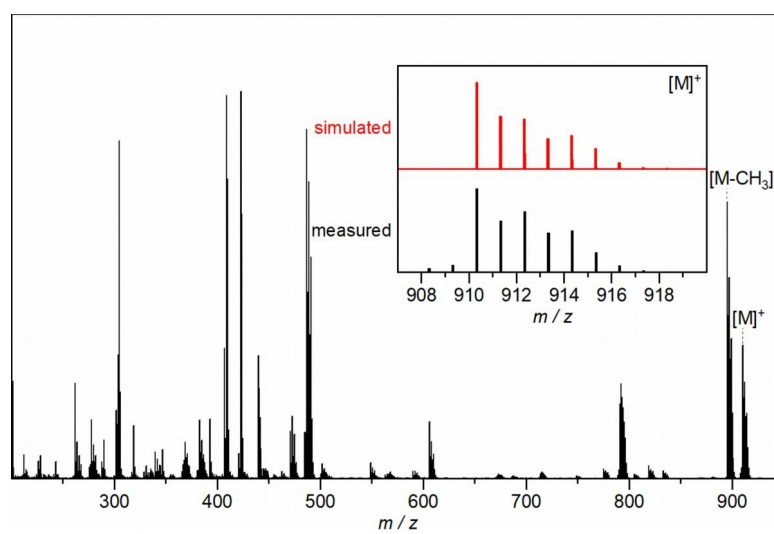


Figure S5.2. EI-MS spectrum of 5.

Supporting Information

6. Crystallographic data

Table S6.1 Crystal data, data collection and refinement for complexes 1-7.

Complex	1	2	3	4	5	6	7
Formula	C ₃₅ H ₃₆ Cu ₂ N ₄ P ₂	C ₁₇ H ₁₈ N ₄ P ₂ Cu ₂	C ₃₉ H ₃₆ Cu ₂ N ₄ P ₂	C ₂₇ H ₁₆ Cu ₂ N ₄ P ₂	C ₃₅ H ₃₆ N ₄ P ₂ Zn	C ₄₁ H ₁₂ N ₄ P ₂ Zn	C ₃₆ H ₃₆ N ₄ P ₂ Zn ₂
D _{calc} /g cm ⁻³	1.300	1.235	1.264	1.360	1.220	1.199	1.187
μ /mm ⁻¹	0.959	0.765	3.902	0.846	0.599	0.531	0.719
Formula Weight	974.06	1178.41	1290.61	1174.29	912.35	1024.56	1356.34
Colour	yellow	colourless	orange	colourless	colourless	yellow	colourless
Shape	needle	prism	block	prism	irregular	prism	plate
Size/mm ³	0.67×0.29×0.10	0.47×0.43×0.38	0.09×0.07×0.05	0.37×0.28×0.20	0.66×0.45×0.22	0.63×0.48×0.36	0.51×0.38×0.19
T/K	200	210	150	100.0	210	220	220
Crystal System	orthorhombic	tetragonal	monoclinic	orthorhombic	triclinic	orthorhombic	monoclinic
Flack Parameter	-0.018(8)	-0.007(6)	-	-0.018(8)	-0.007(5)	-0.020(5)	-
Hooft Parameter	-0.019(4)	0.002(3)	-	-0.004(3)	0.002(5)	-0.009(2)	-
Space Group	P2 ₁ 2 ₁ 2 ₁	P4 ₃ 2 ₁	P2 ₁ /n	P2 ₁ 2 ₁ 2 ₁	P1	P2 ₁ 2 ₁ 2 ₁	P2 ₁ /n
a/Å	12.06660(10)	13.4500(19)	13.6050(5)	10.3351(2)	9.6585(19)	13.930(3)	12.020(2)
b/Å	33.3362(5)	13.4500(19)	11.7346(3)	19.1071(4)	12.736(3)	18.380(4)	40.480(8)
c/Å	61.8831(9)	35.030(7)	21.2378(7)	29.0438(7)	20.345(4)	22.170(4)	15.630(3)
α /°					91.53(3)		
β /°			90.668(3)		92.64(3)		93.50(3)
γ /°					96.14(3)		
V/Å ³	24892.8(6)	6337(2)	3390.37(19)	5735.4(2)	2484.4(9)	5676(2)	7591(3)
Z	20	4	2	4	2	4	4
Z'	5	0.5	0.5	1	2	1	1
Wavelength/Å	0.71073	0.71073	1.34143	0.71073	0.71073	0.71073	0.71073
Radiation type	MoK α	MoK α	GaK α	MoK α	MoK α	MoK α	MoK α
Θ_{min} /°	1.161	1.622	3.339	2.240	1.609	1.439	1.399
Θ_{max} /°	25.186	25.162	64.378	27.032	26.082	25.181	25.155
Measured Refl.	159173	41882	25537	37720	60298	28518	35060
Independent Refl.	44496	5647	8281	11618	18847	10100	13506
Reflections with I > 2(I)	27288	4394	5404	10699	13606	8674	10103
R _{int}	0.0911	0.0360	0.0509	0.0479	0.0424	0.0216	0.0272
Parameters	2901	394	421	725	1143	650	945
Restraints	0	122	42	0	3	0	0
Largest Peak	0.570	0.304	0.693	1.280	0.499	0.390	0.376
Deepest Hole	-0.609	-0.337	-0.880	-0.707	-0.279	-0.156	-0.269
Goof	1.080	1.024	1.062	1.055	0.738	1.018	1.013
wR ₂ (all data)	0.1442	0.0939	0.2006	0.1371	0.0499	0.0814	0.1166
wR ₂	0.1148	0.0911	0.1751	0.1302	0.0478	0.0764	0.1057
R ₁ (all data)	0.1407	0.0452	0.0976	0.0555	0.0481	0.0429	0.0647
R ₁	0.0704	0.0360	0.0653	0.0491	0.0314	0.0324	0.0430

Supporting Information

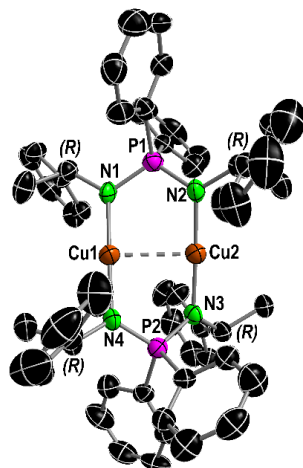


Figure S6.1. Molecular structure of **1** in the solid state with ellipsoids drawn at 50 % probability. All hydrogen atoms are omitted for clarity. Selected bond lengths (Å) and bond angles [°]: Cu1...Cu2 2.534(2), Cu1-N1 1.879(10), Cu1-N4 1.893(10), Cu2-N2 1.860(10), Cu2-N3 1.867(10), P1-N1 1.606(10), P1-N2 1.606(9), P2-N3 1.611(10), P2-N4 1.592(10); N1-Cu1-Cu2 89.4(3), N1-Cu1-N4 178.6(4), N4-Cu1-Cu2 89.4(3), N2-Cu2-Cu1 89.5(3), N2-Cu2-N3 177.9(4), N3-Cu2-Cu1 88.7(3), N1-P1-N2 110.1(5), N4-P2-N3 110.3(5), P1-N1-Cu1 121.0(5), P1-N2-Cu2 117.8(5), P2-N4-Cu1 120.4(6), P2-N3-Cu2 117.0(5), P-P distance [Å]: P1-P2 5.4393(1); NPPN torsion angle [°]: N1-P1-P2-N3 140.223(2).

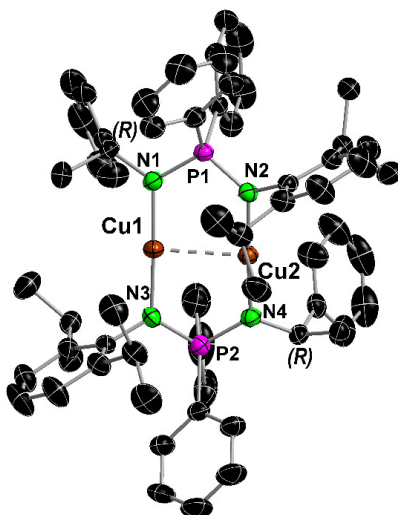


Figure S6.2. Molecular structure of **2** in the solid state with ellipsoids drawn at 40 % probability. All hydrogen atoms are omitted for clarity. Selected bond lengths (Å) and bond angles [°]: Cu1...Cu2 2.5303(7), Cu1-N1 1.866(3), Cu2-N2 1.870(3), Cu1-N3 1.867(3), Cu2-N4 1.866(3), P1-N1 1.608(3), P1-N2 1.611(3), P2-N3 1.609(3), P2-N4 1.613(3); N1-Cu1-N3 177.7(2), N2-Cu2-N4 177.4(2), N1-Cu1-Cu2 92.68(10), N2-Cu2-Cu1 89.33(10), N3-Cu1-Cu2 89.22(10), N4-Cu2-Cu1 92.84(11), P1-N1-Cu1 121.2(2), P1-N2-Cu2 122.1(2), P2-N3-Cu1 122.4(2), P2-N4-Cu2 121.0(2), N1-P1-N2 109.8(2), N3-P2-N4 109.7(2); P-P distance [Å]: P1-P2 5.501(2); NPPN Torsion angle [°]: N1-P1-P2-N4 179.8(2).

Supporting Information

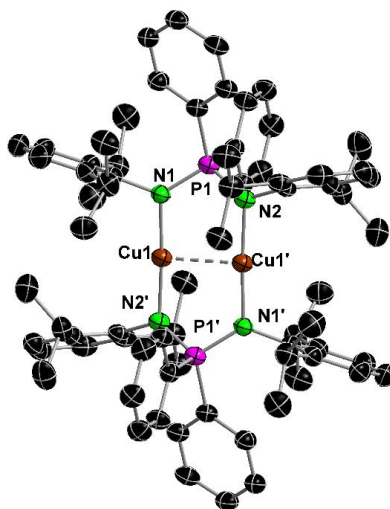


Figure S6.3. Molecular structure of **3** in the solid state with ellipsoids drawn at 50 % probability. All hydrogen atoms are omitted for clarity. Selected bond lengths (Å) and bond angles [°]: Cu1...Cu1' 2.5292(10), Cu1-N1' 1.895(3), Cu1-N2 1.886(3), P1-N1 1.617(3), P1-N2 1.614(3); N1-Cu1-Cu1' 95.85(9), N2-Cu1-Cu1' 86.61(9), N2'-Cu1-N1 176.82(12), N2-P1-N1 107.9(2), P1-N1-Cu1 113.4(2), P1-N2-Cu1 121.3(2), P1-N1-Cu1 113.4(2), P-P distance [Å]: P1-P2 5.4327(12); NPPN torsion angle [°]: N1-P1-P2-N3 180.00(2).

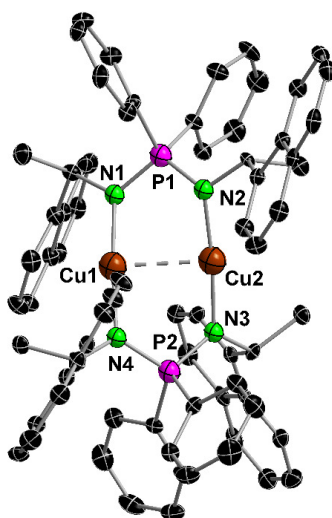


Figure S6.4. Molecular structure of **4** in the solid state with ellipsoids drawn at 50 % probability. All hydrogen atoms are omitted for clarity. Selected bond lengths (Å) and bond angles [°]: Cu1...Cu2 2.5054(8), Cu1-N1 1.892(4), Cu1-N4 1.886(4), Cu2-N2 1.880(4), Cu2-N3 1.881(4), P1-N1 1.611(4), P1-N2 1.608(4), P2-N3 1.611(4), P2-N4 1.612(4); N1-Cu1-Cu2 88.37(13), N4-Cu1-N1 175.6(2), N4-Cu1-Cu2 87.23(13), N2-Cu2-Cu1 86.73(14), N2-Cu2-N3 174.7(2), N3-Cu2-Cu1 88.00(13), N2-P1-N1 109.3(2), N3-P2-N4 109.3(2), P1-N1-Cu1 118.0(2), P1-N2-Cu2 116.7(2), P2-N4-Cu1 119.3(2), P2-N3-Cu2 114.8(2), P-P distance [Å]: P1-P2 5.420(2); NPPN torsion angle [°]: N1-P1-P2-N3 127.59(2).

Supporting Information

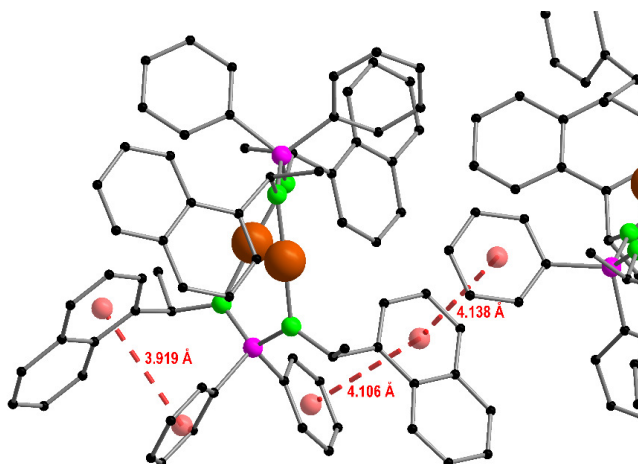


Figure S6.5. Selected intra- and intermolecular interactions between the phenyl and naphthyl groups in the solid state structure of complex **4**. These groups are roughly parallel arranged and form a kind of 1D 'chains' extending through the structure. The distances between the centroids of the phenyl and the closest naphthyl rings are in the range of 3.919 – 4.138 Å. This may enable weak π -stacking interactions.

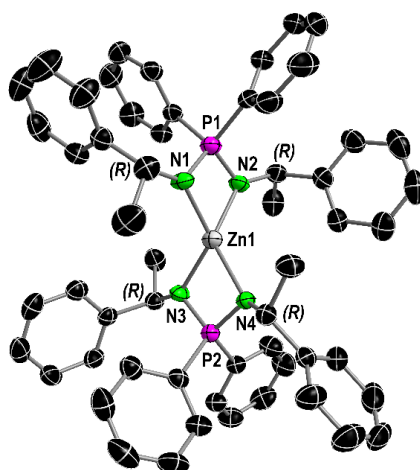


Figure S6.6. Molecular structure of **5** in the solid state with ellipsoids drawn at 50 % probability. All hydrogen atoms are omitted for clarity. Selected bond lengths (Å) and bond angles [°]: Zn1-N1 2.039(3), Zn1-N2 2.025(3), Zn1-N3 2.034(3), Zn1-N4 2.054(3), P1-N1 1.617(3), P1-N2 1.603(3), P2-N3 1.612(3), P2-N4 1.616(3); N1-Zn1-N4 130.83(13), N2-Zn1-N1 74.34(12), N2-Zn1-N3 128.19(13), N2-Zn1-N4 129.87(13), N3-Zn1-N1 128.56(13), N3-Zn1-N4 74.48(12), N2-P1-N1 99.3(2), N3-P2-N4 100.0(2), P1-N1-Zn1 92.6(2), P1-N2-Zn1 93.6(2), P2-N3-Zn1 93.1(2), P2-N4-Zn1 92.26(14). P-P distance [Å]: P1-P2 5.322(2); NPPN torsion angle [°]: N1-P1-P2-N3 92.92(2).

Supporting Information

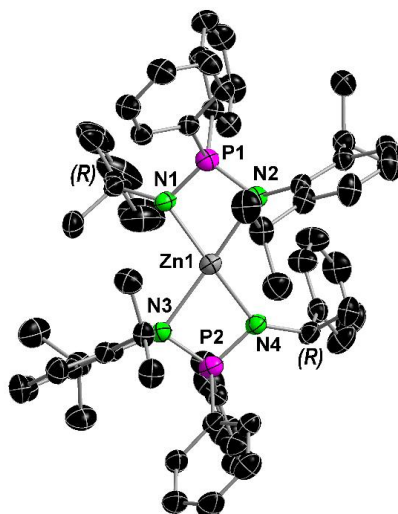


Figure S6.7. Molecular structure of **6** in the solid state with ellipsoids drawn at 40 % probability. All hydrogen atoms are omitted for clarity. Selected bond lengths (Å) and bond angles [°]: Zn1-N1 1.994(3), Zn1-N2 2.197(3), Zn1-N3 2.194(3), Zn1-N4 1.994(3) P1-N1 1.610(3), P1-N2 1.603(3), P2-N3 1.609(3), P2-N4 1.603(3); N1-Zn1-N4 166.25(13), N1-Zn1-N2 72.18(11), N3-Zn1-N2 171.05(11), N4-Zn1-N2 107.50(11), N1-Zn1-N3 110.50(12), N4-Zn1-N3 72.03(11), N2-P1-N1 100.7(2), N4-P2-N3 100.4(2), P1-N1-Zn1 97.2(2), P1-N2-Zn1 89.80(13), P2-N3-Zn1 89.92(13), P2-N4-Zn1 97.6(2). P-P distance [Å]: P1-P2 5.4302(2); NPPN torsion angle [°]: N1-P1-P2-N4 166.33(2).

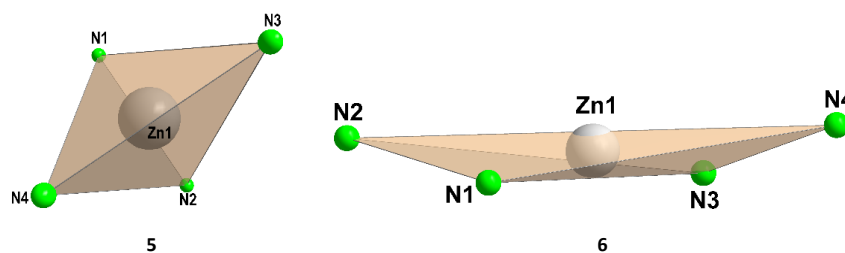


Figure S6.8. Coordination polyhedra of complexes **5** (left) and **6** (right). While **5** shows a nearly tetrahedral coordination sphere **6** is closer to a perfect square tetragonal coordination.

Table S6.2. Distortion parameters towards the four closest geometries of Zn complexes **5** and **6** obtained by continuous shape measurements with the program SHAPE 2.1.^[12]

Complex	SP-4 ^a	T-4 ^b	SS-4 ^c	vTBPY-4 ^d
[Zn{(R)-PEPIA} ₂] (5)	24.959	9.075	11.374	11.939
[Zn{(R)-PE ^{Dipp} PIA} ₂] (6)	3.782	26.596	13.889	27.634

[a] SP-4 = Square (D4h); [b] T-4 = Tetrahedron (Td); [c] SS-4 = Seesaw (C2v); [d] vTBPY-4 = Vacant trigonal bipyramid (C3v).

Supporting Information

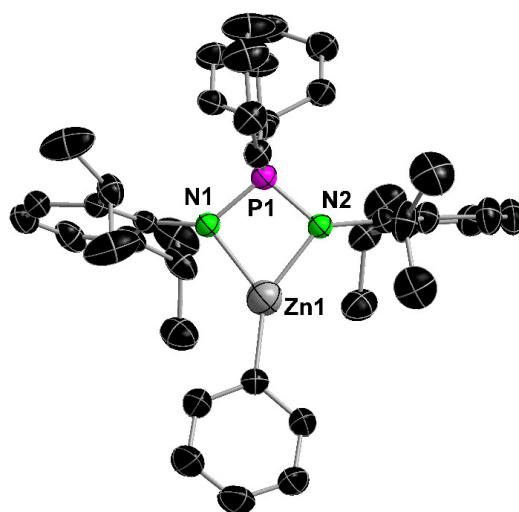


Figure S6.9. Molecular structure of **7** in the solid state with ellipsoids drawn at 40 % probability. All hydrogen atoms are omitted for clarity. Selected bond lengths (Å) and bond angles [°]: Zn-N1 2.026(2), Zn-N2 1.996(2), Zn-C37 1.932(3), P1-N1 1.604(2), P1-N2 1.617(2); N1-Zn-N2 74.51(9), C37-Zn-N1 136.06(11), C37-Zn-N2 148.19(11), N1-P1-N2 98.22(11).

Supporting Information

7. Photoluminescence data

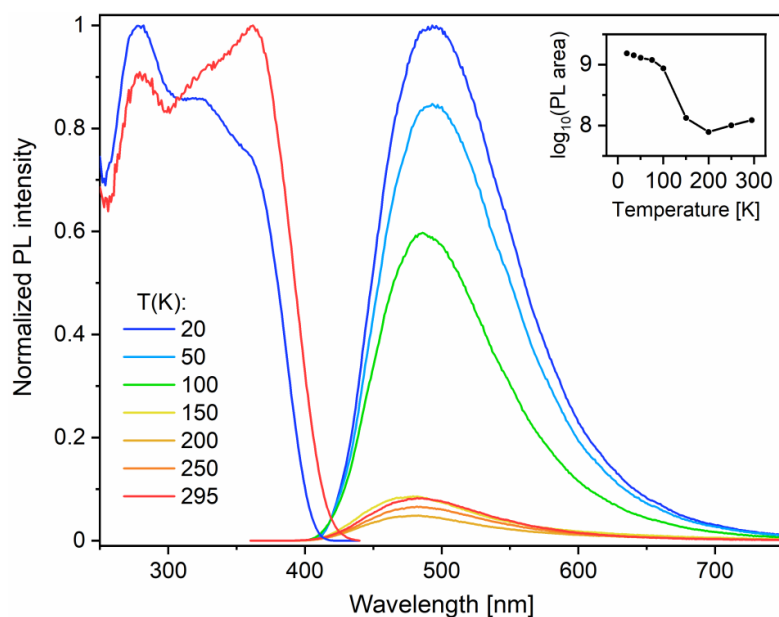


Figure S7.1. Photoluminescence emission (PL) and excitation (PLE) spectra of solid (polycrystalline) complex **1** in a temperature range of 20 K to 295 K. The emission/ PLE spectra were excited/ recorded at 350/ 480 nm. The insert depicts the logarithmic integral PL intensity versus temperature.

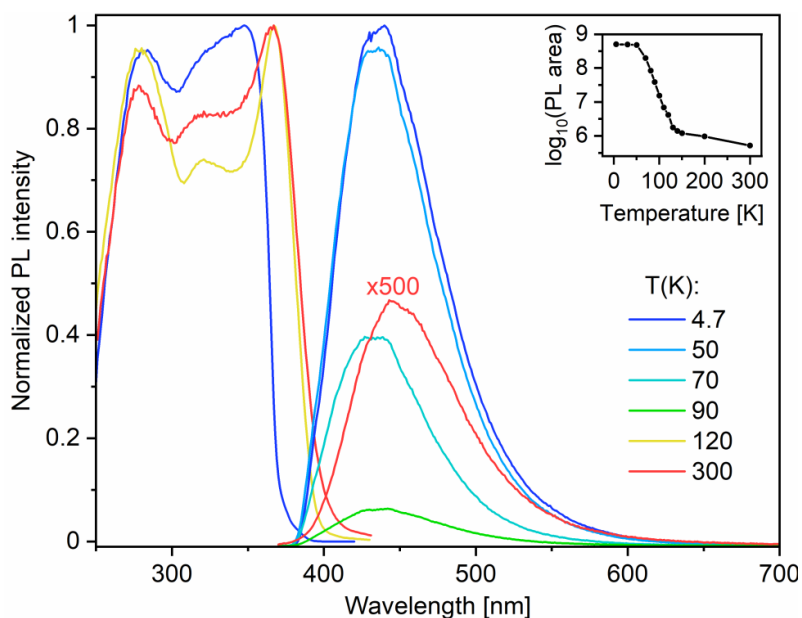


Figure S7.2. Photoluminescence emission (PL) and excitation (PLE) spectra of solid (polycrystalline) complex **2** in a temperature range of 4.7 K to 295 K. The emission/ PLE spectra were excited/ recorded at 340/ 450 nm. The insert depicts the logarithmic integral PL intensity versus temperature.

Supporting Information

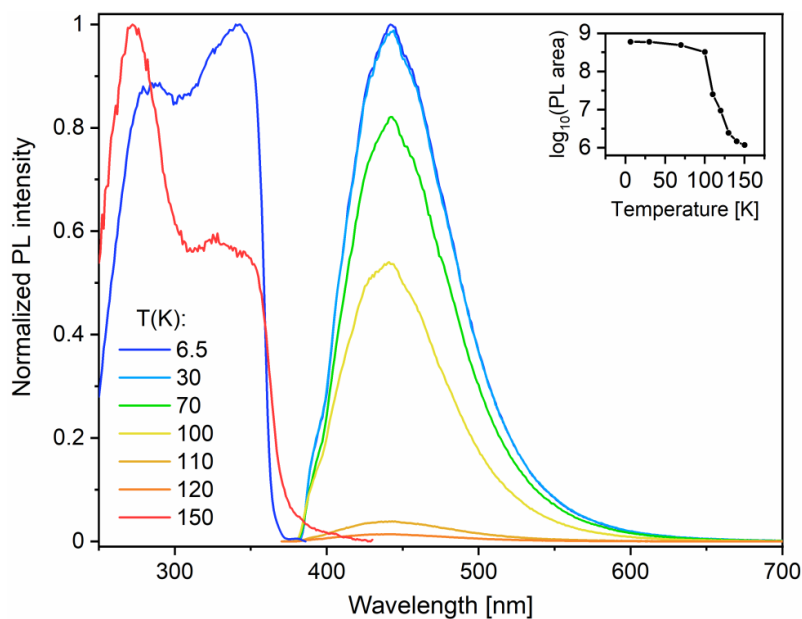


Figure S7.3. Photoluminescence emission (PL) and excitation (PLE) spectra of solid (polycrystalline) complex **3** in a temperature range of 20 K to 295 K. The emission/ PLE spectra were excited/ recorded at 340/ 460 nm. The insert depicts the logarithmic integral PL intensity versus temperature.

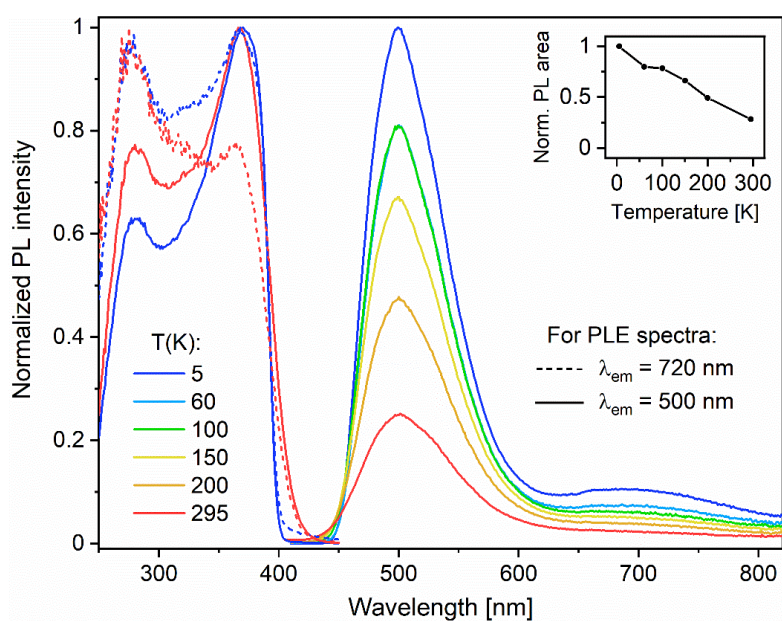


Figure S7.4. Photoluminescence emission (PL) and excitation (PLE) spectra of solid (polycrystalline) complex **4** in a temperature range of 5 K to 295 K. The emission/ PLE spectra were excited/ recorded at 350/ 500 nm. The insert depicts the integral PL intensity versus temperature.

Supporting Information

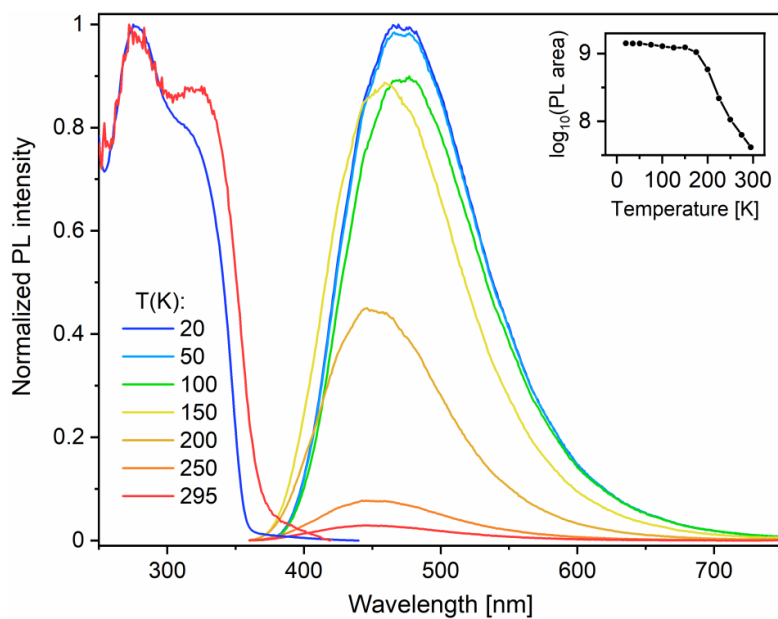


Figure S7.5. Photoluminescence emission (PL) and excitation (PLE) spectra of solid (polycrystalline) complex **5** in a temperature range of 20 K to 295 K. The emission/ PLE spectra were excited/ recorded at 330/ 480 nm. The insert depicts the integral PL intensity versus temperature.

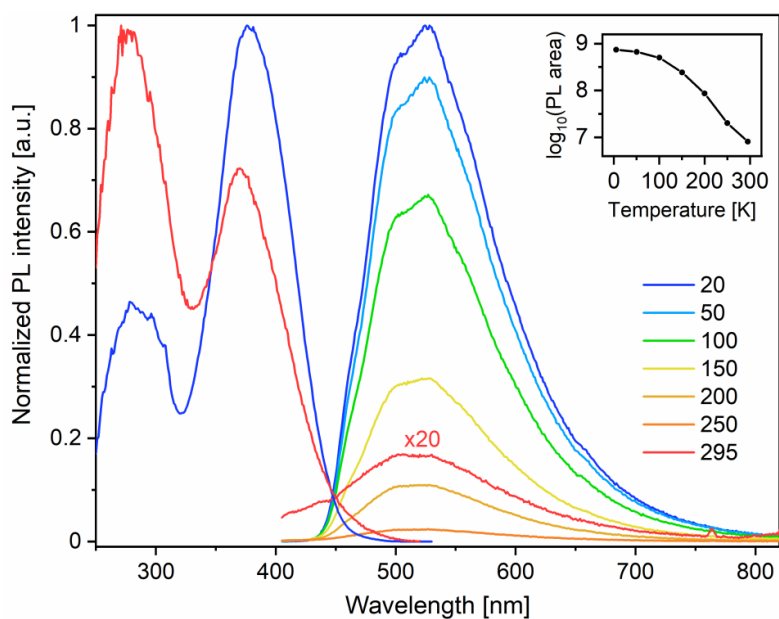


Figure S7.6. Photoluminescence emission (PL) and excitation (PLE) spectra of solid (polycrystalline) complex **6** in a temperature range of 20 K to 295 K. The emission/ PLE spectra were excited/ recorded at 380/ 520 nm. The insert depicts the logarithmic integral PL intensity versus temperature.

Supporting Information

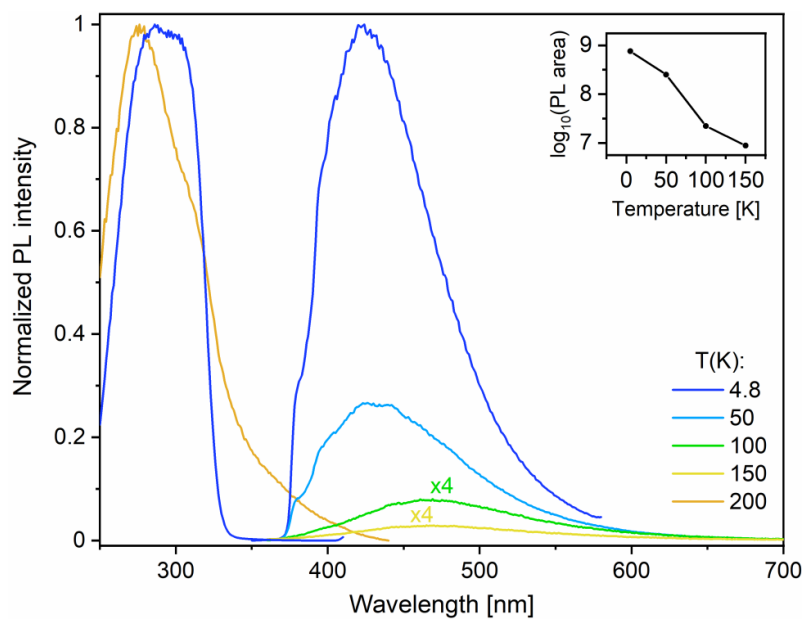


Figure S7.7. Photoluminescence emission (PL) and excitation (PLE) spectra of solid (polycrystalline) complex **7** in a temperature range of 4.8 K to 200 K. The emission/ PLE spectra were excited/ recorded at 300/ 450 nm. The insert depicts the logarithmic integral PL intensity versus temperature.

Supporting Information

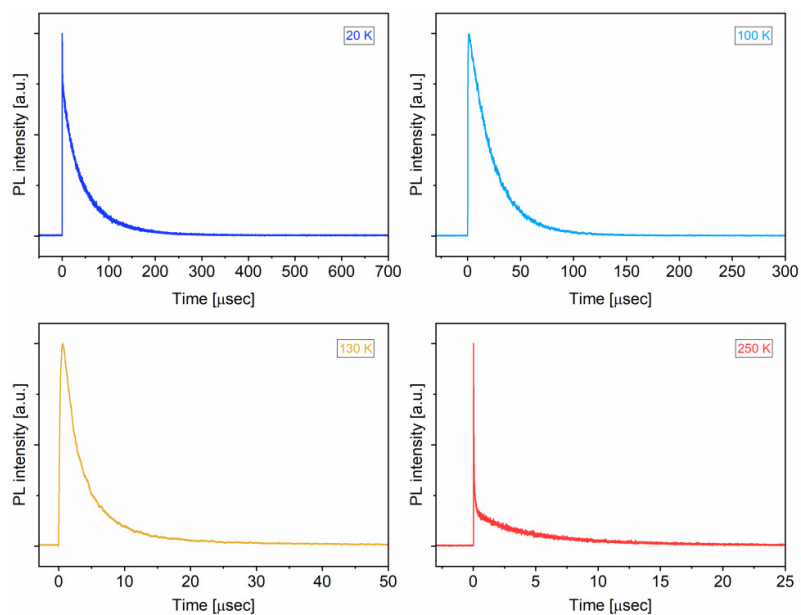


Figure S7.8. PL decay traces for solid complex **1** at selected temperatures. PL was excited at 337 nm with a nsec-pulsed nitrogen laser and recorded at 492 nm emission wavelength. The nsec-fast minor component at 250 K can be attributed to prompt fluorescence. The major μ sec-slow decaying component is contributed by phosphorescence at temperatures below ~ 100 K and by thermally activated delayed fluorescence (TADF) above ~ 150 K (see text).

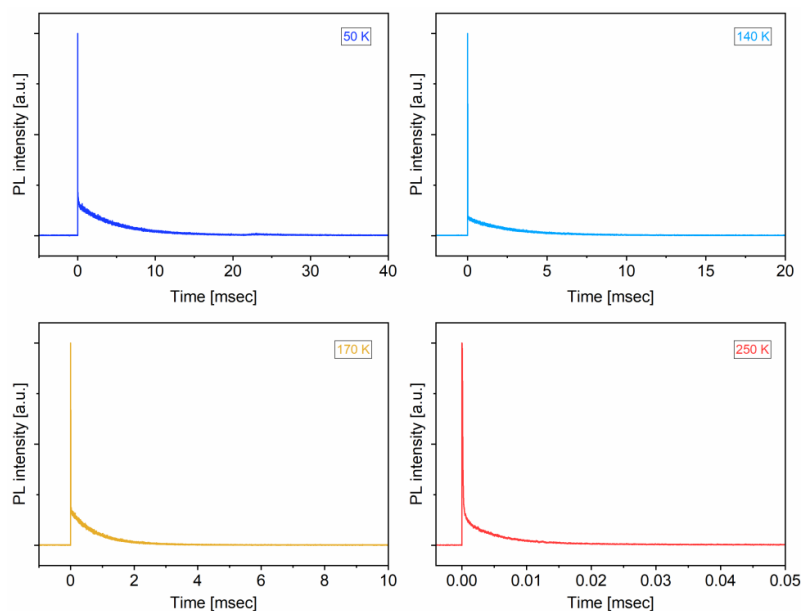


Figure S7.9. PL decay traces of solid complex **5** at selected temperatures. PL was excited at 337 nm with a nsec-pulsed nitrogen laser and recorded at 474 nm emission wavelength. The nsec-fast minor component is attributed to prompt fluorescence. The major PL component is contributed by long-lived phosphorescence at low temperatures (< 100 K) and by thermally activated delayed fluorescence (TADF) above ~ 200 K (see text). Note a large variation of the PL decay time scale depending on the temperature.

Supporting Information

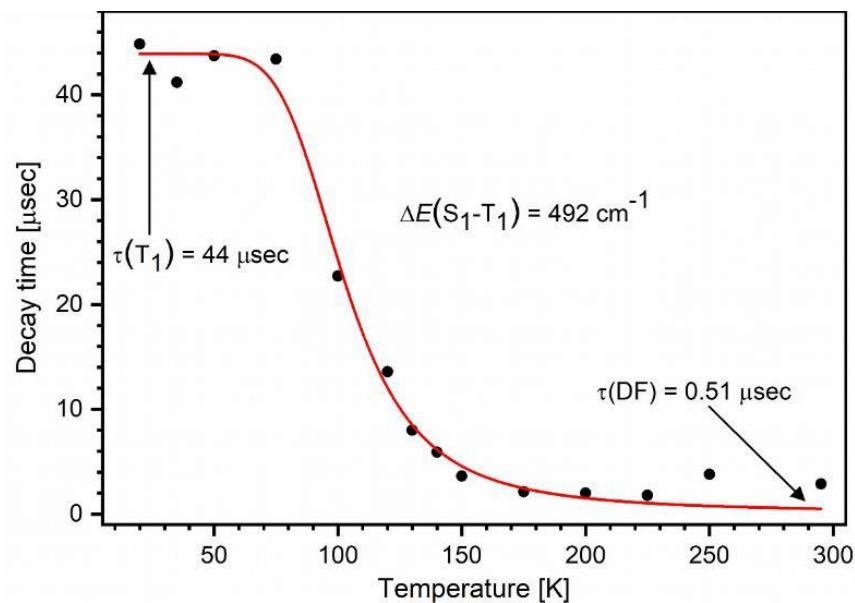


Figure S7.10. PL decay time of solid complex 1 vs. temperature. The indicated PL lifetimes are from monoexponential approximations of the decay curves (see Fig. S6.8). The red curve corresponds to the fit according to eq. (1). The fit yielded the energy separation ΔE between S_1 and T_1 states of about 500 cm^{-1} . Below $T \approx 75 \text{ K}$ the emission is predominantly phosphorescence with the lifetime of $44 \text{ } \mu\text{sec}$. Increasing the temperature activates the TADF mechanism, resulting in the effective PL lifetime of ca. $0.51 \text{ } \mu\text{sec}$ at room temperature.

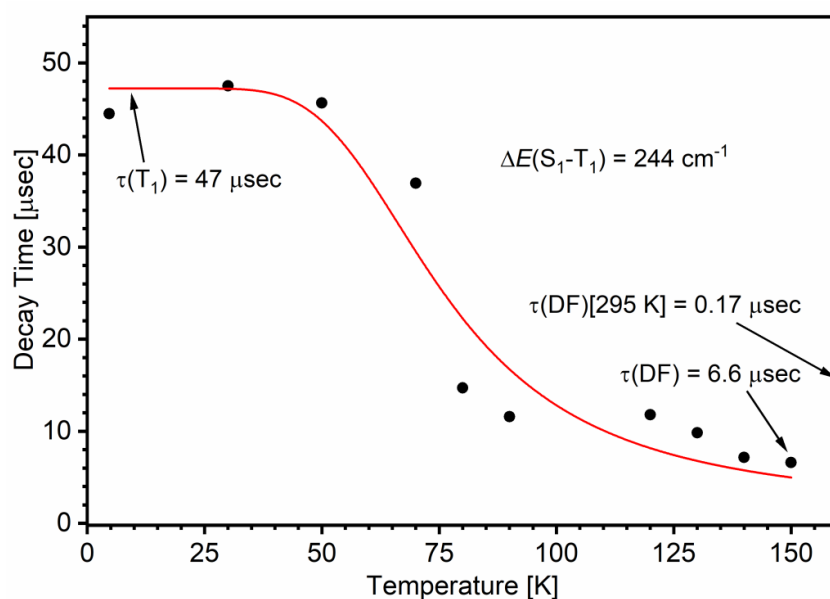


Figure S7.11. PL decay time of solid complex 2 vs. temperature. The red curve corresponds to the fit according to the model of equilibrated S_1 and T_1 states (eq. S1). The fit yielded the energy separation ΔE between S_1 and T_1 states of about 250 cm^{-1} . Below $T \approx 75 \text{ K}$ the emission is phosphorescence with the lifetime of $47 \text{ } \mu\text{sec}$. Increasing the temperature activates the TADF mechanism, resulting in the effective PL lifetime of ca. $0.17 \text{ } \mu\text{sec}$ at 150 K.

Supporting Information

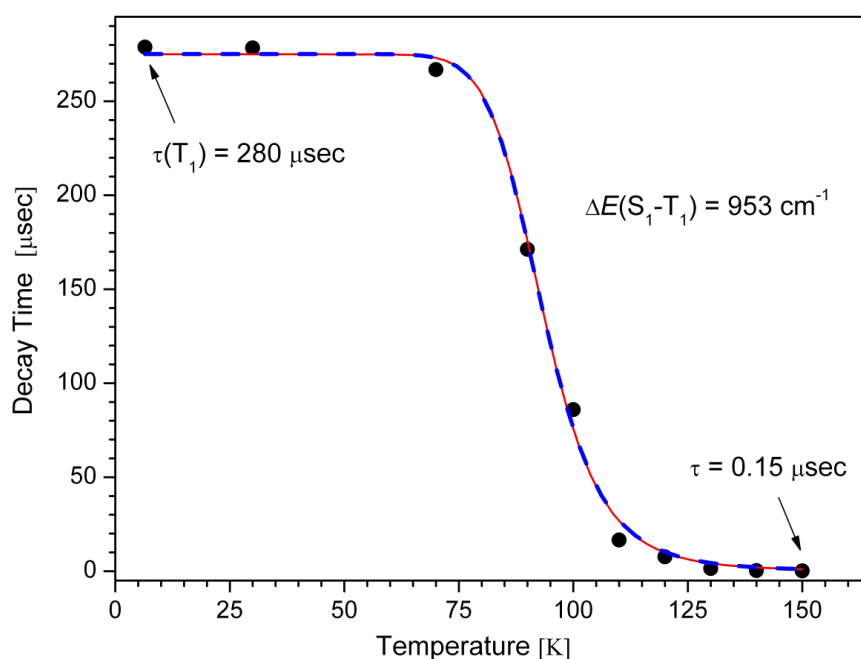


Figure S7.12. PL decay time of solid complex **3** vs. temperature. As indicated, the decay time varies from 280 μsec at 5 K to 0.15 μsec at 150 K. The red curve represents the fit according to the model of equilibrated S_1 and T_1 states (eq. S1). The fit yields the energy separation ΔE between S_1 and T_1 states of $964 \pm 90 \text{ cm}^{-1}$ and the intrinsic S_1 lifetime $\tau(S_1)$ of about 32 psec. Such extremely short S_1 lifetime is another indicator that the assumption of the thermally equilibrated S_1 , T_1 states fails for **3**. The 'kinetic' model of the thermally activated quenching of the phosphorescent T_1 state - *via* fast internal conversion of the S_1 state populated from T_1 - appears in this case more suitable (eq. 1, see text). The blue dashed curve corresponds to the fit according to eq. 1. It yields the energy separation $\Delta E(S_1-T_1) = 953 \pm 90 \text{ cm}^{-1}$ (as indicated in the Figure) and the pre exponential factor (A in eq. 1) of $8.7 \times 10^9 \text{ sec}^{-1}$. The both fit curves are practically identical due to the very large variation of the PL decay time in **3** (over three orders of magnitude within a narrow temperature interval of ~ 70 -120 K). This variation is described by the exponential factor $\exp(-\Delta E/kT)$ in the denominator of both eq. 1 and S1 - yielding practically the same values of ΔE .

Supporting Information

Table S7.1. Characteristic spectroscopic parameters for the photoluminescence (PL) of complexes **1-4**.

Entry	Complex		1	2	3	4
1	$\lambda(\text{Exc})^a$	[nm]	350	340	330	350
2	$\lambda(\text{Em, low T / high T})^a$	[nm]	492 / 482	450 / 450	440 / 460	500 / 500
3	$\lambda(\text{Max}_{\text{exc}}, \text{low T})^b$	[nm]	356	348	344	372
4	$\lambda(\text{Max}_{\text{emis}}, \text{low T})^b$	[nm]	492	442	442	500
5	$\lambda(\text{Max}_{\text{exc}}, \text{high T})^b$	[nm]	362	367	348	368
6	$\lambda(\text{Max}_{\text{emis}}, \text{high T})^b$	[nm]	482	443	443	500
7	FWHM(low T) ^c	[nm]	111	80	80	77
8	FWHM(high T) ^c	[nm]	103	80	88	89
9	Stokes shift(low T) ^d	[eV]	0.96	0.75	0.79	0.85
10	Stokes shift(high T) ^d	[eV]	0.85	0.58	0.76	0.89
11	$\lambda(\text{Exc}, \phi)^e$	[nm]	350	-	-	-
12	$\phi(295 \text{ K})$	[%]	9	-	-	-
13	τ_1	[nsec]	<5	<5	<5	<5 ^g
14	$\tau_2(\text{low T})^f$	[μsec]	44	45	279	6 ^h
15	$\tau_2(\text{high T})^f$	[μsec]	2.9	6.6 (150 K)	0.15 (150 K)	5.3 ^h

[a] Excitation and emission wavelengths applied for recording the PL and PLE spectra; [b] Band maxima (nm) in emission and excitation spectra; [c] Bandwidth of the PL emission; [d] Determined relative to the maximum of the low-energy band in the PLE spectrum; [e] Excitation wavelength used for determination of the PL quantum yield at ambient temperature, $\phi(295 \text{ K})$; [f] Decay times of the PL at 5 and 295 K, if not indicated otherwise, [g] major emission at 500 nm, [h] minor emission band at 700 nm.

Supporting Information

Table S7.2. Characteristic spectroscopic parameters for the photoluminescence (PL) of complexes 5-7.

Entry	Complex		5	6	7
1	$\lambda(\text{Exc})^a$	[nm]	330	380	300
2	$\lambda(\text{Em, low T / high T})^a$	[nm]	474 / 448	600 / 550	430 / 470
3	$\lambda(\text{Max}_{\text{exc}}, \text{low T})^b$	[nm]	320	378	300
4	$\lambda(\text{Max}_{\text{emis}}, \text{low T})^b$	[nm]	474	520	425
5	$\lambda(\text{Max}_{\text{exc}}, \text{high T})^b$	[nm]	325	370	300
6	$\lambda(\text{Max}_{\text{emis}}, \text{high T})^b$	[nm]	448	520	465
7	FWHM(low T) ^c	[nm]	115	120	88
8	FWHM(high T) ^c	[nm]	112	52	131
9	Stokes shift(low T) ^d	[eV]	1.25	0.90	1.21
10	Stokes shift(high T) ^d	[eV]	1.04	0.97	1.46
11	$\lambda(\text{Exc}, \phi)^e$	[nm]	330	-	-
12	$\phi(\text{high T})$	[%]	3	-	-
13	τ_1	[nsec]	<5	<5	<5
14	$\tau_2(\text{Phosph, low T})^f$	[msec]	4.5	-	-
15	$\tau_2(\text{DF, high T})^f$	[μsec]	24.5	-	-

[a] Excitation and emission wavelengths applied for recording the PL and PLE spectra; [b] Band maxima (nm) in emission and excitation spectra; [c] Bandwidth of the PL emission; [d] Determined relative to the maximum of the low-energy band in the PLE spectrum; [e] Excitation wavelength used for determination of the PL quantum yield at ambient temperature, $\phi(295\text{ K})$; [f] Decay times of the PL at 5 and 295 K.

Supporting Information

8. Step-scan FTIR spectroscopy

General description of step-scan FTIR difference spectra (complex 3)

The negative bands result from the depopulation of the electronic ground state and are thus in very good agreement with the ground state absorption features. The deviations of mostly 1 or 2 cm^{-1} for the bleach bands compared to the corresponding ground state vibrations result from the superposition of positive and negative bands in the step-scan difference spectrum. The positive peaks are assigned to the populated electronically excited state(s), with red- or blue-shifted bands compared to the corresponding ground state vibration.

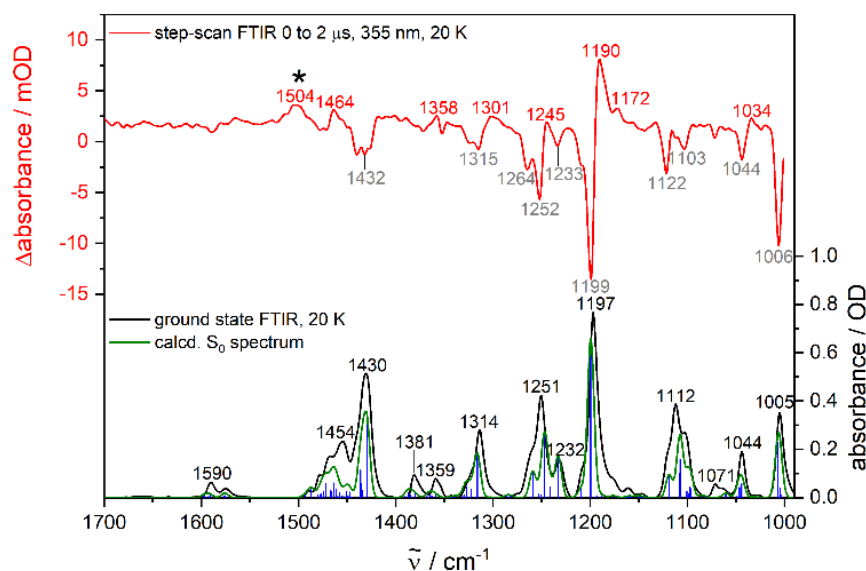


Figure S8.1. Ground state FTIR spectrum (KBr pellet, 20 K) (black), step-scan difference spectrum (0 – 2 μs , $\lambda_{\text{ex}} = 355 \text{ nm}$, KBr pellet, 20 K) (red), DFT calculated S_0 absorption transitions (blue) and simulated S_0 absorption spectrum (green) of **3** (scaled by 0.975, FWHM = 8 cm^{-1} , Gaussian profile) (DFT/B3LYP-D3(BJ)/def2-TZVP).

Supporting Information

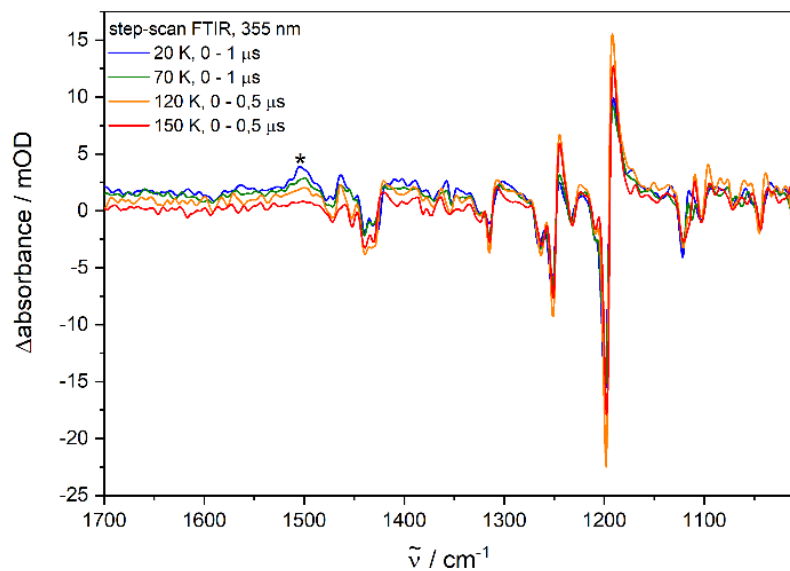


Figure S8.2. Step-scan difference spectra of **3** at 20 K (0 – 1 μs), 70 K (0 – 1 μs), 120 K (0 – 0.5 μs) and 150 K (0 – 0.5 μs) (KBr pellet, $\lambda_{\text{ex}} = 355 \text{ nm}$).

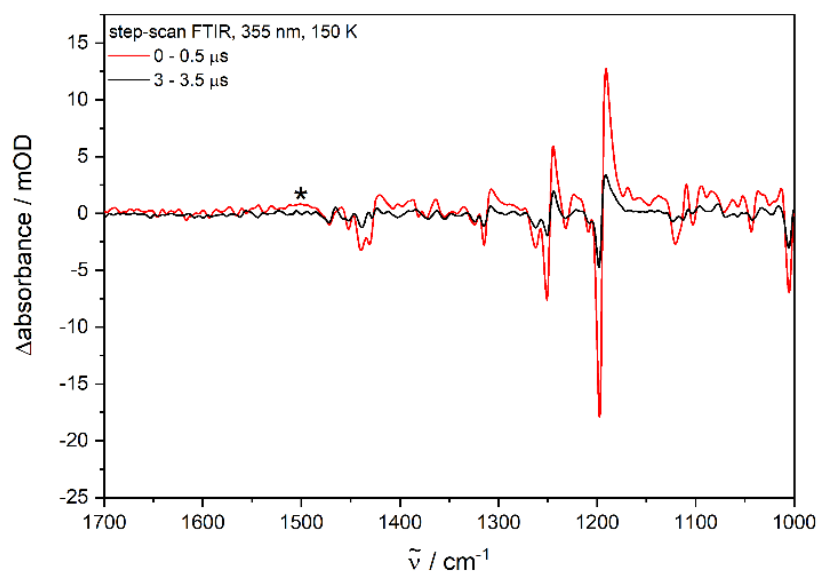


Figure S8.3. Step-scan difference spectra of **3** at 20 K for the time regions of 0 – 0.5 μs (red) and 3.0 – 3.5 μs (black) after laser excitation (KBr pellet, $\lambda_{\text{ex}} = 355 \text{ nm}$).

Supporting Information

Table S8.1. Assignment of the vibrational bands (listed frequencies correspond to the experimental values) of **3** in the S_0 and T_1 states ((U)DFT/B3LYP-D3(BJ)/def2-TZVP).

$\tilde{\nu} / \text{cm}^{-1}$ (ground state)	$\tilde{\nu} / \text{cm}^{-1}$ (excited state)	Character of vibration
1590	-	C-H scissoring combined with C-C stretching in the phenyl rings
1575	1574	C-H scissoring combined with C-C stretching in the phenyl rings
-	1505	C-H scissoring combined with C-C stretching in the P-bonded phenyl rings of one ligand
1488	-	C-H scissoring in the phenyl rings and CH_3 -groups of the isopropyl units
1454	1455	C-H scissoring in the CH_3 -groups of the isopropyl units combined with C-H scissoring in the phenyl rings
1430	1430	C-C stretching and C-H scissoring combined with C-N stretching of the dipp units
1381	1381	symmetrical C-H scissoring in the CH_3 -groups of the isopropyl units
1359	1358	symmetrical C-H scissoring in the CH_3 -groups of the isopropyl units
1314	1314	C-H scissoring of the tertiary H in the isopropyl unit
1260 (shoulder)	-	C-C stretching and C-H scissoring combined with C-N stretching in the dipp units
-	1259	C-C stretching and C-H scissoring combined with C-N stretching on one ligand
1251	1248	C-C stretching combined with C-H scissoring in the phenyl rings and C-H bending in the isopropyl groups
1232	1231	C-C stretching and C-H scissoring in the phenyl rings combined with C-N stretching and bending
-	1207	C-C stretching and C-H scissoring in the phenyl rings combined with C-N stretching
1197	1194	asymmetrical N-P-N stretching combined with C-H scissoring in the phenyl rings
1112	1112	C-P stretching, C-H scissoring in the phenyl rings and CH_3 -groups of the isopropyl units combined with aromatic and aliphatic C-C bending
1071	-	C-H scissoring
1044	1044	C-H scissoring in the isopropyl units combined with phenyl breathing
1005	-	asymmetrical N-P-N stretching combined with breathing in the phenyl rings
969	-	symmetrical N-P-N stretching combined with breathing in the phenyl rings

Supporting Information

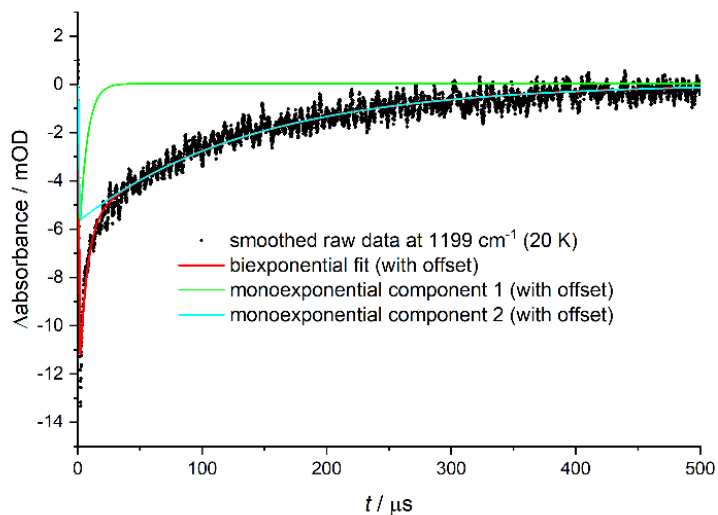


Figure S8.4. Global biexponential fit (red) performed for the negative band at 1199 cm⁻¹ in the step-scan spectrum at 20 K of **3** with an illustration of the underlying monoexponential components (with offset) (green and blue).

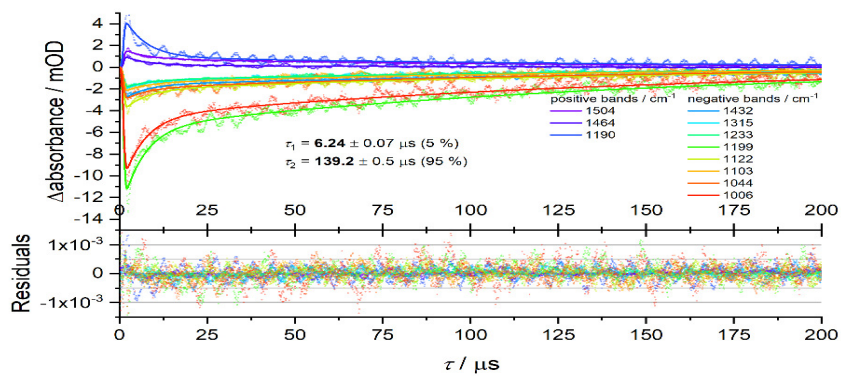
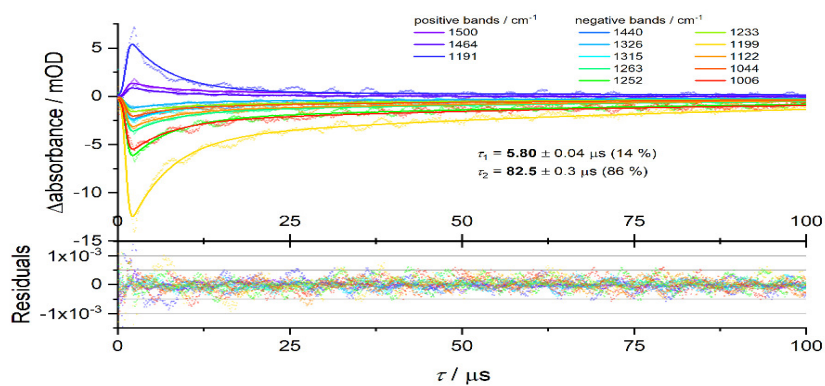
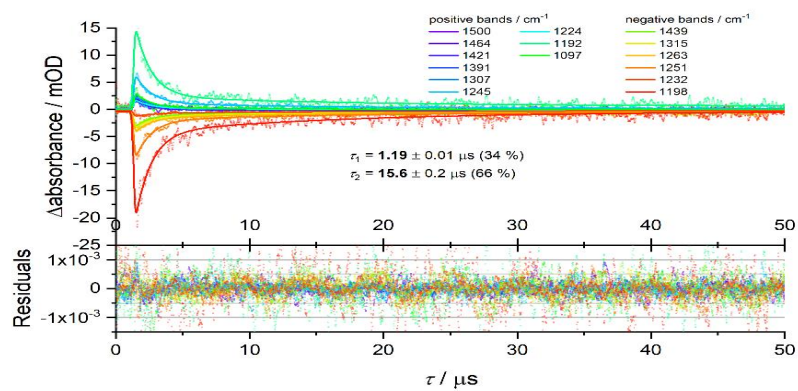


Figure S8.5. Global biexponential fit performed for the step-scan data of **3** at 20 K.

Supporting Information


 Figure S8.6. Global biexponential fit performed for the step-scan data of **3** at 70 K.

 Figure S8.7. Global biexponential fit performed for the step-scan data of **3** at 120 K.

Supporting Information

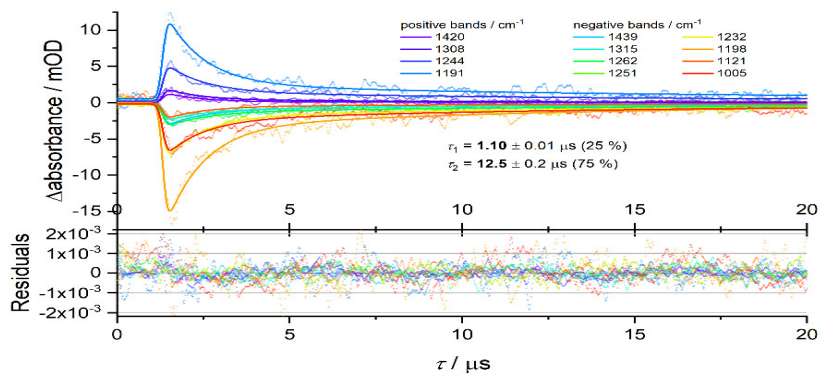


Figure S8.8. Global biexponential fit performed for the step-scan data of **3** at 150 K.

Table S8.2. Excited state lifetimes of **3** obtained from the temperature-dependent step-scan FTIR experiments (KBr pellet, $\lambda_{\text{ex}} = 355 \text{ nm}$).

T / K	$\tau_1 / \mu\text{s}$	$A_1 / \%$	$\tau_2 / \mu\text{s}$	$A_2 / \%$
20	6.24 ± 0.07	5	139.2 ± 0.5	95
70	5.80 ± 0.04	14	82.5 ± 0.3	86
120	1.19 ± 0.01	34	15.6 ± 0.2	66
150	1.10 ± 0.01	25	12.5 ± 0.2	75

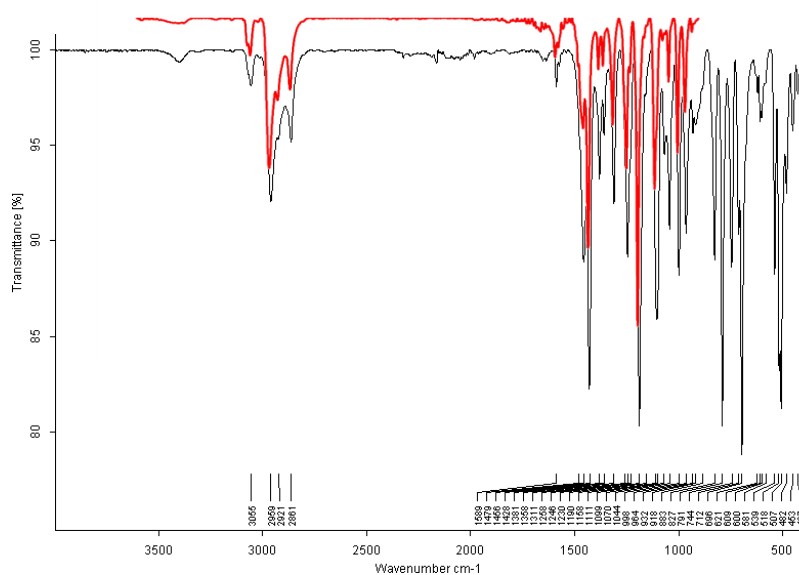


Figure S8.9. Comparison of the ATR spectrum (Fig. S4.3) and the KBR spectrum (red) of complex **3**. The similarity indicates preservation of **3** in the KBR matrix.

Supporting Information

9. Additional calculated data

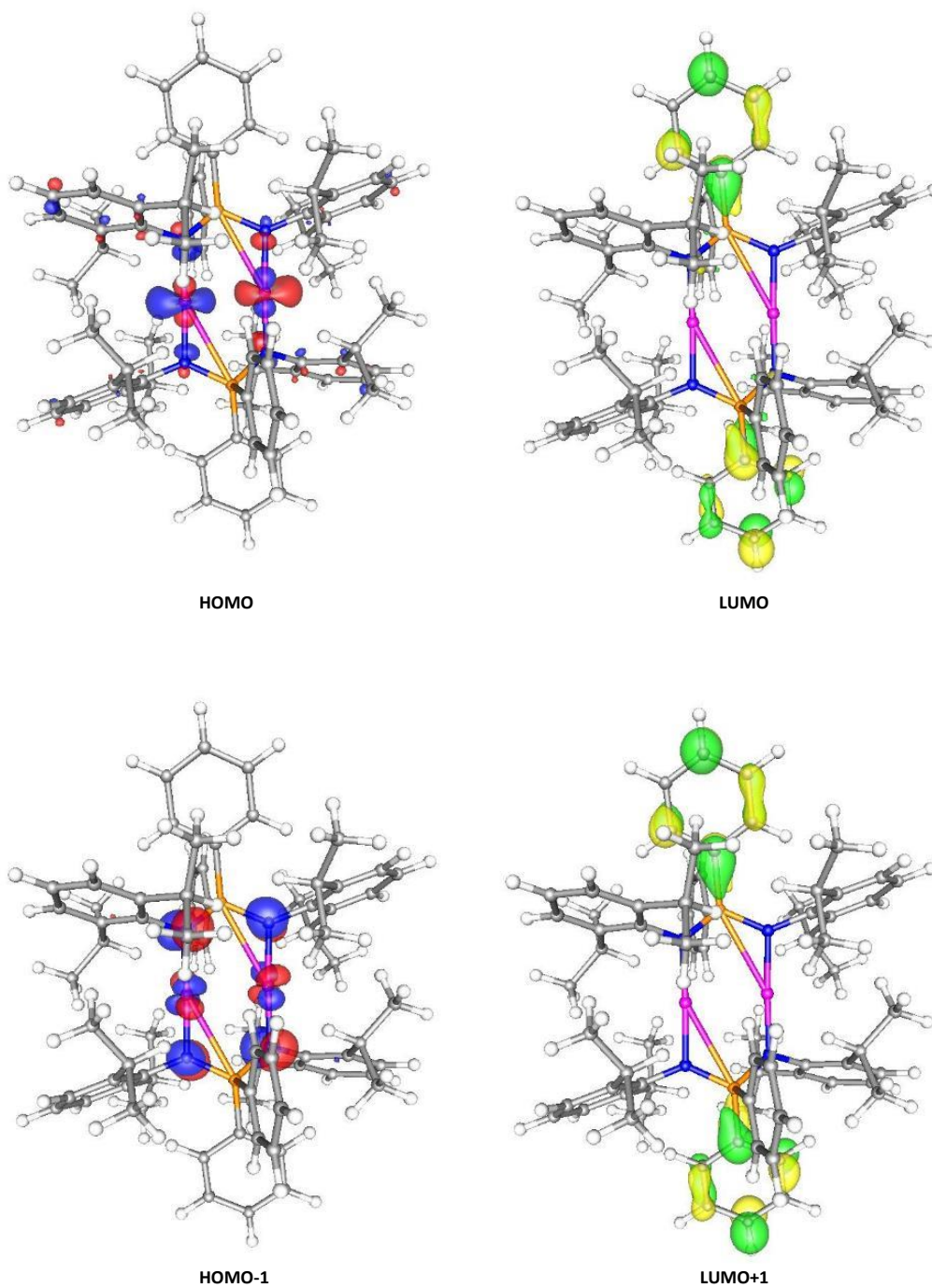
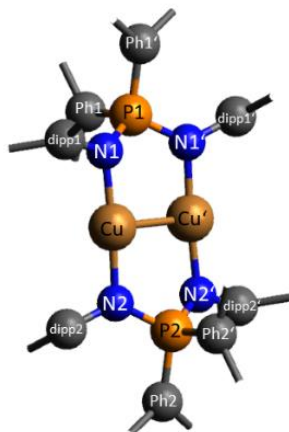


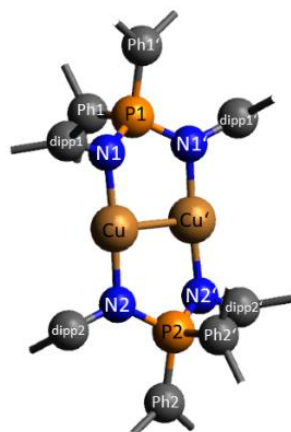
Figure S9.1. Calculated frontier molecular orbitals of **3** in the S_0 state (isovalue: 0.05 a.u.) (DFT/B3LYP-D3(BJ)/def2-TZVP).

Supporting Information

Table S9.1. Calculated bond lengths (Å) and angles (°) of **3** in the S_0 and T_1 states ((U)DFT/B3LYP-D3(BJ)/def2-TZVP).

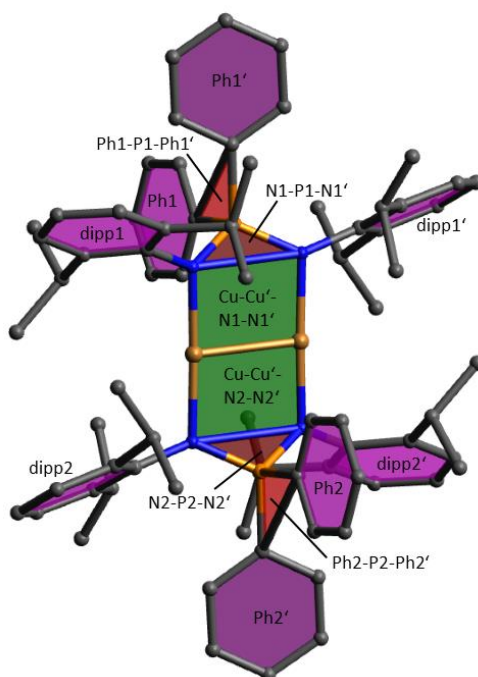
Distances / Å	S_0 vs T_1		
	S_0	T_1	$\Delta(T_1 - S_0)$
Cu-Cu'	2.526	2.508	-0.018
N1-Cu	1.906	1.901	-0.005
N1'-Cu'	1.916	1.912	-0.004
N2-Cu	1.916	1.898	-0.018
N2'-Cu'	1.906	1.871	-0.035
N1...N1'	2.627	2.624	-0.003
N2...N2'	2.627	2.619	-0.008
N1-P1	1.619	1.615	-0.004
N1'-P1	1.617	1.626	0.009
N2-P2	1.617	1.632	0.015
N2'-P2	1.619	1.824	0.205
N1-dipp1	1.423	1.426	0.003
N1'-dipp1'	1.428	1.431	0.003
N2-dipp2	1.428	1.437	0.009
N2'-dipp2'	1.423	1.389	-0.034
P1-Ph1	1.828	1.825	-0.003
P1-Ph1'	1.818	1.817	-0.001
P2-Ph2	1.828	1.766	-0.062
P2-Ph2'	1.818	1.760	-0.058

Supporting Information

Table S9.1. Calculated bond lengths (Å) and angles (°) of **3** in the S_0 and T_1 states ((U)DFT/B3LYP-D3(BJ)/def2-TZVP) (continued).

Angles / °			
	S_0	T_1	$\Delta(T_1 - S_0)$
N1-Cu-N2	176.3	175.4	-0.9
N1'-Cu'-N2'	176.3	174.7	-1.6
N1-P1-N1'	108.5	108.1	-0.4
N2-P2-N2'	108.5	98.4	-10.1
Ph1-P1-Ph1'	102.6	102.1	-0.5
Ph2-P2-Ph2'	102.6	108.5	5.9
N1-Cu-N2	176.3	175.4	-0.9

Supporting Information

Table S9.1. Calculated bond lengths (Å) and angles (°) of **3** in the S_0 and T_1 states ((U)DFT/B3LYP-D3(BJ)/def2-TZVP) (continued).

Dihedral angles / °			
	S_0	T_1	$\Delta(T_1 - S_0)$
ring Ph1 (purple) to Ph1-P1-Ph1' (red)	6.6	6.6	0.0
ring Ph1' (purple) to Ph1-P1-Ph1' (red)	73.0	76.6	3.6
ring Ph2 (purple) to Ph2-P2-Ph2' (red)	-6.6	-8.8	-2.2
ring Ph2' (purple) to Ph2-P2-Ph2' (red)	-73.1	-49.9	23.2
N1-P1-N1' (brown) to Cu-Cu'-N1-N1' (green)	140.2	138.5	-1.7
N2-P2-N2' (brown) to Cu-Cu'-N2-N2' (green)	144.6	143.7	-0.9
ring dipp1 (purple) to Cu-Cu'-N1-N1' (green)	64.8	62.1	-2.7

Supporting Information

10. References

- [1] T. J. Feuerstein, B. Goswami, P. Rauthe, R. Köppe, S. Lebedkin, M. M. Kappes, P. W. Roesky, *Chem. Sci.* **2019**, *10*, 4742-4749.
- [2] B. Goswami, T. J. Feuerstein, R. Yadav, R. Köppe, S. Lebedkin, M. M. Kappes, P. W. Roesky, *Chem. Eur. J.* **2021**, *27*, 4401-4411.
- [3] A. Stasch, *Chem. Eur. J.* **2012**, *18*, 15105-15112.
- [4] a) G. Sheldrick, *Acta Crystallogr. A* **2008**, *64*, 112-122; b) G. Sheldrick, *Acta Crystallogr. C* **2015**, *71*, 3-8.
- [5] O. V. Dolomanov, L. J. Bourhis, R. J. Gildea, J. A. K. Howard, H. Puschmann, *J. Appl. Crystallogr.* **2009**, *42*, 339-341.
- [6] J. C. de Mello, H. F. Wittmann, R. H. Friend, *Adv. Mater.* **1997**, *9*, 230-232.
- [7] M. J. Leitl, F.-R. Küchle, H. A. Mayer, L. Wesemann, H. Yersin, *J. Phys. Chem. A* **2013**, *117*, 11823-11836.
- [8] M. J. Frisch, G. W. Trucks, H. B. Schlegel, G. E. Scuseria, M. A. Robb, J. R. Cheeseman, G. Scalmani, V. Barone, B. Mennucci, G. A. Petersson, H. Nakatsuji, M. Caricato, H. P. H. X. Li, A. F. Izmaylov, J. Bloino, G. Zheng, J. L. Sonnenberg, M. Hada, M. Ehara, K. Toyota, R. Fukuda, J. Hasegawa, M. Ishida, T. Nakajima, Y. Honda, O. Kitao, H. Nakai, T. Vreven, J. J. A. Montgomery, J. E. Peralta, F. Ogliaro, M. Bearpark, J. J. Heyd, E. Brothers, K. N. Kudin, V. N. Staroverov, T. Keith, R. Kobayashi, J. Normand, K. Raghavachari, A. Rendell, J. C. Burant, S. S. Iyengar, J. Tomasi, M. Cossi, N. Rega, J. M. Millam, M. Klene, J. E. Knox, J. B. Cross, V. Bakken, C. Adamo, J. Jaramillo, R. Gomperts, R. E. Stratmann, O. Yazyev, A. J. Austin, R. Cammi, C. Pomelli, J. W. Ochterski, R. L. Martin, K. Morokuma, V. G. Zakrzewski, G. A. Voth, P. Salvador, J. J. Dannenberg, S. Dapprich, A. D. Daniels, O. Farkas, J. B. Foresman, J. V. Ortiz, J. Cioslowski, D. J. Fox, *Gaussian 09, Gaussian, Inc., Wallingford, CT*, **2013**.
- [9] F. Furche, R. Ahlrichs, C. Hättig, W. Klopper, M. Sierka, F. Weigend, *WIREs Computational Molecular Science* **2014**, *4*, 91-100.
- [10] TURBOMOLE V7.4 2019, a development of University of Karlsruhe and Forschungszentrum Karlsruhe GmbH, 1989-2007, TURBOMOLE GmbH, since 2007; available from <http://www.turbomole.com>.
- [11] a) S. Ehrlich, J. Moellmann, W. Reckien, T. Bredow, S. Grimme, *ChemPhysChem* **2011**, *12*, 3414-3420; b) S. Grimme, S. Ehrlich, L. Goerigk, *J. Comput. Chem.* **2011**, *32*, 1456-1465.
- [12] M. Llunell, P. Alemany, S. Alvarez, Shape 2.1 for Windows (32 bit). Available from: http://www.ee.ub.edu/index.php?option=com_jdownloads&view=viewcategories&Itemid=529. Accessed:07/31/2019.

4.4 An Unexpected Boost in Activity of a Cu(I) Photosensitizer by Stabilizing a Transient Excited State

4.4.1 Präambel

In diesem Teil der Arbeit werden die photophysikalischen Eigenschaften und die Katalyseeigenschaften eines Kupfer-Photosensibilisators untersucht. Unter anderem über Step-scan-FTIR- und Lumineszenzspektroskopie sowie Untersuchungen zur Fähigkeit zu Photon Upconversion und Singulett-Sauerstoffbildung konnte eine Verbesserung der für Photosensibilisatoren relevanten Eigenschaften gezeigt werden.

Zusammen mit Pit Boden habe ich die Step-scan-Untersuchungen sowie die Lumineszenzspektroskopie an den Feststoffproben temperaturabhängig durchgeführt. Außerdem haben wir die Singulett-Sauerstoff-Quantenausbeute und die Fähigkeit des Komplexes zu Photon Upconversion bestimmt. Ich habe die DFT-Rechnungen durchgeführt. Pit Boden und ich wurden von Gereon Niedner-Schatteburg betreut.

Martin Rentschler hat die Komplexe synthetisiert und charakterisiert. Er hat außerdem die Untersuchungen zur katalytischen Aktivität durchgeführt. Martin Rentschler wurde von Michael Karnahl und Stefanie Tschierlei betreut. Miguel Argüello Cordero hat die fs-transiente Absorptionsspektroskopie und die ps-zeitaufgelöste Lumineszenz in Lösung durchgeführt. Er wurde betreut von Stefan Lochbrunner. Die elektrochemischen Untersuchungen wurden von Marie-Ann Schmied durchgeführt. Yingya Yang hat die ns-transiente Absorptionsspektroskopie und die ns-zeitaufgelöste Lumineszenz in Lösung untersucht. Marie-Ann Schmied und Yingya Yang wurden von Stefanie Tschierlei betreut. Das Manuskript wurde von allen Autoren gemeinsam geschrieben.

4.4.2 Nachdruck und ergänzende Informationen

Unexpected Boost in Activity of a Cu(I) Photosensitizer by Stabilizing a Transient Excited State

Author: Martin Rentschler, Pit Jean Boden, Miguel A. Argüello Cordero, et al

Publication: Inorganic Chemistry

Publisher: American Chemical Society

Date: Aug 1, 2022

Copyright © 2022, American Chemical Society

PERMISSION/LICENSE IS GRANTED FOR YOUR ORDER AT NO CHARGE

This type of permission/license, instead of the standard Terms and Conditions, is sent to you because no fee is being charged for your order. Please note the following:

- Permission is granted for your request in both print and electronic formats, and translations.
- If figures and/or tables were requested, they may be adapted or used in part.
- Please print this page for your records and send a copy of it to your publisher/graduate school.
- Appropriate credit for the requested material should be given as follows: "Reprinted (adapted) with permission from {COMPLETE REFERENCE CITATION}. Copyright {YEAR} American Chemical Society." Insert appropriate information in place of the capitalized words.
- One-time permission is granted only for the use specified in your RightsLink request. No additional uses are granted (such as derivative works or other editions). For any uses, please submit a new request.

If credit is given to another source for the material you requested from RightsLink, permission must be obtained from that source.

[BACK](#) [CLOSE WINDOW](#)

Unexpected Boost in Activity of a Cu(I) Photosensitizer by Stabilizing a Transient Excited State

Martin Rentschler,^{||} Pit Jean Boden,^{||} Miguel A. Argüello Cordero,^{||} Sophie Theres Steiger, Marie-Ann Schmid, Yingya Yang, Gereon Niedner-Schatteburg,* Michael Karnahl,* Stefan Lochbrunner,* and Stefanie Tschierlei*

Cite This: *Inorg. Chem.* 2022, 61, 12249–12261

Read Online

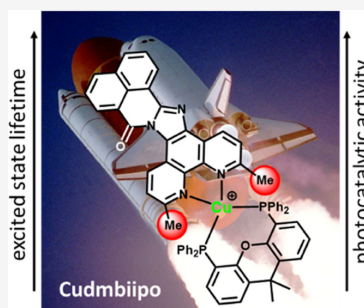
ACCESS |

Metrics & More

Article Recommendations

Supporting Information

ABSTRACT: In this study, we present a slight but surprisingly successful structural modification of the previously reported heteroleptic Cu(I) photosensitizer **Cubiipo** ($[(\text{xantphos})\text{Cu}(\text{biipo})]\text{PF}_6$; **biipo** = 16*H*-benzo-[4',5']-isoquinolino-[2',1':1,2]-imidazo-[4,5-*f*]-[1,10]-phenanthroline-16-one). As a key feature, **biipo** bears a naphthalimide unit at the back, which is directly fused to a phenanthroline moiety to extend the conjugated π -system. This ligand was now altered to include two additional methyl groups at the 2,9-positions at the phenanthroline scaffold. Comparing the novel **Cudmbiipo** complex to its predecessor, ultrafast transient absorption spectroscopy reveals the efficient suppression of a major deactivation pathway by stabilization of a transient triplet state. Furthermore, quantitative measurements of singlet oxygen evolution in solution confirmed that a larger fraction of the excited-state population is transferred to the photocatalytically active ligand-centered triplet ^3LC state with a much longer lifetime of $\sim 30 \mu\text{s}$ compared to **Cubiipo** (2.6 μs). In addition, **Cudmbiipo** was compared with the well-established reference complex **Cubcp** ($[(\text{xantphos})\text{Cu}(\text{bathocuproine})]\text{PF}_6$) in terms of its photophysical and photocatalytic properties by applying time-resolved femto- and nanosecond absorption, step-scan Fourier transform infrared (FTIR), and emission spectroscopies. Superior light-harvesting properties and a greatly enhanced excited-state lifetime with respect to **Cubcp** enable **Cudmbiipo** to be more active in exemplary photocatalytic applications, *i.e.*, in the formation of singlet oxygen and the isomerization of (*E*)-stilbene.



INTRODUCTION

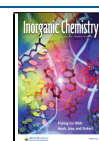
The increased use and conversion of solar energy into electrical or chemical energy can make an essential contribution to solve the problems caused by the rising global energy demand.^{1–3} At the same time, this would conserve valuable fossil resources and reduce the man-made greenhouse effect.^{2,4,5} Furthermore, light-driven reactions enable the efficient production of important compounds, which are used in medicine, chemical industry, and material science.^{6–8} In this context, the effective collection and use of sunlight are of particular relevance. For this reason, there is a long-lasting interest in the design of efficient molecular photosensitizers and photocatalysts.^{9–13} Besides a sufficient (photo)stability and a reversible electrochemical behavior, these molecules should absorb in a wide range of visible light and possess long-lived excited states to enable subsequent chemical reactions.^{10,12,14,15} In addition to organic dyes, especially transition-metal complexes play a crucial role due to their advantageous properties and easy tunability. In fact, traditional noble metal complexes based on Ru(II),^{16–18} Ir(III),^{19–21} or Re(I)^{16,21} have attracted much attention during the last decades and are still under constant development. However, the interest in complexes using more earth-abundant 3d metals such as Cr,^{22–26} Fe,^{27–29} Zn,^{30,31}

and Cu^{12,32–38} is strongly increasing due to advantages in costs and availability.

Although the choice of the metal center is important, the proper selection and optimization of the surrounding ligands are crucial.^{10,38,39} In this regard, we and others have found that particularly large diimine ligands with an extended π -system in their backbone can provide beneficial properties.^{40–44} Consequently, several recent studies report on the successful application of 16*H*-benzo-[4',5']-isoquinolino-[2',1':1,2]-imidazo-[4,5-*f*]-[1,10]-phenanthroline-16-one (**biipo**), a fully conjugated and planar phenanthroline-based ligand (see Figure 1).^{45–47} As a key feature of **biipo**, an imide unit is directly fused to the 1,10-phenanthroline core.^{45–47} When coordinated to a photoactive metal center (see Figure 1), this ligand forms a bichromophoric system consisting of a metal-phenanthroline unit and the fused naphthalimide unit.

Received: April 28, 2022

Published: July 25, 2022



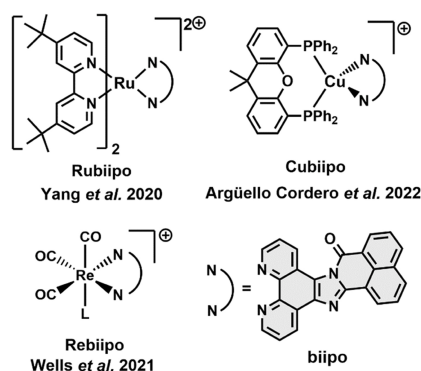


Figure 1. Structure of the **biipo** ligand (bottom right) and of related complexes previously studied.

The naphthalimide unit, as an organic chromophore, exhibits a long-lived and nonemissive excited triplet state (^3LC), which is reached only with a low quantum yield due to the absence of heavy atoms.^{48,49} However, the functional interaction between the metal–phenanthroline part of the resulting complexes and the naphthalimide moiety can circumvent this bottleneck, combining the advantages of purely organic and transition-metal-based chromophores.^{45,47,48,50,51} In these complexes, the absorption of a visible photon causes a transition to an electronically excited singlet state, which can then relax into a ligand-centered ^3LC state.^{47,48,50,51} This relaxation often involves a triplet metal-to-ligand charge-transfer state ($^3\text{MLCT}$). A fast population of the ^3LC state of **biipo** was demonstrated for a corresponding Ru(II) and a Re(I) complex (see Figure 1).^{46,47} Interestingly, in the former case, even a thermal equilibrium between the $^3\text{MLCT}$ and the ^3LC state was found.⁴⁷ As the first example of a complex based on **biipo** and a nonprecious metal, **Cubiipo** was recently studied, which exhibits also a fast relaxation into the ^3LC state.⁴⁷ In this case, the ^3LC state is dark since it is completely localized on the ligand and the triplet state of an organic moiety has no transition dipole moment to the ground state. It exhibits a lifetime of 2.6 μs at room temperature in acetonitrile (MeCN) solution, which is 1 order of magnitude longer than that of the well-known Cu(I) reference photosensitizer (xant)Cu(bcp)PF₆ (0.3 μs , with xant = xantphos and bcp = bathocuproine, **Cubcp**, see Figure 2).⁵² In contrast to the ^3LC state, the excited $^3\text{MLCT}$ states of typical Cu(I) phenanthroline photosensitizers show an oxidized metal center and an accordingly filled π^* -orbital at the phenanthroline unit.^{12,39,53,54} The resulting formal d⁹ electron configuration causes a pseudo-Jahn–Teller distortion (excited-state flat-

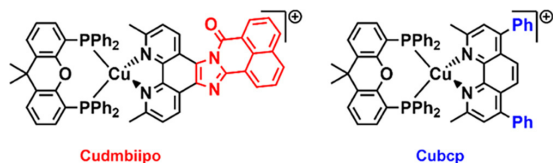


Figure 2. Structural formulae of the new Cu(I) photosensitizer **Cudmbiipo** and the reference complex **Cubcp** investigated in this study together with the plain ligands and the predecessor complex **Cubiipo**.

tening). Consequently, the rather square planar $^3\text{MLCT}$ state undergoes quite efficient nonemissive quenching by nucleophiles attacking the free coordination site that opens in the apical position.^{12,39,54,55}

Despite the rather long-lived ^3LC state of **Cubiipo**, the much lower singlet oxygen yield in MeCN compared to the corresponding Ru(II) complex (tbbpy)₂Ru(biipo)(PF₆)₂ (**Rubiipo**, tbbpy = 4,4'-bis-*tert*-butyl-2,2'-bipyridine)⁴⁷ indicates an unsatisfactory photocatalytic activity. Hence, the aim of the present study is to address this issue and to improve this very promising class of heteroleptic Cu(I) photosensitizers further. To this end, a derivative of the **biipo** ligand with two additional methyl groups in close proximity to the nitrogen donor atoms was developed (**dmbiipo**) and the corresponding heteroleptic Cu(I) complex (xant)Cu(dmbiipo)PF₆ (**Cudmbiipo**) was prepared (see Figure 2).

Bulky groups at the 2,9-positions are often added to the 1,10-phenanthroline scaffold of Cu(I)-based photosensitizers to prevent the flattening distortion of the complex in the excited state.^{12,38,55} In consequence, the metal center is less accessible to nucleophilic quenching, resulting in increased excited-state lifetimes and emission quantum yields.^{38,53,56} As demonstrated by similar copper complexes that only vary in the presence or absence of methyl substituents, the lifetimes and quantum yields can differ by 2 orders of magnitude.^{12,32,38,57}

Therefore, we investigated the impact of this structural modification on the photocatalytic and photophysical properties of **Cudmbiipo** in detail and compared these properties to those of the Cu(I) reference complex **Cubcp**. The selection of **Cubcp** as a reference is based on its state-of-the-art photocatalytic properties with, *e.g.*, an efficient hydrogen production exceeding the capabilities of other structurally related systems.³⁸ Considering our previous studies on **Cubiipo**, which did not reveal a significant flattening distortion in the long-lived excited state,⁴⁷ a large influence of the methylation in **Cudmbiipo** does not seem obvious at first sight. However, the studies presented herein revealed that, interestingly, its photoactivity is strongly boosted. The electrochemical and photophysical properties of the complexes were investigated by cyclic voltammetry, UV/vis absorption and emission spectroscopy, and time-resolved Fourier transform infrared (FTIR) spectroscopy. To characterize the photoinduced intramolecular dynamics, we also performed femto- and nanosecond transient absorption (TA) measurements on **Cudmbiipo** as well as the plain **biipo** and **dmbiipo** ligands. Most importantly, **Cudmbiipo** and **Cubcp** were studied regarding their activity in two different photocatalytic applications, *i.e.*, the isomerization of (*E*)-stilbene and the generation of singlet oxygen ($^1\text{O}_2$). Finally, the suitability of **Cudmbiipo** for photon upconversion was successfully tested, making this complex a promising candidate for numerous other solar energy conversion applications.

EXPERIMENTAL SECTION

Detailed experimental and theoretical data as well as thorough descriptions of experimental setups are given in the Supporting Information (SI).

RESULTS AND DISCUSSION

Synthesis and Structural Characterization. The novel **dmbiipo** ligand was prepared analogously to the previously presented **biipo** ligand.⁴⁵ For this purpose, 2,9-dimethyl-1,10-

phenanthroline-5,6-dioxime^{58,59} was reduced to 5,6-diamino-2,9-dimethyl-1,10-phenanthroline by sodiumdithionite.⁶⁰ The crude product was then directly used for the double condensation reaction with naphthalene dicarboxylic anhydride. This condensation reaction was performed at 140 °C in degassed acetic acid yielding **dmbiipo** in a total yield of 45% over these two steps (see SI, Section S2).

The resulting heteroleptic Cu(I) complex **Cudmbiipo** (see Figure 2) was synthesized by a one-pot two-step procedure, similar to previously prepared heteroleptic Cu(I) photosensitizers.^{41,43,61} Starting from the Cu(MeCN)₄PF₆ precursor, xantphos is introduced first, by refluxing the two compounds in dichloromethane under inert conditions. Hereby, the (xant)-Cu(MeCN)₂⁺ intermediate is formed. After that, the diimine ligand needs to be introduced carefully to avoid the displacement of the xantphos ligand and the formation of the homoleptic bisdiimine complex.^{62–64} This is achieved by the dropwise addition of a solution of the diimine ligand at a decreased temperature (0 °C).⁶¹ Finally, **Cudmbiipo** was obtained as a yellow solid in a 67% yield. This complex was then fully characterized by ¹H, ¹³C, and ³¹P NMR spectroscopy, high-resolution mass spectrometry (HRMS), and elemental analysis. The analytical data obtained are given in the Supporting Information (see Section S3) and are consistent with the proposed structure. The reference complex **Cubcp** was synthesized in an analogous manner.⁶¹

Electrochemical Behavior. The electrochemical data of **Cudmbiipo** and **dmbiipo** were determined by cyclic and differential pulse voltammetry in MeCN solution under inert conditions containing 0.1 M *n*-Bu₄NPF₆ as the supporting electrolyte (see Figures S7–S10). The redox properties are compared with the previously published data of **biipo** and **Cubiipo**.^{45,47} **Cudmbiipo** shows one irreversible oxidation event at 0.96 V vs Fc/Fc⁺, which is typical for this kind of heteroleptic Cu(I) complex.^{12,35,41,65} This can be ascribed to a Cu^{I/II} oxidation followed by a dissociation of the Cu–P bond.^{12,35,41,65} In addition, there is a shoulder at about +0.8 V (see Figure S7), which likely originates from decomposition products of the **dmbiipo** ligand. Furthermore, there are two reversible one-electron reductions at –1.52 and –2.22 V vs Fc/Fc⁺. The first reduction is attributed to the reduction of the naphthaloylene moiety and is also observed in the **dmbiipo** ligand, where it is cathodically shifted by 80 mV to –1.60 V vs Fc/Fc⁺. The second reduction of the **dmbiipo** ligand (–2.23 V) and the **Cudmbiipo** complex (–2.22 V) can be assigned to the phenanthroline moiety. There are only negligible differences compared to the reduction potentials of **Cubiipo** ($E_{\text{red}} = -1.49$ and -2.17 V vs Fc/Fc⁺),⁴⁷ suggesting a small impact of the additional methyl groups on the electrochemical behavior.

Steady-State Absorption and Emission Spectroscopy. The UV/vis absorption spectrum of **Cudmbiipo** in MeCN shows a broad visible absorption band centered at 408 nm with an onset at 500 nm (see Figures 3 and S11). Consequently, **Cudmbiipo** has a broader absorption in the visible region compared to **Cubiipo**, but with a lower extinction coefficient of 8.6×10^3 L mol⁻¹ cm⁻¹ at 408 nm.⁴⁷ Nevertheless, the intensity of the lowest absorption band is stronger compared to the corresponding band of the reference complex **Cubcp** ($\epsilon = 5.2 \times 10^3$ L mol⁻¹ cm⁻¹),⁶⁶ whose lowest-energy maximum is at 387 nm⁶⁶ and thus outside the visible spectral range. The visible absorption of **Cudmbiipo** is also reproduced by time-dependent density functional theory (TDDFT) with three

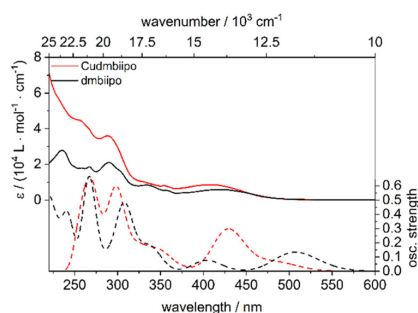


Figure 3. Experimental (solid lines) and theoretical (dashed lines) UV/vis absorption spectra of **Cudmbiipo** (red) and **dmbiipo** (black) in MeCN solution. Calculations: TDDFT/B3LYP-D3(BJ)/def2-TZVP.

vertical transitions of significant intensity (see Table S1), although the experimental energies are slightly underestimated. According to theory, these transitions are of MLCT character with a transfer of electron density from the Cu(I) center to the π -system of the **dmbiipo** ligand with a significant contribution of $\pi \rightarrow \pi^*$ transitions on the **dmbiipo** ligand for the highest of these frequencies. The same assignment applies to the small band experimentally observed at 355 nm, while the high-energy features at 288 and 256 nm also involve the xantphos ligand (see Table S1). Interestingly, the UV/vis absorption spectrum of **dmbiipo** has a similar shape to that of **Cudmbiipo**, but with consistently lower extinction coefficients, confirming the positive impact of the metal center (see Figures 3 and S12). In the case of **dmbiipo**, the visible absorption band is slightly red-shifted by about 10 nm relative to **Cudmbiipo** and has a maximum at 419 nm (see Figure 3). According to the TDDFT calculations, the absorption of **dmbiipo** is mainly composed of $\pi \rightarrow \pi^*$ transitions (see Figure S12 and Table S2).

Furthermore, the UV/vis absorption of **Cudmbiipo** and **dmbiipo** was also determined in the solid state, displaying a red shift compared to the absorption in solution (see Figure S13). At the same time, **Cudmbiipo** is approx. 30 nm blue-shifted relative to **dmbiipo**, which agrees with the trend observed in solution (see Figure S13). In the next step, the emission properties were examined in more detail. The emission spectrum of the plain **dmbiipo** ligand in MeCN shows a broad emission band with a maximum at 572 nm (see Figure 4a) and is red-shifted compared to **biipo** ($\lambda_{\text{em}} = 540$ nm).⁴⁵ In MeCN, **Cudmbiipo** exhibits the same emission spectrum as the solution of the pure ligand, which is identical to the situation already observed for **biipo** and **Cubiipo**.⁴⁷ In solution, both complexes seem to release a small amount of their respective diimine ligand, which is responsible for the observed emission, as the emission spectra of the complex and ligand are identical (see Figure S15 for normalized plots and further explanations).

Due to the much higher solubility of **dmbiipo** and **biipo** in hexafluoroisopropanol (HFIP), required for femtosecond absorption spectroscopy (see below), the emission was also studied in HFIP solutions.⁶⁷ The static absorption and emission spectra as well as the emission lifetimes of 3.3 ns for **biipo** and 4.1 ns for **dmbiipo** in HFIP are comparable to those in MeCN (see Figure S14 for absorption spectra, Figure 4a for emission spectra, and Figures S31 and S32 for an

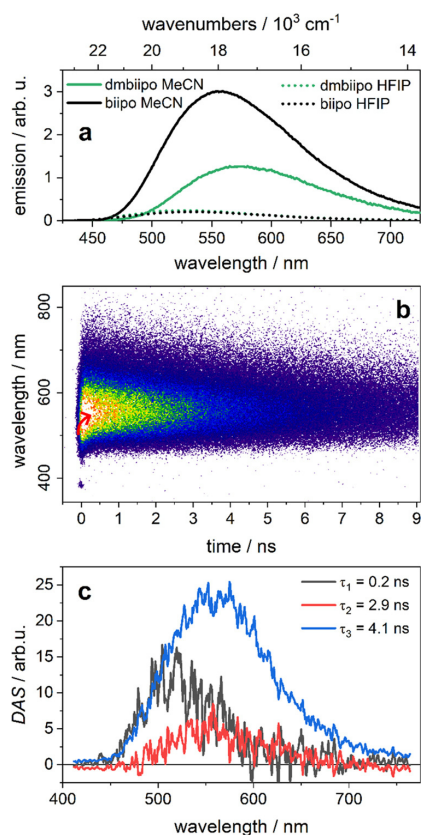


Figure 4. (a) Static emission spectra of **dmbiipo** and **biipo** (data of **biipo** is partly taken from ref 47) dissolved in MeCN (solid) or hexafluoroisopropanol (HFIP) (dotted). (b) Time-dependent emission spectra and (c) decay-associated spectra (DAS) of **dmbiipo** dissolved in HFIP. The DAS are labeled by the corresponding decay constants. All emission measurements were performed with excitation at 388 nm.

emissive lifetime in HFIP). In both cases, the emission decay was fitted with a biexponential function and the average lifetime was calculated using the corresponding amplitudes. The emission with lifetimes of few nanoseconds for both ligands should originate from the same S_1 state as fluorescence in both solutions. The radiative lifetimes τ_{rad} calculated from the corresponding quantum yields ϕ and fluorescence lifetimes τ_{S_1} via $\tau_{\text{rad}} = \tau_{S_1}/\phi$, are very similar for all four solutions (see Table 1), confirming this assumption. The decrease of the excited-state lifetime might be related to the strong hydrogen

Table 1. Summary of the Fluorescence Lifetimes τ_{S_1} , Quantum Yields ϕ , and Calculated Radiative Lifetimes τ_{rad} of the Ligands **biipo** and **dmbiipo** in MeCN and in HFIP Solution

		τ_{S_1} (ns)	ϕ	τ_{rad} (ns)
MeCN	biipo	9.2	0.27	34
	dmbiipo	5.7	0.14	41
HFIP	biipo	3.3	0.08	41
	dmbiipo	4.1	0.11	37

bond donating properties of HFIP,⁶⁷ which slightly changes the energy of the emitting state. This is reflected by a weak blue shift of the emission. The corresponding small increase of the energy of the excited state could reduce a barrier of the nonradiative internal conversion channel, resulting in reduced emission lifetimes and quantum yields.

To get more detailed insights into the fluorescence dynamics, we performed a second measurement of the time-dependent fluorescence of both ligands in HFIP, focussing on the first 10 ns (Figure 4, while those for **biipo** can be found in Figures S33 and S34). The red arrow in Figure 4b indicates a small red shift of the spectra of **dmbiipo** during the first 100 ps. Three exponential decay components ($\tau_1 = 0.2 \text{ ns}$, $\tau_2 = 2.9 \text{ ns}$, and $\tau_3 = 4.1 \text{ ns}$) were found for **dmbiipo** by a global lifetime analysis (see Figure 4c). The decay-associated spectra (DAS) of the fastest component τ_1 reflect the mentioned shift of the fluorescence spectrum. The DAS of the other two components τ_2 and τ_3 provide spectral information about the emission lifetimes that were used to determine the average fluorescence lifetime. Given the fact that these two DAS have almost the same shape and center wavelength, we conclude that the two components parameterize a nonexponential fluorescence decay. It is known that HFIP molecules can form helical aggregates due to their strong hydrogen-bonding properties.⁶⁷ As a result, the interactions of HFIP with the solute can cause complex solvation dynamics on multiple timescales, which is most likely responsible for the fast spectral shift of the fluorescence and its nonexponential decay.^{68–70} A quite similar behavior is also found for the fluorescence and the respective decay constants of **biipo**, as presented in the SI ($\tau_1 = 0.3 \text{ ns}$, $\tau_2 = 2.1 \text{ ns}$, and $\tau_3 = 4.8 \text{ ns}$; see Figure S34).

In addition to the emission studies in solution, temperature-dependent luminescence studies were performed in a KBr matrix to analyze potential thermally activated deactivation processes. In contrast to **Cudmbiipo** in solution, a significant luminescence was observed in the solid state, which is centered at 569 nm at 290 K (see Figure 5). When the sample is cooled to 5 K, the integrated luminescence increases more than 7-fold compared to 290 K (see the inset in Figure 5). Furthermore, the emission maximum blue-shifts to 562 nm, which may result from the literature-known rigidochromism^{71,72} with an inhibited relaxation of the excited state in the rigid matrix at low temperatures. A shoulder can be seen at 654 nm, which

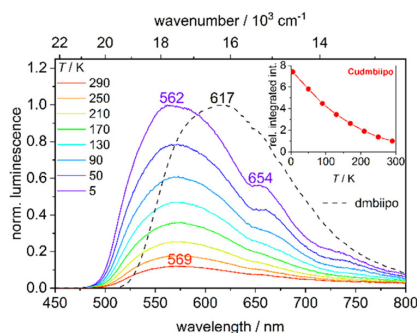


Figure 5. Temperature-dependent solid-state luminescence spectra of **Cudmbiipo** in the range of 290–5 K at an excitation wavelength of 420 nm. The dashed black line represents the solid-state emission of the **dmbiipo** ligand at 5 K. The inset shows the integrated luminescence intensity of **Cudmbiipo** relative to 290 K.

could be due to a vibrational level in the electronic ground state. Interestingly, the solid-state emission of **Cudmbiipo** is clearly blue-shifted relative to the **dmbiipo** ligand, which shows an emission centered at 617 nm independent of the temperature (see Figures 5 and S18). To further exclude the possibility that the luminescence of solid **Cudmbiipo** results from dissociated **dmbiipo** molecules, excitation spectra were recorded of both compounds (see Figure S20), which were then directly compared to the UV/vis absorption spectra of the corresponding solid powder samples (compound diluted with KBr) (see Figure S19). The absorption and excitation spectra of **Cudmbiipo** and **dmbiipo** have almost identical onsets in the visible spectral region, which were determined tangentially to 520 and 568 nm, respectively. Hence, **Cudmbiipo** is blue-shifted compared to **dmbiipo**, as already evident from the luminescence spectra (see above) and the calculated vertical excitation energies (see Figure S13). The very good match between the absorption and excitation spectra strengthens the statement that **Cudmbiipo** indeed exhibits luminescence in the solid state, in contrast to the liquid phase. At the same time, this observation differs from the absence of significant emission in the case of **Cubiipo**, regardless of the medium,⁴⁷ underlining the strong influence of the additional methyl groups in **Cudmbiipo**.

The character of the emission of **Cudmbiipo** in the solid state was further investigated by time-correlated single photon counting (TCSPC) at different temperatures. Triexponential fits on the measured decay curves yielded an amplitude-weighted average lifetime of 2.0–4.3 ns over the whole temperature range of 290–5 K. It should be noted that the underlying triexponential decay (see Table S3) most likely results from different microenvironments in the KBr matrix (e.g. aggregation of several sample molecules or direct contact with KBr on a molecular level) rather than different electronically excited states. The average lifetimes of a few nanoseconds (2.0–4.3 ns) suggest an assignment to pure fluorescence from the S_1 state for **Cudmbiipo** (see Figure S24 and Table S3), which is also true for the lifetimes of 4.6–11 ns of **dmbiipo** (see Figure S25 and Table S3). These results clearly imply that neither **Cudmbiipo** nor the underlying **dmbiipo** ligand possesses a long-lived luminescent excited state (e.g. triplet state).

The reference complex **Cubcp**, prepared as a KBr pellet, shows a broad emission with a maximum at 583 nm at 290 K (see Figure S21), similar to other luminescence studies on powdered samples⁷³ and solutions^{56,73,74} previously reported in the literature. Cooling of the sample induces a progressive red shift to 606 nm at 130 K before the red shift turns into a blue shift at temperatures below 130 K with a maximum at 595 nm at 5 K (see Figures S21 and S22). The blue shift is analogous to the observations for **Cudmbiipo** and is accordingly assigned to rigidochromism.^{71,72} The emission of **Cubcp** is red-shifted by 14 and 33 nm in comparison to **Cudmbiipo** at 290 and 5 K, respectively. In contrast to **Cudmbiipo**, the integrated luminescence hardly changes in the temperature range from 290 to 5 K, but the amplitude-weighted average lifetime of 23 μ s at 290 K shows a strong linear increase to 420 μ s at 5 K (see Table S4). The lifetime of **Cubcp** at 290 K (23 μ s) is in the same order of magnitude as the values reported in the literature for neat powders of the complex at room temperature.⁷³ Importantly, the average decay constant at 290 K and especially the very long lifetime of 420 μ s at 5 K allow an assignment to phosphorescence, which

is of 3 MLCT character according to the unrestricted DFT calculations presented herein (see below) and in the literature.⁷⁴ The more or less linear increase in emission lifetime with the decreasing temperature (see Figure S23) is quite different from the observations made for a large series of Cu(I) complexes showing thermally activated delayed fluorescence (TADF).^{12,75,76} TADF emitters generally show a nonlinear correlation between the luminescence lifetime and temperature with a sharp increase of the luminescence lifetime in the 250–50 K range.^{12,75,76} Thus, a significant contribution of TADF seems improbable for **Cubcp** even at ambient temperature.

Excited-State Dynamics: UV/Vis Femtosecond and Nanosecond Transient Absorption Spectroscopy. The excited-state dynamics of **Cudmbiipo** are studied by ultrafast transient absorption (TA) spectroscopy and compared with the dynamics of **biipo** and **dmbiipo**. The compounds were optically excited by pump pulses at 400 nm and the induced absorption changes were probed with a time resolution of about 100 fs by a white-light continuum (further details can be found in the SI).⁷⁷ TA spectroscopy of the pure **dmbiipo** and **biipo** ligands was performed on HFIP solutions, due to their insufficient solubility in other organic solvents.

The TA spectra of **dmbiipo** are presented in Figure 6. They consist of two distinct bands at around 450 and 650 nm and

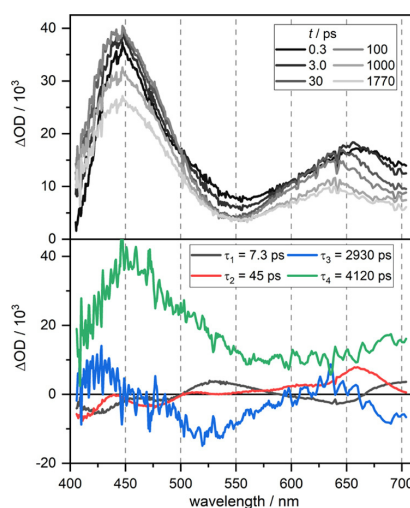


Figure 6. Transient absorption spectra (top) and DAS (bottom) of **dmbiipo** in HFIP solution. The DAS are labeled by the corresponding decay times.

exhibit only small spectral changes as well as a certain decrease during the measured time window of about 2 ns. The minimum at 550 nm, located between the two absorption bands, is at the same spectral location as the fluorescence of **dmbiipo** (see Figure 4a). Most likely, this feature is due to stimulated emission (SE) overlapping the excited-state absorption (ESA). A global lifetime analysis of the TA data revealed four exponential decay components with time constants of 7.3 and 45 ps and of about 2.9 and 4.1 ns. The corresponding DAS are depicted in Figure 6 (bottom). The DAS of the two short time constants seem to reflect small spectral shifts. They may result from vibrational redistribution

and cooling processes after optical excitation.^{70,78} In addition, the solvation dynamics of HFIP contributes probably, too.^{68–70} The two larger time constants were actually taken from the analysis of the streak camera measurements (Figure 4c) because the 2 ns long time window of the TA measurements does not allow for an accurate determination of such large time constants. The DAS of the 2.9 ns component mainly describes a shift of the SE into the red region caused by the solvation dynamics. In contrast, the 4.1 ns component is the by far dominant one and describes the overall decay of the TA signal. Accordingly, it reflects the relaxation from the emissive S_1 state back to the ground state, which is fully consistent with the time-resolved luminescence measurements. Similar TA spectroscopic results were obtained for **biipo** dissolved in HFIP and are presented in the SI (see Figures S56 and S57).

The TA spectra of **Cudmbiipo** in MeCN are depicted in Figure 7. After optical excitation, a pronounced band at

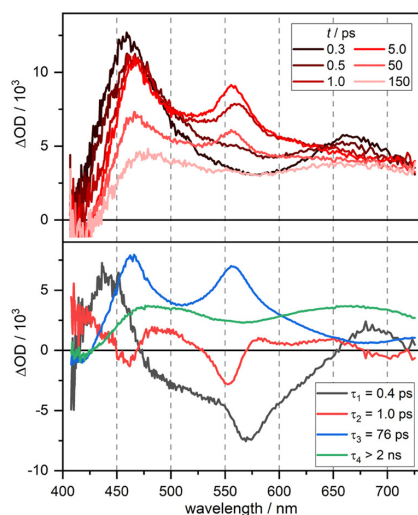


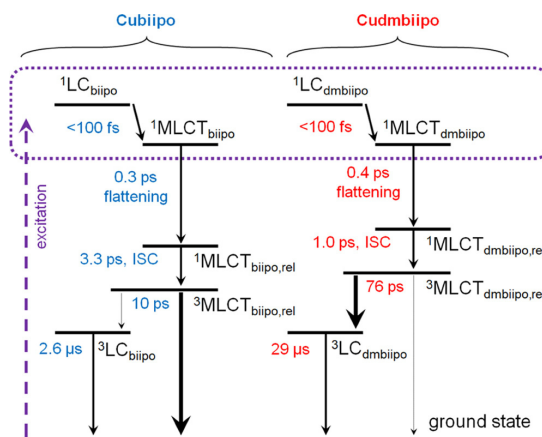
Figure 7. Transient absorption spectra (top) and DAS (bottom) of **Cudmbiipo** in MeCN. The DAS are labeled by the corresponding decay times.

460 nm and a second band at 660 nm are observed. The third band at 560 nm appears after 5 ps. In the spectrum shown after 150 ps (see Figure 7 top), this band as well as the band at 460 nm has disappeared and a broad ESA has formed, which remains constant until the end of the measurement at almost 2 ns.

A global lifetime analysis of the TA data revealed three exponential decay components with lifetimes of 0.4, 1.0, and 76 ps. A fourth, long-lived contribution, which matches exactly the last shown TA spectrum at 150 ps, exhibits a lifetime far beyond the scanned time range of 2 ns and fits to the observations obtained by nanosecond TA (see below). Therefore, the same long-lived species is observed here, *i.e.*, the nonemissive 3LC state, as discussed in more detail below. The results of **Cudmbiipo** agree well with those of **Cubiipo**.⁴⁷ The TA spectra of both Cu(I) complexes are similar and the observed decay times and decay-associated spectra are comparable. Consequently, the model we have already proposed for the ultrafast excited-state dynamics of **Cubiipo**

can also be applied to **Cudmbiipo** and is summarized in Scheme 1. Thus, the different lifetimes can be assigned as

Scheme 1. Simplified Jablonski Diagrams of **Cubiipo** and **Cudmbiipo** Including the Different Relaxation Processes and Time Constants upon Light Excitation⁴⁷



“The label “rel” indicates geometrically relaxed MLCT states after the flattening process.

follows: (i) The fastest time constant τ_1 of 0.4 ps may describe the lifetime of the optically excited singlet state 1MLCT before the flattening process (pseudo-Jahn–Teller distortion). The ligand absorbs at the excitation wavelength of 400 nm, too, and the very early TA spectra of **Cudmbiipo** are similar to those of **dmbiipo**. Hence, we assume that relaxation of the 1LC to the 1MLCT state contributes to the fastest decay component, in line with our previous results on **Cubiipo**.⁴⁷ (ii) The second time constant τ_2 of 1.0 ps is assigned to the intersystem crossing (ISC) of the 1MLCT state into the triplet 3MLCT state. (iii) The third time constant τ_3 of 76 ps reflects an intramolecular electron transfer leading to the final 3LC state, whose spectral signature is given by the long-lived component.

In previous studies by some of us, the impact of different substituents at the 2,9-positions on the phenanthroline moiety of **Cubcp** was investigated.^{56,74} It was found that increasing the size of these substituents from methyl to *n*-butyl did not substantially affect the duration of the flattening process due to the similar inertia of the molecular backbone. In line with this observation, the time constants of **Cubiipo** and **Cudmbiipo** also differ little from each other (0.3 vs 0.4 ps) with respect to the flattening step. The time constant for ISC remains of comparable magnitude upon introduction of the methyl groups. This also matches with observations on **Cubcp** and structurally related Cu(I) complexes such as **Cudppz**, **Cudmdppz**, and **Cutmdppz** (dppz = dipyrrophenazine, dmdppz = dimethyl-dppz, and tm = tetramethyl-dppz).^{41,65,79}

The time constant of 76 ps of **Cudmbiipo** for the population of the 3LC state is remarkably higher compared to **Cubiipo** with only 10 ps. Moreover, the absorption strength of the long-lived component of **Cudmbiipo** is about a factor of 8 larger than that of **Cubiipo**, although it is related to the same state. These facts lead to the assumption, that the final 3LC state is stronger populated in **Cudmbiipo** than in **Cubiipo**. We suspect that there is an additional depopulation channel in

Cubiipo that directly leads from the $^3\text{MLCT}$ state to the ground state. Thus, in **Cubiipo** only a small fraction of the $^3\text{MLCT}$ population reaches the ^3LC state. At the same time, the additional depopulation channel results in a relatively short $^3\text{MLCT}$ lifetime of only 10 ps. In **Cudmbiipo** this additional path seems to be suppressed, causing a prolonged $^3\text{MLCT}$ lifetime and a pretty complete population transfer to the ^3LC state (see Scheme 1). This trend can also be observed in **Cudppz** and **Cudmdppz**.^{41,79} Here, the time constant of the population of the ^3LC increases by a factor of 10 upon introducing two methyl groups at the phenanthroline moiety of the **dppz** ligand.

To study the behavior of the long-lived components of **Cudmbiipo**, **dmbiipo**, and **biipo**, nanosecond TA spectroscopy was introduced (details in the SI, Figures S35–S37). The measurements of the pure **dmbiipo** and **biipo** ligands were performed in HFIP solutions under aerated conditions. The emission strength of the S_1 state is very high for both ligands, but the corresponding time constants are below 10 ns (see above). The single-wavelength analysis of the TA measurements of **biipo** and **dmbiipo** yields a monoexponential decay of 219 and 206 ns, respectively. The time constants are comparable and assigned to the decay of the respective triplet state of **biipo** and **dmbiipo**. In addition, both time constants are also similar to the excited-state lifetime of **Cubiipo**'s ^3LC in aerated MeCN solution ($\tau = 270$ ns).⁴⁷

According to the femtosecond TA of **Cudmbiipo**, a broad and long-lasting ESA was detected after 150 ps. Therefore, the nanosecond TA kinetics were studied in the microsecond range in MeCN under deaerated conditions. Surprisingly, an averaged time constant of 29 μs was obtained, reflecting the relaxation process of the final ^3LC state of **Cudmbiipo** back to the ground state, which is more than 1 order of magnitude longer than that of **Cubiipo** (2.6 μs , Scheme 1).⁴⁷ The nanosecond TA results indicate that the introduction of methyl groups greatly increases the excited-state lifetime of the ^3LC state. A similar trend can also be observed in **Cudppz** and **Cudmdppz**.⁷⁹

Solid-State Step-Scan FTIR Spectroscopy. Step-scan FTIR spectroscopy was applied to **Cubcp** and **Cudmbiipo** to analyze the structures of the long-lived excited triplet states observed in the nanosecond TA investigations and, in the case of **Cubcp**, also by luminescence spectroscopy.

The ground state FTIR spectra of **Cubcp** and **Cudmbiipo** in a KBr matrix are very well described by the calculated IR spectra of the optimized ground state (S_0) structures (see Figures 8 and S46). This good correlation allowed an assignment of the experimental absorption bands to specific vibrations (see Tables S5 and S6). Subsequently, step-scan FTIR spectra of both complexes were recorded upon UV excitation at 355 nm to obtain information on the long-lived electronically excited states. In the step-scan FTIR spectrum of **Cudmbiipo** at 20 K, most ground state vibrations are visible as negative peaks, resulting from the depopulation of the electronic ground state (see Figure S40). The positive bands are assigned to the excited-state absorption of the populated long-lived excited state. At the same time, the step-scan spectrum of **Cubcp** generally shows very intense excited-state absorption features (see Figure S42), so that the positive bands almost fully compensate the negative peaks, which are only weakly visible and mostly show a positive absorbance difference. For further considerations, the pure excited-state absorption spectra were generated by adding a small

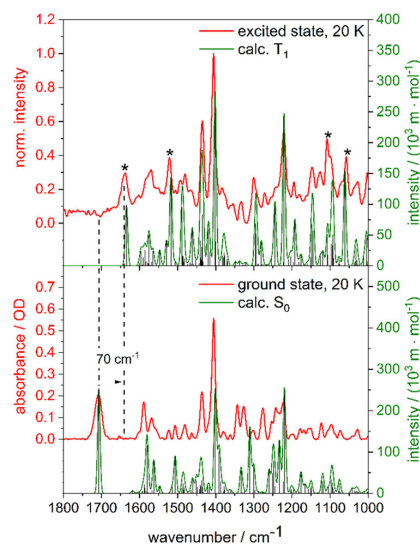


Figure 8. Static FTIR ground state spectrum (KBr pellet, 20 K) and calculated S_0 spectrum of **Cudmbiipo** (bottom). The excited-state IR spectrum (4.0% of the ground state spectrum added to the step-scan difference spectrum) and calculated T_1 spectrum of **Cudmbiipo** (top). Calculations: (U)DFT/B3LYP-D3(BJ)/def2-TZVP, scaled by 0.975, full width at half-maximum (FWHM) = 8 cm^{-1} , Gaussian profile. The bands marked with an asterisk are discussed in detail in the text.

contribution of 3–4% of the ground state spectrum to the step-scan difference spectrum to suppress the negative bands.

The IR absorption of **Cudmbiipo** in the excited state strongly differs from that in the ground state, e.g., by a significant shift of the carbonyl stretching vibration from 1708 cm^{-1} in the ground state to 1638 cm^{-1} in the excited state (see Figure 8). Furthermore, three strong peaks were observed at 1522, 1108, and 1058 cm^{-1} (asterisks in Figure 8), where no significant IR absorption is present in the electronic ground state. For comparison with the experiment, the lowest triplet state of **Cudmbiipo** was optimized by unrestricted DFT calculations. The yielded theoretical IR spectrum describes all three characteristic experimental excited-state absorption bands and, in particular, the strong red shift of the CO stretching vibration (see Figure 8). These specific excited-state vibrations mainly involve the **dmbiipo** ligand and are of rather undefined character with contributions of C–C and C=O stretching as well as C–H bending vibrations according to the DFT calculations (see Table S5). The calculated spin density is fully localized on the **dmbiipo** ligand and thereby mainly on the naphthaloylene part, implying that the lowest triplet state is ligand-centered (^3LC) without a relevant contribution from the Cu(I) center (see Figure 9, top). This behavior is very similar to the closely related **Cubiipo** complex,⁴⁷ which means that the methyl groups do not have a significant influence on the electronic character of the T_1 state. The absence of a direct electronic contribution of the Cu(I) center in the T_1 state with an electron hole on the metal allows bypassing of the most undesired excited-state pseudo-Jahn–Teller flattening distortion observed in many other Cu(I) complexes.^{12,54,80} This also explains the small change of the dihedral angle by 2.1 from 85.5° in the S_0 state to 87.6° in the T_1 state (see Table S7),

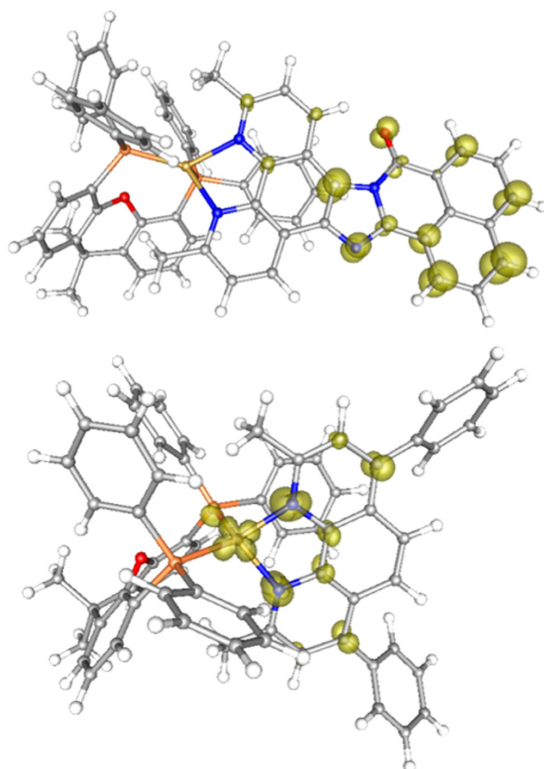


Figure 9. Calculated spin densities (isovalue: 0.01 arb. u.) in the optimized T_1 state of **Cudmbiipo** (top) and **Cubcp** (bottom) (UDFT/B3LYP-D3(BJ)/def2-TZVP).

analogous to the insignificant angular change of 0.2° in **Cubiipo** reported earlier.⁴⁷ These particularly small distortions around the Cu(I) center for **Cudmbiipo** and **Cubiipo** imply that the undesired excited-state flattening is intrinsically inhibited without a relevant impact of the methyl substituents at the 2,9-positions at the phenanthroline moiety, according to the combined analysis by solid-state step-scan FTIR spectroscopy and quantum chemical calculations in the gas phase. The structural changes in the 3LC state of **Cudmbiipo** relative to the S_0 state are more or less limited to the **dmbiipo** ligand (see Table S7), which allows an efficient suppression of potential nonradiative deactivation pathways. Accordingly, the excited-state IR signals of this triplet state are very long-lived. At 20 K, the signals in the step-scan difference spectrum show a biexponential decay with a long-lived time constant of $410 \mu\text{s}$ (97%) and a minor short-lived component of $23 \mu\text{s}$ (3%) (see Figure S47). As the luminescence lifetime of few nanoseconds of solid **Cudmbiipo** was unambiguously assigned to fluorescence, it is obvious that the 3LC state is a dark triplet state, analogous to the observations for **Cubiipo** (3LC lifetime of $439 \mu\text{s}$).⁴⁷ The step-scan FTIR studies on **Cudmbiipo** at 290 K gave essentially the same results compared to 20 K so that the excited-state population also ends up in the described 3LC state at higher thermal energy. The almost temperature-independent excited-state absorption spectra (see Figure S44) strongly suggest that the triplet structure is not significantly affected by temperature, yet exhibits shorter lifetimes at 290 K

($2.5 \mu\text{s}$ (10%) and $47 \mu\text{s}$ (90%)) (see Figure S48). This is due to fast deactivation pathways that are activated when sufficient thermal energy is present. As the step-scan data of **Cudmbiipo** and **Cubiipo**⁴⁷ yielded a very similar temperature dependency for the lifetime of the 3LC state, it is concluded that the introduced methyl groups do not significantly affect its thermal deactivation.

In the case of **Cubcp**, the associated triplet state has mainly 3MLCT character with a transfer of electron density from the Cu(I) core to the phenanthroline ligand (see Figure 9 and the SI, Section S8.1 for the step-scan FTIR results), which is typical for such heteroleptic diimine-bisphosphine Cu(I) complexes.^{12,35,74,81,82} Thus, **Cubcp** is very different compared to **Cudmbiipo** with respect to the electronic character in the T_1 state. The $MLCT$ transition in **Cubcp** involves a partial oxidation of the Cu(I) center, which induces a flattening distortion from 86.1 to 75.7° ($\Delta = 10.4^\circ$) according to the presented DFT calculations (see Table S8). The given change of the dihedral angle upon optical excitation agrees well with previous results on **Cubcp**⁷⁴ and is much larger compared to **Cudmbiipo** and **Cubiipo**, but limited compared to related heteroleptic Cu(I) complexes containing phenanthroline-based ligands without any substituents at the 2,9-positions.^{81,82} As described earlier for **Cubcp**⁷⁴ and related complexes,^{12,35,81,82} methyl groups or other alkyl substituents at the 2,9-positions at the phenanthroline ligand increase the bulkiness and reduce the flattening distortion in the excited state.

Photocatalytic Applications. Subsequent to the in-depth photophysical studies on the electronic and structural properties of **Cudmbiipo** in the ground and excited states, we systematically tested its photocatalytic properties in various applications. In this context, the direct comparison with the reference complex **Cubcp** is particularly important to evaluate the impact of the extended π -system of the **dmbiipo** ligand.

Singlet Oxygen (1O_2) Production. Due to the promising photophysical properties of **Cudmbiipo** and the previously reported **Cubiipo** complex,⁴⁷ they were first investigated in the light-driven production of singlet oxygen (1O_2). Even though 1O_2 is only a short-lived and metastable excited state of molecular oxygen, it represents an important reagent in organic synthesis and for applications in photodynamic therapy (PDT).^{83–86} In our experiments, the quantification of the formed 1O_2 is based on its characteristic sharp near-infrared (NIR) emission, which had been detected at 1285 nm in MeCN for **Cubiipo** in our previous work.⁴⁷ Tetrahydrofuran (THF) was chosen as a suitable solvent because it is commonly used in photocatalysis^{40,56,63,87} and the complexes are readily soluble. For all three complexes **Cubiipo**, **Cudmbiipo**, and **Cubcp**, a clear NIR emission at 1285 nm was found upon excitation with visible light ($\lambda_{\text{ex}} = 420 \text{ nm}$) (see Figure 10), but not for the uncoordinated **biipo** or **dmbiipo** ligands. This confirms the important role of the Cu(I) center and that only the complex is able to act as a photosensitizer. The assignment of the NIR luminescence to 1O_2 was further verified by a decrease in intensity in the presence of the 1O_2 quencher 9-methylanthracene (see Figure S53).⁸⁸ The singlet oxygen quantum yields ($\phi(^1O_2)$) were determined in THF solution relative to the Cr(III) reference complex $\text{Cr}(\text{ddpd})_2(\text{BF}_4)_3$ ($\text{ddpd} = N,N'$ -dimethyl- N,N' -dipyridine-2-ylpyridine-2,6-diamine) ($\phi_{\text{ref}}(^1O_2) = 61\%$ in dimethylformamide (DMF)).⁸⁹ Importantly, **Cudmbiipo** showed the highest $\phi(^1O_2)$ of 68%, outperforming its

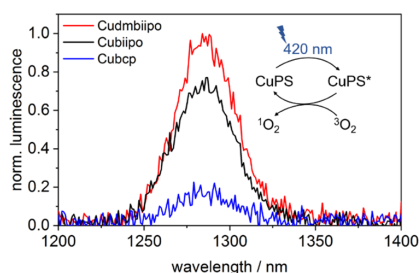


Figure 10. NIR emission of $^1\text{O}_2$ observed for solutions of **Cudmbiipo**, **Cubiipo**, and **Cubcp** in THF excited at a wavelength of 420 nm. Please note that these absolute spectra do not directly reflect the relative trend found for $\phi(^1\text{O}_2)$. The inset shows the underlying photocatalytic cycle.

congener **Cubiipo** (53%) and the reference system **Cubcp** (44%) under identical conditions. The trend for the $\phi(^1\text{O}_2)$ values clearly supports the UV/vis TA results of **Cubiipo** and **Cudmbiipo**, indicating a more efficient population of the photocatalytically relevant long-lived ^3LC state for the latter complex. For verification and better comparison, the ns-TA measurements were also performed in THF (see Figures S38 and S39). The single-wavelength analysis of these measurements yielded averaged biexponential decay constants of $\tau_1 = 20.6 \pm 0.3$, $23.0 \pm 0.3 \mu\text{s}$ and $\tau_2 = 84.9 \pm 1.6$, $103 \pm 2 \mu\text{s}$ for **Cubiipo** and **Cudmbiipo**, respectively. Hence, the difference in the excited-state lifetimes of about 17% agrees well with the difference in the $^1\text{O}_2$ yield of 22%.

It is very likely that oxygen is activated by an intermolecular energy transfer from this ^3LC state to oxygen in its triplet ground state (see the inset in Figure 10),^{90,91} whereby a higher population of the ^3LC state boosts the $^1\text{O}_2$ production. As **Cudmbiipo** showed the highest activity in $^1\text{O}_2$ production, the potential of this photosensitizer and of **Cubcp** in the photoisomerization of stilbene was evaluated and also the light upconversion capabilities of **Cudmbiipo** were tested.

Photocatalytic Isomerization of (E)-Stilbene. The isomerization of the organic substrate (*E*)-stilbene was investigated with a focus on the kinetics of the photocatalytic transformation. Stilbene derivatives are synthesized both naturally and synthetically and make up a class of compounds with a broad set of bioactive properties.^{92,93} In this context, the stereochemical configurations of the molecules are of utmost importance. A common way of transforming the *E*-isomer into the *Z*-isomer is *via* a photocatalytic route where triplet stilbene is formed, which can then relax into either (*E*)- or (*Z*)-stilbene.⁹³ With these properties in mind, stilbene and its derivatives are commonly used as test substrates in a photocatalytic setup.^{94,95} Most photocatalysts used in this reaction are also capable of catalyzing the backreaction. This results in a photostationary state, where both reactions take place at the same rate.⁹³

Both complexes **Cubcp** and **Cudmbiipo** were applied as photocatalysts for the geometrical isomerization of (*E*)- to (*Z*)-stilbene. The alkene substrate (1 mmol) and the photocatalysts (0.01 mol%) were dissolved in dichloromethane (10 mL) and irradiated with visible light (above 410 nm, see the SI, Section S11.2) under inert conditions. Samples of the reaction solution were taken at regular intervals (every 12 h with an additional sample at 6 h for **Cudmbiipo**) and their composition was analyzed *via* gas chromatography. The exact execution of this

experiment is described in the Supporting Information (see Section S11.2)

The novel **Cudmbiipo** complex proved to be much more active than the reference **Cubcp** in terms of initial yields and turnover numbers (TONs, see Figure 11). Both Cu(I)

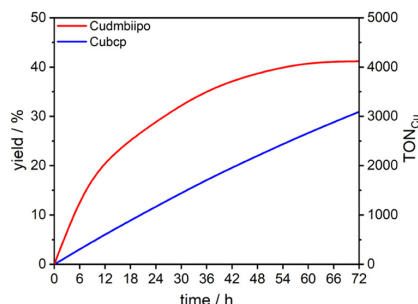


Figure 11. Time evolution of yields and turnover numbers (TONs) for the visible-light-driven photocatalytic isomerization reaction of (*E*)-stilbene using **Cudmbiipo** (red) or **Cubcp** (blue) as photocatalysts. Samples were taken every 12 h (with an additional sample at 6 h for **Cudmbiipo**) and the composition was analyzed *via* gas chromatography.

complexes showed TONs above 1000 within the first 24 h, proving their ability to efficiently complete the (photo)catalytic cycle. However, for **Cudmbiipo**, the initial turnover frequency (TOF) of the isomerization reaction after 12 h is more than 3 times higher than for **Cubcp** ($\text{TOF}_{\text{Cudmbiipo},12\text{h}} = 0.049 \text{ s}^{-1}$ vs $\text{TOF}_{\text{Cubcp},12\text{h}} = 0.014 \text{ s}^{-1}$). In the case of **Cudmbiipo**, the reaction seems to reach a photostationary state after 72 h at a *Z/E*-ratio of 41/59. Nevertheless, the TON of **Cubcp** still increases in an almost linear fashion after that time.

In an additional experiment, the *Z/E*-ratios in the photostationary state were determined for both complexes. (*E*)-Stilbene was converted to *Z*-stilbene using a catalyst loading of 2 mol % and the composition of the reaction mixture was then analyzed by NMR spectroscopy. The experiment is described in more detail in the Supporting Information (see Section S11.2). This experiment confirmed an equilibrium *Z/E*-ratio of 41/59 for **Cudmbiipo** and determined the equilibrium *Z/E*-ratio for **Cubcp** to 82/18. In another control experiment, (*E*)-stilbene (10^{-5} M) and the copper catalysts (0.02 equiv) were directly reacted in a cuvette and the reaction progress was monitored by *in situ* UV/vis spectroscopy (see the SI, Section S11.2). The previous findings were confirmed. **Cudmbiipo** initially converts the substrate faster, but compared to **Cubcp**, the stationary state is reached with a larger amount of substrates still unreacted.

Photon Upconversion Studies. In a preliminary experiment, **Cudmbiipo** was tested to act as a photosensitizer for triplet–triplet upconversion processes in THF in the presence of an excess of anthracene (50 equiv) as an energy acceptor.^{96,97} Indeed, high-energy excitation at 442 nm ($\approx 55 \text{ mW}$) resulted in a clearly resolved high-energy emission of anthracene at $\lambda_{\text{ex}} \leq 410 \text{ nm}$, which was not the case in the absence of **Cudmbiipo** (see Figure 12). Hence, the sensitized photon upconversion is attributed to a nonradiative intermolecular energy transfer from the long-lived ^3LC state of **Cudmbiipo** to the lowest triplet state of anthracene.^{96,97}

This is an important achievement because the number of transition-metal complexes based on earth-abundant metals

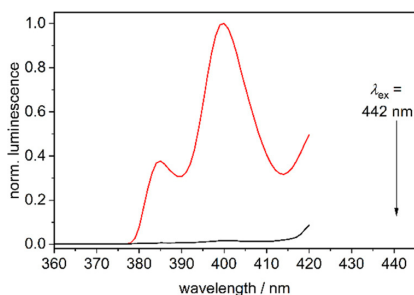


Figure 12. Emission spectra of pure anthracene (black) and of **Cudmbiipo** solutions containing 50 equiv of anthracene (red, $c(\text{Cudmbiipo}) = 2.5 \times 10^{-5}$ M; $c(\text{anthracene}) = 1.3 \times 10^{-3}$ M) upon excitation at $\lambda_{\text{ex}} = 442$ nm.

exhibiting upconversion properties is still very limited.^{97–99} As far as we know, only three homoleptic Cu(I) complexes have been reported in this context so far.⁹⁷ All in all, our successful catalytic tests demonstrate the great potential of **Cudmbiipo** and the advantages of an extended π -system as well as of methyl groups in close proximity to the copper center.

CONCLUSIONS

In this study, the novel Cu(I)-based photosensitizer **Cudmbiipo** was presented, which can be seen as a successor of the previously published **Cubiipo** complex. As the main feature, the **dmbiipo** ligand carries two additional methyl groups next to the nitrogen donors at the phenanthroline unit and a fused naphthaloylene moiety at the back.

Considering the ligand-centered nature of the lowest-lying triplet state of **Cubiipo**, we did not expect much influence of these methyl groups on the photophysical and catalytic properties of the complex. However, the excited-state lifetime of the **Cudmbiipo** complex was strongly increased, about 10-fold to 29 μs , and it outperformed the well-established Cu(I) photosensitizer **Cubcp** in photocatalytic applications, *i.e.*, the formation of singlet oxygen and the isomerization of (*E*)-stilbene. In addition, **Cudmbiipo** was successfully applied as a sensitizer for photon upconversion, one of the very few examples to date based on earth-abundant copper.

Time-resolved spectroscopy, covering the entire time range from femto- to microseconds, was used to analyze the origin of the unexpected enhancement of the excited-state properties of **Cudmbiipo**. The methyl groups were found to prevent the undesired flattening distortion in a transiently populated ³MLCT state, which is thereby stabilized and exhibits a longer lifetime than **Cubiipo**. An ultrafast deactivation path is hampered, associated with a more efficient population of the photoactive ligand-centered lowest triplet state ³LC.

Our design strategy of combining a photoactive charge-transfer metal complex with an organic chromophore has proven to be very powerful. It allowed us to harness the advantage of an organic photosensitizer without any heavy atoms, namely, a long-lived triplet state, while overcoming its major drawback, the inefficient intersystem crossing due to the absence of heavy atoms.

The additional introduction of methyl groups at the 2,9-positions at the phenanthroline unit further improves the relevant properties of the resulting Cu(I) complex, even though the lowest-energy triplet state of the unsubstituted analogue is not significantly flattened. This modification results

in a very potent noble metal-free system, whose full potential has yet to be determined in future studies and applications.

ASSOCIATED CONTENT

Supporting Information

The Supporting Information is available free of charge at <https://pubs.acs.org/doi/10.1021/acs.inorgchem.2c01468>.

Experimental and synthetic details, electrochemistry, NMR, MS, absorption, emission, FTIR, step-scan IR, femtosecond and nanosecond transient absorption spectra, TDDFT calculations, photocatalytic data (PDF)

AUTHOR INFORMATION

Corresponding Authors

Gereon Niedner-Schatteburg – Chemistry Department and State Research Center Optimas, TU Kaiserslautern, 67663 Kaiserslautern, Germany; orcid.org/0000-0001-7240-6673; Email: gns@chemie.uni-kl.de

Michael Karnahl – Department of Energy Conversion, Institute of Physical and Theoretical Chemistry, Technische Universität Braunschweig, 38106 Braunschweig, Germany; orcid.org/0000-0002-6755-0002; Email: michael.karnahl@tu-bs.de

Stefan Lochbrunner – Institute for Physics and Department of Life, Light and Matter, University of Rostock, 18051 Rostock, Germany; orcid.org/0000-0001-9729-8277; Email: stefan.lochbrunner@uni-rostock.de

Stefanie Tschierlei – Department of Energy Conversion, Institute of Physical and Theoretical Chemistry, Technische Universität Braunschweig, 38106 Braunschweig, Germany; orcid.org/0000-0001-9441-7904; Email: s.tschierlei@tu-bs.de

Authors

Martin Rentschler – Department of Energy Conversion, Institute of Physical and Theoretical Chemistry, Technische Universität Braunschweig, 38106 Braunschweig, Germany

Pit Jean Boden – Chemistry Department and State Research Center Optimas, TU Kaiserslautern, 67663 Kaiserslautern, Germany

Miguel A. Argüello Cordero – Institute for Physics and Department of Life, Light and Matter, University of Rostock, 18051 Rostock, Germany

Sophie Theres Steiger – Chemistry Department and State Research Center Optimas, TU Kaiserslautern, 67663 Kaiserslautern, Germany

Marie-Ann Schmid – Department of Energy Conversion, Institute of Physical and Theoretical Chemistry, Technische Universität Braunschweig, 38106 Braunschweig, Germany

Yingya Yang – Department of Energy Conversion, Institute of Physical and Theoretical Chemistry, Technische Universität Braunschweig, 38106 Braunschweig, Germany

Complete contact information is available at: <https://pubs.acs.org/doi/10.1021/acs.inorgchem.2c01468>

Author Contributions

[†]M.R., P.J.B. and M.A.A.C. contributed equally to this work. The manuscript was written through contributions of all authors. All authors have given approval to the final version of the manuscript.

Notes

The authors declare no competing financial interest.

ACKNOWLEDGMENTS

The authors like to thank Christina Kotovich (TU Braunschweig) for support with the photocatalytic isomerization reactions. The authors are grateful to the Deutsche Forschungsgemeinschaft (DFG) within the Priority Program SPP 2102 "Light-controlled reactivity of metal complexes" (KA 4671/2-1, LO 714/11-2, TS 330/4-1) for financial support. M.-A.S. and S.T. acknowledge funding from the Baden-Württemberg Foundation (BW-Stiftung, Germany).

DEDICATION

This paper is dedicated to Prof. Matthias Beller on the occasion of his 60th birthday.

REFERENCES

- Armaroli, N.; Balzani, V. The Future of Energy Supply: Challenges and Opportunities. *Angew. Chem., Int. Ed.* **2007**, *46*, 52–66.
- Detz, R. J.; Reek, J. N. H.; van der Zwaan, B. C. C. The future of solar fuels: when could they become competitive? *Energy Environ. Sci.* **2018**, *11*, 1653–1669.
- Gaedicke, C.; Franke, D.; Ladage, S.; Lutz, R.; Pein, M.; Rebscher, D.; Schauer, M.; Schmidt, S.; von Goerne, G. *BGR Energy Study 2019—Data and Developments Concerning German and Global Energy Supplies*; Federal Institute for Geosciences and Natural Resources: Hannover, 2020; pp 1–200.
- Schiermeier, Q.; Tollefson, J.; Scully, T.; Witze, A.; Morton, O. Electricity without Carbon. *Nature* **2008**, *454*, 816–823.
- Armaroli, N.; Balzani, V. Solar Electricity and Solar Fuels: Status and Perspectives in the Context of the Energy Transition. *Chem.—Eur. J.* **2016**, *22*, 32–57.
- Setoyama, T.; Takewaki, T.; Domen, K.; Tatsumi, T. The challenges of solar hydrogen in chemical industry: how to provide, and how to apply? *Faraday Discuss.* **2017**, *198*, 509–527.
- Soni, V. K.; Lee, S.; Kang, J.; Moon, Y. K.; Hwang, H. S.; You, Y.; Cho, E. J. Reactivity Tuning for Radical–Radical Cross-Coupling via Selective Photocatalytic Energy Transfer: Access to Amine Building Blocks. *ACS Catal.* **2019**, *9*, 10454–10463.
- Kaithal, A.; Hölscher, M.; Leitner, W. Carbon monoxide and hydrogen (syngas) as a C1-building block for selective catalytic methylation. *Chem. Sci.* **2021**, *12*, 976–982.
- Frischmann, P. D.; Mahata, K.; Würthner, F. Powering the future of molecular artificial photosynthesis with light-harvesting metal-supramolecular dye assemblies. *Chem. Soc. Rev.* **2013**, *42*, 1847–1870.
- Yuan, Y.-J.; Yu, Z.-T.; Chen, D.-Q.; Zou, Z.-G. Metal-complex chromophores for solar hydrogen generation. *Chem. Soc. Rev.* **2017**, *46*, 603–631.
- Wenger, O. S. Photoactive Complexes with Earth-Abundant Metals. *J. Am. Chem. Soc.* **2018**, *140*, 13522–13533.
- Zhang, Y.; Schulz, M.; Wächter, M.; Karnahl, M.; Dietzek, B. Heteroleptic diimine–diphosphine Cu(I) complexes as an alternative towards noble-metal based photosensitizers: Design strategies, photophysical properties and perspective applications. *Coord. Chem. Rev.* **2018**, *356*, 127–146.
- Dalle, K. E.; Warnan, J.; Leung, J. J.; Reuillard, B.; Karmel, I. S.; Reisner, E. Electro- and Solar-Driven Fuel Synthesis with First Row Transition Metal Complexes. *Chem. Rev.* **2019**, *119*, 2752–2875.
- Prier, C. K.; Rankic, D. A.; MacMillan, D. W. C. Visible Light Photoredox Catalysis with Transition Metal Complexes: Applications in Organic Synthesis. *Chem. Rev.* **2013**, *113*, 5322–5363.
- Larsen, C. B.; Wenger, O. S. Photoredox Catalysis with Metal Complexes Made from Earth-Abundant Elements. *Chem.—Eur. J.* **2018**, *24*, 2039–2058.
- Kuramochi, Y.; Ishitani, O.; Ishida, H. Reaction mechanisms of catalytic photochemical CO₂ reduction using Re(I) and Ru(II) complexes. *Coord. Chem. Rev.* **2018**, *373*, 333–356.
- Angerani, S.; Winssinger, N. Visible Light Photoredox Catalysis Using Ruthenium Complexes in Chemical Biology. *Chem.—Eur. J.* **2019**, *25*, 6661–6672.
- Rupp, M. T.; Shevchenko, N.; Hanan, G. S.; Kurth, D. G. Enhancing the photophysical properties of Ru(II) complexes by specific design of tridentate ligands. *Coord. Chem. Rev.* **2021**, *446*, No. 214127.
- Costa, R. D.; Ortí, E.; Bolink, H. J.; Monti, F.; Accorsi, G.; Armaroli, N. Luminescent Ionic Transition-Metal Complexes for Light-Emitting Electrochemical Cells. *Angew. Chem., Int. Ed.* **2012**, *51*, 8178–8211.
- Mills, I. N.; Porras, J. A.; Bernhard, S. Judicious Design of Cationic, Cyclometalated Ir(III) Complexes for Photochemical Energy Conversion and Optoelectronics. *Acc. Chem. Res.* **2018**, *51*, 352–364.
- Glaser, F.; Wenger, O. S. Recent progress in the development of transition-metal based photoredox catalysts. *Coord. Chem. Rev.* **2020**, *405*, No. 213129.
- Büldt, L. A.; Wenger, O. S. Chromium(0), Molybdenum(0), and Tungsten(0) Isocyanide Complexes as Luminophores and Photosensitizers with Long-Lived Excited States. *Angew. Chem., Int. Ed.* **2017**, *56*, 5676–5682.
- Treiling, S.; Wang, C.; Förster, C.; Reichenauer, F.; Kalmbach, J.; Boden, P.; Harris, J. P.; Carrella, L. M.; Rentschler, E.; Resch-Genger, U.; Reber, C.; Seitz, M.; Gerhards, M.; Heinze, K. Luminescence and Light-Driven Energy and Electron Transfer from an Exceptionally Long-Lived Excited State of a Non-Innocent Chromium(III) Complex. *Angew. Chem., Int. Ed.* **2019**, *58*, 18075–18085.
- Jiménez, J.-R.; Doistau, B.; Poncet, M.; Piguet, C. Heteroleptic trivalent chromium in coordination chemistry: Novel building blocks for addressing old challenges in multimetallic luminescent complexes. *Coord. Chem. Rev.* **2021**, *434*, No. 213750.
- Reichenauer, F.; Wang, C.; Förster, C.; Boden, P.; Ugur, N.; Báez-Cruz, R.; Kalmbach, J.; Carrella, L. M.; Rentschler, E.; Ramanan, C.; Niedner-Schatteburg, G.; Gerhards, M.; Seitz, M.; Resch-Genger, U.; Heinze, K. Strongly Red-Emissive Molecular Ruby [Cr(bpmp)₂]³⁺ Surpasses [Ru(bpy)₃]²⁺. *J. Am. Chem. Soc.* **2021**, *143*, 11843–11855.
- Sinha, N.; Jiménez, J.-R.; Pfund, B.; Prescimone, A.; Piguet, C.; Wenger, O. S. A Near-Infrared-II Emissive Chromium(III) Complex. *Angew. Chem.* **2021**, *133*, 23915–23921.
- Kjær, K. S.; Kaul, N.; Prakash, O.; Chábera, P.; Rosemann, N. W.; Honarfar, A.; Gordivska, O.; Fredin, L. A.; Bergquist, K.-E.; Häggström, L.; Ericsson, T.; Lindh, L.; Yartsev, A.; Styring, S.; Huang, P.; Uhlig, J.; Bendix, J.; Strand, D.; Sundström, V.; Persson, P.; Lomoth, R.; Wärnmark, K. Luminescence and reactivity of a charge-transfer excited iron complex with nanosecond lifetime. *Science* **2019**, *363*, 249–253.
- Leis, W.; Argüello Cordero, M. A.; Lochbrunner, S.; Schubert, H.; Berkefeld, A. A Photoreactive Iron(II) Complex Luminophore. *J. Am. Chem. Soc.* **2022**, *144*, 1169–1173.
- Dierks, P.; Vukadinovic, Y.; Bauer, M. Photoactive iron complexes: more sustainable, but still a challenge. *Inorg. Chem. Front.* **2022**, *9*, 206–220.
- Bestgen, S.; Schoo, C.; Neumeier, B. L.; Feuerstein, T. J.; Zovko, C.; Köppe, R.; Feldmann, C.; Roesky, P. W. Intensely Photoluminescent Diamidophosphines of the Alkaline-Earth Metals, Aluminum, and Zinc. *Angew. Chem., Int. Ed.* **2018**, *57*, 14265–14269.
- Tungulin, D.; Leier, J.; Carter, A. B.; Powell, A. K.; Albuquerque, R. Q.; Unterreiner, A. N.; Bizzarri, C. Chasing BODIPY: Enhancement of Luminescence in Homoleptic Bis-(dipyrrinato) ZnII Complexes Utilizing Symmetric and Unsymmetrical Dipyrrins. *Chem.—Eur. J.* **2019**, *25*, 3816–3827.
- Lazorski, M. S.; Castellano, F. N. Advances in the light conversion properties of Cu(I)-based photosensitizers. *Polyhedron* **2014**, *82*, 57–70.

- (33) Housecroft, C. E.; Constable, E. C. The emergence of copper(i)-based dye sensitized solar cells. *Chem. Soc. Rev.* **2015**, *44*, 8386–8398.
- (34) Windisch, J.; Oraziotti, M.; Hamm, P.; Alberto, R.; Probst, B. General Scheme for Oxidative Quenching of a Copper Bis-Phenanthroline Photosensitizer for Light-Driven Hydrogen Production. *ChemSusChem* **2016**, *9*, 1719–1726.
- (35) Leoni, E.; Mohanraj, J.; Holler, M.; Mohankumar, M.; Nierengarten, I.; Monti, F.; Sournia-Saquet, A.; Delavaux-Nicot, B.; Nierengarten, J.-F.; Armaroli, N. Heteroleptic Copper(I) Complexes Prepared from Phenanthroline and Bis-Phosphine Ligands: Rationalization of the Photophysical and Electrochemical Properties. *Inorg. Chem.* **2018**, *57*, 15537–15549.
- (36) Hossain, A.; Bhattacharyya, A.; Reiser, O. Copper's rapid ascent in visible-light photoredox catalysis. *Science* **2019**, *364*, No. eaav9713.
- (37) Zhang, X.; Cibian, M.; Call, A.; Yamauchi, K.; Sakai, K. Photochemical CO₂ Reduction Driven by Water-Soluble Copper(I) Photosensitizer with the Catalysis Accelerated by Multi-Electron Chargeable Cobalt Porphyrin. *ACS Catal.* **2019**, *9*, 11263–11273.
- (38) Forero Cortés, P. A.; Marx, M.; Trose, M.; Beller, M. Heteroleptic copper complexes with nitrogen and phosphorus ligands in photocatalysis: Overview and perspectives. *Chem. Catal.* **2021**, *1*, 298–338.
- (39) Förster, C.; Heinze, K. Photophysics and photochemistry with Earth-abundant metals – fundamentals and concepts. *Chem. Soc. Rev.* **2020**, *49*, 1057–1070.
- (40) Luo, S.-P.; Chen, N.-Y.; Sun, Y.-Y.; Xia, L.-M.; Wu, Z.-C.; Junge, H.; Beller, M.; Wu, Q.-A. Heteroleptic copper(I) photosensitizers of dibenzo[b,j]-1,10-phenanthroline derivatives driven hydrogen generation from water reduction. *Dyes Pigm.* **2016**, *134*, 580–585.
- (41) Heberle, M.; Tschierlei, S.; Rockstroh, N.; Ringenberg, M.; Frey, W.; Junge, H.; Beller, M.; Lochbrunner, S.; Karnahl, M. Heteroleptic Copper Photosensitizers: Why an Extended π -System Does Not Automatically Lead to Enhanced Hydrogen Production. *Chem.—Eur. J.* **2017**, *23*, 312–319.
- (42) Soulis, K.; Gourlaouen, C.; Daniel, C.; Quatela, A.; Odobel, F.; Blart, E.; Pellegrin, Y. New luminescent copper(I) complexes with extended π -conjugation. *Polyhedron* **2018**, *140*, 42–50.
- (43) Giereth, R.; Reim, I.; Frey, W.; Junge, H.; Tschierlei, S.; Karnahl, M. Remarkably long-lived excited states of copper photosensitizers containing an extended π -system based on an anthracene moiety. *Sustainable Energy Fuels* **2019**, *3*, 692–700.
- (44) Gernert, M.; Balles-Wolf, L.; Kerner, F.; Müller, U.; Schmiedel, A.; Holzapfel, M.; Marian, C. M.; Pflaum, J.; Lambert, C.; Steffen, A. Cyclic (Amino)(aryl)carbenes Enter the Field of Chromophore Ligands: Expanded π System Leads to Unusually Deep Red Emitting Cu(I) Compounds. *J. Am. Chem. Soc.* **2020**, *142*, 8897–8909.
- (45) Yang, Y.; Brückmann, J.; Frey, W.; Rau, S.; Karnahl, M.; Tschierlei, S. Electron Storage Capability and Singlet Oxygen Productivity of a Ru(II) Photosensitizer Containing a Fused Naphthaloylenebenzene Moiety at the 1,10-Phenanthroline Ligand. *Chem.—Eur. J.* **2020**, *26*, 17027–17034.
- (46) Wells, K. A.; Yarnell, J. E.; Sheykhi, S.; Palmer, J. R.; Yonemoto, D. T.; Joyce, R.; Garakyaraghi, S.; Castellano, F. N. Accessing the triplet manifold of naphthalene benzimidazole-phenanthroline in rhenium(i) bichromophores. *Dalton Trans.* **2021**, *50*, 13086–13095.
- (47) Argüello Cordero, M. A.; Boden, P. J.; Rentschler, M.; Di Martino-Fumo, P.; Frey, W.; Yang, Y.; Gerhards, M.; Karnahl, M.; Lochbrunner, S.; Tschierlei, S. Comprehensive Picture of the Excited State Dynamics of Cu(I)- and Ru(II)-Based Photosensitizers with Long-Lived Triplet States. *Inorg. Chem.* **2022**, *61*, 214–226.
- (48) Tyson, D. S.; Luman, C. R.; Zhou, X.; Castellano, F. N. New Ru(II) Chromophores with Extended Excited-State Lifetimes. *Inorg. Chem.* **2001**, *40*, 4063–4071.
- (49) Polyansky, D. E.; Danilov, E. O.; Castellano, F. N. Observation of Triplet Intraligand Excited States through Nanosecond Step-Scan Fourier Transform Infrared Spectroscopy. *Inorg. Chem.* **2006**, *45*, 2370–2372.
- (50) Wegeberg, C.; Häussinger, D.; Wenger, O. S. Pyrene-Decoration of a Chromium(0) Tris(diisocyanide) Enhances Excited State Delocalization: A Strategy to Improve the Photoluminescence of 3d6 Metal Complexes. *J. Am. Chem. Soc.* **2021**, *143*, 15800–15811.
- (51) Schmid, M.-A.; Brückmann, J.; Bösking, J.; Nauroozi, D.; Karnahl, M.; Rau, S.; Tschierlei, S. Merging of a Perylene Moiety Enables a Ru(II) Photosensitizer with Long-Lived Excited States and the Efficient Production of Singlet Oxygen. *Chem.—Eur. J.* **2022**, *28*, No. e202103609.
- (52) Doettinger, F.; Yang, Y.; Schmid, M.-A.; Frey, W.; Karnahl, M.; Tschierlei, S. Cross-Coupled Phenyl- and Alkynyl-Based Phenanthrolines and Their Effect on the Photophysical and Electrochemical Properties of Heteroleptic Cu(I) Photosensitizers. *Inorg. Chem.* **2021**, *60*, 5391–5401.
- (53) Armaroli, N. Photoactive mono- and polynuclear Cu(-)-phenanthrolines. A viable alternative to Ru(-)polypyridines? *Chem. Soc. Rev.* **2001**, *30*, 113–124.
- (54) Iwamura, M.; Takeuchi, S.; Tahara, T. Ultrafast Excited-State Dynamics of Copper(I) Complexes. *Acc. Chem. Res.* **2015**, *48*, 782–791.
- (55) Mara, M. W.; Fransted, K. A.; Chen, L. X. Interplays of excited state structures and dynamics in copper(I) dimine complexes: Implications and perspectives. *Coord. Chem. Rev.* **2015**, *282–283*, 2–18.
- (56) Mejía, E.; Luo, S.-P.; Karnahl, M.; Friedrich, A.; Tschierlei, S.; Surkus, A.-E.; Junge, H.; Gladiali, S.; Lochbrunner, S.; Beller, M. A Noble-Metal-Free System for Photocatalytic Hydrogen Production from Water. *Chem.—Eur. J.* **2013**, *19*, 15972–15978.
- (57) Tsubomura, T.; Kimura, K.; Nishikawa, M.; Tsukuda, T. Structures and photophysical properties of copper(I) complexes bearing diphenylphenanthroline and bis(diphenylphosphino)alkane: the effect of phenyl groups on the phenanthroline ligand. *Dalton Trans.* **2015**, *44*, 7554–7562.
- (58) Zheng, R. H.; Guo, H. C.; Jiang, H. J.; Xu, K. H.; Liu, B. B.; Sun, W. L.; Shen, Z. Q. A new and convenient synthesis of phenidones oxidated by KBrO₃/H₂SO₄ at room temperature. *Chin. Chem. Lett.* **2010**, *21*, 1270–1272.
- (59) Das, O.; Paria, S.; Zangrando, E.; Paine, T. K. Copper(II)-Mediated Oxidative Transformation of vic-Dioxime to Furoxan: Evidence for a Copper(II)-Dinitrosoalkene Intermediate. *Inorg. Chem.* **2011**, *50*, 11375–11383.
- (60) Comba, P.; Krämer, R.; Mokhir, A.; Naing, K.; Schatz, E. Synthesis of New Phenanthroline-Based Heteroditopic Ligands – Highly Efficient and Selective Fluorescence Sensors for Copper(II) Ions. *Eur. J. Inorg. Chem.* **2006**, *2006*, 4442–4448.
- (61) Rentschler, M.; Schmid, M.-A.; Frey, W.; Tschierlei, S.; Karnahl, M. Multidentate Phenanthroline Ligands Containing Additional Donor Moieties and Their Resulting Cu(I) and Ru(II) Photosensitizers: A Comparative Study. *Inorg. Chem.* **2020**, *59*, 14762–14771.
- (62) Kaeser, A.; Mohankumar, M.; Mohanraj, J.; Monti, F.; Holler, M.; Cid, J.-J.; Moudam, O.; Nierengarten, I.; Karmazin-Brelot, L.; Duhayon, C.; Delavaux-Nicot, B.; Armaroli, N.; Nierengarten, J.-F. Heteroleptic Copper(I) Complexes Prepared from Phenanthroline and Bis-Phosphine Ligands. *Inorg. Chem.* **2013**, *52*, 12140–12151.
- (63) Fischer, S.; Hollmann, D.; Tschierlei, S.; Karnahl, M.; Rockstroh, N.; Barsch, E.; Schwarzbach, P.; Luo, S.-P.; Junge, H.; Beller, M.; Lochbrunner, S.; Ludwig, R.; Brückner, A. Death and Rebirth: Photocatalytic Hydrogen Production by a Self-Organizing Copper-Iron System. *ACS Catal.* **2014**, *4*, 1845–1849.
- (64) Lennox, A. J. J.; Fischer, S.; Jurrat, M.; Luo, S.-P.; Rockstroh, N.; Junge, H.; Ludwig, R.; Beller, M. Copper-Based Photosensitizers in Water Reduction: A More Efficient In Situ Formed System and Improved Mechanistic Understanding. *Chem.—Eur. J.* **2016**, *22*, 1233–1238.
- (65) Zhang, Y.; Traber, P.; Zedler, L.; Kupfer, S.; Gräfe, S.; Schulz, M.; Frey, W.; Karnahl, M.; Dietzek, B. Cu(I) vs. Ru(II) photosensitizers: elucidation of electron transfer processes within a series of

- structurally related complexes containing an extended π -system. *Phys. Chem. Chem. Phys.* **2018**, *20*, 24843–24857.
- (66) Zhang, Y.; Zedler, L.; Karnahl, M.; Dietzek, B. Excited-state dynamics of heteroleptic copper(I) photosensitizers and their electrochemically reduced forms containing a dipyrrophenazine moiety - a spectroelectrochemical transient absorption study. *Phys. Chem. Chem. Phys.* **2019**, *21*, 10716–10725.
- (67) Colomer, I.; Chamberlain, A. E. R.; Haughey, M. B.; Donohoe, T. J. Hexafluoroisopropanol as a highly versatile solvent. *Nat. Rev. Chem.* **2017**, *1*, No. 0088.
- (68) Horng, M. L.; Gardecki, J. A.; Papazyan, A.; Maroncelli, M. Subpicosecond Measurements of Polar Solvation Dynamics: Coumarin 153 Revisited. *J. Phys. Chem. A* **1995**, *99*, 17311–17337.
- (69) Marciniak, H.; Lochbrunner, S. On the interpretation of decay associated spectra in the presence of time dependent spectral shifts. *Chem. Phys. Lett.* **2014**, *609*, 184–188.
- (70) Kumpulainen, T.; Lang, B.; Rosspeintner, A.; Vauthey, E. Ultrafast Elementary Photochemical Processes of Organic Molecules in Liquid Solution. *Chem. Rev.* **2017**, *117*, 10826–10939.
- (71) Lees, A. J. The Luminescence Rigidochromic Effect Exhibited by Organometallic Complexes: Rationale and Applications. *Comments Inorg. Chem.* **1995**, *17*, 319–346.
- (72) Mohankumar, M.; Holler, M.; Meichsner, E.; Nierengarten, J. F.; Niess, F.; Sauvage, J. P.; Delavaux-Nicot, B.; Leoni, E.; Monti, F.; Malicka, J. M.; Cocchi, M.; Bandini, E.; Armaroli, N. Heteroleptic Copper(I) Pseudorotaxanes Incorporating Macrocyclic Phenanthroline Ligands of Different Sizes. *J. Am. Chem. Soc.* **2018**, *140*, 2336–2347.
- (73) Armaroli, N.; Accorsi, G.; Holler, M.; Moudam, O.; Nierengarten, J.-F.; Zhou, Z.; Wegh, R. T.; Welter, R. Highly Luminescent CuI Complexes for Light-Emitting Electrochemical Cells. *Adv. Mater.* **2006**, *18*, 1313–1316.
- (74) Tschierlei, S.; Karnahl, M.; Rockstroh, N.; Junge, H.; Beller, M.; Lochbrunner, S. Substitution-Controlled Excited State Processes in Heteroleptic Copper(I) Photosensitizers Used in Hydrogen Evolving Systems. *ChemPhysChem* **2014**, *15*, 3709–3713.
- (75) Bizzarri, C.; Spuling, E.; Knoll, D. M.; Volz, D.; Bräse, S. Sustainable metal complexes for organic light-emitting diodes (OLEDs). *Coord. Chem. Rev.* **2018**, *373*, 49–82.
- (76) Yersin, H.; Czerwieńiec, R.; Shafigov, M. Z.; Suleymanova, A. F. TADF Material Design: Photophysical Background and Case Studies Focusing on CuI and AgI Complexes. *ChemPhysChem* **2017**, *18*, 3508–3535.
- (77) Pöpcke, A.; Aleksey, F.; Lochbrunner, S. Revealing the initial steps in homogeneous photocatalysis by time-resolved spectroscopy. *J. Phys.: Condens. Matter* **2020**, *32*, No. 153001.
- (78) Elsaesser, T.; Kaiser, W. Vibrational and Vibronic Relaxation of Large Polyatomic Molecules in Liquids. *Annu. Rev. Phys. Chem.* **1991**, *42*, 83–107.
- (79) Zhang, Y.; Zedler, L.; Karnahl, M.; Dietzek, B. Excited-state dynamics of heteroleptic copper(I) photosensitizers and their electrochemically reduced forms containing a dipyrrophenazine moiety - a spectroelectrochemical transient absorption study. *Phys. Chem. Chem. Phys.* **2019**, *21*, 10716–10725.
- (80) Grupe, M.; Bäßler, F.; Theiß, M.; Busch, J. M.; Dietrich, F.; Volz, D.; Gerhards, M.; Bräse, S.; Diller, R. Real-time observation of molecular flattening and intersystem crossing in [(DPEPhos)Cu(i)-(PyrTet)] via ultrafast UV/Vis- and mid-IR spectroscopy on solution and solid samples. *Phys. Chem. Chem. Phys.* **2020**, *22*, 14187–14200.
- (81) Zou, L.-Y.; Cheng, Y.-X.; Li, Y.; Li, H.; Zhang, H.-X.; Ren, A.-M. A theoretical analysis of the phosphorescence efficiencies of Cu(I) complexes. *Dalton Trans.* **2014**, *43*, 11252–11259.
- (82) Kubiček, K.; Thekku Veedu, S.; Storozhuk, D.; Kia, R.; Tschert, S. Geometric and electronic properties in a series of phosphorescent heteroleptic Cu(I) complexes: Crystallographic and computational studies. *Polyhedron* **2017**, *124*, 166–176.
- (83) Zamadar, M.; Greer, A. In *Comprehensive Supramolecular Chemistry*; Albin, A.; Fagnoni, M., Eds.; Wiley-VCH: Weinheim, 2010; Vol. 1, pp 353–386.
- (84) Ghogare, A. A.; Greer, A. Using Singlet Oxygen to Synthesize Natural Products and Drugs. *Chem. Rev.* **2016**, *116*, 9994–10034.
- (85) Pibiri, I.; Buscemi, S.; Palumbo Piccionello, A.; Pace, A. Photochemically Produced Singlet Oxygen: Applications and Perspectives. *ChemPhotoChem* **2018**, *2*, 535–547.
- (86) Imberti, C.; Zhang, P.; Huang, H.; Sadler, P. J. New Designs for Phototherapeutic Transition Metal Complexes. *Angew. Chem., Int. Ed.* **2020**, *59*, 61–73.
- (87) Kim, J.; Whang, D. R.; Park, S. Y. Designing Highly Efficient CuI Photosensitizers for Photocatalytic H₂ Evolution from Water. *ChemSusChem* **2017**, *10*, 1883–1886.
- (88) Sasikumar, D.; Kohara, R.; Takano, Y.; Yuyama, K.-i.; Biju, V. Kinetics of singlet oxygen sensing using 9-substituted anthracene derivatives. *J. Chem. Sci.* **2019**, *131*, No. 5.
- (89) Otto, S.; Nauth, A. M.; Ermilov, E.; Scholz, N.; Friedrich, A.; Resch-Genger, U.; Lochbrunner, S.; Opatz, T.; Heinze, K. Photo-Chromium: Sensitizer for Visible-Light-Induced Oxidative C–H Bond Functionalization—Electron or Energy Transfer? *ChemPhotoChem* **2017**, *1*, 344–349.
- (90) DeRosa, M. C.; Crutchley, R. J. Photosensitized singlet oxygen and its applications. *Coord. Chem. Rev.* **2002**, *233–234*, 351–371.
- (91) Schmidt, R. Photosensitized Generation of Singlet Oxygen. *Photochem. Photobiol.* **2006**, *82*, 1161–1177.
- (92) Giacomini, E.; Rupiani, S.; Guidotti, L.; Recanatini, M.; Roberti, M. The Use of Stilbene Scaffold in Medicinal Chemistry and Multi-Target Drug Design. *Curr. Med. Chem.* **2016**, *23*, 2439–2489.
- (93) Nevesely, T.; Wienhold, M.; Molloy, J. J.; Gilmour, R. Advances in the E \rightarrow Z Isomerization of Alkenes Using Small Molecule Photocatalysts. *Chem. Rev.* **2022**, *122*, 2650–2694.
- (94) Fabry, D. C.; Ronge, M. A.; Rueping, M. Immobilization and Continuous Recycling of Photoredox Catalysts in Ionic Liquids for Applications in Batch Reactions and Flow Systems: Catalytic Alkene Isomerization by Using Visible Light. *Chem.—Eur. J.* **2015**, *21*, 5350–5354.
- (95) Cai, W.; Fan, H.; Ding, D.; Zhang, Y.; Wang, W. Synthesis of Z-alkenes via visible light promoted photocatalytic E \rightarrow Z isomerization under metal-free conditions. *Chem. Commun.* **2017**, *53*, 12918–12921.
- (96) Ruthkosky, M.; Kelly, C. A.; Castellano, F. N.; Meyer, G. J. Electron and energy transfer from CuI MLCT excited states. *Coord. Chem. Rev.* **1998**, *171*, 309–322.
- (97) Castellano, F. N.; McCusker, C. E. MLCT sensitizers in photochemical upconversion: past, present, and potential future directions. *Dalton Trans.* **2015**, *44*, 17906–17910.
- (98) Yang, M.; Sheykhi, S.; Zhang, Y.; Milsman, C.; Castellano, F. N. Low power threshold photochemical upconversion using a zirconium(IV) LMCT photosensitizer. *Chem. Sci.* **2021**, *12*, 9069–9077.
- (99) Herr, P.; Kerzig, C.; Larsen, C. B.; Häussinger, D.; Wenger, O. S. Manganese(i) complexes with metal-to-ligand charge transfer luminescence and photoreactivity. *Nat. Chem.* **2021**, *13*, 956–962.

An Unexpected Boost in Activity of a Cu(I) Photosensitizer by Stabilizing a Transient Excited State

Martin Rentschler,^{#a} Pit Jean Boden,^{#b} Miguel A. Argüello Cordero,^{#c} Sophie Theres Steiger,^b Marie-Ann Schmid,^a Yingya Yang,^a Gereon Niedner-Schatteburg,^{*b} Michael Karnahl,^{*a} Stefan Lochbrunner^{*c} and Stefanie Tschierlei^{*a}

a TU Braunschweig, Institute of Physical and Theoretical Chemistry, Department of Energy Conversion, Rebenring 31, 38106 Braunschweig, Germany

b TU Kaiserslautern, Chemistry Department and State Research Center Optimas, Erwin-Schrödinger-Straße 52, 67663 Kaiserslautern, Germany

c University of Rostock, Institute for Physics and Department of Life, Light and Matter, Albert-Einstein-Straße 23, 18051 Rostock, Germany

equally contributed to this work.

Supporting Information - Table of Contents

1	Experimental Details	page	S2
2	Synthetic Details	page	S7
3	Structural Characterization of Cudmbiipo and dmbiipo	page	S9
	3.1 NMR Spectra	page	S9
	3.2 MS Spectra	page	S11
4	Cyclic Voltammograms and Differential Pulse Voltammograms	page	S13
5	Experimental and Calculated UV/vis Absorption Spectra	page	S14
6	Emission Spectroscopy (steady-state and time-resolved)	page	S18
7	Nanosecond Transient Absorption Spectroscopy	page	S31
8	Step-scan FTIR Spectroscopy and calculated Vibrational Spectra	page	S33
	8.1 Experimental and theoretical ground and excited state IR spectra	page	S33
	8.2 Excited State Lifetimes Obtained by Step-Scan FTIR Spectroscopy	page	S37
	8.3 Characterization of Vibrational Modes	page	S38
9	Calculated Spin Densities	page	S40
10	Calculated Ground and Excited State Geometries	page	S41
11	Photocatalytic applications	page	S46
	11.1 Photocatalytic formation of singlet oxygen	page	S46
	11.2 Photocatalytic isomerization of <i>E</i> -stilbene	page	S47
12	Femtosecond Transient Absorption Spectra of biipo	page	S49
13	Reference Section	page	S50

1 Experimental Details

NMR spectroscopy. Nuclear magnetic resonance (NMR) spectra were measured at 298 K with different Bruker Avance spectrometers operating at Larmor frequencies of 400 MHz or 500 MHz (^1H) and 101 MHz or 126 MHz (^{13}C) and processed with MestreNova software (version 12.0.0). All spectra were referenced to the deuterated solvent as an internal standard.¹ Chemical shifts are given by the residual solvent proton signal. Coupling constants J are presented as absolute values in Hz, without considering the kind of the coupling. For the characterization of the NMR signals the following abbreviations are used: s = singlet, d = doublet, t = triplet, m = multiplet, dd = doublet of doublets.

Mass spectrometry. Mass spectrometric (MS) measurements were performed by the analytical service of the Institute of Organic Chemistry at the University of Stuttgart. High resolution mass spectra were measured using electrospray ionization (ESI) on a Bruker Daltonics microTOF-Q. MS values are given as m/z .

Cyclic voltammetry. Cyclic voltammograms were carried out in acetonitrile solution using 0.1 M Bu_4NPF_6 as supporting electrolyte. An Autolab potentiostat PGSTAT204 from Metrohm was used with a three-electrode configuration. The working electrode was a glassy carbon disc with a 3 mm diameter stick and the counter electrode was a Pt wire. The reference electrode was a non-aqueous Ag/Ag^+ electrode (0.01 M AgNO_3 in acetonitrile) with the ferrocene/ferricenium (Fc/Fc^+) couple as external reference, which was added to the solution after each measurement. All potentials are reported versus the Fc/Fc^+ couple. All scan rates are 0.1 V/s unless otherwise noted.

UV/vis steady-state absorption and emission spectroscopy in solution. Steady-state UV/vis absorption spectra were recorded with a JASCO V-670 spectrophotometer and emission spectra were measured with a JASCO FP-8500 spectrofluorometer. For measurements under air in acetonitrile, ROTISOLV®, UV/IR grade solvents purchased from Carl Roth were used. Quantum yields were determined from the integrated area of emission in comparison to $[\text{Ru}(\text{bpy})_3](\text{PF}_6)_2$ as reference compound ($\Phi = 0.06$ in degassed acetonitrile²), detected at an excitation wavelength of 441 nm.

Additional absorption spectra were measured with an UV/vis absorption spectrophotometer SPECORD 50 (ANALYTIK JENA). The corresponding emission spectra were recorded with a corrected FluoroMax-4 (HORIBA SCIENTIFIC) spectrometer. Acetonitrile (MeCN; UVASOL®-Quality, MERCK) and hexafluoro isopropanol (1,1,1,3,3,3-Hexafluoro-2-propanol, HFIP, $\geq 99\%$, pure, Sigma-Aldrich, Co.) were used as solvents and the samples were filled into 10 mm quartz cuvettes (HELLMA ANALYTICS). Degassed samples were flushed with Ar.

Time-resolved emission spectroscopy. The excited-state lifetimes were determined by means of a streak camera system (Streakscope C10627, HAMAMATSU PHOTONICS) using the frequency doubled output of a femtosecond Ti:Sapphire laser system (CPA 2001, CLARK MXR, INC.) for excitation at 388 nm. All compounds were measured with an optical density of around 0.1 at 388 nm to avoid self-absorption and aggregation. Sample preparation was the same as for steady-state spectroscopy.

UV/vis steady state absorption and emission spectroscopy in the solid state. UV/vis absorption spectra were recorded with a Lambda 900 UV/VIS spectrometer equipped with a diffuse reflectance accessory (Harrick Praying Mantis). The powder samples were prepared by mixing neat powder of the compound with dry KBr in a ratio of ca. 1:100 and grinding to a homogenous mixture.

Steady-state luminescence measurements on KBr pellets were performed on a Fluorolog 3-22 (Horiba Jobin-Yvon) fluorescence spectrometer. A 450 W xenon lamp was used for sample excitation and detection was realized with a R928P photomultiplier detector. All reported spectra are corrected for the wavelength-dependent response sensitivity of the system. The spectral selection was achieved with double grating monochromators in the excitation and emission paths, respectively. Long-wave pass filters with cutoff wavelengths of 455 nm (**Cudmbiipo** and **Cubcp**), 475 nm (**dmbiipo**) or 540 nm (for excitation spectra) were used in the emission channel to avoid higher order excitation light. For the preparation of KBr pellets, the compounds (1.7 mg for **Cudmbiipo** and **Cubcp**; 0.7 mg for **dmbiipo**) were mixed with dry KBr (180 mg, stored in a compartment dryer at 80 °C, purchased from Merck) and ground to a homogenous mixture. This mixture was filled in an evacuable pellet die with a diameter of 13 mm and sintered at a pressure of 0.75 GPa. Temperature-dependent measurements were performed using a closed-cycle helium cryostat (ColdEdge, 101J cryocooler) to cool down the sample to 5 K. The cryocooler was equipped with a pellet holder (copper) and CaF₂ windows. Luminescence lifetimes of KBr pellets were determined by TCSPC (time-correlated single-photon counting) at variable temperature using the same cryostat. In the DeltaFlex (Horiba Scientific) spectrometer the samples were excited with a pulsed excitation source (NanoLED 390 (wavelength: 389 nm, pulse duration: 1.3 ns), NanoLED 350 (wavelength: 345 nm, pulse duration: ~1 ns) for **Cudmbiipo** and **dmbiipo**, SpectralLED 390 (wavelength: 390 nm, pulse duration: ~100 ns) for **Cubcp**). Spectral selection and detection were achieved with a single grating monochromator and a PPD-850 detector, respectively. Long-wave pass filters (cutoff at 510 nm (**Cudmbiipo**) or 540 nm (**Cubcp** and **dmbiipo**)) were set between sample and emission monochromator to suppress the influence of scattered excitation light. Decay curves were analysed by multiexponential fits with the software ORIGIN® and the errors of the decay constants are estimated to ± 10 %.

Femtosecond transient absorption spectroscopy. For transient absorption (TA) spectroscopy a setup based on a regenerative Ti:Sapphire amplifier system (Spitfire Pro, Spectra Physics) was used, providing ultrashort laser pulses centered at 800 nm with a repetition rate of 1 kHz. Excitation (pump) pulses centered at 400 nm were generated by frequency doubling with a BBO crystal. Pulse duration was 60 fs. Absorption changes were probed over the visible spectral range with a white-light continuum. The probe pulses were generated in a rotating CaF₂-plate and their polarisation was set to magic angle (~54.7°) relative to that of the pump-pulses. Relative polarizations of parallel and perpendicular orientation were also measured in order to prove the consistency of the data. Both pulses were focused onto the sample to overlap. Spot diameters of the pulses were approximately 160 µm for the pump and 80 µm for the probe. **Cudmbiipo** was dissolved in acetonitrile (MeCN; UVASOL®-Quality, MERCK) and degassed by flushing Ar through the solution. It was measured in a quartz cuvette with a thickness of 1 mm and an optical density of 0.5 at the excitation wavelength. Pump pulses had a power of 200 µW. The ligands **dmbiipo** and **biipo** were measured in quartz cuvettes with a thickness of 2 mm, diluted in hexafluoro isopropanol (1,1,1,3,3,3-Hexafluoro-2-propanol, HFIP, 99.5+%, pure, ACROS ORGANICS) and an optical density of 0.5 at the excitation wavelength. Pump pulses had a power of 300 µW.

Nanosecond transient absorption spectroscopy. A Q-switched pulsed Nd:YAG laser (Q-smart 450mJ, Quantel laser) was used to generate excitation pulses with an output centered at 355 nm (approx. 6 ns pulse duration. repetition rate of 10 Hz). These pulses were passed through a laser line filter (CWL = 355 ± 2 nm, FWHM = 10 ± 2 nm) to ensure that the samples were only excited by 355 nm light. The power of the

pump beam was about 2–3 mJ per pulse at the sample. The stability of the sample was verified by means of UV/vis spectra before and after each measurement. The spectrometer used was a LP980-K spectrometer from Edinburgh Instruments, where the pump and probe beams spatially overlapped at the sample position in a perpendicular beam setup. The probe lamp was operated in flash mode (150 W ozone-free xenon arc lamp, 30 A), and after passing the sample the probe light was recorded using a photo multiplier tube (Hamamatsu R928P). A standard fused silica cuvette with a layer thickness of 10 mm and a sample OD of approximately 0.2–0.3 at the pump wavelength was used in this setup. The compound **Cudmbiipo** was dissolved in acetonitrile (Carl Roth, ROTISOLV®, UV/IR grade solvents) under inert conditions. The ligands **dmbiipo** and **biipo** were diluted in hexafluoro isopropanol (1,1,1,3,3,3-Hexafluoro-2-propanol, HFIP, ≥99%, pure, Sigma-Aldrich, Co.) under aerated conditions.

Time-resolved Step-scan FTIR spectroscopy. All the time-resolved FTIR experiments were performed with the FTIR spectrometer Bruker Vertex 80v, operated in the step-scan mode. A liquid-nitrogen-cooled mercury cadmium telluride (MCT) detector (Kolmar Tech., Model KV100-1-B-7/190) with a rise time of 25 ns, connected to a fast preamplifier and a 14-bit transient recorder board (Spectrum Germany, M3I4142, 400 MS/s), was used for signal detection and processing. The laser setup used for the measurements includes a Q-switched Nd:YAG laser (Innolas SpitLight Evo I) generating pulses with a bandwidth of about 6 ns at a repetition rate of 100 Hz. The third harmonic (355 nm) of the Nd:YAG laser was used directly for sample excitation. The UV pump beam was attenuated to about 1.5 – 2.0 mJ per shot (1.5 mJ for **Cubcp** and 2.0 mJ for **Cudmbiipo**) at a diameter of 9 mm. The beam was directed onto the sample and adjusted to have a maximal overlap with the IR beam of the spectrometer. The sample chamber was equipped with anti-reflection-coated germanium filters to prevent the entrance of laser radiation into the detector and interferometer compartments. The KBr pellets were prepared as described above (here 0.8 mg for **Cudmbiipo** and 1.5 mg for **Cubcp**, see section on T-dependent emission spectroscopy in the solid state) and cryogenically cooled (20 K or 290 K at the pellet) using a closed-cycle helium cryostat (ARS Model DE-202A). The cryocooler was equipped with a pellet holder and CaF₂ windows, as described for the luminescence spectroscopy. The temporal resolution of the 14-bit transient recorder board was chosen according to the excited state lifetime of the system and was set to 20 ns or 100 ns (**Cudmbiipo**: 100 ns at 20 K, 20 ns at 290 K; **Cubcp**: 20 ns). The time where the laser pulse reached the sample was set as zero point in all spectra. The time delay between the start of the experiment and the laser pulse was controlled with a Stanford Research Systems DG535 delay generator. The spectral region was limited by undersampling to 988 – 1975 cm⁻¹ with a spectral resolution of 4 cm⁻¹ resulting in 555 interferogram points. An IR broadband filter (850 – 1750 cm⁻¹) and CaF₂ windows (no IR transmission ≤ 1000 cm⁻¹) prevented problems when performing a Fourier transformation (i.e. no IR intensity outside the measured region should be observed). FTIR ground state spectra were recorded systematically to check if there is no sample degradation. Estimated uncertainties for the excited state lifetimes are on the order of 10 %.

NIR emission spectroscopy in solution. Static NIR emission spectra were recorded using a Fluorolog 3-22 (Horiba Jobin-Yvon) fluorescence spectrometer equipped with a 450 W xenon lamp and a DSS – IGA020L NIR detector (800 nm ≤ λ_{em} ≤ 1550 nm). Spectral selection was realized with double and single grating monochromators in the excitation and emission paths, respectively. Long-pass filters with cutoff wavelengths of 850 nm and 500 nm were used in the emission channel to avoid higher order excitation light. Spectroscopic grade acetonitrile was purchased from Merck (Uvasol®). The concentration of **Cudmbiipo**, **Cubiipo** and **Cubcp** was set to 2.5 · 10⁻⁵ M in THF and optionally 200 equivalents of 9-methylanthracene (99 %, purchased from Alfa Aesar) were added for quenching experiments. The solutions were measured in 1 cm x 1 cm quartz cuvettes under air.

Singlet oxygen quantum yields. Singlet oxygen quantum yields ($\Phi(^1\text{O}_2)$) in THF were determined relative to the reference complex $[\text{Cr}(\text{ddpd})_2](\text{BF}_4)_3$ (ddpd = *N,N'*-dimethyl-*N,N'*-dipyridine-2-ylpyridine-2,6-diamine) with a known $\Phi_{\text{ref}}(^1\text{O}_2)$ of 0.61 in dimethylformamide.³ Sample and reference were excited with the same excitation wavelength of 420 nm and measured using identical fluorimeter settings. $\Phi(^1\text{O}_2)$ was determined according to the following formula:

$$\Phi(^1\text{O}_2) = \Phi_{\text{ref}}(^1\text{O}_2) \cdot \frac{I_s}{I_{\text{ref}}} \cdot \frac{A_{\text{ref}}}{A_s} \quad \text{Eq. 1}$$

Hereby, I_s and I_{ref} are the integrated emissions of the sample and the reference, respectively. A_s and A_{ref} denote the absorbance of the sample and the reference at the excitation wavelength.

Photoisomerization of *E*-stilbene. The isomerization reactions were conducted under inert conditions. The solvent was dried via freeze-pump-thaw cycles. For the irradiation a white light LED (from StarLight Sensorik-Lichtleitsysteme) with a radiation range from ca. 410-730 nm and a maximum power of 36 W (max. intensity of 730 lm) was used. An emission spectrum of the light source is shown in chapter 11.2.

GC-Measurements. The gas chromatographic measurements were performed by the analytical service of the Institute of Organic Chemistry (IOC) at the University of Stuttgart. The utilized column is 30 m in length and its surface consists of polydimethylsiloxane (PDMS) where 35 % of the methyl groups were substituted for phenyl groups. The following temperature program was applied: heating to 40 °C, holding the temperature at 40 °C for one minute, then heating with 10 K/min until a temperature of 300 °C is reached. Reference samples were prepared to obtain the retention times of the investigated compounds.

***In-situ* UV/vis spectra.** The *in-situ* reaction monitoring via UV-vis spectroscopy was done using an AVA AvaSpec-ULS2048CL-EVO-RS-UA from Avantes with AVA AvaLight-DH-S-BAL as halogen/deuterium light source.

Upconversion experiments. All the investigations were performed using the fluorimeter described in the section on solid state luminescence spectroscopy with the difference that a continuous wave HeCd laser (KIMMON Series IK5651R-G) was used for excitation at 442 nm (~55 mW). Solutions were prepared with concentrations of $2.5 \cdot 10^{-5}$ M for the analyte (**Cudmbiipo**, **Cubcp** and **dmbiipo**) and $1.3 \cdot 10^{-3}$ M for anthracene in THF.

DFT calculations. The crystal structure was used as input structure for **Cubcp** and in the case of **Cudmbiipo** the input was generated by chemical intuition from the optimized minimum structure of **Cubiipo**. Geometry optimizations were performed with the Berny algorithm of Gaussian 09⁴ by using energies and gradients computed by Turbomole 7.4. All calculations were performed with the DFT functional B3LYP with dispersion correction (no three-body interaction) (D3(BJ))⁵ as implemented in Turbomole using the resolution of identity (RI) approximation and the def2-TZVP basis set.

Turbomole 7.4 was used for computing the first hundred electronic excitations in the singlet manifold with TDDFT and simulate the UV/vis spectra using the same functional and basis set as described above. For convolution Gaussian broadening with a full-width at half maximum of 1000 cm^{-1} was used.

Harmonic frequency calculations were performed for the optimized minimum structures. The vibrational frequencies are scaled by a factor of 0.975 to minimize the differences between the experimental and calculated frequencies. A Gaussian convolution with a full-width at half-maximum of 8 cm^{-1} was applied to the calculated vibrational transitions.

2 Synthetic Details

2,9-Dimethylphenanthroline-5,6-dione

2,9-Dimethylphenanthroline-5,6-dione was synthesized according to a previously reported procedure. All analytical data are in accordance to the literature.⁶

2,9-Dimethylphenanthroline-5,6-dioxime

2,9-Dimethylphenanthroline-5,6-dioxime was synthesized according to a previously reported procedure. All analytical data are in accordance to the literature.⁷

5,6-Diamino-2,9-dimethylphenanthroline

5,6-Diamino-2,9-dimethylphenanthroline was synthesized analogously to a previously reported procedure as described below.⁸

2,9-Dimethylphenanthroline-5,6-dioxime (74 mg, 0.275 mmol, 1.0 Eq.) was suspended in degassed 6 mL of ethanol at 70 °C. A solution of sodium dithionite (126 mg, 0.657 mmol, 2.8 Eq.) in 6 mL of 3% ammonia was added via a syringe. After 5-10 minutes, again a solution of sodium dithionite (114 mg, 0.219 mmol, 2.4 Eq.) in 3 mL of 3% ammonia was added via a syringe. After the second addition, the mixture was refluxed for one hour. It was allowed to cool to room temperature and the precipitated product was collected by filtration under a nitrogen atmosphere. The precipitate was washed with ammonia (3 %) and degassed diethyl ether. 63 mg (96 %) of crude product were obtained. The crude product was directly used for the next reaction step.

dmbiipo

Crude 5,6-diamino-2,9-dimethylphenanthroline (63 mg, 0.264 mmol, 1.0 Eq.) and naphthalic anhydride (55 mg, 0.276 mmol, 1.05 Eq.) were dissolved in degassed acetic acid (5 mL) and refluxed for 18 hours. After cooling to room temperature, the product was precipitated by the addition of water (10 mL). It was collected by filtration, washed with water and then taken up in hydrochloric acid (30 %) and again precipitated by careful neutralization, collected by filtration and washed with water. The crude product was then purified by column chromatography with a mixture of dichloromethane and methanol (20:1) as eluent. The ligand **dmbiipo** (49 mg) was obtained as a yellow solid. Yield: 45 % over two steps.

¹H-NMR (CDCl₃, 500 MHz, 25 °C): δ = 10.43 (*d*, 1H, *J* = 8.9, Ar-H), 9.36 (*d*, 1H, *J* = 8.3, Ar-H), 8.96 (*d*, 1H, *J* = 7.6, Ar-H), 8.86 (*d*, 1H, *J* = 7.6, Ar-H), 8.37 (*d*, 1H, *J* = 8.3, Ar-H), 8.23 (*d*, 1H, *J* = 8.3, Ar-H), 7.94 (*d*, 1H, *J* = 8.3, Ar-H), 7.94 (*d*, 1H, *J* = 8.9, Ar-H), 7.88 (*t*, 1H, *J* = 7.7, Ar-H), 7.84 (*t*, 1H, *J* = 7.8, Ar-H), 3.05 (*s*, 3H, CH₃), 3.01 (*s*, 3H, CH₃). ¹³C-NMR (CDCl₃, 126 MHz, 25 °C): δ = 160.6, 159.8, 156.6, 151.9, 142.5, 137.3, 137.2, 136.6, 135.4, 134.8, 134.3, 133.9, 131.9, 129.3, 128.0, 127.8, 127.6, 126.4, 124.0, 121.9, 121.6, 120.0, 118.7, 118.6, 23.1, 22.0. HRMS (ESI) *m/z*: calculated for [M+H]⁺ [C₂₆H₁₇N₄O]⁺: 401.1397; found: 401.1397.

[(xant)Cu(dmbiipo)]PF₆ (Cudmbiipo)

[Cu(MeCN)₄]PF₆ (37 mg, 0.100 mmol, 1.0 Eq.) and xantphos (58 mg, 0.100 mmol, 1.0 Eq.) were refluxed in 20 mL degassed dichloromethane for 16 hours. The reaction mixture was then cooled to 0 °C and **dmbiipo** (40 mg, 0.100 mmol, 1.0 Eq.) in 20 mL dichloromethane was added dropwise via a syringe. After the addition, the reaction mixture was refluxed for 3 hours. *n*-Hexane was added to precipitate the desired complex, which was then washed with diethyl ether. To increase the purity of the complex, it was once

more taken up in dichloromethane and precipitated with *n*-hexane. **Cudmbiipo** was obtained as a yellow solid (80 mg, 67 %).

¹H-NMR (CD₃CN, 700 MHz, 25 °C): δ = 9.66 (*d*, 1H, *J* = 8.3, Ar-H), 8.66 (*d*, 1H, *J* = 7.4, Ar-H), 8.63 (*d*, 1H, *J* = 7.2, Ar-H), 8.61 (*d*, 1H, *J* = 7.1, Ar-H), 8.36 (*d*, 1H, *J* = 8.1, Ar-H), 8.19 (*d*, 1H, *J* = 8.1, Ar-H), 7.80 (*t*, 1H, *J* = 7.6, Ar-H), 7.75 (*t*, 1H, *J* = 7.6, Ar-H), 8.30 (*dd*, 2H, *J* = 7.9, 1.1, Ar-H), 7.42-7.29 (*m*, 3H, Ar-H), 7.25-7.22 (*m*, 1H, Ar-H), 7.17 (*t*, 2H, *J* = 7.7, Ar-H), 7.14-7.10 (*m*, 4H, Ar-H), 7.05-7.00 (*m*, 8H, Ar-H), 6.99-6.95 (*m*, 8H, Ar-H), 6.91-6.88 (*m*, 2H, Ar-H), 2.21 (*s*, 3H, CH₃), 2.19 (*s*, 3H, CH₃), 1.65 (*s*, 3H, CH₃), 1.64 (*s*, 3H, CH₃). **¹³C-NMR (CD₃CN, 176 MHz, 25 °C):** δ = 161.6, 159.1, 157.3, 155.4, 151.7, 142.7, 142.2, 138.4, 137.2, 136.7, 134.5, 134.0, 133.5, 133.3, 133.0, 132.7, 132.5, 132.0, 130.8, 130.7, 130.6, 130.5, 129.4, 129.2, 128.5, 128.3, 128.0, 127.6, 126.7, 126.2, 126.0, 124.9, 124.8, 123.6, 122.3, 122.2, 121.1, 120.2, 36.5, 28.5, 28.4, 27.6, 27.5. **³¹P-NMR (CD₃CN, 283 MHz, 25 °C):** δ = -12.8. **HRMS (ESI) m/z:** calculated for **[M-PF₆]⁺ [C₆₅H₄₈CuN₄O₂P₂]⁺**: 1041.2543; found: 1041.2544. **EA:** calculated for **C₆₅H₄₈CuF₆N₄O₂P₃**: C: 65.74, H: 4.07, N: 4.72; found: C: 65.48, H: 4.18, N: 4.81.

3 Structural Characterization

3.1 NMR Spectra

The **dmbiipo** ligand and the corresponding **Cudmbiipo** complex were characterized by ^1H and ^{13}C NMR spectroscopy (see Figures S3.1 - S3.5).

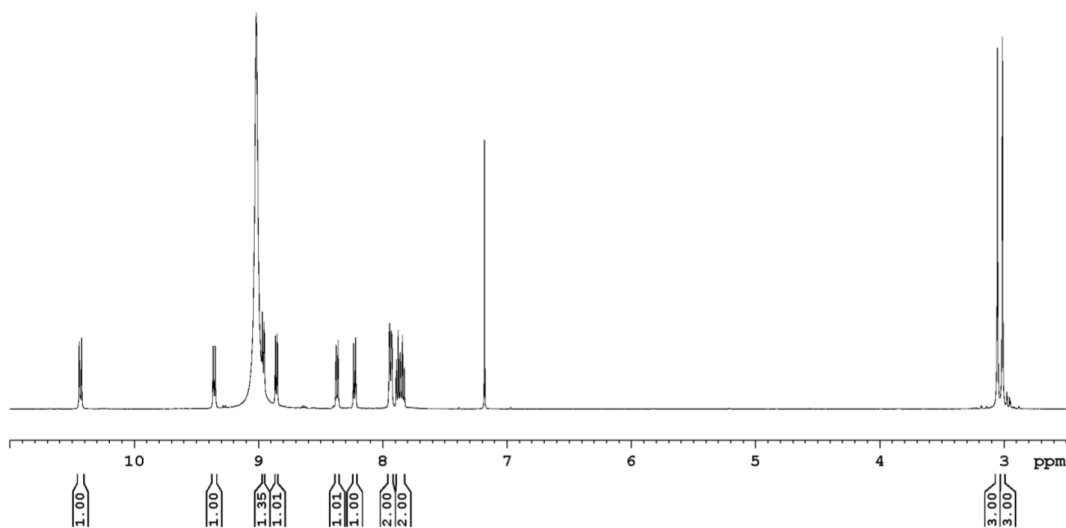


Figure S1. ^1H NMR spectrum of **dmbiipo** in CDCl_3 including a small amount of trifluoroacetic acid to increase the solubility.

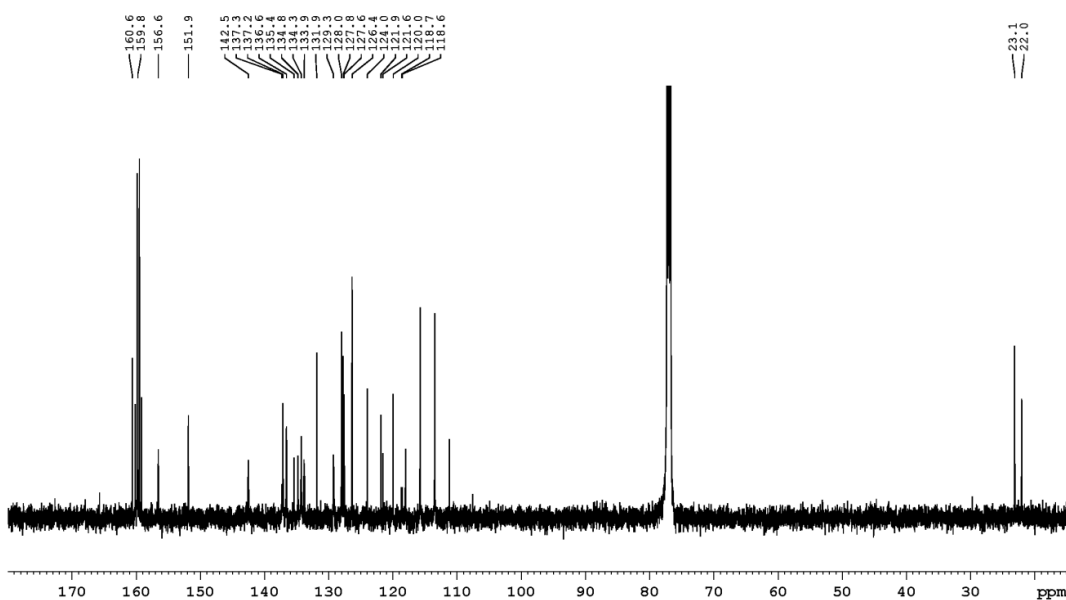


Figure S2. ^{13}C NMR spectrum of **dmbiipo** in CDCl_3 including a small amount of trifluoroacetic acid to increase the solubility.

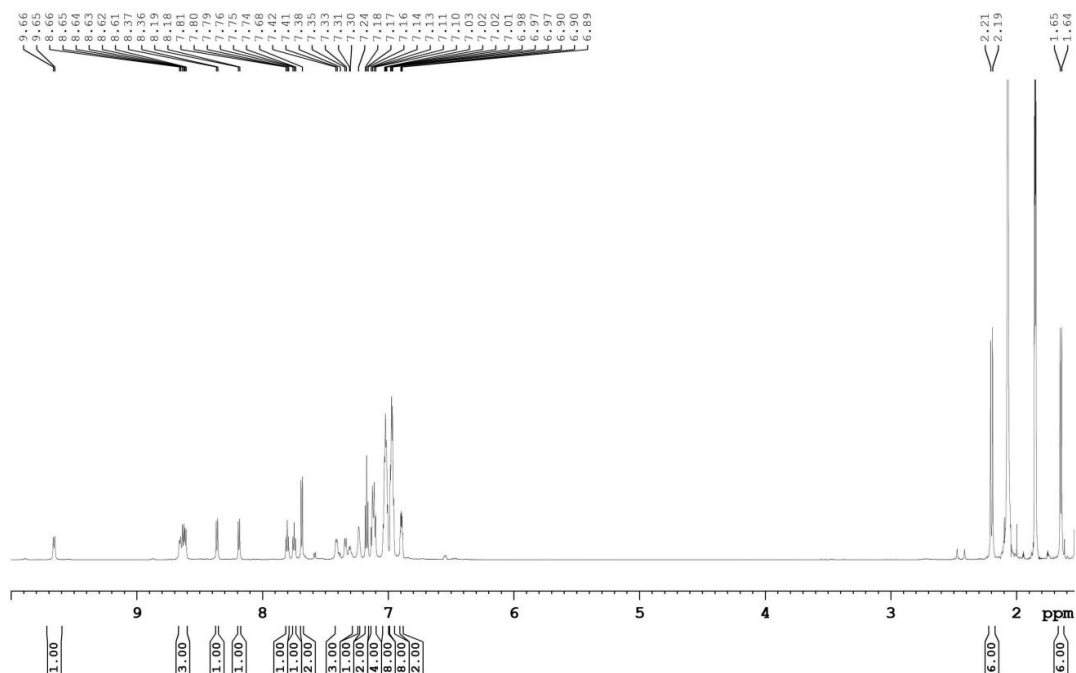


Figure S3. ^1H NMR spectrum of Cudmbiipo in CD_3CN .

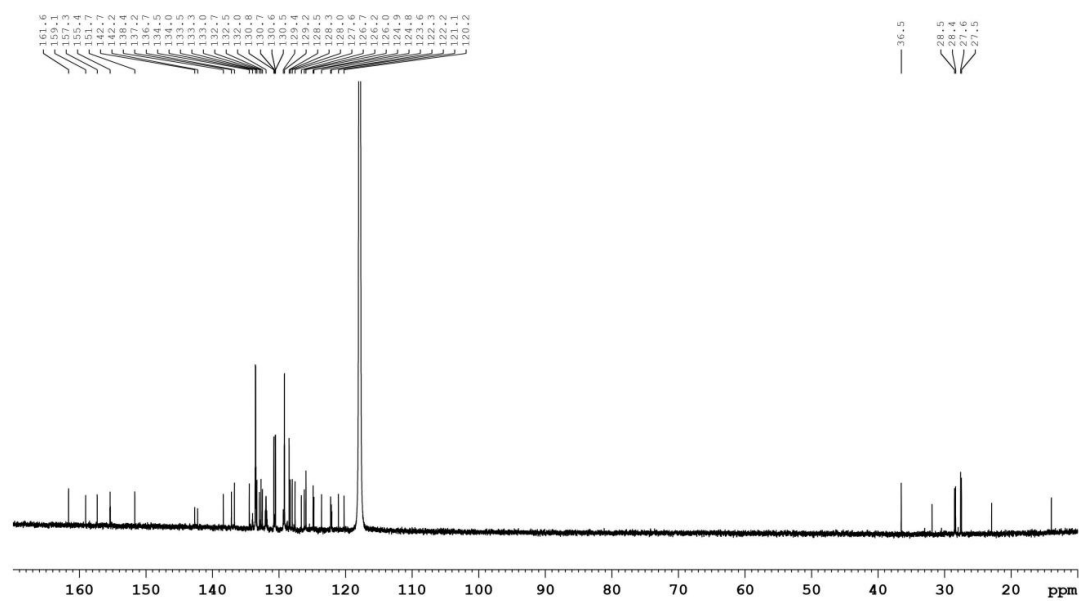


Figure S4. ^{13}C NMR spectrum of Cudmbiipo in CD_3CN .

3.2 MS Spectra

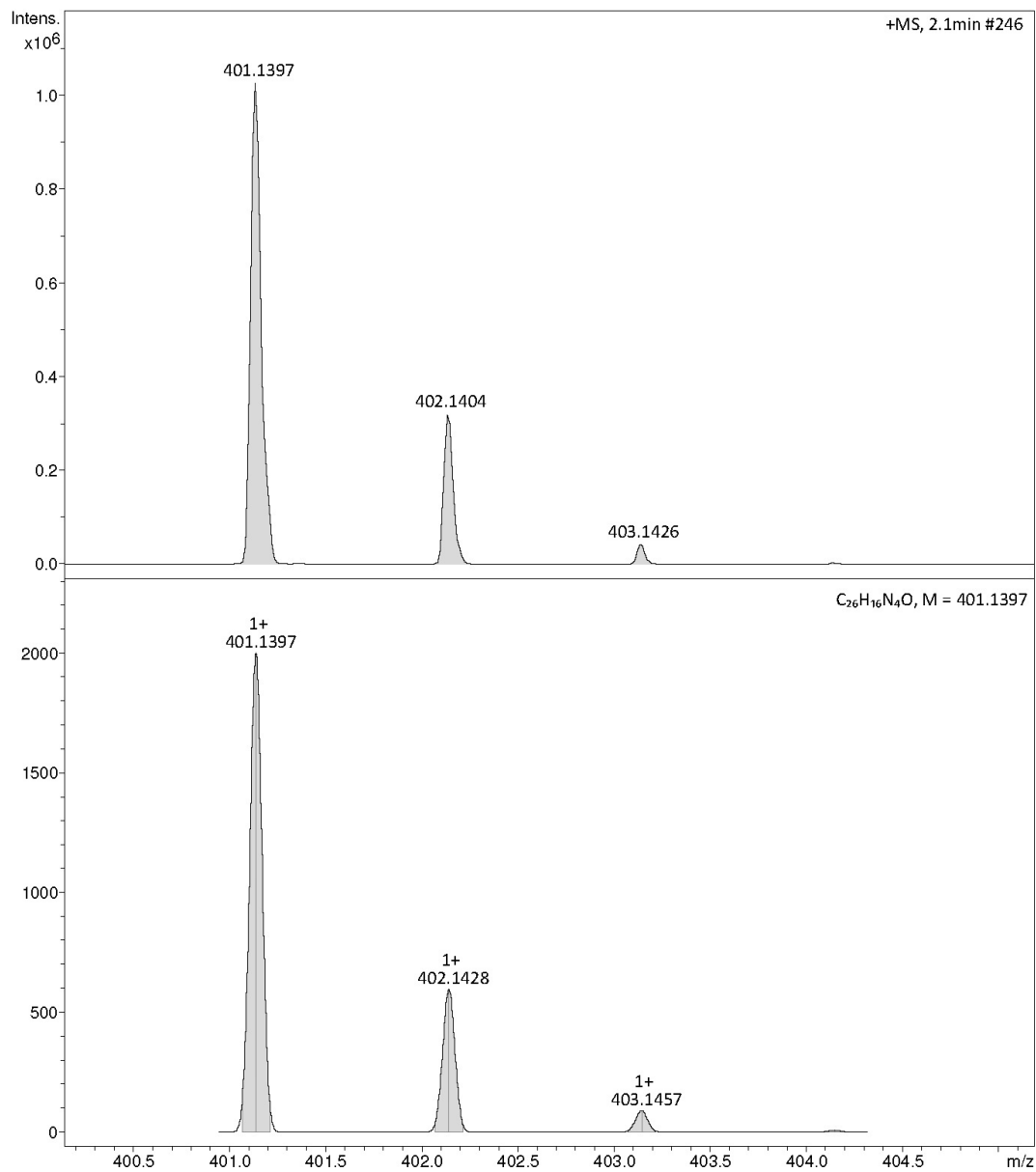


Figure S5. Measured (top) and calculated (bottom) ESI-MS spectrum of dmbiipo.

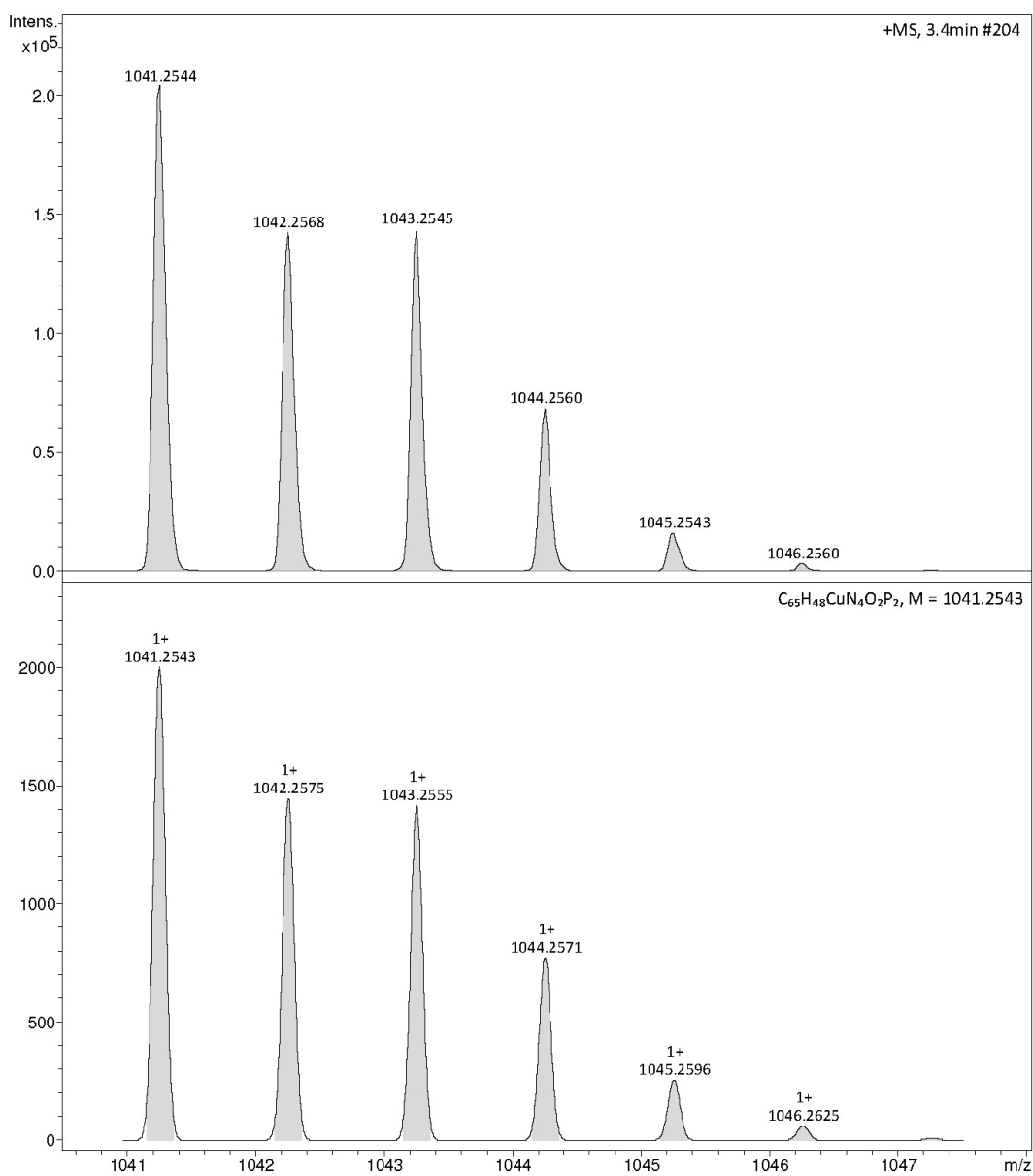


Figure S6. Measured (top) and calculated (bottom) high resolution ESI-MS spectrum of **Cudmbiipo** with matching isotopic pattern.

4 Cyclic Voltammograms and Differential Pulse Voltammograms

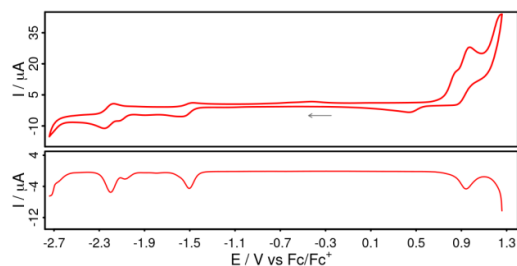


Figure S7. Cyclic voltammogram (top) and differential pulse voltammetry of **Cudmbiipo** ($c < 0.1$ M, due to problems with solubility) in MeCN with 0.1 M $n\text{Bu}_4\text{NPF}_6$ as the supporting electrolyte. The arrow indicates the scan direction.

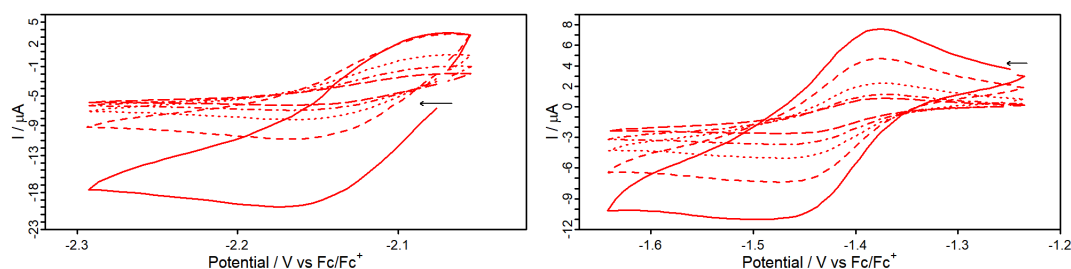


Figure S8. Cyclic voltammograms of the reductions of **Cudmbiipo** in acetonitrile solution with $n\text{Bu}_4\text{NPF}_6$ (0.1 M) as supporting electrolyte measured with different scan rates: 500 mV/s (solid line), 250 mV/s (dashed), 100 mV/s (dotted), 50 mV/s (dotted and dashed), 25 mV/s (long dashes). The arrow indicates the scan direction.

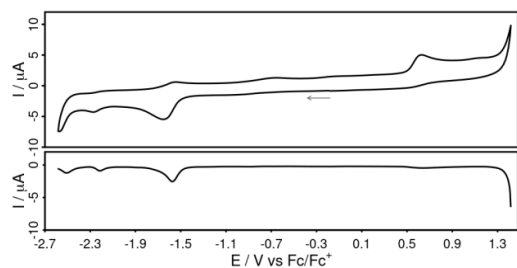


Figure S9. Cyclic voltammogram (top) and differential pulse voltammetry of **dmbiipo** (< 0.1 M, due to problems with solubility) in MeCN with 0.1 M $n\text{Bu}_4\text{NPF}_6$ as the supporting electrolyte. The arrow indicates the scan direction.

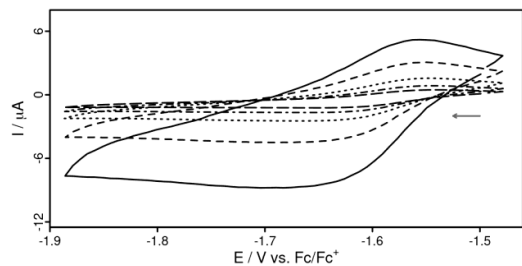


Figure S10. Cyclic voltammograms of the reductions of **dmbiipo** in acetonitrile solution with $n\text{Bu}_4\text{NPF}_6$ (0.1 M) as supporting electrolyte measured with different scan rates: 500 mV/s (solid line), 250 mV/s (dashed), 100 mV/s (dotted), 50 mV/s (dotted and dashed), 25 mV/s (long dashes). The arrow indicates the scan direction.

5 Experimental and Calculated UV/vis Absorption Spectra

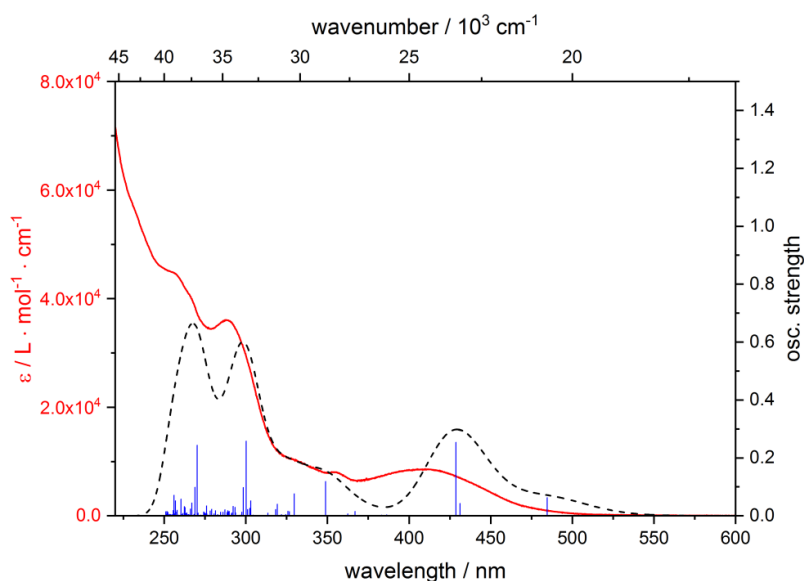


Figure S11. Molar attenuation coefficients of **Cudmbiipo** in acetonitrile (solid) and theoretical UV/vis absorption spectrum (dashed) resulting from the Gaussian convolution (FWHM = 1000 cm^{-1}) of the calculated transitions (vertical bars) (TDDFT/B3LYP-D3(BJ)/def2-TZVP).

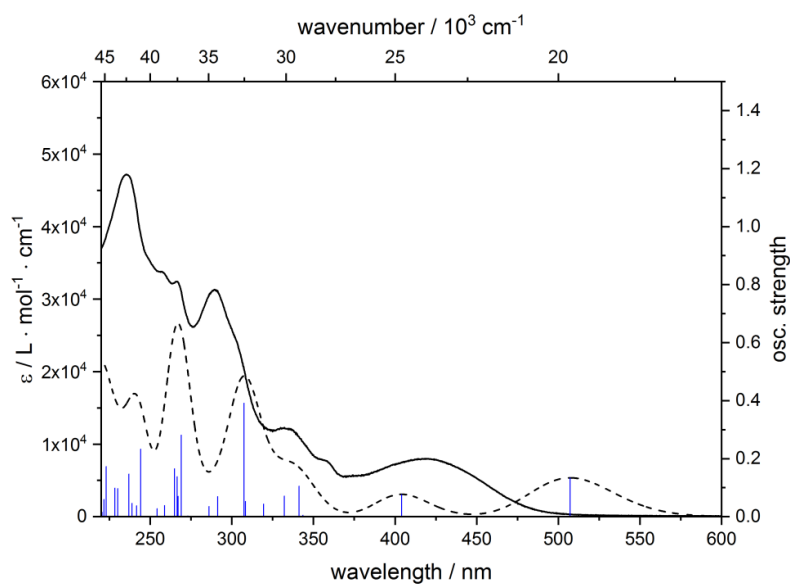


Figure S12. Molar attenuation coefficients of **dmbiipo** in acetonitrile (solid) and theoretical UV/vis absorption spectrum (dashed) resulting from the Gaussian convolution (FWHM = 1000 cm^{-1}) of the calculated transitions (vertical bars) (TDDFT/B3LYP-D3(BJ)/def2-TZVP).

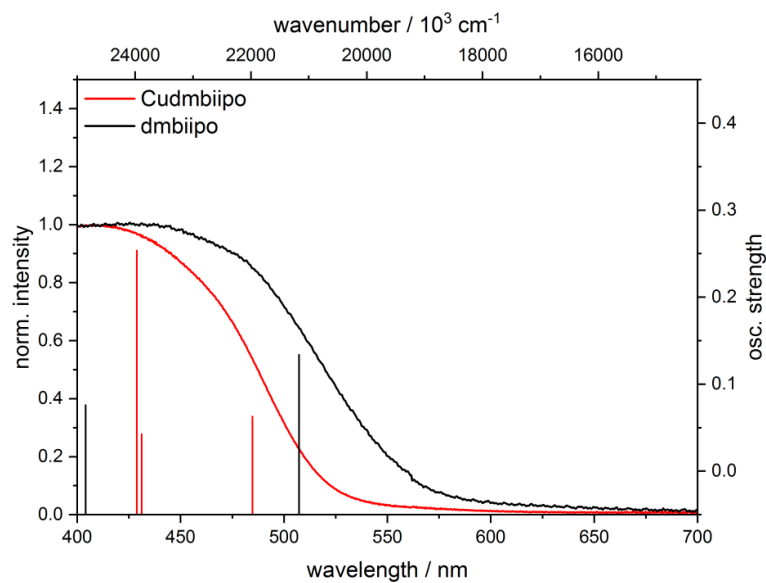


Figure S13 Solid state UV/vis absorption spectra of **Cudmbiipo** (red) and **dmbiipo** (black) (samples diluted with KBr powder) and calculated electronic transitions (TDDFT/B3LYP-D3(BJ)/def2-TZVP).

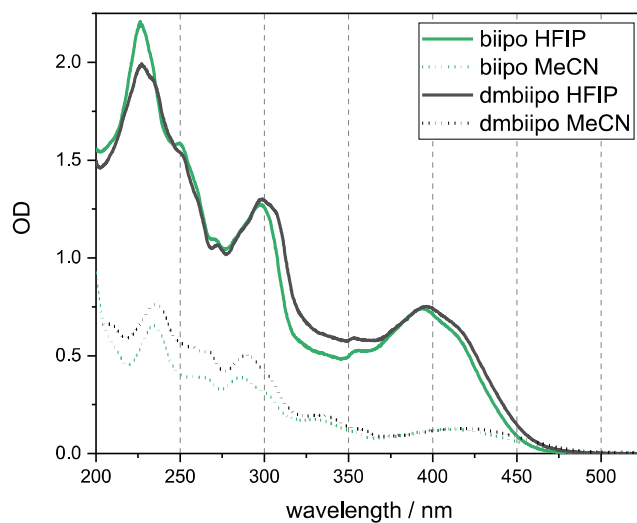


Figure S14. Stationary absorption spectra of **biipo** and **dmbiipo** in acetonitrile and hexafluoro isopropanol solution.

Table S1. Calculated excitation energies, orbital contributions and assignments of **Cudmbiipo** at TDDFT level (B3LYP-D3(BJ)/def2-TZVP) (im = imidazole part, phen = phenanthroline part, naph = naphthaloylene-benzene part, xant = xantphos ligand, xant(Ph) = phenyl rings of xantphos).

transition	$\tilde{\nu} / \text{cm}^{-1}$	λ / nm	%	donor orbital	acceptor orbital	assignment
1	20630	485	98	HOMO	LUMO	$d_{\text{Cu}} \rightarrow \pi_{\text{im, naph}}$
2	23191	431	94	HOMO	LUMO+1	$d_{\text{Cu}} \rightarrow \pi_{\text{phen}}, d_{\text{Cu}}$
3	23321	429	93	HOMO-1	LUMO	$d_{\text{Cu}}, \pi_{\text{im, naph, phen}} \rightarrow \pi_{\text{im, naph}}$
11	28663	349	73	HOMO-5	LUMO	$d_{\text{Cu}}, \pi_{\text{im, phen, naph}} \rightarrow \pi_{\text{im, naph}}$
			12	HOMO-1	LUMO+2	$d_{\text{Cu}}, \pi_{\text{im, naph, phen}} \rightarrow \pi_{\text{im, phen}}$
13	30328	330	47	HOMO-1	LUMO+2	$d_{\text{Cu}}, \pi_{\text{im, naph, phen}} \rightarrow \pi_{\text{im, phen}}$
			14	HOMO-7	LUMO	$d_{\text{Cu}}, \pi_{\text{phen, naph, im}} \rightarrow \pi_{\text{im, naph}}$
			11	HOMO-5	LUMO	$d_{\text{Cu}}, \pi_{\text{im, phen, naph}} \rightarrow \pi_{\text{im, naph}}$
30	33305	300	34	HOMO-1	LUMO+3	$d_{\text{Cu}}, \pi_{\text{im, naph, phen}} \rightarrow \pi_{\text{im, naph, phen}}$
			13	HOMO	LUMO+7	$d_{\text{Cu}} \rightarrow \pi_{\text{xant(Ph)}}$
			12	HOMO-16	LUMO	$d_{\text{Cu}} \rightarrow \pi_{\text{im, naph}}$
			8	HOMO-15	LUMO	$d_{\text{Cu}}, \pi_{\text{xant(Ph)}} \rightarrow \pi_{\text{im, naph}}$
31	33501	298	23	HOMO-1	LUMO+3	$d_{\text{Cu}}, \pi_{\text{im, naph, phen}} \rightarrow \pi_{\text{im, naph, phen}}$
			19	HOMO-11	LUMO	$d_{\text{Cu}}, \pi_{\text{xant}} \rightarrow \pi_{\text{im, naph}}$
			7	HOMO-12	LUMO	$d_{\text{Cu}}, \pi_{\text{xant(Ph)}} \rightarrow \pi_{\text{im, naph}}$
			7	HOMO-15	LUMO	$d_{\text{Cu}}, \pi_{\text{xant(Ph)}} \rightarrow \pi_{\text{im, naph}}$
65	37010	270	39	HOMO-5	LUMO+2	$d_{\text{Cu}}, \pi_{\text{im, phen, naph}} \rightarrow \pi_{\text{im, phen}}$
			9	HOMO	LUMO+14	$d_{\text{Cu}} \rightarrow \pi_{\text{phen, naph, im, xant}}$
			7	HOMO-7	LUMO+2	$d_{\text{Cu}}, \pi_{\text{phen, naph, im}} \rightarrow \pi_{\text{im, phen}}$
66	37182	269	50	HOMO-4	LUMO+5	$d_{\text{Cu}}, \pi_{\text{xant}} \rightarrow \pi_{\text{xant}}$
			11	HOMO-4	LUMO+4	$d_{\text{Cu}}, \pi_{\text{xant}} \rightarrow \pi_{\text{xant}}$
			7	HOMO-4	LUMO+3	$d_{\text{Cu}}, \pi_{\text{xant}} \rightarrow \pi_{\text{im, naph, phen}}$
88	39057	256	23	HOMO-22	LUMO	$d_{\text{Cu}}, \pi_{\text{phen, im, naph}} \rightarrow \pi_{\text{im, naph}}$
			11	HOMO-3	LUMO+9	$d_{\text{Cu}}, \pi_{\text{xant, phen}} \rightarrow \pi_{\text{xant}}$
			8	HOMO-2	LUMO+10	$d_{\text{Cu}}, \pi_{\text{xant(Ph), phen}} \rightarrow \pi_{\text{xant}}$
			7	HOMO-5	LUMO+3	$d_{\text{Cu}}, \pi_{\text{im, phen, naph}} \rightarrow \pi_{\text{im, naph, phen}}$

Table S2. Calculated excitation energies, orbital contributions and assignments of **dmbiipo** at TDDFT level (B3LYP-D3(BJ)/def2-TZVP) (im = imidazole part, phen = phenanthroline part, naph = naphthaloylene-benzene part, Me = methyl group).

transition	$\tilde{\nu} / \text{cm}^{-1}$	λ / nm	%	donor orbital	acceptor orbital	assignment
1	19713	507	98	HOMO	LUMO	$\pi_{\text{phen, im, naph}} \rightarrow \pi_{\text{naph, im}}$
2	24748	404	96	HOMO-1	LUMO	$\pi_{\text{phen, im}} \rightarrow \pi_{\text{naph, im}}$
5	29301	341	81 8	HOMO-3 HOMO-4	LUMO LUMO	$\pi_{\text{naph, im, phen}} \rightarrow \pi_{\text{naph, im}}$ $\sigma_{\text{phen, N}} \rightarrow \pi_{\text{naph, im}}$
11	32520	308	86	HOMO	LUMO+3	$\pi_{\text{phen, im, naph}} \rightarrow \pi_{\text{naph, im, phen}}$
18	37167	269	32 15 11	HOMO-1 HOMO-1 HOMO-1	LUMO+2 LUMO+1 LUMO+3	$\pi_{\text{phen, im}} \rightarrow \pi_{\text{naph, phen, im}}$ $\pi_{\text{phen, im}} \rightarrow \pi_{\text{phen}}$ $\pi_{\text{phen, im}} \rightarrow \pi_{\text{naph, im, phen}}$
20	37517	267	38 21 17	HOMO-1 HOMO-1 HOMO-1	LUMO+1 LUMO+3 LUMO+2	$\pi_{\text{phen, im}} \rightarrow \pi_{\text{phen}}$ $\pi_{\text{phen, im}} \rightarrow \pi_{\text{naph, im, phen}}$ $\pi_{\text{phen, im}} \rightarrow \pi_{\text{naph, phen, im}}$
21	37736	265	36 26 8	HOMO-1 HOMO-8 HOMO-1	LUMO+3 LUMO LUMO+1	$\pi_{\text{phen, im}} \rightarrow \pi_{\text{naph, im, phen}}$ $\pi_{\text{phen}} \rightarrow \pi_{\text{naph, im}}$ $\pi_{\text{phen, im}} \rightarrow \pi_{\text{phen}}$
27	40951	244	41 25 8 7	HOMO-3 HOMO HOMO HOMO-3	LUMO+1 LUMO+5 LUMO+6 LUMO+3	$\pi_{\text{naph, im, phen}} \rightarrow \pi_{\text{phen}}$ $\pi_{\text{phen, im, naph}} \rightarrow \pi_{\text{naph, im, phen}}$ $\pi_{\text{phen, im, naph}} \rightarrow \pi_{\text{phen, im, naph}}$ $\pi_{\text{naph, im, phen}} \rightarrow \pi_{\text{naph, im, phen}}$
31	41298	237	29 22 17 10	HOMO-3 HOMO-3 HOMO HOMO-11	LUMO+3 LUMO+4 LUMO+6 LUMO	$\pi_{\text{naph, im, phen}} \rightarrow \pi_{\text{naph, im, phen}}$ $\pi_{\text{naph, im, phen}} \rightarrow \pi_{\text{naph, phen}}$ $\pi_{\text{phen, im, naph}} \rightarrow \pi_{\text{phen, im, naph}}$ $\pi_{\text{im, phen, Me, O}} \rightarrow \pi_{\text{naph, im}}$
35	44821	223	51 15	HOMO-5 HOMO-5	LUMO+1 LUMO+3	$\pi_{\text{naph}} \rightarrow \pi_{\text{phen}}$ $\pi_{\text{naph}} \rightarrow \pi_{\text{naph, im, phen}}$

6 Emission Spectroscopy (steady state and time-resolved)

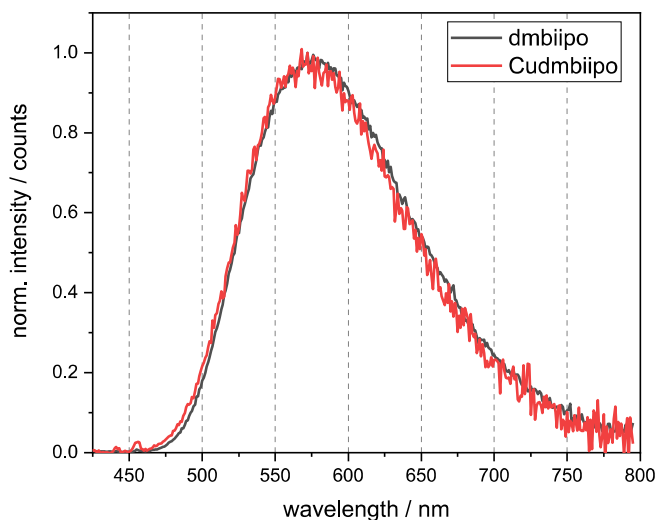


Figure S15. Normalized stationary emission of **dmbiipo** (black) and **Cudmbiipo** (red) in acetonitrile solution saturated with argon, excited at 388 nm.

The mentioned hypothesis is also supported by streak camera measurements, which provide almost the same emissive lifetime of 5.9 and 5.7 ns for the complex and the ligand under an O_2 as well as an argon atmosphere (see Figures S6.14 to S6.16 for time traces and fits). In addition, the excitation spectra of **Cudmbiipo** also match very well with the absorption spectrum of **dmbiipo** (see Figure S6.2). Thus, the emission observed here represents the fluorescence of the ligand, because there is no luminescent triplet state in **dmbiipo**, nor is the 3LC state in **Cudmbiipo** emissive.

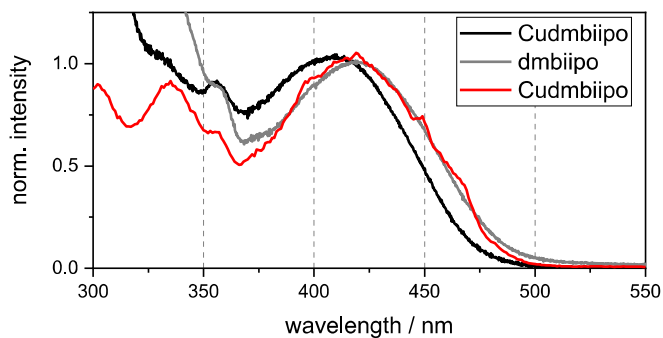


Figure S16. Stationary absorption spectra of **Cudmbiipo** (black) and **dmbiipo** (grey) and excitation spectrum of **Cudmbiipo** (red) in acetonitrile solution. All normalized. Detection of excitation at 576 nm.

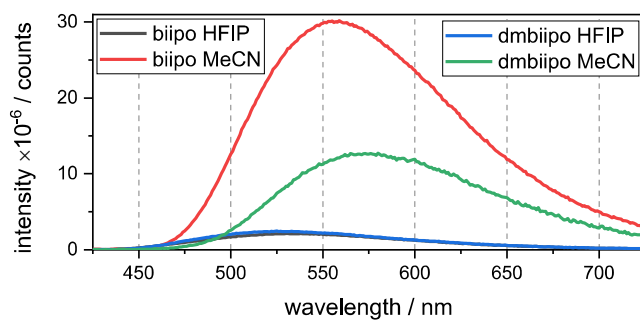


Figure S17. Stationary emission spectra of **dmbiipo** and **biipo** in acetonitrile and in hexafluoro isopropanol solutions in absolute units, excited at 388 nm.

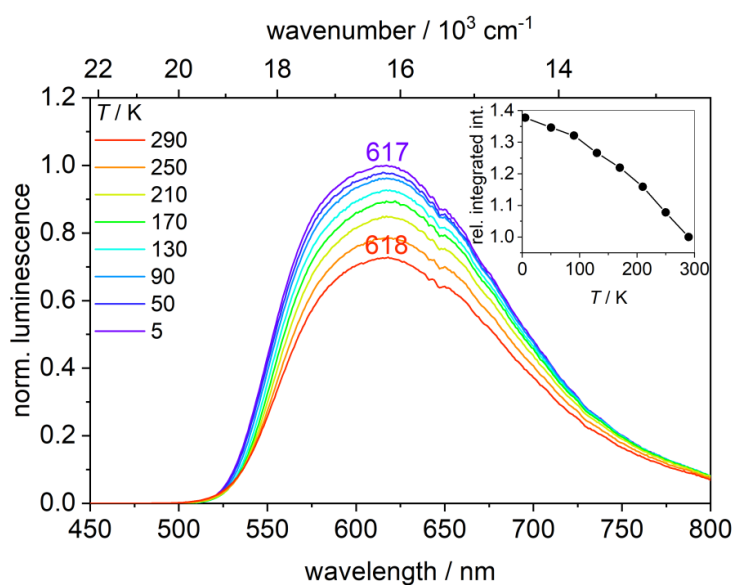


Figure S18. Temperature-dependent solid state luminescence spectra of **dmbiipo** in the temperature range of 290 – 5 K at an excitation wavelength of 420 nm. The inset shows the integrated luminescence intensity relative to 290 K.

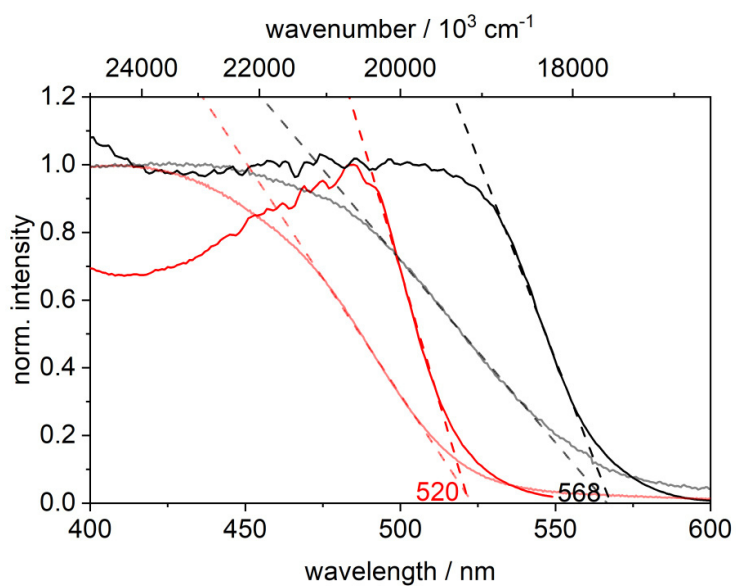


Figure S19. Excitation spectra of **Cudmbiipo** ($\lambda_{em} = 562$ nm, red) and **dmbiipo** ($\lambda_{em} = 617$ nm, black) in a KBr matrix at 5 K. The UV/vis spectra of the solids diluted with KBr powder at room temperature are represented by transparent red and black lines for **Cudmbiipo** and **dmbiipo**, respectively. The onsets of the four spectra were determined tangentially (dashed lines).

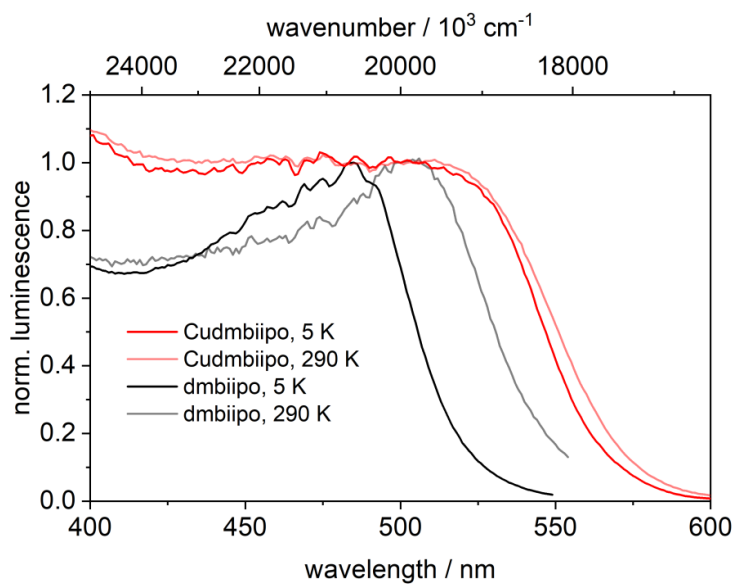


Figure S20. Excitation spectra of **Cudmbiipo** at 5 K ($\lambda_{\text{em}} = 562 \text{ nm}$, red) and 290 K ($\lambda_{\text{em}} = 569 \text{ nm}$, transparent red) and of **dmbiipo** at 5 K ($\lambda_{\text{em}} = 617 \text{ nm}$, black) and 290 K ($\lambda_{\text{em}} = 618 \text{ nm}$, transparent black).

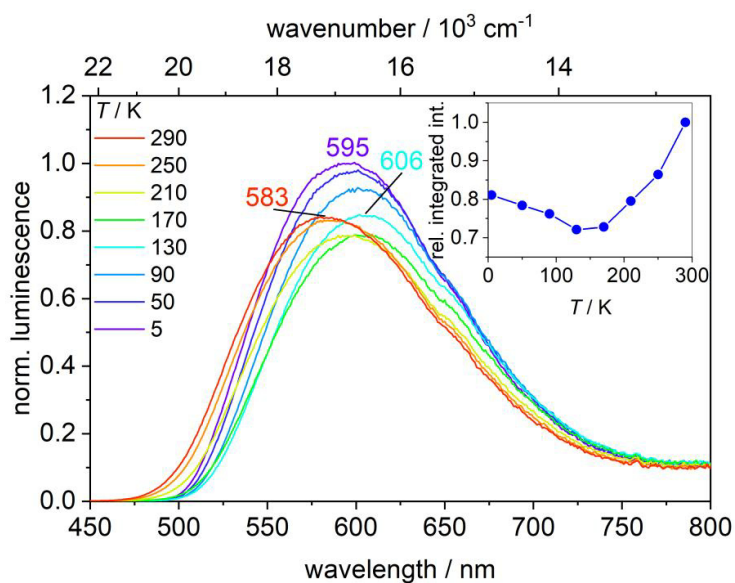


Figure S21. Temperature-dependent solid state luminescence spectra of **Cubcp** in the temperature range of 290 – 5 K at an excitation wavelength of 420 nm. The inset shows the integrated luminescence intensity relative to 290 K.

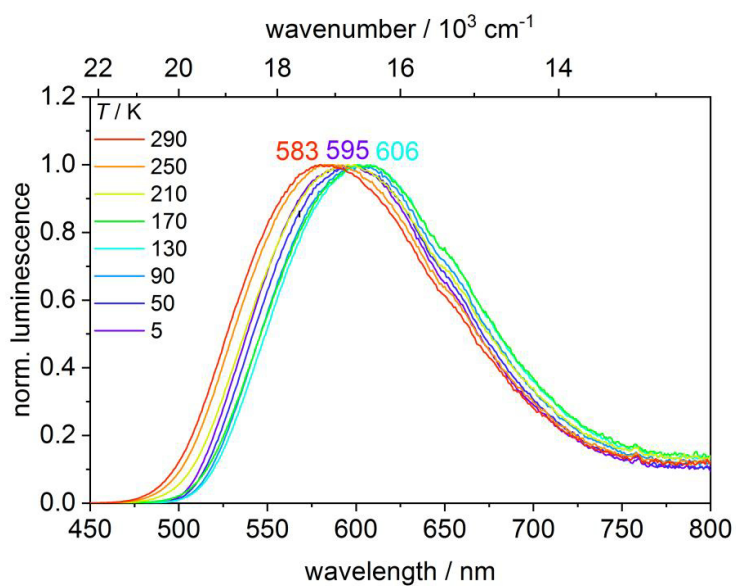


Figure S22. Normalized temperature-dependent solid state luminescence spectra of **Cubcp** in the temperature range of 290 – 5 K at an excitation wavelength of 420 nm.

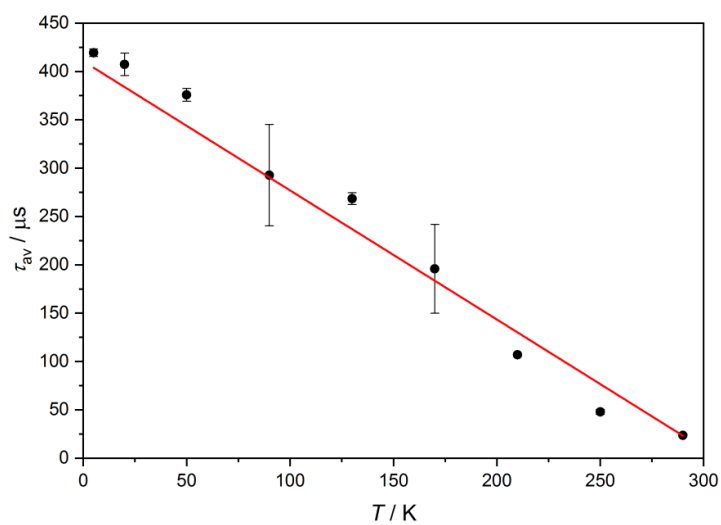


Figure S23. Plot of the average lifetime τ_{av} of **Cubcp** (KBr matrix) against temperature obtained by TCSPC.

Table S3. Temperature-dependent luminescence lifetimes of **Cudmbiipo** and **dmbiipo** (KBr pellets) measured by TCSPC at excitation wavelengths of 345 or 389 nm. The time constants are labelled τ_1 and τ_2 as well as τ_1 , τ_2 and τ_3 for bi- and triexponential fits, respectively, and τ_{av} is the amplitude-weighted average lifetime.

compound	T / K	λ_{ex} / nm (λ_{em} / nm)	τ_1 / ns (% contribution)	τ_2 / ns (% contribution)	τ_3 / ns (% contribution)	τ_{av} / ns
Cudmbiipo	290	345 (555)	0.5 (61 %)	2.1 (26 %)	10 (13 %)	2.1
		389 (555)	0.4 (47 %)	2.2 (36 %)	12 (17 %)	3.0
	130	345 (554)	0.6 (26 %)	2.5 (37 %)	8.5 (37 %)	4.2
		389 (554)	0.6 (28 %)	2.5 (40 %)	9.9 (32 %)	4.3
	5	345 (552)	0.9 (79 %)	3.4 (13 %)	10 (8 %)	2.0
		389 (552)	1.0 (73 %)	3.8 (18 %)	11 (9 %)	2.4
compound	T / K	λ_{em} / nm	τ_1 / ns (% contribution)	τ_1 / ns (% contribution)	τ_3 / ns (% contribution)	τ_{av} / ns
dmbiipo	290	345 (585)	1.8 (47 %)	5.4 (37 %)	11 (16 %)	4.6
		389 (585)	1.5 (45 %)	5.2 (39 %)	11 (16 %)	4.5
	130	345 (582)	2.2 (7 %)	7.3 (58 %)	16 (35 %)	10
		389 (582)	1.9 (15 %)	6.9 (55 %)	16 (30 %)	8.9
	5	345 (580)	2.0 (32 %)	7.2 (44 %)	17 (24 %)	8.0
		389 (580)	2.2 (8 %)	7.3 (50 %)	17 (42 %)	11

Table S4. Temperature-dependent luminescence lifetimes of **Cubcp** (KBr pellets) measured by TCSPC at an excitation wavelength of 390 nm. The time constants are labelled τ_1 and τ_2 as well as τ_1 , τ_2 and τ_3 for bi- and triexponential fits, respectively, and τ_{av} is the amplitude-weighted average lifetime (*continued*).

compound	T / K	λ_{em} / nm	τ_1 / μ s (% contribution)	τ_2 / μ s (% contribution)	τ_3 / μ s (% contribution)	τ_{av} / μ s
Cubcp	290	390 (562)	33 (41 %)	170 (59 %)	-	23
	250	390 (565)	15 (9 %)	42 (77 %)	100 (14 %)	48
	210	390 (572)	49 (30 %)	110 (63 %)	300 (7 %)	110
	170	390 (581)	100 (45 %)	240 (51 %)	700 (4 %)	200
	130	390 (583)	110 (36 %)	280 (54 %)	780 (10 %)	270
	90	390 (579)	80 (37 %)	300 (53 %)	1000 (10 %)	290
	50	390 (573)	120 (36 %)	330 (52 %)	1300 (12 %)	380
	20	390 (572)	160 (55 %)	470 (36 %)	1700 (9 %)	410
	5	390 (571)	160 (55 %)	450 (36 %)	1800 (9 %)	420

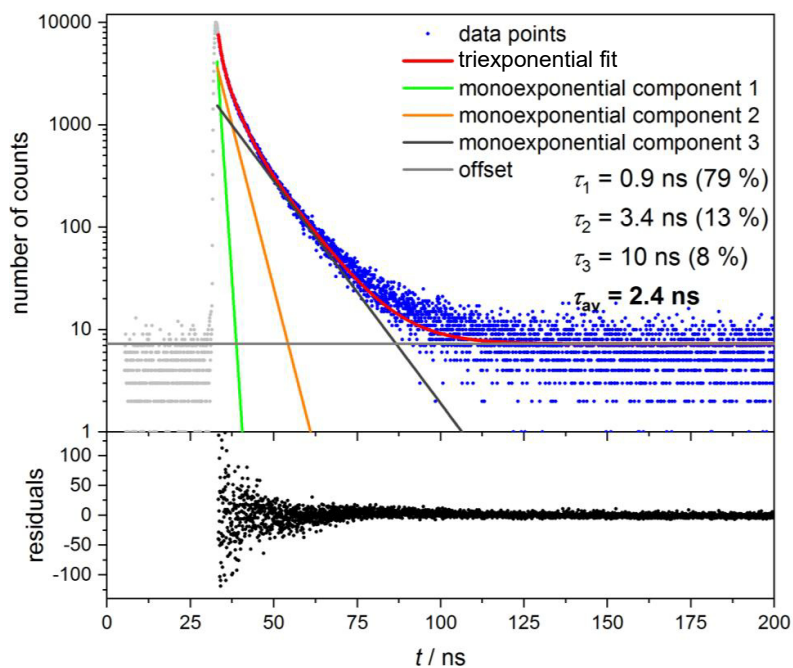


Figure S24. Measured luminescence decay curve (blue dots) of the emission band of **Cudmbiipo** at 5 K ($\lambda_{\text{ex}} = 345 \text{ nm}$; $\lambda_{\text{em}} = 552 \text{ nm}$). The red curve shows the triexponential fit (including an offset) and the green, orange, dark grey and light grey lines represent the underlying monoexponential components and the offset, respectively. The grey dots represent the excitation pulse, which is not considered in the fit. The lower trace shows the residuals of the fit.

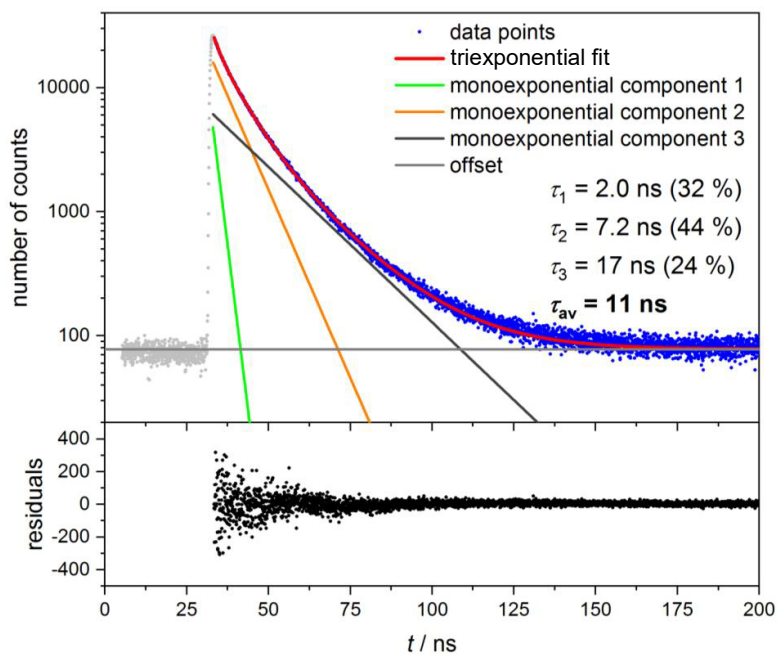


Figure S25. Measured luminescence decay curve (blue dots) of the emission band of **dmbiipo** at 5 K ($\lambda_{\text{ex}} = 345$ nm; $\lambda_{\text{em}} = 580$ nm). The red curve shows the triexponential fit (including an offset) and the green, orange, dark grey and light grey lines represent the underlying monoexponential components and the offset, respectively. The grey dots represent the excitation pulse, which is not considered in the fit. The lower trace shows the residuals of the fit.

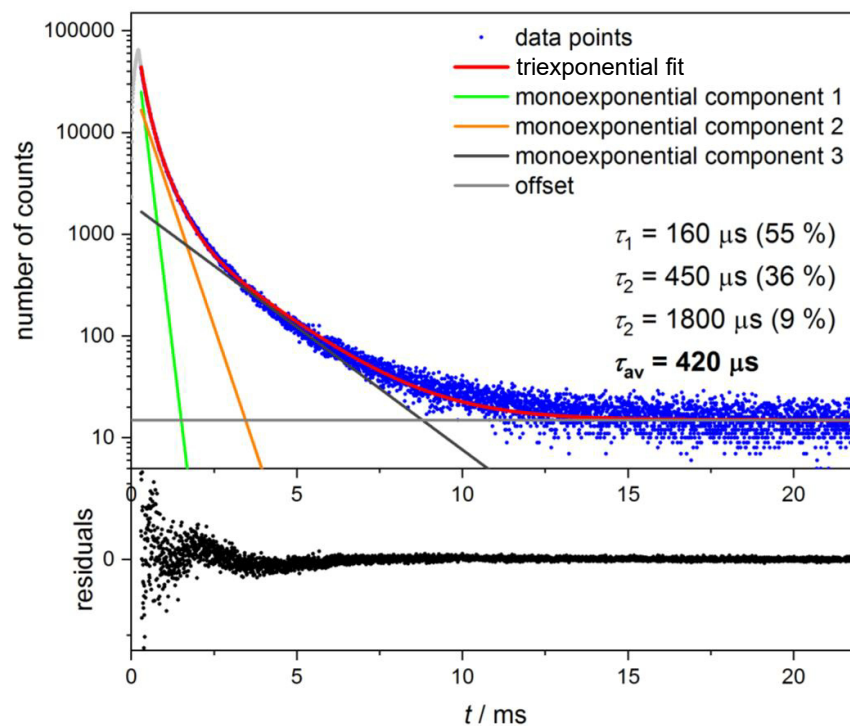


Figure S26. Measured luminescence decay curve (blue dots) of the emission band of **Cubcp** at 5 K ($\lambda_{\text{ex}} = 390 \text{ nm}$; $\lambda_{\text{em}} = 571 \text{ nm}$). The red curve shows the triexponential fit (including an offset) and the green, orange, dark grey and light grey lines represent the underlying monoexponential components and the offset, respectively. The grey dots represent the excitation pulse, which is not considered in the fit. The lower trace shows the residuals of the fit.

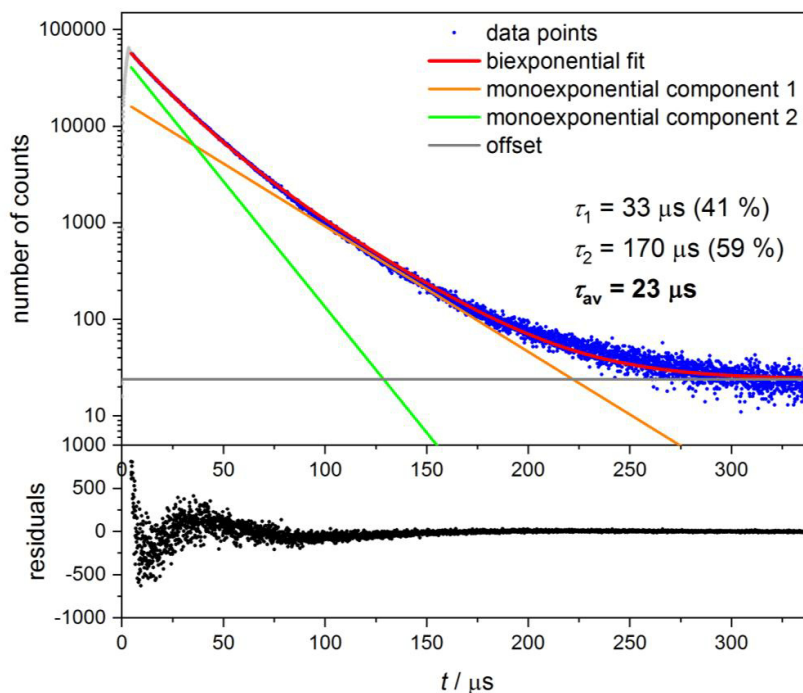


Figure S27. Measured luminescence decay curve (blue dots) of the emission band of **Cubcp** at 290 K ($\lambda_{\text{ex}} = 390$ nm; $\lambda_{\text{em}} = 562$ nm). The red curve shows the biexponential fit (including an offset) and the green, orange and light grey lines represent the underlying monoexponential components and the offset, respectively. The grey dots represent the excitation pulse, which is not considered in the fit. The lower trace shows the residuals of the fit.

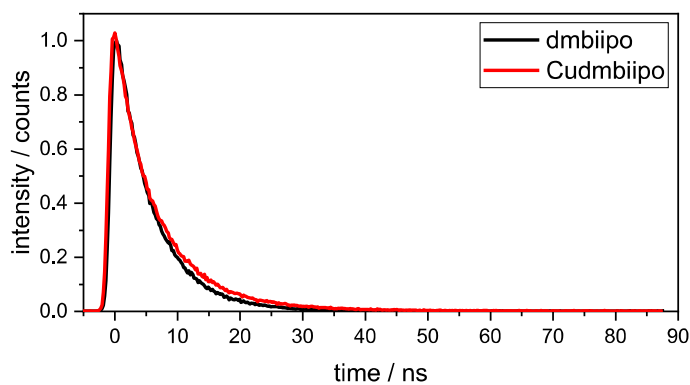


Figure S28. Time-resolved fluorescence signal of **dmbiipo** (black) and **Cudmbiipo** (red) in acetonitrile excited at 388 nm.

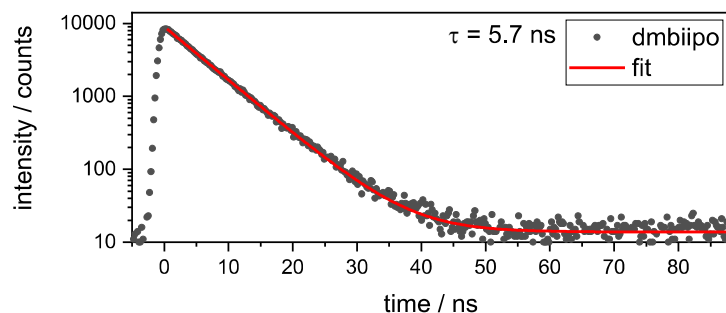


Figure S29. Time-resolved emission signal of **dmbiipo** with a monoexponential fit in acetonitrile excited at 388 nm.

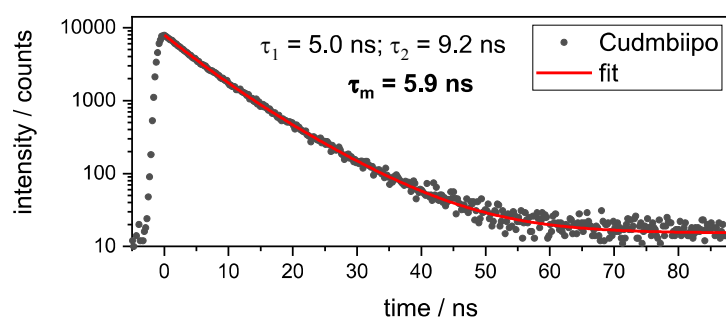


Figure S30. Time-resolved fluorescence signal of **Cudmbiipo** with a biexponential fit in acetonitrile excited at 388 nm.

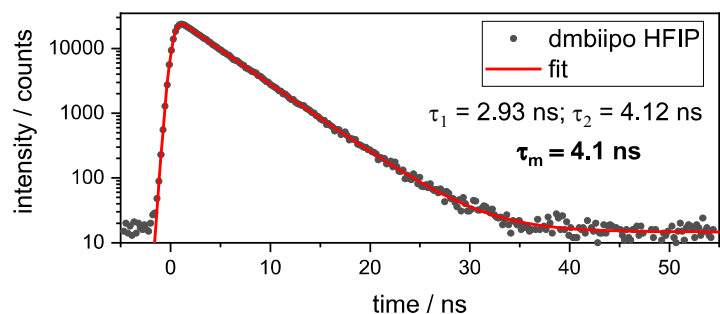


Figure S31. Time-resolved fluorescence signal of **dmbiipo** with a biexponential fit in hexafluoro isopropanol excited at 388 nm.

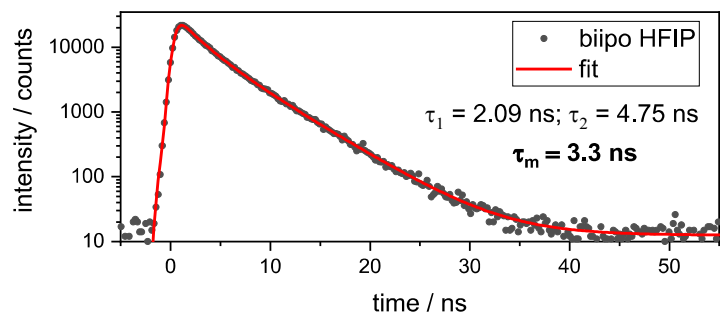


Figure S32. Time-resolved fluorescence signal of **biipo** with a biexponential fit in hexafluoro isopropanol excited at 388 nm.

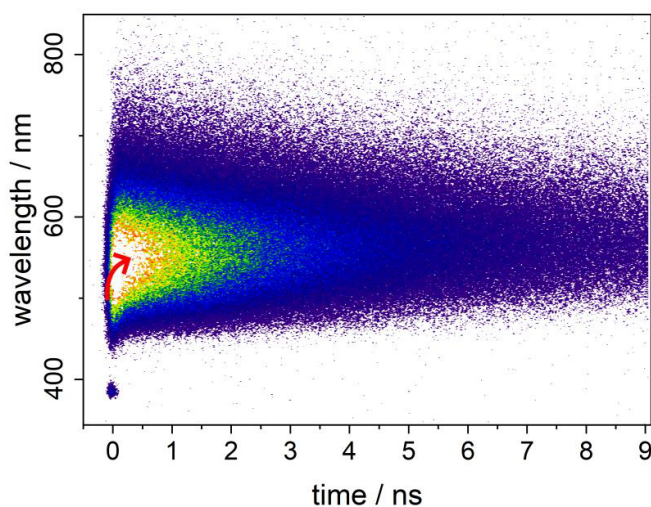


Figure S33. Time-resolved fluorescence spectrum of **biipo** in hexafluoro isopropanol excited at 388 nm (stray-light signal). Red arrow signals the shift of the spectra into the red during the first hundred picoseconds after the excitation.

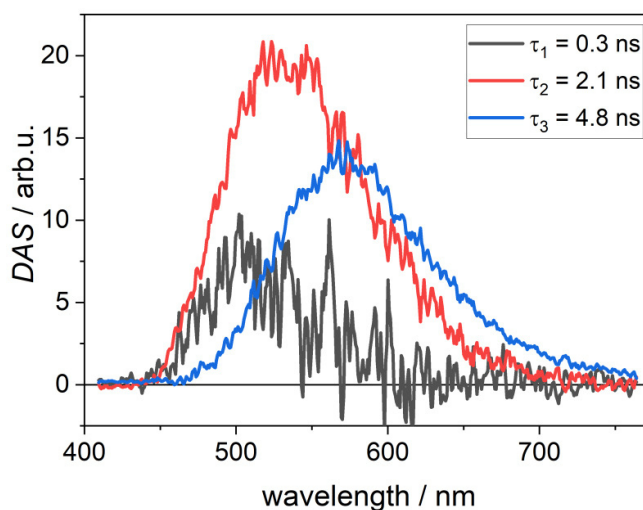


Figure S34. Decay-associated spectra (DAS) of time-resolved fluorescence of **biipo** in hexafluoro isopropanol excited at 388 nm.

Solvent-interaction between the hexafluoro isopropanol and the **dmbiipo** molecules may not be that strong, compared to the solution of **biipo**. Furthermore, the intensity of the DAS of τ_2 is much weaker compared to the DAS of τ_3 resulting in an average lifetime that is almost equal to the lifetime τ_3 . In the case of **biipo** dissolved in hexafluoro isopropanol, we also obtained three DAS with comparable lifetimes (Figure S6.20). Unlike in **dmbiipo**, the last two DAS of 2.1 and 4.8 ns have not only similar intensities and amplitudes, and thus an average lifetime of 3.3 ns, both DAS are also located at different central wavelengths. Here, the interactions between the solvent and the **biipo** molecules may be much stronger compared to **dmbiipo**.

7 Nanosecond Transient Absorption Spectroscopy

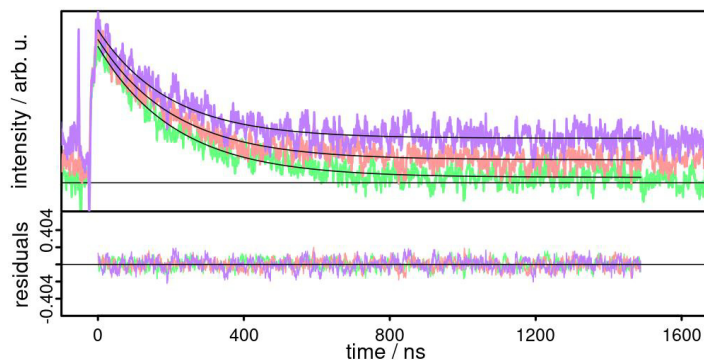


Figure S35. Transient absorption kinetics of **dmbiipo** in hexafluoro isopropanol solution excited at 355 nm under aerated conditions. The black line belongs to the fits with a time constant of 213 ± 2 ns, 209 ± 2 ns and 195 ± 3 ns for 480 (green), 500 (red) and 520 nm (purple), respectively.

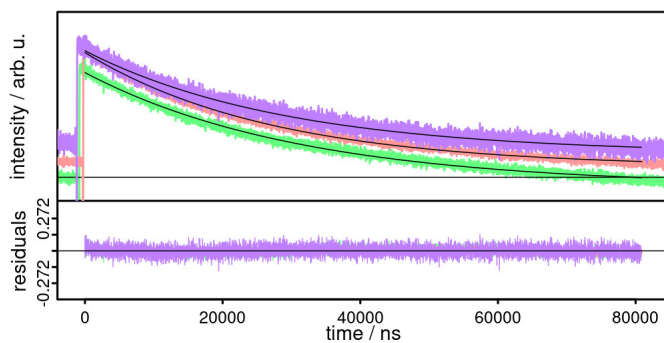


Figure S36. Transient absorption kinetics of **Cudmbiipo** in acetonitrile solution excited at 355 nm under inert conditions. The black line belongs to the fits with a time constant of 31.4 ± 0.1 μ s, 27.1 ± 0.1 μ s and 29.3 ± 0.2 μ s for 460 (green), 500 (red) and 580 nm (purple), respectively.

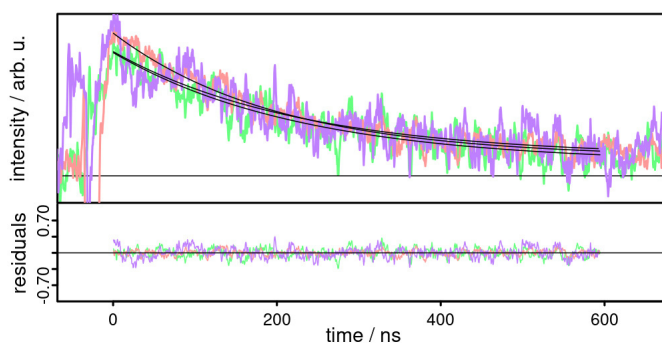


Figure S37. Transient absorption kinetics of **biipo** in hexafluoro isopropanol solution excited at 355 nm under aerated conditions. The black line belongs to the fits with a time constant of 229 ± 9 ns, 200 ± 4 ns and 228 ± 11 ns for 460 (green), 500 (red) and 520 nm (purple), respectively.

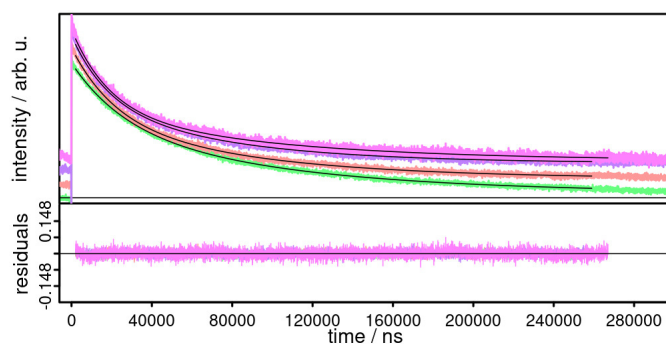


Figure S38. Transient absorption kinetics of **Cubiipo** in tetrahydrofuran solution excited at 355 nm under inert conditions. The black line belongs to the fits with biexponential decay constants of $\tau_1 = 25.6 \pm 0.4 \mu\text{s}$, $21.0 \pm 0.3 \mu\text{s}$, $17.4 \pm 0.3 \mu\text{s}$, $18.3 \pm 0.3 \mu\text{s}$ and $\tau_2 = 96.5 \pm 1.7 \mu\text{s}$, $82.6 \pm 1.3 \mu\text{s}$, $69.5 \pm 1.0 \mu\text{s}$, $91.0 \pm 2.4 \mu\text{s}$ for 480 (green), 500 (red), 520 (purple) and 580 nm (magenta), respectively.

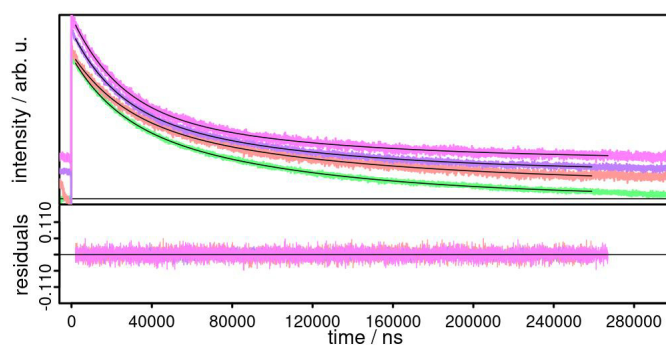


Figure S39. Transient absorption kinetics of **Cudmbiipo** in tetrahydrofuran excited at 355 nm under inert condition. The black line belongs to the fits with biexponential decay constants of $\tau_1 = 21.6 \pm 0.2 \mu\text{s}$, $25.2 \pm 0.5 \mu\text{s}$, $21.8 \pm 0.3 \mu\text{s}$, $23.2 \pm 0.3 \mu\text{s}$ and $\tau_2 = 98.4 \pm 1.0 \mu\text{s}$, $118.2 \pm 0.4 \mu\text{s}$, $94.90 \pm 1.5 \mu\text{s}$, $99.2 \pm 3.1 \mu\text{s}$ for 480 (green), 500 (red), 520 (purple) and 580 nm (magenta), respectively.

8 Step-scan FTIR Spectroscopy and calculated Vibrational Spectra

8.1 Experimental and theoretical ground and excited state IR spectra

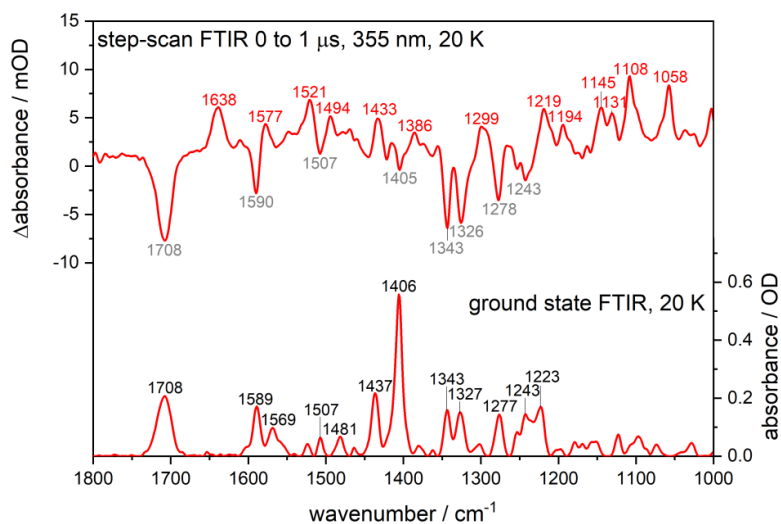


Figure S40. Ground and step-scan FTIR spectra of **Cudmbiipo** measured with an excitation wavelength of 355 nm at 20 K.

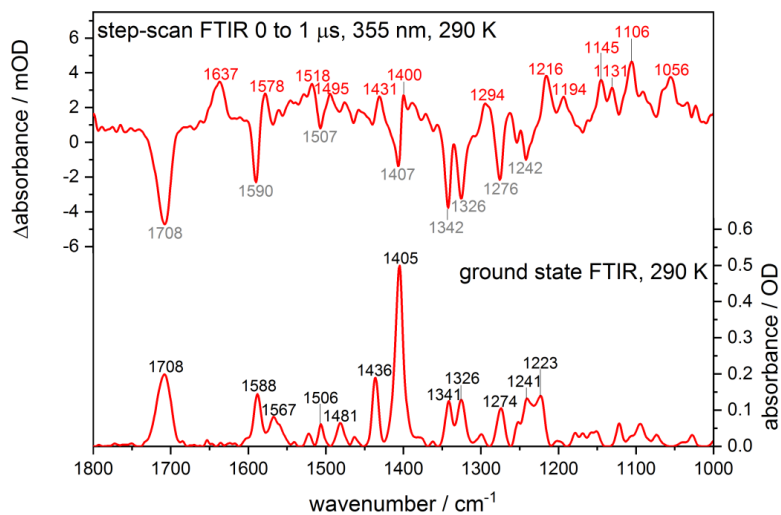


Figure S41. Ground and step-scan FTIR spectra of **Cudmbiipo** measured with an excitation wavelength of 355 nm at 290 K.

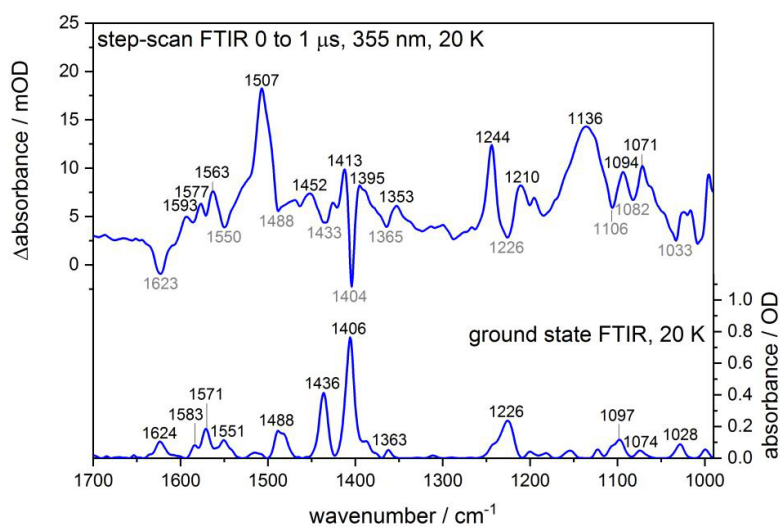


Figure S42. Ground and step-scan FTIR spectra of **Cubcp** measured with an excitation wavelength of 355 nm at 20 K.

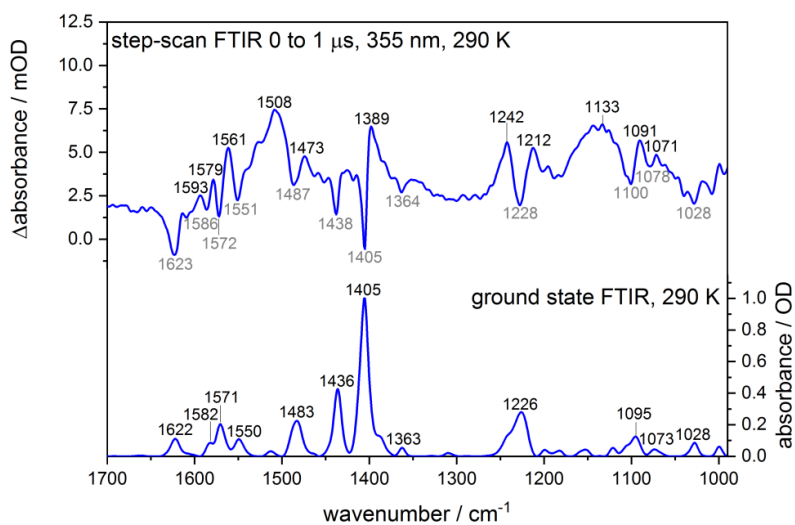


Figure S43. Ground and step-scan FTIR spectra of **Cubcp** measured with an excitation wavelength of 355 nm at 290 K.

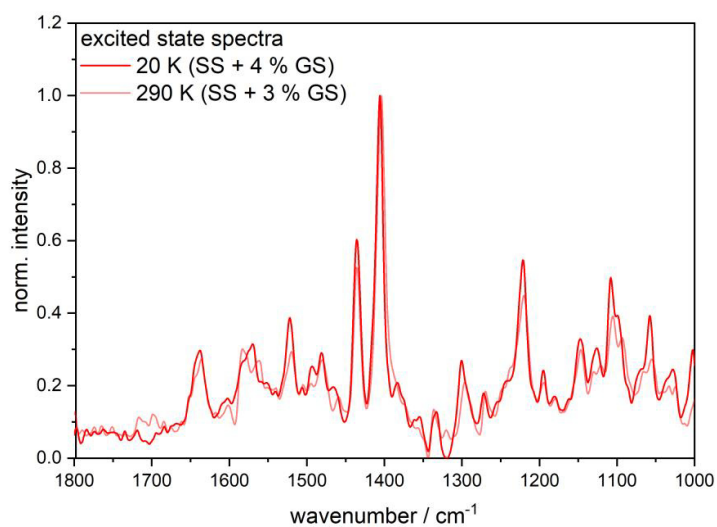


Figure S44. Excited state IR spectra of **Cudmbiipo** measured with an excitation wavelength of 355 nm at 20 and 290 K (3 and 4 % of the ground state spectrum added to the step-scan difference spectrum at 20 and 290 K, respectively).

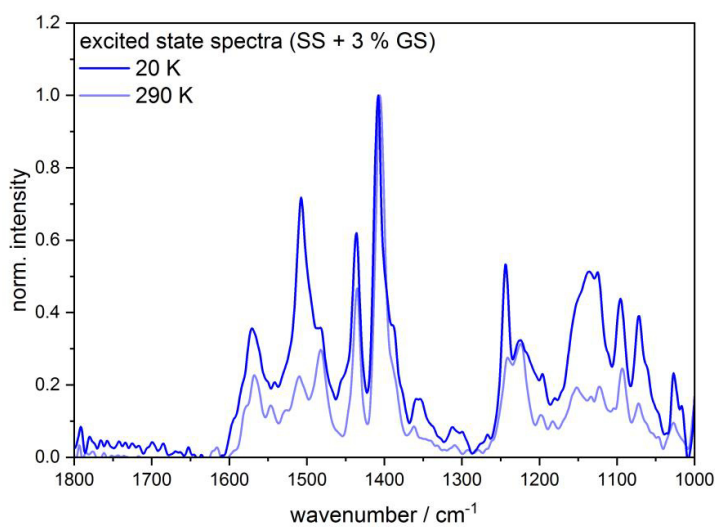


Figure S45. Excited state IR spectra of **Cubcp** measured with an excitation wavelength of 355 nm at 20 and 290 K (3 % of the ground state spectrum added to the step-scan difference spectrum at 20 and 290 K, respectively).

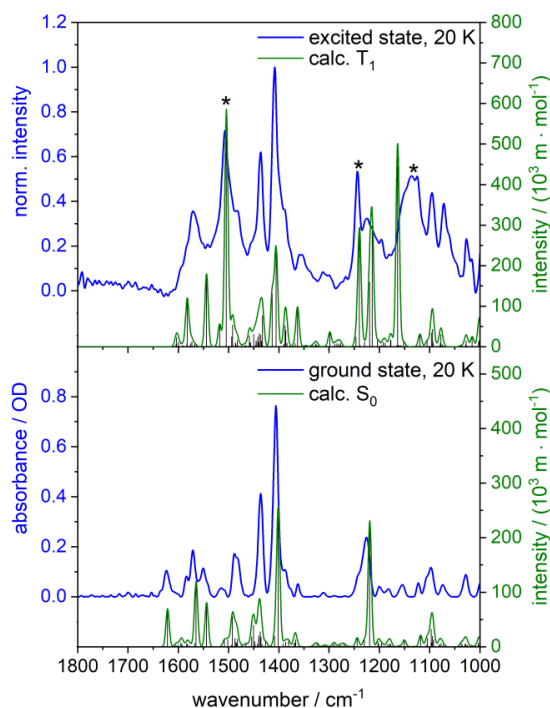


Figure S46. Static FTIR ground state spectrum (KBr pellet, 20 K) and calculated S₀ spectrum of **Cubcp** (bottom). Excited state IR spectrum (3.0 % of the ground state spectrum added to the step-scan difference spectrum) and calculated T₁ spectrum of **Cubcp** (top). Calculations: (U)DFT/B3LYP-D3(BJ)/def2-TZVP, scaled by 0.975, FWHM = 8 cm⁻¹, Gaussian profile. The bands marked with an asterisk are discussed in the text.

The pure excited state IR absorption spectrum of **Cubcp** shows three strong bands at 1507, 1244 and 1136 cm⁻¹ with very low intensities in the ground state spectrum (asterisks in Figure S8.7). The excited state specific features are very well reproduced by the calculated IR spectrum of the T₁ state (see Figure S8.7). The vibrations assigned to the mentioned experimental peaks are localized on the bathocuproine ligand and mainly involve C–C stretching and C–H bending motions (see Table S8.2).

8.2 Excited State Lifetimes Obtained by Step-Scan FTIR Spectroscopy

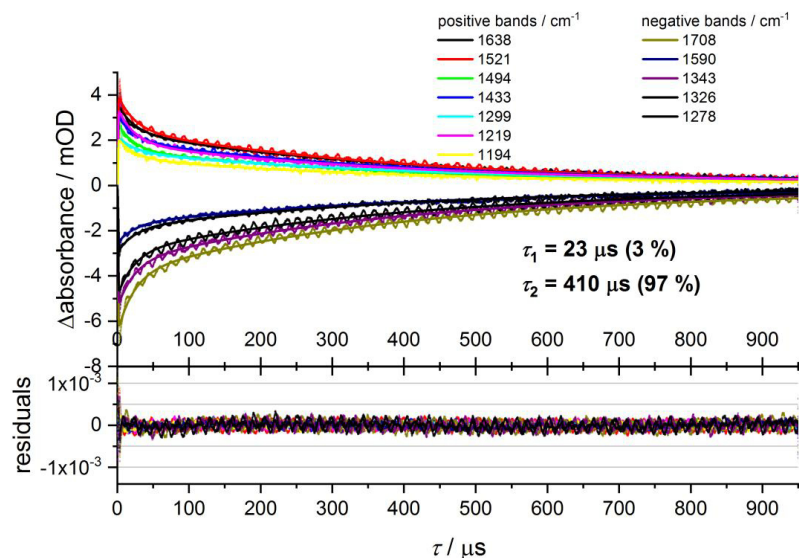


Figure S47. Global biexponential fit performed for the bands in the step-scan difference spectrum of CuDmbiipo at 20 K with a good signal-to-noise ratio.

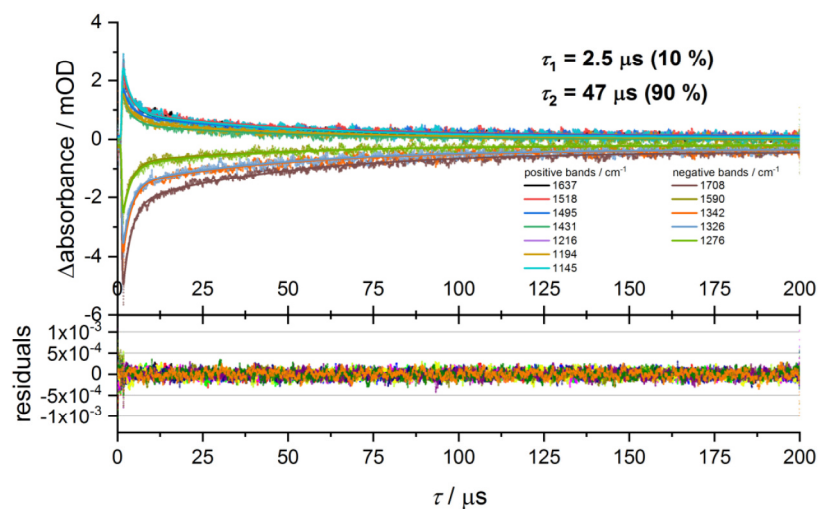


Figure S48. Global biexponential fit performed for the bands in the step-scan difference spectrum of CuDmbiipo at 290 K with a good signal-to-noise ratio.

8.3 Characterization of Vibrational Modes

Table S5. Characterization of vibrational modes of **Cudmbiipo**. The listed frequencies correspond to the experimental values for the ground state and the excited triplet state at 20 K. Calculations: (U)DFT/B3LYP-D3(BJ)/def2-TZVP.

$\tilde{\nu} / \text{cm}^{-1}$ ground state	$\tilde{\nu} / \text{cm}^{-1}$ excited state	Character of the vibration
1708	1638	C=O stretching on dmbiipo
1589	-	C-C and C-N stretching
1569	1570	C-C and C-N stretching on dmbiipo
-	1522	C-H in plane bending coupled with C-C and C=O stretching on dmbiipo
1507	-	C-C and C-N stretching coupled with aromatic C-H in plane bending on dmbiipo
1481	1481	aromatic C-H in plane bending in the phenyl rings of xantphos combined with C-C stretching on dmbiipo
1437	1436	aromatic C-H in plane bending coupled with C-H scissoring in the methyl substituents
1406	1406	C-H in plane bending coupled with C-C stretching in the xanthene subunit of xantphos
1343	-	aromatic C-H bending in the phenyl rings of xantphos coupled with C-N and C-C stretching on dmbiipo
1327	-	C-N and C-C stretching on the phenanthroline moiety of dmbiipo
-	1301	C-C and C-N stretching on dmbiipo
1277	-	C-N and C-C stretching on dmbiipo coupled with C-H in plane bending on the xanthene subunit of xantphos
1243	-	C-H in plane bending on the naphthalene subunit of dmbiipo
1223	1222	C=O stretching coupled with aromatic C-C stretching on the xanthene subunit of xantphos
1179	1195	C-H in plane bending on dmbiipo
1152	1147	C-H in plane bending on dmbiipo combined with C-H in plane bending on the xanthene subunit of xantphos
1123	-	C-C stretching on the xanthene subunit of xantphos combined with C-H in plane bending on the naphthalene unit of dmbiipo
-	1108	C-H in plane bending
1097	-	C-P stretching
1073	-	C-H in plane bending
-	1058	C-H in plane bending on dmbiipo
-	1028	C-C stretching on the phenyl rings of xantphos

Table S6. Characterization of vibrational modes of **Cubcp**. The listed frequencies correspond to the experimental values for the ground state and the excited triplet state at 20 K. Calculations: (U)DFT/B3LYP-D3(BJ)/def2-TZVP.

$\tilde{\nu} / \text{cm}^{-1}$ ground state	$\tilde{\nu} / \text{cm}^{-1}$ excited state	Character of the vibration
1624	-	Symmetric C–C stretching coupled with C–H in plane bending on the phenanthroline subunit
-	1594	Symmetric C–C stretching in the aromatic rings of bcp
1583	-	Symmetric C–C and C–O stretching on the xanthene subunit of xantphos
1571	1570	Symmetric C–C and C–N stretching on bcp coupled with Cu–N rocking
1551		Antisymmetric C–C and C–N stretching on the phenanthroline subunit coupled with Cu–N rocking
-	1541	Symmetric C–C and C–N stretching on the phenanthroline subunit coupled with Cu–N scissoring and aromatic C–H in plane bending
1515	-	C–C stretching coupled with C–H in plane bending on bcp
-	1507	Antisymmetric C–C and C–N stretching coupled with aromatic C–H in plane bending on bcp
1488	1486	C–C stretching in the phenanthroline subunit coupled with C–H rocking of the phenyl rings and C–H bending in the methyl substituents
-	1454	C–H bending in the methyl substituents coupled with C–H rocking on the phenyl substituents of bcp
1436	1436	C–H scissoring in the phenyl rings coupled with C–H bending on the methyl substituents
1406	1408	Antisymmetric C–C and C–O stretching coupled with C–H in plane bending on the xanthene subunit of xantphos
1388	1390	C–H bending on the methyl substituents
1363	1359	C–H bending on the methyl substituents coupled with C–C stretching on the phenanthroline subunit
1241		Aromatic C–H bending on the xantphos ligand
-	1244	Antisymmetric C–C and C–H in plane bending on bcp
1226		C–O stretching coupled with C–H in plane bending
1201	1196	C–H in plane bending coupled with C–O stretching on the xanthene subunit of xantphos
1182	1180	C–H scissoring on the phenyl rings
1154	-	C–H in plane bending on the xanthene subunit of xantphos
-	1136	Antisymmetric C–C stretching coupled with aromatic C–H bending on bcp
1122	1124	C–P stretching coupled with C–C stretching on xantphos

9 Calculated Spin Densities

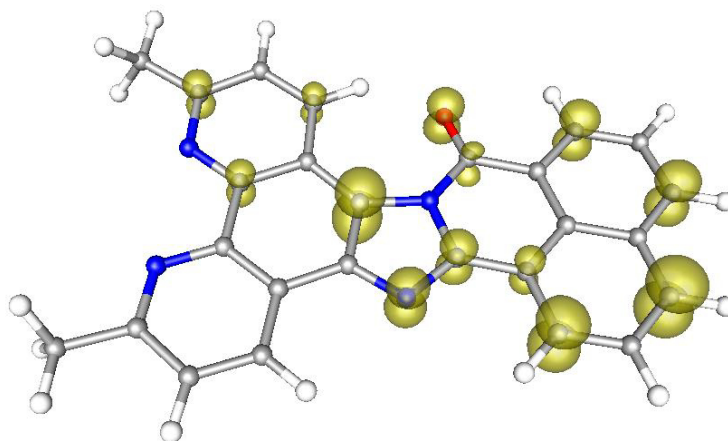


Figure S49. Calculated spin density (isovalue: 0.01 arb. u.) of **dmbiipo** in the optimized triplet state (UDFT/B3LYP-D3(BJ)/def2-TZVP).

10 Calculated Ground and Excited State Geometries

Table S7. Selected calculated bond lengths and angles of **Cudmbiipo** and **dmbiipo** in the S_0 and T_1 states ((U)DFT/B3LYP-D3(BJ)/def2-TZVP). The most important geometrical changes upon excitation from the S_0 state to the T_1 state are highlighted in orange (major) or red (very large).

Bond angles / °			
	Cudmbiipo		
	S_0	T_1	$T_1 - S_0$
P1-Cu-P2	118.6	118.4	-0.2
N1-Cu-N2	78.7	78.1	-0.6
P1-Cu-N2	121.2	122.7	1.5
P1-Cu-N1	129.5	128.8	-0.7
P2-Cu-N1	97.7	98.8	1.1
P2-Cu-N2	102.5	101.0	-1.5
Dihedral angle between the planes N-Cu-N and P-Cu-P	85.5	87.6	2.1

Bond lengths / Å						
	Cudmbiipo			dmbiipo		
	S_0	T_1	$T_1 - S_0$	S_0	T_1	$T_1 - S_0$
Cu-P1	2.270	2.271	0.001			
Cu-P2	2.318	2.324	0.006			
Cu-N1	2.142	2.139	-0.003			
Cu-N2	2.100	2.138	0.038			
N2-C6	1.332	1.336	0.004	1.320	1.328	0.008
N2-C7	1.355	1.350	-0.005	1.348	1.337	-0.011
C6-C _{Me2}	1.495	1.494	-0.001	1.503	1.501	-0.002
C6-C8	1.405	1.402	-0.003	1.413	1.405	-0.008
C8-C10	1.373	1.376	0.003	1.370	1.376	0.006
C10-C9	1.401	1.397	-0.004	1.405	1.398	-0.007
C9-C12	1.423	1.433	0.010	1.424	1.434	0.010
C7-C9	1.407	1.403	-0.004	1.409	1.405	-0.004
C7-C5	1.449	1.459	0.010	1.461	1.476	0.015
N1-C5	1.355	1.344	-0.011	1.344	1.329	-0.015
N1-C2	1.327	1.335	0.008	1.319	1.330	0.011
C2-C _{Me1}	1.494	1.493	-0.001	1.502	1.498	-0.004
C2-C1	1.402	1.398	-0.004	1.406	1.401	-0.005
C1-C3	1.370	1.373	0.003	1.371	1.373	0.002
C3-C4	1.408	1.409	0.001	1.410	1.412	0.002
C5-C4	1.423	1.428	0.005	1.432	1.441	0.009
C4-C11	1.433	1.424	-0.009	1.437	1.424	-0.013
C12-C11	1.388	1.424	0.036	1.388	1.434	0.046
C11-N3	1.410	1.397	-0.013	1.419	1.406	-0.013
C12-N4	1.372	1.329	-0.043	1.375	1.324	-0.051
N3-C15	1.407	1.412	0.005	1.408	1.413	0.005
N4-C15	1.306	1.355	0.049	1.302	1.357	0.055
C15-C18	1.442	1.384	-0.058	1.443	1.383	-0.060
N3-C _{co}	1.416	1.415	-0.001	1.409	1.418	0.009
C _{co} -C17	1.475	1.456	-0.019	1.483	1.456	-0.027
C17-C19	1.416	1.404	-0.012	1.414	1.405	-0.009

C18-C19	1.414	1.431	0.017	1.414	1.429	0.015
C18-C20	1.382	1.438	0.056	1.382	1.434	0.052
C20-C26	1.403	1.368	-0.035	1.404	1.372	-0.032
C26-C24	1.375	1.407	0.032	1.374	1.402	0.028
C24-C22	1.414	1.418	0.004	1.414	1.418	0.004
C19-C22	1.422	1.428	0.006	1.422	1.428	0.006
C17-C21	1.382	1.415	0.033	1.380	1.413	0.033
C21-C25	1.402	1.379	-0.023	1.403	1.381	-0.022
C25-C23	1.375	1.397	0.022	1.374	1.394	0.020
C23-C22	1.413	1.404	-0.009	1.413	1.405	-0.008
C_{co}-O_{co}	1.211	1.226	0.015	1.211	1.226	0.015

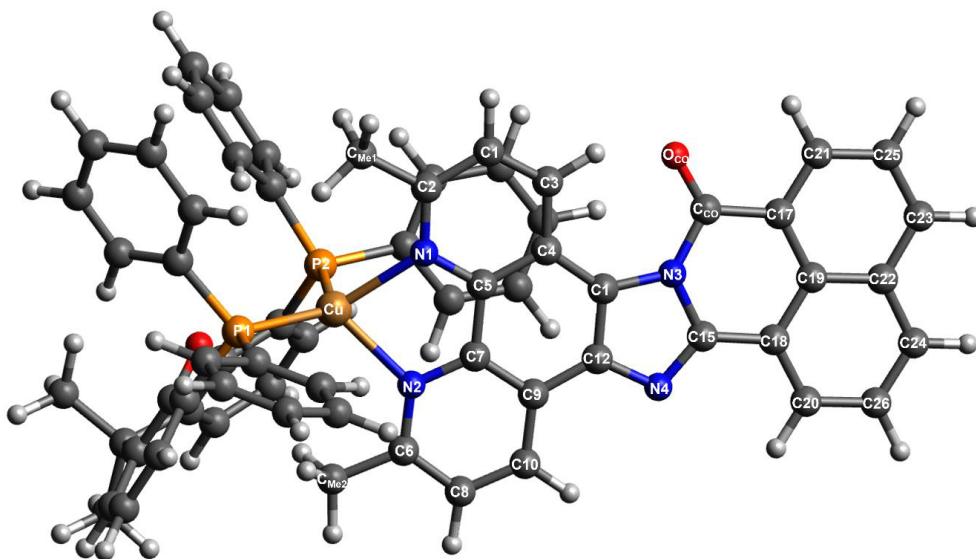


Figure S50. Calculated S_0 structure of **Cudmbiipo** (DFT/B3LYP-D3(BJ)/def2-TZVP).

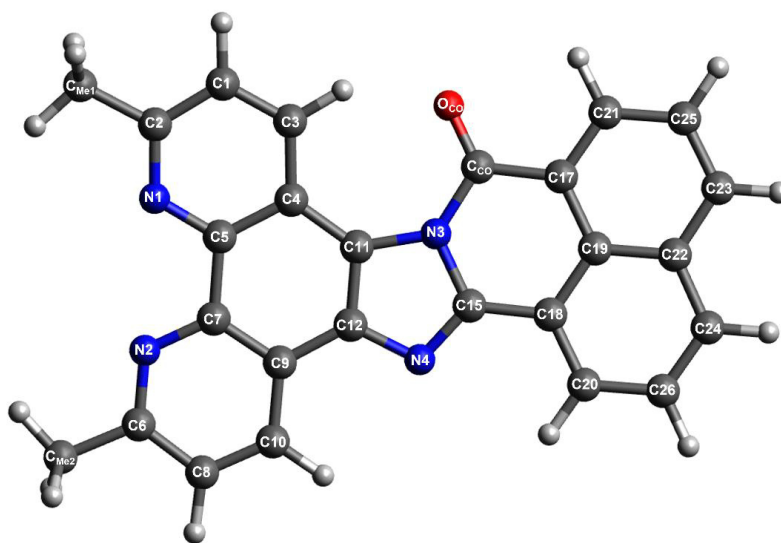


Figure S51. Calculated S_0 structure of **dmbiipo** (DFT/B3LYP-D3(BJ)/def2-TZVP).

Table S8. Selected calculated bond lengths and angles of **Cubcp** in the S_0 and T_1 states ((U)DFT/B3LYP-D3(BJ)/def2-TZVP). The most important geometrical changes upon excitation from the S_0 state to the T_1 state are highlighted in orange (major) or red (very large).

	Bond angles / °		
	S_0	T_1	$T_1 - S_0$
P1-Cu-P2	118.9	112.1	-6.8
N1-Cu-N2	79.0	83.6	4.6
P1-Cu-N2	120.6	112.6	-8.0
P1-Cu-N1	128.8	137.6	8.8
P2-Cu-N1	98.5	96.0	-2.5

P2-Cu-N2	102.3	111.3	9.0
Dihedral angle between the planes N-Cu-N and P-Cu-P	86.1	75.7	-10.4

Bond lengths / Å			
	S ₀	T ₁	T ₁ - S ₀
Cu-P1	2.266	2.352	0.086
Cu-P2	2.313	2.386	0.073
Cu-N1	2.128	1.973	-0.155
Cu-N2	2.126	2.036	-0.090
N2-C6	1.33	1.35	0.020
N2-C7	1.355	1.386	0.031
C6- C _{Me2}	1.495	1.495	0.000
C6-C8	1.401	1.381	-0.020
C8-C10	1.381	1.41	0.029
C10-C9	1.419	1.404	-0.015
C9-C12	1.427	1.431	0.004
C7-C9	1.414	1.424	0.010
C7-C5	1.443	1.401	-0.042
N1-C5	1.356	1.384	0.028
N1-C2	1.327	1.35	0.023
C2- C _{Me1}	1.495	1.495	0.000
C2-C1	1.403	1.378	-0.025
C1-C3	1.378	1.411	0.033
C3-C4	1.421	1.404	-0.017
C4-C5	1.411	1.422	0.011
C4-C11	1.427	1.43	0.003
C12-C11	1.355	1.357	0.002
C10-C13	1.479	1.474	-0.005
C13-C14	1.397	1.4	0.003
C14-C15	1.389	1.388	-0.001
C15-C16	1.39	1.391	0.001
C16-C17	1.391	1.39	-0.001
C17-C18	1.388	1.388	0.000
C18-C13	1.398	1.4	0.002
C3-C19	1.478	1.471	-0.007
C19-C20	1.397	1.401	0.004
C20-C21	1.389	1.387	-0.002
C21-C22	1.39	1.391	0.001
C22-C23	1.391	1.391	0.000
C23-C24	1.388	1.388	0.000
C24-C19	1.398	1.401	0.003

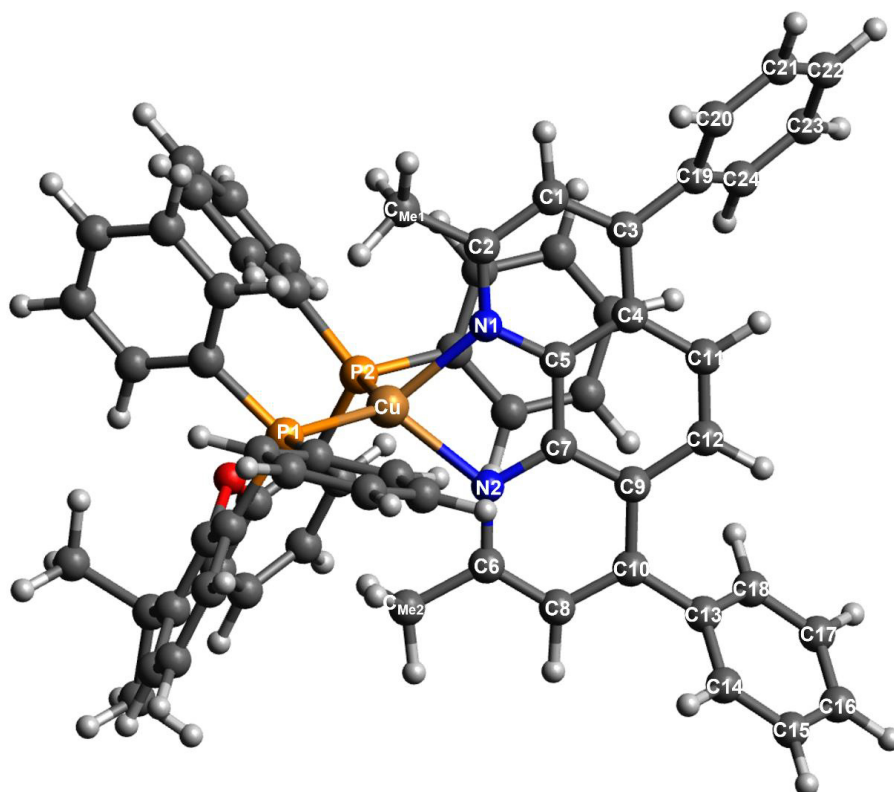


Figure S52. Calculated structure of **Cubcp** (DFT/B3LYP-D3(BJ)/def2-TZVP).

11 Photocatalytic applications

11.1 Photocatalytic formation of singlet oxygen

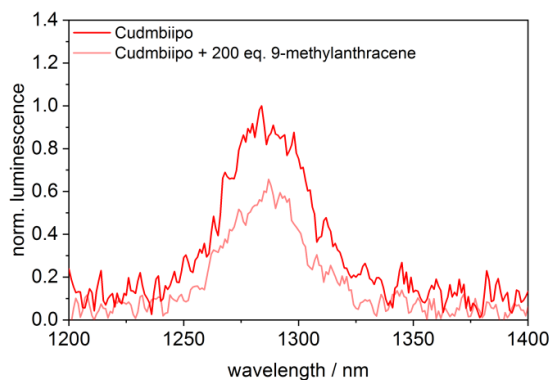


Figure S53. NIR emission of ¹O₂ observed for solutions of **CuDmbiipo** (red) and **CuDmbiipo** with an excess of 200 eq. 9-methylanthracene (light red) ($c(\text{CuDmbiipo}) = 2.5 \cdot 10^{-5} \text{ M}$; $c(9\text{-methylanthracene}) = 5 \cdot 10^{-3} \text{ M}$) ($\lambda_{\text{ex}} = 440 \text{ nm}$).

11.2 Photocatalytic isomerization of *E*-stilbene

In all the isomerization experiments the same LED light source from StarLight Sensorik-Lichtleitsysteme (see Experimental Details above) was used. The light source does not induce the isomerization of *E*-stilbene in the absence of a photosensitizer as it was confirmed via gas chromatographic (GC) analysis.

GC experiment:

A Schlenk tube (diameter: 1 cm, length: 15 cm) was charged with a stirring bar and the respective copper complex (**Cudmbiipo** or **Cubcp**) (0.1 μmol , 0.0001 Eq.). It was weighed in by adding 100 μL of a 0.001 M solution of the complex in dichloromethane. The solvent was removed in an argon stream and afterwards under reduced pressure (10^{-3} mbar). *E*-stilbene (180 mg, 1000 μmol , 1.0 Eq.) was added and the Schlenk tube was again evacuated and flooded with argon five times. Degassed dichloromethane (10 mL) was added and the reaction mixture was irradiated for 72 hours while being stirred. After 6, 12, 24, 48 and 72 hours, samples of 100 μL were taken out of the reaction mixture. These samples were purified via a micro column (2 cm of silica gel inside a Pasteur pipette; eluted with 8-10 ml of dichloromethane) to remove the catalyst. The obtained solution was directly analyzed via gas chromatography. For both catalysts, the experiment was independently performed twice and the deviation from the mean value is below three percent for each datapoint.

NMR experiment:

A Schlenk tube (diameter: 1 cm, length: 15 cm) was charged with a stirring bar and *E*-stilbene (18.0 mg, 0.1 mmol, 1.00 Eq.) Then the respective copper complex (0.2 mmol, 0.02 Eq.) was added as 0.1 mL of a 0.02 M solution in dichloromethane. The dichloromethane was removed under reduced pressure and the reaction vessel was evacuated and flooded with argon five times. Afterwards, 1.0 mL of degassed deuterated dichloromethane was added in under argon counterflow. The Schlenk tube was sealed, placed above a magnetic stirrer and irradiated (see Figure S11.2). After 4 hours nitromethane was added as an internal standard and the reaction mixture was analyzed via ^1H NMR spectroscopy.

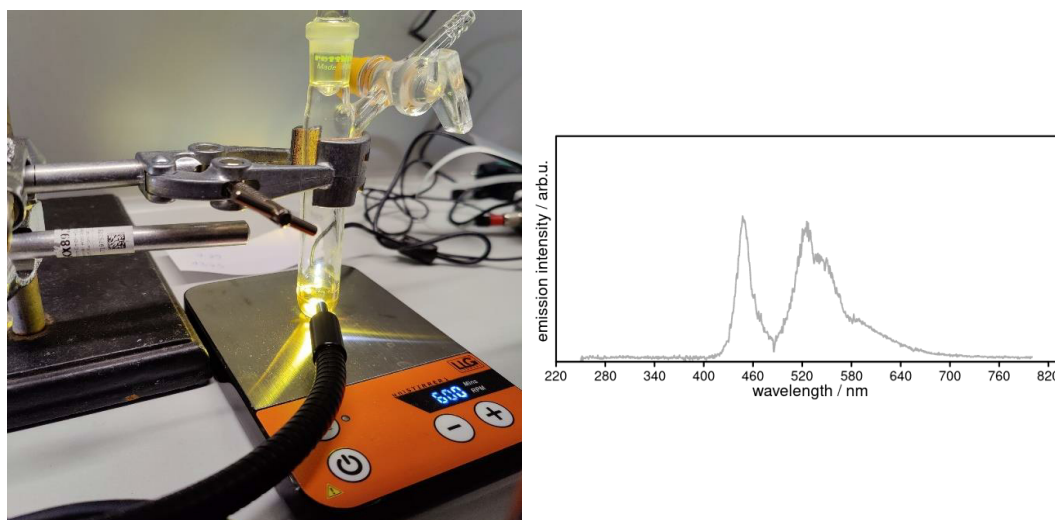


Figure S54. Left: Experimental setup of the isomerization reaction. Right: Emission spectrum of the applied LED light source.

UV/vis experiment:

A cuvette ($V = 4$ mL; $d = 1.0$ cm) was charged with a stirring bar, *E*-stilbene (2 mL; 0.1 mM in dichloromethane) and the respective copper complex (10 μ L; $4 \cdot 10^{-4}$ M in dichloromethane). The solvent was removed first in an argon stream and later under reduced pressure (10^{-3} mbar). The cuvette was placed inside a Schlenk tube and evacuated and flooded with argon five times before 4.0 mL of degassed dichloromethane were added giving a $5 \cdot 10^{-5}$ M solution with 0.02 Eq. of catalyst. A little argon was bubbled through the cuvette to eventually remove residual air. The cuvette was placed inside the Avantes spectrometer (Avantes AvaSpec-ULS2048CL-EVO) above a magnetic stirrer and a UV/vis spectrum was recorded every five minutes (see Figure S11.3). The experiment confirmed the findings of the GC experiment that **Cudmbiipo** compared to **Cubcp** converts the substrate initially with a higher rate constant, but reaches an equilibrium state with more of the substrate still unreacted.

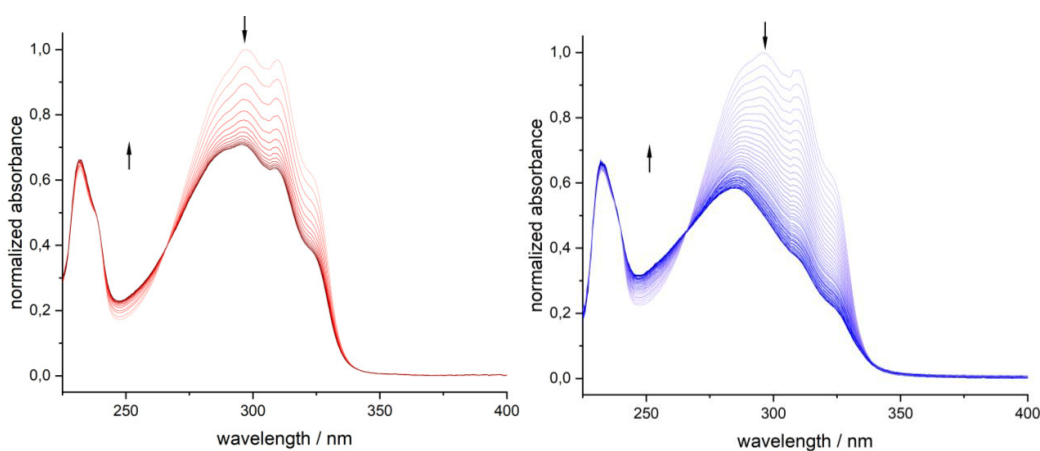


Figure S55. UV/vis spectra monitoring the photoisomerization of *E*-stilbene to *Z*-stilbene using **Cudmbiipo** (left, red) or **Cubcp** (right, blue) as photocatalysts. Each line represents 5 minutes that have passed going from light to dark.

12 Femtosecond Transient Absorption Spectra of biipo

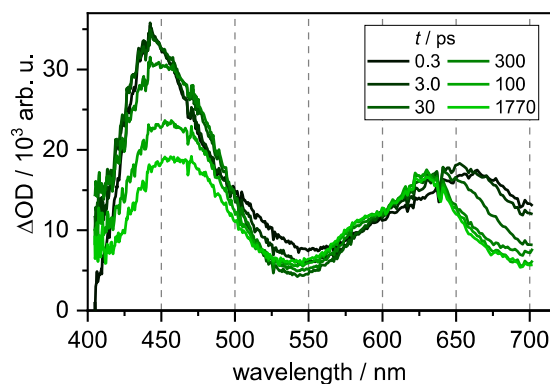


Figure S56. Femtosecond transient absorption spectra of **biipo** in hexafluoro isopropanol with a relative polarization of pump and probe in magic angle. Excited at 400 nm with 300 μ W.

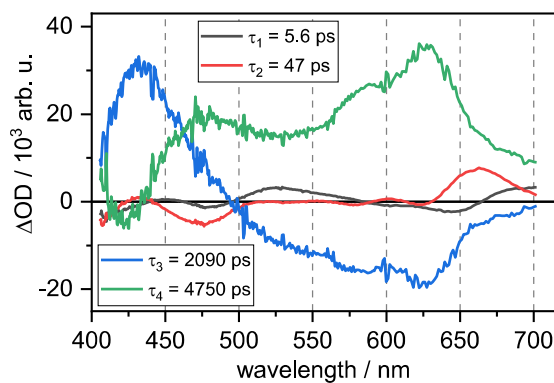


Figure S57. Decay-associated spectra of **biipo** in hexafluoro isopropanol with a relative polarization of pump and probe in magic angle. Excited at 400 nm. Time constants τ_3 and τ_4 were taken from fluorescence-decay.

The DAS of the time constants (2.1 and 4.8 ns) we got from global lifetime analysis describe the fsTA spectra almost equally. This led to DAS that are approximately symmetric to each other along the wavelength axis. This situation is given when the limit of our method is reached. Both DAS have similar intensities and its corresponding lifetimes are both over the measured time range. So, there are not enough data points to distinguish the two components clearly from each other.

13 Reference Section

- 1 Gottlieb, H. E.; Kotlyar, V.; Nudelman, A. NMR Chemical Shifts of Common Laboratory Solvents as Trace Impurities. *J. Org. Chem.* **1997**, *62*, 7512-7515. DOI: 10.1021/jo971176v
- 2 Caspar, J. V.; Meyer, T. J. Photochemistry of MLCT excited states. Effect of nonchromophoric ligand variations on photophysical properties in the series cis-Ru(bpy)₂L₂²⁺. *J. Am. Chem. Soc.* **1983**, *105*, 5583-5590. DOI: 10.1021/ic00159a021
- 3 Otto, S.; Nauth, A. M.; Ermilov, E.; Scholz, N.; Friedrich, A.; Resch-Genger, U.; Lochbrunner, S.; Opatz, T.; Heinze, K. Photo-Chromium: Sensitizer for Visible-Light-Induced Oxidative C-H Bond Functionalization - Electron or Energy Transfer? *ChemPhotoChem* **2017**, *1*, 344-349. DOI: 10.1002/cptc.201700077
- 4 a) F. Furche, R. Ahlrichs, C. Hättig, W. Klopper, M. Sierka, F. Weigend, *Wiley Interdiscip. Rev. Comput. Mol. Sci.* **2014**, *4*, 91-100; b) TURBOMOLE V7.4 2019, a development of University of Karlsruhe and Forschungszentrum Karlsruhe GmbH, 1989-2007, TURBOMOLE GmbH, since 2007; available from <http://www.turbomole.com>.
- 5 Grimme, S.; Antony, J.; Ehrlich, S.; Krieg, H. A consistent and accurate ab initio parametrization of density functional dispersion correction (DFT-D) for the 94 elements H-Pu. *J. Chem. Phys.* **2010**, *132*, 154104 DOI: 10.1063/1.3382344; b) Grimme, S. Ehrlich, S. Goerigk, L. Effect of the damping function in dispersion corrected density functional theory. *J. Comput. Chem.* **2011**, *32*, 1456-1465. DOI: 10.1002/jcc.21759
- 6 Zheng, R. H.; Guo, H. C.; Jiang, H. J.; Xu, K. H.; Liu, B. B.; Sun, W. L.; Shen, Z. Q. A new and convenient synthesis of phendiones oxidated by KBrO₃/H₂SO₄ at room temperature. *Chinese Chem. Lett.*, **2010**, *21*, 1270-1272. DOI: 10.1016/j.ccllet.2010.05.030
- 7 Das, O.; Paria, S.; Zangrando, E.; Paine, T. K. Copper(II)-Mediated Oxidative Transformation of vic-Dioxime to Furoxan: Evidence for a Copper(II)-Dinitrosoalkene Intermediate. *Inorg. Chem.*, **2011**, *50*, 11375-11383. DOI: 10.1021/ic200979q
- 8 Comba, P.; Krämer, R.; Mokhir, A.; Naing, K.; Schatz, E. Synthesis of New Phenanthroline-Based Heteroditopic Ligands – Highly Efficient and Selective Fluorescence Sensors for Copper(II) Ions. *Eur. J. Inorg. Chem.*, **2006**, 4442-4448. DOI: 10.1002/ejic.200600469

Kapitel 5: Thermisch induzierte und photoinduzierte Reaktionen von Übergangsmetallkomplexen

Dieses Kapitel behandelt die Untersuchung von Reaktionen an denen Übergangsmetallkomplexe beteiligt sind. Im ersten Teil wird die Reaktivität eines dinuklearen Kupferkomplexes vorgestellt, welcher thermisch induziert mit Lösungsmitteln reagiert. Der zweite Teil beinhaltet eine photoinduzierte Abspaltungsreaktion bei Chrom-, Molybdän- und Wolfram-Carbonylkomplexen. Mittels zeitaufgelöster FTIR-Spektroskopie werden die Reaktionen verfolgt. Im Vergleich mit quantenchemischen Rechnungen werden Produkte bzw. Intermediate identifiziert und ein Beitrag zur Aufklärung der Reaktionsmechanismen geleistet.

5.1 Cooperativity-Driven Reactivity of a Dinuclear Copper Dimethylglyoxime Complex

5.1.1 Präambel

In diesem Projekt wurde der Reaktionsmechanismus eines Kupferkomplexes untersucht. Über die FTIR-Spektroskopie konnten Produkte nachgewiesen und der Angriff eines Wassermolekül bestätigt werden, was den postulierten Mechanismus unterstützt.

Mein Beitrag besteht in der Durchführung der FTIR-Messungen zusammen mit Pit Boden und der Berechnung der Schwingungsfrequenzen zur Zuordnung der Produkte mit DFT. Maximilian Huber hat die ESI-Massenspektrometrie durchgeführt. Pit Boden, Maximilian Huber und ich wurden betreut von Gereon Niedner-Schatteburg.

Raphael Petrikat hat die Komplexe synthetisiert und charakterisiert. Außerdem hat er die UV/Vis-Daten erhoben. Er wurde betreut von Sabine Becker. Elham Barani hat die DFT-Rechnungen zum Mechanismus und zur Elektronenverteilung durchgeführt. Sie wurde von Karin Fink betreut. Mark Ringenberg hat die EPR-Spektroskopie durchgeführt. Das Manuskript haben alle Autoren zusammen unter der Koordination von Raphael Petrikat und Sabine Becker verfasst.

5.1.2 Nachdruck und ergänzende Informationen

JOHN WILEY AND SONS LICENSE
TERMS AND CONDITIONS

Mar 30, 2023

This Agreement between Sophie Steiger ("You") and John Wiley and Sons ("John Wiley and Sons") consists of your license details and the terms and conditions provided by John Wiley and Sons and Copyright Clearance Center.

License Number	5518761320129	Requestor type	Author of this Wiley article
License date	Mar 30, 2023	Format	Print and electronic
Licensed Content Publisher	John Wiley and Sons	Portion	Full article
Licensed Content Publication	Chemistry - A European Journal	Will you be translating?	No
Licensed Content Title	Cooperativity-Driven Reactivity of a Dinuclear Copper Dimethylglyoxime Complex	Title	Zeitaufgelöste FTIR- und Lumineszenzspektroskopie an Organometallkomplexen und deren Reaktionen
Licensed Content Author	Sabine Becker, Karin Fink, Gereon Niedner-Schatteburg, et al	Institution name	Technische Universität Kaiserslautern
Licensed Content Date	Mar 20, 2023	Expected presentation date	Mar 2023
Licensed Content Volume	0	Requestor Location	Sophie Steiger Erwin-Schrödinger-Straße 52
Licensed Content Issue	0		Kaiserslautern, 67655 Germany Attn: Sophie Steiger
Licensed Content Pages	9	Publisher Tax ID	EU826007151
Type of use	Dissertation/Thesis	Total	0.00 EUR

Cooperativity-Driven Reactivity of a Dinuclear Copper Dimethylglyoxime Complex

Raphael I. Petrikat,^[a] Sophie T. Steiger,^[b] Elham Barani,^[c] Pit J. Boden,^[b] Maximilian E. Huber,^[b] Mark R. Ringenberg,^[d] Gereon Niedner-Schatteburg,^[b] Karin Fink,^[c] and Sabine Becker^{*[a]}

In memory of Prof. Dr. Markus Gerhards.

Abstract: In this report, we present the dinuclear copper(II) dimethylglyoxime (H₂dmg) complex [Cu₂(H₂dmg)(Hdmg)(dmg)]⁺ (1), which, in contrast to its mononuclear analogue [Cu(Hdmg)₂] (2), is subject to a cooperativity-driven hydrolysis. The combined Lewis acidity of both copper centers increases the electrophilicity of the carbon atom in the bridging μ₂-O–N=C-group of H₂dmg and thus, facilitates the nucleophilic attack of H₂O. This hydrolysis

yields butane-2,3-dione monoxime (3) and NH₂OH that, depending on the solvent, is then either oxidized or reduced. In ethanol, NH₂OH is reduced to NH₄⁺, yielding acetaldehyde as the oxidation product. In contrast, in CH₃CN, NH₂OH is oxidized by Cu^{II} to form N₂O and [Cu(CH₃CN)₄]⁺. Herein are presented the combined synthetic, theoretical, spectroscopic and spectrometric methods that indicate and establish the reaction pathway of this solvent-dependent reaction.

Introduction

The cooperative effect, that is, when two or more components achieve a desired reactivity often greater or inaccessible to either of the individual components, is widely found in chemistry and biological systems, for example, in catalysis, metalloenzymes, assembly of compounds on surfaces, and supramolecular polymerization to yield and/or control a desired chemical behavior.^[1–5] On a molecular level, for example, in a complex, cooperativity can occur due to metal–ligand, ligand–ligand, or metal–metal interactions. The coupling of metal centers in multinuclear complexes can influence the magnetic,

catalytic, and optical properties, which leads to a clear distinction in comparison to their mononuclear analogues.^[4,6–8] This cooperativity can either be of functional, enthalpic or entropic nature.^[9] Copper(II) dimethylglyoxime (H₂dmg) complexes are suitable for the investigation of such a cooperative effect because a variety of complexes differing in their composition are known. These complexes include mono-,^[10–12] di-,^[12–15] and tetranuclear^[15,16] complexes, which have been characterized by crystal structure analysis,^[10–16] IR spectroscopy,^[11–13,16,17] UV/Vis spectroscopy,^[12–14,16,18] EPR^[19] and other magnetic methods.^[13,14,16] Additionally, mixtures of Cu^{II} salts and dimethylglyoxime have been applied in catalytic reactions such as the N-arylation of imidazole derivatives^[20] and the decomposition of hydrogen peroxide with subsequent oxidation of benzyl alcohol and ethylbenzene (zeolite encapsulated).^[21]

Due to our interest in multinuclear copper complexes and their reactivity,^[12,22] we focused on the dinuclear complex [Cu₂(H₂dmg)(Hdmg)(dmg)]⁺ (1) and its mononuclear analogue [Cu(Hdmg)₂] (2) as comparison (Figure 1). Two of the possible three isomers of 1 have been reported, whereas isomer I is predominant in literature^[13,14,16] and favored with increasing pH value.^[13] In this article, we report the cooperativity-driven and solvent-dependent degradation of copper-bound H₂dmg to either NH₄⁺ or N₂O.

Results and Discussion

Compound 1 was obtained by the reaction of Cu(ClO₄)₂·6H₂O and H₂dmg in ethanol and subsequent crystallization by pentane diffusion. Similarly, 2 was obtained by the reaction of Cu(OAc)₂·2H₂O and H₂dmg in methanol. Slow evaporation of the solvent led to crystallization. The molecular structures were

[a] R. I. Petrikat, Jun.-Prof. Dr. S. Becker
RPTU Kaiserslautern-Landau
Institut für Anorganische Chemie
Erwin-Schroedinger-Str. 54, 67663 Kaiserslautern (Germany)
E-mail: sbecker@chemie.uni-kl.de

[b] S. T. Steiger, P. J. Boden, M. E. Huber, Prof. Dr. G. Niedner-Schatteburg
RPTU Kaiserslautern-Landau
Institut für Physikalische Chemie
Erwin-Schroedinger-Str. 52, 67663 Kaiserslautern (Germany)

[c] E. Barani, Prof. Dr. K. Fink
Karlsruhe Institute of Technology (KIT)
Institute of Nanotechnology
Hermann-von-Helmholtz-Platz 1
76344 Eggenstein-Leopoldshafen (Germany)

[d] Dr. M. R. Ringenberg
Société Suisse des Explosifs,
Fabrikstrasse 48, CH-3900 Brig (Switzerland)

Supporting information for this article is available on the WWW under <https://doi.org/10.1002/chem.202203438>

© 2023 The Authors. Chemistry – A European Journal published by Wiley-VCH GmbH. This is an open access article under the terms of the Creative Commons Attribution Non-Commercial NoDerivs License, which permits use and distribution in any medium, provided the original work is properly cited, the use is non-commercial and no modifications or adaptations are made.

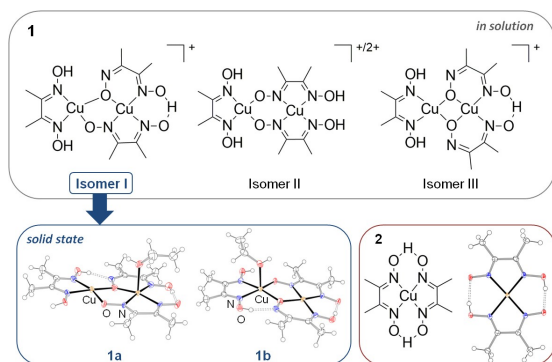


Figure 1. Top: structures of the three isomers of **1** in solution, anion and coordinating solvent molecules not shown for clarity. The charge of isomer II and the positions of the protons are not clarified, depending on the deprotonation state, the charge can be +1 or +2. Bottom: Molecular structures of **1a**, **1b**, and **2** (including Lewis structure). **1a**: d(Cu–Cu): 3.293(8) Å, **1b**: 3.32(1) Å. Ellipsoids are set at the 50% probability level. The counter ions of **1a** and **1b** are omitted for clarity.

determined for both compounds (Figure 1) and resemble comparable structures described in the literature.^[10,12–14,23] Additionally, structure optimization was performed at B3LYP/def2-TZVP level, which showed good geometrical agreement with the experimental results (Figure S47, Table S26 in the Supporting Information).

The structure of **2** resembles that known for nickel(II) ions.^[23–25] Two Hdmg[−] molecules span the pseudo-macrocyclic ligand framework to yield a slightly distorted square-planar coordination geometry for the copper(II) center. The structure of **1** corresponds to that of isomer I (Figure 1). The dimethylglyoxime ligands form distorted square-planar coordination environments for both copper(II) centers, whereas one copper center is coordinated by one Hdmg[−] and one dmg^{2−} molecule, which form a pseudo-macrocyclic coordination environment similar to that in **2**. The pseudo-macrocycle in **1** is, however, not completed by a second proton. Instead, the deprotonated glyoximate residues coordinate the second copper(II) center. An additional H₂dmg ligand completes the square-planar coordination environment. Additionally, one ethanol solvent molecule coordinates one of the copper centers leading to two different isomers **1a** and **1b** with [N₃O₂]/[N₂O₂] and [N₃O]/[N₂O₃] motifs, respectively. **1a** and **1b** (Figure 1, bottom) are found in the same ratio in the crystal structure. In the following, the ratiometric mixture of **1a** and **1b** is referred to as **1**.

Neither isomer II nor III was obtained as solid compound. This experimental result is in agreement with DFT calculations that show that isomer I is the lower energy isomer (Table S26). Further DFT calculations concerning I and II reveal a strong antiferromagnetic exchange coupling of two $S = 1/2$ states, which results in a singlet (broken symmetry state) and a triplet state (Figure 2) in agreement with the experimental results of Ruiz *et al.*^[13,14] The singlet state of I is 5.2 kJ mol^{−1} lower in energy compared to the singlet state of II (Table S26). Isomer III

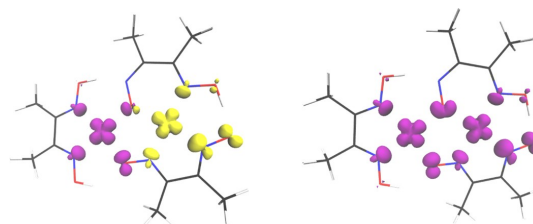


Figure 2. Spin density for singlet (left) and triplet (right) states of isomer I. The isovalue: ± 0.01 , S^2 for singlet is 0.86 (indicating broken-spin solution), for triplet is 2.

was 22.8 kJ mol^{−1} higher in energy than isomer I and was not further considered. In I, the Cu^{II} ions are bridged by the NO-glyoxime groups in a $\mu_2\text{-}\eta^1\text{:}\eta^1$ (N and O each coordinating one copper center) and $\mu_2\text{-}\eta^1$ (O coordinating both copper centers) fashion. In contrast, there are only $\mu_2\text{-}\eta^1\text{:}\eta^1$ motifs in II. The energy difference between the broken symmetry state and the triplet state is 10 kJ mol^{−1} larger in I. This indicates that the purely O-bridged $\mu_2\text{-}\eta^1$ mode dominates the superexchange pathway. However, the calculated singlet triplet gaps also include structural changes and are known to be overestimated by DFT.^[26]

Compounds **1** and **2** were characterized by UV/Vis, IR, MS, EPR, and DFT methods. The UV/Vis spectrum of **1** (Figures S6 and S7) is similar to UV/Vis spectra of comparable compounds^[12–14] and exhibits two strong transitions, 229 and 271 nm, with molar absorption coefficients of approximately 20 000 L mol^{−1} cm^{−1}. The band at 229 nm reflects transitions into LC (ligand centered) states as the spectrum of free H₂dmg displays a band at 227 nm ($\epsilon_m = 11\,302$ L mol^{−1} cm^{−1}). At 435 nm ($\epsilon_m = 2471$ L mol^{−1} cm^{−1}) a weaker absorption maximum is visible, which previously was assigned to transitions into LMCT (ligand-to-metal-charge-transfer) states.^[12–14]

The experimental spectrum is in excellent agreement with the time-dependent (TD) DFT predicted UV/Vis-spectrum that predicted two maxima at 230 and 270 nm and several maxima of lower intensity at higher wavelengths (see the Supporting Information Sections 2, 9.3, and 9.6, Figures S49, S51–S56, and Table S15). The spectroscopic signature of **2** resembles that of **1**, where the main difference is the inverted intensity ratio of the bands at 228 and 275 nm, ($\epsilon_m = 14\,474$ L mol^{−1} cm^{−1} and $\epsilon_m = 9244$ L mol^{−1} cm^{−1}, respectively) caused by the different coordination modes of the ligands. Additionally, a hypsochromic shift and decreased absorption coefficient of the maximum at 435 to 379 nm ($\epsilon_m = 1854$ L mol^{−1} cm^{−1}) was observed.

The characterization of **1** and **2** by ESI mass spectrometry yielded characteristic signals at mass to charge ratios of 471 for **1** (corresponding to [Cu₂(dmg)(Hdmg)(H₂dmg)]⁺) and 294 for **2**, which corresponds to [2 + H⁺]⁺ (see the Supporting Information Section 3).

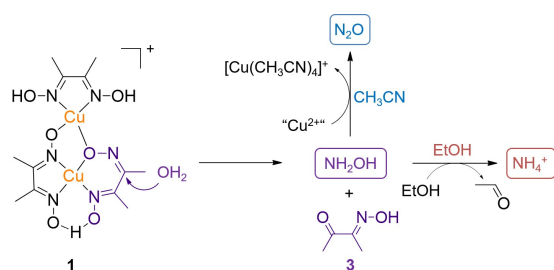
Static FTIR spectra of **1**, **2**, and H₂dmg were recorded in the solid state as KBr pellets with **1** and **2** showing similar vibrational bands. Notably, the CN stretching vibrations are not observed in the spectrum of H₂dmg as a result from a

pronounced impact of the hydrogen bonding.^[17] The assignment of the vibrational bands is discussed in detail in the Supporting Information. It is important to mention that the IR spectrum of **1** in CD₃CN was similar to that in a KBr glass, so that the molecular structure is basically maintained in solution on short timescales (< 1 min; Figure S25).

Compounds **1** and **2** were further analyzed by a qualitative study with X-band EPR spectroscopy (9.5 GHz at 100 K, see the Supporting Information Section 8, Figures S43–S46 as well as the corresponding calculations and simulations in Supporting Information Section 9.7, Figures S59 and S60, Tables S28–S31). These experiments confirmed Cu^{II} centers in axial elongated coordination and indicated that the molecular structure of **1** in the solid state is very likely maintained in solution.

In general, H₂dmg is reported to form rather stable complexes with 3d metal(II/III) ions, such as [Ni(Hdmg)₂],^[23–25] [Cu(Hdmg)₂],^[10] [Co(Hdmg)₂(H₂O)₂],^[27] and [Co(CN)(Hdmg)₂(pyr)].^[28,29] This behavior holds true for **2**, which is stable at air; however, suspensions/solutions of **1** changed color over the course of days, clearly indicating a chemical reaction. Recrystallization of **1** from ethanol/pentane led to red crystals; however, if not separated from the liquid, these crystals dissolved to yield black oil. During this process, the color of the solution changed from red to green and significant amounts of NH₄ClO₄ crystallized (Figure S4). Furthermore, the characteristic and strong odor of acetaldehyde was perceptible. In contrast, when using acetonitrile instead of ethanol, the solution decolorized. Within a day, significant amounts of [Cu(CH₃CN)₄]ClO₄ crystallized (Figure S3). These observations caught our attention. Despite the different reaction outcome, we postulate the same initial reaction step: the nucleophilic attack of H₂O at the glyoxime carbon atom leads to hydrolysis of the Hdmg[−]/dmg^{2−} ligand, which yields butane-2,3-dione monoxime (**3**) and intermediate NH₂OH. Depending on the reaction conditions, NH₂OH was either oxidized to N₂O (yielding Cu⁺ as reduced species) or reduced to NH₄⁺ (yielding acetaldehyde as oxidized species, Scheme 1).

Several spectroscopic and theoretical methods were employed to support this hypothesis. We were able to provide reasonable insight into the reactivity of **1**; however, because of the complexity of the system and the high volatility of diverse



Scheme 1. Postulated nucleophilic attack of H₂O at the glyoxime carbon atom to form intermediate NH₂OH and butane-2,3-dione monoxime (**3**). Depending on the solvent, NH₂OH was either oxidized to N₂O or reduced to NH₄⁺.

reaction products, only a generalized mechanism could be proposed. As a first step, we propose the nucleophilic attack of H₂O at the glyoxime carbon atom of the bridging μ₂-η¹-O–N=C-group. Due to this unique coordination to two Lewis acidic centers, the electron density distribution in comparison to the other O–N=C motifs differs. As shown by analysis of the molecular potential and the Mulliken charges of **1**, the electrophilicity at the carbon atom of this glyoximate group is higher than that of the other carbon atoms, facilitating the nucleophilic attack of H₂O (see the Supporting Information Section 9.4).

The presence of this special Cu–O–Cu coordination motif clearly distinguishes **1** from **2**, in which accordingly a nucleophilic attack of water is not favored, thus, leading to the stability of **2** against moisture and water. Consequently, the favored hydrolysis of the Hdmg[−]/dmg^{2−} molecule can be understood as cooperativity of both Cu^I ions working together to enable the nucleophilic attack of H₂O. This hydrolysis yields NH₂OH and **3** that could be detected in the reaction solutions (see below). To support this initial step, we carried out DFT calculations that focused on the formation of NH₂OH. The mechanism proposed generally represents an oxime hydrolysis (Figure 3). We observed that the energy barrier of the reaction is strongly dependent on the number of water molecules involved in the process, that is, when just one water molecule is involved, the barrier is much higher. This is consistent with results of Rzepa obtained by using a model system.^[30] The first stage is a nucleophilic attack of H₂O on the most electrophilic carbon atom, which is in the μ₂-O–N=C-group (see the Supporting Information Section 9.4.1 and Figure S50, C6). Simultaneously, proton reorganization mediated by a second H₂O molecule takes place at a neighboring oxime group (see TS1 in Figure 3). It is important to note that this proton transfer takes part not from the water molecule, but from the N–OH

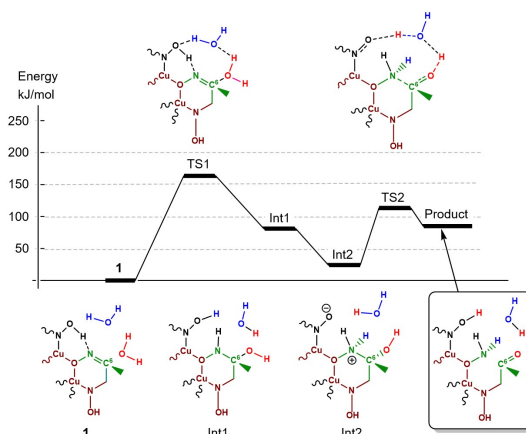


Figure 3. Proposed mechanism and energy diagram for isomer I using B3LYP/def2-TZVP. The atom C6 is labeled because it shows the highest partial charge. The part of the molecule not taking part in the reaction is omitted for clarity. The complete structures are shown in Figure S48.

group of the coordinating oxime (that is reprotonated from the water chain by Grothuss mechanism).^[31] This results in Intermediate 1 (**Int1**) that easily turns into a zwitterionic tautomer (Intermediate 2, **Int2**). The latter tautomerizes with N–C bond splitting into the product, which is a coordinated butane-2,3-dione monoxime (**3**). Thus, the role of the second H₂O molecule (not spent in the hydrolysis process) is the proton transfer during the reaction. Here, one can expect that this can be significantly influenced by the solvent and its pH value. The first barrier of 163 kJ mol⁻¹ (140 kJ mol⁻¹) is noticeably higher than the second one 119 kJ mol⁻¹ (84 kJ mol⁻¹) and thus is rate-controlling. The numbers in parenthesis include thermodynamic corrections (Table S27). This calculated first barrier is rather high; however, we assume that consideration of further solvent effects would lower the activation barrier.

To underline this mechanism, we carried out ESI mass spectrometry measurements and time-dependent UV/Vis and FTIR experiments. EPR did not prove to be a suitable method because the differentiation of the two Cu^{II} centers was not possible (Supporting Information Section 8).

Reactivity of 1 in ethanol

Time-dependent UV/Vis spectroscopic measurements over a time period of 6 d revealed an increase of the absorption maxima at 229 nm referring to ligand internal transitions into LC states and a decrease of the absorption maximum at 460 nm (Figure 4).

Both of these observations are consistent with the decomposition of **1** and liberation of H₂dmg. Notably, the maximum at 270 nm does not decrease but increases and splits into three maxima (251, 257, and 263 nm) that are hypsochromically shifted. Additionally, two shoulders at 287 and 319 nm formed, whereas the shoulder at 287 nm decreases over time, again. This behavior indicates the degradation of H₂dmg and/or formation of new H₂dmg containing species. We calculated the

UV/Vis spectra of diverse possible intermediates such as free and complexed **3**, [Cu(OH)₂(H₂dmg)], and the mixed-valent Cu^{II}/Cu^I species [Cu^{II}Cu^I(H₂dmg)(Hdmg)(dmg)] (Figures S51–S56); however, the identification of the new species formed was not possible because the spectra show similar bands of comparable intensity. Lacking the actual compounds for the spectroscopic comparison, it is unlikely that the identification of either one of those species is possible.

Nevertheless, it was possible to trap and analyze evolving acetaldehyde (see the Supporting Information Sections 5.3 and 7.4, Figures S23 and S27–S29), which clearly supports the suggested decomposition pathway and underlines the oxidation of ethanol.

During subsequent experiments that required a higher concentration solution of **1**, a strong concentration-dependence of the reaction was observed. For example, a higher concentrated solution ($c = 1.84 \times 10^{-4}$ M) of **1** in ethanol did not show significant changes over time in the UV/Vis spectra (Figure S9), indicating that the decomposition of **1** only occurs with high excess ethanol. In accordance with these findings, investigations of high concentration solutions of **1** with ESI mass spectrometry did not show any differences within 24 h, either; however, the measurement of a fresh and low concentration sample revealed the complete decomposition of **1** within a few days. The signal of [Cu₂(dmg)(Hdmg)(H₂dmg)]⁺ (m/z 471, Figures S11, S12, S18, and S20) disappeared, instead, several new signals were observed, for example, at m/z 264 that could correspond to the complex [Cu(3)]⁺, in which one molecule of **3** is deprotonated (Figures S18–S20).

This concentration-dependence further was observed in FTIR mechanistic studies, where concentrations of $c \geq 10$ mM were required. The low solubility of **1** in ethanol as well as strong IR absorptions of ethanol in the region of interest (1700–1100 cm⁻¹) precluded measurements directly in ethanol. Thus, **1** was dissolved in deuterated dimethylsulfoxide ([D₆]DMSO, $c = 15$ mM) and an excess of ethanol (50 equiv.) was added. However, a reaction between **1** and ethanol was not detected over 1.5 h (Figure S26), either.

In summary, we could detect the main reaction products NH₄ClO₄ and acetaldehyde, the latter by IR and NMR (Figures S23 and S27–S29). Additional to its crystallization, we could detect NH₄⁺ in solution by adding Neßler's reagent (K₂[HgI₄]), which forms orange colored [Hg₂N] in the presence of NH₃/NH₄⁺.^[32] In addition, we could detect an intermediate copper(I) species through addition of neocuproine that forms a bright red complex with Cu^I ions, which crystallized from the reaction mixture (Figure S5). Interestingly, **1** can be regenerated by adding new H₂dmg and airing the flask to oxidize Cu^I to Cu^{II}. After some time, the redox reaction and thus, decomposition of **1** starts again, so that we could repeat this cycle four times. Taken together, these findings underline the proposed reaction pathway, in which intermediate NH₂OH is formed by the hydrolysis of H₂dmg. NH₂OH was then *reduced* to NH₄⁺. The redox partner for this reaction is ethanol that is oxidized to acetaldehyde. This redox reaction is mediated by the copper centers, which can be concluded from the detection of intermediate Cu^I species. Most notably, in this reaction pathway,

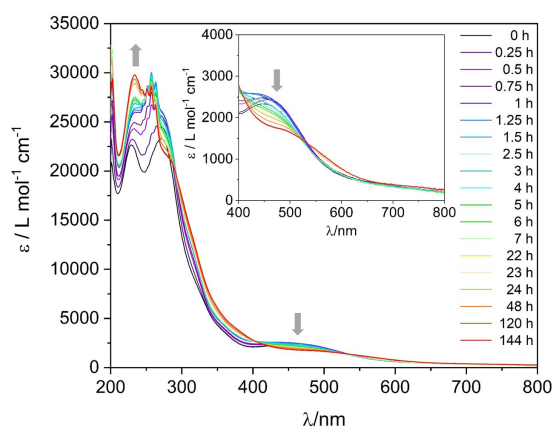


Figure 4. Time-dependent UV/Vis spectra of **1** in ethanol ($c = 3.63 \times 10^{-5}$ mol L⁻¹) over a time period of 6 d.

NH_2OH is reduced, which is chemically challenging ($\epsilon_0(\text{NH}_2\text{OH}^+/\text{NH}_4^+) = +1.35 \text{ V}^{[33]}$) and therefore usually not observed. NH_2OH is a strong reducing agent and thus, typically is oxidized to N_2 and/or N_2O ($\epsilon_0(\text{NH}_2\text{OH}^+/\text{N}_2, \text{N}_2\text{O}) = -1.87 \text{ V}^{[33]}$). In general, Cu^{II} ions do even catalyze this oxidation.^[34] At high concentrations, NH_2OH tends to disproportionate into NH_3 , N_2 , and N_2O ,^[33] however, that is clearly not the case for the reactivity described within this article. First, we do not observe N_2O as oxidation product, but only acetaldehyde, and second, the reaction does only occur at low concentrations. This observation can be explained by the chemically demanding reaction conditions and the concentration-dependence of the electrochemical potential ($\epsilon_0(\text{EtOH}/\text{acetaldehyde}) = -0.197 \text{ at pH } 7$).^[35] It is remarkable that NH_2OH is reduced to NH_4^+ under these conditions. In this context, it is interesting to note that even in nature, there are only few enzymes that are capable of the reduction of NH_2OH to NH_4^+ .^[36–40] Among them is the copper containing nitrite reductase (CuNiR),^[39,40] which notably, uses a dinuclear copper-type two-center for substrate activation.^[41]

Reactivity of 1 in acetonitrile

The time-dependent UV/Vis spectra showed bleaching of the solution and accordingly reduction of the dinuclear 1 to $[\text{Cu}(\text{CH}_3\text{CN})_4]^+$ (Figure 5), which can be obtained as crystalline solid in 68% yield from the reaction solution (Figure S3).

The decomposition of 1 is indicated by the increase in intensity of transitions into LC states (204, 230 nm), which corresponds to a rising amount of free H_2dmg . Further evidence for this decomposition and the reduction of Cu^{II} to Cu^{I} is found in the decrease of all other bands. Based on the UV/Vis spectra, this process is completed within 12 h, which indicates a much faster reaction than observed in ethanol. Results of complementary investigations by ESI mass spectrometry match these

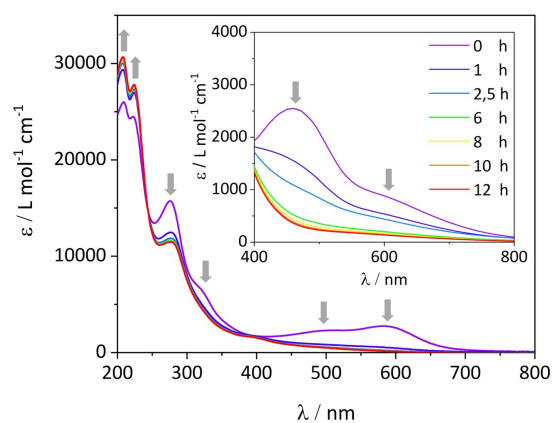


Figure 5. Time-dependent UV/Vis spectra over 12 h of the reaction of 1 in CH_3CN (left: $c = 1.94 \times 10^{-5} \text{ mol L}^{-1}$, right: $c = 7.93 \times 10^{-4} \text{ mol L}^{-1}$). Differences in the spectra for $t = 0 \text{ h}$ derive from the decomposition of 1 that started even in the less-concentrated sample. A comparison with spectra in methanol is given in Figure S8.

findings, where the intensity of the signal of 1 decreases over time and the intensity of the signals of $[\text{Cu}(\text{CH}_3\text{CN})]^+$ (m/z 104) and $[\text{Cu}(\text{CH}_3\text{CN})_2]^+$ (m/z 145) increase. Additionally, several signals that correspond to diverse copper dimethylglyoxime fragments appeared over time, which further underlines the decomposition of 1 (Tables S19 and S20, Figures S14–S17).

The according FTIR investigations were performed in dry CD_3CN over 8 h; however, it was not possible to eliminate all traces of H_2O . In contrast to the observations in $[\text{D}_6]\text{DMSO}$ with ethanol, significant spectral changes were observed already after few minutes (Figure 6).

Hereby, the most important observation is the appearance of a strong new band at 1693 cm^{-1} , which was assigned to a CO stretching vibration and gives a first indication for the formation of 3. This assignment is confirmed by the presence of the same absorption band in the reference IR spectrum of 3 in CD_3CN (Figures S30, S32, and S33). Next to this, a weak band was observed at 2229 cm^{-1} , congruent with the reference of N_2O in CD_3CN (and DMSO , Figure S31), which confirms the suggested product formation (inset in Figure 7, Figure S34). The spectral region of $1650\text{--}1180 \text{ cm}^{-1}$ is discussed in the Supporting Information, with a focus on the conceivable species $[\text{Cu}(\text{CH}_3\text{CN})_4]^+$, H_2dmg , NO_2^- and NO_3^- , the two later ones being present at most as side products. (see the Supporting Information Sections 7.2 and 7.5) In addition to these descriptions, the experimental IR spectra of 1 and 3 are well described by theoretical IR spectra obtained by geometry optimizations and subsequent frequency calculations at DFT level (Figures S41 and S42).

Even though the intrinsic traces of H_2O seemed to be sufficient to initiate the decomposition of 1, we repeated the experiment by adding an excess of H_2O (20 equiv.). Interestingly, the reaction and its kinetics are not significantly influenced during the first hour of the reaction (Figure S39). At longer timescales, however, a follow-up reaction that might relate to complex formation of 3, solvated Cu^{III} ions, and H_2O takes place (see the Supporting Information Section 7.6). To

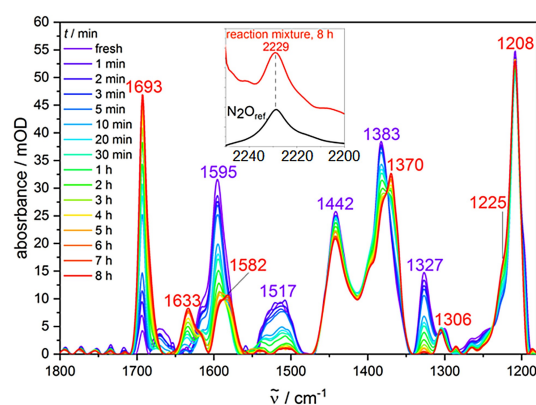


Figure 6. Time-dependent FTIR spectra over 8 h of the reaction of 1 in CD_3CN . The inset is an enlargement of the region around 2230 cm^{-1} (red: reaction mixture after 8 h, black: reference IR spectrum of N_2O in CD_3CN).

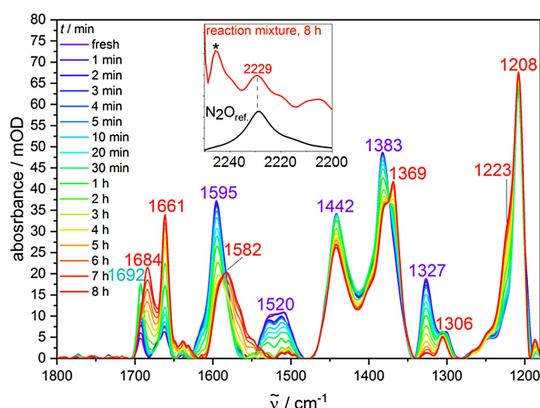


Figure 7. Time-dependent FTIR spectra over 8 h of the reaction of **1** in CD_3CN containing H_2^{18}O (20 equiv.). The inset is an enlargement of the region around 2230 cm^{-1} (red: reaction mixture after 8 h, black: reference IR spectrum of N_2O in CD_3CN). The band marked with an asterisk is an artifact resulting from the strong absorption of CD_3CN in this spectral region.

gain further insight into the mechanism, we carried out experiments with isotopically labeled H_2^{18}O . Based on the proposed mechanism, hydrolysis of H_2dmg would lead to **3**, in which the oxygen atom of the carbonyl function is that of the initially attacking H_2O molecule. Thus, FTIR spectroscopy on **1** in CD_3CN with addition of H_2^{18}O was an ideal tool to experimentally verify this stated mechanism, as the isotope labeled H_2^{18}O should induce a red-shift of the CO stretching vibration by about 40 cm^{-1} (C^{16}O vs. C^{18}O). Indeed, an additional band appeared at 1661 cm^{-1} , which is assigned to the C^{18}O stretching vibration (Figure 7). However, this C^{18}O band coexists with the C^{16}O peak described earlier, which should result from traces of H_2^{16}O that are intrinsically contained in the reaction mixture (despite the use of dry CD_3CN). A more surprising observation is that the C^{16}O signal is stronger than the C^{18}O peak over the first hour of the reaction. This is an indication for preorganized (coordinated) H_2^{16}O molecules that might be present in the solid sample of **1**. Nevertheless, the presence of two distinct CO stretching vibrations (C^{16}O at 1692 cm^{-1} and C^{18}O at 1661 cm^{-1}) clearly strengthens the suggested mechanism. As the C^{16}O peak is logically weaker compared to the investigations without isotope labeled H_2O , the CO stretching vibration attributed to the complexation of formed **3** (see above) is clearly observable as a separate peak at 1684 cm^{-1} . In this particular case, it is only visible as shoulder in the H_2^{16}O experiments. However, it is to mention that in all experiments, the Gaussian deconvolution yielded very similar wavenumbers for the CO vibration of the new species with complexed **3** ($1679\text{--}1682\text{ cm}^{-1}$, Figures S38–S40). The absence of any specific “ ^{18}O band” for this particular vibration might result from similar spectral frequencies of the underlying vibrational modes independent of the isotope (^{16}O or ^{18}O).

In summary, we could detect the main reaction products $[\text{Cu}(\text{CH}_3\text{CN})_4]\text{ClO}_4$, **3**, and N_2O . This finding is in accordance with

the usually observed oxidation of NH_2OH to N_2O ,^[33] which is known to be even catalyzed by Cu^{II} ions.^[34] Furthermore, we could show that the initial step indeed is the nucleophilic attack of H_2O to form **3** and presumably NH_2OH ; however, despite much effort, we were not able to detect intermediate NH_2OH . It is very likely that the nascent NH_2OH is too rapidly oxidized to N_2O to be detected by room-temperature FTIR. Based on the results of the UV/Vis measurements and the good experimental yield of $[\text{Cu}(\text{CH}_3\text{CN})_4]\text{ClO}_4$ (68%), we assume that the decomposition of **1** is rather complete.

Conclusion

We have synthesized and thoroughly characterized the dinuclear copper(II) complex $[\text{Cu}_2(\text{H}_2\text{dmg})(\text{Hdmg})(\text{dmg})]\text{ClO}_4$ (**1**) and its mononuclear analogue $[\text{Cu}(\text{Hdmg})_2]$ (**2**). Three possible coordination isomers I–III of **1** exist; however, based on the spectroscopic signature^[13] and temperature-dependent UV/Vis measurements (see the Supporting Information Section 2.6), we assume that isomer I is dominant. Furthermore, based on the poor match of the calculated and experimental IR spectra, the presence of III is very unlikely (Figure S41).

We found that **1** is sensitive to hydrolysis; this is a result of the cooperative effect of the two Cu^{II} ions, which increases the electrophilia of the glyoxime carbon atom of the bridging $\mu_2\text{-O-N=C}$ -group. DFT calculations reveal a much higher Mulliken charge in comparison to any other carbon atom in the molecule. Therefore, the nucleophilic attack of H_2O is favored at this $\text{Hdmg}/\text{H}_2\text{dmg}$ ligand, and this leads to the hydrolysis products butane-2,3-dione monoxime (**3**) and NH_2OH . Depending on the solvent, NH_2OH is either oxidized or reduced. In CH_3CN , NH_2OH is oxidized to N_2O , which is in accordance with NH_2OH being a strong reducing agent. The reduction product is $[\text{Cu}(\text{CH}_3\text{CN})_4]\text{ClO}_4$, which crystallizes from the reaction mixture. In contrast, in ethanol, NH_2OH is reduced to NH_4^+ , which is obtained in significant amounts as NH_4ClO_4 . The redox partner is ethanol, which is oxidized to acetaldehyde. Based on DFT calculations, we suggest a reaction pathway that is basically glyoxime hydrolysis that yields **3** and NH_2OH . Two H_2O molecules participate in the proposed mechanisms; one nucleophilically attacks the carbon atom and the other one is involved in proton transfer. Even though it was not possible to detect NH_2OH itself and the calculated activation barrier is rather high, the combined approach of theoretical methods, experimental detection and characterization techniques, time-dependent UV/Vis and FTIR spectroscopy, and mass spectrometry allowed the detection of all the main reaction products and thus, underlines the reaction pathway proposed. FTIR spectroscopic measurements with isotopically labeled H_2^{18}O proved the nucleophilic attack of H_2O as initial reaction step.

The possibility of **1** to either oxidize or reduce NH_2OH is remarkable because the electrochemical potentials of both reactions are far apart ($\epsilon_0(\text{NH}_3\text{OH}^+/\text{N}_2, \text{N}_2\text{O}) = -1.87\text{ V}$ and $\epsilon_0(\text{NH}_3\text{OH}^+/\text{NH}_4^+) = +1.35\text{ V}$).^[33] In particular, the reduction of NH_2OH is chemically challenging; this is mirrored by a strong concentration dependence of the hydrolysis of **1** in ethanol. As

a result of the concentration dependence of the electrochemical potential, hydrolysis of **1** with subsequent reduction of NH_2OH to NH_4^+ is only observed at low concentrations/high excess of ethanol.

Experimental Section

Materials and methods: All chemicals used were of p.a. quality and were purchased from Acros Organics, Alfa Aesar, Merck, Roth or Sigma Aldrich if not mentioned otherwise. Solvents for synthesis were degassed but not dried. For time-dependent FTIR spectroscopy, acetonitrile was dried according to literature procedures.^[42] The handling and preparation of air sensitive compounds were performed under a nitrogen atmosphere. Standard Schlenk techniques were used. If not mentioned otherwise all syntheses were performed under inert atmosphere. Analytical data and device parameters (UV/Vis spectroscopy, NMR spectroscopy, IR spectroscopy including corresponding simulations and additional discussion,^[43–48] SC-XRD,^[49–55] elemental analysis, ESI mass spectrometry including corresponding simulations,^[56] and EPR spectroscopy) are given in the Supporting Information.

Deposition Numbers 2203267 (for **1**), 2203268 (for **2**), 2203269 (for $[\text{Cu}(\text{CH}_3\text{CN})_4]\text{ClO}_4$), 2203270 (for $[\text{Cu}(\text{neocuproine})_2]\text{ClO}_4$) contain the supplementary crystallographic data for this paper. These data are provided free of charge by the joint Cambridge Crystallographic Data Centre and Fachinformationszentrum Karlsruhe Access Structures service.

Computational details: All calculations were performed with the program package TURBOMOLE^[45] using density functional theory (DFT). Single-point energy calculations were carried out using tolerances of 10^{-7} Hartrees for the SCF energy change, and default convergence criteria for the geometry optimization. All calculations were performed with the B3LYP functional,^[57–59] def2-TZVP basis set,^[60] and the resolution of the identity (RI) approximation.^[61–63] UV/Vis spectra were calculated with time dependent DFT (TDDFT).^[64,65] Transition states were preoptimized by a reaction path search from Plessow^[66] and then determined by trust region image optimizations.^[67] Solvent effects were not considered. Additionally, computations using the state average complete active space self-consistent field (CASSCF) were done.^[68] With a program developed in Karlsruhe and Kaiserslautern,^[69] spin orbit configuration interaction (SOC) calculations were carried out on the basis of the CASSCF orbitals using a spin orbit mean field technique for the two-electron spin-orbit integrals.^[70,71] The Abragam–Bleaney tensor, as described by Gerloch and McMeeking,^[72] was used to generate the g-tensors (Supporting Information Section 9.7).^[73]

Preparation of $[\text{Cu}_2(\text{H}_2\text{dmg})(\text{Hdmg})(\text{dmg})(\text{EtOH})]\text{ClO}_4$ (1**):** $\text{Cu}(\text{ClO}_4)_2 \cdot 6\text{H}_2\text{O}$ (185 mg, 0.499 mmol) was dissolved in ethanol (ca. 10 mL). H_2dmg (127 mg, 1.09 mmol) was added to the stirred solution. The solution turned deep red and was stirred for 15 min at room temperature. The product could be collected as deep red crystals by pentane diffusion (65 mg, 0.11 mmol, 44%).

Preparation of $[\text{Cu}(\text{Hdmg})_2]$ (2**):** Synthetic procedure using $\text{Cu}(\text{OAc})_2 \cdot 2\text{H}_2\text{O}$: According to literature^[10] $\text{Cu}(\text{OAc})_2 \cdot 2\text{H}_2\text{O}$ (101 mg, 0.506 mmol) was dissolved in methanol (ca. 20 mL). H_2dmg (117 mg, 1.01 mmol) in methanol (ca. 20 mL) was added to the stirred solution of the salt. The solution turned deep red and was stirred for 30 min at room temperature. After slow evaporation of the solvent in air, the product could be collected as red crystals (62 mg, 0.21 mmol, 42%).

Preparation of $[\text{Cu}(\text{CH}_3\text{CN})_4]\text{ClO}_4$: $\text{Cu}(\text{ClO}_4)_2 \cdot 6\text{H}_2\text{O}$ (182 mg, 0.491 mmol) was dissolved in acetonitrile (ca. 15 mL). H_2dmg

(124 mg, 1.07 mmol) was added to the stirred solution. The solution turned deep green. The product was obtained as colorless crystals by diethyl ether diffusion (109 mg, 0.333 mmol, 68%). Among the crystallization process, the solution decolorized.

Acknowledgements

The authors gratefully acknowledge the financial support from TRR/SFB 88 “3MET”. S. B. and R. I. P. thank Dr. Jonathan Becker (JLU Giessen) for his support in crystal measurement. E. B. and K. F. acknowledge support by the state of Baden–Württemberg through bwHPC and the German Research Foundation (DFG) through grant no. INST 40/575-1 FUGG (JUSTUS 2 cluster). Open Access funding enabled and organized by Projekt DEAL.

Conflict of Interest

The authors declare no conflict of interest.

Data Availability Statement

The data that support the findings of this study are available in the supplementary material of this article.

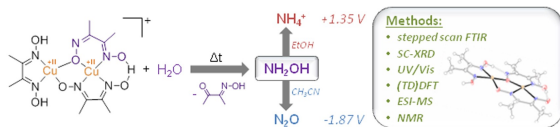
Keywords: cooperative effects · copper complexes · dimethylglyoxime · hydrolysis · hydroxylamine

- [1] N. Sträter, W. N. Lipscomb, T. Klabunde, B. Krebs, *Angew. Chem. Int. Ed. Engl.* **1996**, *35*, 2024–2055.
- [2] B. Bosnich, *Inorg. Chem.* **1999**, *38*, 2554–2562.
- [3] J. I. van der Vlugt, *Eur. J. Inorg. Chem.* **2012**, *2012*, 363–375.
- [4] P. Buchwalter, J. Rosé, P. Braunstein, *Chem. Rev.* **2015**, *115*, 28–126.
- [5] L. Tebben, C. Mück-Lichtenfeld, G. Fernández, S. Grimme, A. Studer, *Chem. Eur. J.* **2017**, *23*, 5864–5873.
- [6] M. H. Prosenč, M. M. Kappes, G. Niedner-Schatteburg, *Chem. Eur. J.* **2021**, *27*, 15019–15020.
- [7] T. Wall, M. Leist, F. Dietrich, W. R. Thiel, M. Gerhards, *ChemPlusChem* **2021**, *86*, 622–628.
- [8] M. Grupe, P. Boden, P. Di Martino-Fumo, X. Gui, C. Bruschi, R. Israil, M. Schmitt, M. Nieger, M. Gerhards, W. Klopfer, C. Riehn, C. Bizzarri, R. Diller, *Chem. Eur. J.* **2021**, *27*, 15252–15271.
- [9] Transregional collaborative research center located at the TU Kaiserslautern (TUK) and Karlsruhe Institute of Technology (KIT), **2009–2022**.
- [10] E. Frasson, R. Bardi, S. Bezzi, *Acta Crystallogr.* **1959**, *12*, 201–205.
- [11] D. H. Svedung, *Acta Chem. Scand.* **1969**, *23*, 2865–2878.
- [12] R. I. Petrikat, S. Becker, *Z. Anorg. Allg. Chem.* **2022**, *648*, e202200150.
- [13] R. Ruiz, J. Sanz, B. Cervera, F. Lloret, M. Julve, C. Bois, J. Faus, M. C. Muñoz, *J. Chem. Soc. Dalton Trans.* **1993**, 1623–1628.
- [14] R. Ruiz, J. Sanz, F. Lloret, M. Julve, J. Faus, C. Bois, M. C. Muñoz, *J. Chem. Soc. Dalton Trans.* **1993**, 3035–3039.
- [15] X.-Y. Chen, P. Cheng, X.-W. Liu, S.-P. Yan, W.-M. Bu, D.-Z. Liao, Z.-H. Jiang, *Chem. Lett.* **2003**, *32*, 118–119.
- [16] C.-H. Li, R.-J. Wang, H.-Z. Kou, Y.-D. Li, *Inorg. Chem. Commun.* **2002**, *5*, 403–406.
- [17] P. K. Panja, S. Bala, C. Pal, P. N. Ghosh, *J. Mol. Struct.* **1991**, *249*, 277–283.
- [18] J. E. Caton, Jr., C. V. Banks, *Talanta* **1966**, *13*, 967–977.
- [19] K. E. Falk, E. Ivanova, B. Roos, T. Vanngard, *Inorg. Chem.* **1970**, *9*, 556–562.
- [20] X. Wu, W. Hu, *Chin. J. Chem.* **2011**, *29*, 2124–2128.
- [21] K. Xavier, *Appl. Catal.* **2004**, *258*, 251–259.

- [22] C. Gawlig, S. Schindler, S. Becker, *Eur. J. Inorg. Chem.* **2020**, 2020, 248–252.
- [23] L. Tschugaeff, *Ber. Dtsch. Chem. Ges.* **1905**, *38*, 2520–2522.
- [24] P. Pfeiffer, *Ber. Dtsch. Chem. Ges. A* **1930**, *63*, 1811–1816.
- [25] L. E. Godycki, R. E. Rundle, R. C. Voter, C. V. Banks, *J. Chem. Phys.* **1951**, *19*, 1205–1206.
- [26] G. Singh, S. Gamboa, M. Orio, D. A. Pantazis, M. Roemelt, *Theor. Chem. Acc.* **2021**, *140*, 139.
- [27] G. N. Schrauzer, R. J. Windgassen, *Chem. Ber.* **1966**, *99*, 602–610.
- [28] G. N. Schrauzer, J. Kohnle, *Chem. Ber.* **1964**, *97*, 3056–3064.
- [29] G. N. Schrauzer, *Acc. Chem. Res.* **1968**, *1*, 97–103.
- [30] H. S. Rzepa, in *Henry Rzepa's Blog*, "Oxime formation from hydroxylamine and ketone", can be found under <https://www.ch.imperial.ac.uk/rzepa/blog/?p=7822>, **2012**.
- [31] N. Agmon, *Chem. Phys. Lett.* **1995**, *244*, 456–462.
- [32] J. Nessler, *Über das Verhalten des Jodquecksilbers und der Quecksilberverbindungen, überhaupt zu Ammoniak und über eine neue Reaktion auf Ammoniak*, Albert-Ludwigs-Universität, Freiburg, **1856**.
- [33] A. F. Holleman, E. Wiberg, N. Wiberg, in *Lehrbuch der anorganischen Chemie*, De Gruyter, Berlin, **1985**.
- [34] J. H. Anderson, *Analyst* **1964**, *89*, 357.
- [35] D. Voet, J. G. Voet, C. W. Pratt, in *Lehrbuch der Biochemie*, Wiley-VCH, Weinheim, **2019**.
- [36] R. Sturms, A. A. DiSpirito, D. B. Fulton, M. S. Hargrove, *Biochemistry* **2011**, *50*, 10829–10835.
- [37] J. Singh, *Biochim. Biophys. Acta Bioenerg.* **1974**, *333*, 28–36.
- [38] O. Einsle, A. Messerschmidt, R. Huber, P. M. H. Kroneck, F. Neese, *J. Am. Chem. Soc.* **2002**, *124*, 11737–11745.
- [39] J. Simon, P. M. H. Kroneck, in *The Metal-Driven Biogeochemistry of Gaseous Compounds in the Environment* (Eds.: P. M. H. Kroneck, M. E. S. Torres), Springer, Dordrecht, **2014**, pp. 211–236.
- [40] P. M. Harrison, in *Metalloproteins. 1: Metal Proteins with Redox Roles*, Verlag Chemie, Weinheim, **1985**.
- [41] M. Sundararajan, I. H. Hillier, N. A. Burton, *J. Phys. Chem. B* **2007**, *111*, 5511–5517.
- [42] J. F. Coetzee, *Pure Appl. Chem.* **1966**, *13*, 427–436.
- [43] M. J. Frisch, G. W. Trucks, H. W. Schlegel, G. E. Scuseria, M. A. Robb, J. R. Cheeseman, G. Scalmani, V. Barone, G. A. Petersson, H. Nakatsuji, X. Li, M. Caricato, A. Marenich, J. Bloino, B. G. Janesko, R. Gomperts, B. Mennucci, H. P. Hratchian, J. V. Ortiz, A. F. Izmaylov, J. L. Sonnenberg, D. Williams-Young, F. Ding, F. Lipparini, F. Egidi, J. Goings, B. Peng, A. Petrone, T. Henderson, D. Ranasinghe, V. G. Zakrzewski, J. Gao, N. Rega, G. Zheng, W. Liang, M. Hada, M. Ehara, K. Throssell, J. A. Montgomery, Jr., J. E. Peralta, F. Ogliaro, M. Bearpark, J. J. Heyd, E. Brothers, K. N. Kudin, V. N. Staroverov, T. Keith, R. Kobayashi, J. Normand, K. Raghavachari, A. Rendell, J. C. Burant, S. S. Iyengar, J. Tomasi, M. Cossi, J. M. Millam, M. Klene, C. Adamo, R. Cammi, J. W. Ochterski, R. L. Martin, K. Morokuma, O. Farkas, J. B. Foresman, D. J. Fox, *Gaussian 09*, Gaussian Inc., Wilford, CT, **2016**.
- [44] F. Furche, R. Ahlrichs, C. Hättig, W. Klopper, M. Sierka, F. Weigend, *WIREs Comput. Mol. Sci.* **2014**, *4*, 91–100.
- [45] a) TURBOMOLE V7.5 **2020**, a development of University of Karlsruhe and Forschungszentrum Karlsruhe GmbH, 1989–2007, TURBOMOLE GmbH, since **2007**; available from <https://www.turbomole.org>; b) S. G. Balasubramani, G. P. Chen, S. Coriani, M. Diedenhofen, M. S. Frank, Y. J. Franzke, F. Furche, R. Grotjahn, M. E. Harding, C. Hättig, A. Hellweg, B. Helmich-Paris, C. Holzer, U. Huniar, M. Kaupp, A. Marefat Khah, S. Karbalaeei Khani, T. Müller, F. Mack, B. D. Nguyen, S. M. Parker, E. Perlt, D. Rappoport, K. Reiter, S. Roy, M. Rückert, G. Schmitz, M. Sierka, E. Tapavicza, D. P. Tew, C. van Wüllen, V. K. Voora, F. Weigend, A. Wodyński, J. M. Yu, *J. Chem. Phys.* **2020**, *152*, 184107.
- [46] S. Grimme, J. Antony, S. Ehrlich, H. Krieg, *J. Chem. Phys.* **2010**, *132*, 154104.
- [47] S. Grimme, S. Ehrlich, L. Goerigk, *J. Comput. Chem.* **2011**, *32*, 1456–1465.
- [48] R. Blinc, D. Hadži, *J. Chem. Soc.* **1958**, 4536–4540.
- [49] L. Krause, R. Herbst-Irmer, G. M. Sheldrick, D. Stalke, *J. Appl. Crystallogr.* **2015**, *48*, 3–10.
- [50] APEX2, Bruker AXS, Inc., Madison, WI, USA.
- [51] XPREP, Bruker AXS, Inc., Madison, WI, USA.
- [52] G. M. Sheldrick, *Acta Crystallogr. Sect. A* **2015**, *71*, 3–8.
- [53] G. M. Sheldrick, *Acta Crystallogr. Sect. C* **2015**, *71*, 3–8.
- [54] C. B. Hübschle, G. M. Sheldrick, B. Dittrich, *J. Appl. Crystallogr.* **2011**, *44*, 1281–1284.
- [55] A. L. Spek, *Platon*, University of Utrecht (The Netherlands), **2008**.
- [56] M. Loos, C. Gerber, F. Corona, J. Hollender, H. Singer, *Anal. Chem.* **2015**, *87*, 5738–5744.
- [57] A. D. Becke, *J. Chem. Phys.* **1993**, *98*, 5648–5652.
- [58] A. D. Becke, *Phys. Rev. A* **1988**, *38*, 3098–3100.
- [59] C. Lee, W. Yang, R. G. Parr, *Phys. Rev. B* **1988**, *37*, 785–789.
- [60] F. Weigend, R. Ahlrichs, *Phys. Chem. Chem. Phys.* **2005**, *7*, 3297–3305.
- [61] K. Eichkorn, O. Treutler, H. Öhm, M. Häser, R. Ahlrichs, *Chem. Phys. Lett.* **1995**, *240*, 283–290.
- [62] K. Eichkorn, F. Weigend, O. Treutler, R. Ahlrichs, *Theor. Chem. Acta* **1997**, *97*, 119–124.
- [63] F. Weigend, *Phys. Chem. Chem. Phys.* **2006**, *8*, 1057–1065.
- [64] R. Bauernschmitt, R. Ahlrichs, *Chem. Phys. Lett.* **1996**, *256*, 454–464.
- [65] R. Bauernschmitt, M. Häser, O. Treutler, R. Ahlrichs, *Chem. Phys. Lett.* **1997**, *264*, 573–578.
- [66] P. Plessow, *J. Chem. Theory Comput.* **2013**, *9*, 1305–1310.
- [67] T. Helgaker, *Chem. Phys. Lett.* **1991**, *182*, 503–510.
- [68] U. Meier, V. Staemmler, *Theor. Chim. Acta* **1989**, *76*, 95–111.
- [69] T. Bodenstein, A. Heimermann, K. Fink, C. van Wüllen, *ChemPhysChem* **2022**, *23*, e202100648.
- [70] F. Neese, *J. Chem. Phys.* **2005**, *122*, 034107.
- [71] B. Helmich-Paris, C. Hättig, C. van Wüllen, *J. Chem. Theory Comput.* **2016**, *12*, 1892–1904.
- [72] M. Gerloch, R. F. McMeeking, *J. Chem. Soc. Dalton Trans.* **1975**, 2443.
- [73] R. Selwin Joseyphus, M. Sivasankaran Nair, *Arab. J. Chem.* **2010**, *3*, 195–204.

Manuscript received: November 5, 2022
 Accepted manuscript online: February 20, 2023
 Version of record online: ■■■

RESEARCH ARTICLE



First check your solvent: In a dinuclear dimethylglyoxime copper(II) complex, hydrolysis of one ligand is facilitated by the cooperative effect of both Cu^{II} ions. Hydrolysis yields butane-2,3-dione monoxime and NH_2OH ; depending on the solvent

used, the latter is either oxidized to N_2O (in CH_3CN) or reduced to NH_4^+ (in ethanol). A combined approach of experimental, theoretical, and spectroscopic methods allowed the reaction mechanism to be suggested.

R. I. Petrikat, S. T. Steiger, E. Barani, P. J. Boden, M. E. Huber, Dr. M. R. Ringenberg, Prof. Dr. G. Niedner-Schatteburg, Prof. Dr. K. Fink, Jun.-Prof. Dr. S. Becker*

1 – 9

Cooperativity-Driven Reactivity of a Dinuclear Copper Dimethylglyoxime Complex



Chemistry–A European Journal

Supporting Information

Cooperativity-Driven Reactivity of a Dinuclear Copper Dimethylglyoxime Complex

Raphael I. Petrikat, Sophie T. Steiger, Elham Barani, Pit J. Boden, Maximilian E. Huber, Mark R. Ringenberg, Gereon Niedner-Schatteburg, Karin Fink, and Sabine Becker*

1.	Single Crystal X-Ray Diffraction	1
1.1.	General Information	1
1.2.	Crystal and Refinement Data of 1	2
1.3.	Crystal and Refinement Data of 2	6
1.4.	Crystal and Refinement Data of $[\text{Cu}(\text{CH}_3\text{CN})_4]\text{ClO}_4$	8
1.5.	Crystal and Refinement Data of NH_4ClO_4	10
1.6.	Crystal and Refinement Data of $[\text{Cu}(\text{neocuproine})_2]\text{ClO}_4$	11
2.	UV/Vis spectroscopy	13
2.1.	General Information	13
2.2.	Spectrum of 1 in methanol	13
2.3.	Spectra of 1 , 2 , and H_2dmg	14
2.4.	Spectra of 1 in different solvents	15
2.5.	Time-dependent measurements of 1 in ethanol	16
2.6.	Temperature-dependent measurements of 1 in methanol	17
3.	ESI mass spectrometry	18
3.1.	General Information	18
3.2.	ESI mass spectrum of 1 in methanol	18
3.3.	ESI mass spectrum of 1 in acetonitrile	20
3.4.	ESI mass spectrum of 1 after reaction in ethanol	23
3.5.	ESI mass spectrum of 2 in methanol	26
4.	Elemental analyses	27
4.1.	General Information	27
4.2.	Elemental analysis for 1	27
4.3.	Elemental analysis for 2	27
5.	NMR spectroscopy	28
5.1.	General Information	28
5.2.	^1H -NMR spectrum of $[\text{Cu}(\text{CH}_3\text{CN})_4]\text{ClO}_4$	28
5.3.	^1H -NMR spectrum of the adsorbed gases obtained by the reaction of $\text{Cu}(\text{ClO}_4)_2 \cdot 6\text{H}_2\text{O}$ and H_2dmg in ethanol	29
6.	Additional synthetic procedures	30
6.1.	Additional synthetic protocols for 2	30
6.2.	Preparation of Neßler's reagent ^[11]	30
7.	IR spectroscopy	31
7.1.	General Information	31
7.2.	Measurements in the solid state	32
7.3.	Time-dependent FTIR spectroscopy of 1 and ethanol in DMSO-d_6	33
7.4.	Measurement of adsorbed gases	34
7.5.	Reference spectra	36

7.6.	Spectra of the reaction of 1 in acetonitrile	40
8.	EPR Spectroscopy	46
8.1.	General Information	46
8.2.	Discussion of data for 1 and 2	46
8.3.	Data for 1	46
8.4.	Data for 2	48
9.	Theoretical calculations	49
9.1.	General information	49
9.2.	Structure Optimization	49
9.3.	Transition density	53
9.4.	Mulliken charges	54
9.4.1.	Mulliken charge of 1	54
9.4.2.	Mulliken charge of 2	54
9.5.	Molecular electrostatic potential	55
9.6.	Calculated UV/Vis spectra	56
9.7.	Electronic states and the magnetic anisotropy	60
10.	Literature	65

1. Single Crystal X-Ray Diffraction

1.1. General Information

Single crystal X-ray diffraction studies were performed with suitable crystals of **1**, **2**, $[\text{Cu}(\text{CH}_3\text{CN})_4]\text{ClO}_4$, NH_4ClO_4 , and $[\text{Cu}(\text{neocuproine})_2]\text{ClO}_4$. A single crystal was mounted on a MiTeGen Dual Thickness MicroMount™ with Fomblin Y oil and transferred to a N_2 cold stream (100 K) by an OXFORD CRYOSYSTEMS 700 low temperature system. Data were collected at low temperatures (100 K) using φ - and ω -scans on a BRUKER D8 Venture system equipped with dual $\lambda\mu\text{S}$ microfocus sources and a PHOTON100 detector. Mo- K_α radiation with wavelength 0.71073 Å and a collimating Quazar multilayer mirror were used. Semi-empirical absorption corrections from equivalents were calculated with SADABS-2016/2.^[1] The space groups were determined using *XPREF*^[2,3] through analysis of the Laue symmetry and systematic absences. The structures were solved with *SHELXT*^[4] and refined by full-matrix least-squares based on F^2 using *SHELXL*^[5] and *SHELXle*^[6] as a graphical interface. All structures were checked for a higher symmetry using *PLATON*.^[7] All non-hydrogen atoms were located and refined anisotropically. Hydrogen atoms were assigned to idealized positions and given thermal parameters equal to either 1.5 (methyl hydrogen atoms and water hydrogen atoms) or 1.2 (non-methyl hydrogen atoms) times the thermal displacement parameters of the atoms to which they were attached. The positions of all OH- and NH-hydrogen atoms were taken from the Fourier synthesis. The bond distances were restrained to idealized distances. Disordered structures were refined by applying advanced Hirshfeld restraints to all atoms in the structures. Similarity restraints on 1,2 distances were used to model the disorder components. U_{ij} components of disordered atoms were restrained with similar ADP restraints. The cif files have been deposited with the Cambridge Structural Database (CSD). All determined parameters such as bond distances, U_{ij} components, etc. can be retrieved free of charge from the CSD (CCDC and CSD numbers: 2203267-2203270). General refinement and structure details for the structures are given below.

1.2. Crystal and Refinement Data of **1****Table S1.** Crystal data and structure refinement for **1**.

CCDC Number	2203267
Empirical formula	C ₁₄ H ₂₇ ClCu ₂ N ₆ O ₁₁
Formula weight	617.94
Temperature	100(2) K
Wavelength	0.71073 Å
Crystal system	Monoclinic
Space group	<i>P2₁/c</i>
Unit cell dimensions	a = 9.5238(6) Å α = 90° b = 22.4310(14) Å β = 92.606(2)° c = 21.2635(13) Å γ = 90°
Volume	4537.8(5) Å ³
Z	8
Density (calculated)	1.809 Mg/m ³
Absorption coefficient	2.061 mm ⁻¹
<i>F</i> (000)	2528
Crystal size	0.470 x 0.328 x 0.080 mm ³
Theta range for data collection	2.325 to 27.877°
Index ranges	12 ≤ h ≤ 12, -29 ≤ k ≤ 29, -27 ≤ l ≤ 27
Reflections collected	100381
Independent reflections	10812 [R(int) = 0.0855]
Completeness to theta = 25.242°	99.9 %
Absorption correction	Semi-empirical from equivalents
Refinement method	Full-matrix least-squares on <i>F</i> ²
Data / restraints / parameters	10812 / 3095 / 1170
Goodness-of-fit on <i>F</i> ²	1.137
Final R indices [I > 2σ(I)]	R1 = 0.0593, wR2 = 0.1012
R indices (all data)	R1 = 0.0923, wR2 = 0.1125
Largest diff. peak and hole	0.744 and -0.727 e.Å ⁻³

1 crystallizes in the monocline space group *P2₁/c* with two complex molecules and two ClO₄⁻ counter ions in the asymmetric unit. The complex molecules differ by the coordination of ethanol and thus, form a pair of isomers. In isomer **1a**, ethanol is bound to the copper center coordinated by an [N₃O] motif and in isomer **1b** to the copper center coordinated by an [N₂O₂] motif. Each isomer shows a whole molecule disorder, in which both disorder components of the complex fragment [Cu₂(H₂dmg)(Hdmg)(dmg)]⁺ are twisted by approximately 180 ° (Figure S1); however it was not possible to reliably link these disorder components to a specific disorder component of the coordinating ethanol molecule. So, for each isomer, the whole molecule disorder of the complex fragment was modeled across two positions. The highest occupied disorder components refined to appr. 76 % for **1a** and 89 % for **1b**. The disorder of the ethanol molecules were modeled across two positions as independent disorders. The occupancies of the highest occupied disorder components refined to approximately 71 % and 81 % for **1a** and **1b**, respectively.

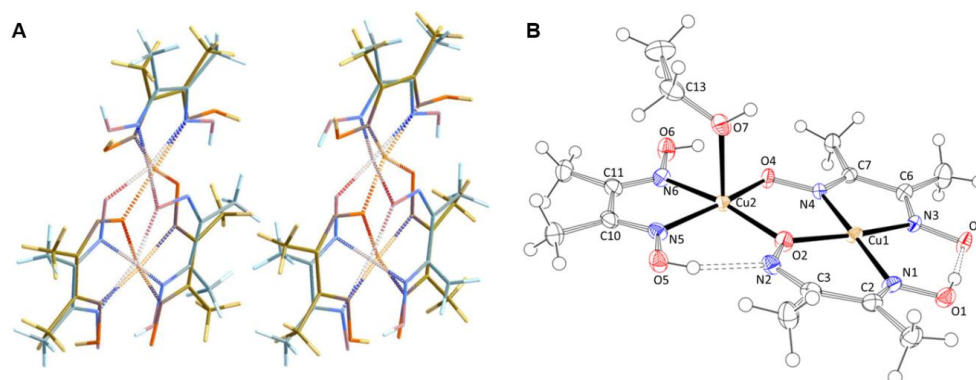


Figure S1 A: stick model representation of the two disordered complex fragments $[\text{Cu}_2(\text{H}_2\text{dmg})(\text{Hdmg})(\text{dmg})]^+$ of **1** in the asymmetric unit, counter ions and coordinating ethanol omitted for clarity. The highest occupied disorder component is highlighted in blue. **B:** molecular structure of **1b** (numbering is identical in **1a**), counter ion is omitted for clarity. Thermal ellipsoids set at 50 %.

Table S2. Corresponding atom numbering for both molecules in the asymmetric unit and their disorder components.

Figure S1 B	isomer 1b	isomer 1a	minor occupied disorder component of 1b	minor occupied disorder component of 1a
Cu1	Cu11	Cu12	Cu1A1	Cu1A2
Cu2	Cu21	Cu22	Cu2A1	Cu2A2
O1	O11	O12	O1A1	O1A2
O2	O21	O22	O2A1	O2A2
O3	O31	O32	O3A1	O3A2
O4	O41	O42	O4A1	O4A2
O5	O51	O52	O5A1	O5A2
O6	O61	O62	O6A1	O6A2
O7	O71	O72	O7A1	O7A2
N1	N11	N12	N1A1	N1A2
N2	N21	N22	N4A1	N4A2
N3	N31	N32	N3A1	N3A2
N4	N41	N42	N2A1	N2A2
N5	N51	N52	N5A1	N5A2
N6	N61	N62	N6A1	N6A2
C2	C21	C22	C2A1	C2A2
C3	C31	C32	/	/
C6	C61	C62	C6A1	C6A2
C7	C71	C72	/	/
C10	C101	C102	C10A1	C10A2
C11	C111	C112	C11A1	C11A2
C13	C131	C132	C13A1	C13A2

Table S3. Selected bond lengths for **1**. For assignment of atoms to specific isomers and disorder components see Table S2.

bond	bond length / Å	bond	bond length / Å
Cu11-O21	1.903(3)	Cu12-N12	1.937(6)
Cu11-N11	1.935(4)	Cu12-N42	1.968(5)
Cu11-N31	1.960(4)	Cu12-N32	1.982(8)
Cu11-N41	1.963(4)	Cu12-O72	2.31(2)
Cu11-O101	2.419(3)	Cu22-O42	1.889(4)
Cu21-O41	1.905(4)	Cu22-O22	1.948(4)
Cu21-O21	1.952(3)	Cu22-N52	1.977(9)
Cu21-N51	1.993(4)	Cu22-N62	1.992(5)
Cu21-N61	1.998(4)	Cu22-O112	2.371(3)
Cu21-O71	2.252(11)	Cu12-N12	1.937(6)
O101-Cu1A1	2.375(10)	O112-Cu2A2	2.413(7)
Cu1A1-O4A1	1.90(2)	Cu1A2-N3A2	1.83(3)
Cu1A1-N1A1	1.91(3)	Cu1A2-N1A2	1.925(19)

S3

Cu1A1-N3A1	1.92(3)	Cu1A2-O4A2	1.937(14)
Cu1A1-N2A1	1.96(3)	Cu1A2-N2A2	1.989(18)
Cu2A1-O2A1	1.80(3)	Cu1A2-O7A2	2.31(6)
Cu2A1-O4A1	1.96(2)	Cu2A2-O2A2	1.813(17)
Cu2A1-N5A1	1.96(4)	Cu2A2-N5A2	1.91(3)
Cu2A1-N6A1	2.02(3)	Cu2A2-O4A2	1.924(13)
Cu2A1-O7A1	2.29(4)	Cu2A2-N6A2	1.960(17)

Table S4. Selected bond angles **1**. For assignment of atoms to specific isomers and disorder components see Table S2.

angle	angle / °	angle	angle / °
C21-N11-Cu11	125.9(4)	O22-Cu12-N12	93.4(2)
O11-N11-Cu11	116.7(3)	O22-Cu12-N42	87.6(2)
N21-O21-Cu11	126.9(3)	N12-Cu12-N42	172.8(3)
N21-O21-Cu21	113.4(3)	O22-Cu12-N32	164.4(4)
Cu11-O21-Cu21	118.89(16)	N12-Cu12-N32	97.8(3)
O21-Cu11-N11	93.54(17)	N42-Cu12-N32	80.0(3)
O21-Cu11-N31	167.43(18)	O22-Cu12-O72	94.8(6)
N11-Cu11-N31	98.29(19)	N12-Cu12-O72	96.9(5)
O21-Cu11-N41	87.81(16)	N42-Cu12-O72	90.1(5)
N11-Cu11-N41	176.6(2)	N32-Cu12-O72	94.5(7)
N31-Cu11-N41	80.14(17)	O42-Cu22-O22	92.37(18)
O21-Cu11-O101	98.40(13)	O42-Cu22-N52	163.6(4)
N11-Cu11-O101	87.57(18)	O22-Cu22-N52	102.5(3)
N31-Cu11-O101	86.37(19)	O42-Cu22-N62	87.01(19)
N41-Cu11-O101	95.32(13)	O22-Cu22-N62	176.9(2)
O41-Cu21-O21	92.13(14)	N52-Cu22-N62	77.8(3)
O41-Cu21-N51	163.51(19)	O42-Cu22-O112	100.48(16)
O21-Cu21-N51	100.92(18)	O22-Cu22-O112	82.90(14)
O41-Cu21-N61	87.66(16)	N52-Cu22-O112	88.3(9)
O21-Cu21-N61	169.17(19)	N62-Cu22-O112	100.2(2)
N51-Cu21-N61	77.62(19)	N22-O22-Cu12	127.8(4)
O41-Cu21-O71	99.6(3)	N22-O22-Cu22	112.7(3)
O21-Cu21-O71	98.3(2)	Cu12-O22-Cu22	117.5(2)
N51-Cu21-O71	88.6(3)	C22-N12-Cu12	126.9(5)
N61-Cu21-O71	92.4(2)	O12-N12-Cu12	116.8(4)
N41-O41-Cu21	116.3(3)	N42-O42-Cu22	115.9(3)
C61-N31-Cu11	116.4(3)	C62-N32-Cu12	115.8(4)
O31-N31-Cu11	124.1(4)	O32-N32-Cu12	123.7(7)
C71-N41-Cu11	115.7(3)	C72-N42-Cu12	115.8(4)
O41-N41-Cu11	124.8(3)	O42-N42-Cu12	123.9(3)
C101-N51-Cu21	117.5(4)	C102-N52-Cu22	118.1(5)
O51-N51-Cu21	125.5(3)	O52-N52-Cu22	125.4(7)
C111-N61-Cu21	118.4(4)	C112-N62-Cu22	117.8(4)
O61-N61-Cu21	125.4(3)	O62-N62-Cu22	124.3(4)
Cl11-O101-Cu1A1	128.1(3)	Cl12-O112-Cu22	131.27(18)
Cl11-O101-Cu11	136.95(18)	Cl12-O112-Cu2A2	134.8(2)
C131-O71-Cu21	127.2(5)	C132-O72-Cu12	135.2(13)
Cu21-O71-HO71	123.3	Cu12-O72-HO72	111.9
O4A1-Cu1A1-N1A1	166.9(14)	N3A2-Cu1A2-N1A2	100.6(10)
O4A1-Cu1A1-N3A1	94.2(12)	N3A2-Cu1A2-O4A2	94.5(9)
N1A1-Cu1A1-N3A1	96.9(14)	N1A2-Cu1A2-O4A2	163.7(9)
O4A1-Cu1A1-N2A1	85.2(10)	N3A2-Cu1A2-N2A2	173.6(16)
N1A1-Cu1A1-N2A1	83.2(11)	N1A2-Cu1A2-N2A2	81.5(7)
N3A1-Cu1A1-N2A1	176(2)	O4A2-Cu1A2-N2A2	82.8(6)
O4A1-Cu1A1-O101	94.2(8)	N3A2-Cu1A2-O7A2	92(2)
N1A1-Cu1A1-O101	94.0(17)	N1A2-Cu1A2-O7A2	95.8(14)
N3A1-Cu1A1-O101	84.1(18)	O4A2-Cu1A2-O7A2	89.7(13)
N2A1-Cu1A1-O101	100.3(10)	N2A2-Cu1A2-O7A2	94.2(16)
O2A1-Cu2A1-O4A1	92.0(11)	O2A2-Cu2A2-N5A2	84.4(9)
O2A1-Cu2A1-N5A1	85.4(13)	O2A2-Cu2A2-O4A2	91.0(6)
O4A1-Cu2A1-N5A1	167(2)	N5A2-Cu2A2-O4A2	174.9(16)
O2A1-Cu2A1-N6A1	161.7(14)	O2A2-Cu2A2-N6A2	162.8(8)
O4A1-Cu2A1-N6A1	103.7(11)	N5A2-Cu2A2-N6A2	79.6(8)
N5A1-Cu2A1-N6A1	77.2(13)	O4A2-Cu2A2-N6A2	104.8(6)
O2A1-Cu2A1-O7A1	98.4(16)	O2A2-Cu2A2-O112	95.6(6)
O4A1-Cu2A1-O7A1	89.7(14)	N5A2-Cu2A2-O112	91(3)
N5A1-Cu2A1-O7A1	103(2)	O4A2-Cu2A2-O112	91.2(4)
N6A1-Cu2A1-O7A1	91.0(18)	N6A2-Cu2A2-O112	91.0(7)
N2A1-O2A1-Cu2A1	118(2)	N2A2-O2A2-Cu2A2	116.2(12)
C2A1-N1A1-Cu1A1	113.8(18)	C2A2-N1A2-Cu1A2	116.5(13)
O1A1-N1A1-Cu1A1	129(3)	O1A2-N1A2-Cu1A2	124.4(15)

C3A1-N2A1-Cu1A1	112.3(16)	C3A2-N2A2-Cu1A2	112.8(11)
O2A1-N2A1-Cu1A1	125(2)	O2A2-N2A2-Cu1A2	125.4(11)
N4A1-O4A1-Cu1A1	125.7(18)	N4A2-O4A2-Cu2A2	110.5(10)
N4A1-O4A1-Cu2A1	114.3(17)	N4A2-O4A2-Cu1A2	126.0(12)
Cu1A1-O4A1-Cu2A1	119.9(11)	Cu2A2-O4A2-Cu1A2	120.4(7)
C6A1-N3A1-Cu1A1	127(2)	C6A2-N3A2-Cu1A2	127.5(16)
O3A1-N3A1-Cu1A1	119(3)	O3A2-N3A2-Cu1A2	116(2)
N4A1-O4A1-Cu1A1	125.7(18)	C10A2-N5A2-Cu2A2	118.2(15)
C10A1-N5A1-Cu2A1	119.9(18)	O5A2-N5A2-Cu2A2	126(2)
O5A1-N5A1-Cu2A1	124(3)	C11A2-N6A2-Cu2A2	117.3(11)
C11A1-N6A1-Cu2A1	117(2)	O6A2-N6A2-Cu2A2	125.3(12)
O6A1-N6A1-Cu2A1	126(2)	C13A2-O7A2-Cu1A2	131(4)
C13A1-O7A1-Cu2A1	124(3)	Cu1A2-O7A2-HO7A2	91.6
Cu2A1-O7A1-HO7A1	24.2		

1.3. Crystal and Refinement Data of **2****Table S5.** Crystal data and structure refinement for **2**.

CCDC Number	2203268
Empirical formula	C ₈ H ₁₄ CuN ₄ O ₄
Formula weight	293.77
Temperature	100(2) K
Wavelength	0.71073 Å
Crystal system	Monoclinic
Space group	<i>P2₁/n</i>
Unit cell dimensions	a = 7.0694(8) Å α = 90° b = 16.865(2) Å β = 108.663(4)° c = 9.7340(12) Å γ = 90°
Volume	1099.5(2) Å ³
Z	4
Density (calculated)	1.775 Mg/m ³
Absorption coefficient	1.997 mm ⁻¹
F(000)	604
Crystal size	0.273 x 0.093 x 0.053 mm ³
Theta range for data collection	2.415 to 27.483°
Index ranges	9<=h<=8, -21<=k<=21, -12<=l<=12
Reflections collected	48024
Independent reflections	2521 [R(int) = 0.1058]
Completeness to theta = 25.242°	100.0 %
Absorption correction	Semi-empirical from equivalents
Refinement method	Full-matrix least-squares on F ²
Data / restraints / parameters	2521 / 2 / 164
Goodness-of-fit on F ²	1.049
Final R indices [I>2σ(I)]	R1 = 0.0318, wR2 = 0.0732
R indices (all data)	R1 = 0.0457, wR2 = 0.0792
Largest diff. peak and hole	0.479 and -0.574 e.Å ⁻³

2 crystallizes in the monoclinic space group *P2₁/n* with one molecule in the asymmetric unit. The copper center is coordinated by two Hdmg⁻ ligands forming a pseudo-macrocycle via hydrogen bonding (Figure S2).

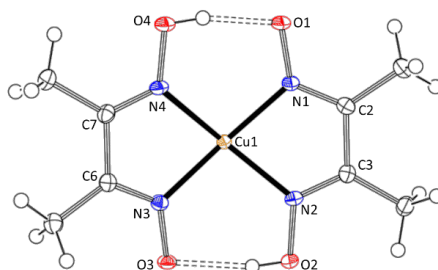
**Figure S2** Molecular structure of **2**. Thermal ellipsoids set at 50 %.

Table S6. Selected bond lengths for **2**.

bond	bond length / Å	bond	bond length / Å
Cu(1)-N(3)	1.9462(19)	Cu(1)-N(2)	1.954(2)
Cu(1)-N(1)	1.9520(19)	Cu(1)-N(4)	1.967(2)

Table S7. Selected bond angles for **2**.

angle	angle / °	angle	angle / °
N(3)-Cu(1)-N(1)	165.57(8)	N(1)-O(1)-Cu(1)#1	101.21(12)
N(3)-Cu(1)-N(2)	95.97(8)	C(2)-N(1)-Cu(1)	115.59(16)
N(1)-Cu(1)-N(2)	80.75(8)	O(1)-N(1)-Cu(1)	122.94(14)
N(3)-Cu(1)-N(4)	80.38(8)	C(3)-N(2)-Cu(1)	115.93(16)
N(1)-Cu(1)-N(4)	97.54(8)	O(2)-N(2)-Cu(1)	123.48(14)
N(2)-Cu(1)-N(4)	158.67(9)	C(6)-N(3)-Cu(1)	116.07(16)
N(3)-Cu(1)-O(1)#1	102.22(7)	O(3)-N(3)-Cu(1)	122.39(14)
N(1)-Cu(1)-O(1)#1	92.21(7)	C(7)-N(4)-Cu(1)	116.00(16)
N(2)-Cu(1)-O(1)#1	103.23(7)	O(4)-N(4)-Cu(1)	124.88(14)
N(4)-Cu(1)-O(1)#1	98.08(7)		

1.4. Crystal and Refinement Data of $[\text{Cu}(\text{CH}_3\text{CN})_4]\text{ClO}_4$ **Table S8.** Crystal data and structure refinement for $[\text{Cu}(\text{CH}_3\text{CN})_4]\text{ClO}_4$.

CCDC number	2203269
Empirical formula	$\text{C}_8\text{H}_{12}\text{ClCuN}_4\text{O}_4$
Formula weight	327.21
Temperature	100(2) K
Wavelength	0.71073 Å
Crystal system	Orthorhombic
Space group	$Pna2_1$
Unit cell dimensions	$a = 23.7835(17)$ Å $\alpha = 90^\circ$ $b = 8.3209(6)$ Å $\beta = 90^\circ$ $c = 20.3339(14)$ Å $\gamma = 90^\circ$
Volume	$4024.1(5)$ Å ³
Z	12
Density (calculated)	1.620 Mg/m ³
Absorption coefficient	1.839 mm ⁻¹
$F(000)$	1992
Crystal size	$0.887 \times 0.205 \times 0.166$ mm ³
Theta range for data collection	1.712 to 29.129°
Index ranges	$-32 \leq h \leq 32$, $-11 \leq k \leq 11$, $-27 \leq l \leq 27$
Reflections collected	121386
Independent reflections	10848 [R(int) = 0.1294]
Completeness to theta = 25.242°	100.0 %
Absorption correction	Semi-empirical from equivalents
Max. and min. transmission	0.7461 and 0.4679
Refinement method	Full-matrix least-squares on F^2
Data / restraints / parameters	10848 / 1 / 501
Goodness-of-fit on F^2	1.014
Final R indices [$I > 2\sigma(I)$]	R1 = 0.0429, wR2 = 0.0850
R indices (all data)	R1 = 0.0715, wR2 = 0.0964
Absolute structure parameter	0.414(15)
Extinction coefficient	0.00081(9)
Largest diff. peak and hole	0.769 and -0.809 e.Å ⁻³

$[\text{Cu}(\text{CH}_3\text{CN})_4]\text{ClO}_4$ crystallizes in the orthorhombic space group $Pna2_1$ with three complex and three ClO_4^- molecules in the asymmetric unit. Copper is tetrahedrally coordinated by four acetonitrile molecules (Figure S3).

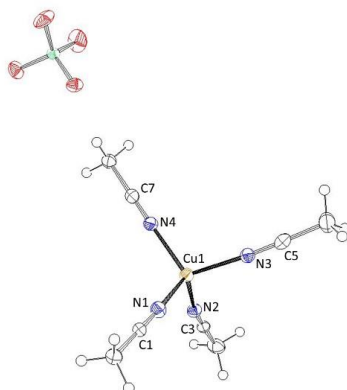


Figure S3. Molecular structure of $[\text{Cu}(\text{CH}_3\text{CN})_4]\text{ClO}_4$. Thermal ellipsoids are set to 50 % probability.

Table S9. Selected bond lengths for $[\text{Cu}(\text{CH}_3\text{CN})_4]\text{ClO}_4$.

bond	bond length / Å	bond	bond length / Å
Cu(1)-N(1)	1.976(5)	Cu(2)-N(7)	1.984(5)
Cu(1)-N(3)	1.997(5)	Cu(2)-N(5)	2.001(4)
Cu(1)-N(4)	2.002(4)	Cu(3)-N(9)	1.977(5)
Cu(1)-N(2)	2.014(5)	Cu(3)-N(11)	1.992(4)
Cu(2)-N(8)	1.978(5)	Cu(3)-N(12)	2.008(5)
Cu(2)-N(6)	1.980(4)	Cu(3)-N(10)	2.010(4)

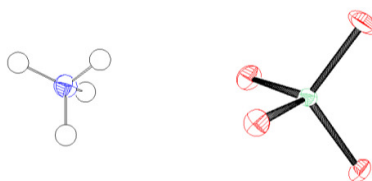
Table S10. Selected bond angles for $[\text{Cu}(\text{CH}_3\text{CN})_4]\text{ClO}_4$.

angle	angle / °	angle	angle / °
N(1)-Cu(1)-N(3)	110.4(2)	N(9)-Cu(3)-N(10)	109.03(19)
N(1)-Cu(1)-N(4)	111.52(18)	N(11)-Cu(3)-N(10)	108.63(17)
N(3)-Cu(1)-N(4)	110.17(19)	N(12)-Cu(3)-N(10)	105.06(18)
N(1)-Cu(1)-N(2)	112.4(2)	C(1)-N(1)-Cu(1)	177.4(5)
N(3)-Cu(1)-N(2)	105.41(18)	C(3)-N(2)-Cu(1)	170.7(5)
N(4)-Cu(1)-N(2)	106.69(19)	C(5)-N(3)-Cu(1)	175.1(5)
N(8)-Cu(2)-N(6)	111.6(2)	C(7)-N(4)-Cu(1)	174.0(4)
N(8)-Cu(2)-N(7)	111.37(16)	C(9)-N(5)-Cu(2)	179.2(6)
N(6)-Cu(2)-N(7)	109.2(2)	C(11)-N(6)-Cu(2)	170.8(4)
N(8)-Cu(2)-N(5)	108.8(2)	C(13)-N(7)-Cu(2)	171.7(5)
N(6)-Cu(2)-N(5)	107.91(16)	C(15)-N(8)-Cu(2)	172.4(5)
N(7)-Cu(2)-N(5)	107.8(2)	C(17)-N(9)-Cu(3)	178.6(6)
N(9)-Cu(3)-N(11)	112.6(2)	C(19)-N(10)-Cu(3)	173.4(5)
N(9)-Cu(3)-N(12)	110.67(19)	C(21)-N(11)-Cu(3)	174.0(5)
N(11)-Cu(3)-N(12)	110.50(18)	C(23)-N(12)-Cu(3)	174.0(4)

1.5. Crystal and Refinement Data of NH_4ClO_4 **Table S11.** Crystal data and structure refinement for NH_4ClO_4 .

Empirical formula	ClH_4NO_4
Formula weight	116.48
Temperature	100(2) K
Wavelength	0.71073 Å
Crystal system	Orthorhombic
Space group	<i>Pnma</i>
Unit cell dimensions	$a = 9.0691(3)$ Å $\alpha = 90^\circ$ $b = 5.7911(2)$ Å $\beta = 90^\circ$ $c = 7.3466(2)$ Å $\gamma = 90^\circ$
Volume	$385.84(2)$ Å ³
Z	4
Density (calculated)	2.005 Mg/m ³
Absorption coefficient	0.860 mm ⁻¹
<i>F</i> (000)	236
Crystal size	0.228 x 0.110 x 0.089 mm ³
Theta range for data collection	3.569 to 45.288°
Index ranges	-18 ≤ <i>h</i> ≤ 18, -11 ≤ <i>k</i> ≤ 11, -14 ≤ <i>l</i> ≤ 14
Reflections collected	72729
Independent reflections	1719 [R(int) = 0.0407]
Completeness to theta = 25.242°	99.5 %
Absorption correction	Semi-empirical from equivalents
Refinement method	Full-matrix least-squares on <i>F</i> ²
Data / restraints / parameters	1719 / 3 / 42
Goodness-of-fit on <i>F</i> ²	1.131
Final R indices [<i>I</i> > 2σ(<i>I</i>)]	R1 = 0.0228, wR2 = 0.0640
R indices (all data)	R1 = 0.0261, wR2 = 0.0654
Extinction coefficient	0.100(6)
Largest diff. peak and hole	0.580 and -0.728 e.Å ⁻³

NH_4ClO_4 crystallizes in the orthorhombic space group *Pnma* with one molecule in the asymmetric unit (Figure S4).

**Figure S4.** Molecular structure of NH_4ClO_4 . Thermal ellipsoids are set to 50 % probability.

1.6. Crystal and Refinement Data of [Cu(neocuproine)₂]ClO₄**Table S12.** Crystal data and structure refinement for [Cu(neocuproine)₂]ClO₄.

CCDC number	2203270
Empirical formula	C ₂₈ H ₂₄ ClCuN ₄ O ₄
Formula weight	579.50
Temperature	100(2) K
Wavelength	0.71073 Å
Crystal system	Monoclinic
Space group	<i>P2₁/n</i>
Unit cell dimensions	a = 13.4114(11) Å α = 90° b = 10.7218(8) Å β = 95.268(3)° c = 17.6702(14) Å γ = 90°
Volume	2530.1(3) Å ³
Z	4
Density (calculated)	1.521 Mg/m ³
Absorption coefficient	1.012 mm ⁻¹
<i>F</i> (000)	1192
Crystal size	0.203 x 0.183 x 0.165 mm ³
Theta range for data collection	2.224 to 30.507°
Index ranges	-19 ≤ <i>h</i> ≤ 19, -15 ≤ <i>k</i> ≤ 15, -25 ≤ <i>l</i> ≤ 25
Reflections collected	317741
Independent reflections	7737 [R(int) = 0.0585]
Completeness to theta = 25.242°	99.9 %
Absorption correction	Semi-empirical from equivalents
Refinement method	Full-matrix least-squares on <i>F</i> ²
Data / restraints / parameters	7737 / 0 / 348
Goodness-of-fit on <i>F</i> ²	1.034
Final R indices [<i>I</i> > 2σ(<i>I</i>)]	R1 = 0.0380, wR2 = 0.1007
R indices (all data)	R1 = 0.0470, wR2 = 0.1064
Extinction coefficient	0.0032(4)
Largest diff. peak and hole	0.650 and -0.687 e.Å ⁻³

[Cu(neocuproine)₂]ClO₄ crystallizes in the monoclinic space group *P2₁/n* with one complex molecule and one ClO₄⁻ counter ion in the asymmetric unit. The copper center is tetrahedral coordinated by the nitrogen atoms of the phenanthroline unit of the neocuproine molecule (Figure S5).

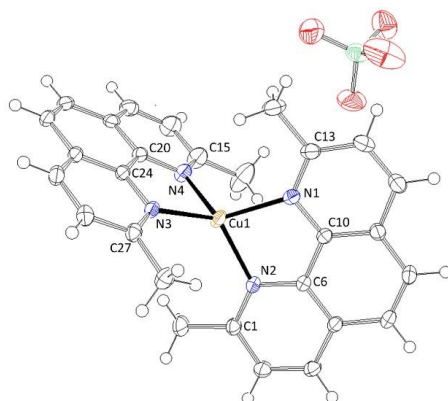


Figure S5. Molecular structure of $[\text{Cu}(\text{neocuproine})_2]\text{ClO}_4$. Thermal ellipsoids are set to 50 % probability.

Table S13. Selected bond lengths for $[\text{Cu}(\text{neocuproine})_2]\text{ClO}_4$.

bond	bond length / Å	bond	bond length / Å
Cu(1)-N(2)	2.0328(13)	Cu(1)-N(3)	2.0561(13)
Cu(1)-N(4)	2.0414(14)	Cu(1)-N(1)	2.0725(14)

Table S14. Selected bond angles for $[\text{Cu}(\text{neocuproine})_2]\text{ClO}_4$.

angle	angle / °	angle	angle / °
N(2)-Cu(1)-N(3)	125.56(5)	C(1)-N(2)-Cu(1)	128.89(11)
N(4)-Cu(1)-N(3)	81.82(5)	C(6)-N(2)-Cu(1)	112.28(10)
N(2)-Cu(1)-N(1)	81.90(5)	C(27)-N(3)-Cu(1)	130.81(11)
N(4)-Cu(1)-N(1)	115.11(6)	C(24)-N(3)-Cu(1)	111.01(10)
N(3)-Cu(1)-N(1)	128.02(5)	C(15)-N(4)-Cu(1)	129.56(12)
N(2)-Cu(1)-N(4)	130.40(6)	C(20)-N(4)-Cu(1)	111.95(11)
C(13)-N(1)-Cu(1)	130.82(11)	C(10)-N(1)-Cu(1)	111.28(10)

2. UV/Vis spectroscopy

2.1. General Information

All samples were measured on an Agilent Cary 60 spectrometer. The samples were measured in methanol, ethanol or acetonitrile. For measurement in solution, a quartz glass cuvette of a 1 cm diameter was used. The measurement was performed at room temperature.

2.2. Spectrum of **1** in methanol

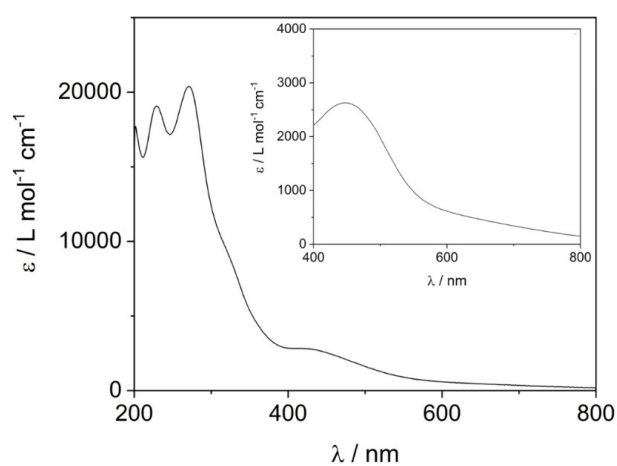


Figure S6: UV/Vis spectrum of **1** in methanol ($c = 3.56 \cdot 10^{-5}$ M). The inset shows a measurement of **1** in methanol with higher concentration ($c = 1.94 \cdot 10^{-4}$ M).

Table S15: Observed UV/Vis absorption bands and suggested transitions of **1**. Transition assignments are based on TD-DFT calculations (see Section 9.6).

UV/Vis absorption band / nm	$\epsilon / \text{L mol}^{-1} \text{cm}^{-1}$	assigned transition
229	17,744	LC
271	19,722	LC
435	2,471	MLCT
633	239	MLCT

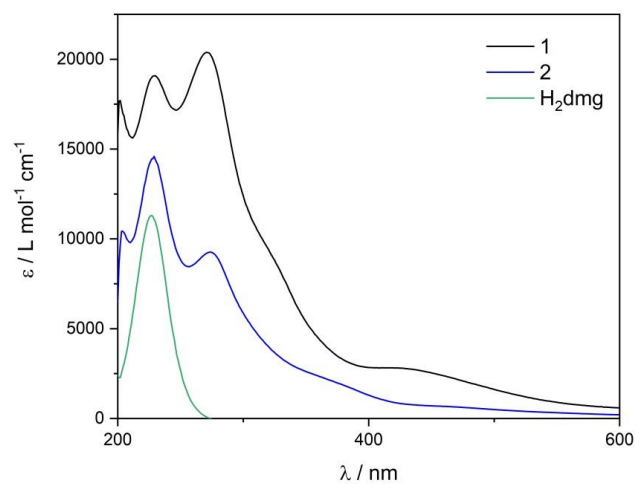
2.3. Spectra of **1**, **2**, and H₂dmg

Figure S7. UV/Vis spectra of **1** ($c = 3.56 \cdot 10^{-5}$ M, black), **2** ($c = 1.85 \cdot 10^{-4}$ M, blue), and H₂dmg ($c = 6.03 \cdot 10^{-5}$ M, green) in methanol.

Table S16: Observed UV/Vis absorption bands and suggested transitions of **2**. Transition assignments are based on TD-DFT calculations (see Section 9.6).

UV/Vis absorption band / nm	$\epsilon / \text{L mol}^{-1} \text{cm}^{-1}$	assigned transition
228	14,474	LC
275	9,244	LC
379	1,854	MLCT

Table S17: Observed UV/Vis absorption bands and suggested transitions of H₂dmg. Transition assignments are based on TD-DFT calculations (see Section 9.6).

UV/Vis absorption band / nm	$\epsilon / \text{L mol}^{-1} \text{cm}^{-1}$	assigned transition
227	11,302	LC

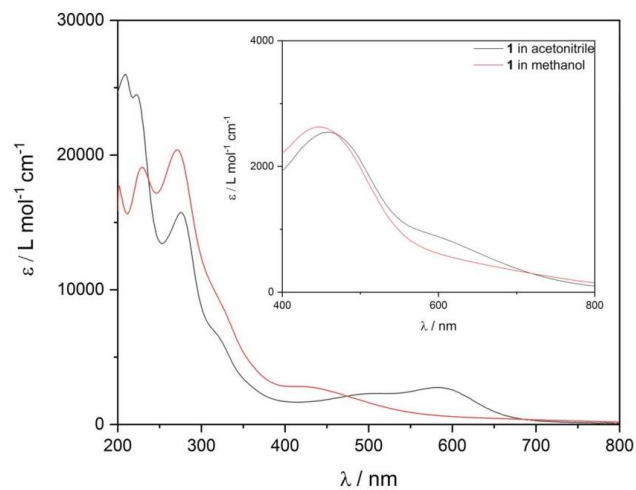
2.4. Spectra of **1** in different solvents

Figure S8. UV/vis spectrum of **1** in methanol ($c = 3.56 \cdot 10^{-5} \text{ M}$, red) and in acetonitrile ($c = 1.94 \cdot 10^{-5} \text{ M}$, black). The inset shows a measurement of **1** in methanol and acetonitrile with higher concentration ($c = 1.94 \cdot 10^{-4} \text{ M}$, $c = 7.93 \cdot 10^{-4} \text{ M}$, black). The differences in the spectra of low and high concentration samples in CH_3CN are caused by the already beginning decomposition of **1** in the low concentration sample.

2.5. Time-dependent measurements of **1** in ethanol

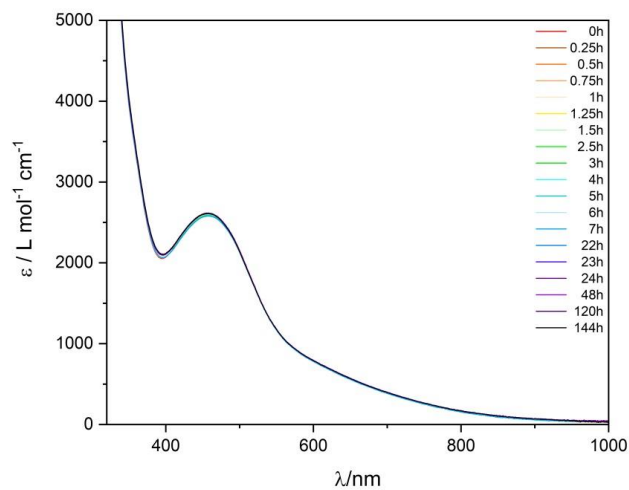


Figure S9. Time-dependent UV/Vis spectra of **1** ($c = 1.84 \cdot 10^{-4} \text{ M}$) in ethanol over 144 h.

2.6. Temperature-dependent measurements of **1** in methanol

Ruiz *et al.*^[8,9] present UV/Vis data for isomer I and II, which are in a pH-dependent equilibrium. Based on their spectroscopic data, we can assign our experimental data to isomer I; however, we could not observe a significant alteration in the spectroscopic signature of isomer I (e.g. indicating formation of isomer II) during the temperature-depending measurements. With increasing temperature, the absorption bands decrease (Figure S10). We assume that this decrease is either caused by concentration differences due to expansion of the solvent at higher temperatures or by the decomposition of the complex with increasing temperature.

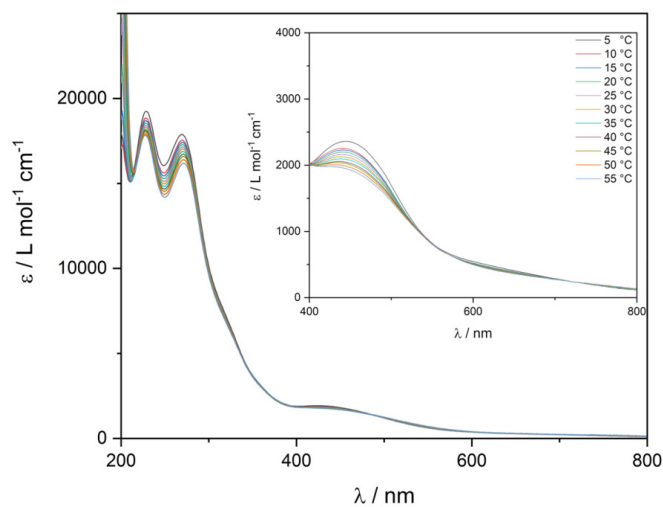


Figure S10. Temperature-dependent UV/Vis spectra of **1** ($c = 5.71 \cdot 10^{-5} \text{ M}$) in methanol. The inset shows the spectra of a higher concentrated solution ($c = 2.27 \cdot 10^{-4} \text{ M}$).

3. ESI mass spectrometry

3.1. General Information

The measurements were performed on a Bruker AmaZon SL device. Simulations were performed using enviPat.^[10] Characterization of **1** in methanol via ESI mass spectrometry yielded an intense signal at a mass to charge ratio of 471, which corresponds to the complex cation $[\text{Cu}_2(\text{dmg})(\text{Hdmg})(\text{H}_2\text{dmg})]^+$. Usage of different solvents such as ethanol or CH_3CN led to additional signals that indicate the decomposition of the complex. Caused by the neutral charge of **2**, the ESI mass spectrum of **2** only shows a signal of weak intensity at a mass to charge ratio of 294, which corresponds to $[\mathbf{2}+\text{H}]^+$. Additionally, the signal for **1** at $m/z = 471$ was observed. At this point, it was unclear if this finding mirrors a chemical equilibrium of **1** and **2**, or if small portions of **1** were formed during the ionization process of **2**. Notably, the signal of $[\mathbf{2}+\text{H}]^+$ is observed to a minor amount in the mass spectrum of **1**, as well

3.2. ESI mass spectrum of **1** in methanol

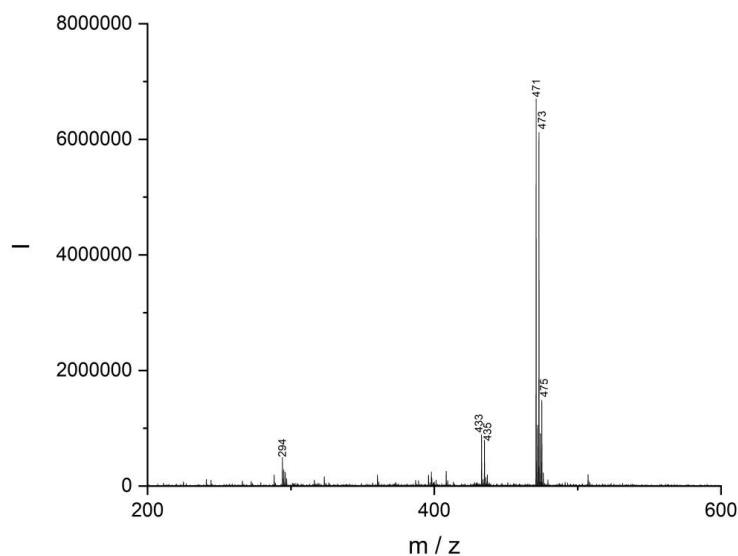


Figure S11. ESI mass spectrum of **1** (positive mode, overview, sprayed in methanol).

Table S18. ESI-MS signals (m/z) and fragments assigned.

m/z	fragment	exact mass of fragment (calculated)
294	$[\text{Cu}(\text{Hdmg})_2]+\text{H}^+$	294.04
471	$[\text{Cu}_2(\text{dmg})(\text{Hdmg})(\text{H}_2\text{dmg})]^+$	471.01

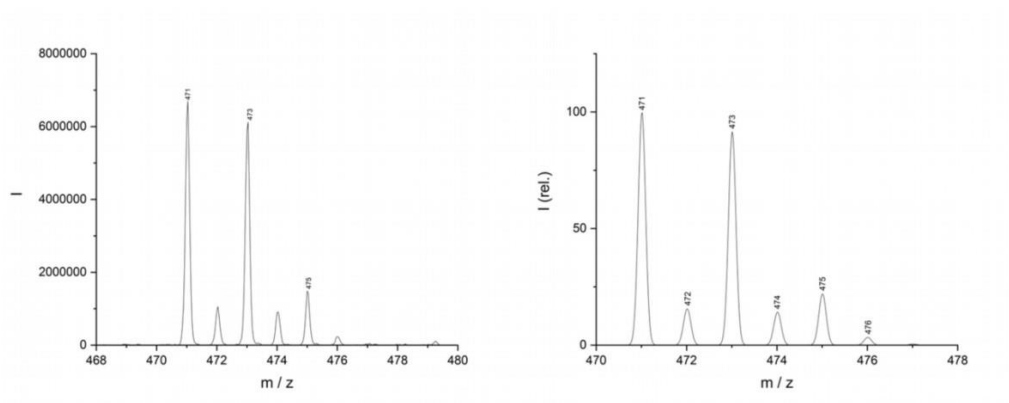


Figure S12. ESI mass spectrum of **1** (sprayed in methanol). Isolation of signal at $m/z = 471$ (left) and simulation of $[\text{Cu}_2(\text{dmg})(\text{Hdmg})(\text{H}_2\text{dmg})]^+$ (enviPat¹⁰; right).

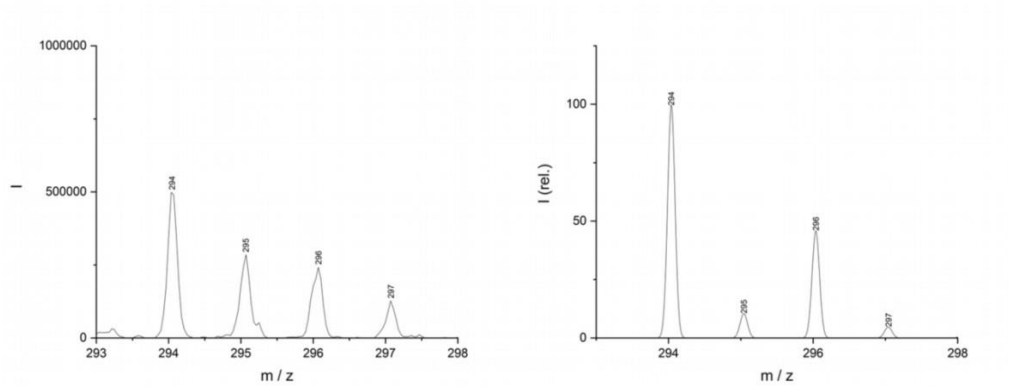


Figure S13. ESI mass spectrum of **1** (sprayed in methanol). Isolation of the signal at $m/z = 294$ (left) and simulation of $[\text{Cu}(\text{Hdmg})_2] + \text{H}^+$ (enviPat¹⁰; right).

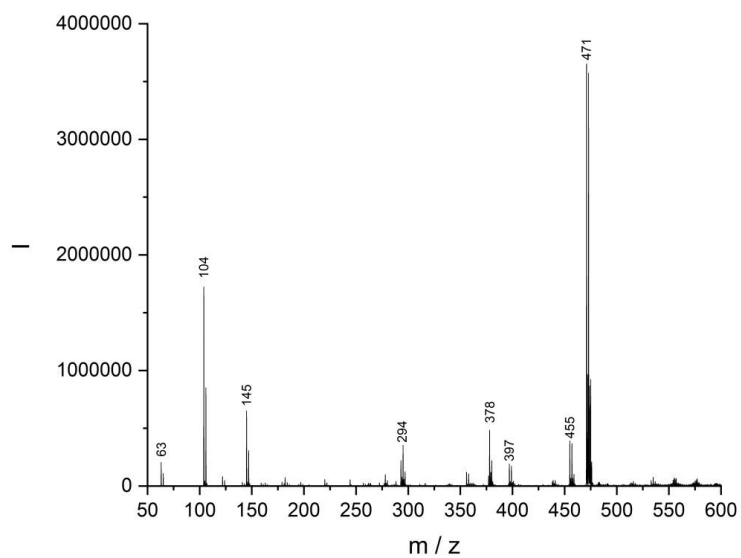
3.3. ESI mass spectrum of **1** in acetonitrile

Figure S14. ESI mass spectrum of **1** direct after dissolving in acetonitrile (positive mode, overview, sprayed in acetonitrile).

Table S19. ESI-MS signals (m/z) and fragments assigned.

m/z	fragment	exact mass of fragment (calculated)
63	Cu ⁺	62.93
104	[Cu(CH ₃ CN)] ⁺	103.96
145	[Cu(CH ₃ CN) ₂] ⁺	144.98
294	[Cu(Hdmg) ₂] ⁺ H ⁺	294.04
471	[Cu ₂ (dmg)(Hdmg)(H ₂ dmg)] ⁺	471.01

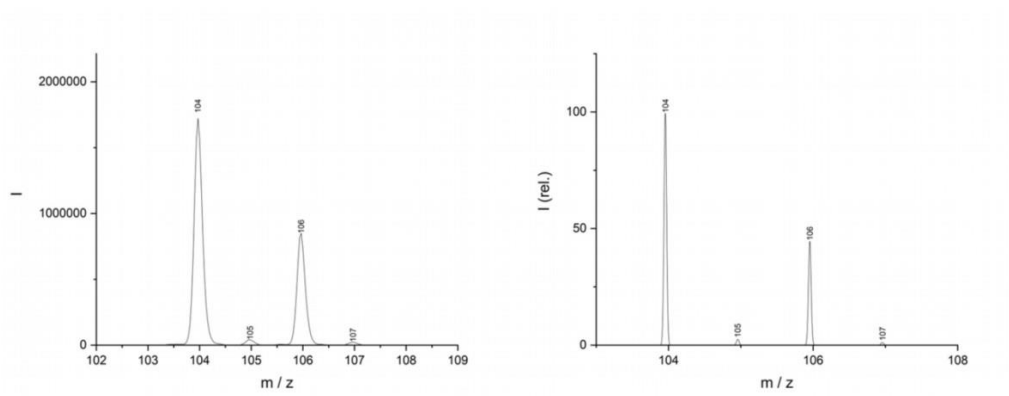


Figure S15. ESI mass spectrum of **1** (sprayed in acetonitrile). Isolation of the signal at $m/z = 104$ (left) and simulation of $[\text{Cu}(\text{CH}_3\text{CN})]^+$ (enviPat¹⁰, right).

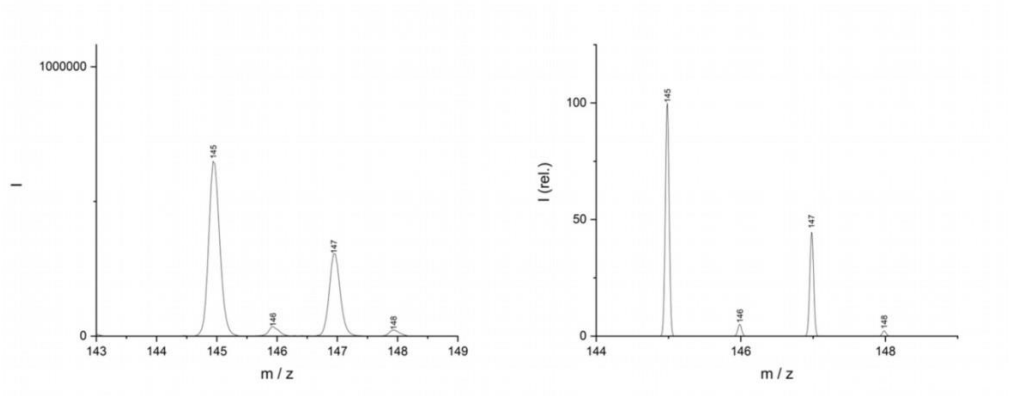


Figure S16. ESI mass spectrum of **1** (sprayed in acetonitrile). Isolation of the signal at $m/z = 145$ (left) and simulation of $[\text{Cu}(\text{CH}_3\text{CN})]^+$ (enviPat¹⁰, right).

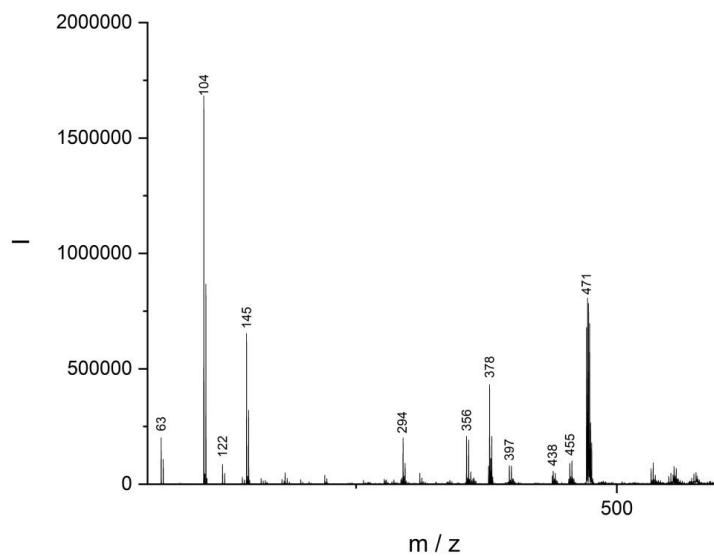


Figure S17. ESI mass spectrum of 1 24 h after dissolving in acetonitrile (positive mode, overview, sprayed in acetonitrile).

Table S20. ESI-MS signals (m/z) and fragments assigned.

m/z	fragment	exact mass of fragment (calculated)
63	Cu ⁺	62.93
104	[Cu(CH ₃ CN)] ⁺	103.96
122	[Cu(CH ₃ CN)(H ₂ O)] ⁺	121.97
145	[Cu(CH ₃ CN) ₂] ⁺	144.98
294	[Cu(Hdmg) ₂] ⁺ H ⁺	294.04
471	[Cu ₂ (dmg)(Hdmg)(H ₂ dmg)] ⁺	471.01

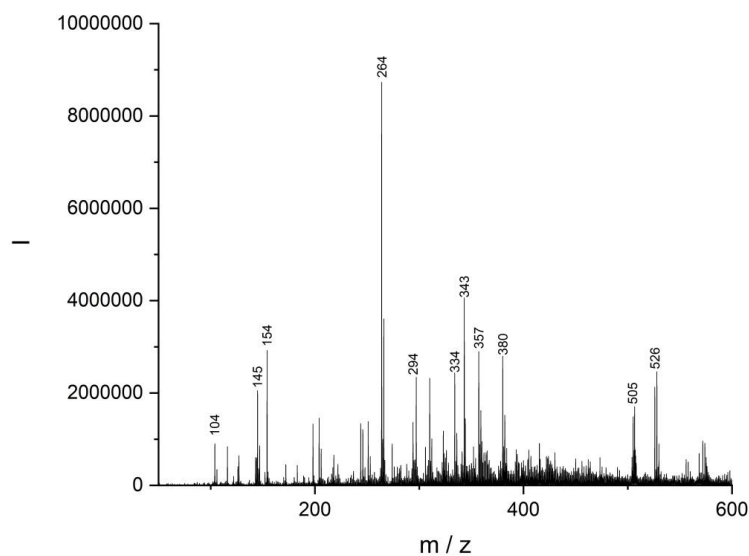
3.4. ESI mass spectrum of **1** after reaction in ethanol

Figure S18. ESI mass spectrum of **1**, 5 d after reaction in ethanol (solution, positive mode, overview, sprayed in methanol).

Table S21. ESI-MS signals (m/z) and fragments assigned.

m/z	fragment	exact mass of fragment (calculated)	comment
104	$[\text{Cu}(\text{CH}_3\text{CN})]^+$	103.96	impurity in spectrometer (CH_3CN)
145	$[\text{Cu}(\text{CH}_3\text{CN})_2]^+$	144.98	impurity in spectrometer (CH_3CN)
264	$[\text{Cu}(\text{C}_4\text{H}_6\text{NO}_2)(\text{C}_4\text{H}_7\text{NO}_2)]^+$	264.02	
294	$[\text{Cu}(\text{Hdmg})_2]^+\text{H}^+$	294.04	

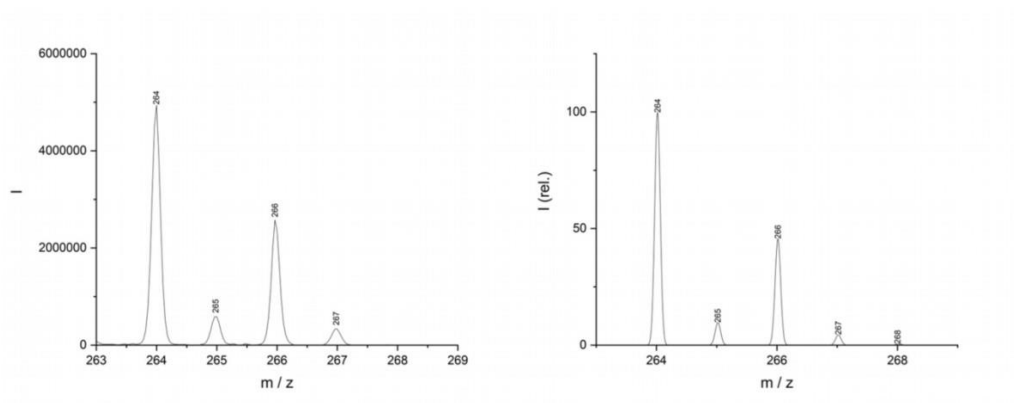


Figure S19. ESI mass spectrum of **1 5 d** after reaction in ethanol. Isolation of the signal at $m/z = 264$ (left) and simulation of $[\text{Cu}(\text{C}_4\text{H}_6\text{NO}_2)(\text{C}_4\text{H}_7\text{NO}_2)]^+$ (enviPat¹⁰; right).

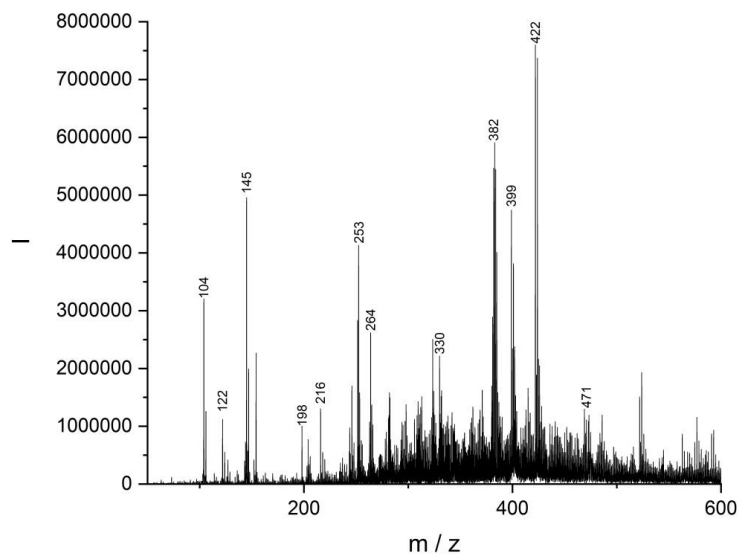


Figure S20. ESI mass spectrum of 1, 5 d after reaction in ethanol (residue, positive mode, overview, sprayed in methanol).

Table S22. ESI-MS signals (m/z) and fragments assigned.

m/z	fragment	exact mass of fragment (calculated)	comment
104	$[\text{Cu}(\text{CH}_3\text{CN})]^+$	103.96	impurity in spectrometer (CH_3CN)
122	$[\text{Cu}(\text{CH}_3\text{CN})(\text{H}_2\text{O})]^+$	121.97	impurity in spectrometer (CH_3CN)
145	$[\text{Cu}(\text{CH}_3\text{CN})_2]^+$	144.98	impurity in spectrometer (CH_3CN)
264	$[\text{Cu}(\text{C}_4\text{H}_6\text{NO}_2)(\text{C}_4\text{H}_7\text{NO}_2)]^+$	264.02	
471	$[\text{Cu}_2(\text{dmg})(\text{Hdmg})(\text{H}_2\text{dmg})]^+$	471.01	

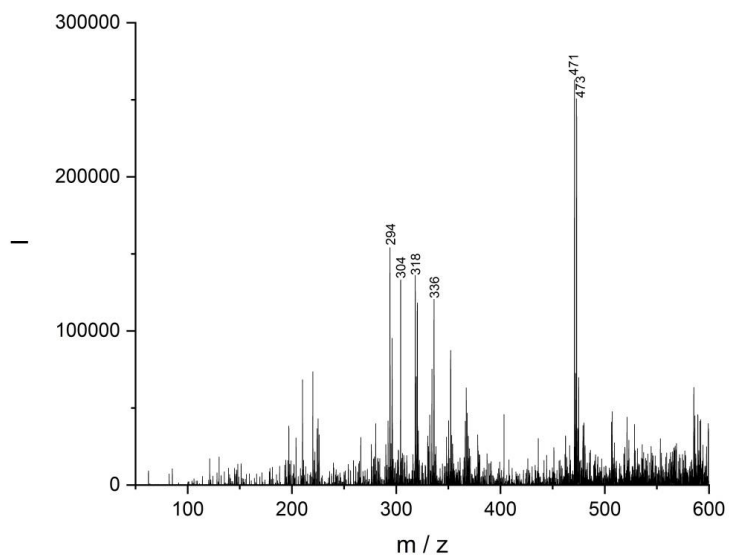
3.5. ESI mass spectrum of **2** in methanol

Figure S21. ESI mass spectrum of **2** (positive mode, overview, sprayed in methanol).

Table S23. ESI-MS signals (m/z) and fragments assigned.

m/z	fragment	exact mass of fragment (calculated)	comment
294	[Cu(Hdmg) ₂]+H ⁺	294.04	poor resolution because of uncharged target 2
471	[Cu ₂ (dmg)(Hdmg)(H ₂ dmg)] ⁺	471.01	poor resolution because of uncharged target 2

4. Elemental analyses

4.1. General Information

The measurements were performed in the analytical division of the organic chemistry department of the TU Kaiserslautern. The measurements were performed on an Elementar Analysensysteme vario MICRO cube device.

4.2. Elemental analysis for **1**

Table S24. Elemental analysis results for **1**.

	Carbon / %	Hydrogen / %	Nitrogen / %
Calculated	27.21	4.40	13.60
Measurement	27.13	4.33	13.71

4.3. Elemental analysis for **2**

Table S25. Elemental analysis for **2**.

	Carbon / %	Hydrogen / %	Nitrogen / %
Calculated	32.71	4.80	19.07
Measurement	32.59	4.83	18.79

5. NMR spectroscopy

5.1. General Information

The NMR spectra were measured on a Bruker Avance 400 device. Measurements were performed at 400 MHz. The chemical shift of the used solvent CD_3CN was set to 1.96 ppm (^1H). The resulting signal for water is 2.18 ppm.

5.2. ^1H -NMR spectrum of $[\text{Cu}(\text{CH}_3\text{CN})_4]\text{ClO}_4$

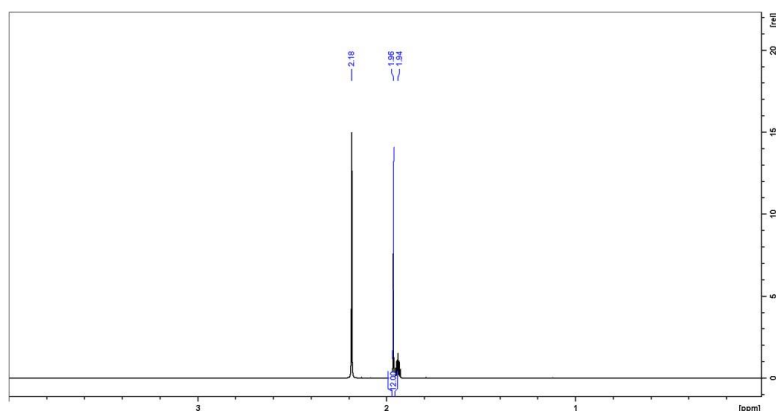


Figure S22. ^1H -NMR spectrum of $[\text{Cu}(\text{CH}_3\text{CN})_4]\text{ClO}_4$ (CD_3CN , 400 MHz).

^1H -NMR (400 MHz, CD_3CN , rt): $\delta = 1.96$ (s, 12H, $-\text{CH}_3$) ppm.

5.3. $^1\text{H-NMR}$ spectrum of the adsorbed gases obtained by the reaction of $\text{Cu}(\text{ClO}_4)_2 \cdot 6\text{H}_2\text{O}$ and H_2dmg in ethanol

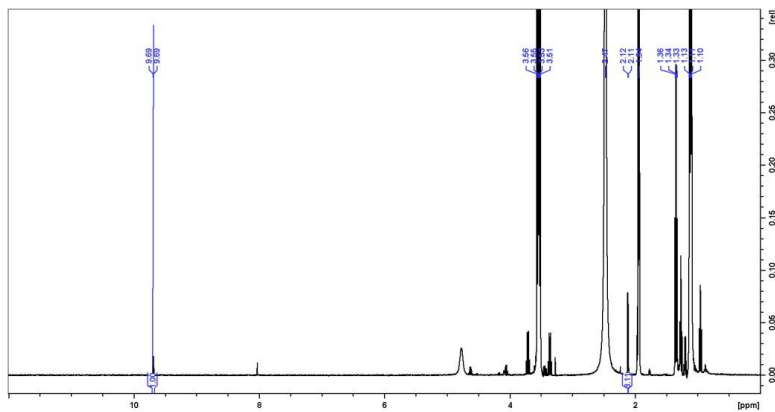


Figure S23. $^1\text{H-NMR}$ spectrum of the adsorbed gases obtained by the reaction of $\text{Cu}(\text{ClO}_4)_2 \cdot 6\text{H}_2\text{O}$ and H_2dmg in ethanol (CD_3CN , 400 MHz).

$^1\text{H-NMR}$ (400 MHz, CD_3CN , rt): $\delta = 2.12$ (d, 3H, $-\text{CH}_3$), 9.69 (q, 1H, $-\text{CHO}$) ppm.

6. Additional synthetic procedures

6.1. Additional synthetic protocols for **2**

$\text{CuClO}_4 \cdot 6\text{H}_2\text{O}$ (177 mg, 0.478 mmol, 1 eq.) was dissolved in ethanol (20 mL). H_2dmg (55 mg, 0.47 mmol, 1 eq.) and Na_2dmg (146 mg, 0.480 mmol, 1 eq.) were added to the stirred solution. The solution turned deep red. The product could be collected per pentane diffusion as deep red crystals (79 mg, 0.27 mmol, 56 %).

The described syntheses to obtain **2** could also be carried out in acetonitrile. Here, **2** did not crystallize but precipitated as deep red powder because of its insolubility in acetonitrile. The product thus, is of less purity.

6.2. Preparation of Neßler's reagent^[11]

HgCl_2 (987 mg, 3.64 mmol, 1 eq) was dissolved in H_2O (20 mL) and KI (1.25 g, 7.53 mmol, 2 eq.) in H_2O (15 mL) was added. A red precipitate appeared. The solution was decanted off. The precipitate was washed three times with H_2O (3-15 mL). Another portion of KI (840 mg, 5.06 mmol, 1.5 eq) in H_2O (10 mL) was added. The precipitate was solved and NaOH (3.31 g, 82.8 mmol, 20 eq.) in H_2O (10 mL) was added. Then, H_2O was added until a volume of 50 mL was reached.

7. IR spectroscopy

7.1. General Information

Static FTIR spectroscopy in the solid state: FTIR investigations on samples prepared as KBr pellets were performed with the FTIR spectrometer Bruker Invenio R, whereby the sample chamber was purged continuously with dry air. KBr pellets were prepared by mixing neat powder of the compound (0.5 – 1.2 mg, depending on the substance) with dry KBr (ca. 180 mg, stored in a compartment dryer at 80 °C, purchased from Merck) and grinding to a homogenous mixture. This mixture was filled in an evacuable pellet die with a diameter of 13 mm and sintered at a pressure of 0.75 GPa.

Time-dependent FTIR spectroscopy in solution: All measurements were performed with the FTIR spectrometer Bruker Vertex 80v, whereby the sample chamber was purged continuously with argon. Solutions were measured in a sealed optical cell (Specac Omni-Cell®) with two CaF₂ windows separated by 200 µm. Isotope labeled solvents were purchased from Deutero. Deuterated solvents were selected for their lower IR absorption in the relevant spectral region of 1700 – 1100 cm⁻¹.

The reactivity of **1** with ethanol (50 eq.) was investigated in deuterated dimethylsulfoxide (DMSO-d₆) at a complex concentration of c = 15 mM. Investigations in deuterated acetonitrile (CD₃CN) were performed at a concentration of c = 30 mM with optionally addition of either H₂O or H₂¹⁸O (20 eq.) as second reagent. For the experiments under presence of H₂¹⁸O, the used deuterated acetonitrile was dried before usage according to literature known procedures.^[12]

Compound **3** was measured in CD₃CN at concentrations of c = 3 – 33 mM with optionally addition of either H₂O or H₂¹⁸O as reagent. The salts Cu(NO₃)₂ and NaNO₂ were measured in CD₃CN by addition of H₂O for the latter one (5 µL H₂O on 500 µL CD₃CN) for better solubility. Solutions of N₂O were prepared by purging the corresponding solvent (CD₃CN or DMSO) with N₂O gas for few minutes under ambient conditions.

Simulation of IR absorption spectra: The crystal structure and a molecular structure generated by chemical intuition were used as input structures for **1** and **3**, respectively. Geometry optimizations were performed with the Berny algorithm of Gaussian 09^[13] by using energies and gradients computed by Turbomole 7.4.^[14,15] All calculations were performed with the DFT functional B3LYP with dispersion correction (no three-body interaction) (D3(BJ))^[16,17] as implemented in Turbomole using the resolution of identity (RI) approximation and the def2-TZVP basis set.

Harmonic frequency calculations were performed for the optimized minimum structures. The influence of CH₃CN was modulated by using the conductor-like screening model (COSMO). The vibrational frequencies are scaled by a factor of 0.98 to minimize the differences between the experimental and calculated frequencies. A Gaussian convolution with a full-width at half-maximum of 8 cm⁻¹ was applied to the calculated vibrational transitions.

7.2. Measurements in the solid state

Both, **1** and **2**, show a strong sharp band at 1208 and 1210 cm^{-1} , respectively, which was assigned to the NO stretching vibration (Figure S24).^[8,18-20] Further intense bands are observed at ca. 1380 cm^{-1} as well as at 1430 – 1440 cm^{-1} . These bands, which are ligand in character, are attributed to asymmetric and symmetric CH bending vibrations, respectively.^[21] The CN stretching vibrations are found at 1661 and 1598 cm^{-1} for **1** and at 1586 as well as 1541 cm^{-1} for **2**.^[8,18-21] These stretching vibrations are not observed in the spectrum of H_2dmg as a result from a pronounced impact of the hydrogen bonding.^[21] In the spectrum of **1**, the region below 1200 cm^{-1} is overlaid by the strong signal from the ClO_4^- counterion.

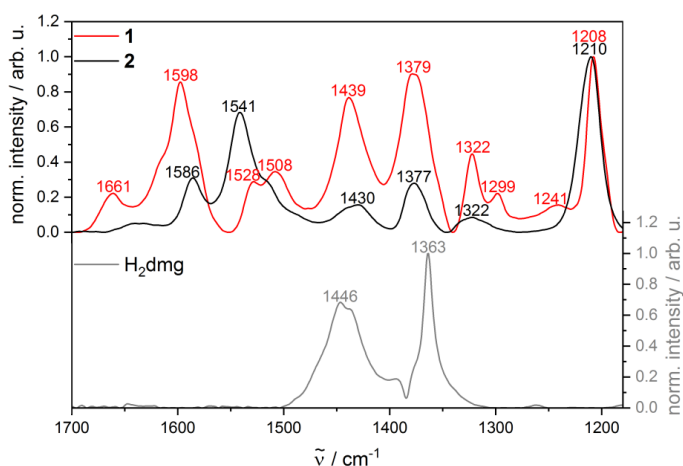


Figure S24. Solid state FTIR spectra (KBr pellets) of **1** (red), **2** (black) and H_2dmg (grey).

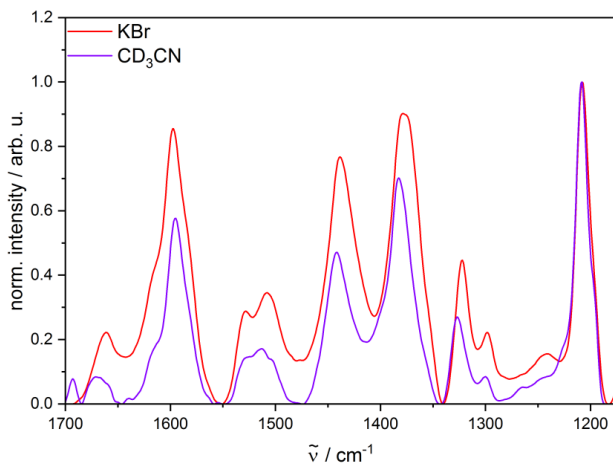


Figure S25. FTIR spectra of **1** in a KBr matrix (red) and in CD_3CN (purple).

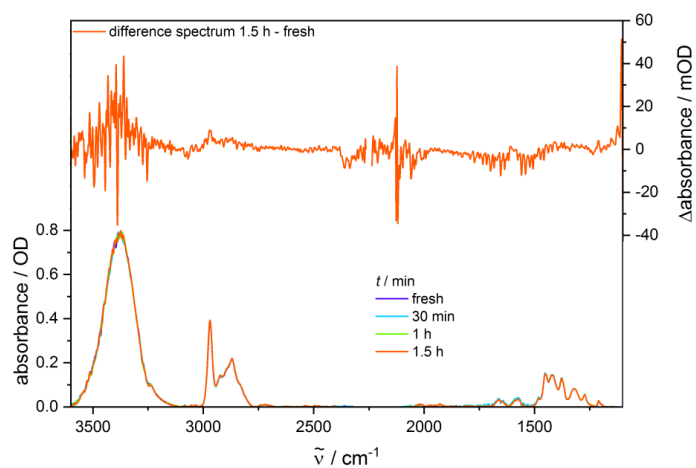
7.3. Time-dependent FTIR spectroscopy of **1** and ethanol in DMSO-d₆

Figure S26. Time-dependent FTIR spectra over 1.5 h of the reaction of **1** in DMSO-d₆ with ethanol (50 eq.) as reagent (lower trace). The upper trace is the corresponding difference spectrum that shows no signals apart from a slight variation of the content of gaseous water in the sample chamber.

7.4. Measurement of adsorbed gases

Therefore, a syringe equipped with a syringe filter and filled with CD_3CN was pierced through a septum that sealed the reaction solution. Due to this set-up, only gaseous reaction products were allowed to diffuse into the CD_3CN solution in the syringe.

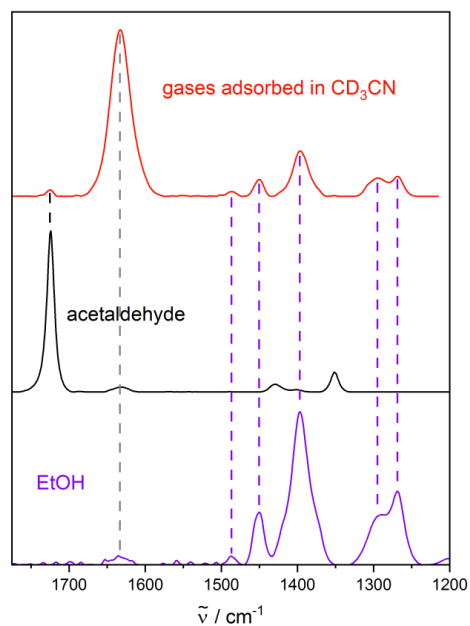


Figure S27. FTIR spectrum of gases dissolved in CD_3CN due to adsorption from the gas phase above a solution of **1** in ethanol (red). The spectra of acetaldehyde (black) and ethanol (purple) in CD_3CN are shown for comparison.

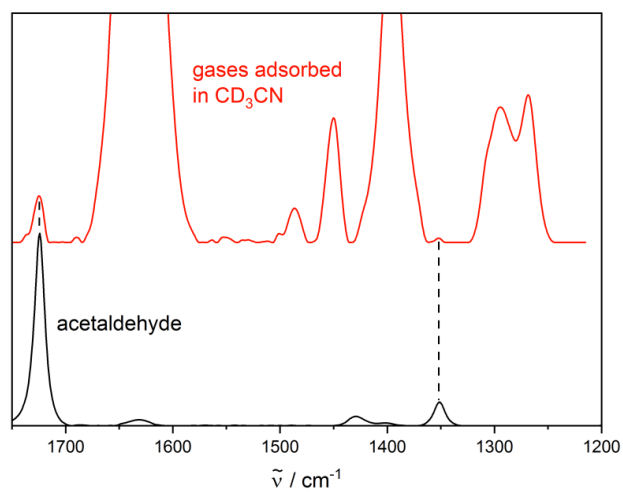


Figure S28. Enlarged detection of the FTIR spectrum of gases dissolved in CD_3CN due to adsorption from the gas phase above a solution of **1** in ethanol (red). The spectrum of acetaldehyde (black) in CD_3CN is shown for comparison.

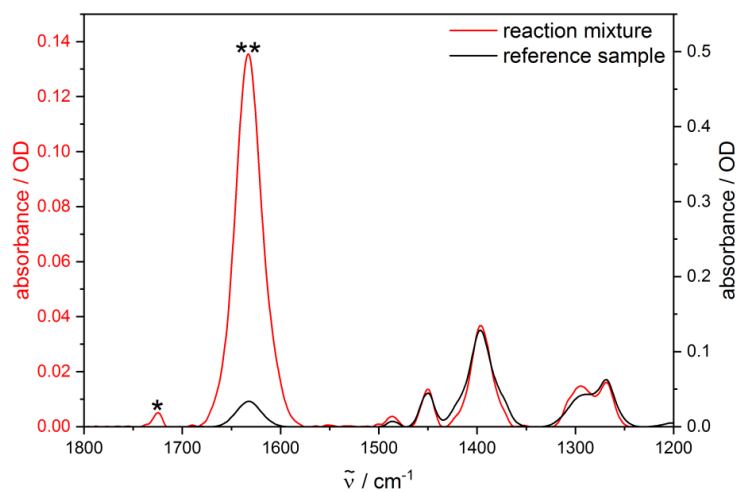


Figure S29. FTIR spectrum of gases dissolved in CD_3CN due to adsorption from the gas phase above a solution of **1** in ethanol (red). The spectrum of the reference experiment with the gases adsorbed from the gas phase above pure ethanol is shown in black. The bands marked with one and two asterisks are assigned to acetaldehyde and H_2O , respectively.

7.5. Reference spectra

Next to the reference experiments on **3** and N_2O discussed in detail in the manuscript, other conceivable species that could be present in the reaction mixture are discussed in the following lines. The potential oxidation products NO_2^- and NO_3^- could be ruled out as major products; however, the reference IR spectrum of NO_2^- in CD_3CN (measured as NaNO_2 , H_2O added to CD_3CN to increase solubility) might be assigned to the blue tail of the strong band at 1208 cm^{-1} , but can be excluded as main reaction product (Figure S30). The production of NO_3^- is even less probable, as the reference IR spectrum of $\text{Cu}(\text{NO}_3)_2$ does not show any agreement with the spectra of **1** in CD_3CN . Apart from these discussed species, the absorption bands observed for the reaction mixture can in principle be assigned to **3**, $[\text{Cu}(\text{CH}_3\text{CN})_4]^+$ and uncoordinated H_2dmg (Figure S30). The rather unspecific absorption bands at $1650 - 1180\text{ cm}^{-1}$ should not be over interpreted. During the reaction, a peak appears at 1633 cm^{-1} , which is attributed to H_2O and most probably originates from the dissolution of surrounding atmospheric H_2O traces over hours.

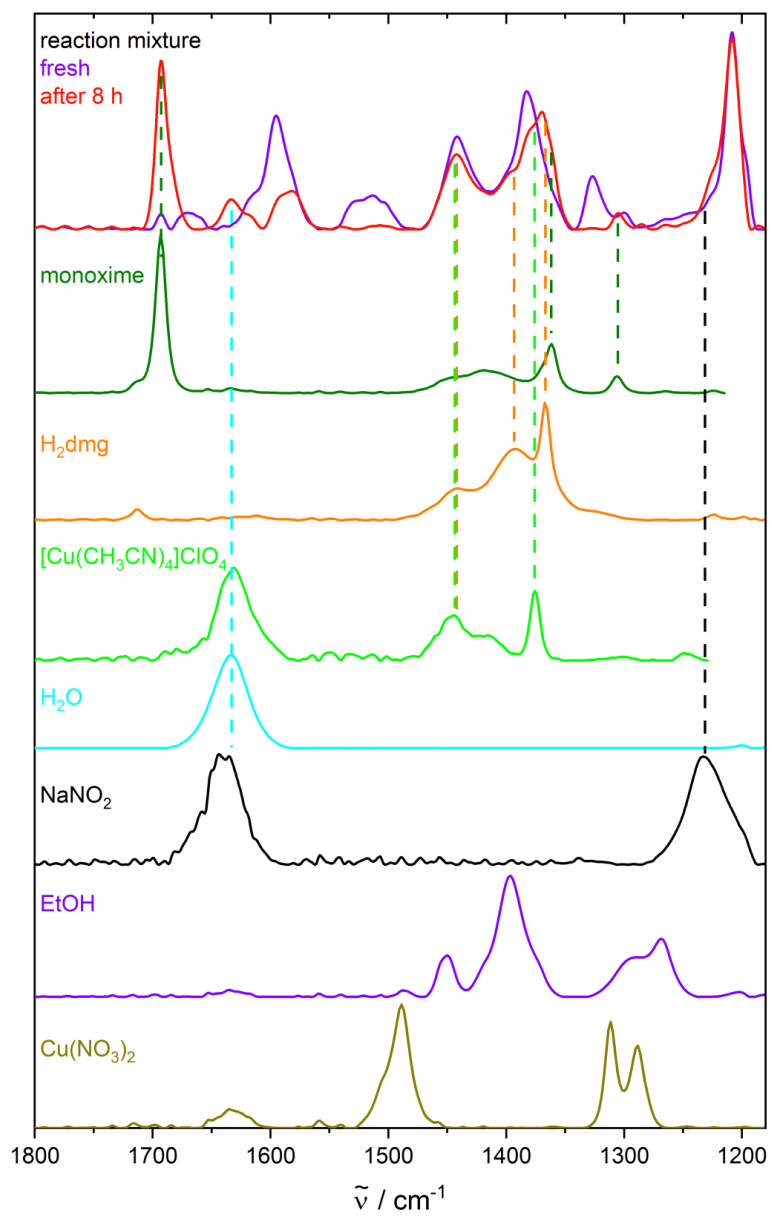


Figure S30. FTIR spectra of solutions of **1** (fresh and 8 h), **3** (2,3-butanedione monoxime), H₂dmg, [Cu(CH₃CN)₄]ClO₄, H₂O, NaNO₂, ethanol and Cu(NO₃)₂ in CD₃CN (5 μL H₂O for 500 μL CD₃CN in the case of NaNO₂).

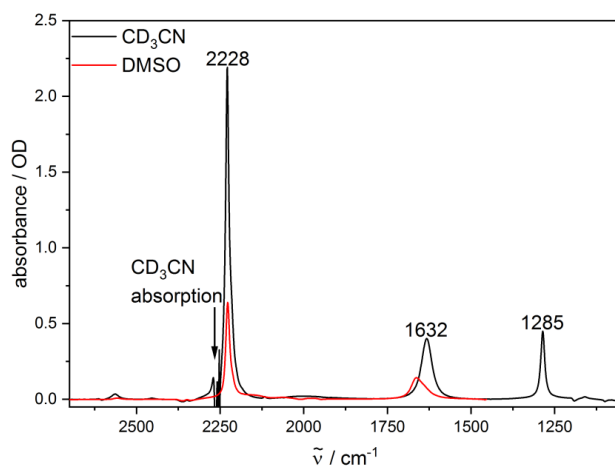


Figure S31. FTIR spectra of N_2O in CD_3CN and DMSO .

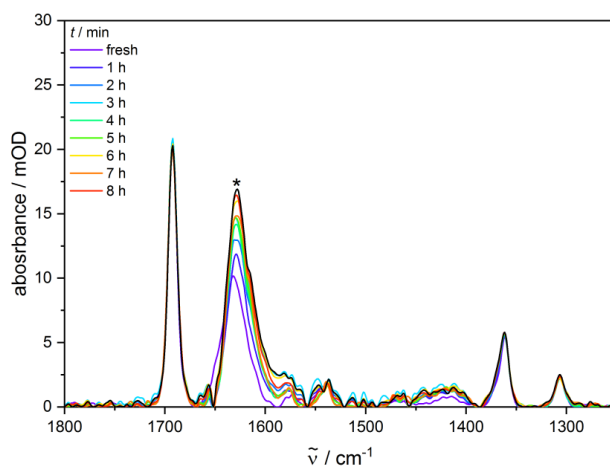


Figure S32. Time-dependent FTIR spectra over 8 h of **3** in CD_3CN containing H_2O (200 eq.). The band marked with asterisk is assigned to H_2O .

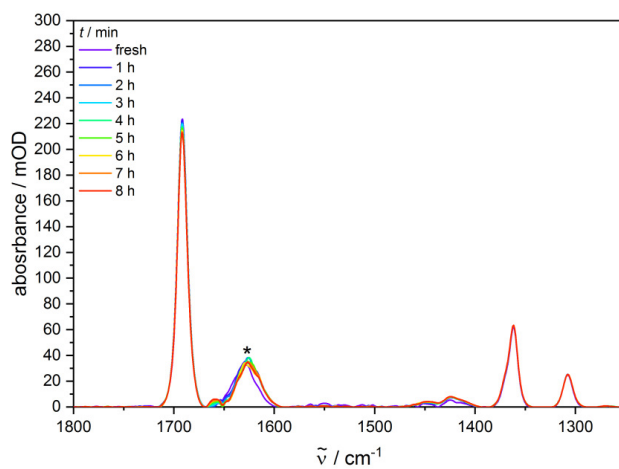


Figure S33. Time-dependent FTIR spectra over 8 h of **3** in CD₃CN containing H₂¹⁸O (15 eq.). The band marked with asterisk is assigned to H₂O.

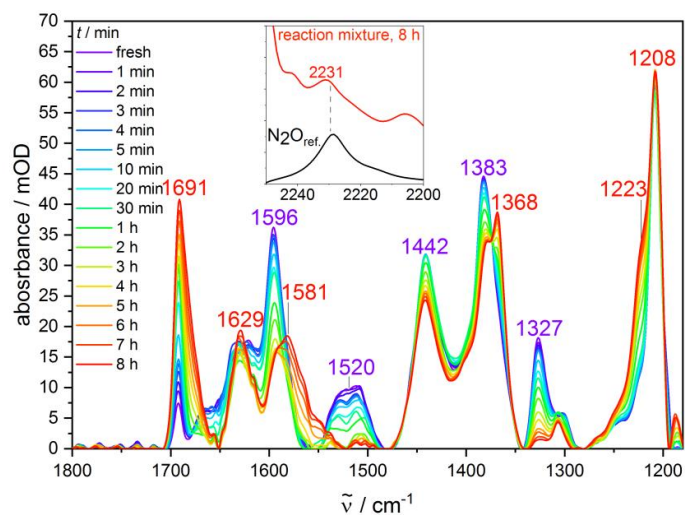
7.6. Spectra of the reaction of **1** in acetonitrile

Figure S34. Time-dependent FTIR spectra over 8 h of the reaction of **1** in CD_3CN containing H_2O (20 eq.). The inset is an enlarged section of the spectral region around 2230 cm^{-1} (red: reaction mixture after 8 h, black: reference IR spectrum of N_2O in CD_3CN).

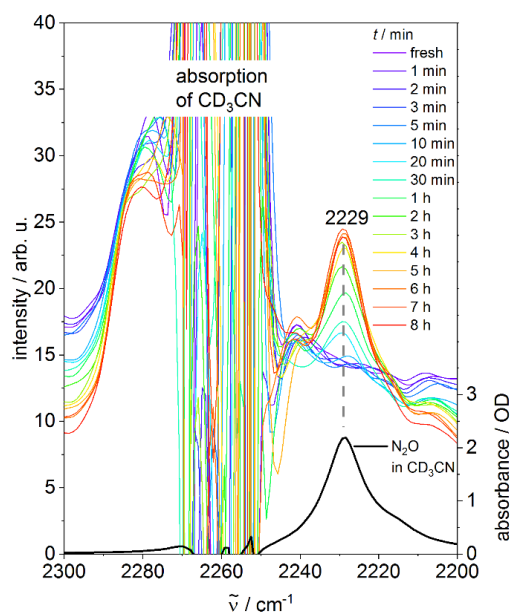


Figure S35. Time-dependent FTIR spectra ($2300 - 2200\text{ cm}^{-1}$) over 8 h of the reaction of **1** in CD_3CN . The black curve is a reference IR spectrum of N_2O in CD_3CN .

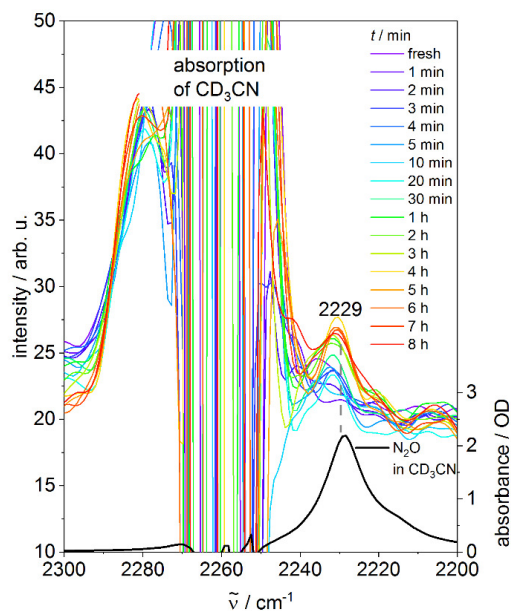


Figure S36. Time-dependent FTIR spectra (2300 – 2200 cm^{-1}) over 8 h of the reaction of **1** in CD_3CN containing H_2O (20 eq.). The black curve is a reference IR spectrum of N_2O in CD_3CN .

The reaction and its kinetics are not significantly influenced by the addition of H_2O at least over the first hour of reaction (Figure S39). At longer time scales, however, the CO band assigned to forming **3** broadens, which is an indication for a follow-up reaction. The experimental CO band obtained after 8 h of reaction can be deconvoluted into two Gaussian-shaped bands, whereby one frequency is that of the initial CO band and a second Gaussian pulse is red-shifted by ca. 10 cm^{-1} (Figure S38-S39). The appearance of this lower-frequency CO band is only visible as a shoulder after a reaction time of 8 h if no water is added to the used CD_3CN (Figures S34 and S38). Interestingly, the broadening of the CO band is not observed when a pure solution of **3** in CD_3CN is followed over time under comparable conditions (Figure S32). Accordingly, there might be complexation of formed **3** by e.g. solvated Cu ions in the reaction mixture, supported by H_2O molecules that could then act as co-ligands.

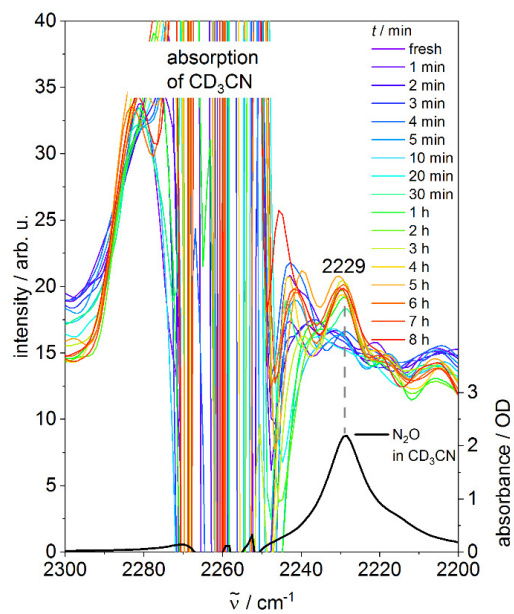


Figure S37. Time-dependent FTIR spectra (2300 – 2200 cm^{-1}) over 8 h of the reaction of **1** in CD_3CN containing H_2^{18}O (20 eq.). The black curve is a reference IR spectrum of N_2O in CD_3CN .

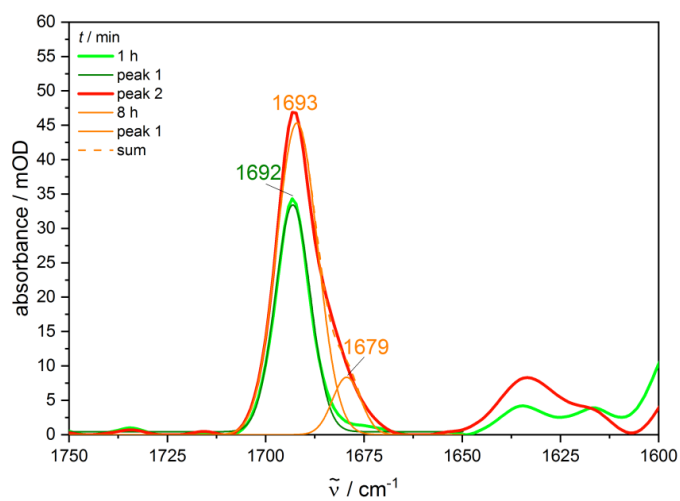


Figure S38. FTIR spectra (1750 – 1600 cm⁻¹) of **1** in CD₃CN after 1 and 8 h (thick lines). The thin lines represent the Gaussian deconvolution of the measured CO band.

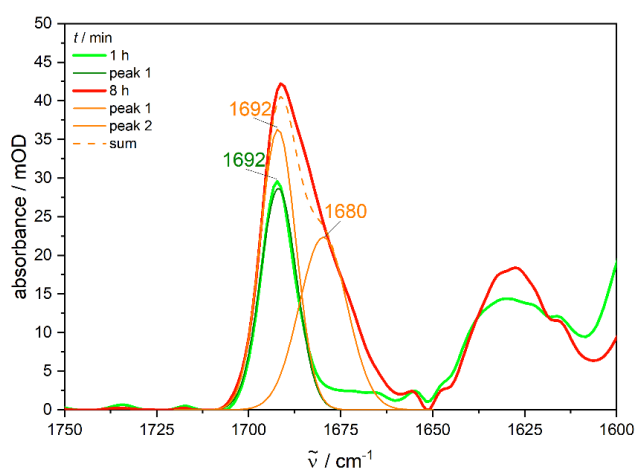


Figure S39. FTIR spectra (1750 – 1600 cm⁻¹) of **1** in CD₃CN containing H₂O (20 eq.) after 1 and 8 h (thick lines). The thin lines represent the Gaussian deconvolution of the measured CO band.

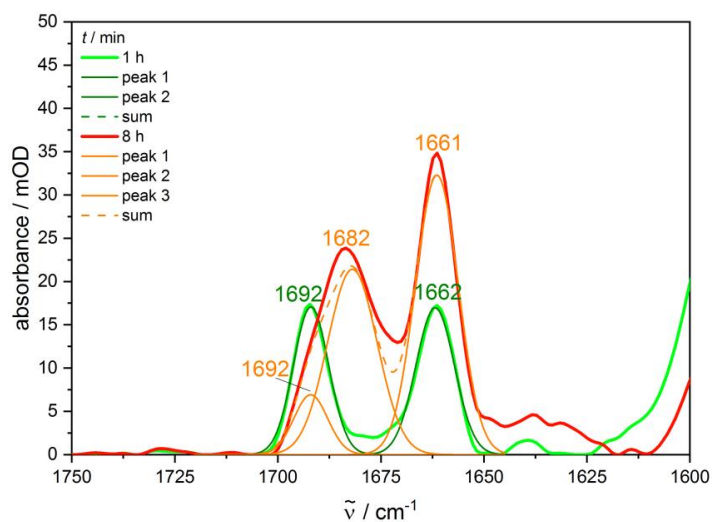


Figure S40. FTIR spectra (1750 – 1600 cm^{-1}) of **1** in CD_3CN containing H_2^{18}O (20 eq.) after 1 and 8 h (thick lines). The thin lines represent the Gaussian deconvolution of the measured CO band.

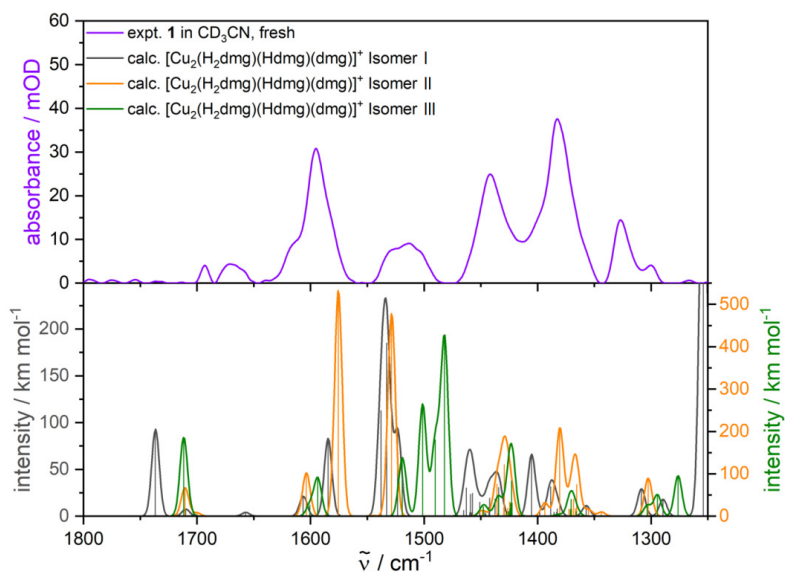


Figure S41. FTIR spectrum (purple) of **1** in CD_3CN and calculated vibrational spectra of the three conceivable isomers of $[\text{Cu}_2(\text{H}_2\text{dmg})(\text{Hdmg})(\text{dmg})]^+$ (grey, orange, green). Calculations: DFT/B3LYP-D3(BJ)/def2-TZVP/COSMO, scaling factor: 0.98, Gaussian convolution with FWHM = 8 cm^{-1} .

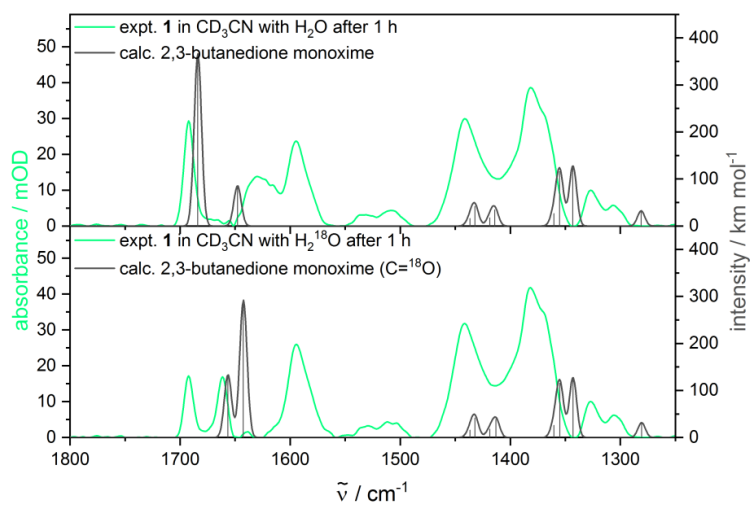


Figure S42. Time-dependent FTIR spectra after 1 h of the reaction mixture of **1** in CD₃CN containing H₂¹⁶O (orange, upper trace) or H₂¹⁸O (orange, lower trace) (20 eq.). The calculated vibrational spectra of **3** (C=¹⁶O, grey, upper trace) and **3** (C=¹⁸O, grey, lower trace) are shown for comparison. Calculations: DFT/B3LYP-D3(BJ)/def2-TZVP/COSMO, scaling factor: 0.98, Gaussian convolution with FWHM = 8 cm⁻¹.

8. EPR Spectroscopy

8.1. General Information

EPR spectra in the X band were recorded with a Bruker EMX System. Solid state samples were placed in a quartz tube under argon. The samples in solution were dissolved in dried, degassed DMSO and transferred under argon to an EPR 4 mm quartz tube. The solution was frozen in liquid nitrogen and the sample was placed in the resonator at 100 K. Measurements were carried out with a frequency of 9.46 GHz (the exact frequency of the measurements is given for each compound below).

8.2. Discussion of data for **1** and **2**

The spectra of the solid state and frozen solution were measured (Figure S43-S46). A major difference can be found in the EPR spectra of the frozen solution (100 K) and solid state of **1**. The frozen solution spectrum (Figure S44) showed a large g anisotropy, $g_{\parallel} = 2.411$ and $g_{\perp} = 2.073$, indicating the presence of different axial ligands than found in the solid state EPR spectrum (Figure S43) that showed $g_{\parallel} = 2.200$, $g_{\perp} = 2.033$. This finding can be explained by the use of DMSO as solvent for the frozen solution spectra; i.e., in a DMSO solution, the axial EtOH, and ClO_4^- ligands are likely displaced by a stronger field DMSO ligand(s). The frozen solution spectrum of **2** (Figure S46) displayed a lower g anisotropy ($g_{\parallel} = 2.153$, $g_{\perp} = 2.055$), and is shifted from the observed g values of the dinuclear **1**. Additionally, there was essentially no change in the g values in the solid-state spectrum of **1** ($g_{\parallel} = 2.16$, $g_{\perp} = 2.055$, Figure S45), indicating that the molecular structure found in the solid state is very likely maintained in solution. Unfortunately, a differentiation of the two copper centers was not possible, so it was not possible to use EPR measurements to probe the reactivity of **1**. For a comparison with theoretical data and discussion of the electronic states and magnetic anisotropy, please see 9.7.

8.3. Data for **1**

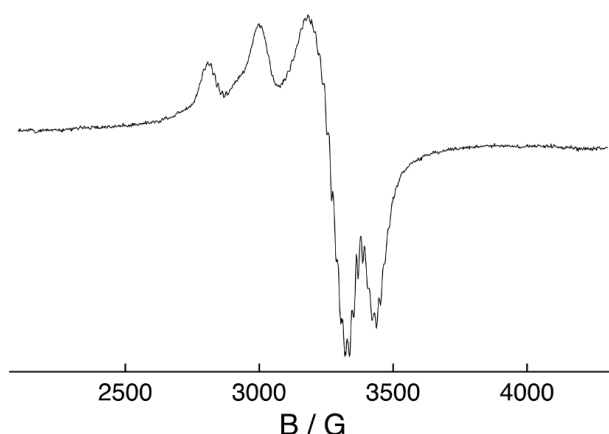


Figure S43. Solid state EPR spectrum of **1** ($g_{\parallel} = 2.200$, $g_{\perp} = 2.033$, 9.4603 GHz).

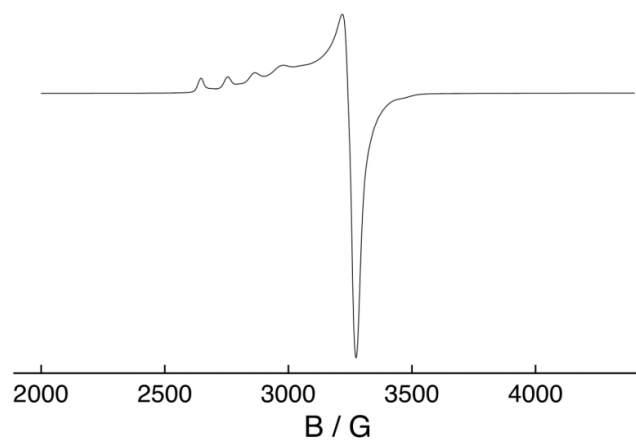


Figure S44. Frozen solution EPR spectrum (100K) of **1** in DMSO ($g_{\parallel} = 2.411$, $g_{\perp} = 2.073$, 9.4673 GHz).

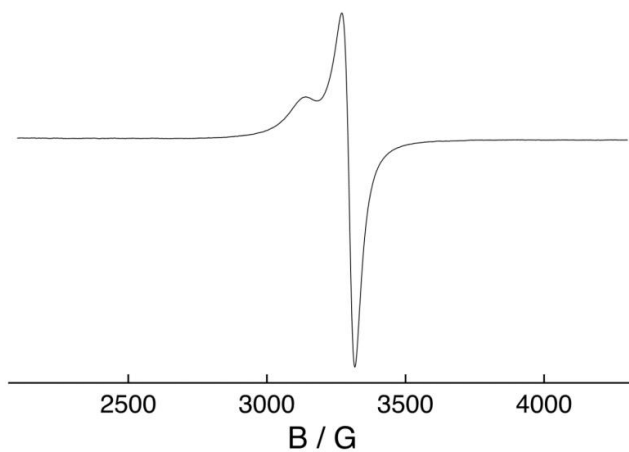
8.4. Data for **2**

Figure S45. Solid state EPR spectrum of **2** ($g_{\parallel} = 2.16$, $g_{\perp} = 2.055$, 9.4659 GHz).

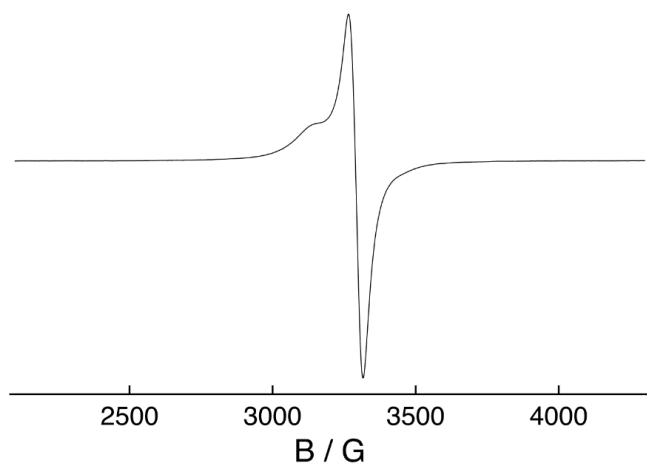


Figure S46. Frozen solution EPR spectrum (100K) of **2** in DMSO ($g_{\parallel} = 2.153$, $g_{\perp} = 2.055$, 9.4616 GHz).

The EPR spectra of **2** show the typical behavior of Cu(II) in an elongated octahedral ligand field with ($g_{\parallel} > g_{\perp} > g_e$).^[22] This behavior is in good agreement with the *ab initio* calculations shown in section 9.7.

For the frozen solution of **1**, the spectrum agrees well with simulations with the program PHI^[23] for Cu(II). The exchange coupled singlet and triplet state with $J = -475 \text{ cm}^{-1}$ and a triplet state with $g_{\parallel} = 2.5$ and $g_{\perp} = 2.1$ were compared in Figure S59. The temperature dependence of the spectrum of the exchange coupled system is shown in Figure S60.

9. Theoretical calculations

9.1. General information

All calculations were carried out using the TURBOMOLE rev. V7.5.0.^[15] Single-point energy calculations were carried out using tolerances of 10^{-7} Hartrees for the SCF energy change, and default convergence criteria for the geometry optimization. To speed up the calculations, the resolution of identity approximation was employed.^[24–26] The integration grid “3” was used. All associated geometries can be found as xyz files in the attached file. Electronic energy and thermodynamic data for the corresponding reaction is summarized in Table S27.

9.2. Structure Optimization

Table S26. Electronic energy (a.u.) for optimized structures of isomers I-III for different multiplicities and functionals. Basis set: def2-TZVP

Structure	Multiplicity	Energy (a.u.)				Rel. energy (kJ/mol)
		B3LYP	PBE0	M06	PBE	B3LYP
I	Singlet	-4530.1491	-4529.0719	-4530.0787	-4529.1089	0
	Triplet	-4530.1435	-4529.0670	-4529.0670	-4529.0897	14.3
II	Singlet	-4530.1471	-4529.0684	-4530.0791	-4529.1017	5.2
	Triplet	-4530.1438	-4529.0658	-4530.0751	-4529.0880	9.1
III	Singlet	-4530.1404				22.8

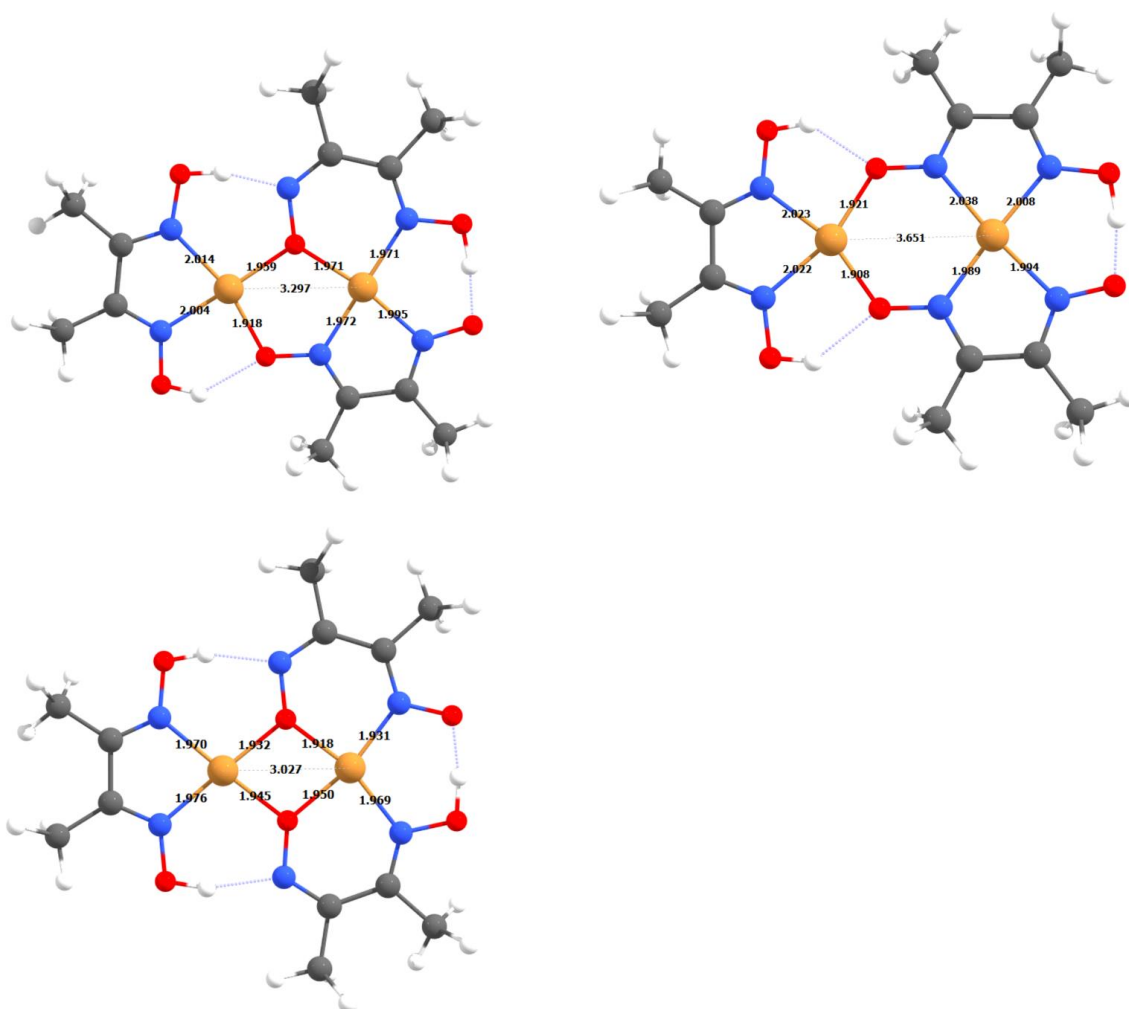


Figure S47. Molecular structures of isomers I-III I (left) and II (right) and III (bottom) after optimization. Bond lengths are in Å. Basis set: def2-TZVP; functional: B3LYP. Cu: brown, O: red, N: blue, C: grey, H: white.

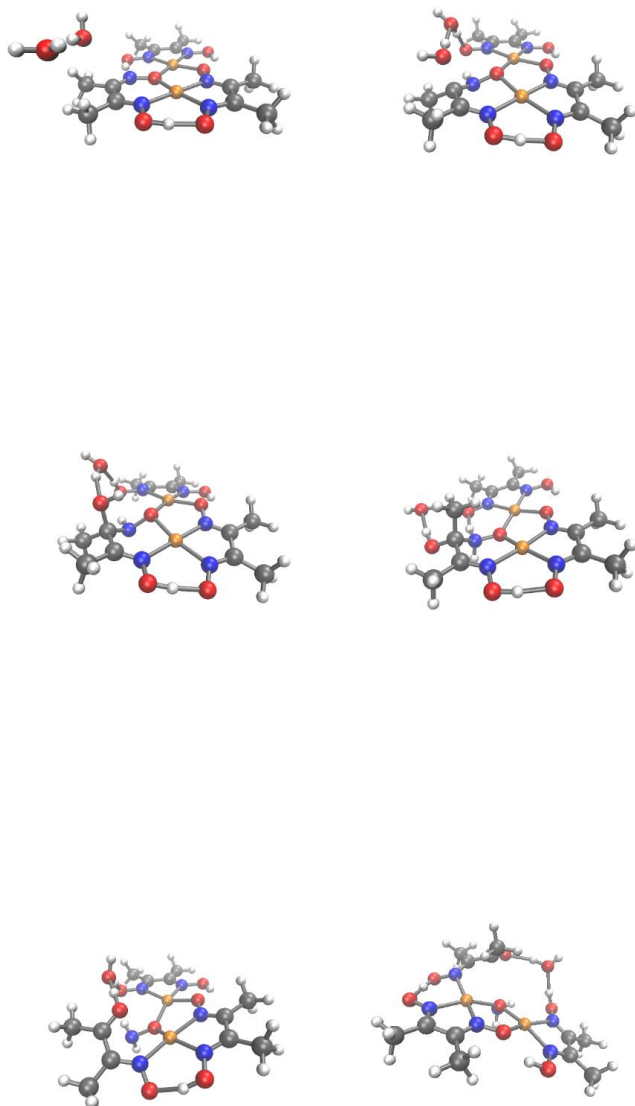
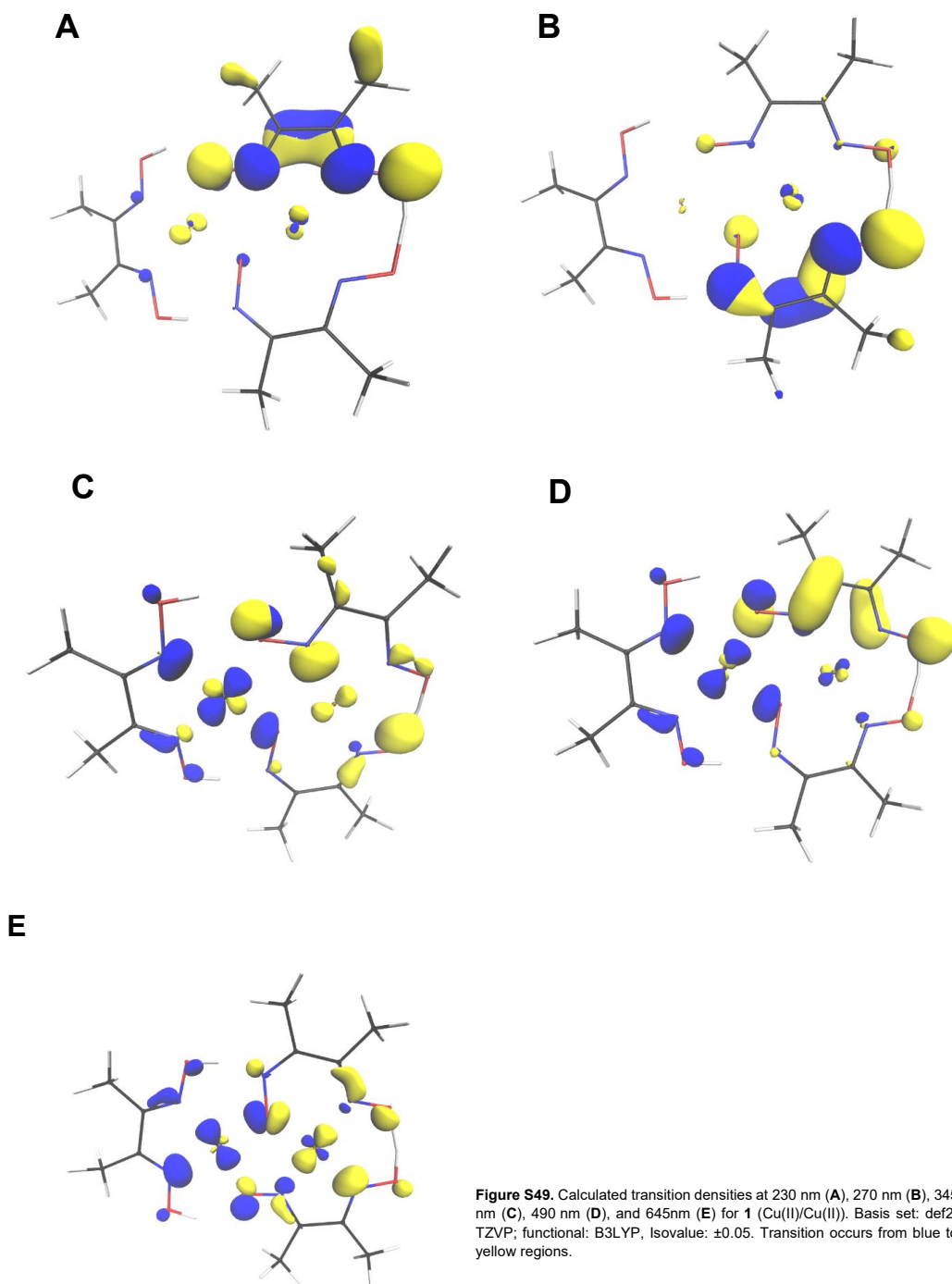


Figure S48. Calculated structures along the reaction path for the reaction of **1**. Top: reactants (left), TS1 (right), middle: intermediate **1** (left), intermediate **2** (right), bottom: TS2 (left), product (right).

Table S27. Electronic energy (a.u.) and Thermodynamic data for the reaction. T=298.15 K, P= 0.1Mpa

Species	Energy (Hartree)	Relative Energy (kJ/mol)	ZPE (kJ/mol)	Entropy (kJ/mol/K)	ZPE corrected energy (kJ/mol)	Gibbs free energy (kJ/mol)	Relative ΔG (kJ/mol)
Reactant	-4683.0168	0.00	1040	1.0086	-12294220.61	-12293918.03	0.00
TS1	-4682.9548	162.68	1048	0.9051	-12294049.83	-12293778.30	139.72
Intermediate1	-4682.9941	59.47	1054	0.9150	-12294147.01	-12293872.50	45.52
Intermediate2	-4683.0042	33.03	1053	0.9180	-12294174.52	-12293899.13	18.89
TS2	-4682.9715	118.95	1042	0.8852	-12294099.67	-12293834.12	83.90
Product	-4682.9905	69.13	1046	0.9480	-12294145.56	-12293861.14	56.87

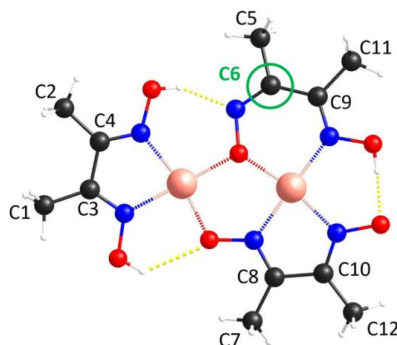
9.3. Transition density



9.4. Mulliken charges

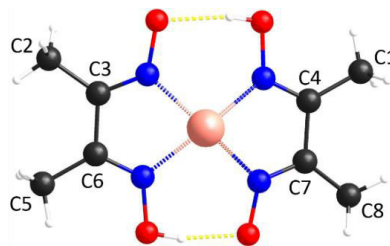
9.4.1. Mulliken charge of 1

Atoms	Mulliken charges
C1	-0.37779
C2	-0.36744
C3	0.12118
C4	0.10261
C5	-0.41054
C6	0.21212
C7	-0.38240
C8	0.18775
C9	0.10364
C10	0.06000
C11	-0.33945
C12	-0.41424



9.4.2. Mulliken charge of 2

Atoms	Mulliken charges
C1	-0.35800
C2	-0.38370
C3	0.15971
C4	0.06139
C5	-0.36958
C6	0.06115
C7	0.16113
C8	-0.38892



9.5. Molecular electrostatic potential

A map of the molecular electrostatic potential onto the surface of **1** reveals a higher attraction to nucleophiles (red color) in the neighborhood of C6 (bridging $\mu_2\text{-}\eta^1\text{-O-N=C}$ -group) than C8 (Figure S50). This observation also is supported by the Mulliken charges (see SI 9.4), where C6 has a much higher Mulliken charge than any other carbon atom of the O-N=C motifs. Notably, the Mulliken charge for C6 in **1** is significantly higher than for the carbon atoms in **2** (see SI 9.4).

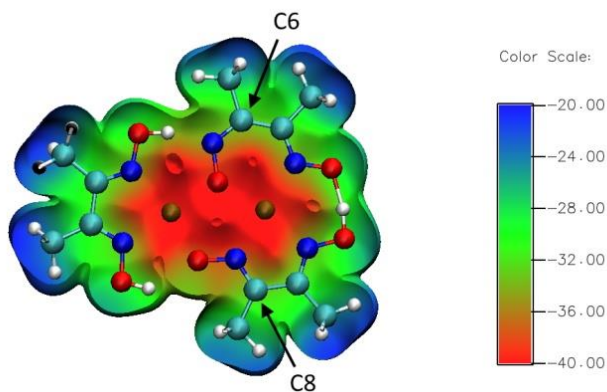


Figure S50 Mapping of the molecular electrostatic potential onto the surface of **1**. The colour scale shows the force acting on a positive test charge in the vicinity of the molecule in kJ/mol (the more negative values the higher attraction).

9.6. Calculated UV/Vis spectra

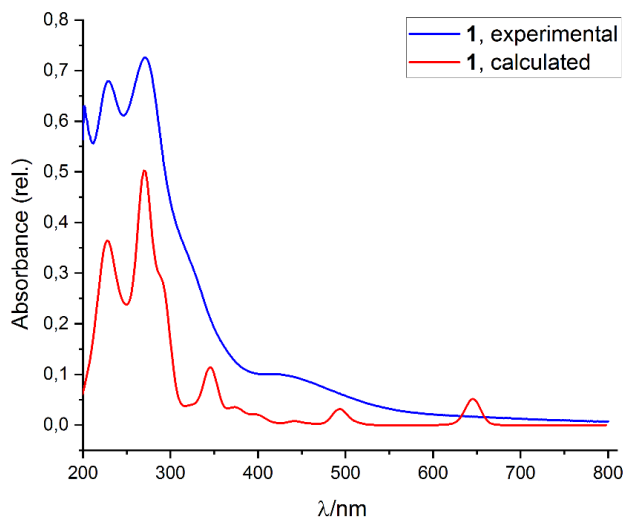


Figure S51. Comparison of the experimental and calculated UV/Vis spectra of **1**. Basis set: def2-TZVP; functional: B3LYP.

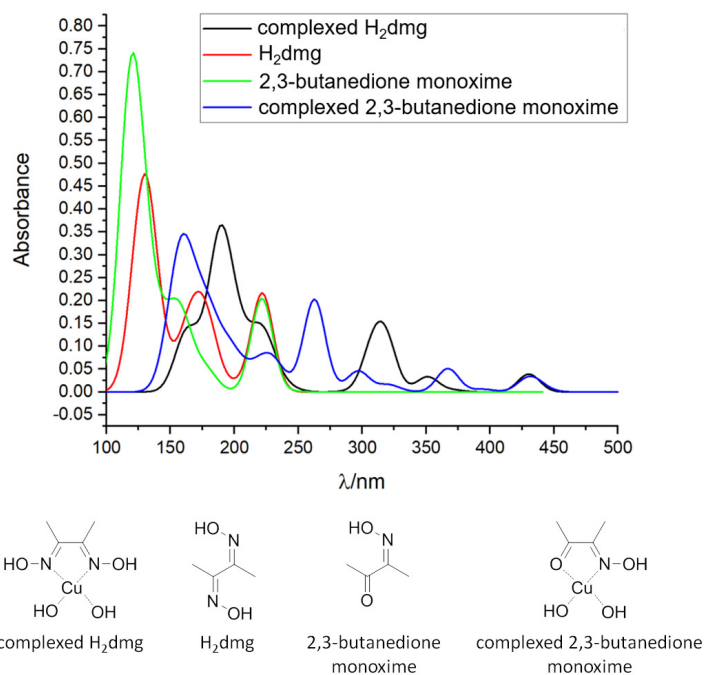


Figure S52. Calculated UV/Vis spectra for H₂dmg and 2,3-butanedione monoxime. Basis set: def2-TZVP; functional: B3LYP.

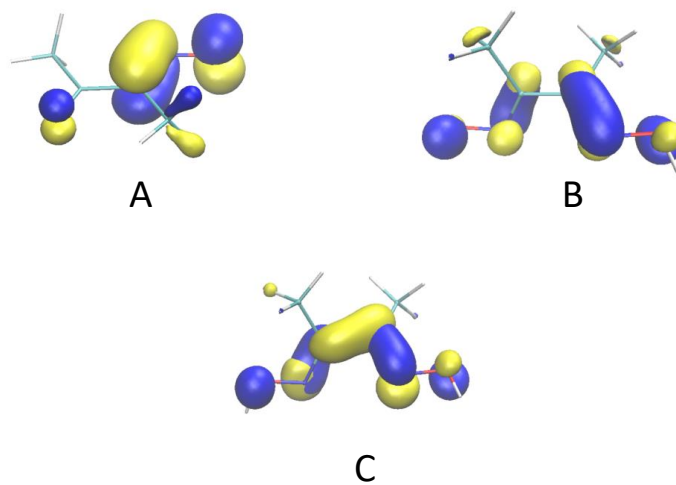


Figure S53. Calculated transition densities for free 2,3-butanedione monoxime at 221 nm (A) and free dimethylglyoxime at 179 nm (B) and at 222 nm (C). Basis set: def2-TZVP; functional: B3LYP. Isovalue: ± 0.1 . Transition occurs from blue to yellow regions.

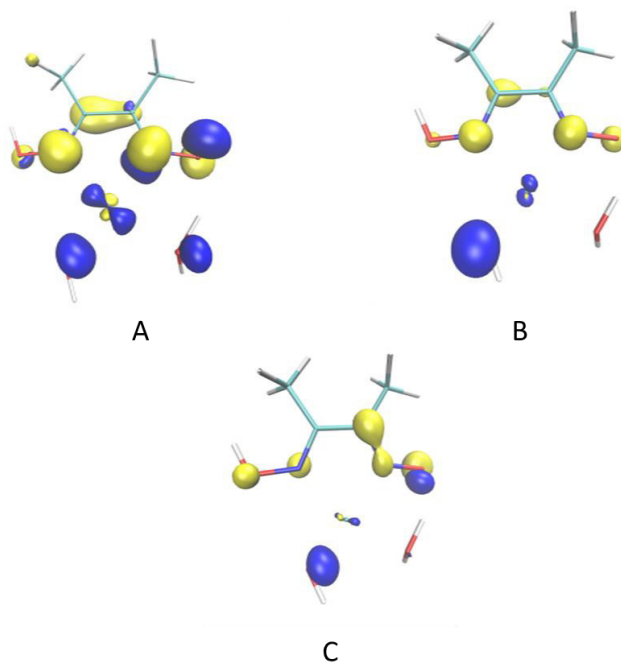


Figure S54. Calculated transition densities for complexed dimethylglyoxime at 307 nm (A), at 350 nm (B) and at 430 nm (C). Basis set: def2-TZVP; functional: B3LYP. Isovalue: ± 0.1 . Transition occurs from blue to yellow regions.

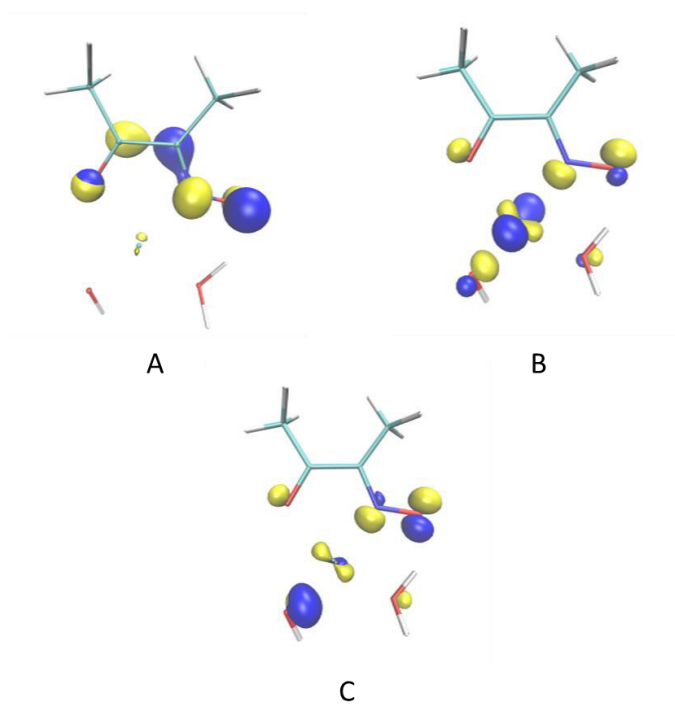


Figure S55. Calculated transition densities for complexed 2,3-butanedione monoxime at 262 nm (A), at 366 nm (B) and at 430 nm (C). Basis set: def2-TZVP; functional: B3LYP. Isovalue: ± 0.1 . Transition occurs from blue to yellow regions.

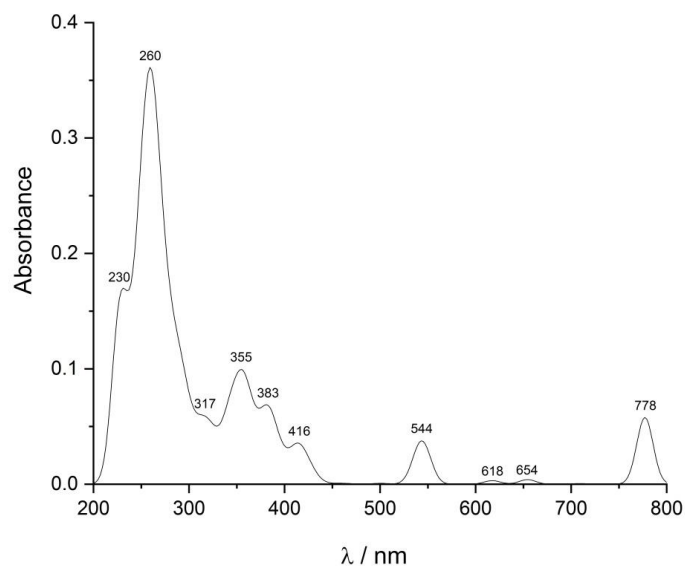


Figure S56. Calculated UV/Vis spectrum for the mixed valent species of **1** (Cu(I)/Cu(II)). Basis set: def2-TZVP; functional: B3LYP.

9.7. Electronic states and the magnetic anisotropy

To gain information about the electronic states and the magnetic anisotropy, complete-active-space self-consistent field (CASSCF) and spin-orbit configuration interaction (SOC) calculations were performed for **1** and **2**. When doing CASSCF calculations for **1**, the active space CAS(18, 10) with 18 valence electrons located in the 10 3d orbitals of the two copper centers. The results of the CASSCF and SOC calculations are presented in Table S28. The lowest triplet state has an energy that is 62 cm⁻¹ higher than the ground singlet. Typically for CASSCF, this value is significantly lower^[27] than the one experimentally obtained by Ruiz *et al.* (950 cm⁻¹).^[9] Therefore, the experimental value is used in the simulation of the EPR spectra.

Additionally, the g values and the magnetic axes of the triplet state of **1** are listed in Table S29 and visualized in Figure S57. g is rather anisotropic, g_⊥ = 2.08 and g_∥ = 2.47 which is common for complexes containing Cu(II).^[28] Moreover, calculations using the active space CAS(9, 5) in CASSCF, i.e. 9 valence electrons distributed in five 3d orbitals, were performed for **2** with and without an additional ethanol ligand. Table S33 displays the results of the CASSCF and SOC computations. The next excited state has an energy that is 13000 cm⁻¹ higher than the ground state. Additionally, the g values and magnetic axes are listed in Table S30 and visualized in Figure S58. For **2** the g values were estimated for the lowest Kramer's doublet from SOC calculations with a pseudospin of S = 1/2, for which g is rather anisotropic. For the chosen method the anisotropy is expected to be slightly overestimated. Singh *et al.*^[29] showed in a systematic study that there is a strong change when the ligand orbital which interacts strongly with the d_{x²-y²} orbital in square planar coordination is included in the active space while neglectation of dynamic correlation is not changing the results significantly for chelating ligands.

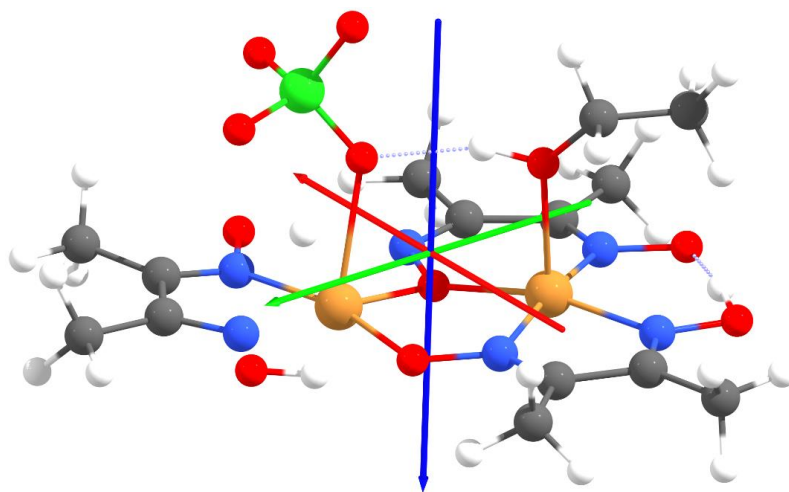
The EPR spectra are simulated with the program package PHI.^[23] In Figure S57 three situations are compared for T=100 K. An isolated Cu(II) center with g_⊥ = 2.1 and g_∥ = 2.5, the excited triplet state of **1** with the same g values and the lowest singlet and triplet state present in **1**. The energy difference of the singlet and the triplet state is considered as twice the experimental exchange coupling constant J = -475 cm⁻¹ determined by Ruiz *et al.*^[9] In PHI, the Heisenberg Hamiltonian is defined as $\hat{H} = -2J\hat{S}_1\hat{S}_2$, where \hat{S}_1 and \hat{S}_2 are the spin operators of the two Cu centers. All three models show exactly the same EPR spectra. Taking into account that the hyperfine coupling is missing in this description, the spectra agree well with the measurements of **1** in frozen solution. In Figure S60, the temperature dependence of the spectrum of **1** is shown. The form remains unchanged while the intensity increases because of the higher occupation of the triplet state.

Table S28. Energies (in cm⁻¹) of the lowest electronic states for **1** with inclusion of Spin-Orbit Coupling, CAS (18,10) SCF/CI.

		CASSCF (18, 10)		SOC	
Spin= 1	States			States	
1	¹ A ₁	0		¹ A ₁	0
2	³ A ₁	62		³ A ₁	62.429 62.435 62.615
3	³ A ₁	11273			
4	¹ A ₁	11274			

Table S29. g-values and magnetic axes of the triplet state of **1** with two ligands.

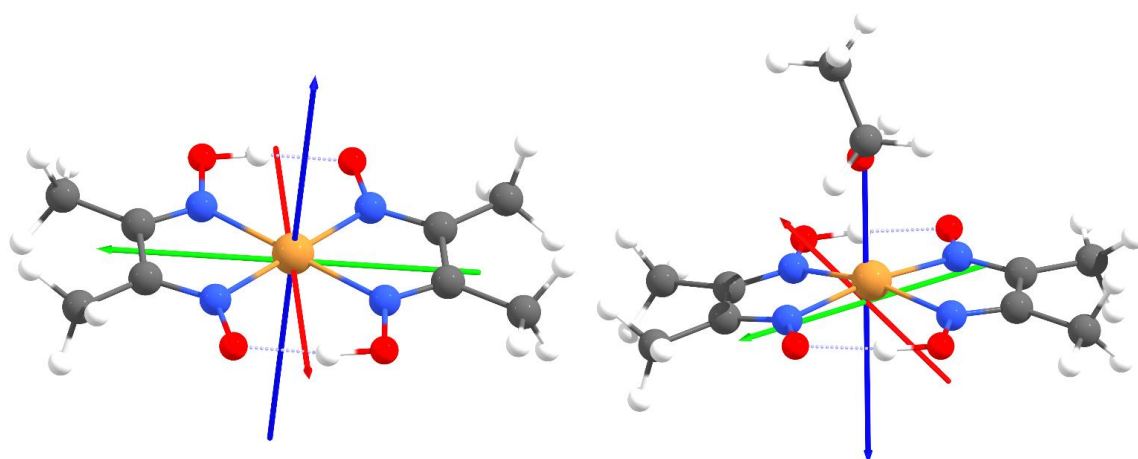
S=1.0	g1	g2	g3
	2.08	2.09	2.47
Magnetic main axes			
X	-0.83	-0.53	-0.13
Y	0.42	-0.48	-0.76
Z	-0.34	0.69	-0.63

**Figure S57.** Magnetic axes of the triplet state, g1 (red), g2 (green), g3 (blue) for **1** with two ligands.**Table S30.** CASSCF (9,5) and SOCI energies (in cm^{-1}) for the lowest electronic states of **2** with and without ethanol based on a state average for 5 doublets.

Spin= 1/2	CASSCF (9,5)			SOCI	
	2	2 with ethanol	KD	2	2 with ethanol
1	0	0	K1	0	0
2	13337	12265	K2	13233	11953
3	14994	12810	K3	14484	12411
4	15314	13416	K4	15106	13662
5	15332	13715	K5	16511	14560

Table S31. g-values and magnetic axes of the lowest Kramer's doublet for **2** with and without ethanol, spin $S=1/2$.

$S=1/2$	2			2 with Ethanol		
	g1	g2	g3	g1	g2	g3
	2.09	2.09	2.43	2.10	2.09	2.45
Magnetic main axes						
X	0.04	0.99	-0.01	-0.65	-0.76	0.06
Y	-0.88	0.03	-0.47	-0.62	0.57	0.53
Z	0.47	-0.03	-0.88	0.43	-0.31	0.84

**Figure S58.** Magnetic axes g_1 (red), g_2 (green), g_3 (blue) for **2** without ethanol (left) and **2** with ethanol (right). g_3 corresponds to g_{\perp} and is perpendicular to the $\text{Cu}(\text{dmgl})_2$ plane.

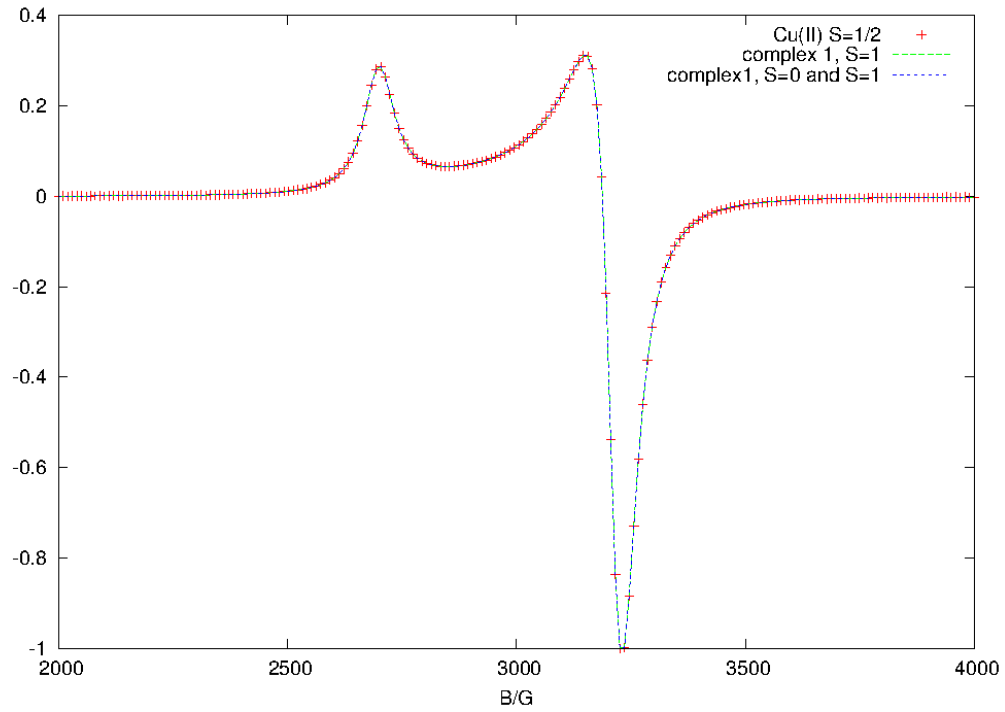


Figure S59. Simulation of the EPR spectra with the program package PHI^[23] for T = 100K and a frequency of 9.45 GHz.

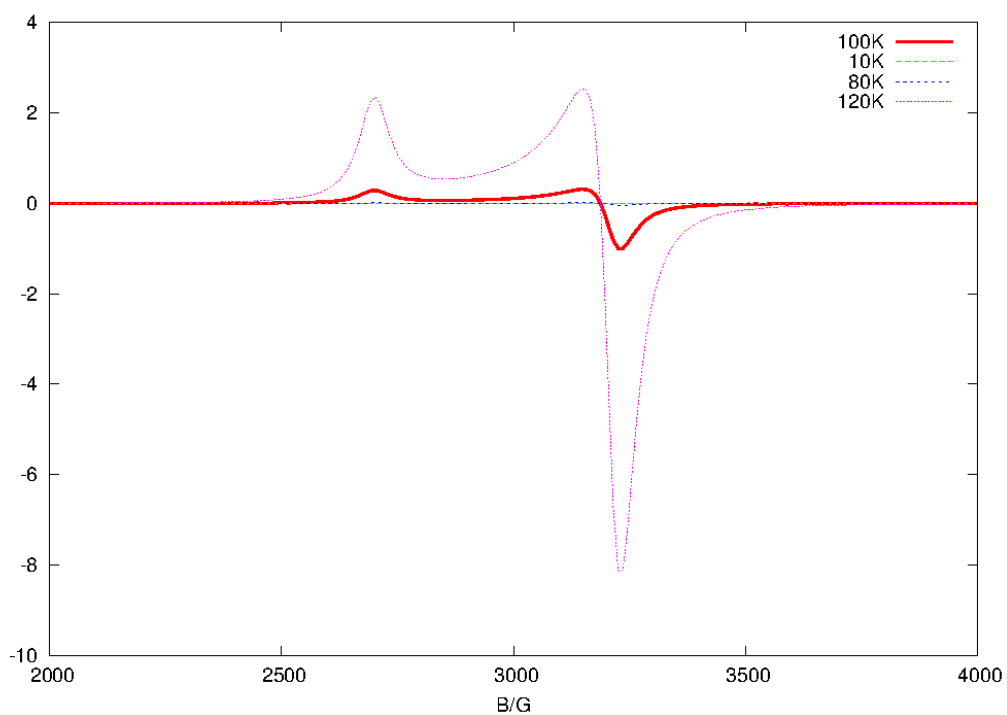


Figure S60. Temperature dependence of the simulated spectra of **1** from the lowest singlet and triplet state. With temperature the occupation of the triplet state increases (Boltzmann statistics). Therefore, the intensity is growing while the form of the spectrum remains unchanged. Parameters: $J = -475 \text{ cm}^{-1}$, taken from experimental findings by *Ruiz et al.*^[9], frequency 9.45 GHz.

10. Literature

- [1] L. Krause, R. Herbst-Irmer, G. M. Sheldrick, D. Stalke, *J. Appl. Crystallogr.* **2015**, *48*, 3–10.
- [2] APEX2, Bruker AXS, Inc., Madison, WI, USA.
- [3] XPREP, Bruker AXS, Inc., Madison, WI, USA. [4] G. M. Sheldrick, *Acta Cryst. A Found Adv.* **2015**, *71*, 3–8.
- [5] G. M. Sheldrick, *Acta Cryst. C Struct. Chem.* **2015**, *71*, 3–8.
- [6] C. B. Hübschle, G. M. Sheldrick, B. Dittrich, *J. Appl. Crystallogr.* **2011**, *44*, 1281–1284.
- [7] A.L. Spek, Platon, University Of Utrecht, The Netherlands, **2008**. [8] R. Ruiz, J. Sanz, B. Cervera, F. Lloret, M. Julve, C. Bois, J. Faus, M. C. Muñoz, *J. Chem. Soc., Dalton Trans.* **1993**, 1623–1628.
- [9] R. Ruiz, J. Sanz, F. Lloret, M. Julve, J. Faus, C. Bois, M. C. Muñoz, *J. Chem. Soc., Dalton Trans.* **1993**, 3035–3039.
- [10] M. Loos, C. Gerber, F. Corona, J. Hollender, H. Singer, *Anal. Chem.* **2015**, *87*, 5738–5744.
- [11] J. Nessler, Über Das Verhalten Des Jodquecksilbers Und Der Quecksilberverbindungen Überhaupt Zu Ammoniak Und Über Eine Neue Reaction Auf Ammoniak, Albert-Ludwigs-Universität Freiburg, **1856**.
- [12] J. F. Coetzee, *Pure Appl. Chem.* **1966**, *13*, 427–436.
- [13] M. J. Frisch, G. W. Trucks, H. W. Schlegel, G. E. Scuseria, M. A. Robb, J. R. Cheeseman, G. Scalmani, V. Barone, G. A. Petersson, H. Nakatsuji, X. Li, M. Caricato, A. Marenich, J. Bloino, B. G. Janesko, R. Gomperts, B. Mennucci, H. P. Hratchian, J. V. Ortiz, A. F. Izmaylov, J. L. Sonnenberg, D. Williams-Young, F. Ding, F. Lipparini, F. Egidi, J. Goings, B. Peng, A. Petrone, T. Henderson, D. Ranasinghe, V. G. Zakrzewski, J. Gao, N. Rega, G. Zheng, W. Liang, M. Hada, M. Ehara, K. Throssell, J. A. Montgomery Jr., J. E. Peralta, F. Ogliaro, M. Bearpark, J. J. Heyd, E. Brothers, K. N. Kudin, V. N. Staroverov, T. Keith, R. Kobayashi, J. Normand, K. Raghavachari, A. Rendell, J. C. Burant, S. S. Iyengar, J. Tomasi, M. Cossi, J. M. Millam, M. Klene, C. Adamo, R. Cammi, J. W. Ochterski, R. L. Martin, K. Morokuma, O. Farkas, J. B. Foresman, D. J. Fox, Gaussian 09, Gaussian Inc., Wilford CT., **2016**.
- [14] F. Furche, R. Ahlrichs, C. Hättig, W. Klopper, M. Sierka, F. Weigend, *WIREs Comput Mol Sci* **2014**, *4*, 91–100.
- [15] a) TURBOMOLE V7.5 **2020**, a development of University of Karlsruhe and Forschungszentrum Karlsruhe GmbH, 1989-2007, TURBOMOLE GmbH, since 2007; available from <https://www.turbomole.org>. b) S. G. Balasubramani, G. P. Chen, S. Coriani, M. Diedenhofen, M. S. Frank, Y. J. Franzke, F. Furche, R. Grotjahn, M. E. Harding, C. Hättig, A. Hellweg, B. Helmich-Paris, C. Holzer, U. Huniar, M. Kaupp, A. Marefat Khah, S. Karbalaei Khani, T. Müller, F. Mack, B. D. Nguyen, S. M. Parker, E. Perit, D. Rappoport, K. Reiter, S. Roy, M. Rückert, G. Schmitz, M. Sierka, E. Tapavicza, D. P. Tew, C. van Wüllen, V. K. Voora, F. Weigend, A. Wodyński, J. M. Yu, *J. Chem. Phys.* **2020**, *152*, 184107.
- [16] S. Grimme, J. Antony, S. Ehrlich, H. Krieg, *J. Chem. Phys.* **2010**, *132*, 154104.
- [17] S. Grimme, S. Ehrlich, L. Goerigk, *J. Comput. Chem.* **2011**, *32*, 1456–1465.
- [18] R. I. Petrikat, S. Becker, *Z. anorg. allg. Chem.* **2022**, *648*, DOI 10.1002/zaac.202200150.
- [19] C.-H. Li, R.-J. Wang, H.-Z. Kou, Y.-D. Li, *Inorg. Chem. Commun.* **2002**, *5*, 403–406.
- [20] R. Blinc, D. Hadži, *J. Chem. Soc.* **1958**, *0*, 4536–4540.
- [21] P. K. Panja, S. Bala, C. Pal, P. N. Ghosh, *J. Mol. Struct.* **1991**, *249*, 277–283.
- [22] E. Garribba, G. Micera, *J. Chem. Educ.* **2006**, *83*, 1229.
- [23] N. F. Chilton, R. P. Anderson, L. D. Turner, A. Soncini, K. S. Murray, *J. Comput. Chem.* **2013**, *34*, 1164–1175.
- [24] K. Eichkorn, O. Treutler, H. Öhm, M. Häser, R. Ahlrichs, *Chem. Phys. Lett.* **1995**, *240*, 283–290.
- [25] K. Eichkorn, F. Weigend, O. Treutler, R. Ahlrichs, *Theor. Chem. Acta* **1997**, *97*, 119–124.
- [26] F. Weigend, *Phys. Chem. Chem. Phys.* **2006**, *8*, 1057.
- [27] G. Singh, S. Gamboa, M. Orío, D. A. Pantazis, M. Roemelt, *Theor. Chem. Acc.* **2021**, *140*, 139.
- [28] R. Selwin Joseyphus, M. Sivasankaran Nair, *Arab. J. Chem.* **2010**, *3*, 195–204.
- [29] S. K. Singh, M. Atanasov, F. Neese, *J. Chem. Theory Comput.* **2018**, *14*, 4662–4677.

5.2 Mechanistic and Kinetic Investigations of ON/OFF (Photo)Switchable Binding of Carbon Monoxide by Chromium(0), Molybdenum(0) and Tungsten(0) Carbonyl Complexes with a Pyridyl-Mesoionic Carbene Ligand

5.2.1 Präambel

In diesem Projekt wird die photoinduzierte Reaktivität von Chrom(0)-, Molybdän(0)- und Wolfram(0)-Carbonylkomplexen verfolgt. Diese Komplexe zeigen auch eine dunkle Rückreaktion nach der Bestrahlung, welche auch kinetisch untersucht wird.

Zusammen mit Pit Boden und Daniel Marhöfer habe ich die experimentellen Untersuchungen durchgeführt. Patrick Di Martino-Fumo hat die DFT-Rechnungen durchgeführt. Ich habe die DFT-Rechnungen ergänzt und die Auswertung für alle DFT-Rechnungen vollzogen. Pit Boden, Patrick Di Martino-Fumo, Daniel Marhöfer und ich wurden von Gereon Niedner-Schatteburg betreut.

Tobias Bens hat die Komplexe synthetisiert. Er wurde von Biprajit Sarkar betreut. Pit Boden und Biprajit Sarkar haben das Konzept entworfen. Das Manuskript wurde von Pit Boden geschrieben und von allen Autoren gemeinsam überarbeitet.

5.2.2 Nachdruck und ergänzende Informationen

JOHN WILEY AND SONS LICENSE
TERMS AND CONDITIONS

Dec 07, 2022

This Agreement between Sophie Steiger ("You") and John Wiley and Sons ("John Wiley and Sons") consists of your license details and the terms and conditions provided by John Wiley and Sons and Copyright Clearance Center.

Type of use	Dissertation/Thesis
License Number	5443830989219
Requestor type	Author of this Wiley article
License date	Dec 07, 2022
Format	Print and electronic
Licensed Content Publisher	John Wiley and Sons
Portion	Full article
Licensed Content Publication	Chemistry - A European Journal
Will you be translating?	No
Licensed Content Title	Mechanistic and Kinetic Investigations of ON/OFF (Photo)Switchable Binding of Carbon Monoxide by Chromium(0), Molybdenum(0) and Tungsten(0) Carbonyl Complexes with a Pyridyl-Mesoionic Carbene Ligand
Title	Zeitaufgelöste FTIR- und Lumineszenzspektroskopie an Organometallkomplexen und deren Reaktionen
Licensed Content Author	Pit J. Boden, Patrick Di Martino-Fumo, Tobias Bens, et al
Institution name	Technische Universität Kaiserslautern
Expected presentation date	Feb 2023
Licensed Content Date	Sep 1, 2022
Requestor Location	Sophie Steiger Erwin-Schrodinger-Straße 52
Licensed Content Volume	28
Requestor Location	Kaiserslautern, 67655 Germany Attn: Sophie Steiger
Licensed Content Issue	51
Publisher Tax ID	EU826007151
Licensed Content Pages	2
Total	0.00 EUR

Mechanistic and Kinetic Investigations of ON/OFF (Photo)Switchable Binding of Carbon Monoxide by Chromium(0), Molybdenum(0) and Tungsten(0) Carbonyl Complexes with a Pyridyl-Mesoionic Carbene Ligand

Pit J. Boden,^[a] Patrick Di Martino-Fumo,^[a] Tobias Bens,^[b] Sophie T. Steiger,^[a] Daniel Marhöfer,^[a] Gereon Niedner-Schatteburg,^{*,[a]} and Biprajit Sarkar^{*,[b]}

Abstract: This work tackles the photochemistry of a series of mononuclear Cr⁰, Mo⁰ and W⁰ carbonyl complexes containing a bidentate mesoionic carbene ligand of the 1,2,3-triazol-5-ylidene type. FTIR spectroscopy, combined with density functional theory calculations, revealed a clean photo-induced reaction in organic solvents (acetonitrile, pyridine, valeronitrile) to give mainly one photoproduct with mono-substitution of a carbonyl ligand for a solvent molecule. The highest photodissociation quantum yields were reached for

the Cr⁰ complex under UV irradiation (266 nm). Based on previous investigations, the kinetics of the dark reverse reactions have now been determined, with reaction times of up to several hours in pyridine. Photochemical studies in the solid state (KBr matrix, frozen solution) also showed light-induced reactivity with stabilization of the metastable intermediate with a free coordination site at very low temperature. The identified reactive species emphasizes a mechanism without ligand–sphere reorganization.

Introduction

Light-driven chemical reactivity is an elegant way to generate new classes of chemical substances, and to induce unusual types of catalysis.^[1] Oftentimes photo-induced reactions tend to be very different from their thermal counterparts, as light can be used to selectively access states that might not be accessible in a selective manner in thermal reactions. In this context, carbonyl complexes of zero-valent group 6 metals are well-known for their mostly irreversible loss of carbon monoxide (CO) on irradiation with light.^[2–14] Such reactions are well established for the parent [M(CO)₆] (M = Cr, Mo, W) complexes,^[9–13,15,16] systems of the type [LM(CO)₅] (L is usually a monodentate N-donor),^[2,3,17] but also for complexes of the type [LM(CO)₄] (M = Cr, Mo, W), where L is usually a chelating ligand

containing N-donors such as 2,2'-bipyridine.^[2,5–8,14,18] In the aforementioned metal complexes, apart from the specific case of W(CO)₆ in acetonitrile (MeCN),^[9] irradiation with UV/VIS light leads to an irreversible loss of CO in solution, and such a method is often used for performing facile substitution reactions on these complexes.

In recent years, N-heterocyclic carbenes (NHCs), and in particular mesoionic carbenes (MICs) of the 1,2,3-triazol-5-ylidene type have been established as privileged ligands in the fields of photochemistry and photophysics.^[19–22,23,24–26] It was shown that MIC containing transition metal complexes often display much more promising excited state properties for applications in comparison to metal complexes that contain only N-donor ligands. Additionally, MIC ligands were also shown to form luminescent metal complexes with 3d transition metals^[20–22,24,26] as well as with main group metals.^[25,26] We have recently reported Cr⁰, Mo⁰ and W⁰ carbonyl complexes with a pyridyl-MIC ligand (L; Figure 1).^[19,20] These compounds display electrochemical, photophysical and photochemical properties that are largely different from related complexes with exclusively N-donor ligands. The Cr⁰ complex displays a completely

[a] Dr. P. J. Boden, P. Di Martino-Fumo, S. T. Steiger, D. Marhöfer, Prof. Dr. G. Niedner-Schatteburg
Department of Chemistry and State Research Center Optimas
TU Kaiserslautern
Erwin-Schrödinger-Straße 52, 67663 Kaiserslautern (Germany)
E-mail: gns@chemie.uni-kl.de

[b] T. Bens, Prof. Dr. B. Sarkar
Chair of Inorganic Coordination Chemistry
Institute of Inorganic Chemistry
University of Stuttgart
Pfaffenwaldring 55, 70569 Stuttgart (Germany)
E-mail: biprajit.sarkar@iac.uni-stuttgart.de

Supporting information for this article is available on the WWW under <https://doi.org/10.1002/chem.202201038>

© 2022 The Authors. Chemistry - A European Journal published by Wiley-VCH GmbH. This is an open access article under the terms of the Creative Commons Attribution License, which permits use, distribution and reproduction in any medium, provided the original work is properly cited.

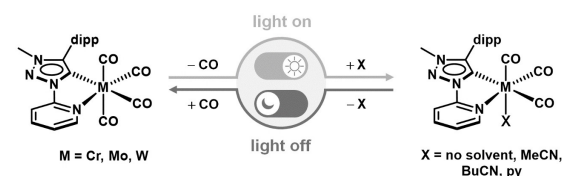


Figure 1. Photochemical reactivity of Cr, Mo, and W.

reversible oxidation to the corresponding Cr^{I} complex at ambient temperatures.^[19] In solution, they display a completely light-driven reversible bond activation reaction, with an almost complete recovery of the initial species when left in the dark.^[19] This observation is very distinct from photochemical reactions observed for other related group 6 carbonyl complexes in which the photo-induced CO ligand loss is always completely irreversible.^[2,5–8,14,18] In the literature, a (photo)switchable coordination of CO by a 3d metal complex is only known for very few Cu^{I} pyridylalkylamine systems so far, to the best of our knowledge.^[27]

In this contribution, we tackle the question of the reversible photochemical bond activation reaction in the abovementioned complexes of Cr^0 (**Cr**), Mo^0 (**Mo**) and W^0 (**W**; Figure 1) from a mechanistic perspective by using a combination of experimental and theoretical methods. The photochemical reactivity in solution and in the solid state was followed by FTIR spectroscopy, including investigations at low temperature to stabilize reactive intermediates, and interpreted by considering density functional theory (DFT) calculations. Beyond these mechanistic insights, the photodissociation quantum yields and the kinetics of the dark reverse reaction were determined on basis of the evolution of IR spectra over time. To the best of our knowledge, this is the first mechanistic investigation on group 6 metal complexes of the type $[\text{LM}(\text{CO})_4]$ in which the photochemical bond activation reactions are almost completely reversible.

Results and Discussion

Based on our preliminary studies of the photochemistry of **Cr** and **Mo** in different organic solvents acetonitrile (MeCN), pyridine (py), dichloromethane,^[19] we proceeded with refined photochemical studies by FTIR spectroscopy on **Cr**, **Mo** and **W** in MeCN and pyridine. The experimental procedure was optimized by irradiation of the liquid sample cell with two separate laser beams from opposite directions to ensure a homogenous illumination of the cell volume. This procedure enabled in particular the determination of the photodissociation quantum yields and kinetic studies, as presented below.

Fresh solutions of the complexes **Cr**, **Mo** and **W** show three strong IR absorption bands localized at 1995–2006, 1877–1892 and 1827–1835 cm^{-1} , with respect to the metal center and the solvent (Figures 2 and S30).^[19,20] The experimental IR spectra are very well described by the theoretical spectra calculated by DFT with simulation of solvent effects through the conductor-like screening model (COSMO). Hereby, the COSMO model is crucial for an accurate description of the CO stretching frequencies. The comparison between experiment and theory also confirmed the assignment of the abovementioned experimental bands to the four CO stretching vibrations.

Irradiation of the respective solutions was performed at 355 nm over 15 or 20 s for **Cr** and 60 s for **Mo** and **W** to stimulate the photochemical reaction. Excitation times were selected to achieve an almost complete conversion to the photoproducts, but prevent eventual follow-up reactions, which would impede a clear identification of photoproducts and

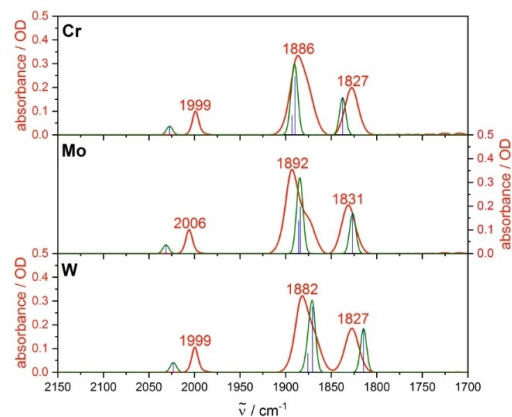


Figure 2. Experimental IR spectra of **Cr**, **Mo**, and **W** in MeCN (red) as well as calculated IR frequencies (blue) and convoluted spectra (green). Calculations: DFT/B3LYP-D3(BJ)/def2-TZVP/COSMO, scaling factor: 0.99, Gaussian convolution with FWHM = 8 cm^{-1} .

reaction pathways. Experiments were performed at concentrations of 3 and 6 mM to analyze potential concentration effects on the photo-induced reaction products. In MeCN, intense bands were observed at 1892–1900 and 1779–1783 cm^{-1} upon irradiation independent of concentration, with a slight shift of the spectral frequencies with respect to the metal center (Figures 3 and S1–S5). Only minor traces of side products were observed at 1927 cm^{-1} (**Cr**) and 1932 cm^{-1} (**Mo**, $c = 6$ mM), revealing a clean conversion of the starting complex. A red-shift of 4 cm^{-1} was found for the initial band at about 1830 cm^{-1} in the case of **Cr** and **Mo**, which could result from the same side product. Interestingly, a weak IR signal was observed at 2135–2138 cm^{-1} in the difference spectra of all three complexes (Figures 3 and S1–S5). This feature is in good agreement with the IR spectrum of CO gas dissolved in MeCN, which shows a sharp band at 2138 cm^{-1} (Figure S8). The control experiment clearly points to dissolved free CO in solutions of the three complexes upon irradiation, where the broader band most likely results from solvation effects.

Performing the experiment in pyridine yielded similar observations with weak side bands at 1718 (**Mo**) and 1727 cm^{-1} (**Cr**, only recognizable in the difference spectrum), which are assigned to a minor side product (Figures S9–S14). Analogous to MeCN, a weak broad band was found at 2132–2133 cm^{-1} , consistent with the spectrum of free CO gas dissolved in pyridine with a sharp peak at 2133 cm^{-1} (Figure S16).

As the presence or absence of free CO molecules in solutions of the complexes upon irradiation is a key point in the identification of the photochemical reaction, we conducted further analysis with the CO detection reagent $\text{PdCl}_2(\text{MeCN})_2$. Pd^{II} is known to oxidize CO to CO_2 in presence of water,^[28] a reaction that only occurs with uncoordinated CO molecules. The formed CO_2 is an ideal IR probe as it shows an intense IR absorption in a region, where an interference with other absorption bands is not to be expected. Indeed, a sharp and

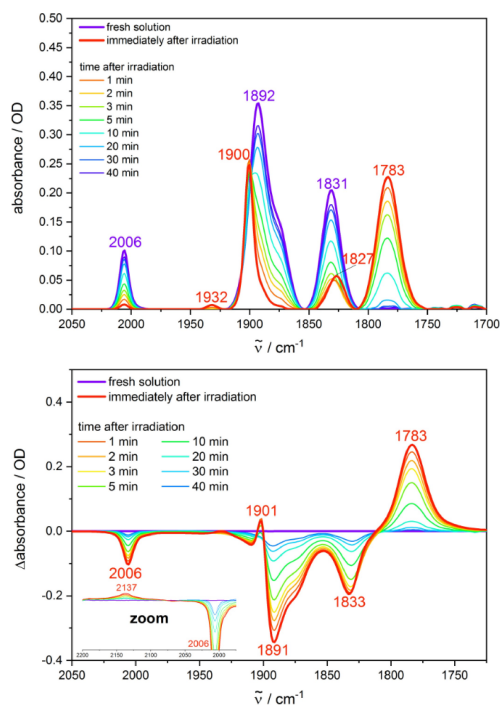


Figure 3. Irradiation ($\lambda_{\text{ex}} = 355$ nm) of a fresh solution of **Mo** in MeCN ($c = 6$ mM), and spectra recorded in the dark after irradiation (top: absolute absorption spectra, bottom: difference spectra).

quite intense absorption band was observed at 2335 cm^{-1} in pyridine (containing traces of H_2O) for all three complexes, which is assigned to CO_2 and confirms indirectly the formation of free CO molecules (Figures 4, S28, and S29). Unfortunately, the photochemical studies in MeCN under presence of

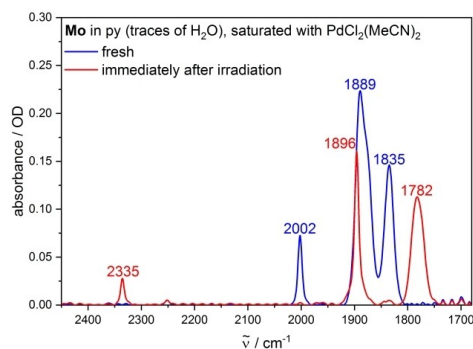


Figure 4. IR spectra of a solution of **Mo** in py (containing traces of H_2O , $c = 6$ mM), saturated with $\text{PdCl}_2(\text{MeCN})_2$, before and after irradiation ($\lambda_{\text{ex}} = 355$ nm).

$\text{PdCl}_2(\text{MeCN})_2$ failed due to undesired dark reactions taking place before irradiation.

Concerning the irradiation of **Cr**, **Mo**, and **W** in MeCN and pyridine, experimental data suggest the formation of one main photoproduct, next to minor contributions of side products. Hereby, side reactions seem to play a larger role for **Cr**. For a clear identification of the formed photoproducts, in-depth quantum chemical calculations (including COSMO) were performed for a large series of conceivable photoproducts. Considering the presented experimental results, a substitution of a CO ligand for a solvent molecule plays a key role ($[\text{LM}(\text{CO})_3(\text{X})]$, with $\text{X} = \text{MeCN}$ or py). Accordingly, all three potential isomeric photoproducts were optimized, followed by harmonic frequency calculations. Interestingly, the isomer with a substitution of an axial CO ligand for a solvent molecule ($[\text{LM}(\text{CO})_3(\text{X}_{\text{ax}})]$) is in very good agreement with the experimental data independent of the metal center or the solvent. The theoretical spectra of the two equatorially substituted isomers of the remaining two isomers ($[\text{LM}(\text{CO})_3(\text{X}_{\text{eq}})]$) give only a limited description of the experiment (Figures 5 and S31–S35), but could be responsible for the small side bands observed experimentally in MeCN at 1927 (**Cr**) and 1932 cm^{-1} (**Mo**) as well as the abovementioned red-shift of 4 cm^{-1} for the band at approx. 1830 cm^{-1} .

At the same time, the axial monosubstitution was throughout the photoproduct with the smallest predicted enthalpy of reaction with values of $31.7\text{--}66.5\text{ kJ mol}^{-1}$, depending on the metal center and the solvent (Figures 5 and S31–S35). Hereby, the values are higher in MeCN ($55.1\text{--}66.5\text{ kJ mol}^{-1}$) compared to

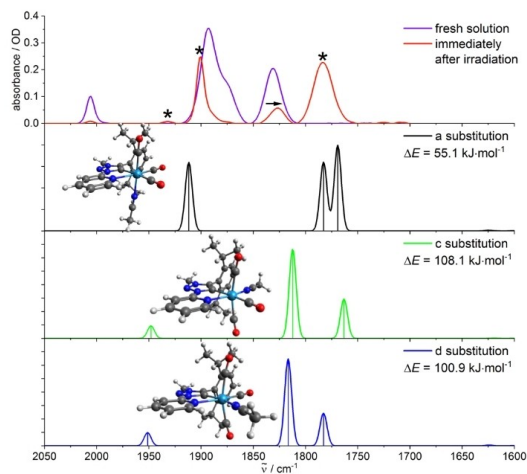


Figure 5. Experimental IR spectra of **Mo** in MeCN before and after irradiation (upper trace, bands marked with asterisks result from the formed photoproduct(s)) and calculated IR spectra of the photoproducts with the substitution of a CO ligand for a MeCN molecule (three lower traces), including the optimized structures and calculated enthalpies of reaction. The substitution occurs in the axial position for isomer a ($[\text{LMo}(\text{CO})_3\text{MeCN}_{\text{ax}}]$) and in the equatorial position for isomers c/d ($[\text{LMo}(\text{CO})_3\text{MeCN}_{\text{eq}}]$), respectively. Calculations: DFT/B3LYP–D3(BJ)/def2-TZVP/COSMO, scaling factor: 0.99, Gaussian convolution with $\text{FWHM} = 8\text{ cm}^{-1}$.

pyridine ($31.7\text{--}43.6\text{ kJ mol}^{-1}$) and follow the trend $\text{Cr} > \text{W} > \text{Mo}$. At first sight, these values might appear rather high, but the reaction enthalpies are far below the energy input resulting from the absorbed 355 nm photon in the experiment (337 kJ mol^{-1}). Thus, $[\text{LM}(\text{CO})_3(\text{X}_{\text{ax}})]$ can be assigned as main product from an energetic point of view, even though the isomers $[\text{LM}(\text{CO})_3(\text{X}_{\text{eq}})]$ could also contribute to a small extent. A bisubstitution with exchange of two CO ligands for solvent molecules ($[\text{LM}(\text{CO})_2(\text{X})_2]$) is not in good agreement with the experimental IR spectra at least for three of the four isomers, as their theoretical spectra show two strong bands in the region of $1825\text{--}1675\text{ cm}^{-1}$ versus only one in the experiment (Figures S36–S41). Only the fourth isomer $[\text{LM}(\text{CO})_2(\text{X}_{\text{eq}})_2]$ shows one single calculated band in the mentioned spectral region ($1825\text{--}1675\text{ cm}^{-1}$) that might be assigned to the experiment. However, it is energetically the most unfavorable bisubstitution ($\geq 207.6\text{ kJ mol}^{-1}$). Concerning the weak side bands observed experimentally in py at 1718 and 1727 cm^{-1} for Mo (Figures S10 and S13) and Cr (Figures S9 and S12), respectively, an assignment to $[\text{LM}(\text{CO})_2(\text{py}_{\text{ax}})(\text{py}_{\text{eq}})]$ is conceivable (Figures S39 and S40). However, the calculated spectra of $[\text{LM}(\text{CO})_2(\text{py}_{\text{ax}})_2]$ and $[\text{LM}(\text{CO})_2(\text{py}_{\text{ax}})(\text{py}_{\text{eq}})]$ are similar, making an unambiguous assignment difficult from that point of view. It can only be mentioned that the formation of $[\text{LM}(\text{CO})_2(\text{py}_{\text{ax}})(\text{py}_{\text{eq}})]$ gives the smallest enthalpy of reaction. A trisubstitution is excluded as the predicted bands are too far red-shifted with respect to the experiment and the reaction enthalpies are much higher ($\geq 228.0\text{ kJ mol}^{-1}$; Figures S42–S47). Next, the formation of a metallaketene upon irradiation was considered, whereby a CO ligand is inserted into the initial metal–carbene bond and the vacant coordination site is occupied by a solvent molecule (Figure 6). A related photochemical reactivity has been reported for a Fischer–carbene complex of Cr^0 with conversion to a metal–ketene upon visible light excitation.^[29] This pathway occurs without a loss of CO ligands, inconsistent with the free CO observed experimentally. However, the calculated IR spectrum of the metallaketene with insertion of a CO ligand

into the metal–carbene bond of the starting species and a solvent molecule coordinated in axial position (metal ketenes a or d, Figures S48–S53) is in good agreement with the experimental new absorption bands, so that a contribution of this reaction cannot be fully excluded at the current state of investigation. Nevertheless, the higher reaction enthalpies of $\geq 90.8\text{ kJ mol}^{-1}$ compared to the monosubstitution ($\geq 31.7\text{ kJ mol}^{-1}$) suggest that the formation of a metallaketene most likely takes place at most as side reaction and is not the main reaction product. Beyond this, a photoproduct with cleavage of the initial metal–carbene bond, followed by a rotation around the C–N bond bridging the triazole and pyridine rings and coordination of the triazole via the free nitrogen to the metal center was considered in the calculations (isomer e in Figures 6 and S54–S59).

The calculated IR spectra of this structure are only partly in agreement with the experiment and do not explain the strong product band at $1778\text{--}1784\text{ cm}^{-1}$, so that this species could only occur as side product. Furthermore, it is unlikely that this photoproduct with an uncoordinated carbene is stable in solution over a longer period at ambient temperature under experimental conditions (e.g., protonation of the carbene), which is inconsistent with the slow dark reverse reaction described in more detail in the following section. This drawback is in principle circumvented by isomers f and g with cleavage of the metal–pyridyl bond instead of the coordination of the carbene to the metal center (Figures 6 and S54–S59). The resulting vacant coordination site at the metal is occupied by a solvent molecule. Herewith, the two isomeric structures only differ by the position of the coordinated solvent molecule relative to the now monodentate pyridyl–MIC ligand. The calculated IR spectra show similar bands, which could contribute to the experimental IR spectrum, but do not explain the new band observed experimentally at $1778\text{--}1784\text{ cm}^{-1}$ upon irradiation. The low reaction enthalpies of $4.0\text{--}35.9\text{ kJ mol}^{-1}$ suggest the two isomers as conceivable side products, but can be excluded as main photoproducts. A similar description is

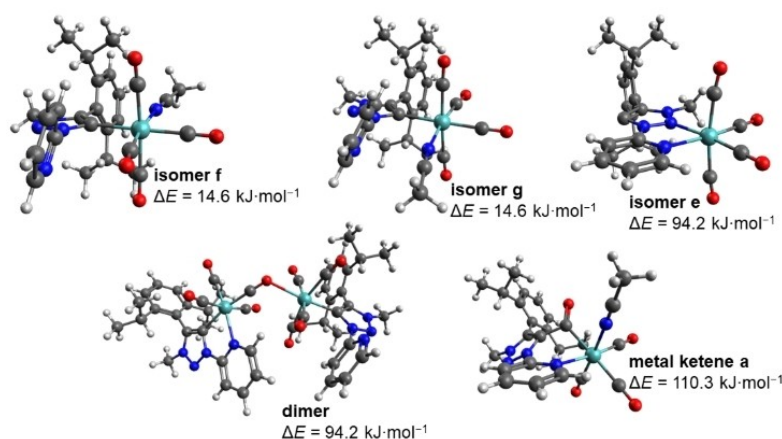


Figure 6. Optimized structures and enthalpies of reaction of selected photoproducts of Mo in MeCN. Calculations: DFT/B3LYP–D3(BJ)/def2-TZVP/COSMO.

valid for a dimeric structure formed out of two complex molecules with a CO ligand bridging the two metal centers and loss of one CO molecule per formed dimer (Figures 6 and S54–S59). Hereby, it should be mentioned that no optimized minimum structures were found for other conceivable dimers. However, dimerization would require a collision between one photoexcited species and a second molecule of the complex, which is rather unlikely at sample concentrations of 3 and 6 mM.

By considering the full set of experimental IR spectra and the calculations, including the predicted reaction enthalpies, it can be concluded that $[\text{LM}(\text{CO})_3(\text{X}_{\text{ax}})]$ is probably the main product of the photochemical reaction upon irradiation at 355 nm, independent of the solvent (MeCN and py) and the metal center (Cr, Mo, W). The conceivable primary reaction step with loss of a CO ligand was further analyzed by IR spectroscopy in the solid state (KBr matrix and frozen solution) at low temperature (see below). This assignment with photofragmentation of one M–CO bond and formation of the respective photoproduct with an axially coordinated solvent molecule is in accordance with literature reports on related systems such as $[\text{Mo}(\text{CO})_4(\text{iPr-DAB})]$ (DAB: 1,4-diaza-butadiene) and $[\text{Cr}(\text{CO})_4(\text{bpy})]$ (bpy: 2,2'-bipyridine).^[14,18]

A powerful tool to further investigate photo-induced reactivity is represented by UV/VIS spectroscopy and consideration of absorption spectra of all three complexes in py after irradiation at 355 nm. Pyridine was the solvent of choice due to the higher stability of the formed photoproducts compared to MeCN (see below and ref. [19]). For the three complexes two low-energy absorption bands are localized at 499–465 and 377–398 nm in py (Figure S64), which had been assigned to MLCT transitions earlier.^[20] The spectral blue-shift from Cr via W to Mo for the lowest-energy absorption band is in accordance with the absorption in other organic solvents.^[20] Interestingly, the UV/VIS spectrum clearly changes upon intense laser irradiation with a significant blue-shift of the strong low-energy visible absorption band to 449–470 nm (Figure S65). The mentioned absorption band is very well described by the theoretical UV/VIS spectra of $[\text{LM}(\text{CO})_3(\text{py}_{\text{ax}})]$, as calculated by time-dependent DFT (Figure S66). The strong visible absorption band of the photoproduct is a charge transfer transition from the metal center and the CO ligands to the coordinated pyridine ring and the bidentate pyridyl-MIC ligand (Tables S2–S4). Thus, UV/VIS spectroscopy further strengthens the suggestions that are based on IR spectroscopy.

The eventual influence of the excitation wavelength on the formed photoproducts was investigated by irradiation of fresh solutions of the complexes at 532 and 266 nm, complementary to the investigations at 355 nm excitation presented above. The investigations at 266 nm had to be restricted to MeCN solutions, as pyridine shows an intense absorption at 266 nm. Interestingly, the IR spectra after irradiation at 532 and 266 nm show the same product bands as at 355 nm irradiation (Figures S6, S7 and S15), indicating that the photon energy has no significant influence on the formed photoproducts. Particular attention should be paid to the reactivity at 532 nm upon visible excitation into the lowest energy absorption band (see

Figure S64 for the absorption in py and ref. [20] for MeCN). These observations clearly showed that at least one of the low-lying electronically excited states is photochemically reactive. It should also be mentioned that the lower photon energy at 532 nm (225 kJ mol^{-1}) is still far above the calculated reaction enthalpies of most potential photoproducts.

As irradiation at 532, 355 and 266 nm did not reveal any significant changes with respect to the formed main photoproduct, potential differences in the efficiency of reaction were considered by determination of the photodissociation quantum yields at these excitation wavelengths. The quantum yield of the photochemical reaction was determined from the fraction of reacted complex molecules relative to the number of absorbed photons, independent of the type of photoproduct which is formed. This evaluation was performed by considering the evolution of the IR spectrum during a short period of irradiation of few seconds at 532, 355 and 266 nm. The number of absorbed photons was determined from the respective UV/VIS extinction coefficients (Table S1). Irradiation times were kept short to minimize an undesired influence of the dark reverse reaction (see the next section) and follow-up reactions induced by absorption of a second photon by the initially formed photoproducts. Cr revealed to be the most reactive complex with a photodissociation quantum yield (Φ_{diss}) of 43% at 355 nm in MeCN with Mo and W showing lower quantum efficiencies of 15 and 5%, respectively (Table 1). No significant influence was observed using pyridine as solvent instead of MeCN. The quantum yields obtained for Cr, Mo, and W in MeCN and pyridine are of the order of those reported for related $\text{M}(\text{CO})_4(\text{diimine})$ complexes in the literature.^[5–8,14] The described trend of $\text{Cr} \gg \text{Mo} > \text{W}$ is known from the related α -diimine carbonyl complexes of Cr^0 , Mo^0 and W^0 .^[6,7,14,30] and could result from efficient intersystem crossing towards low-reactive $^3\text{MLCT}$ states for W with its heavy tungsten center.^[14] Indeed, our previous photophysical studies on solid samples of Cr, Mo, and W yielded the highest phosphorescence quantum yields for tungsten.^[20] Interestingly, the quantum yields of the photochemical dissociation increase with decreasing irradiation wavelength resulting in a rise by more than one order of magnitude from 532 to 266 nm excitation (Table 1). This means on the one hand, that at least one low-energy excited state is photochemically reactive and on the other hand, that also one or several higher energy excited states show photochemical reactivity. The increase of the quantum efficiency with decreasing excitation wavelength is known from related α -diimine carbonyl complexes and is assigned to a higher photochemical reactivity of energetically higher MLCT states compared to the lower

Table 1. Photodissociation quantum yields of Cr, Mo, and W in MeCN ($\lambda_{\text{ex}} = 532, 355, 266 \text{ nm}$) and py ($\lambda_{\text{ex}} = 532, 355 \text{ nm}$).

	λ_{ex} [nm]	Φ_{diss} [%]		
		Cr	Mo	W
MeCN	532	0.9	0.6	0.3
	355	43	15	5
	266	46	44	10
py	532	0.9	0.5	0.3
	355	36	14	3.4

ones.^[5,6,8,14,18] Beyond this, extensive studies on $[\text{Cr}(\text{CO})_4(2,2\text{-bipyridine})]$ revealed that the excitation wavelength has a significant influence on the ultrafast dynamics in the first hundreds of femtoseconds after excitation and herewith on the relative population of reactive and unreactive excited states. Excitation with high energy photons favors the population of reactive $^1\text{MLCT}$ states.^[31,32]

At this point, we wish to highlight the reversibility of the presented complexes to their initial species in a slow dark reaction. This reversibility is quite surprising for the investigated carbonyl complexes, as it has, to the best of our knowledge, only been reported for the homoleptic hexacarbonyl complex $\text{W}(\text{CO})_6$ so far.^[9,11] Preliminary observations concerning the reverse reactions for the systems **Cr** and **Mo** have been presented in an earlier publication,^[19] but profound kinetic studies were up to now hampered by limited reproducibility. Herein, we report on the kinetics of the dark reverse reaction, which were analyzed under optimized conditions with a homogenous irradiation of the sample volume by two laser beams.

Concretely, the kinetics of the dark reverse reaction were analyzed in MeCN and pyridine by considering the decrease of the strong new band at $1778\text{--}1784\text{ cm}^{-1}$, which is clearly assigned to the main photoproduct and is well separated from the other absorption features. The dark reaction was monitored subsequent to a period of irradiation at 355 nm (15 or 20 s for **Cr**, 60 s for **Mo** and **W**) or 532 nm (15 s for **Cr**, 60 or 120 s for **Mo** and **W**) with conversion of significant amounts of the initial complex to the photoproducts (Figures 3, S1–S6 and S9–S15). Hereby, the experimental IR intensity of the considered photoproduct band at the end of the irradiation period was normalized to 1 as the photoproduct concentration could not be accurately determined with the available techniques. Experiments were performed at concentrations of 6 and 3 mM with the laser power being adapted accordingly. The decay of the photoproduct band can be described by a first-order kinetic fit for all three complexes, yet with deviations at longer time scales for **Mo** and **W** (Figures 7 and S67–S69). At the same time, the second order model kinetic plots do not yield the linear slopes expected for a bimolecular reaction (Figures S70–S73). For the second order evaluation, it was assumed that the photoproduct concentration is throughout identical to that of solvated CO. At first sight, the much better agreement of the first-order kinetics is surprising for this bimolecular reverse reaction. However, it may be explained by a rate limiting initial thermal loss of the coordinated solvent molecule, before the formed reactive intermediate with 16 valence electrons reacts with CO to the initial complex (**Cr**, **Mo**, **W**).

Interestingly, the obtained reaction constants in MeCN strongly depend on the metal center as the dark reverse reaction is about one order of magnitude faster for **Cr** ($k_{\text{Cr}}(\text{MeCN}) = 0.019\text{--}0.026\text{ s}^{-1}$) compared to the lower values of **Mo** and **W** ($k_{\text{Mo}}(\text{MeCN}) = (1.3\text{--}1.9) \times 10^{-3}\text{ s}^{-1}$; $k_{\text{W}}(\text{MeCN}) = (1.1\text{--}2.4) \times 10^{-3}\text{ s}^{-1}$ (Table 2).

In pyridine no clear trend was observed with respect to the correlation between the kinetics and the metal. **Cr** only gave clearly the highest kinetic rate at an irradiation wavelength of

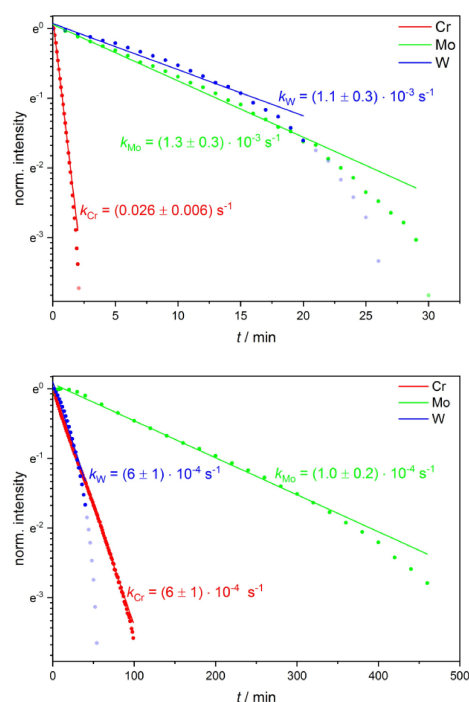


Figure 7. First-order kinetic plots and fits of the dark reverse reaction of **Cr**, **Mo**, and **W** measured in MeCN (top) and py (bottom; $c = 6\text{ mM}$). The shown kinetics were recorded after irradiation at 532 nm. The IR intensity at the end of the irradiation period ($t = 0$) was normalized to 1.

355 nm and a concentration of 6 mM. At 532 nm irradiation in pyridine the reaction constants of **W** surpass those of **Cr**. Furthermore, the obtained results for **Mo** and **W** in pyridine strongly depend on the wavelength of the preceding irradiation (355 vs. 532 nm) and on concentration (6 vs. 3 mM). These observations for **Mo** and **W** in pyridine suggest at least two competing pathways for the reverse reaction under these conditions and are not yet fully understood. The impact of the solvent is more pronounced and obvious with reverse reactions that are at least one order of magnitude slower in pyridine compared to MeCN (Table 2, Figures 7 and S67–S69). In pyridine the photoproduct of **Mo** is clearly detectable several hours after the irradiation period and is thus particularly stable. This is in accordance with the observations reported in an earlier publication.^[19] The higher stability of the photoproducts containing pyridine relative to those with MeCN can be explained by the strong π -backbonding in case of the py ligand. Selected absolute and difference spectra of the kinetic experiments are represented in Figures 3, S1–S5 and S9–S14.

It is concluded that the general trend of $\text{Cr} \gg \text{Mo} \approx \text{W}$ found for the dark kinetics in MeCN is similar to the results for the photodissociation quantum yields ($\text{Cr} \gg \text{Mo} > \text{W}$). The initial photochemical reaction and the subsequent dark reaction seem to be more favorable for **Cr**. The initial step is best described as cleavage of a coordinative M–CO and M–solvent

	c [mM]	λ_{ex} [nm]	K [s ⁻¹]		
			Cr	Mo	W
MeCN	6	532	0.026±0.006	$(1.3\pm 0.3)\times 10^{-3}$	$(1.1\pm 0.3)\times 10^{-3}$
	3	532	0.019±0.005	$(1.4\pm 0.4)\times 10^{-3}$	$(2.4\pm 0.6)\times 10^{-3}$
	6	355	0.023±0.006	$(1.9\pm 0.5)\times 10^{-3}$	$(1.7\pm 0.4)\times 10^{-3}$
	3	355	0.025±0.006	$(1.7\pm 0.4)\times 10^{-3}$	$(1.4\pm 0.4)\times 10^{-3}$
py	6	532	$(6\pm 1)\times 10^{-4}$	$(1.0\pm 0.2)\times 10^{-4}$	$(6\pm 1)\times 10^{-4}$
	3	532	$(5\pm 1)\times 10^{-4}$	$(2.0\pm 0.5)\times 10^{-4}$	$(1.2\pm 0.3)\times 10^{-4}$
	6	355	$(8\pm 2)\times 10^{-4}$	$(1.7\pm 0.4)\times 10^{-4*}$	$(1.5\pm 0.4)\times 10^{-4}$
	3	355	$(6.1\pm 0.2)\times 10^{-4}$	$(4\pm 1)\times 10^{-4}$	$(8\pm 2)\times 10^{-4}$

* It should be noted that the underlying fit shows larger deviations from the experimental data.

(acetonitrile/pyridine) bond, respectively (see low-temperature IR spectroscopy). Such a dissociative mechanism has also been reported for related Cr complexes such as [Cr(CO)₄phen] (phen = phenanthroline) by van Eldik et al., but the analogous Mo and W complexes rather follow associative substitution pathways.^[8,33]

Temperature-dependent photochemical studies on Cr, Mo, and W were performed in a KBr matrix to obtain more insights with respect to the reaction pathway and long-lived intermediates. Irradiation at 355 nm of KBr pellets cooled down to 10 K yielded weak new absorption bands/shoulders in the regions of 1918–1905 cm⁻¹ (one signal) and 1813–1763 cm⁻¹ (two signals), with small spectral shifts depending on the metal center (Figures 8 and S60–S61). Furthermore, small signals appeared at 2123–2183 cm⁻¹ in the respective difference spectra, which are

assigned to traces of unbound or weakly bound CO in the matrix upon irradiation (Figure S18). Thus, reactivity was obtained in the solid state without the presence of any obvious reaction partner. The traces of free CO indicate the cleavage of M–CO bonds, similar to the observations in liquid solution. Considering the experimental spectra, theoretical calculations were performed for three potential photoproducts in the solid state with loss of a single CO ligand and a vacant coordination site ([LM(CO)₃]) (Figures 8, S60, and S61). The theoretical spectra of the optimized structures with loss of an axial CO ligand are indeed in very good agreement with the experiment for all three complexes. The isomers with a vacant equatorial coordination site describe the recorded IR spectra only to a smaller extent and are higher in energy.

These statements are in perfect agreement with the conclusions deduced from the photochemical studies in solution, where [LM(CO)₅(X_{ax})] was best described as the main photoproduct.

In the KBr matrix with absence of a suitable reaction partner, it is conceivable that the assigned species [LM(CO)₃] with 16 valence electrons is stabilized at 10 K. The weak product features must result from a very limited conversion of the initial species to the photoproducts in the solid sample. A specific orientation and packing on a molecular level may be required for photo-induced reactivity. The formed photoproduct is stabilized to full extent at 10 K over at least 30 min in the dark. However, the intensity of the product features decreases steadily upon heating stepwise to 290 K after irradiation at 10 K, accompanied by an increase of the absorption bands of the initial complex. Hence, the reaction in the solid state is reversible at least at sufficient thermal energy (Figures S19–S21). This means that a certain amount of photoproduct is efficiently stabilized over time at a specific temperature and, accordingly, irradiation of a fresh sample at a chosen temperature yields a certain amount of stable photoproduct (Figures S22–S24). No reaction was observed in the static spectra at 290 K, which most probably results from a very fast reverse reaction, impeding the accumulation of detectable amounts of photoproduct. The fast reverse reaction at higher temperature may be a result of stronger fluctuations within the KBr matrix at higher thermal energy, making the trapping of uncoordinated

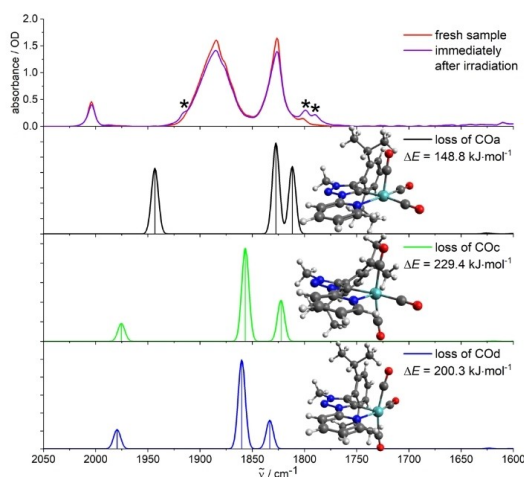


Figure 8. Irradiation ($\lambda_{\text{ex}} = 355$ nm) of fresh samples of Mo (KBr pellet) at 10 K and calculated IR spectra of different photoproducts with loss of a CO ligand, including the optimized structures and calculated enthalpies of reaction. The vacant coordination site is localized in the axial position for isomer a and in the equatorial position for structures c/d. Calculations: DFT/B3LYP–D3(BJ)/def2-TZVP/COSMO, scaling factor: 0.99, Gaussian convolution with FWHM = 8 cm⁻¹.

CO less efficient and leading to its recombination with the very reactive 16 valence electron species. $[\text{LM}(\text{CO})_3]$ is far too short-lived to be detectable with the applied techniques in solution at room temperature. In this context, it should be noticed that the transient femtosecond pump-probe experiments required for the observation of such short-lived intermediates would most likely be hampered by the rather low photochemical reactivity of the systems (in particular **Mo** and **W**). This drawback had led to very weak step-scan FTIR signals in preliminary works.^[19] In accordance with the reported photodissociation quantum yields in solution (MeCN and py), the photochemical reaction in the solid state is, compared to excitation at 355 nm, less efficient at 532 nm and more pronounced at 266 nm according to the relative spectral intensities (Figures S25–S27). This photochemistry in the solid state is closely related to the reported reactivity of the hexacarbonyls of chromium, molybdenum and tungsten in a cold matrix (KBr,^[9] PMMA (poly(methyl methacrylate))^[15] and inert-gas matrix^[10] with a loss of a CO ligand and formation of the reactive species $\text{M}(\text{CO})_5$ ($\text{M} = \text{Cr}^0$, Mo^0 or W^0).

Complementary studies were performed in frozen valeronitrile (BuCN) at 10 K in order to confirm the formation of the reactive species $[\text{LM}(\text{CO})_3]$ also under conditions that are closer to the studies in liquid solution. BuCN was selected not only for its ability to form a clear glass at the melting point, but also for its ligand properties comparable to MeCN. As expected, irradiation ($\lambda_{\text{ex}} = 355$ nm) of fresh solutions of **Cr**, **Mo**, and **W** in BuCN at room temperature yielded IR spectra with product bands very similar to those in MeCN and pyridine (Figure S17). Concerning the experiments in frozen solution, the measurement of absolute spectra turned out to be difficult due to varying scattering effects induced by the glass matrix when comparing the sample scans with the reference consisting of pure valeronitrile. Hence, the following discussions are limited to difference spectra representing the spectral changes induced by irradiation at 355 nm. The difference spectrum of **Mo** shows intense positive peaks at 1917 and 1904 cm^{-1} as well as a broad positive band at 1793 cm^{-1} (Figure 9). A weak positive band was observed at 2133 cm^{-1} , which can be assigned to free CO under consideration of the studies in solution and KBr presented before. Surprisingly, the negative bands in the difference spectrum obtained in frozen BuCN are very weak compared to the positive ones, which might be explained by higher oscillator strengths of the photoproduct peaks in this medium. The comparison of the difference spectra of **Mo** obtained in liquid and frozen BuCN revealed that the peaks at 1903 cm^{-1} in liquid solution and at 1904 cm^{-1} in frozen solution result from the same product species (Figure 9). The positive peak at 1792 cm^{-1} is broader in frozen glass compared to the liquid phase and could indicate the superposition of the absorption features of at least two different structures in this spectral region for the frozen matrix. Furthermore, an additional band was observed at 1917 cm^{-1} in the glass, which was completely absent at room temperature. Under consideration of this experimental result, the new peak at 1917 cm^{-1} was preliminarily attributed to a reactive intermediate, similar to the observations in a KBr matrix at low temperature. For clarifica-

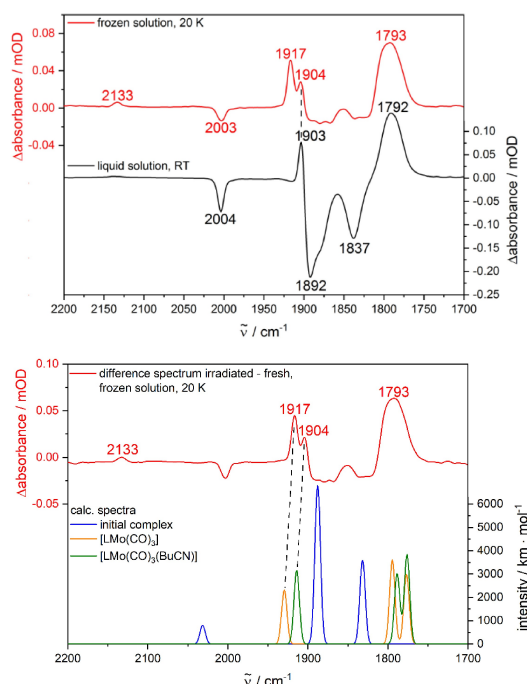


Figure 9. Top: Difference spectra (irradiated–fresh) of **Mo** recorded in frozen (20 K) and liquid (RT) solutions. Bottom: Comparison of the difference spectrum at 20 K with calculated IR spectra of the initial complex as well as the photoproducts $[\text{LMo}(\text{CO})_3]$ (vacant coordination site in axial position) and $[\text{LMo}(\text{CO})_3]_2(\text{BuCN})_x$. The dashed lines are guides to the eye. Calculations: DFT/B3LYP–D3(BJ)/def2-TZVP/COSMO, scaling factor: 0.99, Gaussian convolution with FWHM = 8 cm^{-1} .

tion, theoretical calculations were performed in BuCN. Indeed, the calculated IR spectra of $[\text{LMo}(\text{CO})_3]$ and $[\text{LMo}(\text{CO})_3]_2(\text{BuCN})_x$ suggest their coexistence in frozen solution. Concerning the experimental double band around 1910 cm^{-1} , theory predicts a slight red-shift for the structure with a bound BuCN molecule, in agreement with the experimental difference spectra in frozen and liquid BuCN (Figure 9). The same descriptions are valid for **Cr** and **W** (Figures S62 and S63), both from an experimental and theoretical point of view. Finally, the photochemical studies in frozen solution clearly show that the mechanistic pathway in organic solvents involves the presented species $[\text{LM}(\text{CO})_3]$ as metastable intermediate, followed by formation of $[\text{LM}(\text{CO})_3(\text{X}_{\text{ax}})]$ with a solvent molecule in axial position.

The first step in the reaction mechanism is preferably a cleavage of an axial M–CO bond as these are elongated compared to those of the equatorial CO ligands according to theory (Table S5) and the crystal structures reported earlier.^[19,20] In this case, the mechanism could take place without ligand-sphere reorganization with respect to the orientation of the CO ligands. This suggestion is in full agreement with ultrafast spectroscopy on $[\text{Cr}(\text{CO})_4(2,2'\text{-bipyridine})]$, which did not show any structural reorganization after the initial photochemical loss of CO .^[32]

Conclusion

In conclusion, profound spectroscopic and theoretical studies were performed on the photochemical properties of a series of pseudo-octahedral Cr⁰, Mo⁰ and W⁰ carbonyl complexes containing a bidentate pyridyl-mesoionic carbene ligand (Figure 10). According to IR spectroscopy in combination with density functional theory (DFT), in common coordinating organic solvents (acetonitrile, valeronitrile and pyridine), UV and visible irradiation induce a clean photochemistry with monosubstitution of an axial CO ligand for a solvent molecule. FTIR spectroscopy at low temperatures revealed a metastable reactive intermediate with a vacant axial coordination site, thereby pointing to a reaction without ligand–sphere reorganization upon photo-induced cleavage of one of the two weakest coordinative bonds (CO_{axial}). The photodissociation quantum yield increases from W⁰ over Mo⁰ to Cr⁰ (values of up to 46%) independently of the solvent. The values in acetonitrile are higher throughout compared to those in pyridine and increase with decreasing irradiation wavelength. The most remarkable observation for the investigated complexes is definitely the reversibility of the photochemical reaction with recovery of at least the majority of the starting complex in a dark reverse reaction consecutive to irradiation. The reverse reaction is faster for Cr⁰ (minutes) than for Mo⁰ and W⁰ in MeCN and can take several hours for Mo⁰ and W⁰ in pyridine. This atypical reversibility will be investigated by further theoretical studies in the future with a focus on mechanistic pathways and, in particular, energy barriers. The photochemistry, with one preferred reaction pathway, would be extremely useful for applications in highly selective photochemical synthesis, and its reversibility opens a new field of (photo)switchable transition metal complexes.

Experimental Section

Experimental details are provided in the Supporting Information.

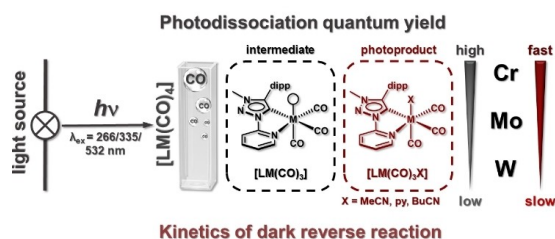


Figure 10. Graphical summary of the (photo)chemistry of Cr, Mo, and W in organic solution (MeCN, py, BuCN). The given molecular structures of intermediate and photoproduct are those of the species mainly observed. The illustrated trends for the photodissociation quantum yield and the kinetics of the dark reverse reaction are fully valid for MeCN, with a few exceptions for py.

Acknowledgements

We gratefully acknowledge financial support from the Deutsche Forschungsgemeinschaft (DFG, Priority Program SPP 2102 "Light-controlled reactivity of metal complexes", SA1840/7-2, Ni 325/12-2). Open access funding enabled and organized by Projekt DEAL. Open Access funding enabled and organized by Projekt DEAL.

Conflict of Interest

The authors declare no conflict of interest.

Data Availability Statement

The data that support the findings of this study are available in the supplementary material of this article.

Keywords: group 6 metals · mesoionic carbene · metastable compounds · photochemistry · reversible reactions · time-resolved FTIR spectroscopy

- [1] a) W.-M. Cheng, R. Shang, *ACS Catal.* **2020**, *10*, 9170–9196; b) S. P. Pitre, L. E. Overman, *Chem. Rev.* **2022**, *122*, 1717–1751; c) K. P. S. Cheung, S. Sarkar, V. Gevorgyan, *Chem. Rev.* **2022**, *122*, 1543–1625.
- [2] M. Wrighton, *Chem. Rev.* **1974**, *74*, 401–430.
- [3] R. M. Dahlgren, J. I. Zink, *J. Am. Chem. Soc.* **1979**, *101*, 1448–1454.
- [4] C. Garino, L. Salassa, *Philos. Trans. R. Soc. London Ser. A* **2013**, *371*, 20120134.
- [5] R. S. Panesar, N. Dunwoody, A. J. Lees, *Inorg. Chem.* **1998**, *37*, 1648–1650.
- [6] R. W. Balk, T. Snoeck, D. J. Stufkens, A. Oskam, *Inorg. Chem.* **1980**, *19*, 3015–3021.
- [7] D. M. Manuta, A. J. Lees, *Inorg. Chem.* **1986**, *25*, 1354–1359.
- [8] S. Wieland, K. B. Reddy, R. van Eldik, *Organometallics* **1990**, *9*, 1802–1806.
- [9] G. R. Dobson, M. F. A. El Sayed, I. W. Stolz, R. K. Sheline, *Inorg. Chem.* **1962**, *1*, 526–530.
- [10] M. A. Graham, M. Poliakoff, J. J. Turner, *J. Chem. Soc. A* **1971**, 2939.
- [11] I. W. Stolz, G. R. Dobson, R. K. Sheline, *J. Am. Chem. Soc.* **1962**, *84*, 3589–3590.
- [12] L. Zhu, S. Saha, Y. Wang, D. A. Keszler, C. Fang, *J. Phys. Chem. B* **2016**, *120*, 13161–13168.
- [13] G. M. Greetham, D. Sole, I. P. Clark, A. W. Parker, M. R. Pollard, M. Towrie, *Rev. Sci. Instrum.* **2012**, *83*, 103107.
- [14] A. Vlček Jr., *Coord. Chem. Rev.* **2002**, *230*, 225–242.
- [15] A. G. Massey, L. E. Orgel, *Nature* **1961**, *191*, 1387.
- [16] a) J. Burdett, R. N. Perutz, M. Poliakoff, J. J. Turner, *J. Am. Chem. Soc.* **1975**, 4805–4808; b) M. J. Boylan, J. D. Black, P. S. Braterman, *J. Chem. Soc. Dalton Trans.* **1980**, 1646; c) R. N. Perutz, J. J. Turner, *Inorg. Chem.* **1975**, *14*, 262–270.
- [17] a) R. M. Dahlgren, J. I. Zink, *Inorg. Chem.* **1977**, *16*, 3154–3161; b) M. Wrighton, *Inorg. Chem.* **1974**, *13*, 905–909; c) L. Tutt, J. I. Zink, *J. Am. Chem. Soc.* **1986**, *108*, 5830–5836.
- [18] A. Vlček Jr., I. R. Farrell, D. J. Liard, P. Matousek, M. Towrie, A. W. Parker, D. C. Grills, M. W. George, *J. Chem. Soc. Dalton Trans.* **2002**, 701–712.
- [19] T. Bens, P. Boden, P. Di Martino-Fumo, J. Beerhues, U. Albold, S. Sobottka, N. I. Neuman, M. Gerhards, B. Sarkar, *Inorg. Chem.* **2020**, *59*, 15504–15513.
- [20] P. Boden, P. Di Martino-Fumo, T. Bens, S. Steiger, U. Albold, G. Niedner-Schatteburg, M. Gerhards, B. Sarkar, *Chem. Eur. J.* **2021**, *27*, 12959–12964.
- [21] P. Chábbera, Y. Liu, O. Prakash, E. Thyraug, A. E. Nahhas, A. Honarfar, S. Essén, L. A. Fredin, T. C. B. Harlang, K. S. Kjær, K. Handrup, F. Ericson, H.

- Tatsuno, K. Morgan, J. Schnadt, L. Häggström, T. Ericsson, A. Sobkowiak, S. Lidin, P. Huang, S. Styring, J. Uhlig, J. Bendix, R. Lomoth, V. Sundström, P. Persson, K. Wärnmark, *Nature* **2017**, *543*, 695–699.
- [22] G. Kleinhans, A. K.-W. Chan, M.-Y. Leung, D. C. Liles, M. A. Fernandes, V. W.-W. Yam, I. Fernández, D. I. Bezuidenhout, *Chem. Eur. J.* **2020**, *26*, 6993–6998.
- [23] a) L. Suntrup, F. Stein, G. Hermann, M. Kleoff, M. Kuss-Petermann, J. Klein, O. S. Wenger, J. C. Tremblay, B. Sarkar, *Inorg. Chem.* **2018**, *57*, 13973–13984; b) S. K. Verma, P. Kumari, S. N. Ansari, M. O. Ansari, D. Deori, S. M. Mobin, *Dalton Trans.* **2018**, *47*, 15646–15650; c) L. Suntrup, F. Stein, J. Klein, A. Wiltling, F. G. L. Parlane, C. M. Brown, J. Fiedler, C. P. Berlinguette, I. Siewert, B. Sarkar, *Inorg. Chem.* **2020**, *59*, 4215–4227; d) E. Matteucci, F. Monti, R. Mazzoni, A. Baschieri, C. Bizzarri, L. Sambri, *Inorg. Chem.* **2018**, *57*, 11673–11686; e) J. Soellner, T. Strassner, *Chem. Eur. J.* **2018**, *24*, 5584–5590; f) L. Cao, S. Huang, W. Liu, H. Zhao, X.-G. Xiong, J.-P. Zhang, L.-M. Fu, X. Yan, *Chem. Eur. J.* **2020**, *26*, 17222–17229; g) L. Hettmanczyk, S. J. P. Spall, S. Klenk, M. van der Meer, S. Hohloch, J. A. Weinstein, B. Sarkar, *Eur. J. Inorg. Chem.* **2017**, *2017*, 2112–2121; h) P. Dierks, A. Kruse, O. S. Bokareva, M. J. Al-Marri, J. Kalmbach, M. Baltrun, A. Neuba, R. Schoch, S. Hohloch, K. Heinze, M. Seitz, O. Kühn, S. Lochbrunner, M. Bauer, *Chem. Commun.* **2021**, *57*, 6640–6643; i) Á. Vivancos, A. Jiménez-García, D. Bautista, P. González-Herrero, *Inorg. Chem.* **2021**, *60*, 7900–7913; j) B. Sarkar, L. Suntrup, *Angew. Chem. Int. Ed.* **2017**, *56*, 8938–8940; *Angew. Chem.* **2017**, *129*, 9064–9066; k) A. R. Naziruddin, C.-S. Lee, W.-J. Lin, B.-J. Sun, K.-H. Chao, A. H. H. Chang, W.-S. Hwang, *Dalton Trans.* **2016**, *45*, 5848–5859.
- [24] S. S. Nair, O. A. Bysewski, S. Kupfer, M. Wächtler, A. Winter, U. S. Schubert, B. Dietzek, *Inorg. Chem.* **2021**, *60*, 9157–9173.
- [25] P. Pinter, C. M. Schüßlbauer, F. A. Watt, N. Dickmann, R. Herbst-Irmer, B. Morgenstern, A. Grünwald, T. Ullrich, M. Zimmer, S. Hohloch, D. M. Guldi, D. Munz, *Chem. Sci.* **2021**, *12*, 7401–7410.
- [26] R. Maity, B. Sarkar, *JACS Au* **2022**, *2*, 22–57.
- [27] H. C. Fry, H. R. Lucas, A. A. N. Sarjeant, K. D. Karlin, G. J. Meyer, *Inorg. Chem.* **2008**, *47*, 241–256.
- [28] a) A. A. Christman, E. L. Randall, *J. Biol. Chem.* **1933**, *102*, 595–609; b) C. H. Gray, M. Sandiford, *The Analyst* **1946**, *71*, 107–110.
- [29] S. C. Nguyen, J. P. Lomont, M. C. Zoerb, P. V. Pham, J. F. Cahoon, C. B. Harris, *Organometallics* **2014**, *33*, 6149–6153.
- [30] K. R. Mann, H. B. Gray, G. S. Hammond, *J. Am. Chem. Soc.* **1977**, *99*, 306–307.
- [31] a) J. Vichova, F. Hartl, A. Vlcek, *J. Am. Chem. Soc.* **1992**, *114*, 10903–10910; b) I. G. Virrels, M. W. George, J. J. Turner, J. Peters, A. Vlček, *Organometallics* **1996**, *15*, 4089–4092; c) I. R. Farrell, P. Matousek, A. Vlček, *J. Am. Chem. Soc.* **1999**, *121*, 5296–5301.
- [32] I. R. Farrell, P. Matousek, M. Towrie, A. W. Parker, D. C. Grills, M. W. George, A. Vlcek, *Inorg. Chem.* **2002**, *41*, 4318–4323.
- [33] K. J. Schneider, R. van Eldik, *Organometallics* **1990**, *9*, 92–96.

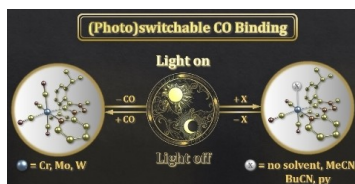
Manuscript received: April 5, 2022

Accepted manuscript online: June 15, 2022

Version of record online: ■■■, ■■■■

RESEARCH ARTICLE

Shining light on group 6 photochemistry: The reversible (photo)chemistry of chromium(0), molybdenum(0) and tungsten(0) carbonyl complexes containing a mesoionic carbene ligand has been investigated. Kinetic and mechanistic studies were performed by using (temperature-dependent) FTIR and UV/VIS spectroscopy, in combination with density functional theory calculations.



Dr. P. J. Boden, P. Di Martino-Fumo, T. Bens, S. T. Steiger, D. Marhöfer, Prof. Dr. Dr. G. Niedner-Schatteburg, Prof. Dr. B. Sarkar**

1 – 11

Mechanistic and Kinetic Investigations of ON/OFF (Photo)Switchable Binding of Carbon Monoxide by Chromium(0), Molybdenum(0) and Tungsten(0) Carbonyl Complexes with a Pyridyl-Mesoionic Carbene Ligand



Chemistry–A European Journal

Supporting Information

Mechanistic and Kinetic Investigations of ON/OFF (Photo)Switchable Binding of Carbon Monoxide by Chromium(0), Molybdenum(0) and Tungsten(0) Carbonyl Complexes with a Pyridyl-Mesoionic Carbene Ligand

Pit J. Boden, Patrick Di Martino-Fumo, Tobias Bens, Sophie T. Steiger, Daniel Marhöfer, Gereon Niedner-Schatteburg,* and Biprajit Sarkar*

Table of Contents

1	Experimental Details	3
1.1	Static and time-resolved FTIR spectroscopy	3
1.1.1	General setup for time-resolved FTIR experiments.....	3
1.1.2	Sample preparations for FTIR spectroscopy in solution at room temperature.....	3
1.1.3	Kinetic studies by time-resolved FTIR spectroscopy.....	3
1.1.4	Determination of photodissociation quantum yields by FTIR spectroscopy	4
1.1.5	FTIR spectroscopy in frozen solution	4
1.1.6	FTIR spectroscopy in the solid state	4
1.2	UV/VIS absorption spectroscopy	5
1.3	Theoretical calculations	5
2	Experimental IR spectra.....	6
2.1	Acetonitrile.....	6
2.2	Pyridine	14
2.3	Valeronitrile	21
2.4	KBr matrix	22
3	Detection of CO with the detection reagent PdCl ₂ (MeCN) ₂	30
4	Comparison between experimental and theoretical IR spectra	31
4.1	IR spectra of Cr, Mo and W	31
4.2	Monosubstitution	32
4.2.1	Monosubstitution in acetonitrile.....	32
4.2.2	Monosubstitution in pyridine	34
4.3	Bisubstitution.....	37
4.3.1	Bisubstitution in acetonitrile	37
4.3.2	Bisubstitution in pyridine.....	40
4.4	Trisubstitution.....	43
4.4.1	Trisubstitution in acetonitrile	43
4.4.2	Trisubstitution in pyridine.....	46

4.5	Formation of a metallaketene	49
4.5.1	Formation of a metallaketene in acetonitrile	49
4.5.2	Formation of a metallaketene in pyridine	52
4.6	Further isomerizations	55
4.6.1	Further isomerizations in acetonitrile	55
4.6.2	Further isomerizations in pyridine	58
4.7	Loss of a CO ligand in a KBr matrix	61
4.8	Photochemistry in frozen valeronitrile	63
5	Comparison between experimental and theoretical UV/VIS spectra	65
6	Kinetic data for the dark reverse reaction	69
7	Calculated bond lengths	76
8	References	77

1 Experimental Details

1.1 Static and time-resolved FTIR spectroscopy

1.1.1 General setup for time-resolved FTIR experiments

IR spectroscopy was performed with the FTIR spectrometer Bruker Vertex 80v. A liquid-nitrogen-cooled mercury cadmium telluride (MCT) detector (Kolmar Tech., Model KV100-1-B-7/190) with a rise time of 25 ns, connected to a fast preamplifier, was used for signal detection and processing. The laser setup includes a Q-switched Nd:YAG laser (Innolas SpitLight Evo I) generating pulses with a band-width of 6 – 8 ns at a repetition rate of 100 Hz. Either the second, third or fourth harmonic of the Nd:YAG laser (532, 355 and 266 nm, respectively) was used directly for sample excitation. The homogeneity of the irradiation of the whole sample volume was optimized by dividing the incoming beam of the Nd:YAG laser (8.0 mJ/shot at 532 nm, 4.0 – 5.5 mJ/shot at 355 nm, 4.0 – 5.0 mJ/shot at 266 nm if not stated otherwise) into two partial beams, which irradiated the sample from opposite directions.

The sample chamber was purged with argon and was equipped with anti-reflection-coated germanium filters to prevent the entrance of laser radiation into the detector and interferometer compartments. The spectral region was limited by undersampling either to 0 – 3949.5 cm^{-1} or 0 – 2633.5 cm^{-1} with a spectral resolution of 4 cm^{-1} resulting in 2221 and 1481 interferogram points, respectively. The germanium windows also prevented problems when performing a Fourier transformation as IR radiation outside the measured spectral window of 0 – 3949.5 cm^{-1} was efficiently absorbed, which was further guaranteed by the CaF_2 windows of the sample cell (no transmission < 1000 cm^{-1}). In the case of measurements covering the spectral range of 0 – 2633.5 cm^{-1} , the spectral region was limited by use of an IR longpass filter (no transmission > 2400 cm^{-1}).

1.1.2 Sample preparations for FTIR spectroscopy in solution at room temperature

Experiments in solution at room temperature were performed in a sealed optical cell (Specac Omni-Cell®) with two CaF_2 windows separated by 200 μm . Solutions of the complexes for IR spectroscopy were prepared at concentrations of 3 or 6 mM, depending on the experiment. Acetonitrile was purchased from Merck (Uvasol Grade) and pyridine from Acros Organics (anhydrous, $\geq 99.5\%$). Solutions were handled under air if not stated otherwise. Investigations with $\text{PdCl}_2(\text{MeCN})_2$ were performed with saturated solutions of the reagent, which was purchased from Sigma-Aldrich. Saturation of acetonitrile and pyridine solutions with carbon monoxide (CO) was performed by purging the solutions with argon and subsequently with CO for at least 20 min, respectively.

1.1.3 Kinetic studies by time-resolved FTIR spectroscopy

For the kinetic studies on the dark reverse reactions following an initial period of irradiation of 15 – 60 s (depending on the experiment) at 532 or 355 nm, FTIR spectra were recorded at regular intervals of 15 – 120 s in the dark subsequent to irradiation. Experiments were performed at concentrations of 6 and 3 mM with the laser power being adapted accordingly (355 nm: 4 mJ at 6 mM and 2 mJ at 3 mM; 532 nm: 8 mJ at 6 mM and 4 mJ at 3 mM). The decrease of the intensity of the strong new band at

1779 – 1784 cm^{-1} was considered over time, which is clearly assigned to the main photoproduct. The IR intensity of this photoproduct band at the end of the irradiation period ($t = 0$) was normalized to 1. The error bars for the kinetic rates are estimated to $\pm 25\%$.

1.1.4 Determination of photodissociation quantum yields by FTIR spectroscopy

Photodissociation quantum yields were determined by constant irradiation of solutions ($c = 3$ or 6 mM) at 532, 355 or 266 nm and consideration of the photo-induced decrease of the isolated band of the initial complex at 1995 – 2006 cm^{-1} . The considered time region was limited to an irradiation period of ≤ 70 s at 532 nm and ≤ 5 s at 355 nm and 266 nm to avoid a large influence of the formed photoproduct(s) (in particular the photon absorption at 266 nm) and the much slower dark reverse reaction on the obtained quantum yields. Irradiation intensities (8.0 mJ/shot at 532 nm, 4.2 mJ at 355 nm/shot and 4.5 mJ/shot at 266 nm) were determined using a power meter and UV/VIS extinction coefficients were obtained *via* UV/VIS absorption spectroscopy. The higher laser power at 532 nm was selected to induce considerable conversion to the photoproducts for an accurate determination of the quantum yields despite the throughout poor efficiency at this wavelength. The time of irradiation, the irradiation power, the sample concentration, the cell volume (80 μL), the extinction coefficient and the IR intensity then yielded information on the number of reacted complex molecules per number of irradiated photons. The error bars for the photodissociation quantum yields are estimated to $\pm 25\%$.

1.1.5 FTIR spectroscopy in frozen solution

Investigations on frozen solutions at 20 K were performed in valeronitrile ($\geq 99\%$, purchased from Sigma-Aldrich) at a concentration of 6 mM. The samples were measured in a home-built cell consisting of two CaF_2 windows separated by 1 mm, which was sealed with high vacuum grease. The cell was cooled to 20 K with a closed-cycle helium cryostat (ARS Model DE-202A). The cryocooler was equipped with a cell holder and CaF_2 windows. Photochemical experiments were performed by irradiation over 8 min at 355 nm (3.0 mJ/shot).

1.1.6 FTIR spectroscopy in the solid state

KBr pellets were prepared by mixing neat powder of the compound (ca. 0.4 mg) with dry KBr (ca. 180 mg, stored in a compartment dryer at 80 °C, purchased from Merck) and grinding to a homogenous mixture. This mixture was filled in an evacuable pellet die with a diameter of 13 mm and sintered at a pressure of 0.75 GPa. The strongest peak in the ground state spectrum showed an absorption of ≥ 1 OD with the mentioned concentration. The measurements were performed at temperatures of 20 – 290 K using a closed-cycle helium cryostat (ARS Model DE-202A). The cryocooler was equipped with a pellet holder and CaF_2 windows. Photochemical investigations were performed by irradiation of the pellets over 8 min at 532, 355 or 266 nm (2.0 mJ/shot).

1.2 UV/VIS absorption spectroscopy

UV/VIS absorption experiments in solution were performed with a Lambda 900 UV/VIS/NIR spectrometer using 10 mm path length quartz cells at 25°C. The solutions were prepared at a concentration of $2 \cdot 10^{-5}$ M. The spectra were recorded relative to the pure solvent. The UV/VIS spectra of the photoproducts were recorded subsequent to a period of laser irradiation (3 min at 2.0 mJ/pulse at 100 Hz, 355 nm, Innolas SpitLight Evo I). The yielded solutions were centrifugated before the measurement of the UV/VIS spectrum of the photoproduct to prevent scattering losses due to insoluble photoproducts, which most probably resulted from side reactions.

1.3 Theoretical calculations

The crystal structures were used as input structures for the initial complexes and starting structures for conceivable photoproducts were generated by chemical intuition. Geometry optimizations were performed with the Bery algorithm of Gaussian 09^[1] by using energies and gradients computed by Turbomole 7.4.^[2,3] All calculations were performed with the DFT functional B3LYP with dispersion correction (no three-body interaction) (D3(BJ))^[4] as implemented in Turbomole using the resolution of identity (RI) approximation and the def2-TZVP basis set.

Harmonic frequency calculations were performed for the optimized minimum structures. The influence of the medium (MeCN, valeronitrile, pyridine, KBr) was modulated by using the conductor-like screening model (COSMO). The vibrational frequencies are scaled by a factor of 0.99 to minimize the differences between the experimental and calculated frequencies. A Gaussian convolution with a full-width at half-maximum of 8 cm^{-1} was applied to the calculated vibrational transitions.

2 Experimental IR spectra

2.1 Acetonitrile

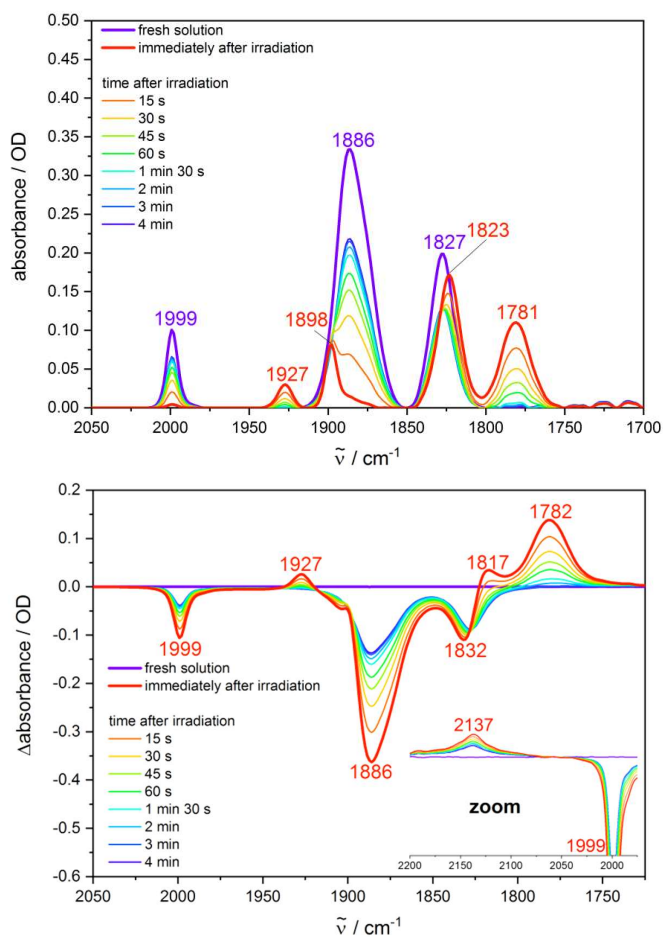


Figure S1. Irradiation ($\lambda_{\text{ex}} = 355 \text{ nm}$) of a fresh solution of **Cr** in MeCN ($c = 6 \text{ mM}$) and spectra recorded in the dark after irradiation (top: absolute absorption spectra, bottom: difference spectra).

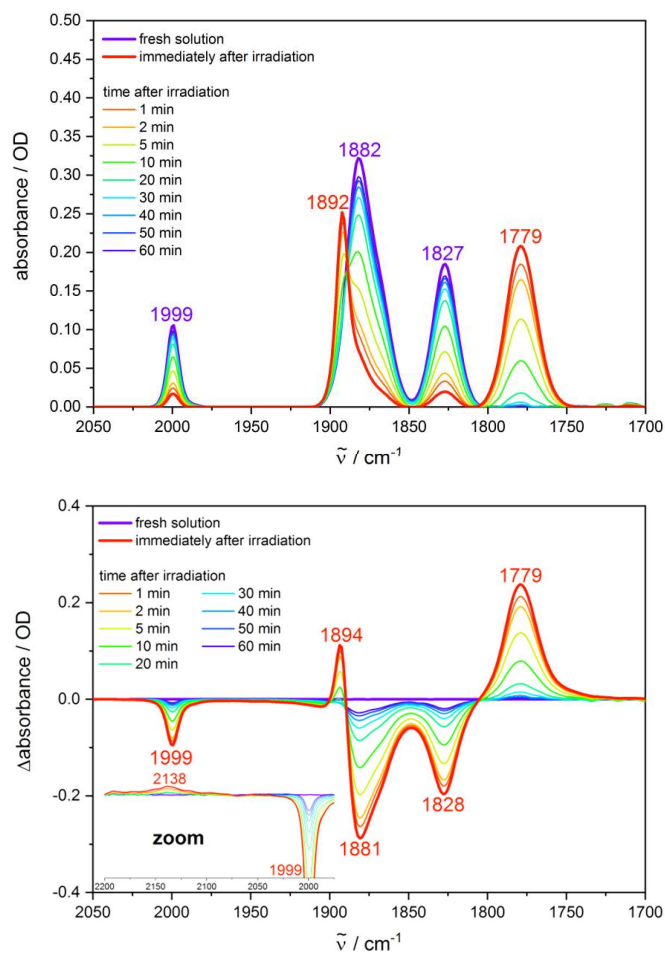


Figure S2. Irradiation ($\lambda_{\text{ex}} = 355 \text{ nm}$) of a fresh solution of **W** in MeCN ($c = 6 \text{ mM}$) and spectra recorded in the dark after irradiation (top: absolute absorption spectra, bottom: difference spectra).

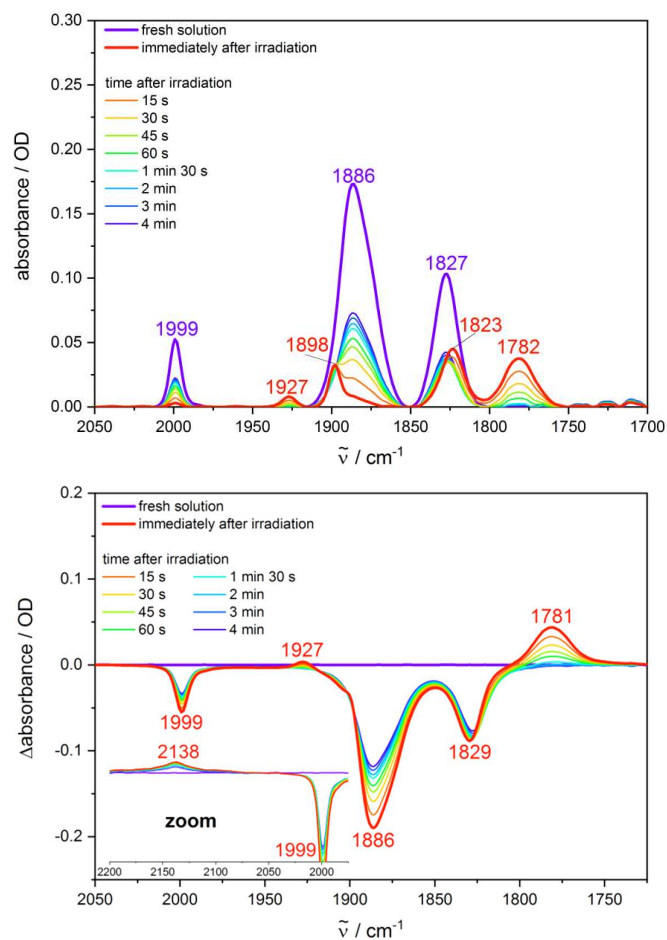


Figure S3. Irradiation ($\lambda_{\text{ex}} = 355 \text{ nm}$) of a fresh solution of **Cr** in MeCN ($c = 3 \text{ mM}$) and spectra recorded in the dark after irradiation (top: absolute absorption spectra, bottom: difference spectra).

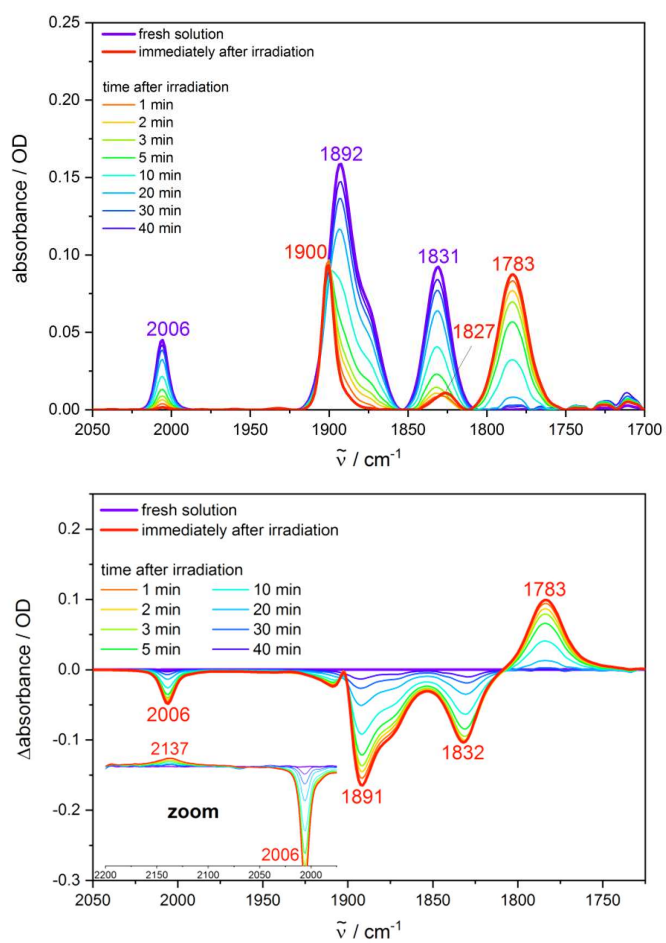


Figure S4. Irradiation ($\lambda_{\text{ex}} = 355 \text{ nm}$) of a fresh solution of **Mo** in MeCN ($c = 3 \text{ mM}$) and spectra recorded in the dark after irradiation (top: absolute absorption spectra, bottom: difference spectra).

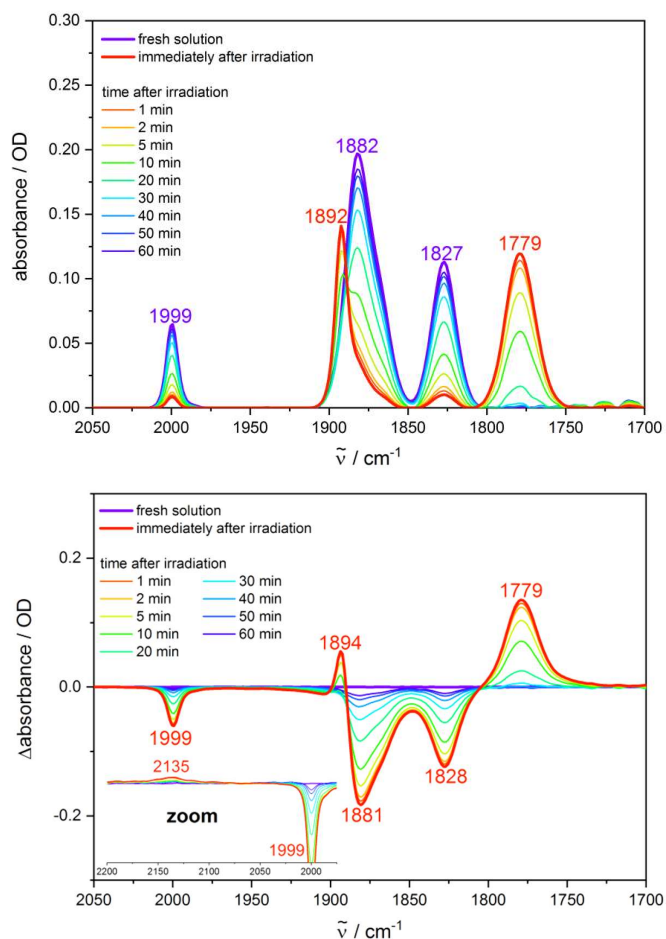


Figure S5. Irradiation ($\lambda_{\text{ex}} = 355 \text{ nm}$) of a fresh solution of **W** in MeCN ($c = 3 \text{ mM}$) and spectra recorded in the dark after irradiation (top: absolute absorption spectra, bottom: difference spectra).

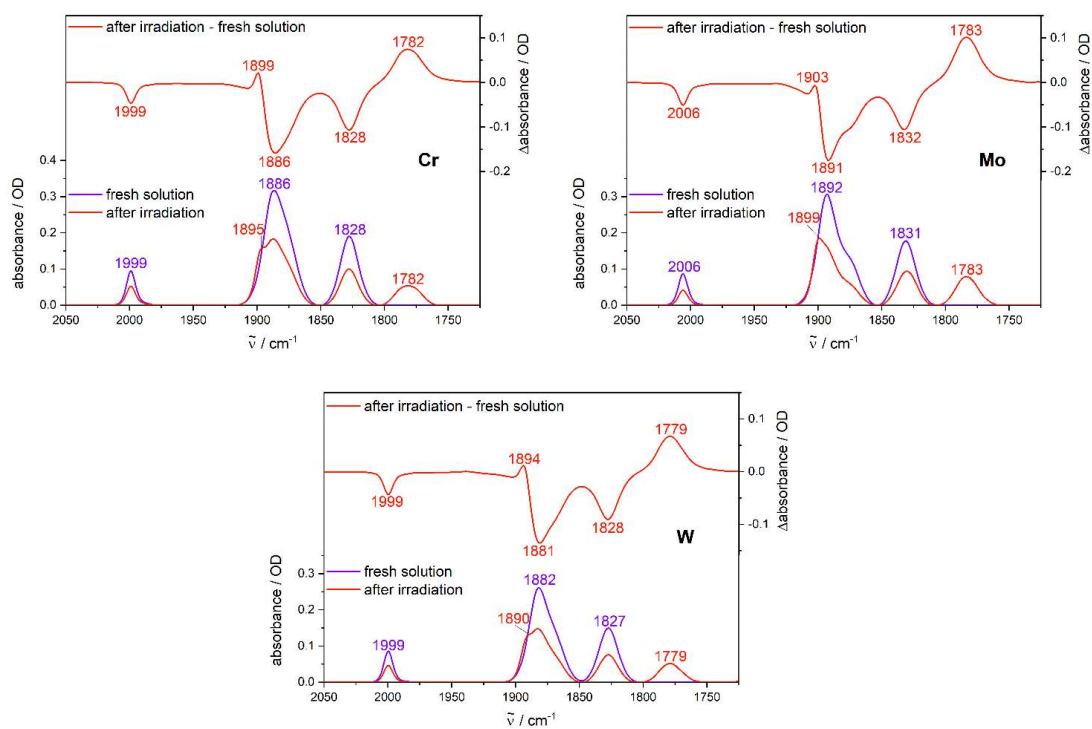


Figure S6. Irradiation ($\lambda_{\text{ex}} = 532 \text{ nm}$) of fresh solutions of **Cr** (top, left), **Mo** (top, right) and **W** (bottom) in MeCN ($c = 6 \text{ mM}$) with representation of the absolute spectra before and immediately after irradiation as well as the corresponding difference spectrum (irradiated – fresh).

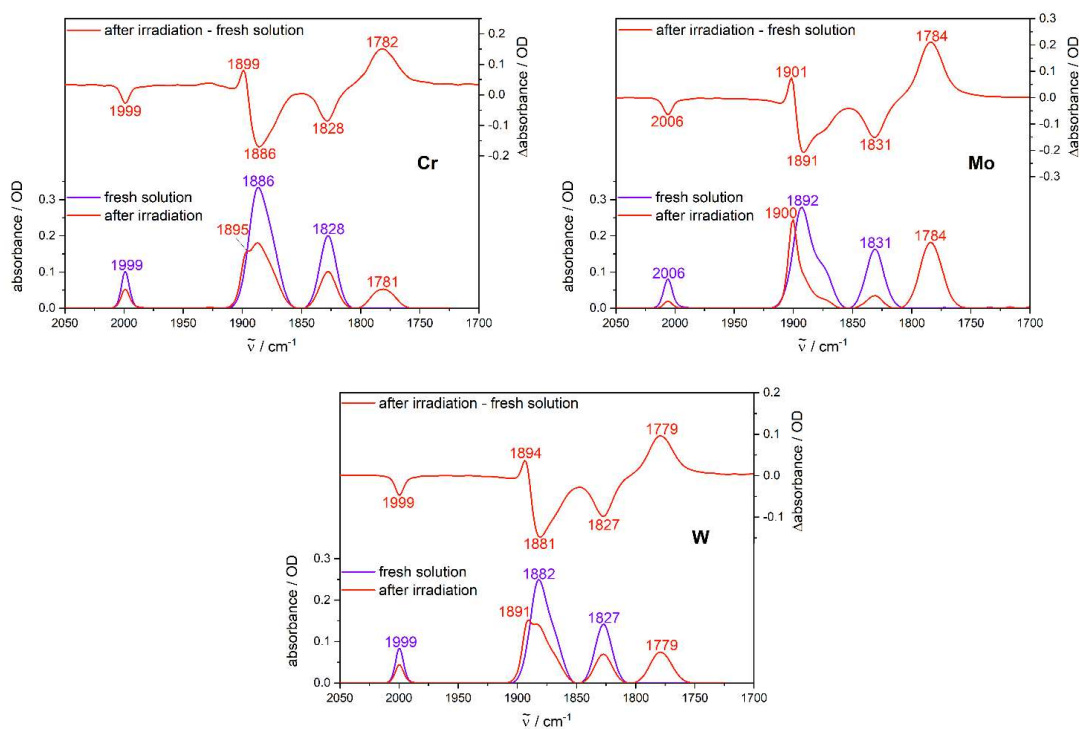
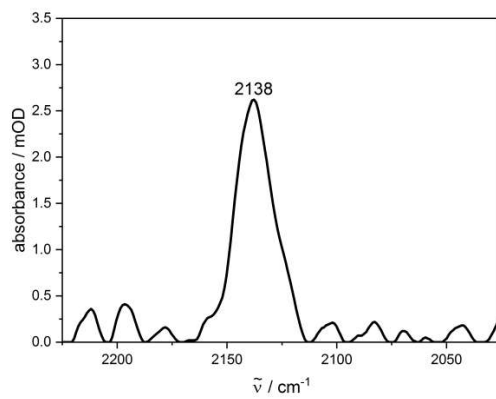


Figure S7. Irradiation ($\lambda_{\text{ex}} = 266 \text{ nm}$) of fresh solutions of **Cr** (top, left), **Mo** (top, right) and **W** (bottom) in MeCN ($c = 6 \text{ mM}$) with representation of the absolute spectra before and immediately after irradiation as well as the corresponding difference spectrum (irradiated – fresh).

Figure S8. IR spectrum of CO dissolved in MeCN.

2.2 Pyridine

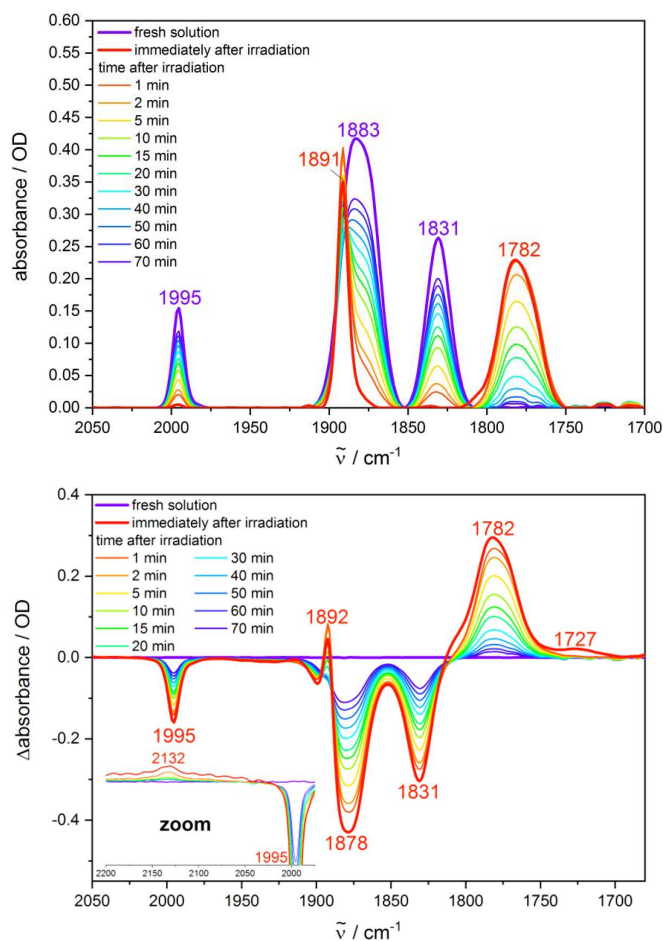


Figure S9. Irradiation ($\lambda_{\text{ex}} = 355 \text{ nm}$) of a fresh solution of Cr in py ($c = 6 \text{ mM}$) and spectra recorded in the dark after irradiation (top: absolute absorption spectra, bottom: difference spectra).

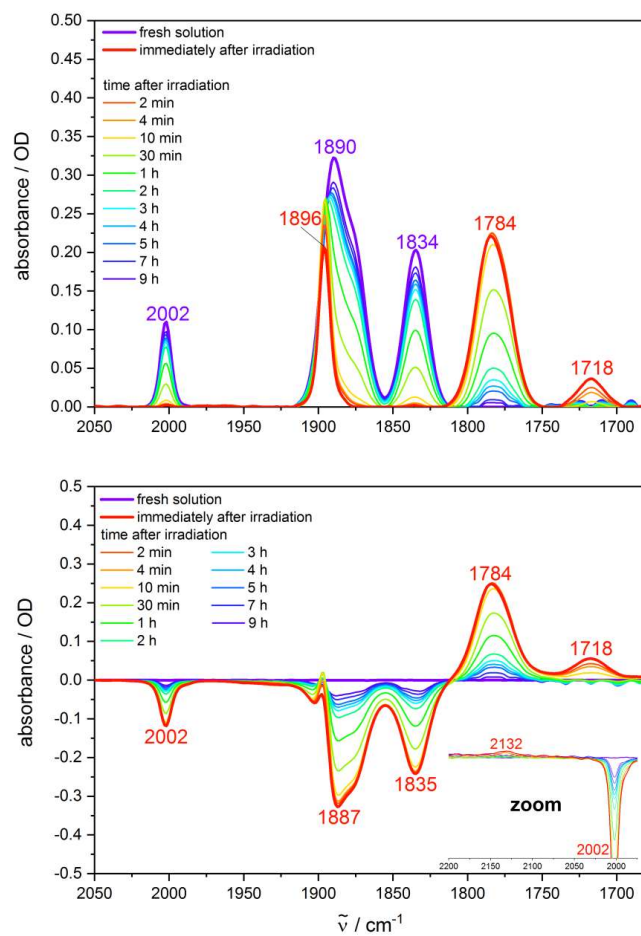


Figure S10. Irradiation ($\lambda_{\text{ex}} = 355 \text{ nm}$) of a fresh solution of **Mo** in py ($c = 6 \text{ mM}$) and spectra recorded in the dark after irradiation (top: absolute absorption spectra, bottom: difference spectra).

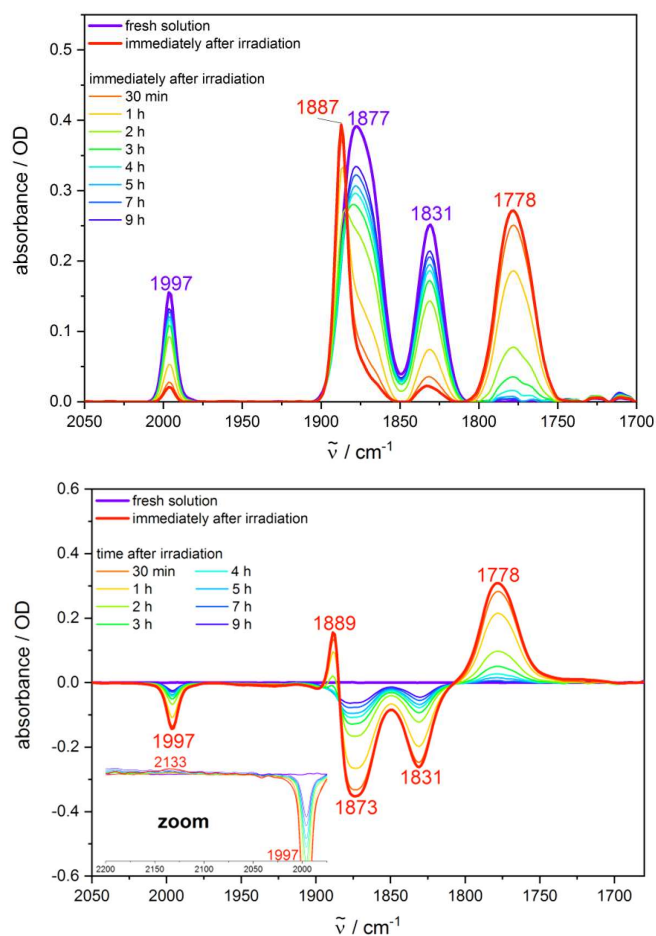


Figure S11. Irradiation ($\lambda_{\text{ex}} = 355 \text{ nm}$) of a fresh solution of **W** in py ($c = 6 \text{ mM}$) and spectra recorded in the dark after irradiation (top: absolute absorption spectra, bottom: difference spectra).

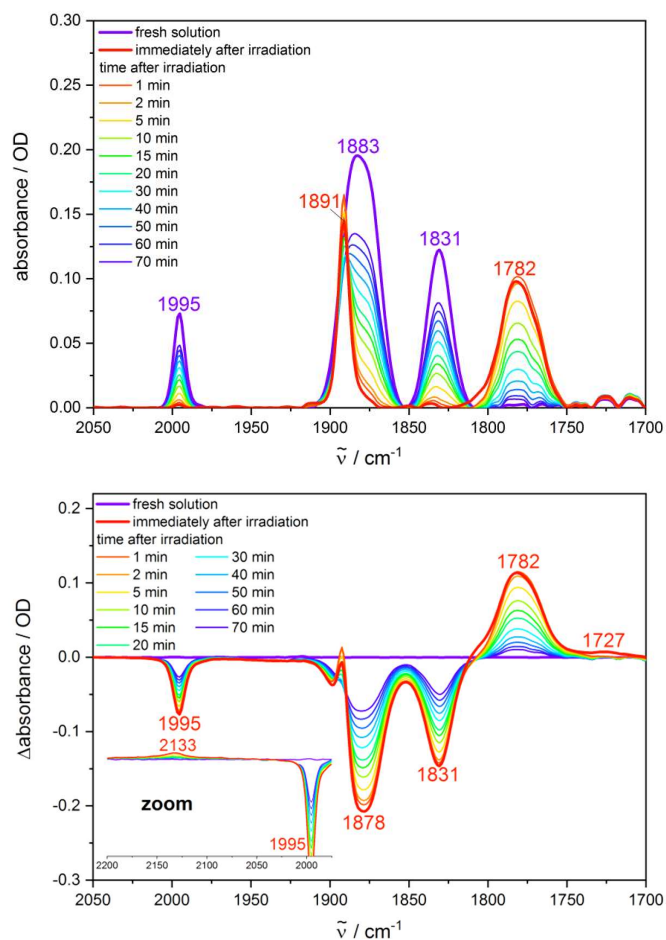


Figure S12. Irradiation ($\lambda_{\text{ex}} = 355 \text{ nm}$) of a fresh solution of **Cr** in py ($c = 3 \text{ mM}$) and spectra recorded in the dark after irradiation (top: absolute absorption spectra, bottom: difference spectra).

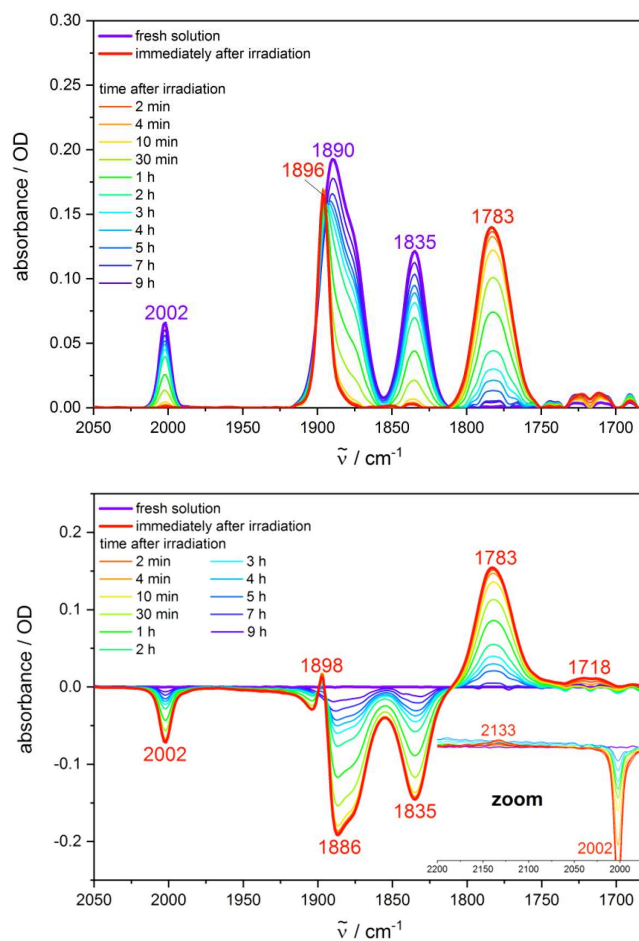


Figure S13. Irradiation ($\lambda_{\text{ex}} = 355 \text{ nm}$) of a fresh solution of **Mo** in py ($c = 3 \text{ mM}$) and spectra recorded in the dark after irradiation (top: absolute absorption spectra, bottom: difference spectra).

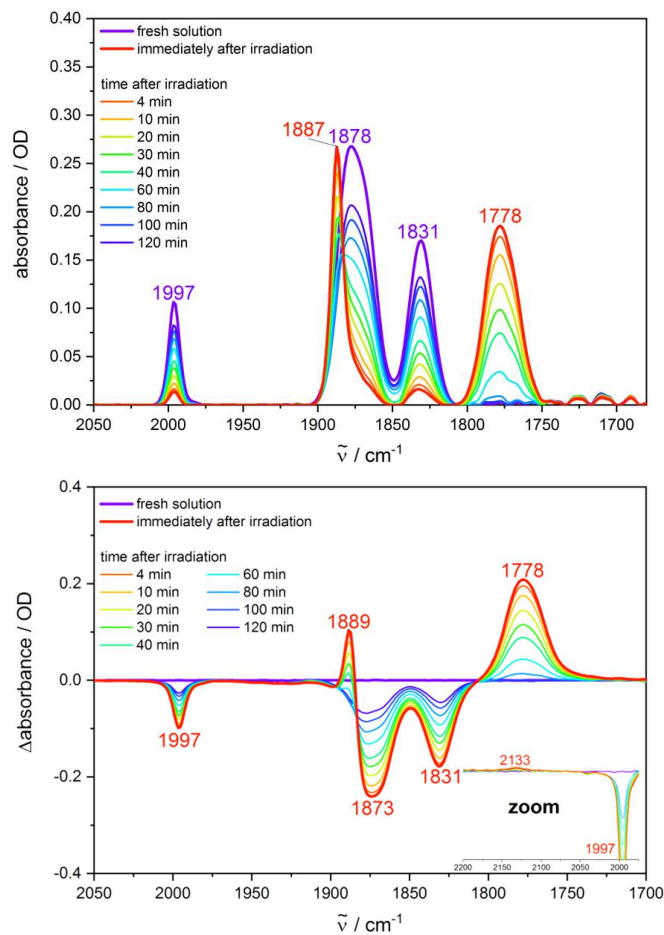


Figure S14. Irradiation ($\lambda_{\text{ex}} = 355 \text{ nm}$) of a fresh solution of **W** in py ($c = 3 \text{ mM}$) and spectra recorded in the dark after irradiation (top: absolute absorption spectra, bottom: difference spectra).

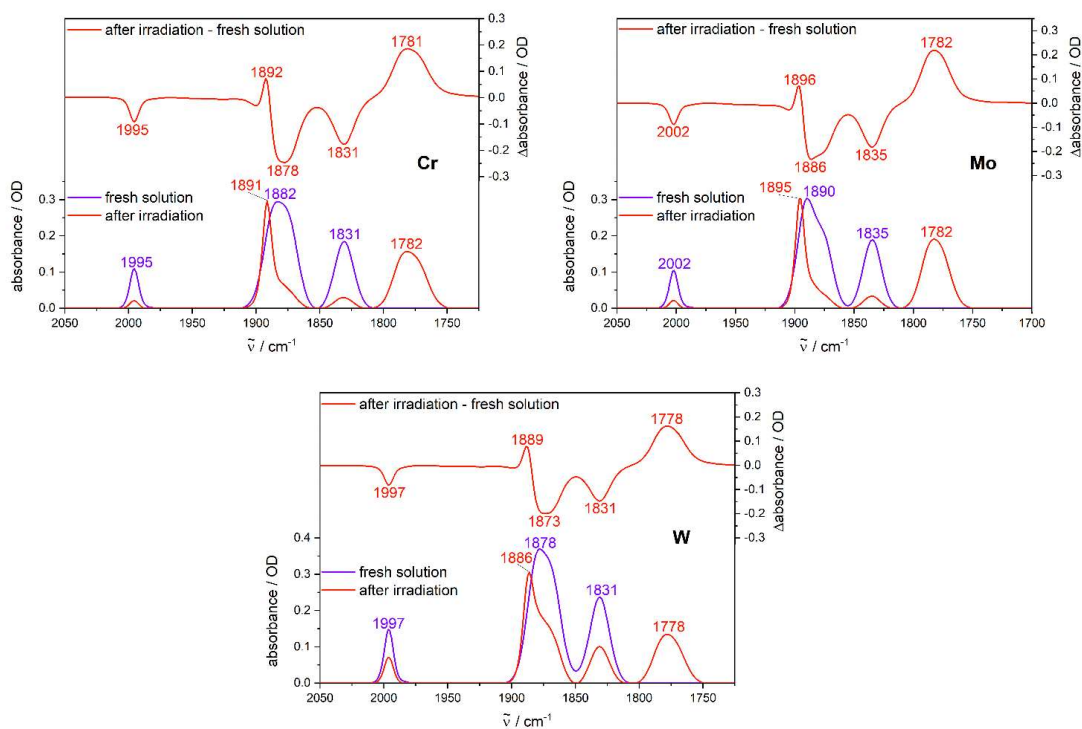


Figure S15. Irradiation ($\lambda_{\text{ex}} = 532 \text{ nm}$) of fresh solutions of **Cr** (top, left), **Mo** (top, right) and **W** (bottom) in py ($c = 6 \text{ mM}$) with representation of the absolute spectra before and immediately after irradiation as well as the corresponding difference spectrum (irradiated – fresh).

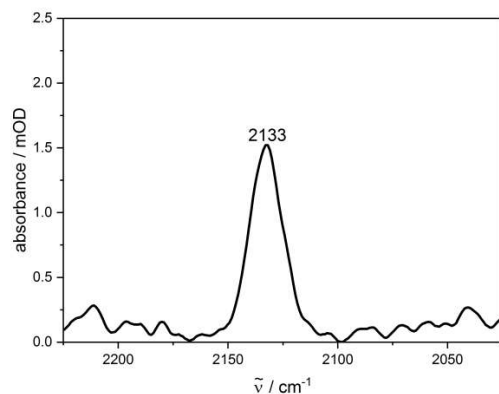
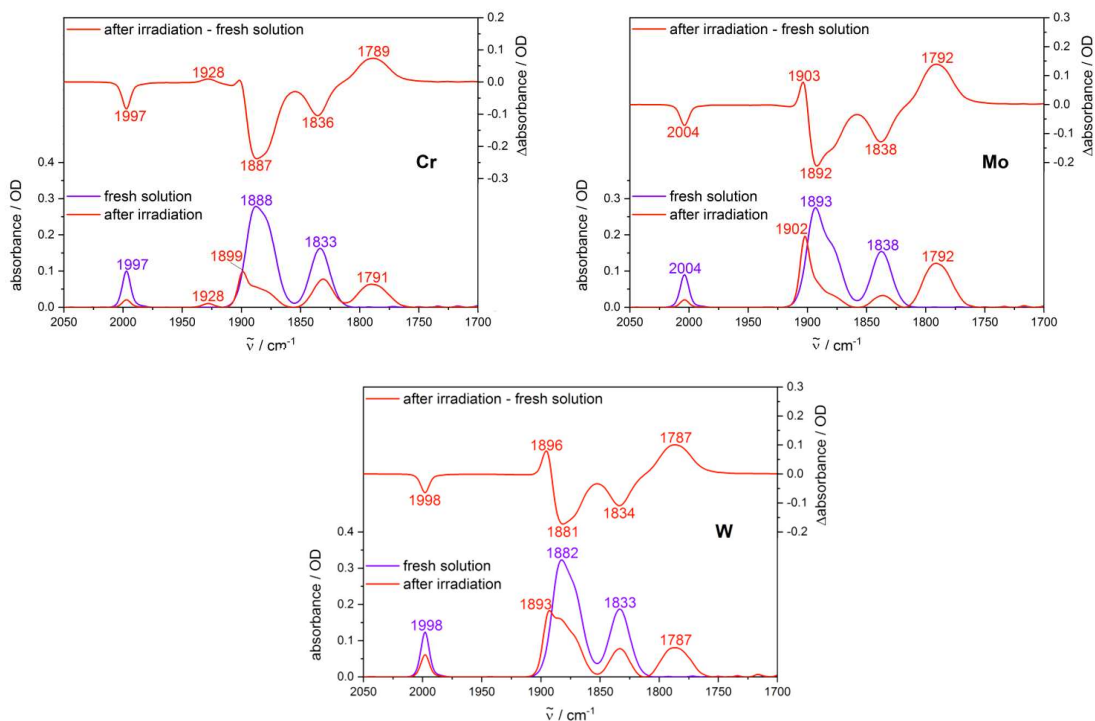


Figure S16. IR spectrum of CO dissolved in py.

2.3 Valeronitrile

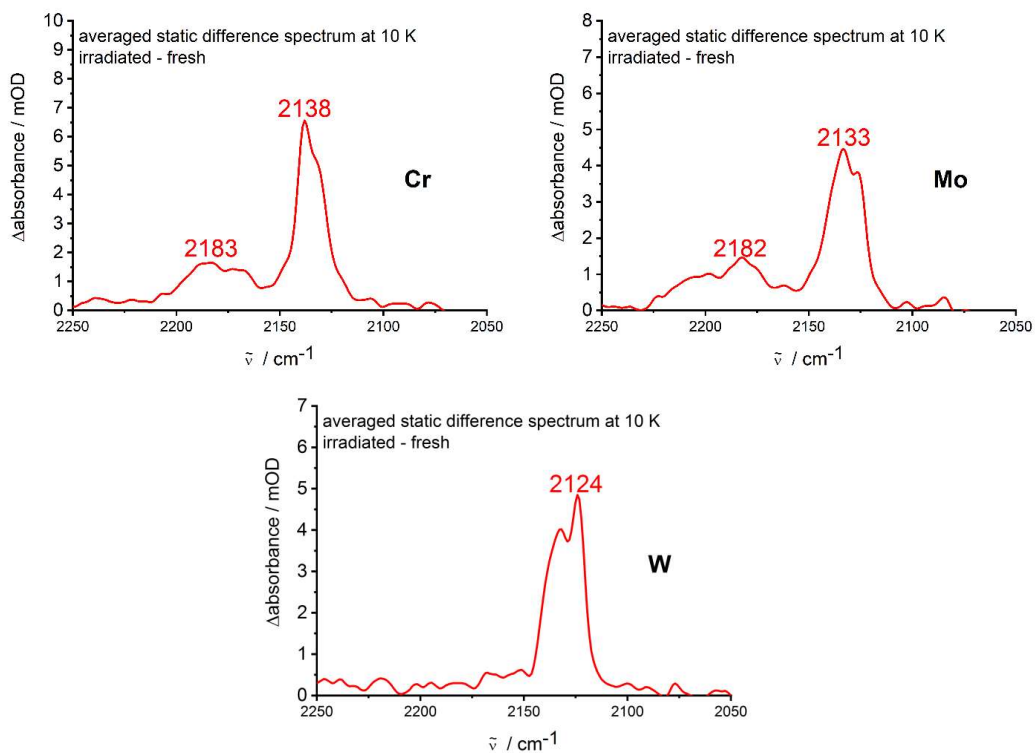
Figure S17. Irradiation ($\lambda_{\text{ex}} = 355 \text{ nm}$) of fresh solutions of **Cr** (top, left), **Mo** (top, right) and **W** (bottom)



in BuCN ($c = 6 \text{ mM}$) with representation of the absolute spectra before and immediately after irradiation as well as the corresponding difference spectrum (irradiated – fresh).

2.4 KBr matrix

Figure S18. Positive signals in the region of free CO in the difference spectra (irradiated – fresh sample)



of **Cr**, **Mo** and **W** (KBr pellets) at 10 K after irradiation ($\lambda_{\text{ex}} = 355 \text{ nm}$).

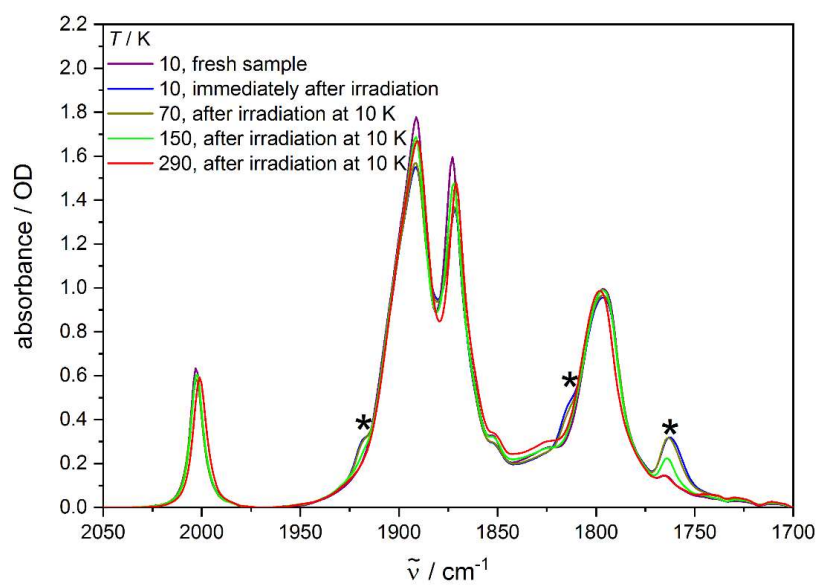


Figure S19. Irradiation ($\lambda_{\text{ex}} = 355 \text{ nm}$) of a fresh sample of Cr (KBr pellets) at 10 K and subsequent heating to 70 K, 150 K and 290 K. Product bands are marked with asterisks.

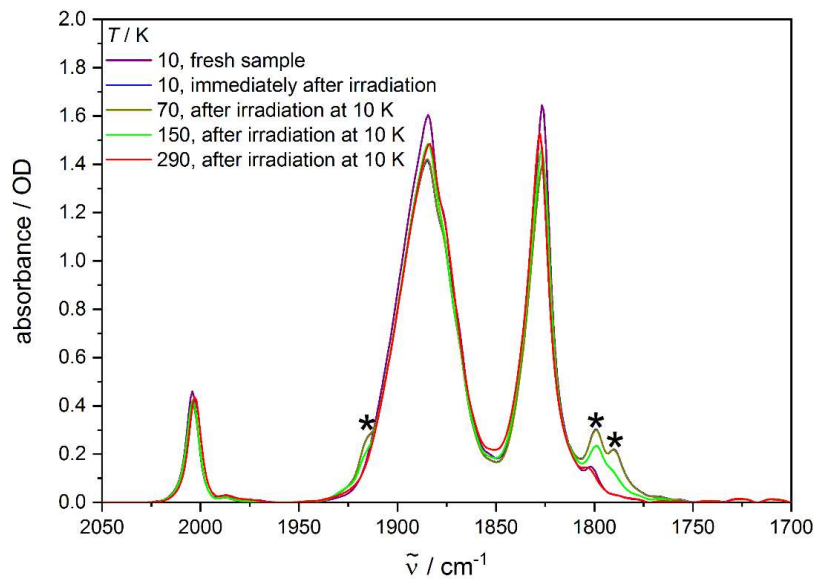


Figure S20. Irradiation ($\lambda_{\text{ex}} = 355 \text{ nm}$) of a fresh sample of **Mo** (KBr pellets) at 10 K and subsequent heating to 70 K, 150 K and 290 K. Product bands are marked with asterisks.

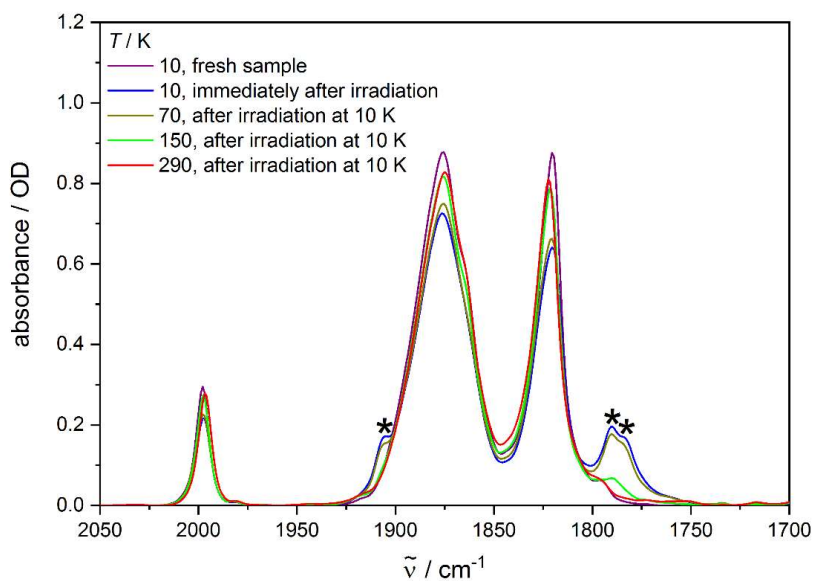


Figure S21. Irradiation ($\lambda_{\text{ex}} = 355 \text{ nm}$) of a fresh sample of **W** (KBr pellets) at 10 K and subsequent heating to 70 K, 150 K and 290 K. Product bands are marked with asterisks.

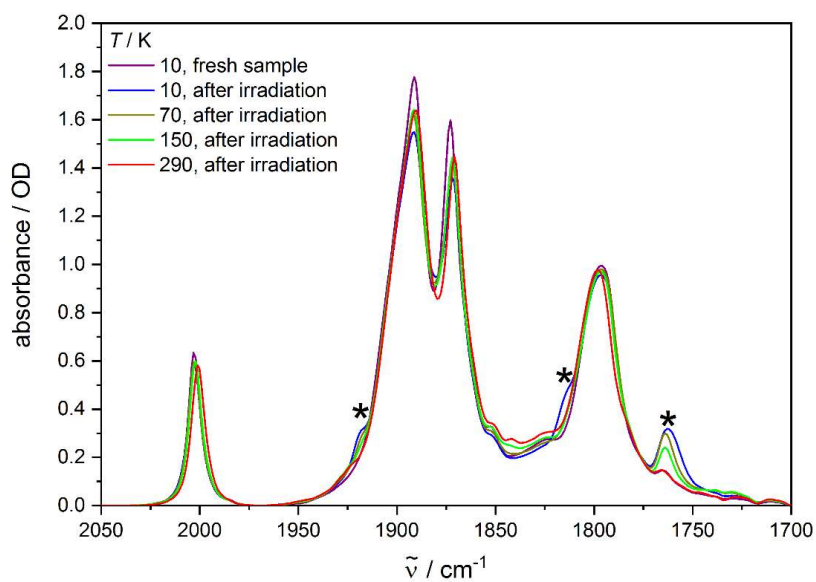


Figure S22. Irradiation ($\lambda_{\text{ex}} = 355 \text{ nm}$) of fresh samples of **Cr** (KBr pellet) at 10 K, 70 K, 150 K and 290 K. Product bands are marked with asterisks.

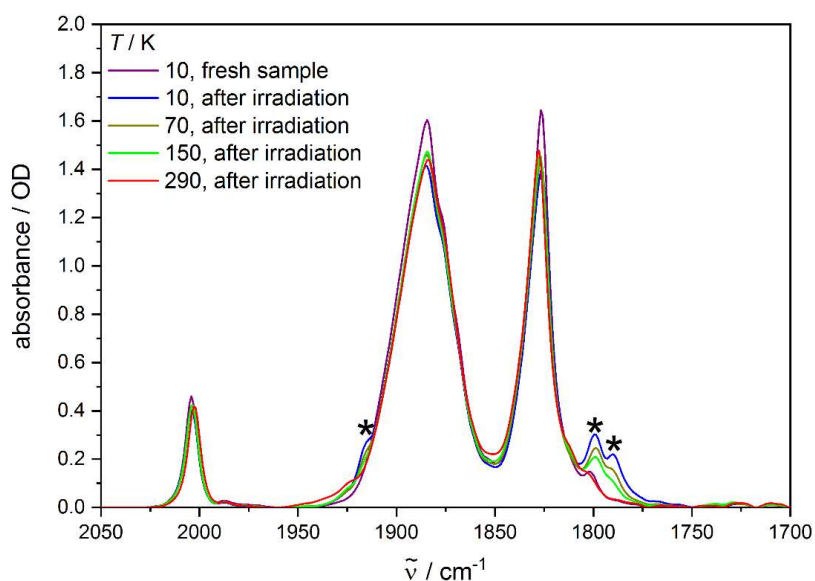
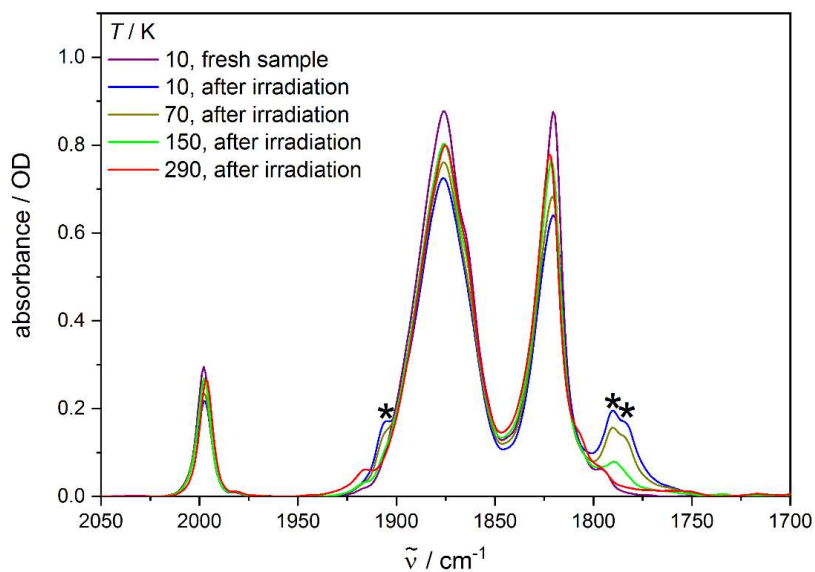


Figure S23. Irradiation ($\lambda_{\text{ex}} = 355 \text{ nm}$) of fresh samples of **Mo** (KBr pellet) at 10 K, 70 K, 150 K and 290 K. Product bands are marked with asterisks.

Figure S24. Irradiation ($\lambda_{\text{ex}} = 355 \text{ nm}$) of fresh samples of **W** (KBr pellet) at 10 K, 70 K, 150 K and 290 K. Product bands are marked with asterisks.



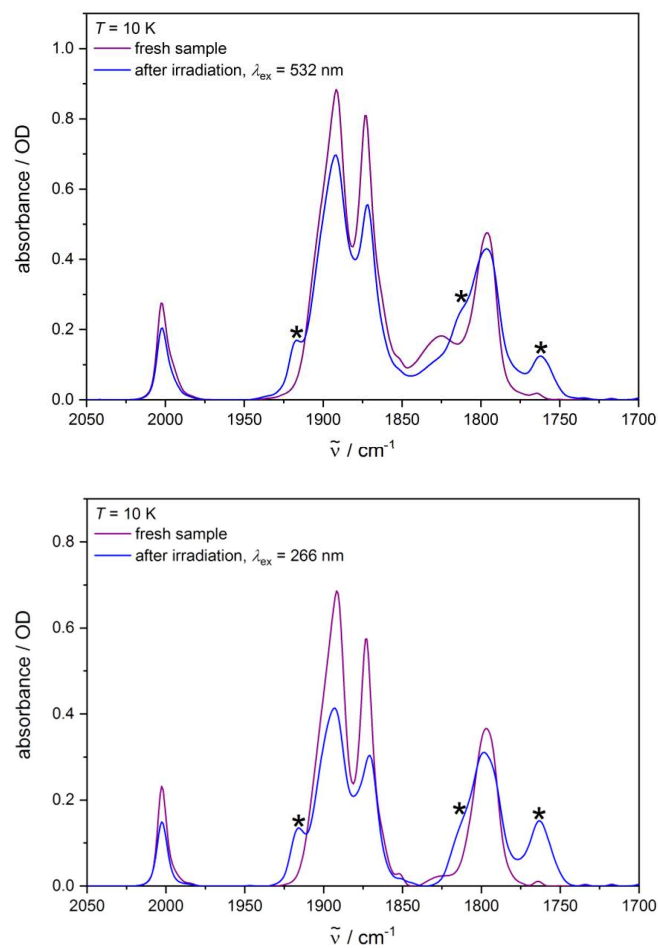


Figure S25. Irradiation of fresh samples of Cr (KBr pellets) at $\lambda_{\text{ex}} = 532$ nm (top) and 266 nm (bottom) at 10 K. Product bands are marked with asterisks.

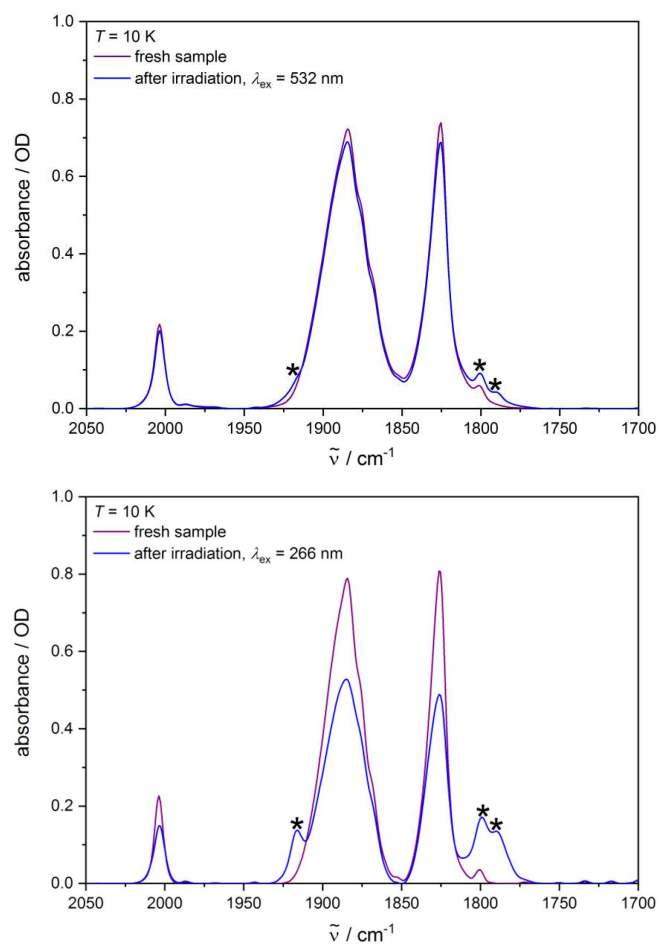


Figure S26. Irradiation of fresh samples of **Mo** (KBr pellets) at $\lambda_{\text{ex}} = 532$ nm (top) and 266 nm (bottom) at 10 K. Product bands are marked with asterisks.

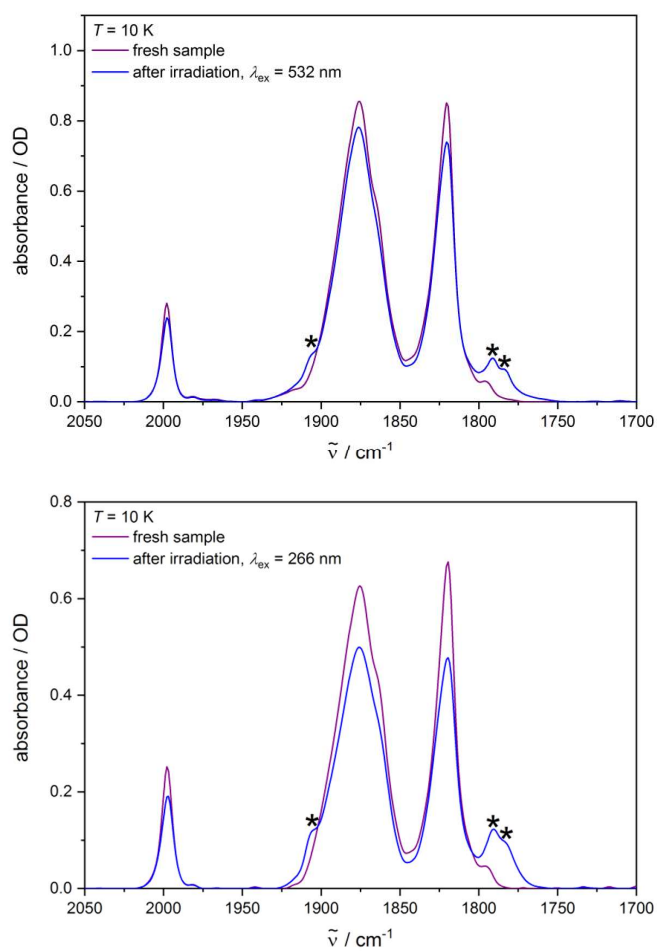
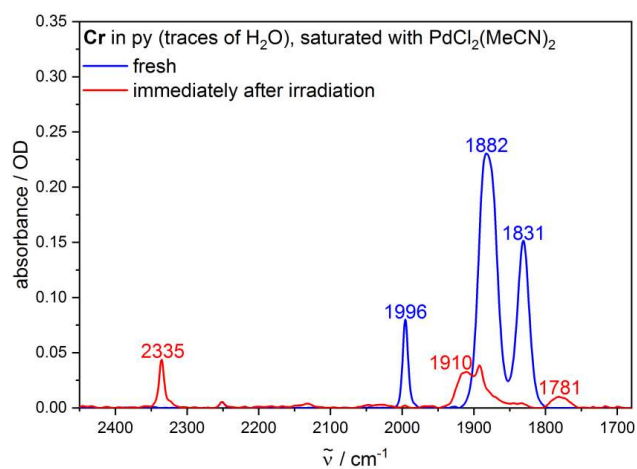


Figure S27. Irradiation of fresh samples of **W** (KBr pellets) at $\lambda_{\text{ex}} = 532$ nm (top) and 266 nm (bottom) at 10 K. Product bands are marked with asterisks.



3 Detection of CO with the detection reagent PdCl₂(MeCN)₂

Figure S28. IR spectra of a solution of **Cr** in py (containing traces of H₂O, $c = 6 \text{ mM}$), saturated with PdCl₂(MeCN)₂, before and after irradiation ($\lambda_{\text{ex}} = 355 \text{ nm}$).

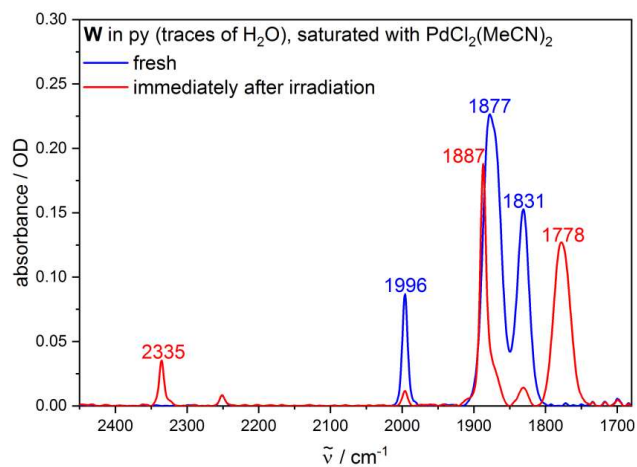


Figure S29. IR spectra of a solution of **W** in py (containing traces of H₂O, *c* = 6 mM), saturated with PdCl₂(MeCN)₂, before and after irradiation (λ_{ex} = 355 nm).

4 Comparison between experimental and theoretical IR spectra

4.1 IR spectra of Cr, Mo and W

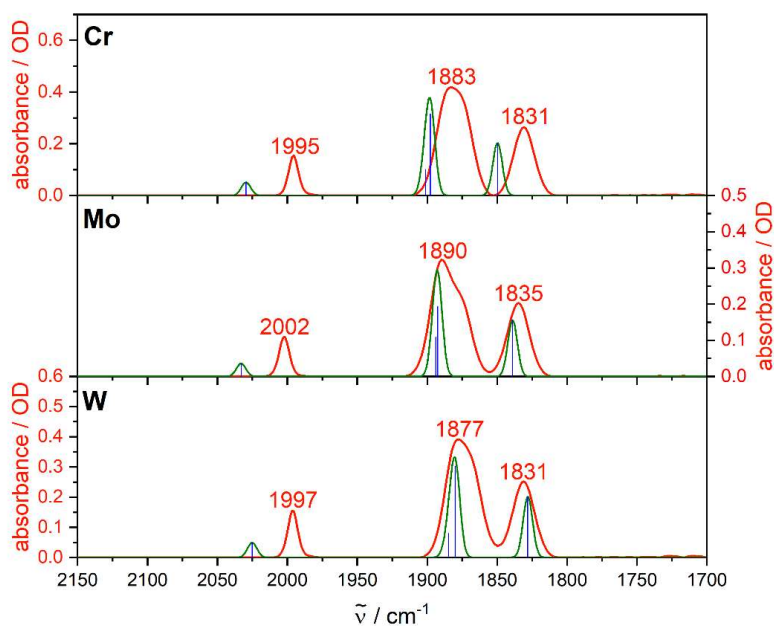


Figure S30. Experimental IR spectra of **Cr**, **Mo** and **W** in py (red) as well as calculated IR frequencies (blue) and convoluted spectra (green). Calculations: DFT/B3LYP-D3(BJ)/def2-TZVP/COSMO, scaling factor: 0.99, Gaussian convolution with FWHM=8 cm⁻¹.

4.2 Monosubstitution

4.2.1 Monosubstitution in acetonitrile

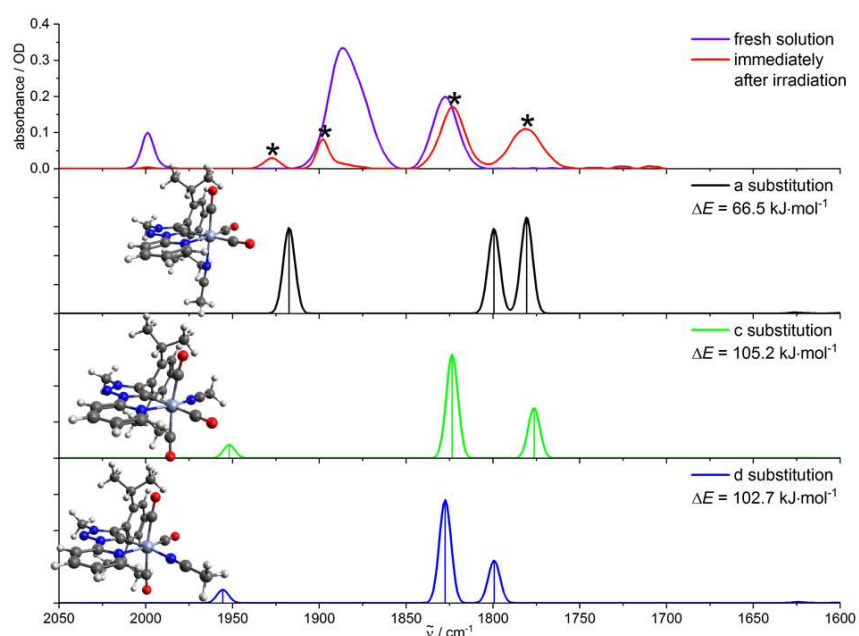


Figure S31. Experimental IR spectra of **Cr** in MeCN before and after irradiation (upper trace, bands marked with asterisks result from the formed photoproduct(s)) and calculated IR spectra of the photoproducts with a substitution of a CO ligand for a MeCN molecule (three lower traces), including the optimized structures and calculated enthalpies of reaction. The substitution occurs in axial position for isomer a ($[\text{LCr}(\text{CO})_3\text{MeCN}_{\text{ax}}]$) and in equatorial position for isomers c/d ($[\text{LMo}(\text{CO})_3\text{MeCN}_{\text{eq}}]$), respectively. Calculations: DFT/B3LYP-D3(BJ)/def2-TZVP/COSMO, scaling factor: 0.99, Gaussian convolution with $\text{FWHM}=8 \text{ cm}^{-1}$.

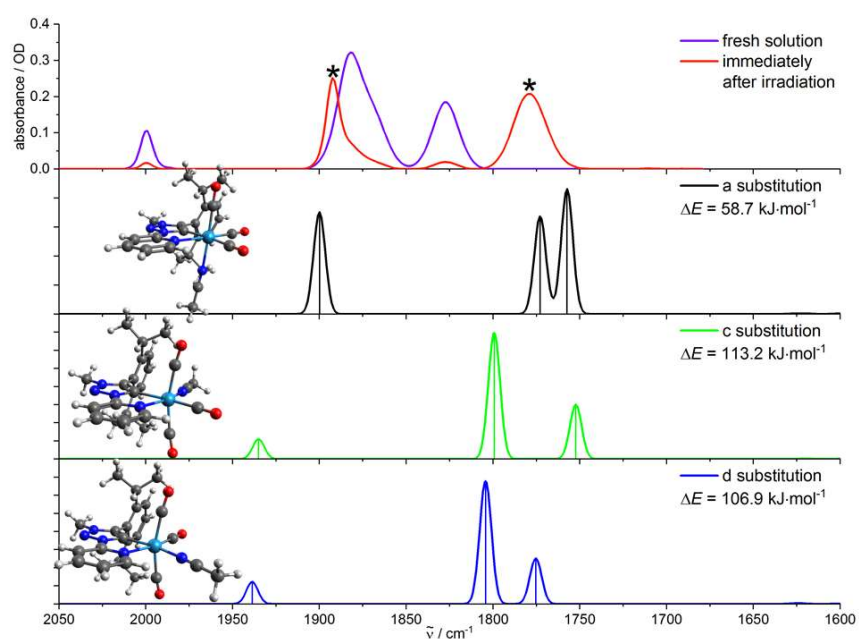
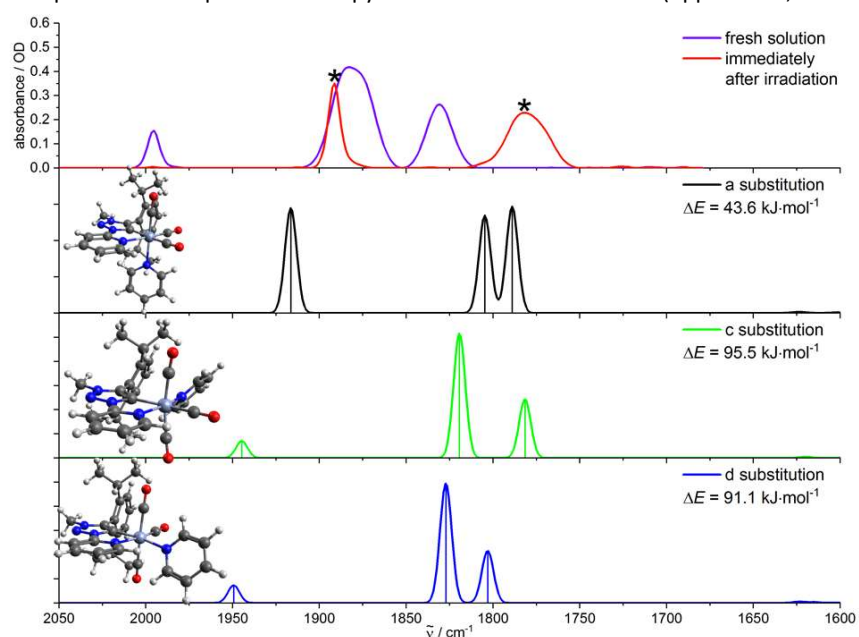


Figure S32. Experimental IR spectra of **W** in MeCN before and after irradiation (upper trace, bands marked with asterisks result from the formed photoproduct(s)) and calculated IR spectra of the photoproducts with a substitution of a CO ligand for a MeCN molecule (three lower traces), including the optimized structures and calculated enthalpies of reaction. The substitution occurs in axial position for isomer a ($[\text{LW}(\text{CO})_3\text{MeCN}_{\text{ax}}]$) and in equatorial position for isomers c/d ($[\text{LW}(\text{CO})_3\text{MeCN}_{\text{eq}}]$), respectively. Calculations: DFT/B3LYP-D3(BJ)/def2-TZVP/COSMO, scaling factor: 0.99, Gaussian convolution with $\text{FWHM}=8 \text{ cm}^{-1}$.

4.2.2 Monosubstitution in pyridine

Figure S33. Experimental IR spectra of Cr in py before and after irradiation (upper trace, bands marked



with asterisks result from the formed photoproduct(s) and calculated IR spectra of the photoproducts with a substitution of a CO ligand for a py molecule (three lower traces), including the optimized structures and calculated enthalpies of reaction. The substitution occurs in axial position for isomer a ($[\text{LCr}(\text{CO})_3\text{py}_{\text{ax}}]$) and in equatorial position for isomers c/d ($[\text{LCr}(\text{CO})_3\text{py}_{\text{eq}}]$), respectively. Calculations: DFT/B3LYP-D3(BJ)/def2-TZVP/COSMO, scaling factor: 0.99, Gaussian convolution with $\text{FWHM}=8 \text{ cm}^{-1}$.

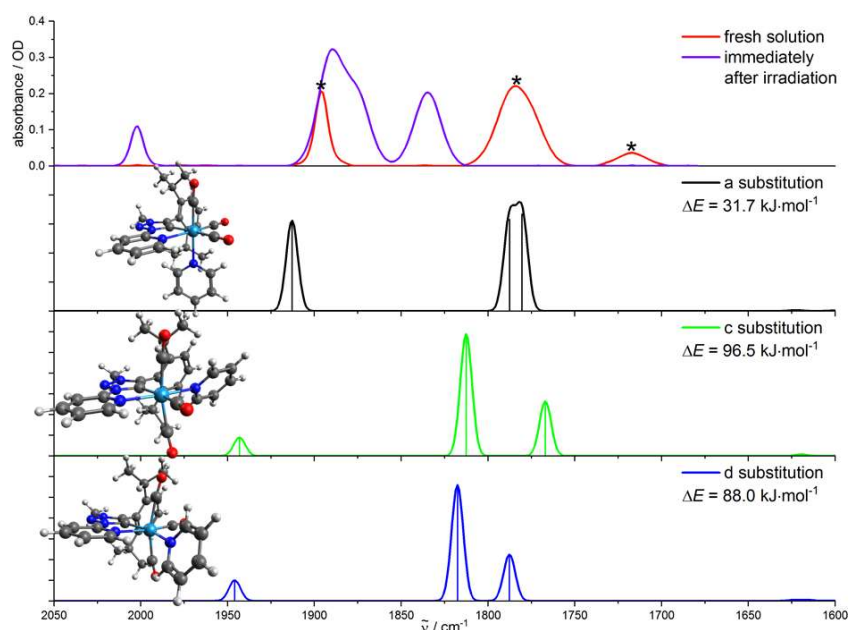


Figure S34. Experimental IR spectra of **Mo** in py before and after irradiation (upper trace, bands marked with asterisks result from the formed photoproduct(s)) and calculated IR spectra of the photoproducts with a substitution of a CO ligand for a py molecule (three lower traces), including the optimized structures and calculated enthalpies of reaction. The substitution occurs in axial position for isomer a ($[\text{LMo}(\text{CO})_3\text{py}_{\text{ax}}]$) and in equatorial position for isomers c/d ($[\text{LMo}(\text{CO})_3\text{py}_{\text{eq}}]$), respectively. Calculations: DFT/B3LYP-D3(BJ)/def2-TZVP/COSMO, scaling factor: 0.99, Gaussian convolution with $\text{FWHM}=8 \text{ cm}^{-1}$.

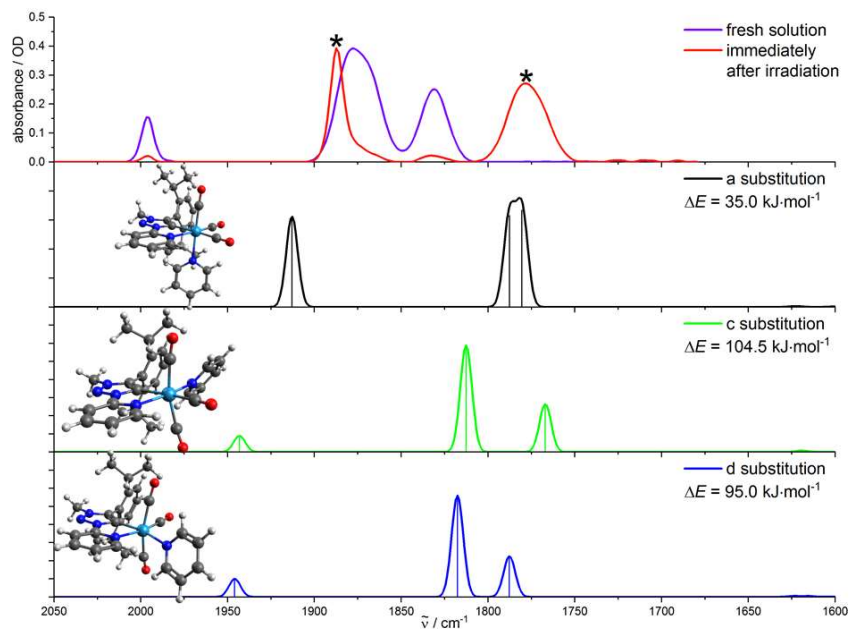


Figure S35. Experimental IR spectra of **W** in py before and after irradiation (upper trace, bands marked with asterisks result from the formed photoproduct(s)) and calculated IR spectra of the photoproducts with a substitution of a CO ligand for a py molecule (three lower traces), including the optimized structures and calculated enthalpies of reaction. The substitution occurs in axial position for isomer a ($[\text{LW}(\text{CO})_3\text{py}_{\text{ax}}]$) and in equatorial position for isomers c/d ($[\text{LW}(\text{CO})_3\text{py}_{\text{eq}}]$), respectively. Calculations: DFT/B3LYP-D3(BJ)/def2-TZVP/COSMO, scaling factor: 0.99, Gaussian convolution with FWHM=8 cm^{-1} .

4.3 Bisubstitution

4.3.1 Bisubstitution in acetonitrile

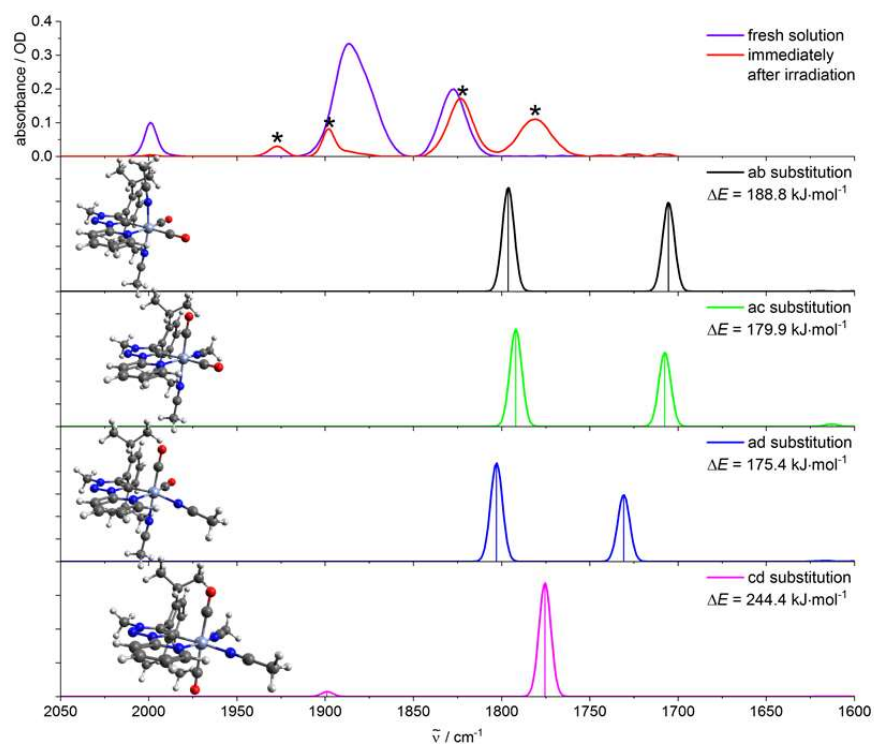


Figure S36. Experimental IR spectra of **Cr** in MeCN before and after irradiation (upper trace, bands marked with asterisks result from the formed photoproduct(s)) and calculated IR spectra of the photoproducts with a substitution of two CO ligands for two MeCN molecules (three lower traces), including the optimized structures and calculated enthalpies of reaction. The bisubstitution occurs in the two axial positions for isomer ab ($[\text{LCr}(\text{CO})_3(\text{MeCN}_{\text{ax}})_2]$), in an axial and an equatorial position for isomers ac/ad ($[\text{LCr}(\text{CO})_3(\text{MeCN}_{\text{ax}})(\text{MeCN}_{\text{eq}})]$) and in the two equatorial positions for isomer cd ($[\text{LCr}(\text{CO})_3(\text{MeCN}_{\text{eq}})_2]$), respectively. Calculations: DFT/B3LYP-D3(BJ)/def2-TZVP/COSMO, scaling factor: 0.99, Gaussian convolution with FWHM=8 cm^{-1} .

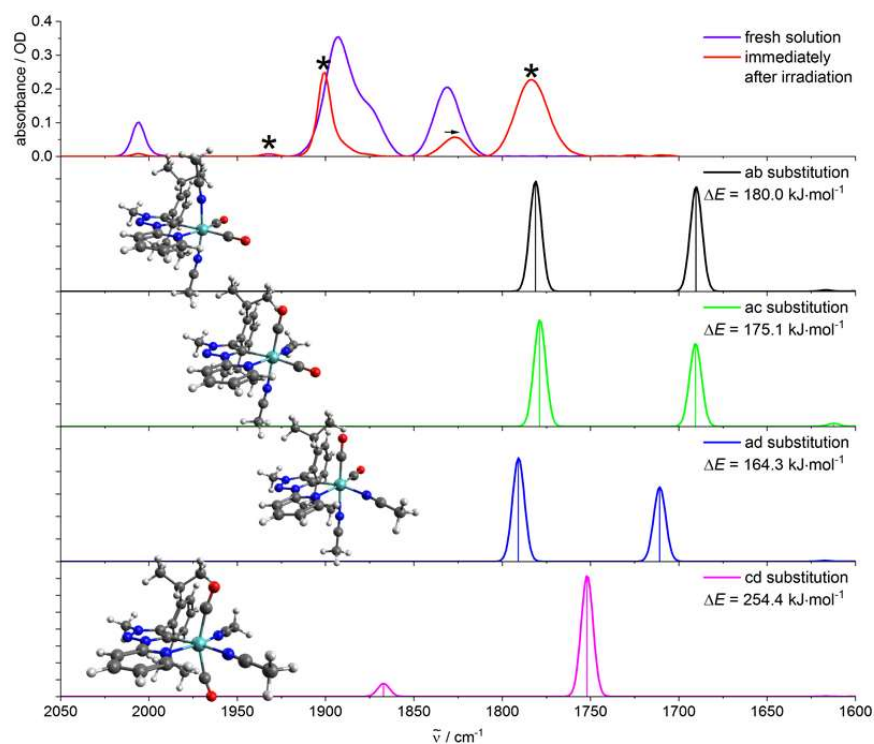


Figure S37. Experimental IR spectra of **Mo** in MeCN before and after irradiation (upper trace, bands marked with asterisks result from the formed photoproduct(s)) and calculated IR spectra of the photoproducts with a substitution of two CO ligands for two MeCN molecules (three lower traces), including the optimized structures and calculated enthalpies of reaction. The bisubstitution occurs in the two axial positions for isomer ab ($[\text{LMo}(\text{CO})_3(\text{MeCN}_{\text{ax}})_2]$), in an axial and an equatorial position for isomers ac/ad ($[\text{LMo}(\text{CO})_3(\text{MeCN}_{\text{ax}})(\text{MeCN}_{\text{eq}})]$) and in the two equatorial positions for isomer cd ($[\text{LMo}(\text{CO})_3(\text{MeCN}_{\text{eq}})_2]$), respectively. Calculations: DFT/B3LYP-D3(BJ)/def2-TZVP/COSMO, scaling factor: 0.99, Gaussian convolution with FWHM=8 cm^{-1} .

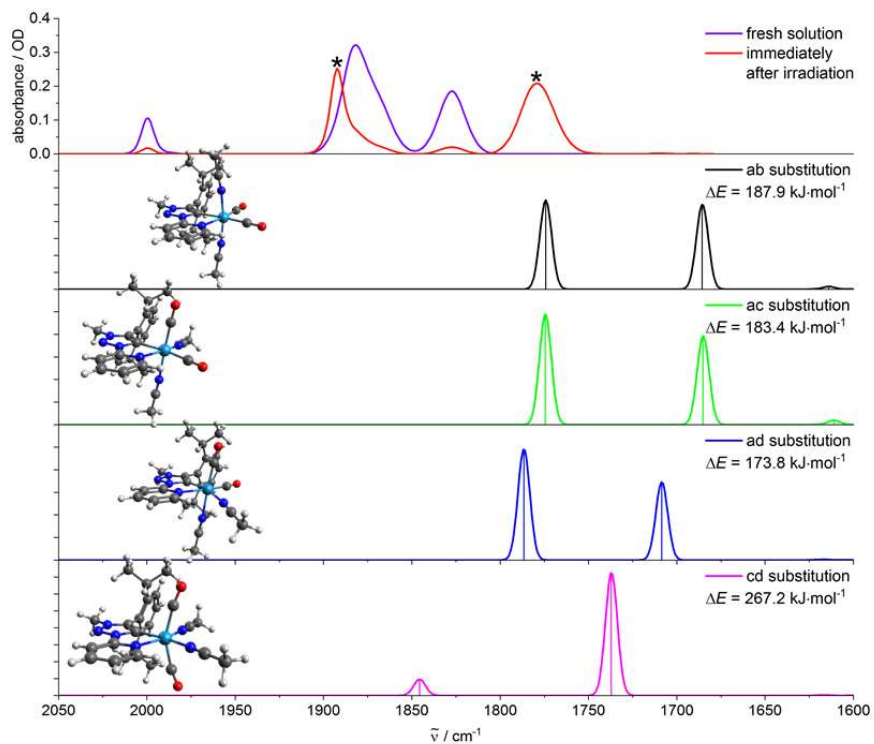


Figure S38. Experimental IR spectra of **W** in MeCN before and after irradiation (upper trace, bands marked with asterisks result from the formed photoproduct(s)) and calculated IR spectra of the photoproducts with a substitution of two CO ligands for two MeCN molecules (three lower traces), including the optimized structures and calculated enthalpies of reaction. The bisubstitution occurs in the two axial positions for isomer ab ($[\text{LW}(\text{CO})_3(\text{MeCN}_{\text{ax}})_2]$), in an axial and an equatorial position for isomers ac/ad ($[\text{LW}(\text{CO})_3(\text{MeCN}_{\text{ax}})(\text{MeCN}_{\text{eq}})]$) and in the two equatorial positions for isomer cd ($[\text{LW}(\text{CO})_3(\text{MeCN}_{\text{eq}})_2]$), respectively. Calculations: DFT/B3LYP-D3(BJ)/def2-TZVP/COSMO, scaling factor: 0.99, Gaussian convolution with FWHM=8 cm^{-1} .

4.3.2 Bisubstitution in pyridine

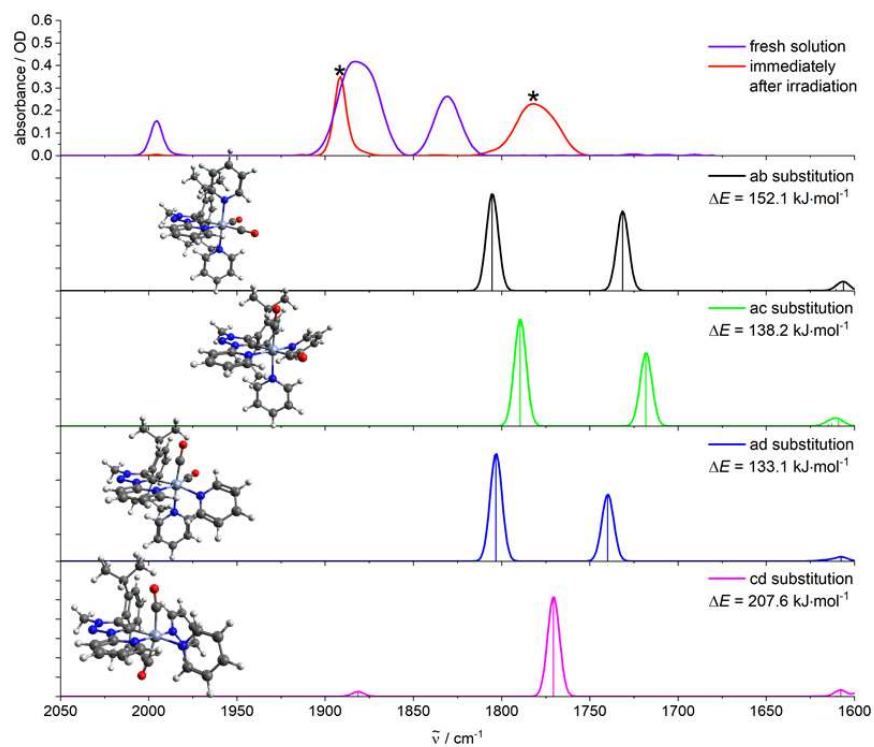


Figure S39. Experimental IR spectra of **Cr** in py before and after irradiation (upper trace, bands marked with asterisks result from the formed photoproduct(s)) and calculated IR spectra of the photoproducts with a substitution of two CO ligands for two py molecules (three lower traces), including the optimized structures and calculated enthalpies of reaction. The bisubstitution occurs in the two axial positions for isomer ab ($[\text{LCr}(\text{CO})_3(\text{py}_{\text{ax}})_2]$), in an axial and an equatorial position for isomers ac/ad ($[\text{LCr}(\text{CO})_3(\text{py}_{\text{ax}})(\text{py}_{\text{eq}})]$) and in the two equatorial positions for isomer cd ($[\text{LCr}(\text{CO})_3(\text{py}_{\text{eq}})_2]$), respectively. Calculations: DFT/B3LYP-D3(BJ)/def2-TZVP/COSMO, scaling factor: 0.99, Gaussian convolution with FWHM=8 cm⁻¹.

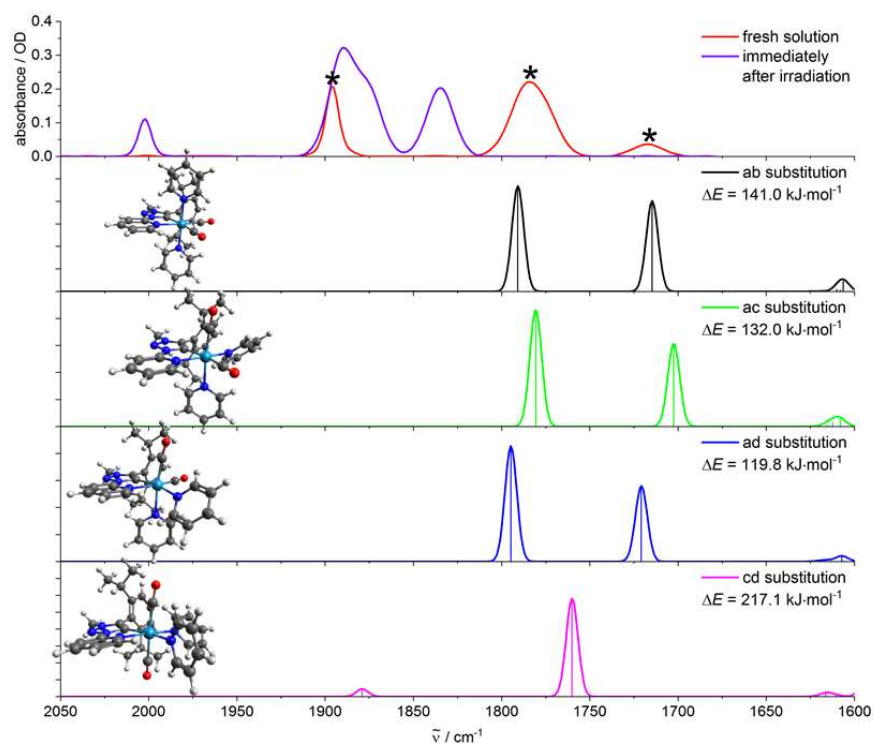


Figure S40. Experimental IR spectra of **Mo** in py before and after irradiation (upper trace, bands marked with asterisks result from the formed photoproduct(s)) and calculated IR spectra of the photoproducts with a substitution of two CO ligands for two py molecules (three lower traces), including the optimized structures and calculated enthalpies of reaction. The bisubstitution occurs in the two axial positions for isomer ab ($[\text{LMo}(\text{CO})_3(\text{py}_{\text{ax}})_2]$), in an axial and an equatorial position for isomers ac/ad ($[\text{LMo}(\text{CO})_3(\text{py}_{\text{ax}})(\text{py}_{\text{eq}})]$) and in the two equatorial positions for isomer cd ($[\text{LMo}(\text{CO})_3(\text{py}_{\text{eq}})_2]$), respectively. Calculations: DFT/B3LYP-D3(BJ)/def2-TZVP/COSMO, scaling factor: 0.99, Gaussian convolution with FWHM=8 cm^{-1} .

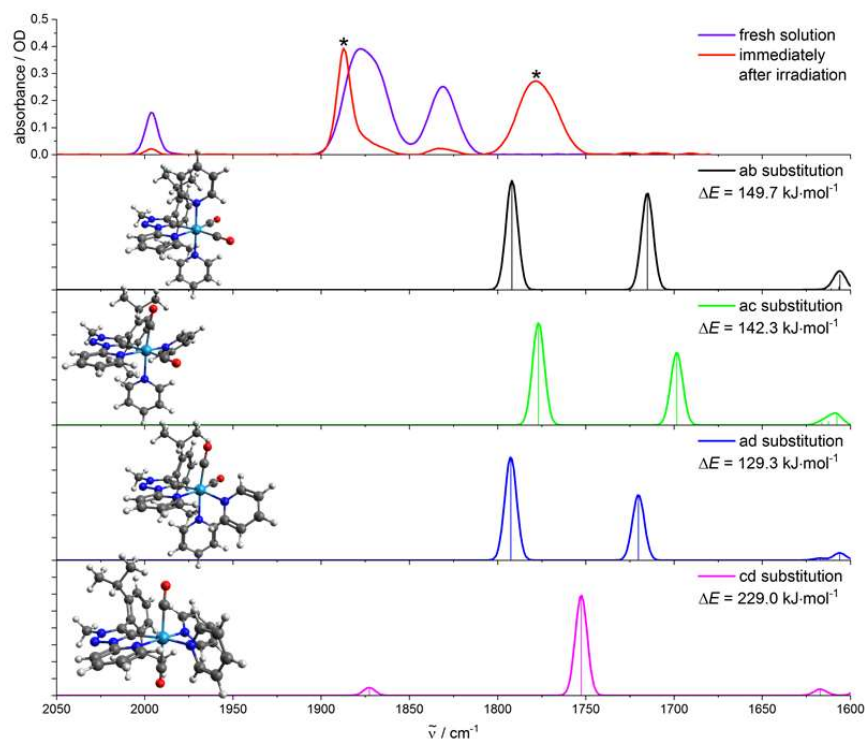


Figure S41. Experimental IR spectra of **W** in py before and after irradiation (upper trace, bands marked with asterisks result from the formed photoproduct(s)) and calculated IR spectra of the photoproducts with a substitution of two CO ligands for two py molecules (three lower traces), including the optimized structures and calculated enthalpies of reaction. The bisubstitution occurs in the two axial positions for isomer ab ($[\text{LW}(\text{CO})_3(\text{py}_{\text{ax}})_2]$), in an axial and an equatorial position for isomers ac/ad ($[\text{LW}(\text{CO})_3(\text{py}_{\text{ax}})(\text{py}_{\text{eq}})]$) and in the two equatorial positions for isomer cd ($[\text{LW}(\text{CO})_3(\text{py}_{\text{eq}})_2]$), respectively. Calculations: DFT/B3LYP-D3(BJ)/def2-TZVP/COSMO, scaling factor: 0.99, Gaussian convolution with $\text{FWHM}=8 \text{ cm}^{-1}$.

4.4 Trisubstitution

4.4.1 Trisubstitution in acetonitrile

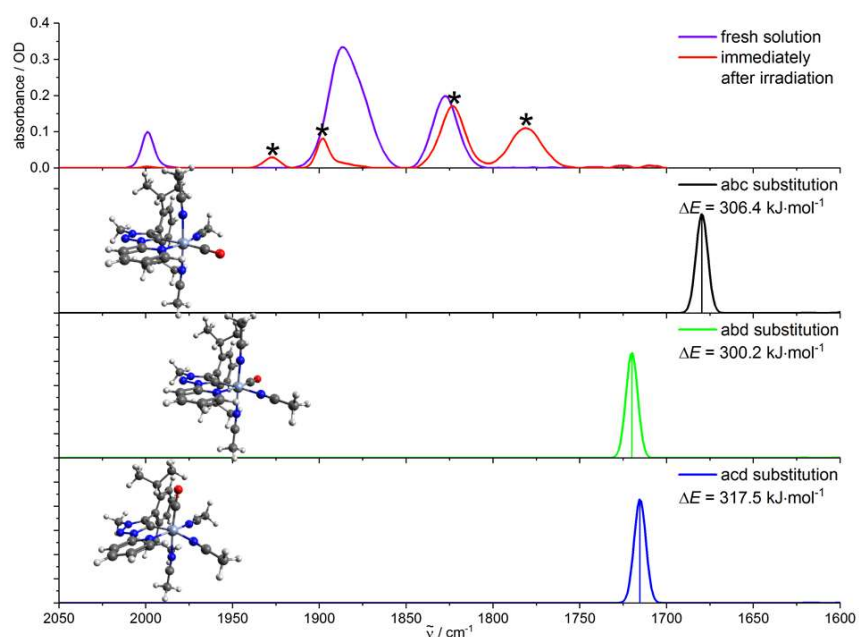


Figure S42. Experimental IR spectra of **Cr** in MeCN before and after irradiation (upper trace, bands marked with asterisks result from the formed photoproduct(s)) and calculated IR spectra of the photoproducts with a substitution of three CO ligands for three MeCN molecules (three lower traces), including the optimized structures and calculated enthalpies of reaction. A coordinated CO ligand remains in equatorial position for isomers abc/abd and in axial position for isomer acd. Calculations: DFT/B3LYP-D3(BJ)/def2-TZVP/COSMO, scaling factor: 0.99, Gaussian convolution with FWHM=8 cm^{-1} .

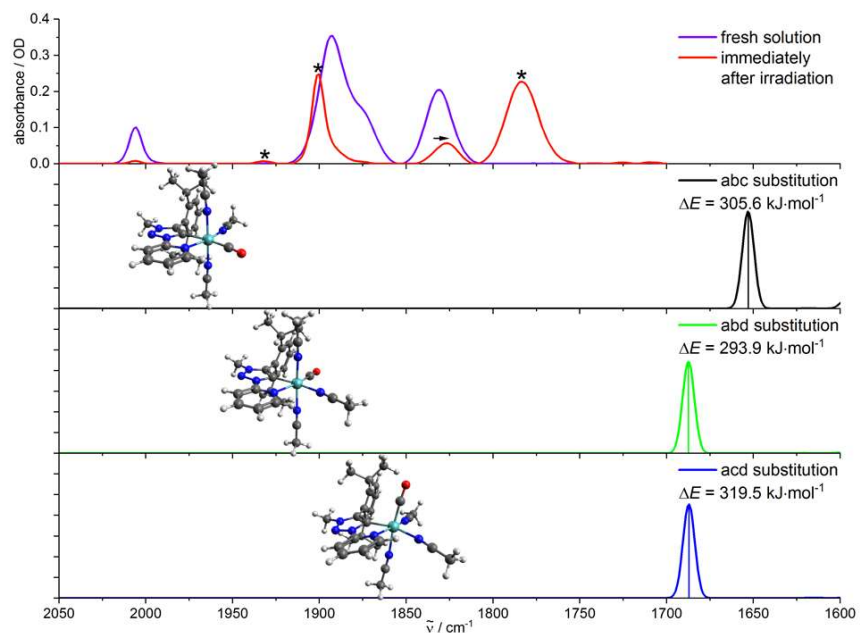


Figure S43. Experimental IR spectra of **Mo** in MeCN before and after irradiation (upper trace, bands marked with asterisks result from the formed photoproduct(s)) and calculated IR spectra of the photoproducts with a substitution of three CO ligands for three MeCN molecules (three lower traces), including the optimized structures and calculated enthalpies of reaction. A coordinated CO ligand remains in equatorial position for isomers abc/abd and in axial position for isomer acd. Calculations: DFT/B3LYP-D3(BJ)/def2-TZVP/COSMO, scaling factor: 0.99, Gaussian convolution with FWHM=8 cm⁻¹.

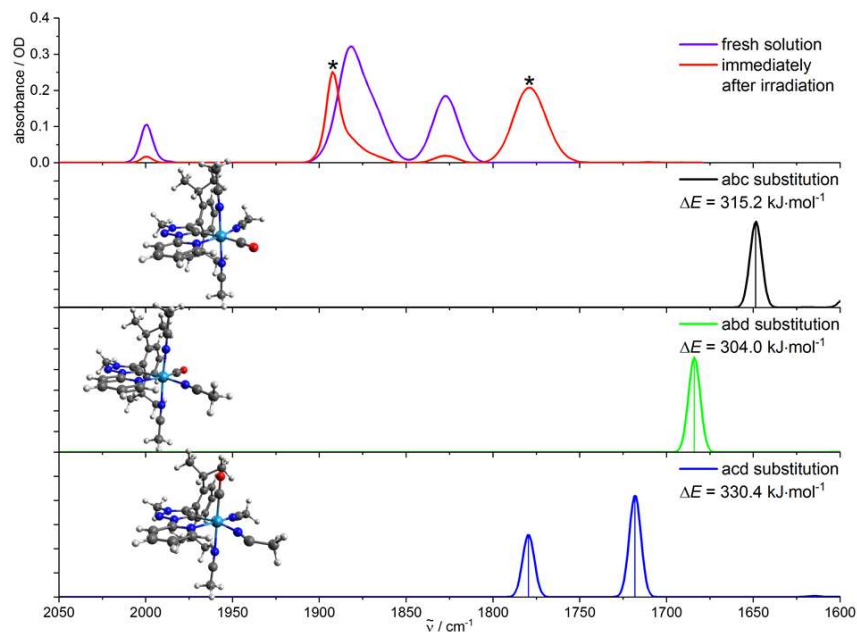
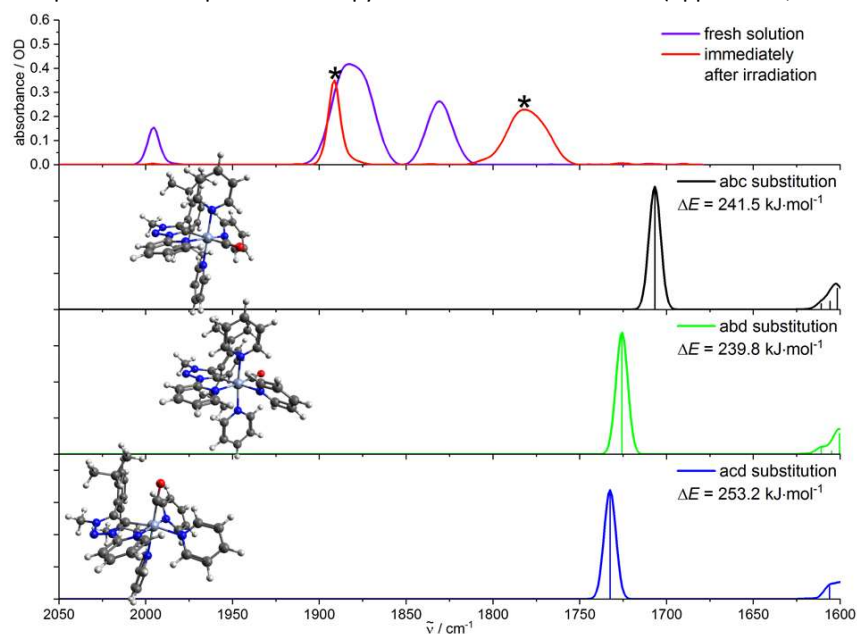


Figure S44. Experimental IR spectra of **W** in MeCN before and after irradiation (upper trace, bands marked with asterisks result from the formed photoproduct(s)) and calculated IR spectra of the photoproducts with a substitution of three CO ligands for three MeCN molecules (three lower traces), including the optimized structures and calculated enthalpies of reaction. A coordinated CO ligand remains in equatorial position for isomers abc/abd and in axial position for isomer acd. Calculations: DFT/B3LYP-D3(BJ)/def2-TZVP/COSMO, scaling factor: 0.99, Gaussian convolution with $\text{FWHM}=8 \text{ cm}^{-1}$.

4.4.2 Trisubstitution in pyridine

Figure S45. Experimental IR spectra of Cr in py before and after irradiation (upper trace, bands marked



with asterisks result from the formed photoproduct(s) and calculated IR spectra of the photoproducts with a substitution of three CO ligands for three py molecules (three lower traces), including the optimized structures and calculated enthalpies of reaction. A coordinated CO ligand remains in equatorial position for isomers abc/abd and in axial position for isomer acd. Calculations: DFT/B3LYP-D3(BJ)/def2-TZVP/COSMO, scaling factor: 0.99, Gaussian convolution with FWHM=8 cm⁻¹.

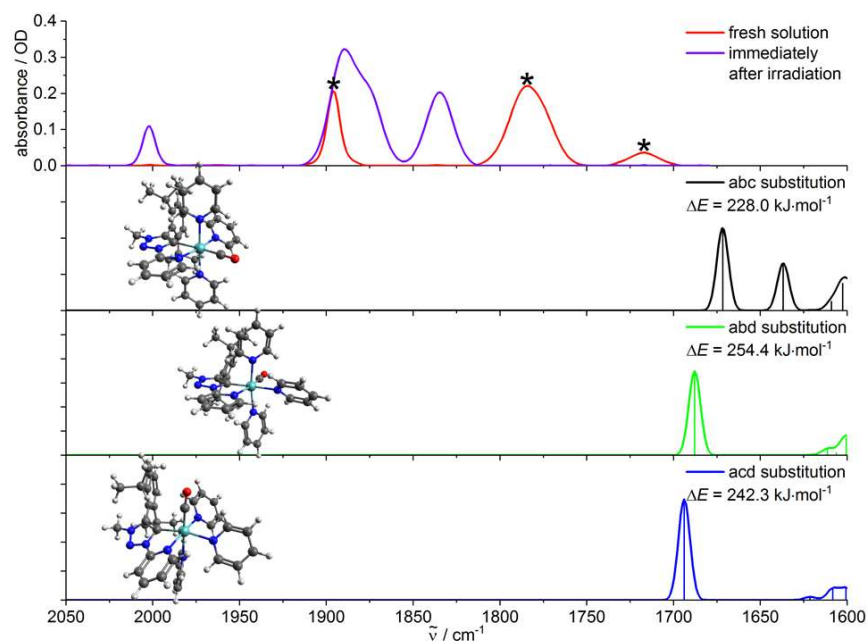


Figure S46. Experimental IR spectra of **Mo** in py before and after irradiation (upper trace, bands marked with asterisks result from the formed photoproduct(s)) and calculated IR spectra of the photoproduct(s) with a substitution of three CO ligands for three py molecules (three lower traces), including the optimized structures and calculated enthalpies of reaction. A coordinated CO ligand remains in equatorial position for isomers abc/abd and in axial position for isomer acd. Calculations: DFT/B3LYP-D3(BJ)/def2-TZVP/COSMO, scaling factor: 0.99, Gaussian convolution with FWHM=8 cm^{-1} .

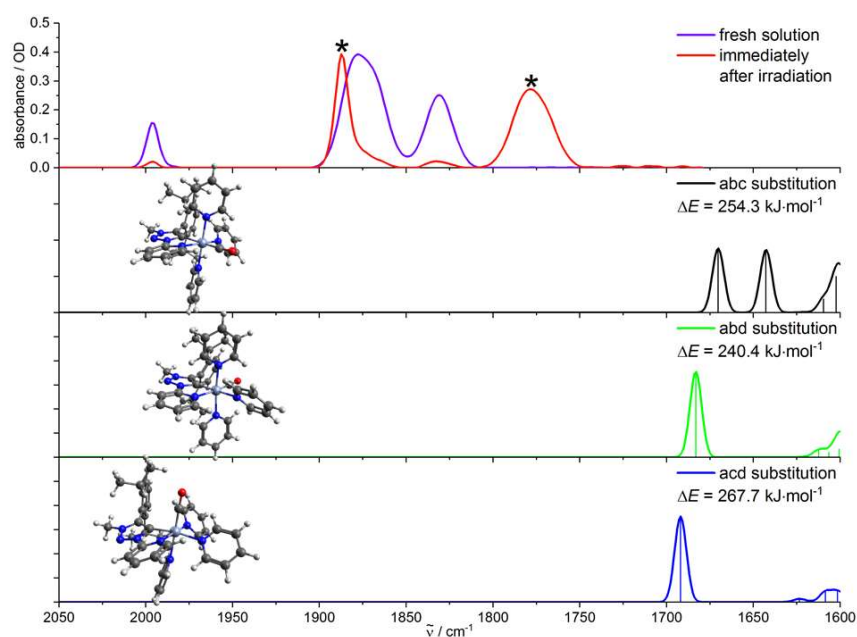


Figure S47. Experimental IR spectra of **W** in py before and after irradiation (upper trace, bands marked with asterisks result from the formed photoproduct(s)) and calculated IR spectra of the photoproducts with a substitution of three CO ligands for three py molecules (three lower traces), including the optimized structures and calculated enthalpies of reaction. A coordinated CO ligand remains in equatorial position for isomers abc/abd and in axial position for isomer acd. Calculations: DFT/B3LYP-D3(BJ)/def2-TZVP/COSMO, scaling factor: 0.99, Gaussian convolution with FWHM=8 cm⁻¹.

4.5 Formation of a metallaketene

4.5.1 Formation of a metallaketene in acetonitrile

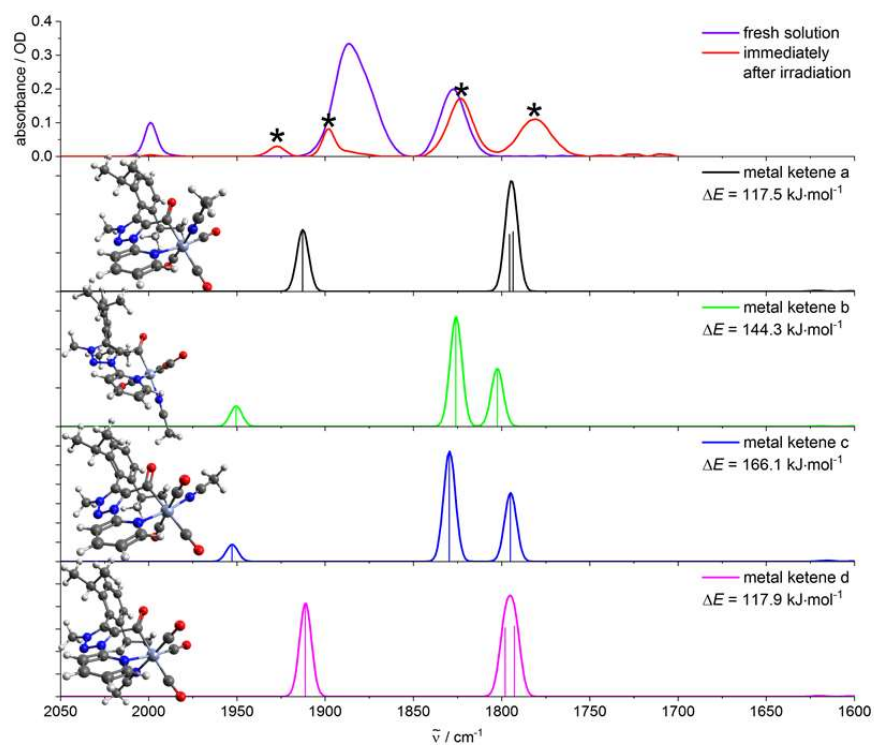


Figure S48. Experimental IR spectra of Cr in MeCN before and after irradiation (upper trace, bands marked with asterisks result from the formed photoproduct(s)) and calculated IR spectra of the photoproducts with formation of a metallaketene (four lower traces), including the optimized structures and calculated enthalpies of reaction. The coordinated MeCN is localized in axial position for isomers a/d and in equatorial position for b/c. Calculations: DFT/B3LYP-D3(BJ)/def2-TZVP/COSMO, scaling factor: 0.99), Gaussian convolution with FWHM=8 cm^{-1} .

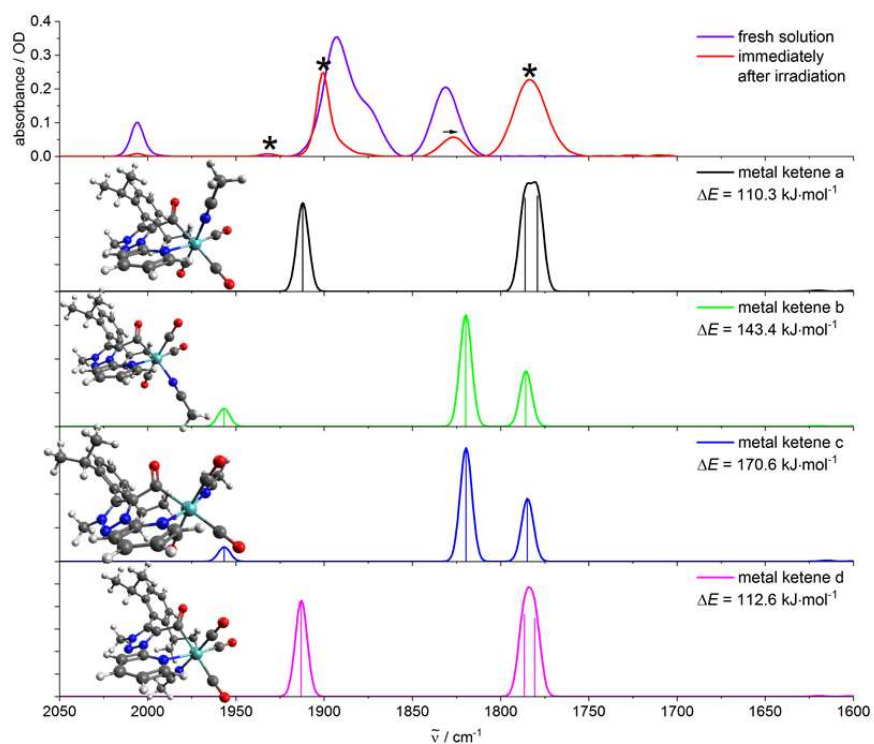


Figure S49. Experimental IR spectra of **Mo** in MeCN before and after irradiation (upper trace, bands marked with asterisks result from the formed photoproduct(s)) and calculated IR spectra of the photoproducts with formation of a metallaketene (four lower traces), including the optimized structures and calculated enthalpies of reaction. The coordinated MeCN is localized in axial position for isomers a/d and in equatorial position for b/c. Calculations: DFT/B3LYP-D3(BJ)/def2-TZVP/COSMO, scaling factor: 0.99), Gaussian convolution with FWHM=8 cm⁻¹.

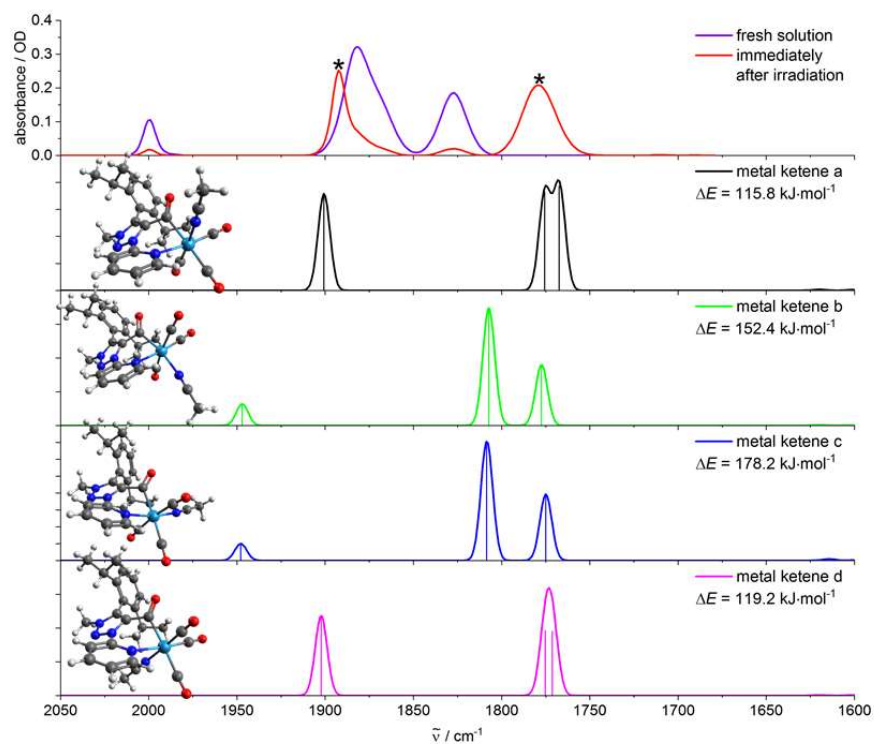


Figure S50. Experimental IR spectra of **W** in MeCN before and after irradiation (upper trace, bands marked with asterisks result from the formed photoproduct(s)) and calculated IR spectra of the photoproducts with formation of a metallaketene (four lower traces), including the optimized structures and calculated enthalpies of reaction. The coordinated MeCN is localized in axial position for isomers a/d and in equatorial position for b/c. Calculations: DFT/B3LYP-D3(BJ)/def2-TZVP/COSMO, scaling factor: 0.99, Gaussian convolution with FWHM=8 cm^{-1} .

4.5.2 Formation of a metallaketene in pyridine

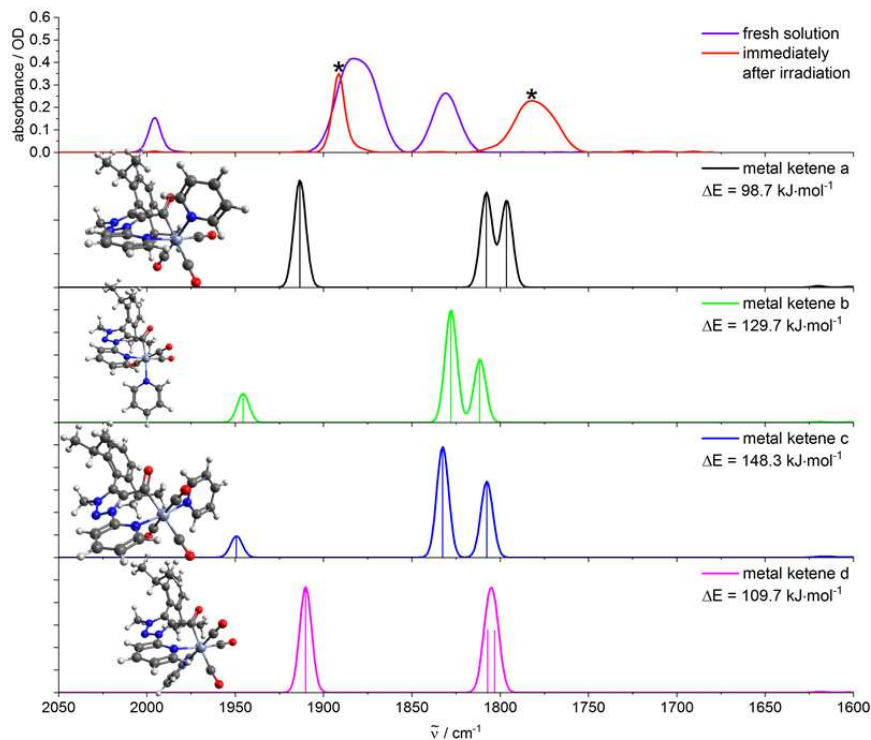


Figure S51. Experimental IR spectra of Cr in py before and after irradiation (upper trace, bands marked with asterisks result from the formed photoproduct(s)) and calculated IR spectra of the photoproducts with formation of a metallaketene (four lower traces), including the optimized structures and calculated enthalpies of reaction. The coordinated py is localized in axial position for isomers a/d and in equatorial position for b/c. Calculations: DFT/B3LYP-D3(BJ)/def2-TZVP/COSMO, scaling factor: 0.99, Gaussian convolution with FWHM=8 cm⁻¹.

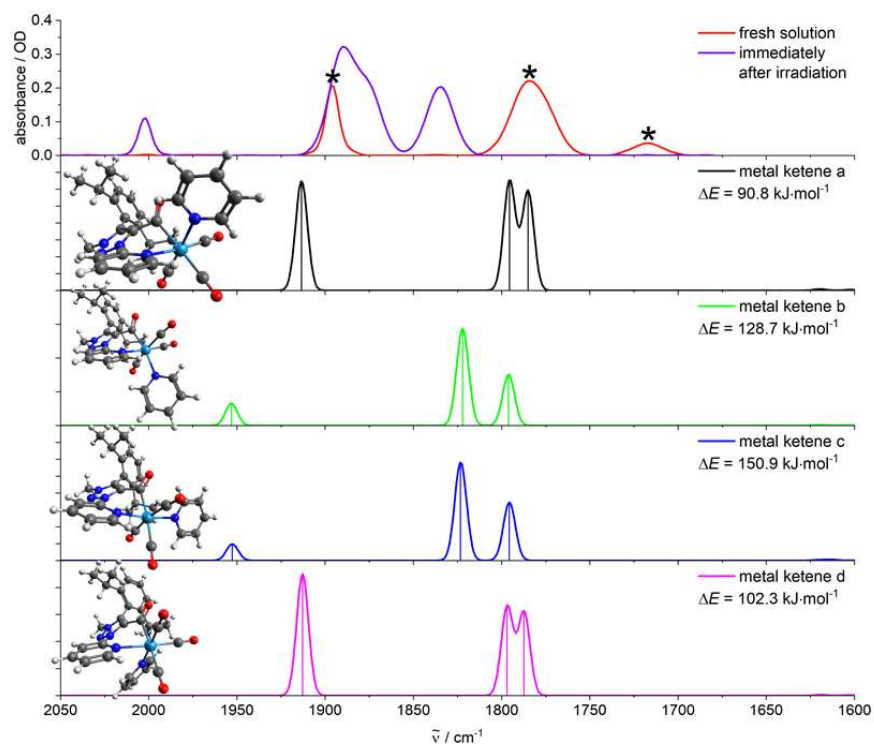


Figure S52. Experimental IR spectra of **Mo** in py before and after irradiation (upper trace, bands marked with asterisks result from the formed photoproduct(s)) and calculated IR spectra of the photoproducts with formation of a metallaketene (four lower traces), including the optimized structures and calculated enthalpies of reaction. The coordinated py is localized in axial position for isomers a/d and in equatorial position for b/c. Calculations: DFT/B3LYP-D3(BJ)/def2-TZVP/COSMO, scaling factor: 0.99, Gaussian convolution with FWHM=8 cm^{-1} .

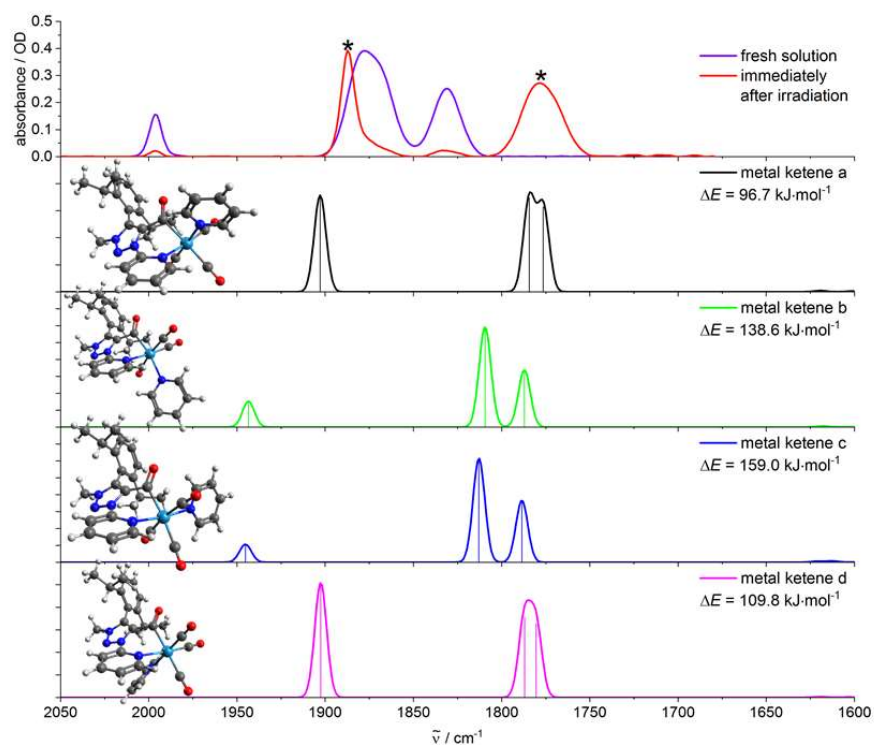


Figure S53. Experimental IR spectra of **W** in py before and after irradiation (upper trace, bands marked with asterisks result from the formed photoproduct(s)) and calculated IR spectra of the photoproducts with formation of a metallaketene (four lower traces), including the optimized structures and calculated enthalpies of reaction. The coordinated py is localized in axial position for isomers a/d and in equatorial position for b/c. Calculations: DFT/B3LYP-D3(BJ)/def2-TZVP/COSMO, scaling factor: 0.99, Gaussian convolution with FWHM=8 cm⁻¹.

4.6 Further isomerizations

4.6.1 Further isomerizations in acetonitrile

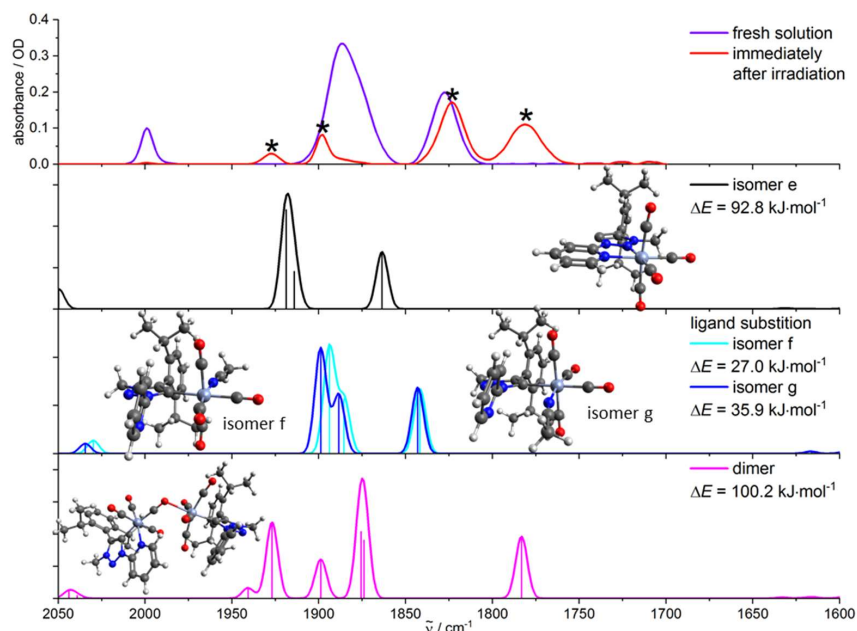


Figure S54. Experimental IR spectra of **Cr** in MeCN before and after irradiation (upper trace, bands marked with asterisks result from the formed photoproduct(s)) and calculated IR spectra of isomers e, f and g as well as a dimer structure (three lower traces), including the optimized structures and calculated enthalpies of reaction. Calculations: DFT/B3LYP-D3(BJ)/def2-TZVP/COSMO, scaling factor: 0.99, Gaussian convolution with FWHM=8 cm⁻¹.

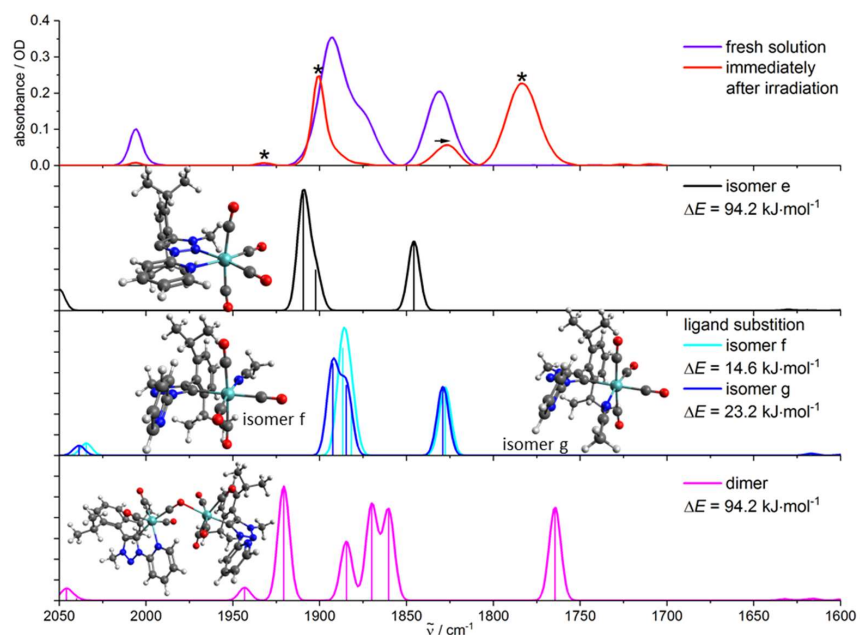


Figure S55. Experimental IR spectra of **Mo** in MeCN before and after irradiation (upper trace, bands marked with asterisks result from the formed photoproduct(s)) and calculated IR spectra of isomers e, f and g as well as a dimer structure (three lower traces), including the optimized structures and calculated enthalpies of reaction. Calculations: DFT/B3LYP-D3(BJ)/def2-TZVP/COSMO, scaling factor: 0.99, Gaussian convolution with FWHM=8 cm^{-1} .

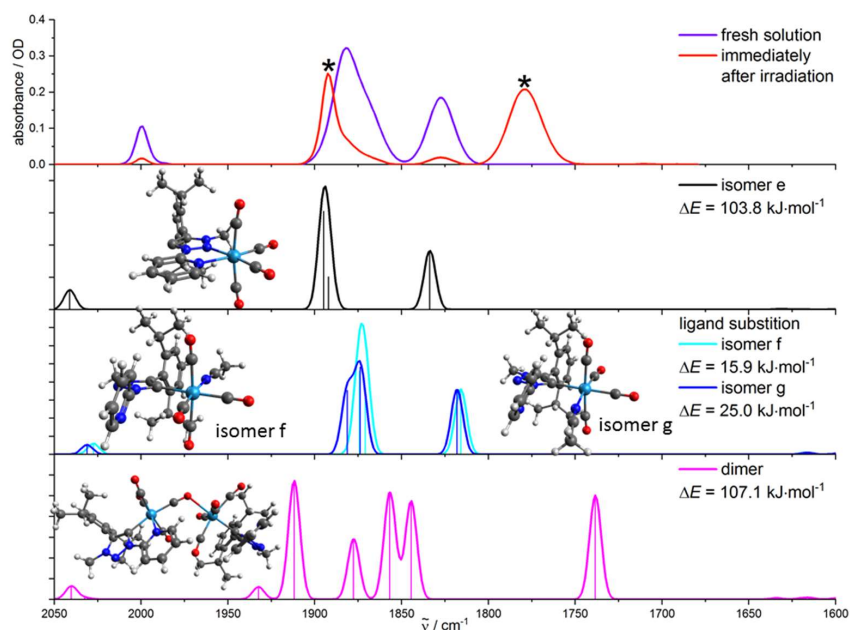


Figure S56. Experimental IR spectra of **W** in MeCN before and after irradiation (upper trace, bands marked with asterisks result from the formed photoproduct(s)) and calculated IR spectra of isomers e, f and g as well as a dimer structure (three lower traces), including the optimized structures and calculated enthalpies of reaction. Calculations: DFT/B3LYP-D3(BJ)/def2-TZVP/COSMO, scaling factor: 0.99, Gaussian convolution with FWHM=8 cm⁻¹.

4.6.2 Further isomerizations in pyridine

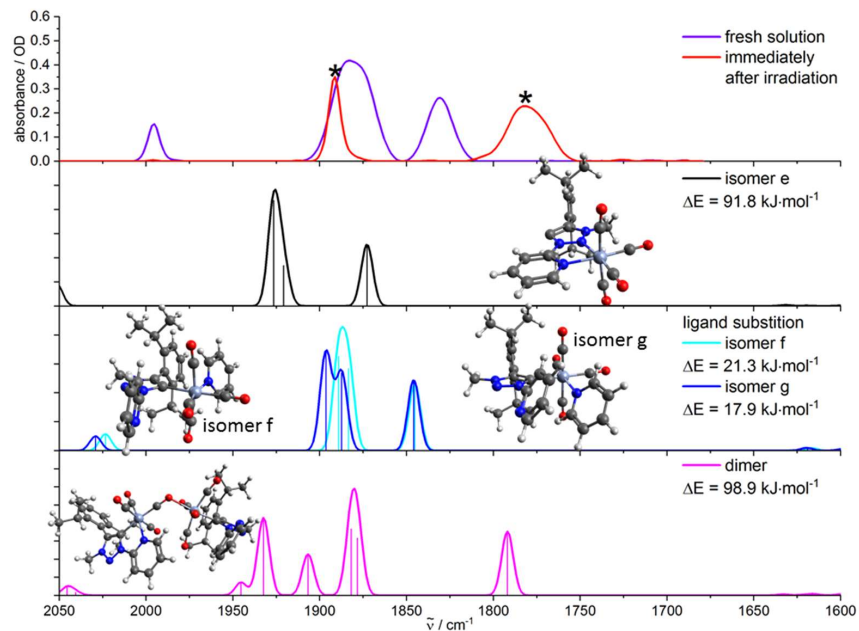


Figure S57. Experimental IR spectra of **Cr** in py before and after irradiation (upper trace, bands marked with asterisks result from the formed photoproduct(s)) and calculated IR spectra of isomers e, f and g as well as a dimer structure (three lower traces), including the optimized structures and calculated enthalpies of reaction. Calculations: DFT/B3LYP-D3(BJ)/def2-TZVP/COSMO, scaling factor: 0.99, Gaussian convolution with FWHM=8 cm⁻¹.

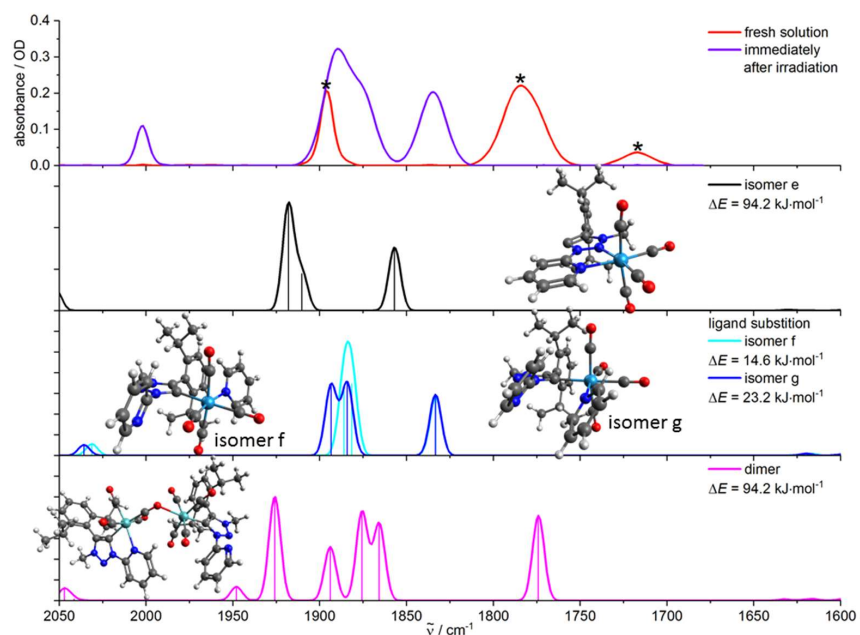


Figure S58. Experimental IR spectra of **Mo** in py before and after irradiation (upper trace, bands marked with asterisks result from the formed photoproduct(s)) and calculated IR spectra of isomers e, f and g as well as a dimer structure (three lower traces), including the optimized structures and calculated enthalpies of reaction. Calculations: DFT/B3LYP-D3(BJ)/def2-TZVP/COSMO, scaling factor: 0.99, Gaussian convolution with FWHM=8 cm^{-1} .

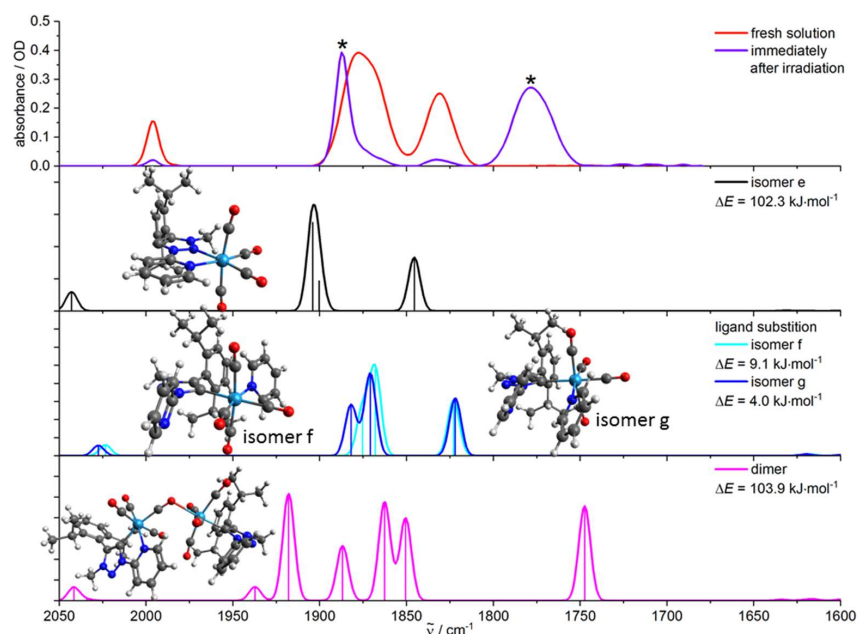


Figure S59. Experimental IR spectra of **W** in py before and after irradiation (upper trace, bands marked with asterisks result from the formed photoproduct(s)) and calculated IR spectra of isomers e, f and g as well as a dimer structure (three lower traces), including the optimized structures and calculated enthalpies of reaction. Calculations: DFT/B3LYP-D3(BJ)/def2-TZVP/COSMO, scaling factor: 0.99, Gaussian convolution with FWHM=8 cm^{-1} .

4.7 Loss of a CO ligand in a KBr matrix

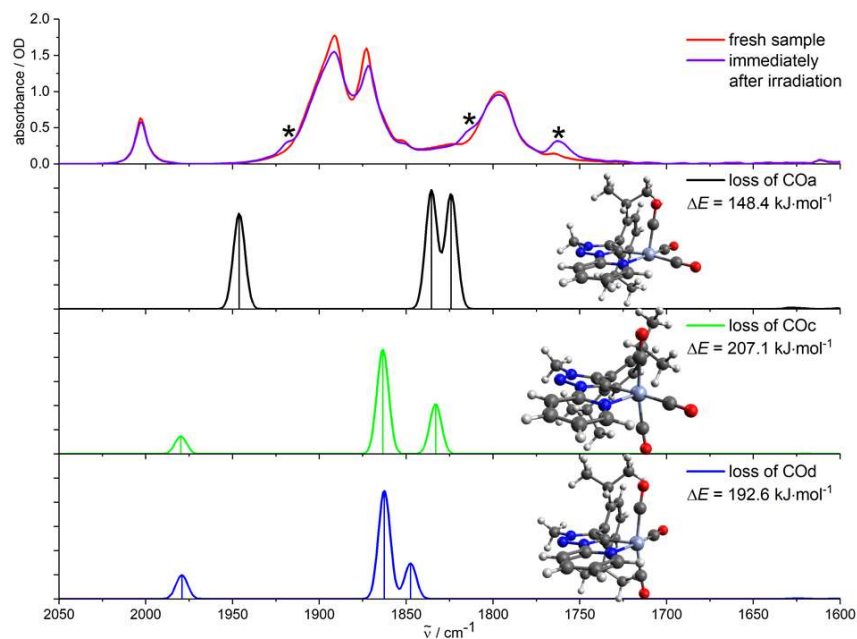


Figure S60. Irradiation ($\lambda_{\text{ex}} = 355 \text{ nm}$) of fresh samples of Cr (KBr pellet) at 10 K and calculated IR spectra of different photoproducts with loss of a CO ligand, including the optimized structures and calculated enthalpies of reaction. The vacant coordination site is localized in axial position for isomer a and in equatorial position for structures c and d, respectively. Calculations: DFT/B3LYP-D3(BJ)/def2-TZVP/COSMO, scaling factor: 0.99, Gaussian convolution with FWHM=8 cm^{-1} .

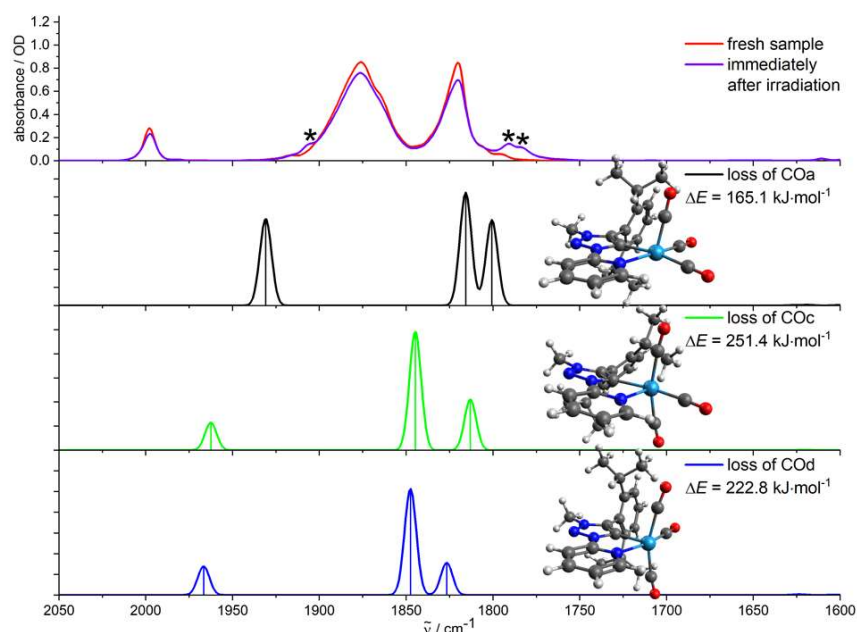
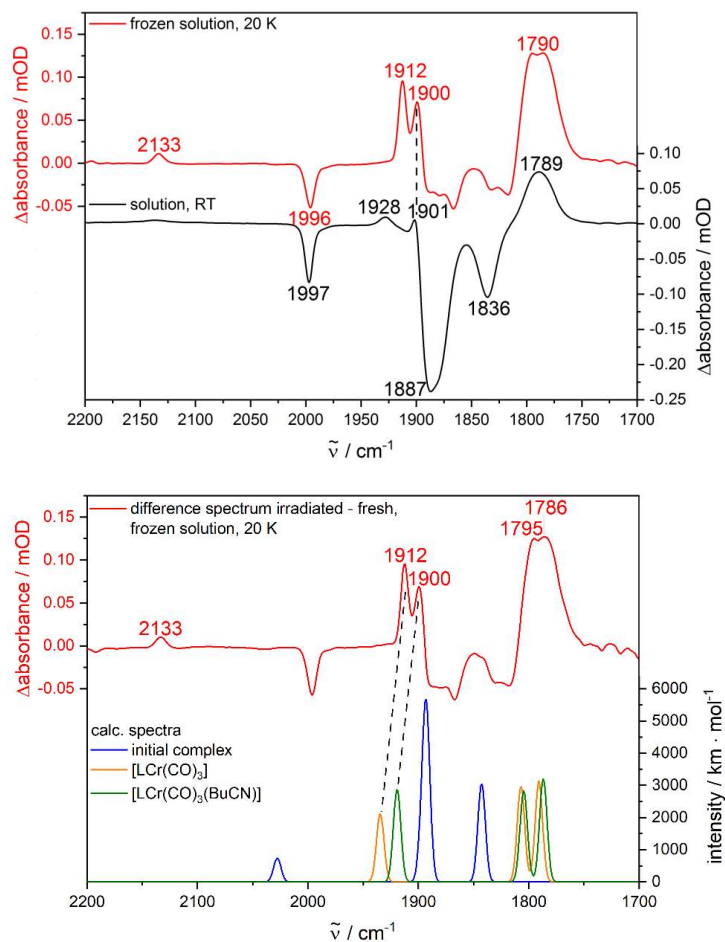


Figure S61. Irradiation ($\lambda_{\text{ex}} = 355 \text{ nm}$) of fresh samples of **W** (KBr pellet) at 10 K and calculated IR spectra of different photoproducts with loss of a CO ligand, including the optimized structures and calculated enthalpies of reaction. The vacant coordination site is localized in axial position for isomer a and in equatorial position for structures c and d, respectively. Calculations: DFT/B3LYP-D3(BJ)/def2-TZVP/COSMO, scaling factor: 0.99, Gaussian convolution with FWHM=8 cm^{-1} .

4.8 Photochemistry in frozen valeronitrile

Figure S62. Difference spectra (irradiated – fresh) of Cr recorded in frozen and liquid solution at 20 K



and at room temperature, respectively (top). Comparison of the difference spectrum at 20 K with calculated IR spectra of the initial complex as well as the photoproducts $[\text{LCr}(\text{CO})_3]$ (vacant coordination site in axial position) and $[\text{LCr}(\text{CO})_2\text{BuCN}_{\text{ax}}]$ (bottom). The dashed lines are guides to the eye. Calculations: DFT/B3LYP-D3(BJ)/def2-TZVP/COSMO, scaling factor: 0.99, Gaussian convolution with $\text{FWHM}=8 \text{ cm}^{-1}$.

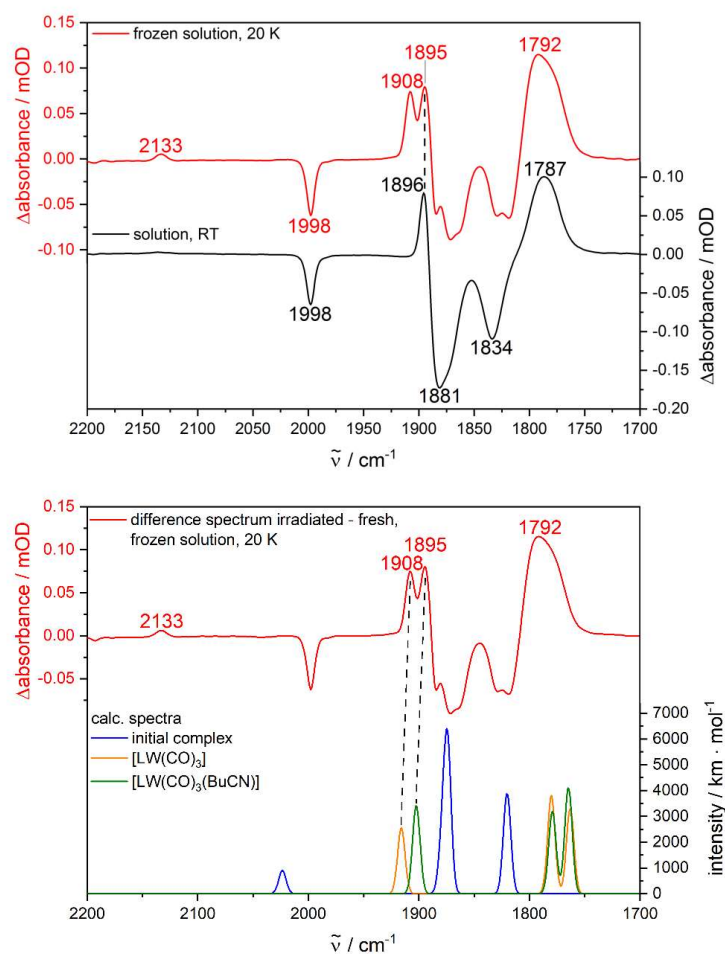


Figure S63. Difference spectra (irradiated – fresh) of **W** recorded in frozen and liquid solution at 20 K and at room temperature, respectively (top). Comparison of the difference spectrum at 20 K with calculated IR spectra of the initial complex as well as the photoproducts [LW(CO)₃] (vacant coordination site in axial position) and [LW(CO)₃(BuCN)] (bottom). The dashed lines are guides to the eye. Calculations: DFT/B3LYP-D3(BJ)/def2-TZVP/COSMO, scaling factor: 0.99, Gaussian convolution with FWHM=8 cm^{-1} .

5 Comparison between experimental and theoretical UV/VIS spectra

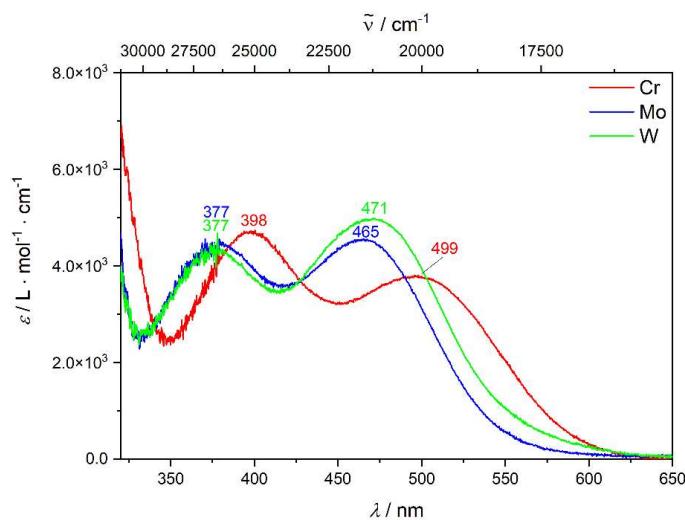


Figure S64. Experimental UV/VIS spectra (extinction coefficients) of fresh solutions of **Cr**, **Mo** and **W** in py.

Table S1. Extinction coefficients of **Cr**, **Mo** and **W** in MeCN as well as py at the wavelengths of 532, 355 and 266 nm.

Complex	solvent	λ / nm	$\epsilon / \text{L} \cdot \text{mol}^{-1} \cdot \text{cm}^{-1}$
Cr	MeCN*	532	1741
		355	2746
		266	25730
	py	532	2910
		355	2634
Mo	MeCN*	532	621
		355	3897
		266	31797
	py	532	1150
		355	3795
W	MeCN*	532	987
		355	3247
		266	24486
	py	532	1775
		355	3630

(*): values taken from ref. [5]

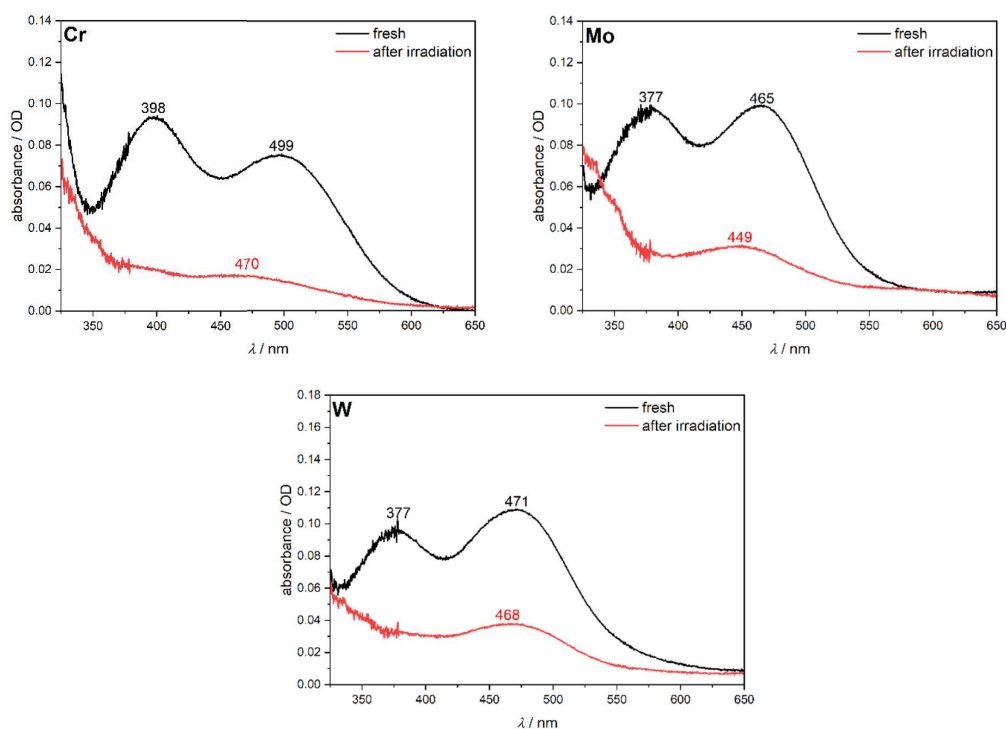


Figure S65. Experimental UV/VIS absorption spectra of **Cr** (top, left), **Mo** (top, right) and **W** (bottom) recorded of fresh solutions and immediately after irradiation at $\lambda_{\text{ex}} = 355$ nm.

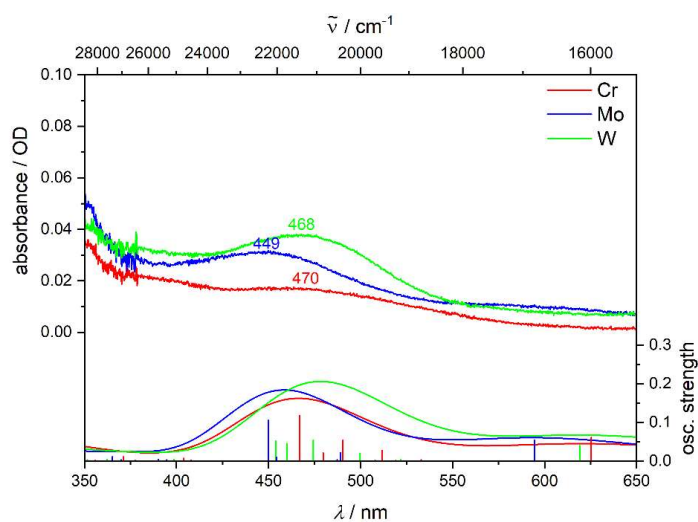


Figure S66. Experimental UV/VIS spectra of solutions of **Cr**, **Mo** and **W** in py after irradiation at 355 nm (upper trace) as well as calculated UV/VIS absorption frequencies (sticks) and convoluted spectra (curves) of the conceivable photoproducts with substitution of an axial CO ligand for a py molecule

(lower trace). Calculations: TDDFT/B3LYP-D3(BJ)/def2-TZVP/COSMO, convolution with FWHM = 1500 cm^{-1} .

Table S2. Assignment of the calculated lowest electronic excitations in the singlet manifold for the photoproduct with an axial CO ligand substituted by a py molecule for Cr in py (TDDFT/B3LYP D3(BJ)/def2-TZVP/COSMO: py).

transition	$\tilde{\nu} / \text{cm}^{-1}$	λ / nm	%	donor orbital	acceptor orbital	assignment
7	21082	474	42.7	HOMO	LUMO+2	$d_{\text{Cr}}, \pi_{\text{Cr-CO}} \rightarrow \pi_{\text{pyridine}}$
			40.1	HOMO-2	LUMO+1	$d_{\text{Cr}}, \pi_{\text{Cr-CO}} \rightarrow \pi_{\text{ligand-pyr}}$
			11.2	HOMO-1	LUMO+2	$d_{\text{Cr}}, \pi_{\text{Cr-CO}} \rightarrow \pi_{\text{ligand-pyr}}$
8	21473	460	37.0	HOMO-2	LUMO+2	$d_{\text{Cr}}, \pi_{\text{Cr-CO}} \rightarrow \pi_{\text{pyridine}}$
			36.5	HOMO-2	LUMO+1	$d_{\text{Cr}}, \pi_{\text{Cr-CO}} \rightarrow \pi_{\text{ligand-pyr}}$
			12.0	HOMO	LUMO+2	$d_{\text{Cr}}, \pi_{\text{Cr-CO}} \rightarrow \pi_{\text{pyridine}}$
			7.8	HOMO-1	LUMO+1	$d_{\text{Cr}}, \pi_{\text{Cr-CO}} \rightarrow \pi_{\text{ligand-pyr}}$
9	22029	454	57.9	HOMO-2	LUMO+2	$d_{\text{Cr}}, \pi_{\text{Cr-CO}} \rightarrow \pi_{\text{pyridine}}$
			19.4	HOMO	LUMO+2	$d_{\text{Cr}}, \pi_{\text{Cr-CO}} \rightarrow \pi_{\text{pyridine}}$
			10.6	HOMO-2	LUMO+1	$d_{\text{Cr}}, \pi_{\text{Cr-CO}} \rightarrow \pi_{\text{ligand-pyr}}$
			6.1	HOMO	LUMO+2	$d_{\text{Cr}}, \pi_{\text{Cr-CO}} \rightarrow \pi_{\text{pyridine}}$

Table S3. Assignment of the calculated lowest electronic excitations in the singlet manifold for the photoproduct with an axial CO ligand substituted by a py molecule for Mo in py (TDDFT/B3LYP D3(BJ)/def2-TZVP/COSMO: py).

transition	$\tilde{\nu} / \text{cm}^{-1}$	λ / nm	%	donor orbital	acceptor orbital	assignment
7	21421	467	39.4	HOMO-2	LUMO+1	$d_{\text{Mo}}, \pi_{\text{Mo-CO}} \rightarrow \pi_{\text{ligand-pyr}}$
			36.0	HOMO	LUMO+2	$d_{\text{Mo}}, \pi_{\text{Mo-CO}} \rightarrow \pi_{\text{pyridine}}$
			16.0	HOMO-1	LUMO+2	$d_{\text{Mo}}, \pi_{\text{Mo-CO}} \rightarrow \pi_{\text{pyridine}}$
9	22233	450	39.3	HOMO-2	LUMO+1	$d_{\text{Mo}}, \pi_{\text{Mo-CO}} \rightarrow \pi_{\text{ligand-pyr}}$
			30.5	HOMO	LUMO+2	$d_{\text{Mo}}, \pi_{\text{Mo-CO}} \rightarrow \pi_{\text{pyridine}}$
			12.2	HOMO-1	LUMO+2	$d_{\text{Mo}}, \pi_{\text{Mo-CO}} \rightarrow \pi_{\text{pyridine}}$
			9.5	HOMO-1	LUMO+1	$d_{\text{Mo}}, \pi_{\text{Mo-CO}} \rightarrow \pi_{\text{ligand-pyr}}$

Table S4. Assignment of the calculated lowest electronic excitations in the singlet manifold for the photoproduct with an axial CO ligand substituted by a py molecule for W in py (TDDFT/B3LYP D3(BJ)/def2-TZVP/COSMO: py).

transition	$\tilde{\nu} / \text{cm}^{-1}$	λ / nm	%	donor orbital	acceptor orbital	assignment
7	20390	490	41.5	HOMO	LUMO+2	$d_{\text{W}}, \pi_{\text{W-CO}} \rightarrow \pi_{\text{pyridine}}$
			30.0	HOMO-2	LUMO+1	$d_{\text{W}}, \pi_{\text{W-CO}} \rightarrow \pi_{\text{ligand-pyr}}$
			18.3	HOMO-2	LUMO+2	$d_{\text{W}}, \pi_{\text{W-CO}} \rightarrow \pi_{\text{pyridine}}$
			8.9	HOMO-1	LUMO+2	$d_{\text{W}}, \pi_{\text{W-CO}} \rightarrow \pi_{\text{pyridine}}$
9	21419	467	49.3	HOMO-2	LUMO+1	$d_{\text{W}}, \pi_{\text{W-CO}} \rightarrow \pi_{\text{ligand-pyr}}$
			26.4	HOMO	LUMO+2	$d_{\text{W}}, \pi_{\text{W-CO}} \rightarrow \pi_{\text{pyridine}}$
			11.7	HOMO-1	LUMO+1	$d_{\text{W}}, \pi_{\text{W-CO}} \rightarrow \pi_{\text{ligand-pyr}}$
			5.8	HOMO-1	LUMO+2	$d_{\text{W}}, \pi_{\text{W-CO}} \rightarrow \pi_{\text{pyridine}}$

6 Kinetic data for the dark reverse reaction

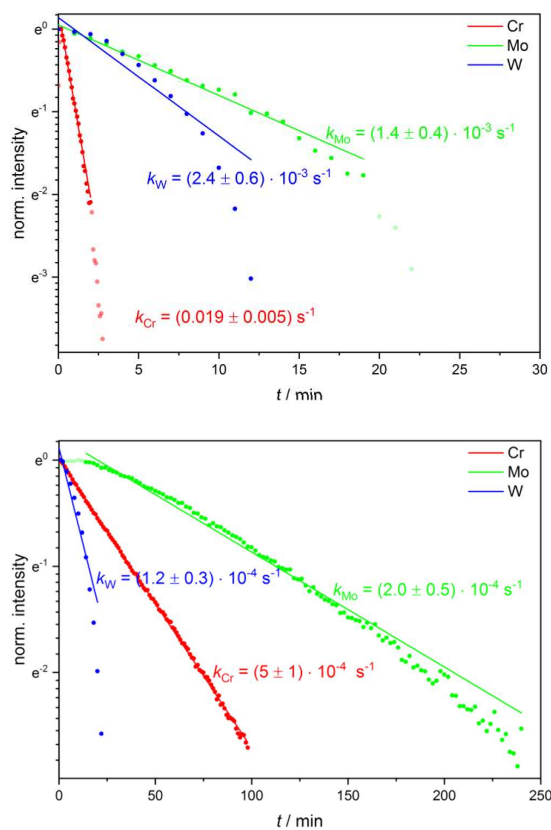


Figure S67. First order kinetic plots and fits of the dark reverse reaction of **Cr**, **Mo** and **W** measured in MeCN (top) and py (bottom) ($c = 3 \text{ mM}$). The shown kinetics were recorded subsequent to irradiation at 532 nm. The IR intensity at the end of the irradiation period ($t = 0$) was normalized to 1.

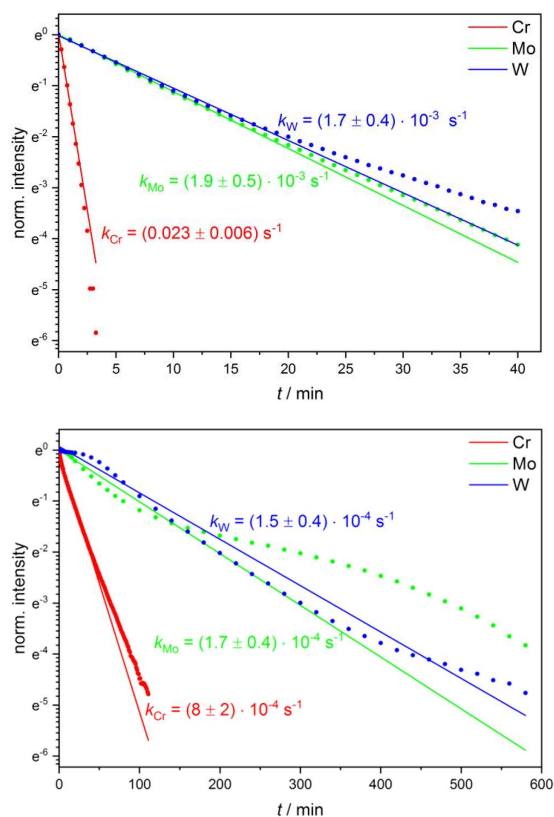


Figure S68. First order kinetic plots and fits of the dark reverse reaction of **Cr**, **Mo** and **W** measured in MeCN (top) and py (bottom) ($c = 6 \text{ mM}$). The shown kinetics were recorded subsequent to irradiation at 355 nm. The IR intensity at the end of the irradiation period ($t = 0$) was normalized to 1.

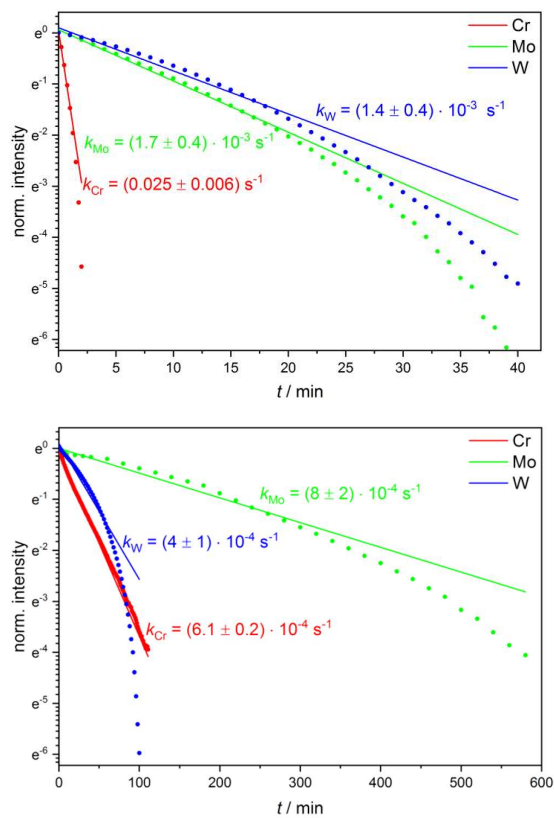


Figure S69. First order kinetic plots and fits of the dark reverse reaction of **Cr**, **Mo** and **W** measured in MeCN (top) and py (bottom) ($c = 3 \text{ mM}$). The shown kinetics were recorded subsequent to irradiation at 355 nm. The IR intensity at the end of the irradiation period ($t = 0$) was normalized to 1.

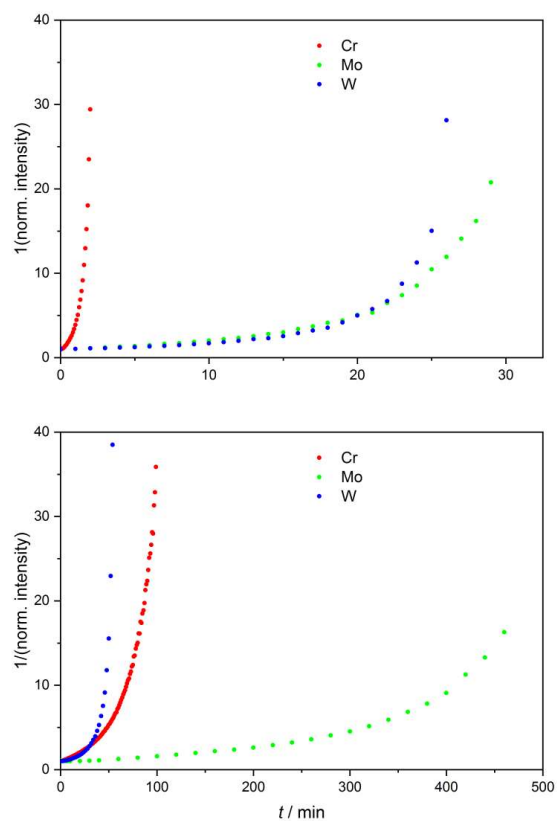


Figure S70. Second order kinetic plot of the dark reverse reaction of **Cr**, **Mo** and **W** measured in MeCN (top) and py (bottom) ($c = 6 \text{ mM}$). The shown kinetics were recorded subsequent to irradiation at 532 nm. The IR intensity at the end of the irradiation period ($t = 0$) was normalized to 1.

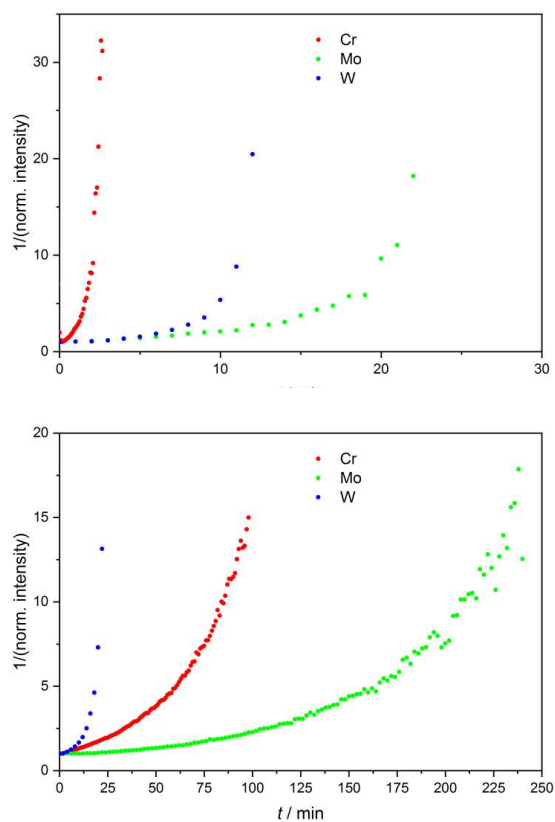


Figure S71. Second order kinetic plot of the dark reverse reaction of **Cr**, **Mo** and **W** measured in MeCN (top) and py (bottom) ($c = 3 \text{ mM}$). The shown kinetics were recorded subsequent to irradiation at 532 nm. The IR intensity at the end of the irradiation period ($t = 0$) was normalized to 1.

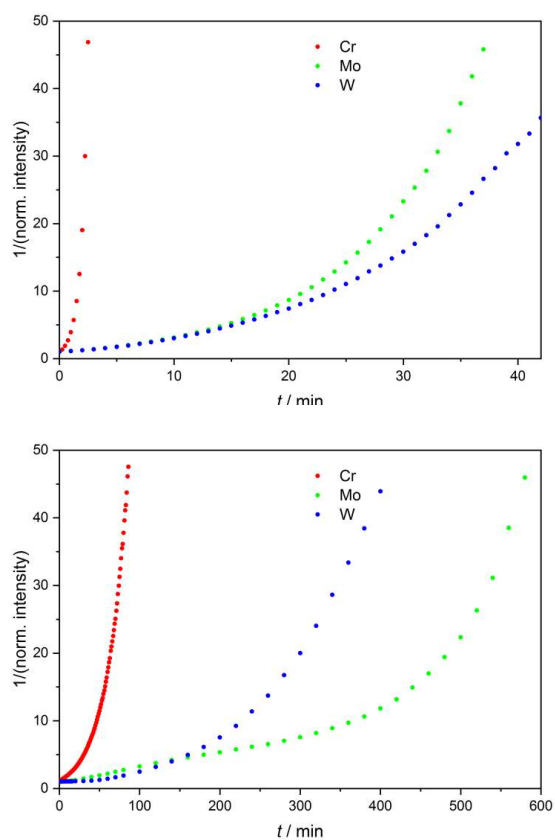


Figure S72. Second order kinetic plot of the dark reverse reaction of **Cr**, **Mo** and **W** measured in MeCN (top) and py (bottom) ($c = 6 \text{ mM}$). The shown kinetics were recorded subsequent to irradiation at 355 nm. The IR intensity at the end of the irradiation period ($t = 0$) was normalized to 1.

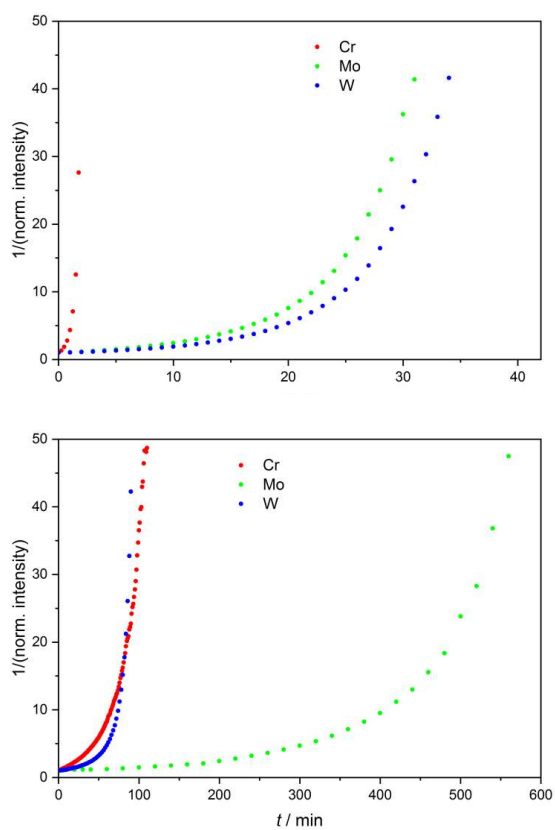
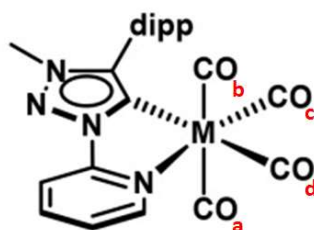


Figure S73. Second order kinetic plot of the dark reverse reaction of **Cr**, **Mo** and **W** measured in MeCN (top) and py (bottom) ($c = 3 \text{ mM}$). The shown kinetics were recorded subsequent to irradiation at 355 nm. The IR intensity at the end of the irradiation period ($t = 0$) was normalized to 1.

7 Calculated bond lengths

Table S5. Calculated M–CO and C–O bond lengths in Å for **Cr**, **Mo** and **W** (DFT/B3LYP D3(BJ)/def2-TZVP/COSMO).



complex	medium	M-COa	COa	M-COb	COb	M-COc	COc	M-COd	COd
Cr	KBr ^[5]	1.894	1.151	1.894	1.151	1.839	1.159	1.853	1.160
	MeCN	1.893	1.152	1.892	1.152	1.835	1.161	1.848	1.163
	py	1.893	1.151	1.892	1.151	1.836	1.160	1.849	1.162
	BuCN	1.893	1.151	1.892	1.152	1.836	1.160	1.848	1.162
Mo	KBr ^[5]	2.043	1.151	2.044	1.151	1.966	1.161	1.997	1.160
	MeCN	2.042	1.151	2.043	1.151	1.962	1.163	1.992	1.163
	py	2.042	1.151	2.043	1.151	1.964	1.162	1.994	1.162
	BuCN	2.042	1.151	2.043	1.151	1.963	1.163	1.993	1.162
W	KBr ^[5]	2.052	1.153	2.052	1.153	1.981	1.163	2.009	1.163
	MeCN	2.051	1.153	2.052	1.153	1.976	1.165	2.004	1.165
	py	2.051	1.153	2.052	1.153	1.978	1.165	2.006	1.164
	BuCN	2.051	1.153	2.052	1.153	1.977	1.165	2.005	1.165

8 References

- [1] M. J. Frisch, G. W. Trucks, H. B. Schlegel, G. E. Scuseria, M. A. Robb, J. R. Cheeseman, G. Scalmani, V. Barone, B. Mennucci, G. A. Petersson, H. Nakatsuji, M. Caricato, X. Li, H. P. Hratchian, A. F. Izmaylov, J. Bloino, G. Zheng, J. L. Sonnenberg, M. Hada, M. Ehara, K. Toyota, R. Fukuda, J. Hasegawa, M. Ishida, T. Nakajima, Y. Honda, O. Kitao, H. Nakai, T. Vreven, J. A. Montgomery, Jr., J. E. Peralta, F. Ogliaro, M. Bearpark, J. J. Heyd, E. Brothers, K. N. Kudin, V. N. Staroverov, T. Keith, R. Kobayashi, J. Normand, K. Raghavachari, A. Rendell, J. C. Burant, S. S. Iyengar, J. Tomasi, M. Cossi, N. Rega, J. M. Millam, M. Klene, J. E. Knox, J. B. Cross, V. Bakken, C. Adamo, J. Jaramillo, R. Gomperts, R. E. Stratmann, O. Yazyev, A. J. Austin, R. Cammi, C. Pomelli, J. W. Ochterski, R. L. Martin, K. Morokuma, V. G. Zakrzewski, G. A. Voth, P. Salvador, J. J. Dannenberg, S. Dapprich, A. D. Daniels, O. Farkas, J. B. Foresman, J. V. Ortiz, J. Cioslowski, D. J. Fox, Gaussian 09, Gaussian, Inc., Wallingfort, CT, **2013**.
- [2] F. Furche, R. Ahlrichs, C. Hättig, W. Klopper, M. Sierka, F. Weigend, *Wiley Interdiscip. Rev. Comput. Mol. Sci.* **2014**, 4, 91.
- [3] *TURBOMOLE V7.4 2019, a development of University of Karlsruhe and Forschungszentrum Karlsruhe GmbH, 1989-2007, TURBOMOLE GmbH, since 2007; available from <http://www.turbomole.com>.*
- [4] a) S. Grimme, J. Antony, S. Ehrlich, H. Krieg, *J. Chem. Phys.* **2010**, 132, 154104; b) S. Grimme, S. Ehrlich, L. Goerigk, *J. Comput. Chem.* **2011**, 32, 1456.
- [5] P. Boden, P. Di Martino-Fumo, T. Bens, S. Steiger, U. Albold, G. Niedner-Schatteburg, M. Gerhards, B. Sarkar, *Chem. Eur. J.* **2021**, 27, 12959–12964.

Kapitel 6: Zusammenfassung und Ausblick

Diese Arbeit beschäftigte sich einerseits mit der Untersuchung der photophysikalischen Eigenschaften von Organometallkomplexen mittels multispektroskopischer Methoden und andererseits mit der Verfolgung von Reaktionen mit Beteiligung von Organometallkomplexen mittels zeitaufgelöster FTIR-Spektroskopie. Die untersuchten Komplexe sind Übergangsmetallkomplexe, die im Hinblick auf die Entwicklung von OLEDs oder Katalysatoren bzw. Photosensibilisatoren interessante Eigenschaften aufweisen. Dabei sind insbesondere die Leuchteigenschaften für die Anwendung als OLEDs sowie die Lebensdauer und Geometrie im angeregten Zustand für Katalysatoren und Photosensibilisatoren von Bedeutung. Die Komplexe enthalten dabei keine Seltenerdmetalle, mit denen diese Eigenschaften erzielt werden, sondern häufiger vorkommende Metalle wie Kupfer. Durch die Verfolgung von Reaktionen wird ein wichtiges Verständnis für die Reaktivität von verschiedenen Organometallkomplexen erhalten.

Um diese Eigenschaften zu untersuchen, wurde eine Kombination aus (zeitaufgelöster) Lumineszenz- und Fourier-Transformations-Infrarot-Spektroskopie verwendet. Die Lumineszenzspektroskopie wurde für die Untersuchung der Leuchteigenschaften, sowie der lumineszenten Zustände angewandt, wobei mit der zeitaufgelösten Lumineszenzspektroskopie Lebensdauern dieser erhalten wurden. Die FTIR-Spektroskopie, insbesondere die zeitaufgelöste Step-scan-Methode, wurde in Kombination mit quantenchemischen Rechnungen für die strukturelle Bestimmung angeregter Zustände verwendet. Um auch das temperaturabhängige Verhalten der angeregten Zustände charakterisieren zu können, wurden die Messungen in einem Temperaturbereich von 5-290 K durchgeführt. Das zweite große Kapitel dieser Arbeit beschäftigt sich mit der Verfolgung von Reaktionen von Organometallkomplexen mit zeitaufgelöster FTIR-Spektroskopie. Dabei kamen die Technik der wiederholten statischen Messungen sowie die Rapid-scan-Methode zum Einsatz.

6.1 Photophysik lumineszenter Kupferkomplexe

Der erste Teil dieser Arbeit beschäftigt sich mit der Charakterisierung der Lumineszenz und der lumineszenten Zustände von dinuklearen Kupfer- und Silberkomplexen, welche von Dr. Jasmin Busch im Arbeitskreis von Prof. Dr. Stefan Bräse am KIT synthetisiert wurden. Dabei wurde ein Quartett an Komplexen bestehend aus einem Cu_2Br_2 -, Cu_2Cl_2 -, Ag_2Br_2 - oder Ag_2Cl_2 -Zentrum und jeweils einem verbrückenden und zwei endständigen 2-(Diphenylphosphino)pyridin-Liganden untersucht und der Einfluss der Kooperativität auf die Lumineszenz bestimmt. Die Komplexe emittieren im sichtbaren Bereich zwischen ca. 480

und 580 nm, wobei die Kupferkomplexe die rottere Emission zeigen. Interessanterweise emittieren die Silberkomplexe bei Raumtemperatur nur sehr schwach, während die Kupferkomplexe eine intensive Emission aufweisen. Temperaturabhängige Lumineszenzmessungen zeigen für die Kupferkomplexe TADF-typisches Verhalten bei Raumtemperatur und Phosphoreszenz bei tiefer Temperatur mit einer Rotverschiebung der Emissionsbandenlage und einem deutlichen Anstieg der Lebensdauern. Die Halogenide beeinflussen dabei das Lumineszenzverhalten kaum. Im Gegensatz dazu weist das temperaturabhängige Verhalten der Silberkomplexe deutliche Unterschiede zu dem der Kupferkomplexe auf. Die Emissionsbandenlage ist nahezu temperaturunabhängig, jedoch nimmt die Intensität zu tiefen Temperaturen hin stark zu. Damit weisen die Silberkomplexe kein TADF-Verhalten auf, aber eine signifikante Unterdrückung nicht-strahlender Deaktivierungskanäle bei tiefer Temperatur. Aus den Step-scan-FTIR-Untersuchungen im Vergleich mit quantenchemischen Rechnungen (Durchgeführt von Florian Rehak aus der Arbeitsgruppe von Prof. Dr. Willem Klopper, KIT) wurden die Triplett-Zustände anhand ihrer Struktur motive charakterisiert. Diese Untersuchung ergab für die Silberkomplexe die Zuordnung zu einem energetisch höher liegenden ligandzentrierten Triplett-Zustand, in dem die Komplexe anscheinend kinetisch gefangen sind und somit den TADF-fähigen energetisch niedrigeren M/XLCT-Triplett-Zustand nicht erreichen können. Die TADF-fähigen M/XLCT-Triplettzustände finden sich auch für die Kupferkomplexe und wurden dem experimentell beobachteten langlebigen elektronisch angeregten Zustand zugeordnet. Da die Silberkomplexe diese Zustände laut DFT-Rechnungen auch aufweisen, diese bei den vorliegenden Komplexen jedoch nicht besetzt werden, scheint die Synthese eines TADF-fähigen Silberkomplexes auf Basis dieser Ergebnisse möglich.

Verwandt mit dem zuvor beschriebenen Projekt sind die Untersuchung der Lumineszenzeigenschaften sowie der lumineszenten Zustände in verschiedenen Medien (KBr-Pressling, Pulver, teilweise Kristalle) der vierkernige Kupferkomplexe mit den Halogeniden Iodid, Bromid und Chlorid und zwei verbrückenden 2-(Diphenylphosphino)pyridin-Liganden bzw. deren Derivaten 4-Methyl-2-(Diphenylphosphino)pyridin und 1-(Diphenylphosphino)isochinolin. Diese Komplexe wurden ebenfalls von Dr. Jasmin Busch aus dem Arbeitskreis von Prof. Dr. Stefan Bräse am KIT synthetisiert und wurden aufgrund der Thermochromie-aufweisenden verwandten vierkernigen Komplexe mit 6-Methyl-2-(Diphenylphosphino)pyridin-Liganden^[53] auf dieses Verhalten hin untersucht. Das temperaturabhängige Lumineszenzverhalten ergab für die Komplexreihe mit den 4-Methyl-2-(Diphenylphosphino)pyridin-Liganden kein thermochromes Verhalten mit erkennbarer Beteiligung von zwei verschiedenen Triplett-

Zuständen. Dagegen zeigte sich für die Komplexe, mit Ausnahme des entsprechenden Iodid-Komplexes im KBr-Pressling, eine leichte Rotverschiebung zu tiefen Temperaturen, wobei jedoch der Temperaturverlauf der Lumineszenzlebensdauern, welche alle im Bereich der Phosphoreszenz ($\geq 5 \mu\text{s}$) liegen, einen TADF-Mechanismus widerlegt. Die Rotverschiebung erklärt sich möglicherweise über eine Destabilisierung des Grundzustands oder eine Stabilisierung des Triplett-Zustands bei tiefer Temperatur. Die Emissionsbande des Iodid-Komplexes im KBr-Pressling schiebt zu tieferen Temperaturen in den blauerer Bereich, was über einen im KBr-Pressling im Gegensatz zu den Pulverproben stärker ausgeprägten rigidochromen Effekt erklärt wird. Der Bromid- und der Chlorid-Komplex ohne Methylsubstituenten am Liganden (2-(Diphenylphosphino)pyridin-Ligand) zeigen ein vergleichbares temperaturabhängiges Lumineszenzverhalten wie die analogen 4-Methyl-Komplexe. Für den Iodid-Komplex ohne Methylgruppe ließ sich dagegen ein thermochromes Verhalten beobachten. Dieses war in der reinen Pulverprobe deutlich aufgelöster als im KBr-Pressling. Mit der Step-scan-FTIR-Spektroskopie konnten für den Iodid-Komplex ohne Methylgruppe am Liganden bei 20 K und 290 K unterschiedliche Triplett-Zustände zugeordnet werden, was die beobachtete Thermochromie bestätigt. Ebenfalls untersucht wurde ein Komplex mit erweitertem π -System am Liganden, indem die Pyridineinheit durch eine Isochinolin-Einheit ersetzt wurde. Dieser unterscheidet sich in seinem Lumineszenzverhalten deutlich von den Komplexen mit Pyridinring und zeigt Anzeichen für einen TADF-Mechanismus.

Interessantes temperaturabhängiges Lumineszenzverhalten wurde auch für verschiedene zweikernige Kupfer- und einkernige Zinkkomplexe aus der Arbeitsgruppe von Prof. Dr. Peter Roesky am KIT festgestellt. Diese zeigen in etwa einen temperaturabhängigen TADF-Mechanismus, der jedoch bei höherer Temperatur (ab 150 K) keine verzögerte Fluoreszenz, sondern ein effizientes Quenching aufweist. Für den $[\text{Cu}_2\{\text{DippPIA}\}_2]$ -Komplex (DippPIA = *P,P*-Diphenyl-*N,N'*-bis(2,6-diisopropylphenyl)phosphinimidamin) wurde mittels Step-scan-FTIR-Spektroskopie im Vergleich mit quantenchemischen Rechnungen auf DFT-Niveau der angeregte Zustand von 20 bis 150 K für einen Vergleich mit den Lumineszenzdaten charakterisiert. Der experimentell untersuchte angeregte Zustand des Kupferkomplexes wurde anhand charakteristischer Banden einem ligandzentrierten Triplett-Zustand zugeordnet. Die Lebensdauern des angeregten Zustands aus den Step-scan-Daten bei 20 und 70 K bestätigen die Lumineszenzlebensdauern, gemessen am KIT. Die lange Lebensdauer aus den Step-scan-Daten bei 150 K, wo keine deutliche Lumineszenz mehr detektiert wurde, führt zu der Annahme, dass bei höheren Temperaturen weiterhin ein Triplett-Zustand besetzt wird, welcher jedoch effizient über nicht-strahlende Kanäle deaktiviert wird.

6.2 Photophysik und Energieübertragung von Kupfer-Photosensibilisatoren

Kupferkomplexe sind nicht nur aufgrund ihrer möglichen Anwendung in OLEDs relevant, sie werden auch zur Verwendung als neue, effiziente Photosensibilisatoren entwickelt. Dazu wurde ein Kupferkomplex im Arbeitskreis von Prof. Dr. Stefanie Tschierlei und Dr. Michael Karnahl an der TU Braunschweig synthetisiert, welcher einmal den Xantphos-Liganden und einen um zwei Methylgruppen in 2- und 9-Position an der Phenanthrolineinheit erweiterten biipo-Liganden (biipo = 16*H*-Benzo-[4',5']-isochinolino-[2',1':1,2]-imidazo-[4,5-*f*]-[1,10]-phenanthrolin-16-on) enthält. Im Vergleich zum Kupferkomplex mit dem nicht-methylierten biipo-Liganden erhält man eine Verzehnfachung der Lebensdauer des angeregten Zustands und damit eine bessere potentielle Eignung als Photosensibilisator. Auch die Untersuchung der Singulett-Sauerstoff-Bildung und der Energieübertragung, durch Photon-Upconversion auf Anthracen, waren erfolgreich und zeigen die Eignung des Komplexes als Photosensibilisator, was für einen Komplex ohne seltene Metalle bemerkenswert ist. In den Step-scan-FTIR-Messungen im Feststoff wurde ein im Gegensatz zu den Lumineszenzdaten sehr langlebiger und daher dunkler angeregter Zustand beobachtet und im Vergleich mit quantenchemischen Rechnungen einem auf dem methylierten biipo-Liganden zentrierten Triplett-Zustand zugeordnet. Mit der Kombination aus großem organischen Chromophor und Metallatom konnte ein langlebiger, katalytisch aktiver, elektronisch angeregter Zustand durch effizientes Intersystem Crossing populiert werden. Auf Basis dieser Ergebnisse können weitere Systeme ohne seltene und teure Metalle als effiziente Photokatalysatoren entwickelt und untersucht werden.

6.3 Thermische Reaktionen eines Kupferkomplexes

Dieser Teil beschäftigt sich mit der Aufklärung des Reaktionsmechanismus der Reaktion des dinuklearen Kupfer-Dimethylglyoxim (dmg)-Komplexes $[\text{Cu}_2(\text{H}_2\text{dmg})(\text{Hdmg})(\text{dmg})]^+$ mit den Lösungsmitteln Acetonitril (CH_3CN) und Ethanol (EtOH). Die Reaktion in CH_3CN wurde mittels Aufnahme von statischen FTIR-Messungen in festgelegten, regelmäßigen Zeitabständen über 8 h verfolgt. Außerdem wurden Referenzspektren möglicher Produkte aufgenommen. Der mononukleare Referenzkomplex $[\text{Cu}(\text{Hdmg})_2]$ zeigt keine Reaktivität in den genannten Lösungsmitteln, während der dinukleare Komplex eine deutliche Reaktivität aufweist, was für einen kooperativen Effekt zwischen den Kupferzentren spricht. Je nach Reaktionspartner, EtOH oder CH_3CN , wird der dinukleare Komplex reduziert oder oxidiert. Die Reduktion in Ethanol konnte nicht mit FTIR-Spektroskopie verfolgt werden, da der benötigte Überschuss an EtOH mit gleichzeitig ausreichend hoher Konzentration des Komplexes, aufgrund der schlechten Löslichkeit in Ethanol nicht erreicht werden konnte. Stattdessen wurde das Gasgemisch über der Reaktionslösung abgefangen und in

deutertem Acetonitril (CD_3CN) aufgenommen, worin das Oxidationsprodukt des Ethanol, Acetaldehyd, mittels FTIR-Spektroskopie nachgewiesen werden konnte. Die Reaktion in CD_3CN ließ sich über deutliche Veränderungen im FTIR-Spektrum bereits innerhalb der ersten Minuten der Reaktion gut verfolgen. Im Produktspektrum nach 8 h konnten der hydrolysierte Ligand als 2,3-Butandionmonoxim, das Kupferprodukt $[\text{Cu}(\text{CH}_3\text{CN})_4]^+$ und unkoordiniertes H_2dmg anhand von Referenzmessungen zugeordnet werden. Der postulierte und durch DFT-Rechnungen vorgeschlagene Reaktionsmechanismus beinhaltet als ersten Schritt den nukleophilen Angriff von H_2O an den zweikernigen Komplex, welches anschließend den angegriffenen Liganden zu 2,3-Butandionmonoxim hydrolysiert. Um diesen Mechanismus mit experimentellen Ergebnissen bestätigen zu können, wurde die Reaktion in CD_3CN unter Zugabe von ^{18}O -isotopiertem Wasser abermals mittels FTIR-Spektroskopie verfolgt. Es wurde eine Rotverschiebung der dem Monoxim zugeordneten C-O-Schwingungen beobachtet. Dieses Ergebnis bestätigt eindeutig die Beteiligung von Wasser am ablaufenden Reaktionsmechanismus. Da das Intermediat der Reaktion mit an dem Komplex gebundenem Hydroxylamin, vermutlich aufgrund einer schnellen Oxidation zu N_2O , mittels FTIR-Spektroskopie in der Reaktionslösung nicht nachgewiesen werden konnte, wurde das Produkt N_2O in CD_3CN untersucht. Dazu wurde das Gas in reines CD_3CN geleitet und das von der resultierenden Lösung aufgenommene Referenzspektrum mit dem Produktspektrum verglichen. Somit konnte die Bildung von N_2O bei der Reaktion in CD_3CN bestätigt werden, was den postulierten Mechanismus ebenfalls bekräftigt.

6.4 Photochemische Reaktivität von Cr(0)-, Mo(0)-, W(0)-Carbonyl-Komplexen

Im zweiten Projekt im Bereich der Reaktionen von Organometallkomplexen wurde die photochemische Reaktivität von Chrom(0)-, Molybdän(0) und Wolfram(0)-Carbonylkomplexen mit einem bidentaten Pyridyl-mesoionischen Carben-Liganden des 1,2,3-Triazol-5-yliden-Typs und vier Carbonyl (CO)-Liganden untersucht. Die Komplexe wurden von Tobias Bens aus der Arbeitsgruppe von Prof. Dr. Biprajit Sarkar an der Universität Stuttgart synthetisiert. Es wurde zeitaufgelöste FTIR-Spektroskopie (wiederholte, statische Messungen; Rapid-scan-Methode) für die Charakterisierung der Produkte, Intermediate und der Kinetik der Reaktionen angewandt. Diese Komplexe zeigen in den Lösungsmitteln CH_3CN und Pyridin eine photochemisch induzierte Abspaltung eines CO-Liganden, welche interessanterweise im Dunkeln nach der Bestrahlung reversibel ist. Von der photochemischen Reaktion wurde in beiden Lösungsmitteln die Quantenausbeute bestimmt und die dunkle Rückreaktion kinetisch untersucht. Für die Reaktionen des Chrom-Komplexes wurde im Vergleich mit den Molybdän- und Wolframsystemen die höchste Reaktivität festgestellt (je nach Bedingungen Quantenausbeuten von bis zu 46 %). Als

Photoprodukt wurde im Vergleich mit quantenchemischen Rechnungen die Substitution eines axialen Carbonyl-Liganden durch ein Lösungsmittelmolekül zugeordnet. Die Rückreaktion läuft zunächst nach einer Kinetik erster Ordnung ab und ist für den Chrom-Komplex am schnellsten. Dabei ist die Geschwindigkeitskonstante auch abhängig vom Lösungsmittel, wobei die Reaktion in Pyridin aufgrund der stärkeren π -Rückbindung des Pyridins an das Metall im Photoprodukt langsamer abläuft. Die Zeitskala der Rückreaktion liegt damit zwischen einigen Minuten für den Chrom-Komplex in CH_3CN und mehreren Stunden für den Molybdän- und Wolfram-Komplex in Pyridin. Auch das freie Kohlenstoffmonoxid, welches durch die Abspaltung des CO-Liganden entsteht, konnte in der Reaktionslösung nachgewiesen werden. In fester Phase (KBr-Pressling) ist ebenfalls eine Reaktion zu beobachten. Dabei entstand ein bei tiefen Temperaturen stabiles Intermediat mit einer vakanten Koordinationsstelle in axialer Position. In fester Phase in gefrorenem Valeronitril konnten das Intermediat und das Produkt mit der Substitution des axialen CO-Liganden gegen ein Lösungsmittelmolekül in den FTIR-Spektren nachgewiesen werden. Somit konnte ein Reaktionsmechanismus ohne Umlagerung oder Reorganisation der an der Reaktion nicht beteiligten Liganden bestätigt werden. Weitere Untersuchungen und erweiterte quantenchemische Berechnungen insbesondere im Hinblick auf die genaue Aufklärung des Reaktionsmechanismus, einschließlich der energetischen Barrieren, sollen folgen, um die reversible Reaktion besser zu verstehen. Auf Basis dieser Untersuchungen könnten solche reversiblen photochemischen Reaktionen an Organometallkomplexen gezielt beispielsweise in der Synthese genutzt werden. Analoge Systeme mit einem Isomer des Pyridyl-mesoionischen Carben-Liganden wurden bereits in der Arbeitsgruppe Sarkar synthetisiert und sollen in Folgeprojekten mittels Lumineszenzspektroskopie und zeitaufgelöster FTIR-Spektroskopie auf vergleichbare Effekte und Reaktivitäten hin untersucht werden.

Im Rahmen dieser Arbeit wurden Organometallkomplexe aus dem Bereich der Leuchtstoffe sowie der Katalysatoren und Photosensibilisatoren mittels zeitaufgelöster Lumineszenz- und FTIR-Spektroskopie charakterisiert und Reaktionen der Komplexe mittels zeitaufgelöster FTIR-Spektroskopie verfolgt. Die erlangten Erkenntnisse über den Einfluss verschiedener Ligandmodifikationen, Halogenide oder Metallzentren auf die gewünschten Eigenschaften der Organometallkomplexe tragen zu der Entwicklung verbesserter Systeme bei, was eine Motivation zur Untersuchung verwandter Systeme mit den vorgestellten experimentellen und theoretischen Methoden darstellt. Langfristig sollen so Systeme entwickelt werden, die komplett ohne Metallzentren die gewünschten lumineszenten oder katalytischen Eigenschaften aufweisen und dabei Energie effizient nutzen.

Kapitel 7: Summary and Outlook

This work dealt on the one hand with the investigation of the photophysical properties of organometallic complexes by multispectroscopic methods and on the other hand with the tracking of reactions involving organometallic complexes by time-resolved FTIR spectroscopy. The investigated complexes are transition metal complexes that show interesting properties with regard to the development of OLEDs or catalysts or photosensitizers. In particular, the luminescent properties are important for the application as OLEDs and the lifetime and geometry in the excited state for catalysts and photosensitizers. The complexes do not contain rare earth elements to achieve these properties, but more abundant metals such as copper. By following reactions, an important understanding of the reactivity of different organometallic complexes is obtained.

To investigate these properties, a combination of (time-resolved) luminescence and Fourier transform infrared spectroscopy was performed. Luminescence spectroscopy was applied to study the luminescence properties, as well as the luminescent states, whereby the lifetime of these excited states are obtained by time-resolved luminescence spectroscopy. FTIR spectroscopy, in particular the time-resolved step-scan method, in combination with quantum chemical calculations was required for the structural determination of excited states. In order to also be able to characterise the temperature-dependent behaviour of the excited states, the measurements were carried out in a temperature range of 5-290 K. The second major chapter of this thesis deals with the tracking of reactions of organometallic complexes by time-resolved FTIR spectroscopy. The technique of repeated static measurements and the rapid-scan method were used.

7.1 Photophysics of luminescent copper complexes

The first part of this thesis deals with the characterisation of the luminescence and the luminescent states of dinuclear copper and silver complexes, which were synthesised by Dr. Jasmin Busch in the group of Prof. Dr. Stefan Bräse at KIT. A quartet of complexes containing a Cu_2Br_2 , Cu_2Cl_2 , Ag_2Br_2 or Ag_2Cl_2 centre, each with one bridging and two terminal 2-(diphenylphosphino)pyridine ligands, was investigated and the influence of cooperativity on the luminescence was determined. The complexes emit light in the visible range between about 480 and 580 nm, with the copper complexes showing emission at lower energy. Interestingly, the silver complexes emit only very weakly at room temperature, while the copper complexes show intense emission. Temperature-dependent luminescence measurements show TADF-typical behaviour for the copper complexes at room temperature and phosphorescence at low temperature with a red shift of the emission band position and

a clear increase of the lifetimes. The halides hardly influence the luminescence behaviour. In contrast, the temperature-dependent behaviour of the silver complexes shows clear differences to that of the copper complexes. The emission band position is almost independent of temperature, but the intensity increases strongly towards low temperatures. Thus, the silver complexes show no TADF behaviour, but a significant suppression of non-radiative deactivation channels at low temperature. From the step-scan FTIR investigations in comparison with quantum chemical calculations (performed by Florian Rehak from the group of Prof. Dr. Willem Klopper, KIT), the triplet states were structurally characterised. This investigation resulted in the assignment of the silver complexes to an energetically higher ligand-centred triplet state, in which the complexes could be kinetically trapped and thus cannot reach the TADF-capable lower M/XLCT triplet state. The TADF-capable M/XLCT triplet states were found as energetically lowest excited states for the copper complexes and were assigned to the experiment. Since these states also exist in the silver complexes according to DFT calculations, but these are not occupied in the present complexes, the synthesis of a TADF-capable silver complex seems possible on the basis of these results.

Related to the previously described project are the investigation of the luminescence properties and the luminescent states in different media (KBr compact, powder, partly crystals) of the tetranuclear copper complexes with the halides iodide, bromide and chloride and two bridging 2-(diphenylphosphino)pyridine ligands or their derivatives 4-methyl-2-(diphenylphosphino)pyridine and 1-(diphenylphosphino)isoquinoline. These complexes were also provided by Dr. Jasmin Busch from the group of Prof. Dr. Stefan Bräse at KIT and were investigated to examine an eventual thermochromic behaviour on the basis of related thermochromic tetranuclear complexes with 6-methyl-2-(diphenylphosphino)pyridine ligands^[53]. The temperature-dependent luminescence behaviour showed no thermochromic effects for the complex series with the 4-methyl-2-(diphenylphosphino)pyridine ligands with an obvious contribution of two different triplet states. In contrast, these complexes, except for the iodide complex in a KBr pellet, showed a slight red shift to low temperatures, although the temperature profile of the luminescence lifetimes, which are all in the phosphorescence range ($\geq 5 \mu\text{s}$), refutes a TADF mechanism. The red shift may be explained by a destabilisation of the ground state or a stabilisation of the luminescent triplet state at low temperature. The emission band of the iodide complex in the KBr matrix shifts to higher energy at lower temperatures, which is explained by a more pronounced rigidochromic effect in the KBr pellet in contrast to the powder samples. The bromide and chloride complexes without a methyl substituent on the ligand (2-(diphenylphosphino)pyridine ligand) show a comparable temperature-dependent luminescence behaviour as the analogous 4-methyl complexes. In

contrast, a thermochromic behaviour was observed for the iodide complex without methyl group. The thermochromic behaviour with two separate emission bands was better resolved in the neat powder sample than in the KBr pellet. With step-scan FTIR spectroscopy, two different triplet states could be assigned for the iodide complex without methyl group at the ligand at 20 K and 290 K, which confirms the observed thermochromism. In addition, investigations were performed on a complex with an extended π -system of the ligand by replacing the pyridine moiety with an isoquinoline moiety. This system differs significantly in its luminescence behaviour from the complexes with pyridine ring and shows signs of a TADF mechanism.

Interesting temperature-dependent luminescence behaviour was also found for various binuclear copper and mononuclear zinc complexes from Prof. Dr. Peter Roesky's research group at KIT. These show approximately a temperature-dependent TADF mechanism, which, however, does not show delayed fluorescence at higher temperature (from 150 K), but efficient luminescence quenching. For the $[\text{Cu}_2\{\text{DippPIA}\}_2]$ complex (DippPIA = *P,P*-diphenyl-*N,N'*-bis(2,6-diisopropylphenyl)phosphinimidic amine), step-scan FTIR spectroscopy was used to characterise the excited state from 20 to 150 K for comparison with the luminescence data. The experimentally investigated excited state of the copper complex was assigned, with the help of quantum chemical calculations at the DFT level, to a ligand-centred triplet state on the basis of characteristic bands. The lifetimes of the excited state from the step-scan data at 20 and 70 K confirm the luminescence lifetimes measured at KIT. The long lifetime from the step-scan data at 150 K, where no clear luminescence was detected, leads to the assumption that a triplet state is still occupied at higher temperatures, however, it is efficiently deactivated via non-radiating channels.

7.2 Photophysics and energy transfer of copper photosensitizers

Copper complexes are not only relevant because of their potential application in OLEDs, they are also being developed for use as new efficient photosensitizers. For this purpose, a copper complex was synthesised in the working group of Prof. Dr. Stefanie Tschierlei and Dr. Michael Karnahl at the TU Braunschweig, which contains the xantphos ligand and the biipo ligand (biipo = 16H-benzo[4',5']-isoquinolino-[2',1':1,2]-imidazo-[4,5-f]-[1,10]-phenanthroline-16-one) extended by two methyl groups in the 2- and 9-positions at the phenanthroline unit. Compared to the copper complex with the non-methylated biipo ligand, a tenfold increase in the lifetime of the excited state is obtained and thus a better potential suitability as a photosensitizer. The investigation of singlet oxygen formation and energy transfer by photon upconversion on anthracene were also successful and show the suitability of the complex as a photosensitizer, which is striking for a complex without rare metals. In the step-scan FTIR

measurements, a very long-lived dark excited state was observed in contrast to the luminescence data and assigned to a dark triplet state centred on the methylated biipo ligand, in comparison with quantum chemical calculations. With the combination of large organic chromophore and metal atom, a long-lived, catalytically active state could be populated by efficient intersystem crossing. Based on these results, further systems without rare and expensive metals can be developed and investigated as efficient photocatalysts.

7.3 Thermal-induced reactions of a copper complex

This part deals with the elucidation of the reaction mechanism of the dinuclear copper dimethylglyoxime (dmg) complex $[\text{Cu}_2(\text{H}_2(\text{dmg})(\text{Hdmg})(\text{dmg}))^+]$ with the solvents acetonitrile (CH_3CN) and ethanol (EtOH). The reaction in CH_3CN was followed with static FTIR measurements repeated at fixed time intervals over 8 h. Reference spectra of conceivable products were also recorded. The mononuclear reference complex $[\text{Cu}(\text{Hdmg})_2]$ shows no reactivity in the solvents mentioned above, whereas the dinuclear complex clearly shows a reactivity, which indicates a cooperative effect between the copper centres. Depending on the reaction partner, EtOH or CH_3CN , the dinuclear complex is reduced or oxidised. The reduction in ethanol could not be followed with FTIR spectroscopy, because the required excess of EtOH with a sufficiently high complex concentration could not be achieved due to its poor solubility in ethanol. Instead, the gas mixture above the reaction solution of the complex in EtOH was trapped and dissolved in deuterated acetonitrile (CD_3CN), wherewith the oxidation product of ethanol, acetaldehyde, was detected by FTIR spectroscopy.

The reaction in CD_3CN could be easily followed by FTIR spectroscopy with clear changes already within the first minutes of the reaction. In the product spectrum after 8 h, the hydrolysed ligand and other products could be detected as 2,3-butanedione monoxime, the copper compound $[\text{Cu}(\text{CH}_3\text{CN})_4]^+$ and uncoordinated H_2dmg according to reference measurements. The postulated reaction mechanism proposed by DFT calculations involves as a first step the nucleophilic attack of H_2O on the dinuclear complex, which subsequently hydrolyses the attacked ligand to 2,3-butanedione monoxime. In order to confirm this mechanism with experimental results, the reaction in CD_3CN with the addition of ^{18}O -isotoped water was again monitored by FTIR spectroscopy. A red shift of the C-O stretching vibration assigned to the monoxime was observed. This result clearly confirms the involvement of water in the reaction mechanism. Since the intermediate of the reaction with hydroxylamine bound to the complex could not be detected by FTIR spectroscopy in the reaction solution, presumably due to a rapid oxidation to N_2O , the product N_2O in CD_3CN was investigated. For this purpose, N_2O gas was passed through pure CD_3CN and the recorded reference spectrum

was compared to that of the product mixture. Thus, the formation of N_2O during the reaction in CD_3CN could be confirmed, which also corroborates the postulated mechanism.

7.4 Photochemical reactivity of Cr(0)-, Mo(0)-, W(0)-carbonyl complexes

In the second project in the field of reactions of organometallic complexes in this thesis, the photochemical reactivity of chromium(0), molybdenum(0) and tungsten(0) carbonyl complexes containing a bidentate pyridyl-mesoionic carbene ligand of 1,2,3-triazol-5-ylidene type and four carbonyl (CO) ligands was investigated. The complexes were synthesised by Tobias Bens from the group of Prof. Dr. Sarkar at the University of Stuttgart. Time-resolved FTIR spectroscopy (repeated, static measurements; rapid-scan method) was applied for the characterisation of the products and intermediates and analysis of the kinetics of the reactions. These complexes show photochemically induced cleavage of a CO ligand in the solvents CH_3CN and pyridine, which interestingly is reversible in the dark after irradiation. The quantum yield of the photochemical reaction was determined in both solvents and the dark reverse reaction was kinetically investigated. For the reactions of the chromium complex, the highest reactivity (depending of the conditions, quantum yields of up to 46 %) was found in comparison with the molybdenum and tungsten systems. The substitution of an axial carbonyl ligand by a solvent molecule was assigned as the photoproduct in comparison with quantum chemical calculations. The reverse reaction initially proceeds according to first-order kinetics and is fastest for the chromium complex. Here, the rate constant is also dependent on the solvent, with the reaction proceeding more slowly in pyridine due to the stronger π -backbonding of the pyridine to the metal centre in the corresponding photoproduct. The time scale of the reverse reaction thus ranges from a few minutes for the chromium complex in CH_3CN to several hours for the molybdenum and tungsten complexes in pyridine. The free carbon monoxide, which is formed by the cleavage of the CO ligand, could be detected in the reaction solution. A reaction can also be observed in the solid phase in the KBr pellet. A stable intermediate with a vacant coordination site in the axial position was observed at low temperature. In solid phase in frozen valeronitrile, the intermediate and the product with the substitution of the axial CO ligand against a solvent molecule could be observed in the FTIR spectra. Thus, a reaction mechanism without rearrangement or reorganisation of the ligand sphere could be confirmed. Further investigations and extended quantum chemical calculations, especially with regard to the exact elucidation of the reaction mechanism, including the energetic barriers, should follow in order to a better understanding of the reversible reaction. Based on these investigations, such regioselective and reversible photochemical reactions on organometallic complexes could be used, for example, in synthesis. Analogue systems with an isomer of the pyridyl-mesoionic carbene ligand have

already been synthesised in the Sarkar group and are to be investigated in follow-up projects using luminescence spectroscopy and time-resolved FTIR spectroscopy for comparable effects and reactivities.

In this work, organometallic complexes from the field of luminophors as well as catalysts and photosensitizers were characterised by time-resolved luminescence and FTIR spectroscopy and reactions of the complexes were followed by time-resolved FTIR spectroscopy. The obtained knowledge about the influence of different ligand modifications, halides or metal centres on the desired properties of the organometallic complexes contributes to the development of improved systems, which motivates further investigations with the presented methods on related systems. In the long term, the aim is to develop systems that exhibit the desired luminescent or catalytic properties completely without metal centres, while making efficient use of energy.

Kapitel 8: Literaturverzeichnis

- [1] K. E. Dalle, J. Warnan, J. J. Leung, B. Reuillard, I. S. Karmel, E. Reisner, *Chemical reviews* **2019**, *119*, 2752–2875.
- [2] S.-P. Luo, E. Mejía, A. Friedrich, A. Pazidis, H. Junge, A.-E. Surkus, R. Jackstell, S. Denurra, S. Gladiali, S. Lochbrunner, M. Beller, *Angew. Chem.* **2013**, *125*, 437–441.
- [3] R. Giereth, I. Reim, W. Frey, H. Junge, S. Tschierlei, M. Karnahl, *Sustainable Energy Fuels* **2019**, *3*, 692–700.
- [4] K. Heinze, C. Förster, P. Vöhringer, B. Sarkar, *Nachr. Chem.* **2019**, *67*, 54–59.
- [5] J. G. de Vries, S. D. Jackson, *Catal. Sci. Technol.* **2012**, *2*, 2009.
- [6] P. Linares, X. Labandeira, *Journal of Economic Surveys* **2010**.
- [7] D. Volz, *J. Photon. Energy* **2016**, *6*, 20901.
- [8] K. Tanaka, *Energy Policy* **2011**, *39*, 6532–6550.
- [9] M. Hack, M. S. Weaver, J. J. Brown, L.-H. Chang, C.-K. Wu, Y.-H. Lin, *SID Symposium Digest* **2010**, *41*, 894.
- [10] Deutsche Bunsen-Gesellschaft für Physikalische Chemie (Hrsg.), **2008**.
- [11] M. Karnahl, *Bunsenmagazin* **2015**, *17*, 232–238.
- [12] D. F. Fernández, J. L. Mascareñas, F. López, *Chemical Society reviews* **2020**, *49*, 7378–7405.
- [13] Ł. Woźniak, J.-F. Tan, Q.-H. Nguyen, A. Du Madron Vigné, V. Smal, Y.-X. Cao, N. Cramer, *Chemical reviews* **2020**, *120*, 10516–10543.
- [14] S. Chu, A. Majumdar, *Nature* **2012**, *488*, 294–303.
- [15] M. S. Lazorski, F. N. Castellano, *Polyhedron* **2014**, *82*, 57–70.
- [16] Y. Liu, S.-C. Yiu, C.-L. Ho, W.-Y. Wong, *Coordination Chemistry Reviews* **2018**, *375*, 514–557.
- [17] J. K. McCusker, *Science (New York, N.Y.)* **2019**, *363*, 484–488.
- [18] S. Neumann, O. S. Wenger, C. Kerzig, *Chemistry (Weinheim an der Bergstrasse, Germany)* **2021**, *27*, 4115–4123.
- [19] M. Ruthkosky, C. A. Kelly, F. N. Castellano, G. J. Meyer, *Coordination Chemistry Reviews* **1998**, *171*, 309–322.
- [20] H. Yersin, R. Czerwieńiec, M. Z. Shafikov, A. F. Suleymanova, *Chemphyschem : a European journal of chemical physics and physical chemistry* **2017**, *18*, 3508–3535.
- [21] C. Förster, K. Heinze, *Chemical Society reviews* **2020**, *49*, 1057–1070.
- [22] L. P. Ravaro, K. P. Zaroni, A. S. de Camargo, *Energy Reports* **2020**, *6*, 37–45.
- [23] Y. Ma, C.-M. Che, H.-Y. Chao, X. Zhou, W.-H. Chan, J. Shen, *Adv. Mater.* **1999**, *11*, 852–857.

- [24] G. Hong, X. Gan, C. Leonhardt, Z. Zhang, J. Seibert, J. M. Busch, S. Bräse, *Adv. Mater.* **2021**, *33*, e2005630.
- [25] C. Bizzarri, E. Spuling, D. M. Knoll, D. Volz, S. Bräse, *Coordination Chemistry Reviews* **2018**, *373*, 49–82.
- [26] J. M. Busch, D. S. Koshelev, A. A. Vashchenko, O. Fuhr, M. Nieger, V. V. Utochnikova, S. Bräse, *Inorg. Chem.* **2021**, *60*, 2315–2332.
- [27] A. Hossain, A. Bhattacharyya, O. Reiser, *Science (New York, N.Y.)* **2019**, *364*.
- [28] R. Malmberg, T. von Arx, M. Hasan, O. Blacque, A. Shukla, S. K. M. McGregor, S.-C. Lo, E. B. Namdas, K. Venkatesan, *Chemistry (Weinheim an der Bergstrasse, Germany)* **2021**, *27*, 7265–7274.
- [29] I. Omae, *Coordination Chemistry Reviews* **2016**, *310*, 154–169.
- [30] S. Perruchas, C. Tard, X. F. Le Goff, A. Fargues, A. Garcia, S. Kahlal, J.-Y. Saillard, T. Gacoin, J.-P. Boilot, *Inorg. Chem.* **2011**, *50*, 10682–10692.
- [31] Y. Zhang, M. Schulz, M. Wächtler, M. Karnahl, B. Dietzek, *Coordination Chemistry Reviews* **2018**, *356*, 127–146.
- [32] M. Pujadas, L. Rodríguez, *Coordination Chemistry Reviews* **2020**, *408*, 213179.
- [33] S. Witzel, A. S. K. Hashmi, J. Xie, *Chemical reviews* **2021**, *121*, 8868–8925.
- [34] M. Chaaban, C. Zhou, H. Lin, B. Chyi, B. Ma, *J. Mater. Chem. C* **2019**, *7*, 5910–5924.
- [35] H. Cheng, T.-L. Lam, Y. Liu, Z. Tang, C.-M. Che, *Angewandte Chemie International Edition in English* **2021**, *60*, 1383–1389.
- [36] E. V. Puttock, M. T. Walden, J. G. Williams, *Coordination Chemistry Reviews* **2018**, *367*, 127–162.
- [37] S. DiLuzio, V. Mdluli, T. U. Connell, J. Lewis, V. VanBenschoten, S. Bernhard, *Journal of the American Chemical Society* **2021**, *143*, 1179–1194.
- [38] E. A. Medlycott, G. S. Hanan, *Chemical Society reviews* **2005**, *34*, 133–142.
- [39] L. A. Büldt, O. S. Wenger, *Angewandte Chemie International Edition in English* **2017**, *56*, 5676–5682.
- [40] B. M. Hockin, C. Li, N. Robertson, E. Zysman-Colman, *Catal. Sci. Technol.* **2019**, *9*, 889–915.
- [41] O. S. Wenger, *Journal of the American Chemical Society* **2018**, *140*, 13522–13533.
- [42] H. Yersin, A. F. Rausch, R. Czerwieniec, T. Hofbeck, T. Fischer, *Coordination Chemistry Reviews* **2011**, *255*, 2622–2652.
- [43] K. P. S. Cheung, S. Sarkar, V. Gevorgyan, *Chemical reviews* **2022**, *122*, 1543–1625.
- [44] M. H. Prosenč, M. M. Kappes, G. Niedner-Schatteburg, *Chemistry (Weinheim an der Bergstrasse, Germany)* **2021**, *27*, 15018–15019.

- [45] T. Wall, M. Leist, F. Dietrich, W. R. Thiel, M. Gerhards, *ChemPlusChem* **2021**, *86*, 622–628.
- [46] M. Grupe, P. Boden, P. Di Martino-Fumo, X. Gui, C. Bruschi, R. Israil, M. Schmitt, M. Nieger, M. Gerhards, W. Klopper, C. Riehn, C. Bizzarri, R. Diller, *Chemistry (Weinheim an der Bergstrasse, Germany)* **2021**, *27*, 15251–15270.
- [47] M. Zimmer, F. Dietrich, D. Volz, S. Bräse, M. Gerhards, *Chemphyschem : a European journal of chemical physics and physical chemistry* **2017**, *18*, 3023–3029.
- [48] R. Maity, B. S. Birenheide, F. Breher, B. Sarkar, *ChemCatChem* **2021**, *13*, 2337–2370.
- [49] G. Niedner-Schatteburg, M. M. Kappes, *Chemistry (Weinheim an der Bergstrasse, Germany)* **2021**, *27*, 15027–15042.
- [50] K. Heinze, *Bunsenmagazin* **2021**, *23*, 305.
- [51] J. M. Busch, D. M. Zink, P. Di Martino-Fumo, F. R. Rehak, P. Boden, S. Steiger, O. Fuhr, M. Nieger, W. Klopper, M. Gerhards, S. Bräse, *Dalton transactions (Cambridge, England : 2003)* **2019**, *48*, 15687–15698.
- [52] M. A. Argüello Cordero, P. J. Boden, M. Rentschler, P. Di Martino-Fumo, W. Frey, Y. Yang, M. Gerhards, M. Karnahl, S. Lochbrunner, S. Tschierlei, *Inorg. Chem.* **2022**, *61*, 214–226.
- [53] P. Boden, P. Di Martino-Fumo, J. M. Busch, F. R. Rehak, S. Steiger, O. Fuhr, M. Nieger, D. Volz, W. Klopper, S. Bräse, M. Gerhards, *Chemistry (Weinheim an der Bergstrasse, Germany)* **2021**, *27*, 5439–5452.
- [54] T. Bens, P. Boden, P. Di Martino-Fumo, J. Beerhues, U. Albold, S. Sobottka, N. I. Neuman, M. Gerhards, B. Sarkar, *Inorg. Chem.* **2020**, *59*, 15504–15513.
- [55] M. Dahlen, E. H. Hollesen, M. Kehry, M. T. Gamer, S. Lebedkin, D. Schooss, M. M. Kappes, W. Klopper, P. W. Roesky, *Angewandte Chemie International Edition in English* **2021**, *60*, 23365–23372.
- [56] K. M. Omberg, J. R. Schoonover, T. J. Meyer, *J. Phys. Chem. A* **1997**, *101*, 9531–9536.
- [57] J. R. Schoonover, G. F. Strouse, *Chemical reviews* **1998**, *98*, 1335–1356.
- [58] M. George, *Coordination Chemistry Reviews* **1998**, *177*, 201–217.
- [59] J. M. Butler, M. W. George, J. R. Schoonover, D. M. Dattelbaum, T. J. Meyer, *Coordination Chemistry Reviews* **2007**, *251*, 492–514.
- [60] D. Volz, M. Wallesch, S. L. Grage, J. Göttlicher, R. Steininger, D. Batchelor, T. Vitova, A. S. Ulrich, C. Heske, L. Weinhardt, T. Baumann, S. Bräse, *Inorg. Chem.* **2014**, *53*, 7837–7847.
- [61] R.-P. Xu, Y.-Q. Li, J.-X. Tang, *J. Mater. Chem. C* **2016**, *4*, 9116–9142.
- [62] S. Y. Lee, T. Yasuda, H. Komiyama, J. Lee, C. Adachi, *Advanced materials (Deerfield Beach, Fla.)* **2016**, *28*, 4019–4024.
- [63] M. Wallesch, A. Verma, C. Fléchon, H. Flügge, D. M. Zink, S. M. Seifermann, J. M. Navarro, T. Vitova, J. Göttlicher, R. Steininger, L. Weinhardt, M. Zimmer, M. Gerhards, C. Heske, S.

- Bräse, T. Baumann, D. Volz, *Chemistry (Weinheim an der Bergstrasse, Germany)* **2016**, *22*, 16400–16405.
- [64] T. Hofbeck, U. Monkowius, H. Yersin, *Journal of the American Chemical Society* **2015**, *137*, 399–404.
- [65] D. Volz, D. M. Zink, T. Bocksrocker, J. Friedrichs, M. Nieger, T. Baumann, U. Lemmer, S. Bräse, *Chem. Mater.* **2013**, *25*, 3414–3426.
- [66] D. M. Zink, M. Bächle, T. Baumann, M. Nieger, M. Kühn, C. Wang, W. Klopper, U. Monkowius, T. Hofbeck, H. Yersin, S. Bräse, *Inorganic chemistry* **2013**, *52*, 2292–2305.
- [67] D. M. Zink, D. Volz, T. Baumann, M. Mydlak, H. Flügge, J. Friedrichs, M. Nieger, S. Bräse, *Chem. Mater.* **2013**, *25*, 4471–4486.
- [68] J. Troyano, F. Zamora, S. Delgado, *Chemical Society reviews* **2021**, *50*, 4606–4628.
- [69] A. Y. Baranov, A. S. Berezin, D. G. Samsonenko, A. S. Mazur, P. M. Tolstoy, V. F. Plyusnin, I. E. Kolesnikov, A. V. Artem'ev, *Dalton transactions (Cambridge, England : 2003)* **2020**, *49*, 3155–3163.
- [70] D. Volz, Y. Chen, M. Wallesch, R. Liu, C. Fléchon, D. M. Zink, J. Friedrichs, H. Flügge, R. Steininger, J. Göttlicher, C. Heske, L. Weinhardt, S. Bräse, F. So, T. Baumann, *Advanced materials (Deerfield Beach, Fla.)* **2015**, *27*, 2538–2543.
- [71] K. Tsuge, Y. Chishina, H. Hashiguchi, Y. Sasaki, M. Kato, S. Ishizaka, N. Kitamura, *Coordination Chemistry Reviews* **2016**, *306*, 636–651.
- [72] R. Czerwieniec, M. J. Leidl, H. H. Homeier, H. Yersin, *Coordination Chemistry Reviews* **2016**, *325*, 2–28.
- [73] F. Bäßler, M. Zimmer, F. Dietrich, M. Grupe, M. Wallesch, D. Volz, S. Bräse, M. Gerhards, R. Diller, *Physical chemistry chemical physics : PCCP* **2017**, *19*, 29438–29448.
- [74] X.-L. Chen, R. Yu, X.-Y. Wu, D. Liang, J.-H. Jia, C.-Z. Lu, *Chemical communications (Cambridge, England)* **2016**, *52*, 6288–6291.
- [75] K. Chen, J. Shearer, V. J. Catalano, *Inorganic chemistry* **2015**, *54*, 6245–6256.
- [76] A. Lapprand, M. Dutartre, N. Khiri, E. Levert, D. Fortin, Y. Rousselin, A. Soldera, S. Jugé, P. D. Harvey, *Inorg. Chem.* **2013**, *52*, 7958–7967.
- [77] D. M. Zink, T. Grab, T. Baumann, M. Nieger, E. C. Barnes, W. Klopper, S. Bräse, *Organometallics* **2011**, *30*, 3275–3283.
- [78] W.-H. Chan, Z.-Z. Zhang, T. C. Mak, C.-M. Che, *Journal of Organometallic Chemistry* **1998**, *556*, 169–172.
- [79] Z. Liu, P. I. Djurovich, M. T. Whited, M. E. Thompson, *Inorganic chemistry* **2012**, *51*, 230–236.
- [80] E. I. Musina, A. V. Shamsieva, I. D. Strel'nik, T. P. Gerasimova, D. B. Krivolapov, I. E. Kolesnikov, E. V. Grachova, S. P. Tunik, C. Bannwarth, S. Grimme, S. A. Katsyuba, A. A.

- Karasik, O. G. Sinyashin, *Dalton transactions (Cambridge, England : 2003)* **2016**, *45*, 2250–2260.
- [81] Y.-D. Yu, L.-B. Meng, Q.-C. Chen, G.-H. Chen, X.-C. Huang, *New J. Chem.* **2018**, *42*, 8426–8437.
- [82] A. V. Shamsieva, I. E. Kolesnikov, I. D. Strel'nik, T. P. Gerasimova, A. A. Kalinichev, S. A. Katsyuba, E. I. Musina, E. Lähderanta, A. A. Karasik, O. G. Sinyashin, *J. Phys. Chem. C* **2019**, *123*, 25863–25870.
- [83] T. J. Feuerstein, B. Goswami, P. Rauthe, R. Köppe, S. Lebedkin, M. M. Kappes, P. W. Roesky, *Chemical science* **2019**, *10*, 4742–4749.
- [84] B. Sarkar, P. Vöhringer, K. Heinze, C. Förster, *Nachr. Chem.* **2019**, *67*, 67–71.
- [85] P. A. Forero Cortés, M. Marx, M. Trose, M. Beller, *Chem Catalysis* **2021**, *1*, 298–338.
- [86] M. Rentschler, P. J. Boden, M. A. Argüello Cordero, S. T. Steiger, M.-A. Schmid, Y. Yang, G. Niedner-Schatteburg, M. Karnahl, S. Lochbrunner, S. Tschierlei, *Inorganic chemistry* **2022**, *61*, 12249–12261.
- [87] N. P. E. Barry, P. J. Sadler, *Pure and Applied Chemistry* **2014**, *86*, 1897–1910.
- [88] W. von Philipsborn, *Chem. Soc. Rev.* **1999**, *28*, 95–105.
- [89] N. Sträter, W. N. Lipscomb, T. Klabunde, B. Krebs, *Angewandte Chemie International Edition in English* **1996**, *35*, 2024–2055.
- [90] B. Bosnich, *Inorg. Chem.* **1999**, *38*, 2554–2562.
- [91] P. Buchwalter, J. Rosé, P. Braunstein, *Chemical reviews* **2015**, *115*, 28–126.
- [92] L. Tebben, C. Mück-Lichtenfeld, G. Fernández, S. Grimme, A. Studer, *Chemistry (Weinheim an der Bergstrasse, Germany)* **2017**, *23*, 5864–5873.
- [93] R. I. Petrikat, S. T. Steiger, E. Barani, P. J. Boden, M. E. Huber, M. R. Ringenberg, G. Niedner-Schatteburg, K. Fink, S. Becker, *Chemistry (Weinheim an der Bergstrasse, Germany)* **2023**, e202203438.
- [94] M. Wrighton, *Chem. Rev.* **1974**, *74*, 401–430.
- [95] R. W. Balk, T. Snoeck, D. J. Stufkens, A. Oskam, *Inorg. Chem.* **1980**, *19*, 3015–3021.
- [96] D. M. Manuta, A. J. Lees, *Inorg. Chem.* **1986**, *25*, 1354–1359.
- [97] A. Vlček Jr., *Coordination Chemistry Reviews* **2002**, *230*, 225–242.
- [98] G. R. Dobson, M. F. A. El Sayed, I. W. Stolz, R. K. Sheline, *Inorg. Chem.* **1962**, *1*, 526–530.
- [99] A. Vlček Jr., I. R. Farrell, D. J. Liard, P. Matousek, M. Towrie, A. W. Parker, D. C. Grills, M. W. George, *J. Chem. Soc., Dalton Trans.* **2002**, 701–712.
- [100] P. Boden, P. Di Martino-Fumo, T. Bens, S. Steiger, U. Albold, G. Niedner-Schatteburg, M. Gerhards, B. Sarkar, *Chemistry (Weinheim an der Bergstrasse, Germany)* **2021**, *27*, 12959–12964.

- [101] W. W. Parson, *Modern optical spectroscopy. With exercises and examples from biophysics and biochemistry*, Springer, Heidelberg, London, New York, N.Y., **2009**.
- [102] D. C. Harris, *Lehrbuch der Quantitativen Analyse*, Springer Berlin Heidelberg, **2014**.
- [103] Y. Song, Y. Cong, B. Wang, N. Zhang, *Expert opinion on drug delivery* **2020**, *17*, 551–571.
- [104] C. T. Pinheiro, R. Rendall, M. J. Quina, M. S. Reis, L. M. Gando-Ferreira, *Energy Fuels* **2017**, *31*, 179–187.
- [105] S. O. Fakayode, G. A. Baker, D. K. Bwambok, N. Bhawawet, B. Elzey, N. Siraj, S. Macchi, D. A. Pollard, R. L. Perez, A. V. Duncan, I. M. Warner, *Applied Spectroscopy Reviews* **2020**, *55*, 647–723.
- [106] H. Günzler, H.-U. Gremlich, *IR spectroscopy. An introduction*, Wiley-VCH, Weinheim, Cambridge, **2002**.
- [107] D. M. Dattelbaum, K. M. Omberg, P. J. Hay, N. L. Gebhart, R. L. Martin, J. R. Schoonover, T. J. Meyer, *J. Phys. Chem. A* **2004**, *108*, 3527–3536.
- [108] P. Linstrom, *NIST Chemistry WebBook, NIST Standard Reference Database 69* **1997**.
- [109] National Institute of Advanced Industrial Science and Technology (AIST), "Spectral Database for Organic Compounds SDBS", zu finden unter https://sdb.sdb.aist.go.jp/sdb/sdb/cgi-bin/cre_list.cgi.
- [110] P. M. Chu, F. R. Guenther, G. C. Rhoderick, W. J. Lafferty, *J. Res. Natl. Inst. Stand. Technol.* **1999**, *104*, 59.
- [111] M. Orio, D. A. Pantazis, F. Neese, *Photosynthesis research* **2009**, *102*, 443–453.
- [112] Porezag, Pederson, *Physical review. B, Condensed matter* **1996**, *54*, 7830–7836.
- [113] L. Glasser, *J. Chem. Educ.* **1987**, *64*, A260.
- [114] W. D. Perkins, *J. Chem. Educ.* **1987**, *64*, A269.
- [115] P. Chen, R. A. Palmer, *Appl. Spectrosc., AS* **1997**, *51*, 580–583.
- [116] T. J. Johnson, A. Simon, J. M. Weil, G. W. Harris, *Appl. Spectrosc., AS* **1993**, *47*, 1376–1381.
- [117] W. Mäntele, *Trends in Biochemical Sciences* **1993**, *18*, 197–202.
- [118] C. Kötting, J. Güldenhaupt, K. Gerwert, *Chemical Physics* **2012**, *396*, 72–83.
- [119] I. Radu, M. Schlegler, C. Bolwien, J. Heberle, *Photochemical & photobiological sciences : Official journal of the European Photochemistry Association and the European Society for Photobiology* **2009**, *8*, 1517–1528.
- [120] J. R. Lakowicz, *Principles of fluorescence spectroscopy (3rd ed)*, 3. Aufl., Springer, New York, Berlin, **2006**.
- [121] K. S. McCain, D. C. Hanley, J. M. Harris, *Analytical chemistry* **2003**, *75*, 4351–4359.
- [122] M. V. Gorbunova, S. V. Gutorova, D. A. Berseneva, V. V. Apyari, V. D. Zaitsev, S. G. Dmitrienko, Y. A. Zolotov, *Applied Spectroscopy Reviews* **2019**, *54*, 631–652.
- [123] S. S. Deshpande, *Critical reviews in food science and nutrition* **2001**, *41*, 155–224.

- [124] A. B. Aletti, D. M. Gillen, T. Gunnlaugsson, *Coordination Chemistry Reviews* **2018**, *354*, 98–120.
- [125] L. Prodi, *Coordination Chemistry Reviews* **2000**, *205*, 59–83.
- [126] X. Pei, Y. Pan, L. Zhang, Y. Lv, *Applied Spectroscopy Reviews* **2021**, *56*, 324–345.
- [127] X.-Y. Dong, Y. Si, J.-S. Yang, C. Zhang, Z. Han, P. Luo, Z.-Y. Wang, S.-Q. Zang, T. C. W. Mak, *Nature communications* **2020**, *11*, 3678.
- [128] J. C. Schlothauer, C. Peter, C. Hirschl, G. Oreski, B. Röder, *J Polym Res* **2017**, *24*.
- [129] Kenry, C. Chen, B. Liu, *Nature communications* **2019**, *10*, 2111.
- [130] M. Shimizu, T. Sakurai, *ChemPlusChem* **2021**, *86*, 446–459.
- [131] R. Mazzaro, A. Vomiero, *Adv. Energy Mater.* **2018**, *8*, 1801903.
- [132] W. Herres, J. Gronholz, *Understanding FT-IR Data Processing, part1-3* **1985**.
- [133] W. D. Perkins, *J. Chem. Educ.* **1986**, *63*, A5.
- [134] T. J. Johnson, G. Zachmann, *Introduction to Step-scan FTIR*.
- [135] P. W. Atkins, J. de Paula, *Kurzlehrbuch physikalische Chemie. Für natur- und ingenieurwissenschaftliche Studiengänge*, 5. Aufl., Wiley-VCH Verlag GmbH & Co. KGaA, Weinheim, **2020**.
- [136] F. J. Harris, *Proc. IEEE* **1978**, *66*, 51–83.
- [137] S. Egbert, C. Carpenter, *Journal of Applied Engineering Mathematics* **2017**.
- [138] R. S. Bretzlaff, T. B. Bahder, *Rev. Phys. Appl. (Paris)* **1986**, *21*, 833–844.
- [139] G. D. Smith, R. A. Palmer in *Handbook of vibrational spectroscopy* (Hrsg.: P. R. Griffiths, J. M. Chalmers), Wiley, Chichester, **2002**.
- [140] Bruker, "Step-Scan / Rapid-Scan. Akquisitionsrate", zu finden unter <https://www.bruker.com/de/products-and-solutions/infrared-and-raman/ft-ir-research-spectrometers/vertex-research-ft-ir-spectrometer/step-scan---rapid-scan-interleaved-trs.html>.
- [141] W. Uhmann, A. Becker, C. Taran, F. Siebert, *Appl. Spectrosc., AS* **1991**, *45*, 390–397.
- [142] M. Zimmer, *Dissertation*, Technische Universität Kaiserslautern, Kaiserslautern, **2017**.
- [143] H. Haken, H. C. Wolf, *Molekülphysik und Quantenchemie. Einführung in die experimentellen und theoretischen Grundlagen*, 4. Aufl., Springer, Berlin, **2003**.
- [144] J. M. Hollas, *Modern spectroscopy*, 4. Aufl., J. Wiley, New York, **2004**.
- [145] G. Wedler, H.-J. Freund, *Lehr- und Arbeitsbuch Physikalische Chemie*, 7. Aufl., Wiley-VCH Verlag GmbH & Co. KGaA, Weinheim, **2019**.
- [146] M. Kasha, *Discuss. Faraday Soc.* **1950**, *9*, 14.
- [147] I. V. Hertel, C.-P. Schulz, *Moleküle und Photonen - Spektroskopie und Streuphysik*, Springer, Berlin, **2010**.
- [148] C. A. Parker, *Photoluminescence of Solutions*, Elsevier Publishing Company, **1968**.

- [149] T. J. Penfold, E. Gindensperger, C. Daniel, C. M. Marian, *Chemical reviews* **2018**, *118*, 6975–7025.
- [150] T. Förster, *Angew. Chem. Int. Ed. Engl.* **1969**, *8*, 333–343.
- [151] Horiba Scientific, *Time-resolved fluorescence lifetime measurements, Time-Resolved Fluorescence Technical Note TRFT-1*.
- [152] Horiba Jobin Yvon, *A practical guide to time-resolved luminescence lifetime determination using dedicated Time-Correlated Single-Photon Counting systems*.
- [153] Horiba Scientific, *Time-resolved emission spectra / decay associated spectra, Time-Resolved Fluorescence Technical Note TRFT-4*.
- [154] J. B. Foresman, E. Frisch, *Exploring Chemistry with Electronic Structure Methods*, **1996**.
- [155] J. Reinhold, *Quantentheorie der Moleküle. Eine Einführung*, 4. Aufl., Springer Spektrum, Wiesbaden, **2013**.
- [156] N. H. March, *J. Phys. Chem.* **1982**, *86*, 2262–2267.
- [157] L. H. Thomas, *Math. Proc. Camb. Phil. Soc.* **1927**, *23*, 542–548.
- [158] E. Fermi, *Z. Physik* **1928**, *48*, 73–79.
- [159] P. Hohenberg, W. Kohn, *Phys. Rev.* **1964**, *136*, B864–B871.
- [160] W. Kohn, L. J. Sham, *Phys. Rev.* **1965**, *140*, A1133–A1138.
- [161] R. G. Parr, W. Yang, *Annual review of physical chemistry* **1995**, *46*, 701–728.
- [162] W. Kohn, A. D. Becke, R. G. Parr, *J. Phys. Chem.* **1996**, *100*, 12974–12980.
- [163] A. J. Cohen, P. Mori-Sánchez, W. Yang, *Chemical reviews* **2012**, *112*, 289–320.
- [164] Á. Nagy, *Physics Reports* **1998**, *298*, 1–79.
- [165] J. P. Perdew, M. Ernzerhof, K. Burke, *The Journal of chemical physics* **1996**, *105*, 9982–9985.
- [166] A. D. Becke, *The Journal of chemical physics* **1993**, *98*, 1372–1377.
- [167] P. J. Hasnip, K. Refson, M. I. J. Probert, J. R. Yates, S. J. Clark, C. J. Pickard, *Philosophical transactions. Series A, Mathematical, physical, and engineering sciences* **2014**, *372*, 20130270.
- [168] K. Burke, *The Journal of chemical physics* **2012**, *136*, 150901.
- [169] Bruker, *VERTEX 80 & 80v FT-IR Spectrometers Flyer*.
- [170] Bruker Optik GmbH, *VERTEX 80v, User Manual*.
- [171] P. J. Boden, *Dissertation*, Technische Universität Kaiserslautern, Kaiserslautern, **2022**.
- [172] PerkinElmer, *Lambda 800/900 - User's Guide*.
- [173] I. Harrick Scientific Products, *The Praying Mantis™. User's Manual*.
- [174] Horiba Jobin Yvon, *FluoroLog3. Operation Manual*.
- [175] Horiba Jobin Yvon, *FluoroMax-2 With DataMax for Windows Hardware, Operation Manual*.

- [176] Horiba Scientific, *DeltaFlex™. Modular Fluorescence Lifetime System, System guide*.
- [177] J. M. Busch, *Synthesevorschrift Vierkernige Cu-Komplexe*. unveröffentlichte Arbeit.
- [178] D. M. Manuta, A. J. Lees, *Inorg. Chem.* **1986**, *25*, 3212–3218.
- [179] W. Kaim, S. Kohlmann, S. Ernst, B. Olbrich-Deussner, C. Bessenbacher, A. Schulz, *Journal of Organometallic Chemistry* **1987**, *321*, 215–226.
- [180] A. J. Lees, *Comments on Inorganic Chemistry* **1995**, *17*, 319–346.
- [181] I. Roppolo, E. Celasco, M. Sangermano, A. Garcia, T. Gacoin, J.-P. Boilot, S. Perruchas, *J. Mater. Chem. C* **2013**, *1*, 5725.
- [182] D. Volz, D. M. Zink, T. Bocksrocker, J. Friedrichs, M. Nieger, T. Baumann, U. Lemmer, S. Bräse, *Chem. Mater.* **2013**, *25*, 3414–3426.
- [183] D. Volz, M. Nieger, J. Friedrichs, T. Baumann, S. Bräse, *Langmuir : the ACS journal of surfaces and colloids* **2013**, *29*, 3034–3044.
- [184] A. Makal, J. Benedict, E. Trzop, J. Sokolow, B. Fournier, Y. Chen, J. A. Kalinowski, T. Graber, R. Henning, P. Coppens, *J. Phys. Chem. A* **2012**, *116*, 3359–3365.
- [185] D. V. O'Connor, W. R. Ware, J. C. Andre, *J. Phys. Chem.* **1979**, *83*, 1333–1343.
- [186] M. J. Leitl, F.-R. Kühle, H. A. Mayer, L. Wesemann, H. Yersin, *J. Phys. Chem. A* **2013**, *117*, 11823–11836.
- [187] R. Thomas, S. Varghese, G. U. Kulkarni, *J. Mater. Chem.* **2009**, *19*, 4401.

Kapitel 9: Anhang

9.1 Beteiligung an weiteren Veröffentlichungen

9.1.1 Investigation of Luminescent Triplet States in Tetranuclear Cu(I) Complexes:

Thermochromism and Structural Characterization

9.1.1.1 Präambel

Das temperaturabhängige Lumineszenzverhalten vierkerniger Kupferkomplexe wurde untersucht und ein thermochromes Verhalten konnte für einige Komplexe nachgewiesen werden. Dabei wurde das thermochrome Verhalten mittels temperaturabhängiger Lumineszenzspektroskopie untersucht und die an der Thermochromie beteiligten Triplett-Zustände wurden mittels Step-scan-FTIR-Spektroskopie im Vergleich mit quantenchemischen Rechnungen charakterisiert.

Die temperaturabhängige Lumineszenz- und die Step-scan-FTIR-Spektroskopie an KBr-Presslingen sowie die Untersuchungen der Lumineszenz und der UV/Vis-Absorption in Lösung wurden von Pit Boden und mir durchgeführt. Pit Boden und Markus Gerhards haben das Manuskript entworfen. Patrick di Martino-Fumo hat DFT-Rechnungen beigetragen. Patrick Di Martino-Fumo, Pit Boden und ich wurden von Markus Gerhards betreut.

Jasmin Busch und Daniel Volz haben die Komplexe synthetisiert und analytisch charakterisiert. Außerdem haben sie die Pulverproben mittels Lumineszenzspektroskopie untersucht. Sie wurden von Stefan Bräse betreut. Florian Rehak hat zusätzliche DFT-Rechnungen und die Bethe-Salpeter-Rechnungen durchgeführt. Er wurde von Willem Klopper betreut. Olaf Fuhr und Martin Nieger haben die Kristallstrukturen bestimmt. Das Manuskript wurde von allen Autoren gemeinsam überarbeitet.

9.1.1.2 Referenz

Pit Boden, Patrick Di Martino-Fumo, Jasmin M. Busch, Florian R. Rehak, Sophie Steiger, Olaf Fuhr, Martin Nieger, Daniel Volz, Willem Klopper, Stefan Bräse, and Markus Gerhards, *Chem. Eur. J.* **2021**, 27, 5439 –5452. DOI: 10.1002/chem.202004539

9.1.2 NIR-Emissive Chromium(0), Molybdenum(0), and Tungsten(0) Complexes in the Solid State at Room Temperature

9.1.2.1 Präambel

Für die Chrom-, Molybdän- und Wolfram-Carbonylkomplexe mit einem Pyridyl-mesoionischen Carben-basierten Liganden wurde eine Lumineszenz mit einer Emission bis

in den NIR-Bereich nachgewiesen und die langlebigen Triplett-Zustände wurden mittels Step-scan-FTIR-Spektroskopie untersucht.

Die UV/Vis-Absorptions- und die Lumineszenzspektroskopie sowie die Step-scan-FTIR-Spektroskopie wurden von Pit Boden und mir durchgeführt. Patrick Di Martino-Fumo hat die DFT-Rechnungen durchgeführt. Patrick Di Martino-Fumo, Pit Boden und ich wurden betreut von Markus Gerhards und Gereon Niedner-Schatteburg.

Tobias Bens hat die Komplexe synthetisiert und den Wolfram-Komplex analytisch charakterisiert. Er wurde von Biprajit Sarkar betreut. Uta Albold hat die Kristallstruktur des Wolfram-Komplexes bestimmt. Das Projekt wurde von Pit Boden, Biprajit Sarkar und Markus Gerhards gestaltet und das Manuskript von Pit Boden geschrieben. Allen Autoren haben bei der Überarbeitung des Manuskripts beigetragen.

9.1.2.2 Referenz

Pit Boden, Patrick Di Martino-Fumo, Tobias Bens, Sophie Steiger, Uta Albold, Gereon Niedner-Schatteburg, Markus Gerhards, and Biprajit Sarkar, *Chem. Eur. J.* **2021**, *27*, 12959–12964. DOI: 10.1002/chem.202102208

9.2 Weitere Projekte in Zusammenarbeit mit Dissertationen aus der anorganischen Chemie an der TU Kaiserslautern

9.2.1 Lumineszenz- und FTIR-Untersuchungen an einem dinuklearen Iridium(III)-Komplex und den beiden entsprechenden mononuklearen Komplexen

Yanik Becker aus der Arbeitsgruppe von Prof. Dr. Werner Thiel (TU Kaiserslautern) untersuchte in seiner Dissertation den Einfluss verschiedener bipyridinartiger Liganden auf die roll-over Cyclometallierung. Drei im Rahmen seiner Arbeit synthetisierten Iridium-Komplexe wurden auf ihre photophysikalischen Eigenschaften hin untersucht. Diese drei Komplexe bilden eine Serie mit einem zweikernigen Komplex und zwei einkernigen Komplexen. Der zweikernige Komplex enthält einen verbrückenden, bipyridinähnlichen Liganden zwischen beiden Iridiumzentren und an beiden Metallzentren jeweils einen Chlorid- und einen Cp^* -Liganden (Cp^* = Pentamethylcyclopentadienyl) (Ir-Zweikerner) (Abb. 9.1, Mitte) Die beiden einkernigen Komplexe bestehen aus den beiden Hälften des zweikernigen Komplexes, jeweils einschließlich des bipyridinähnlichen Liganden, welcher NV -koordiniert (NV -Ir-Einkerner, Abb. 9.1, rechts) oder CN -koordiniert (CN -Ir-Einkerner, Abb. 9.1, links) sein kann. Daher eignet sich diese Serie auch im Rahmen des SFB/TRR88 (3MET) zur Untersuchung des kooperativen Effekts bei diesen Ir-Verbindungen.

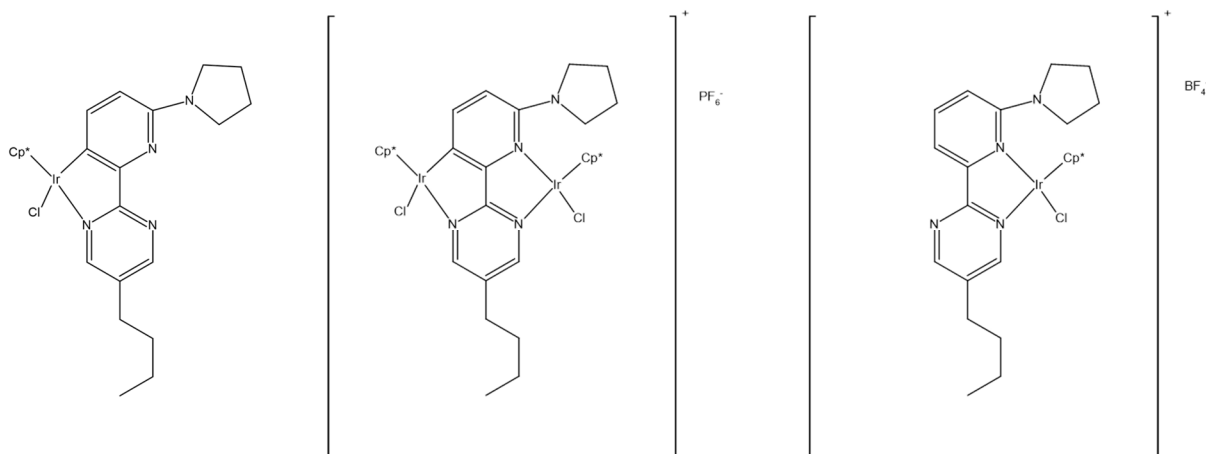


Abb. 9.1: Schematische Strukturen der drei untersuchten Ir-Komplexe. Links: CN-kordinierter Einkerner (ungeladen), Mitte: Zweikerner (Gegenion PF₆⁻), rechts: NN-kordinierter Einkerner (Gegenion BF₄⁻).

9.2.1.1 UV/Vis-Absorptionsspektroskopie

Die drei Komplexe zeigen in Dichlormethan sehr unterschiedliche Absorptionsspektren im Bezug auf Lage sowie das Absorptionmuster (Abb. 9.2). Der Zweikerner weist den rotesten Onset bei ca. 590 nm auf, der *NW*-Einkerner absorbiert erst bei ca. 500 nm und zeigt somit den blauesten Anstieg. Der Zweikerner hat mehrere Absorptionsmaxima, das roteste bei ca. 520 nm. Die Absorption des *CN*-Einkerners weist eine breite, kaum aufgelöste Absorption auf, das erste und einzige deutliche Maximum liegt bei ca. 240 nm. Oberhalb von 600 nm war bei keinem der Komplexe eine Absorptionsbande zu erkennen.

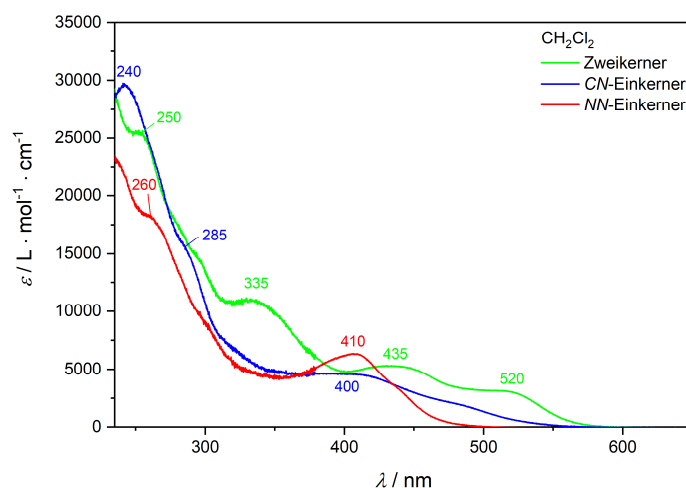


Abb. 9.2: UV/Vis-Spektren der drei Komplexe in Dichlormethan. Es ist der Extinktionskoeffizient gegen die Wellenlänge aufgetragen. Die erkennbaren Maxima sind gekennzeichnet.

Im Feststoff (vermischt mit KBr-Pulver) dagegen zeigen alle drei Komplexe ein Absorptionsspektrum ohne erkennbare Bandenstruktur (Abb. 9.3). Auch hier weist der Ir-Zweikerner den rotesten Onset ab ca. 740 nm auf, der *CN*-Einkerner liegt in der Mitte mit

einem Onset bei ca. 690 nm und die Absorption des *NV*-koordinierten liegt am weitesten im blauen Bereich mit einem Onset von ca. 580 nm. Damit ist der Trend identisch mit den Spektren in Dichlormethan, jedoch ist die Absorption insgesamt deutlich rotverschoben.

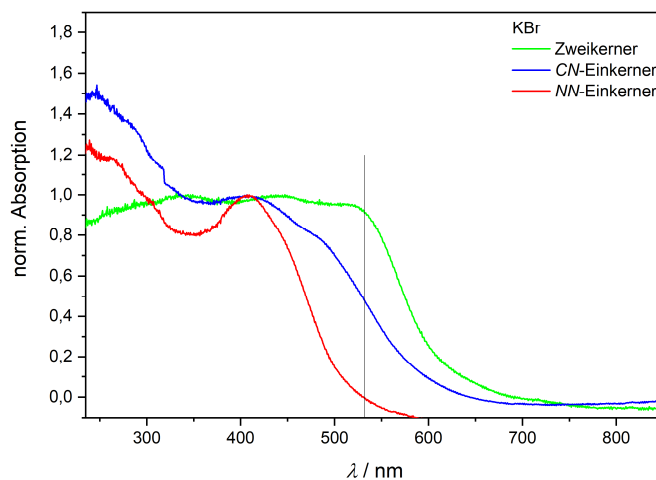


Abb. 9.3: UV/Vis-Spektren der drei Komplexe im KBr-Pulver mit der Reflektionseinheit bei Raumtemperatur gemessen. Die senkrechte Markierung kennzeichnet die Anregungswellenlänge für die Step-scan-FTIR-Messungen bei 532 nm.

9.2.1.2 Emissionsspektroskopie in Lösung

Der Ir-Zweikerner zeigt eine schwache, breite Emission in Dichlormethan im sichtbaren Bereich mit zwei erkennbaren Maxima bei 700 und 755 nm (Abb. 9.4, links). Die breite Bande stammt von der nicht aufgelösten Schwingungsprogression. Die Bande ist ab einer Anregungswellenlänge von 580 nm zu erkennen. Auch im NIR-Bereich von 800 nm bis 1550 nm ist eine Emission zu sehen (Abb. 9.4, rechts). Die blaue Anstiegsflanke im Spektrum ist jedoch apparativ bedingt und das Spektrum zeigt lediglich den roten Ausläufer der Emissionsbande mit dem Maximum im sichtbaren Bereich. Die Bande reicht bis ca. 1150 nm in den roten Bereich hinein. Dies spricht für einen energetisch im Vergleich zum Grundzustand tief liegenden Triplett-Zustand, aus dem die Emission ausgeht.

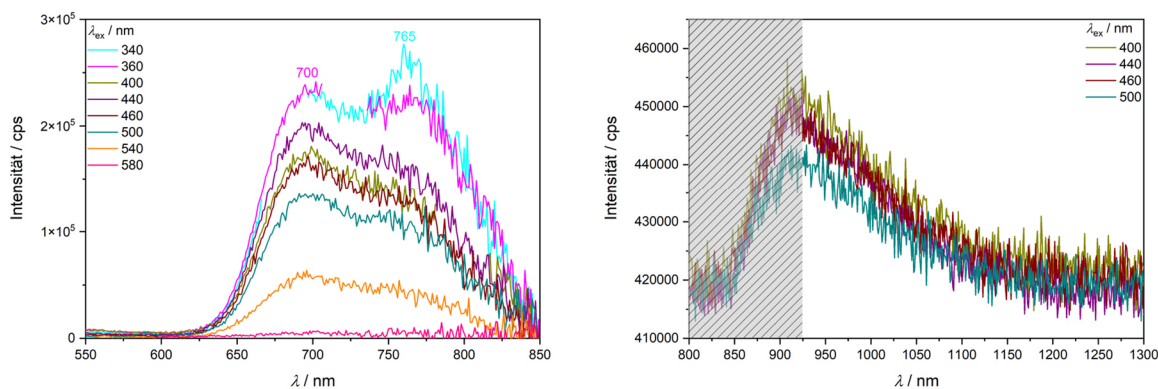


Abb. 9.4: Emissionsspektren des Ir-Zweikerners in Dichlormethan im sichtbaren (links) bis NIR-Bereich (rechts) bei verschiedenen Anregungswellenlängen. Die Emission im NIR-Bereich ist der rote Ausläufer der Emissionbande mit Maxima im sichtbaren Bereich. Der Einbruch der Intensität unterhalb von 920 nm ist apparativ bedingt (grau markiert).

Vom *NV*-Ir-Einkerner konnte kein Lumineszenzspektrum in Dichlormethan aufgenommen werden, da der Komplex zerfällt und die Emission daher direkt vom ebenfalls lumineszenten Zerfallsprodukt überlagert wird.

Die Probe des *CM*-koordinierten Ir-Einkerners zeigt dagegen eine deutliche Emission, die je nach Anregungswellenlänge ihr Maximum verschiebt (Abb. 9.5). Die blaueste Emission wird für eine Anregungswellenlänge von 340 nm erhalten und die rotteste bei 440 nm. Die Lage und Intensität bleibt auch nach Bestrahlung durch eine gesamte Messreihe identisch, der Komplex bleibt also stabil. Die Verschiebung der Emissionswellenlänge bei den verschiedenen Anregungswellenlängen kann daher von verschiedenen Isomeren in der Probe kommen, die leicht unterschiedliche Emissionen zeigen und bei den unterschiedlichen Anregungswellenlängen unterschiedlich effizient angeregt werden. Damit unterscheiden sich auch die Absorptionsspektren der Isomere, wofür auch das breite UV-Absorptionsspektrum (Abb. 9.2) des ungeladenen Einkerners spricht.

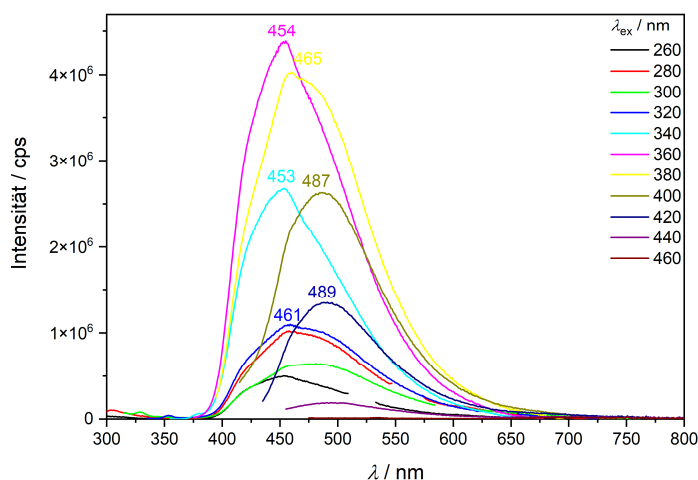


Abb. 9.5: Emissionsspektren des CN-kooordinierten Ir-Einkerners in Dichlormethan im UV/Vis-Bereich bei verschiedenen Anregungswellenlängen.

Die Lebensdauer des Ir-Zweikerners lässt sich gut über einen biexponentiellen Fit beschreiben, wobei die kleine Komponente einen sehr geringen Beitrag von unter 1 % aufweist und nur dazu dient die kleine, methodenbedingte Spitze zu beschreiben (Abb. 9.6). Die Hauptkomponente mit einem Anteil von über 99 % ergibt eine Lebensdauer von 107 ns. Der Fehler der Lebensdauern wird allgemein mit $\pm 10\%$ angenommen. Die Lebensdauer des CN-Einkerners ist wesentlich kürzer und beträgt ca. 14 ns. Diese Messung wurde bei zwei verschiedenen Anregungs- und damit auch Emissionswellenlängen durchgeführt. Beide Messungen ergeben eine monoexponentielle Abklingkurve mit einer nahezu identischen Lebensdauer (Abb. 9.7). Die Lebensdauer der verschiedenen Isomere muss demnach sehr ähnlich sein.

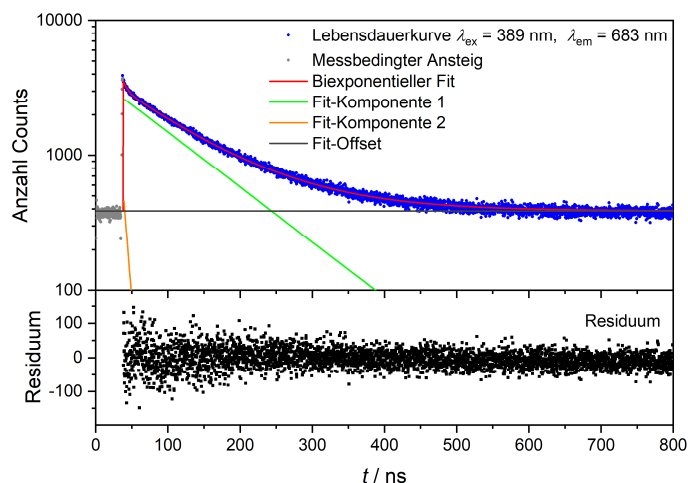


Abb. 9.6: Oben: TCSPC-Lebensdauerkurve des Ir-Zweikerners in Dichlormethan ($\lambda_{\text{ex}} = 389$ nm und $\lambda_{\text{em}} = 683$ nm) (blau) mit biexponentiellem Fit (rot), der Hauptkomponente (grün), der zweiten Komponente (orange, beschreibt nur die apparativ bedingte Spitze in den ersten 10 ns) und dem Offset (dunkelgrau). Unten: Das Residuum des biexponentiellen Fits.

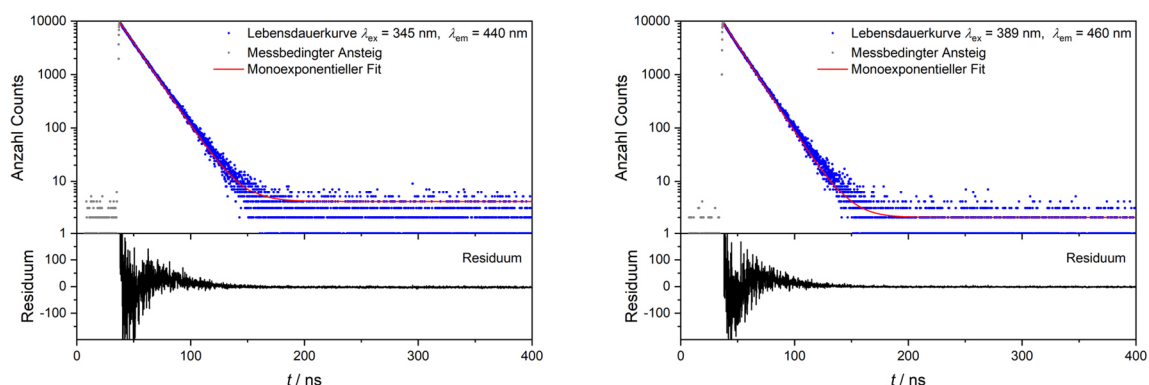


Abb. 9.7: TCSPC-Lebensdauerkurven des CN-kooordinierten Einkerners in Dichlormethan (oben) mit Residuen (unten) für die Anregungswellenlängen $\lambda_{\text{ex}} = 345$ nm (links) und $\lambda_{\text{ex}} = 389$ nm (rechts) mit den Emissionswellenlängen $\lambda_{\text{em}} = 440$ nm und $\lambda_{\text{em}} = 460$ nm (blau) mit monoexponentiellem Fit (rot). Die erhaltenen Lebensdauern sind identisch. Jeweils unten: Das Residuum des monoexponentiellen Fits.

Damit weist der Ir-Zweikerner eindeutig kooperative Effekte in Bezug auf die Lumineszenzeigenschaften auf. Durch die Kombination zweier Iridiumzentren wird die Emission rotverschoben und die Lebensdauer deutlich verlängert.

9.2.1.3 Temperaturabhängige Emission im KBr-Pressling

Die Lumineszenz der Ir-Komplexe in KBr-Presslingen wurde im Temperaturbereich von 290 – 5 K im UV/Vis- bis NIR-Bereich untersucht. Der Ir-Zweikerner im KBr-Pressling bei 290 K zeigt wie auch in Dichlormethan eine schwache, breite Emission mit nahezu identischer Bandenlage im Vergleich zum Spektrum in Lösung (Abb. 9.8). Lediglich die Form der breiten Bande mit den zwei Maxima unterscheidet sich. Im KBr-Pressling ist das rottere Maximum im Verhältnis schwächer und die Maxima sind schlechter separiert. Auch im KBr-Pressling reicht

die Emission bis ca. 1250 nm in den NIR-Bereich (Abb. 9.9, rechts). Zu tiefen Temperaturen hin nimmt die Emission auf das ca. 7-fache bei 5 K zu (Abb. 9.9, links). Auch die Auflösung der Schwingungsbanden verbessert sich. Bei 5 K sind drei Maxima bei 688, 751 und 778 nm zu erkennen, womit die Bandenlage über den gesamten Temperaturbereich kaum verändert (Abb. 9.10). Die Bandenlage und das Intensitätsmuster sind anregungswellenlängenunabhängig.

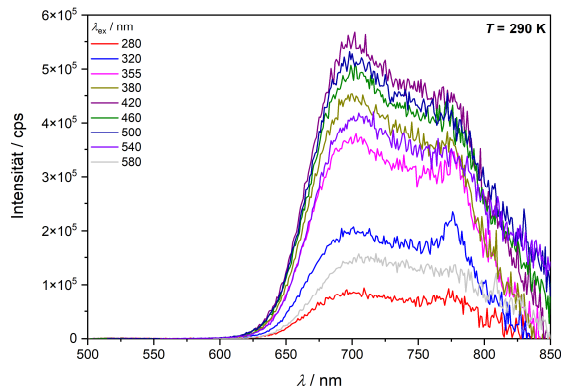


Abb. 9.8: Emissionsspektren des Ir-Zweikerners im KBr-Pressling bei 290 K bei verschiedenen Anregungswellenlängen.

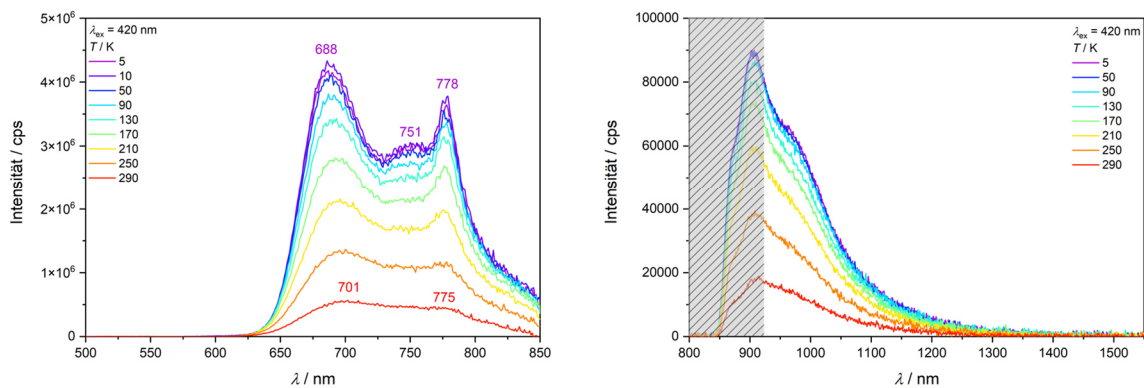


Abb. 9.9: Emissionsspektren des Ir-Zweikerners im KBr-Pressling im Temperaturbereich von 5 – 290 K bei einer Anregungswellenlänge von $\lambda_{\text{ex}} = 420$ nm im sichtbaren Bereich (links) und im NIR-Bereich (rechts). Der Anstieg im NIR-Bereich unterhalb von 920 nm ist apparativ bedingt (grau markiert). Die Emission zeigt lediglich den Ausläufer der Emission mit Maxima im sichtbaren Bereich.

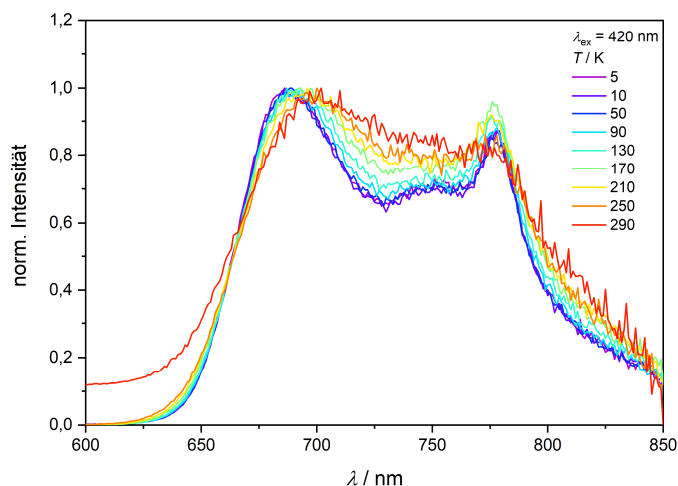


Abb. 9.10: Normierte Emission des Ir-Zweikerners im KBr-Pressling im Temperaturbereich von 5 - 290 K bei einer Anregungswellenlänge von $\lambda_{\text{ex}} = 420$ nm.

Der CN-koordinierte Einkerner im KBr-Pressling zeigt bei 290 K im Vergleich zum Spektrum in Dichlormethan eine rotverschobene Emission bei ca. 715 nm (Abb. 9.11, rechts). Die Emission ist jedoch sehr schwach und breit, weshalb die Lage deutlich vom Untergrundrauschen des Detektors beeinflusst ist. Die Intensität nimmt von 290 K bis 5 K auf das etwa 30-fache zu, wobei gleichzeitig ein zweiter Peak bei 785 nm in der breiten Bande mit einem Maximum bei 681 nm zu erkennen ist (Abb. 9.12, links). Dieser Peak könnte auf eine aufgelöste Schwingungsbande zurückzuführen sein. Auch im NIR-Bereich ist die Emission zu detektieren und die Emissionsbande reicht dabei vom sichtbaren bis ca. 1300 nm (Abb. 9.12, rechts). Die Anregungswellenlängenabhängigkeit ist im KBr-Pressling schwächer ausgeprägt wie in Dichlormethan, jedoch zeigen die Anregungsspektren (Abb. 9.13) im roten und blauen Bereich der breiten Emissionsbande einen abweichenden Onset von 550 nm für die blaue Flanke und 590 nm für die rote.

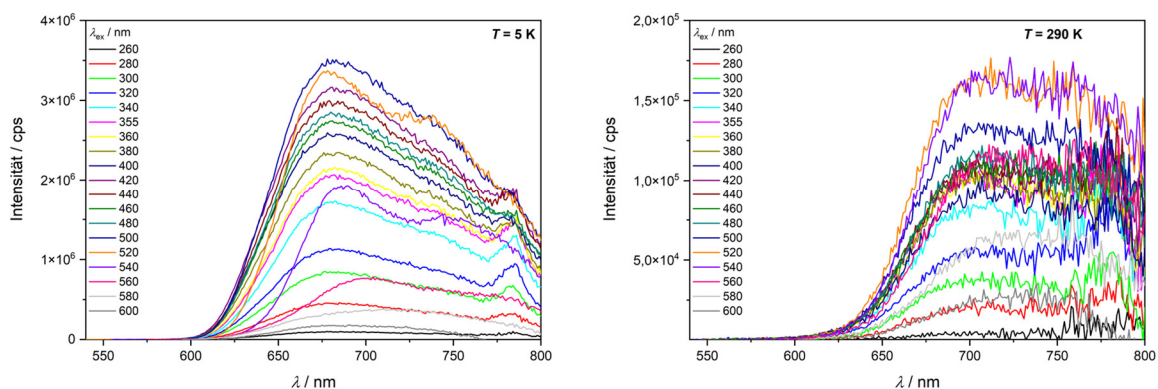


Abb. 9.11: Emissionsspektren des CN-koordinierten Ir-Einkerners im KBr-Pressling bei 5 K (links) und 290 K (rechts) bei verschiedenen Anregungswellenlängen.

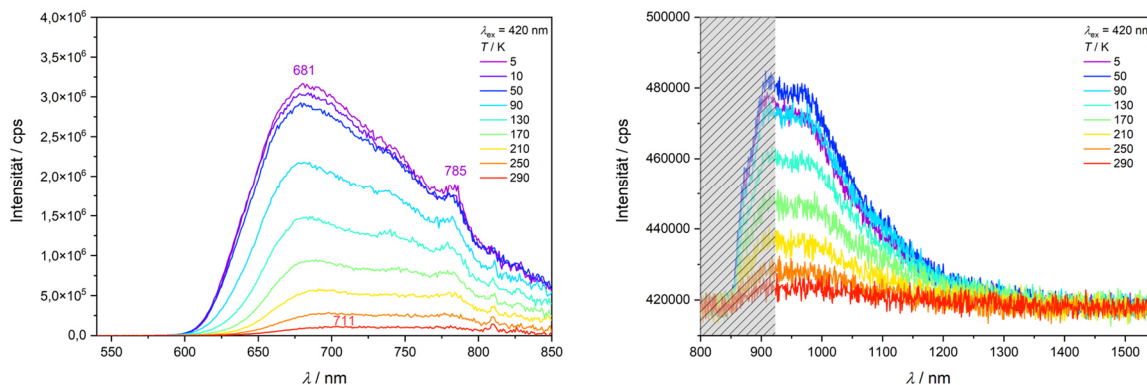


Abb. 9.12: Emissionsspektren des CN-kordinierten Ir-Einkerners im KBr-Pressling im Temperaturbereich von 5 – 290 K bei einer Anregungswellenlänge von $\lambda_{\text{ex}} = 420$ nm im sichtbaren Bereich (links) und im NIR-Bereich (rechts). Der Anstieg im NIR-Bereich unterhalb von 920 nm ist apparativ bedingt (grau markiert). Die Emission zeigt lediglich den Ausläufer der Emission mit Maxima im sichtbaren Bereich.

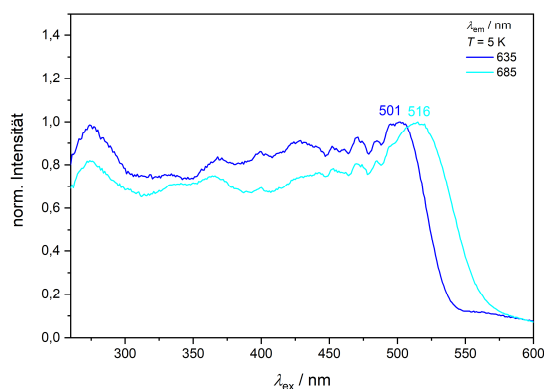


Abb. 9.13: Anregungsspektren des CN-kordinierten Ir-Einkerners im KBr-Pressling bei 5 K für die das blaue (dunkelblau) und das rote (hellblau) Maximum der Emissionbande. Die gewählten Emissionswellenlängen entsprechen den Maxima am Detektor ohne Korrektur.

Im Gegensatz zu den Messungen in Dichlormethan lässt sich im KBr-Pressling auch für den *NV*-Einkerner eine schwache Emission bei 290 K detektieren. Die Emission liegt bei ca. 700 nm. Bei Raumtemperatur ist die Emission zu schwach, um im NIR-Bereich noch detektiert zu werden, während bei 5 K eine Zunahme der Emission um das 170-fache gemessen wurde (Abb. 9.14). Hierbei wird durch die höhere Intensität auch die Auflösung deutlicher und die Bandenstruktur hängt stark von der Anregungswellenlänge ab (Abb. 9.15, links). Dies deutet auf eine Probe mit verschiedenen Isomeren hin. Bei 355 nm und 420 nm Anregungswellenlänge zeigt sich beispielsweise eine breite Bande mit zwei bzw. drei Maxima bei 595 nm und 634 nm (und 786 nm), während die Emission bei $\lambda_{\text{ex}} = 500$ nm nur ein einziges deutliches Maximum bei 671 nm aufweist. Bei tiefer Temperatur ist die Emission für alle Anregungswellenlängen bis in den NIR-Bereich zu beobachten und reicht für $\lambda_{\text{ex}} = 355/420$ nm bis ca. 1270 nm sowie bei $\lambda_{\text{ex}} = 500$ nm bis ca. 1200 nm (Abb. 9.15, rechts).

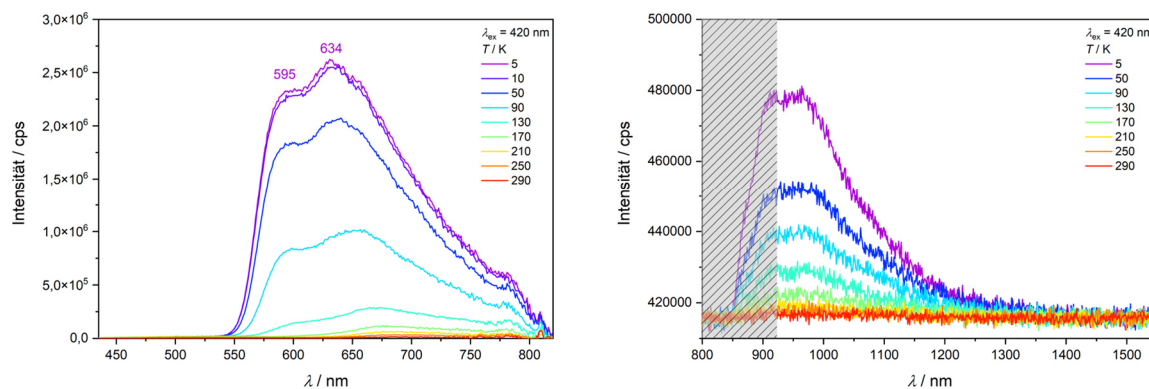


Abb. 9.14: Emissionsspektren des NN-koodinierten Ir-Einkerners im KBr-Pressling im Temperaturbereich von 5 – 290 K bei einer Anregungswellenlänge von $\lambda_{\text{ex}} = 420$ nm im sichtbaren Bereich (links) und im NIR-Bereich (rechts). Der Anstieg im NIR-Bereich unterhalb von 920 nm ist apparativ bedingt (grau markiert). Die Emission zeigt lediglich den Ausläufer der Emission mit Maxima im sichtbaren Bereich.

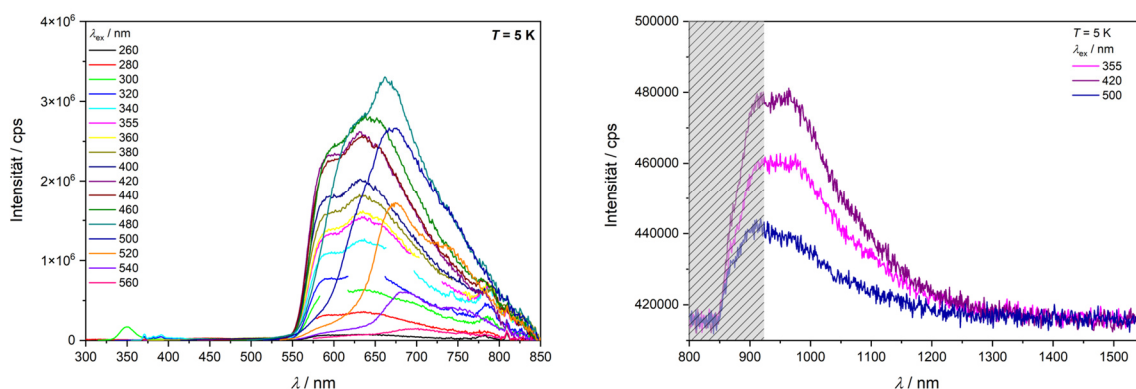


Abb. 9.15: Emissionsspektren des NN-koodinierten Ir-Einkerners im KBr-Pressling bei 5 K im sichtbaren (links) und NIR-Bereich (rechts) bei verschiedenen Anregungswellenlängen. Der Anstieg im NIR-Bereich unterhalb von 920 nm ist apparativ bedingt (grau markiert). Die Emission zeigt lediglich den Ausläufer der Emission mit Maxima im sichtbaren Bereich.

Lumineszenzlebensdauer-Messungen ließen sich an den drei Komplexen im KBr-Pressling nicht durchführen, da Abklingkurven durch die geringe Intensität stark von Untergrundeffekten überlagert wurden.

Im Vergleich der drei Komplexe bei 5 K liegt die Emission des *NN*-koodinierten Einkerners bei allen Anregungswellenlängen höherenergetisch im Vergleich mit den beiden anderen Komplexen. Der *CN*-Einkerner und der Zweikerner zeigen von der Bandenlage ein ähnliches Emissionsspektrum. Die Anstiegsflanke im blauen Bereich ist für den Zweikerner rotverschoben zum Einkerner. Im Vergleich mit dem *CN*-Einkerner zeigt der Zweikerner eine deutliche Spitze im roten Bereich der breiten Emissionsbande bei 778 nm, während die rote Flanke beider Spektren nahezu identisch ist. Die Vergleiche sind in Abb. 9.16 gezeigt.

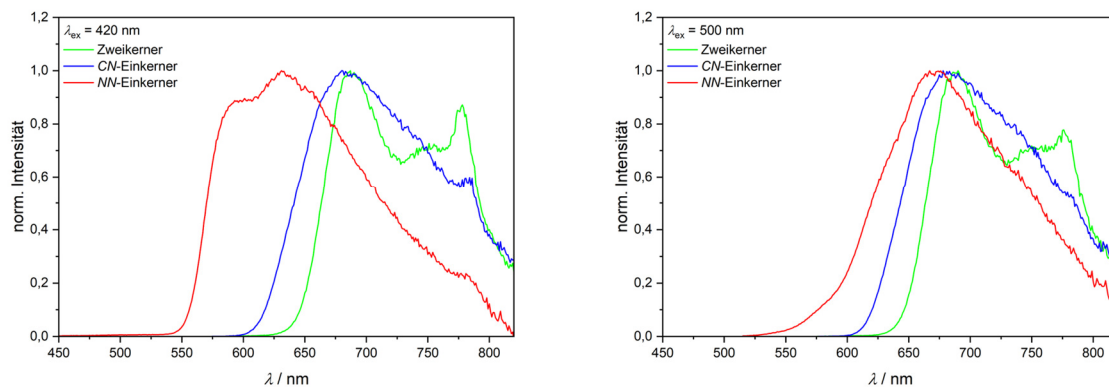


Abb. 9.16: Vergleich der Emissionsspektren der drei Ir-Komplexe bei 5 K bei einer Anregungswellenlänge von $\lambda_{\text{ex}} = 420$ nm (links) und $\lambda_{\text{ex}} = 500$ nm (rechts).

9.2.1.4 Statische FTIR-Spektren des elektronischen Grundzustands

Im elektronischen Grundzustand wurden die FTIR-Spektren bei 290 und 20 K für alle drei Komplexe (KBr-Presslinge) aufgenommen. Die Spektren des Zweikerners und des *CN*-koordinierten Einkerners sind ähnlich, während das Spektrum des *NN*-koordinierten Einkerners sich von den andern unterscheidet (Abb. 9.17). Die größten Unterschiede finden sich bei den CH-Biege- und CC-Streckschwingungen im Pyridinring, welcher je nach Komplex C-, N- oder verbrückend an die Iridiumzentren koordiniert ist. Die Zuordnung erfolgt über DFT-Rechnungen, wobei die Frequenzen der optimierten Strukturen die experimentellen Spektren sehr gut beschreiben (Abb. 9.18). Lediglich der *NN*-Koordinierte Komplex zeigt eine breite, unstrukturierte Absorption im Bereich von $1000 - 1150 \text{ cm}^{-1}$, welche vom Gegenion BF_4^- stammt. Die Spektren des elektronischen Grundzustands sind jeweils bei 20 K und 290 K identisch.

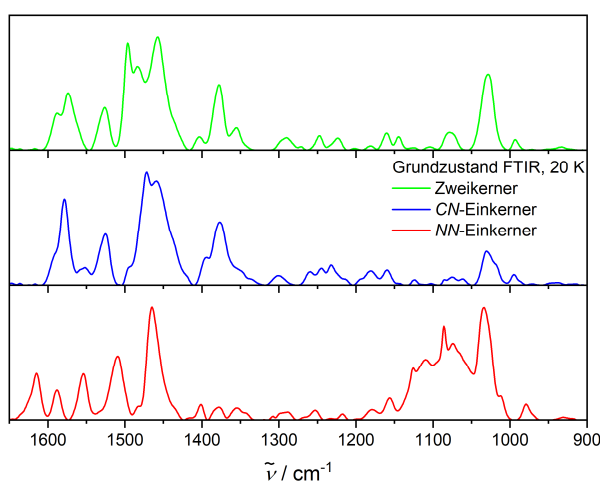


Abb. 9.17: Vergleich der FTIR-Grundzustandsspektren der drei untersuchten Ir-Komplexe bei 20 K.

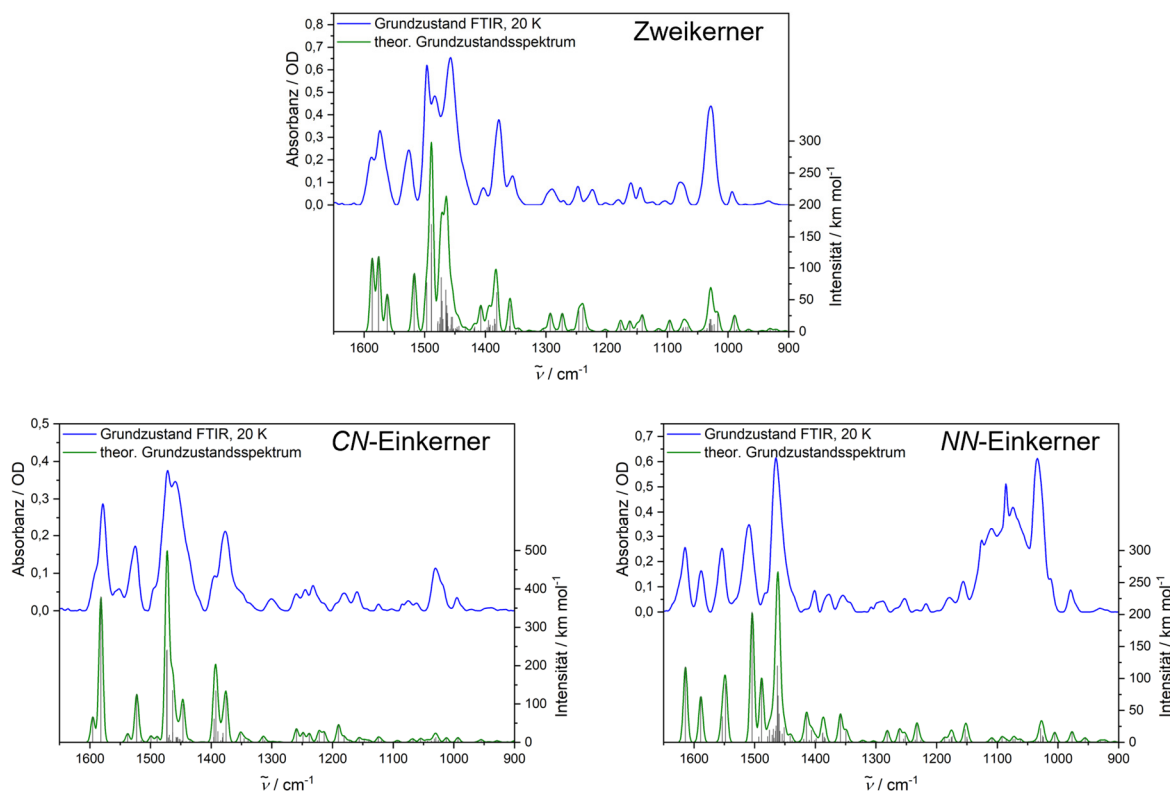


Abb. 9.18: Vergleich der FTIR-Grundzustandsspektren bei 20 K mit der DFT-Grundzustandsrechnung (DFT/B3LYP-D3(BJ)/def2-TZVP, Skalierungsfaktor 0,975) für den Ir-Zweikerner (oben), den CN-koodinierten Ir-Einkerner (unten links) und den NN-koodinierten Ir-Einkerner (unten rechts).

9.2.1.5 Step-scan-FTIR-Spektroskopie zur Untersuchung des elektronisch angeregten Zustands

Auch die FTIR-Spektren des angeregten Zustands wurden mittels Step-scan-Methode untersucht. Die Komplexe wurden mit einer Wellenlänge von 532 nm angeregt. Der Ir-Zweikerner zeigt bei Anregung einige negative Banden, welche mit dem Grundzustand übereinstimmen sowie eine intensive positive Bande bei 1335 cm^{-1} (Abb. 9.19). Die Spektren bei 20 K und 290 K unterscheiden sich lediglich im Intensitätsverhältnis der Banden. Das Spektrum des angeregten Zustands wird durch die Aufaddierung mit 1,5 % des Grundzustandsspektrums erhalten. Das erhaltene Spektrum wird vom theoretischen Spektrum aus der DFT-Rechnung des niedrigsten Triplett-Zustands gut beschrieben (Abb. 9.20). Die charakteristische Bande bei 1335 cm^{-1} stellt CH-Biegeschwingungen in den Ringen des verbrückenden Liganden dar. Die Spindichte des zugeordneten Triplett-Zustands liegt ausschließlich auf dem CN-koodinierten Iridiumzentrum und den Ringen des verbrückenden Liganden (Abb. 9.20), weshalb dort lokalisierte Schwingungen für den angeregten Zustand charakteristisch sind.

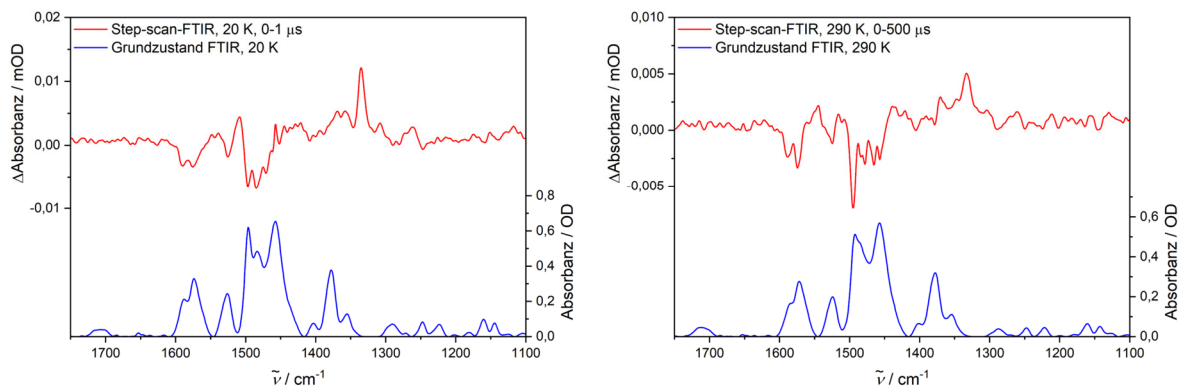


Abb. 9.19: Vergleich des Step-scan-FTIR-Spektrums (rot) mit dem Grundzustandsspektrum (blau) bei 20 K (links) und 290 K (rechts) für den Ir-Zweikerner. Für das dargestellt Step-scan-FTIR-Spektrum wurden die gemessenen Spektren über 1 μs bzw. 500 ns nach der Anregung gemittelt. Negative Banden entsprechen den Banden des Grundzustands, positive denen des angeregten Zustands.

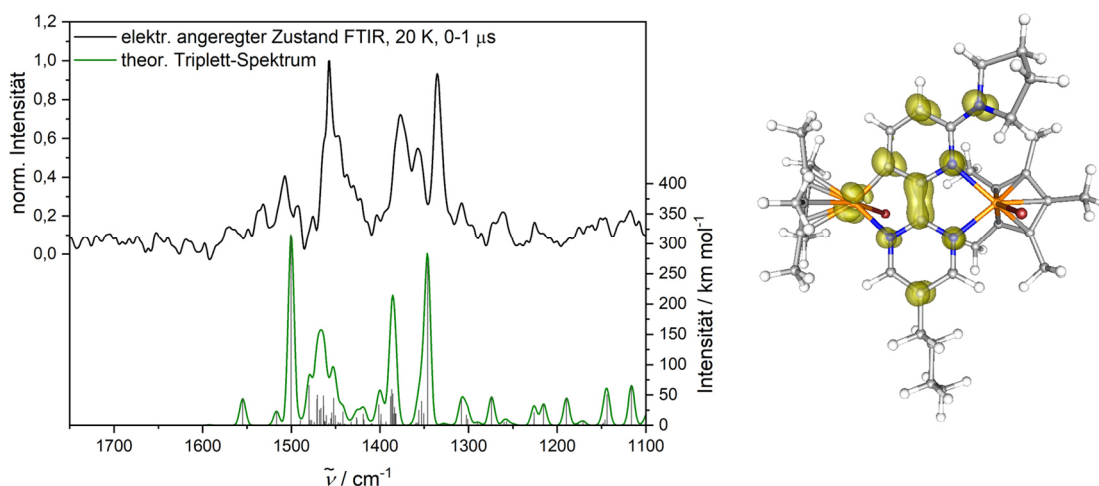


Abb. 9.20: Links: Das Spektrum des angeregten Zustands des Ir-Zweikers bei 20 K (Step-scan + 1,5 % Grundzustand) (schwarz) im Vergleich mit dem theoretischen Spektrum der DFT-Rechnung (UDFT/B3LYP-D3(BJ)/def2-TZVP, Skalierungsfaktor 0,975). Rechts: Spindichte des gerechneten Triplett-Zustands (Isovalue 0,01).

Auch für die einkernigen Komplexe konnten Step-scan-Spektren aufgenommen werden. Die Intensität der Differenzspektren ist jedoch, vor allem für den *MN*-koordinierten Komplex, sehr gering. Die geringe Intensität lässt sich über die schwächere Absorption bei 532 nm für die beiden einkernigen Komplexe im Vergleich mit dem zweikernigen Komplex erklären. Die negativen Banden stimmen mit dem Grundzustand überein, wobei die Auflösung der negativen Banden ungewöhnlicherweise bei 290 K besser ist als bei 20 K (Abb. 9.21 und Abb. 9.22). Dies könnte an einer geringeren Stabilität der Proben bei 290 K liegen, weshalb die Abnahme des Grundzustands bei der Anregung durch Zersetzung der Probe begünstigt ist. Bei 20 K kommen jedoch die positiven Banden wesentlich besser heraus, sodass in den Spektren des angeregten Zustands bei 20 K mehr bzw. deutlichere charakteristische Banden

zu erkennen sind als bei 290 K. Die DFT-Rechnungen beschreiben die experimentellen Spektren jedoch wesentlich weniger gut als beim Zweikerner, weshalb eine Zuordnung schwierig ist (Abb. 9.23).

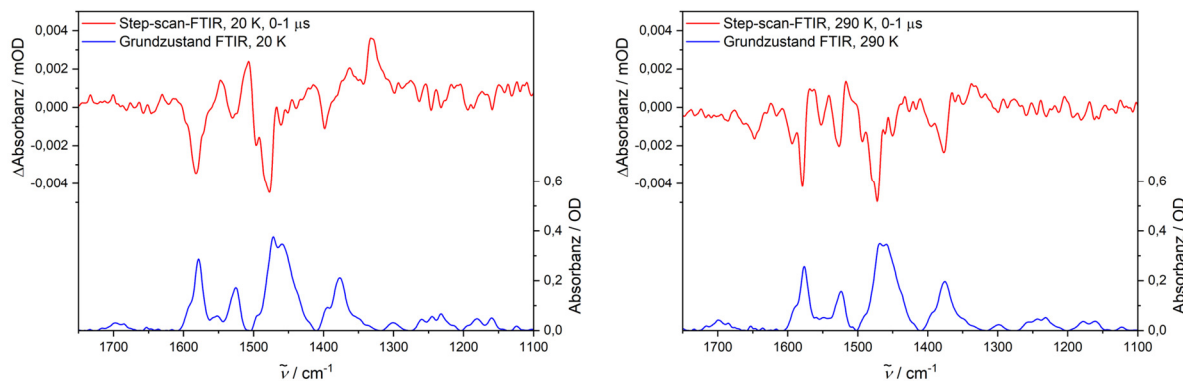


Abb. 9.21: Vergleich des Step-scan-FTIR-Spektrums (rot) mit dem Grundzustandsspektrum (blau) bei 20 K (links) und 290 K (rechts) für den CN-kooordinierten Ir-Einkerner. Für das dargestellt Step-scan-FTIR-Spektrum wurden die gemessenen Spektren über 1 μ s nach der Anregung gemittelt. Negative Banden entsprechen den Banden des Grundzustands, positive denen des angeregten Zustands.

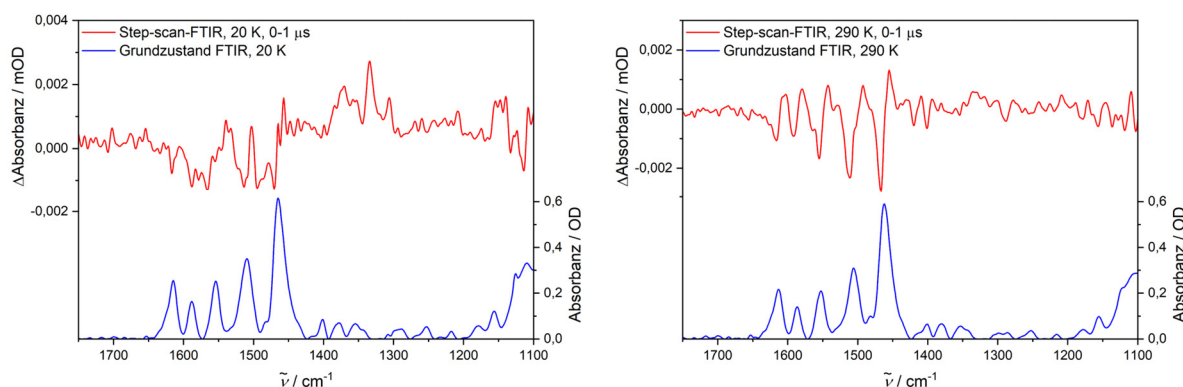


Abb. 9.22: Vergleich des Step-scan-FTIR-Spektrums (rot) mit dem Grundzustandsspektrum (blau) bei 20 K (links) und 290 K (rechts) für den NN-kooordinierten Ir-Einkerner. Für das dargestellt Step-scan-FTIR-Spektrum wurden die gemessenen Spektren über 1 μ s nach der Anregung gemittelt. Negative Banden entsprechen den Banden des Grundzustands, positive denen des angeregten Zustands.

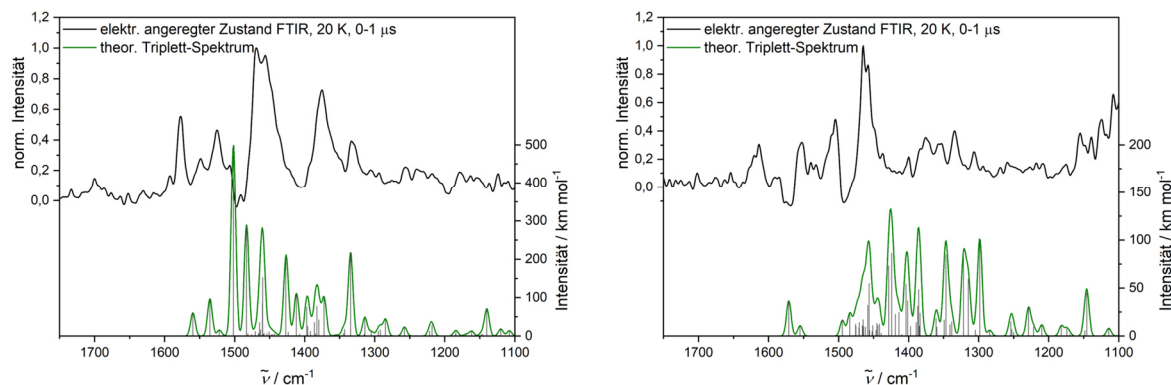


Abb. 9.23: Die Spektren des angeregten Zustands des CN- (links) und des NN-kordinierten (rechts) Ir-Einkerners bei 20 K (Step-scan + 3 bzw. 1 % Grundzustand) (schwarz) im Vergleich mit dem theoretischen Spektrum der DFT-Rechnung (UDFT/B3LYP-D3(BJ)/def2-TZVP, Skalierungsfaktor 0,975).

9.2.2 Untersuchung der Lumineszenzeigenschaften eines Platin-Komplexes

Im Rahmen der Dissertation von Tobias Grimm aus der Arbeitsgruppe von Prof. Dr. Werner Thiel (TU Kaiserslautern) wurde ein cyclometallierter Platin(II)-Komplex synthetisiert, der einen um zwei *n*-Butylgruppen erweiterten NCN-Pinzettenliganden enthält (Abb. 9.24). Aufgrund seiner ähnlichen Struktur zu anderen Platin-Komplexen mit interessanten photophysikalischen Eigenschaften wurde dieses System ebenfalls auf diese hin untersucht.

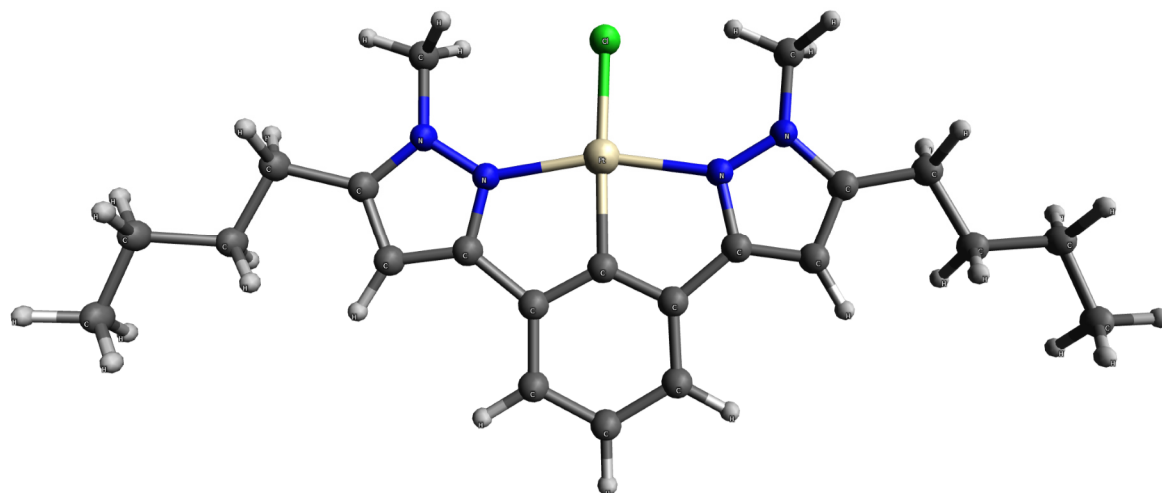


Abb. 9.24: Struktur des Pt(II)-Komplexes nach der quantenchemischen Rechnung (DFT/B3LYP/def2-TZVP), angesetzt aus der Kristallstruktur.

Der Komplex hat eine quadratisch planare Koordinationsumgebung mit einem Chloridion an der vierten Koordinationsstelle. Im Feststoff liegt er laut Kristallstruktur nahezu komplett planar vor. Durch das Platinzentrum ist eine starke Spin-Bahn-Kopplung und damit bei elektronischer Anregung ein Übergang in den Triplett-Zustand zu erwarten.

9.2.2.1 UV/Vis-Absorptionsspektroskopie

Das UV/Vis-Absorptionsspektrum (Abb. 9.25) in Lösung ist aufgelöst und es sind im Bereich zwischen 260 – 290 nm und zwischen 335 – 360 nm je zwei separierte Banden zu erkennen. Der Onset liegt bei ca. 370 nm. Die energetisch niedrigeren Übergänge sind im Vergleich mit Literatur^[1-5] Metal-zu-Ligand-Ladungsübertragung (eng. Metal-to-Ligand-Charge-Transfer (MLCT)) gemischt mit π - π^* -Übergängen auf dem Liganden, während die höherenergetischen π - π^* -Übergänge auf dem Liganden (engl. Ligand centred (LC)) zugeordnet werden. In den Lösungsmitteln Dichlormethan, Aceton, Ethanol und Toluol sind die Absorptionsspektren nahezu identisch und es kann kein solvatochromer Einfluss auf die Absorption im UV/Vis-Bereich festgestellt werden.

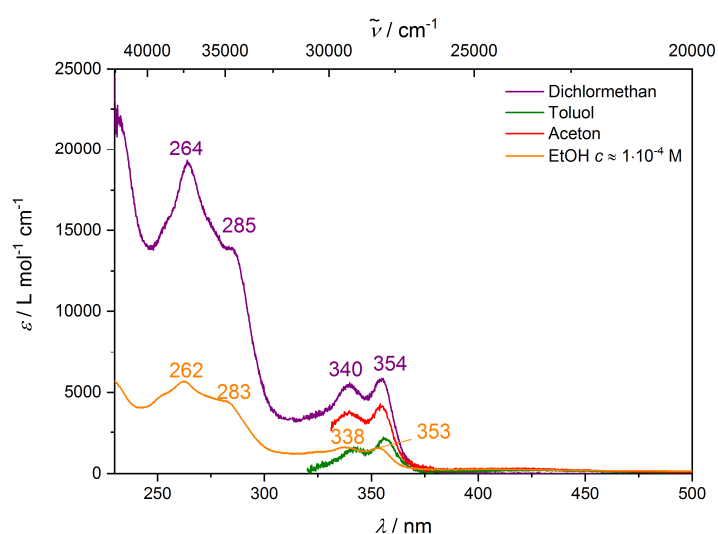


Abb. 9.25: UV/Vis-Absorptionsspektren des Pt(II)-Komplexes in den Lösungsmitteln Dichlormethan (lila), Toluol (grün), Aceton (rot) und Ethanol (orange). Das Spektrum in Ethanol ist bei einer höheren Konzentration von $c = 1 \cdot 10^{-4} \text{ mol L}^{-1}$ aufgenommen worden, die anderen Spektren bei der Standardkonzentration von $c = 2 \cdot 10^{-5} \text{ mol L}^{-1}$.

9.2.2.2 Emission in Lösung

Der untersuchte Pt-Komplex zeigt nur eine schwache Emissionsintensität bei Raumtemperatur in Lösung. In Dichlormethan und Ethanol konnten Lumineszenzspektren aufgenommen werden (Abb. 9.26), wobei in Ethanol, aufgrund der sehr geringen Intensität der Emission, die Konzentration gegenüber der Standard-Konzentration verfünffacht wurde. Diese zeigen eine erkennbare Schwingungsauflösung mit drei scharfen Banden. Die Bandenlage ist in Dichlormethan etwas rotverschoben gegenüber dem Spektrum in Ethanol und das Intensitätsmuster unterscheidet sich. Diese solvatochromen Effekte sprechen für eine unterschiedlich stark ausgeprägte Stabilisierung des elektronisch angeregten Zustands im Vergleich zum elektronischen Grundzustand in den beiden Lösungsmitteln. Unter Bestrahlung ist der Komplex in Ethanol stabiler. Die Lebensdauern des Komplexes in Lösung liegen im niedrigen Nanosekundenbereich (Tabelle 9.1). In Dichlormethan wurden zwei

Komponenten erhalten, was auf zwei Konformere des Komplexes hindeuten könnte. In Ethanol ist die zweite Komponente im Vergleich ungewöhnlich lang, was auf eine Überlagerung mit Störsignalen aufgrund der geringen Emissionsintensität zurückzuführen ist.

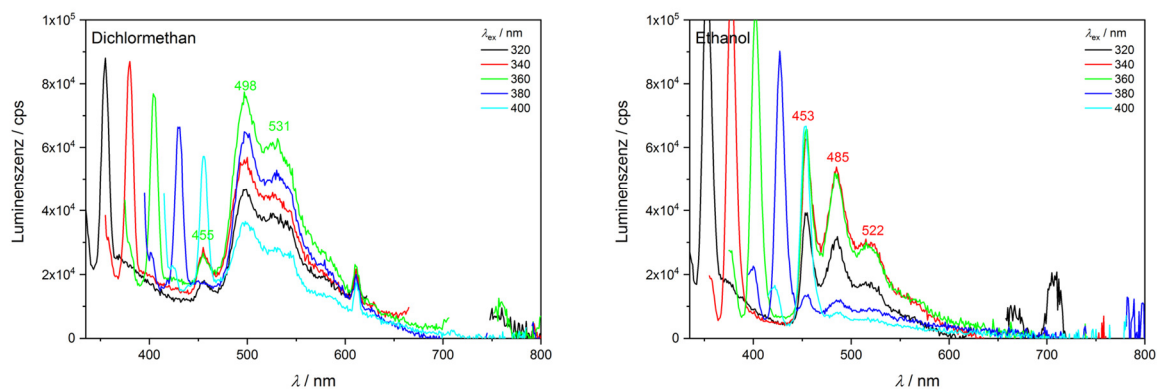


Abb. 9.26: Lumineszenzspektren des Pt(II)-Komplexes in den Lösungsmitteln Dichlormethan (links) und Ethanol (rechts) bei jeweils vier verschiedenen Anregungswellenlängen. Die scharfen Spitzen im energetisch höheren Bereich stammen von der Raman-Streuung des Lösungsmittels, die Banden der Probe sind beschriftet.

Tabelle 9.1: Lumineszenzlebensdauern des Pt(II)-Komplexes in den Lösungsmitteln Dichlormethan und Ethanol (Fehler $\pm 10\%$).

	$\lambda_{em} /$ nm	$\lambda_{ex} /$ nm	$\tau_1 /$ ns	$A_1 /$ %	$\tau_2 /$ ns	$A_2 /$ %
Dichlormethan	496	345	8,7	67	2,4	33
Ethanol	454	345	30,9*	30	3,4	70

9.2.2.3 Temperaturabhängige Emission im Feststoff

Auch das Spektrum am KBr-Pressling der Probe zeigt bei Raumtemperatur eine schwache, aber deutlich schwingungsaufgelöste Emission (Abb. 9.27). Die Bandenlage und das Intensitätsmuster der drei scharfen Banden sind identisch zum Spektrum in Ethanol.

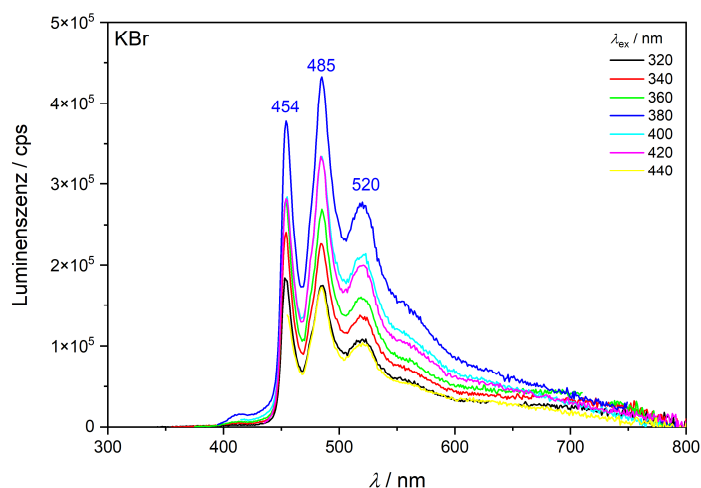


Abb. 9.27: Lumineszenzspektren des Pt(II)-Komplexes im KBr-Pressling bei Raumtemperatur bei verschiedenen Anregungswellenlängen.

Die Intensität der Emission nimmt zu tiefen Temperaturen hin auf das ca. 450-fache zu (Abb. 9.28), was über eine sehr effiziente Unterdrückung der nicht-strahlenden Kanäle bei tiefer Temperatur zu erklären ist. Bei hohen Temperaturen (Raumtemperatur) sorgen nicht-strahlende Deaktivierungskanäle, begünstigt durch die langen Alkylgruppen, für die sehr schwache Emissionsintensität^[6,7]. Die starre Matrix bei tiefer Temperatur verhindert die Bewegungen im Komplex und somit die nicht-strahlende Deaktivierung über Schwingungen und Stöße. Die Bandenlage bleibt über den gesamten untersuchten Temperaturbereich nahezu unverändert, während sich das Intensitätsmuster verschiebt, was für eine temperaturabhängige Besetzung der Schwingungsniveaus innerhalb der Schwingungsprogression spricht (Abb. 9.28). Bei den intensiven Emissionen in den Spektren bei 5 – 30 K wurden Nebenbanden für die Bande bei 485 und 525 nm beobachtet (Sternchen in Abb. 9.28), was, wie schon die beiden Komponenten der Lebensdauern in Dichlormethan-Lösung, auf die Existenz von zwei verschiedenen Isomeren (Konformeren) in der Probe hindeutet. Die Abstände der Schwingungsprogression von ca. 1400 cm^{-1} entsprechen, im Vergleich mit den über DFT-Rechnungen ermittelten Frequenzen, CH-Biegeschwingungen am NCN-Liganden.

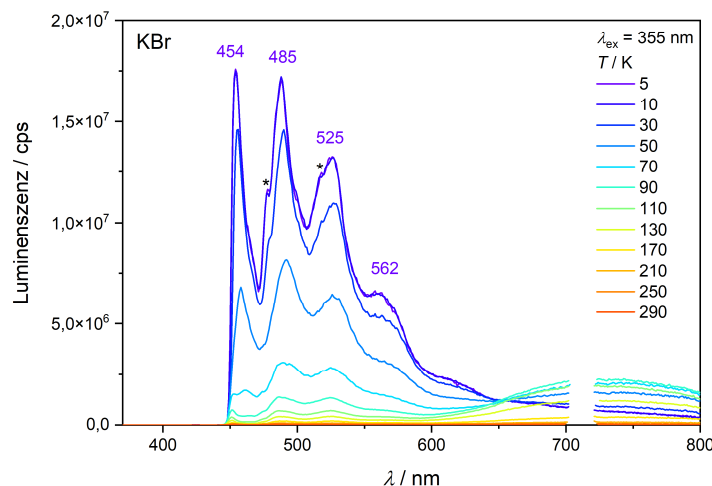


Abb. 9.28: Lumineszenzspektren des Pt(II)-Komplexes im KBr-Pressling im Temperaturbereich von 5 – 290 K bei einer Anregungswellenlänge von $\lambda_{\text{ex}} = 355$ nm. Mit Sternchen markiert sind die Nebenbanden, die vermutlich von einem Isomer des Komplexes stammen. Der Anstieg oberhalb von 600 nm in den Spektren bei höheren Temperaturen erklärt sich über die Emission von Spuren des freien NCN-Liganden in der Probe, welche, aufgrund der sehr schwachen Intensität des gesamten Spektrums und des damit großen Einflusses des Untergrundrauschens, von der Korrekturfunktion überschätzt wird.

Die Lumineszenzlebensdauern im Feststoff wurden im Temperaturbereich von 5 – 170 K untersucht. Bei Temperaturen oberhalb von 170 K war die Emissionsintensität zu schwach, um aussagekräftige Ergebnisse zu erhalten. Bei 170 K wurden zwei Komponenten mit ca. 0,5 und 15 ns gemessen, wobei die Verteilung der Komponenten von der untersuchten Emissionswellenlänge abhängt. Mit abnehmender Temperatur nimmt die Lebensdauer zunächst leicht und ab ca. 90 K stark zu bis sie bei 5 K etwa das 1000-fache der Lebensdauer bei 170 K erreicht (Abb. 9.29). Auch dieses Verhalten ist wie die Intensitätszunahme auf die Unterdrückung der nicht-strahlenden Deaktivierung bei tiefer Temperatur zurückzuführen. Die Lebensdauer liegt bei 5 K bei ca. 5 μs . Da die zweite Komponente bei allen Emissionswellenlängen $< 6\%$ beträgt und deutlich kürzer ist, ist davon auszugehen, dass sie wie für diese Messungen üblich lediglich apparativen Ursprungs ist, und beide Isomere eine im Rahmen des Messfehlers identische Lebensdauer aufweisen. Die Lebensdauern bei tiefer Temperatur sowie der Einfluss des Platinzentrums auf die Spin-Bahn-Kopplung sprechen für die Besetzung eines Triplettzustands und somit für Phosphoreszenz. Bei höheren Temperaturen ist die Lebensdauer durch die nicht-strahlende Deaktivierung über die Alkylgruppen stark verkürzt.

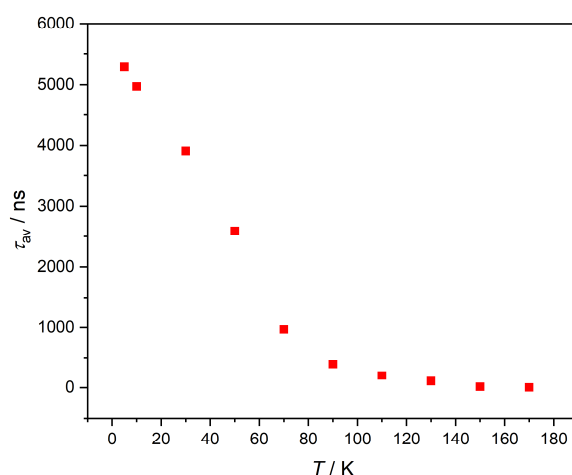


Abb. 9.29: Temperaturverlauf der Lumineszenzlebensdauern des Pt(II)-Komplexes. Die aufgetragene Werte sind aus Gründen der Übersicht die gemittelte komponentengewichtete Lumineszenzlebensdauer.

9.2.2.4 Literatur

- [1] A. K.-W. Chan, M. Ng, Y.-C. Wong, M.-Y. Chan, W.-T. Wong, V. W.-W. Yam, *Journal of the American Chemical Society* **2017**, *139*, 10750–10761.
- [2] Z. Wang, E. Turner, V. Mahoney, S. Madakuni, T. Groy, J. Li, *Inorg. Chem.* **2010**, *49*, 11276–11286.
- [3] A. K.-W. Chan, E. S.-H. Lam, A. Y.-Y. Tam, D. P.-K. Tsang, W. H. Lam, M.-Y. Chan, W.-T. Wong, V. W.-W. Yam, *Chemistry (Weinheim an der Bergstrasse, Germany)* **2013**, *19*, 13910–13924.
- [4] J. A. G. Williams, A. Beeby, E. S. Davies, J. A. Weinstein, C. Wilson, *Inorg. Chem.* **2003**, *42*, 8609–8611.
- [5] V. M. Miskowski, V. H. Houlding, C. M. Che, Y. Wang, *Inorg. Chem.* **1993**, *32*, 2518–2524.
- [6] C. Xu, R. Ye, H. Shen, J. W. Y. Lam, Z. Zhao, B. Zhong Tang, *Angew. Chem.* **2022**, *134*.
- [7] Y. Ai, Y. Li, H. Ma, C.-Y. Su, V. W.-W. Yam, *Inorg. Chem.* **2016**, *55*, 11920–11929.

Publikationsliste

1. *Highly soluble fluorine containing Cu(I) AlkylPyrPhos TADF complexes*
Jasmin M. Busch, Daniel M. Zink, Patrick Di Martino-Fumo, Florian R. Rehak, Pit Boden, **Sophie Steiger**, Olaf Fuhr, Martin Nieger, Wim Klopper, Markus Gerhards, and Stefan Bräse
Dalton Trans. **2019**, 48, 15687–15698.
DOI: 10.1039/c9dt02447f
2. *Investigation of Luminescent Triplet States in Tetranuclear Cu^I Complexes: Thermochromism and Structural Characterization*
Pit Boden, Patrick Di Martino-Fumo, Jasmin M. Busch, Florian R. Rehak, **Sophie Steiger**, Olaf Fuhr, Martin Nieger, Daniel Volz, Willem Klopper, Stefan Bräse, and Markus Gerhards
Chem. Eur. J. **2021**, 27, 5439–5452.
DOI: 10.1002/chem.202004539
3. *Thermally Activated Delayed Fluorescence and Phosphorescence Quenching in Iminophosphonamide Copper and Zinc Complexes*
Bhupendra Goswami, Thomas J. Feuerstein, Ravi Yadav, Sergei Lebedkin, Pit J. Boden, **Sophie T. Steiger**, Gereon Niedner-Schatteburg, Markus Gerhards, Manfred M. Kappes, and Peter W. Roesky
Chem. Eur. J. **2021**, 27, 15110–15119.
DOI: 10.1002/chem.202101247
4. *NIR-Emissive Chromium(0), Molybdenum(0), and Tungsten(0) Complexes in the Solid State at Room Temperature*
Pit Boden, Patrick Di Martino-Fumo, Tobias Bens, **Sophie Steiger**, Uta Albold, Gereon Niedner-Schatteburg, Markus Gerhards, and Biprajit Sarkar
Chem. Eur. J. **2021**, 27, 12959–12964.
DOI: 10.1002/chem.202102208
5. *Unexpected Boost in Activity of a Cu(I) Photosensitizer by Stabilizing a Transient Excited State*
Martin Rentschler, Pit Jean Boden, Miguel A. Argüello Cordero, **Sophie Theres Steiger**, Marie-Ann Schmid, Yingya Yang, Gereon Niedner-Schatteburg, Michael Karnahl, Stefan Lochbrunner, and Stefanie Tschierlei
Inorg. Chem. **2022**, 61, 12249–12261.
DOI: 10.1021/acs.inorgchem.2c01468

6. *Mechanistic and Kinetic Investigations of ON/OFF (Photo)Switchable Binding of Carbon Monoxide by Chromium(0), Molybdenum(0) and Tungsten(0) Carbonyl Complexes with a Pyridyl-Mesoionic Carbene Ligand*

Pit J. Boden, Patrick Di Martino-Fumo, Tobias Bens, **Sophie T. Steiger**, Daniel Marhöfer, Gereon Niedner-Schatteburg, and Biprajit Sarkar

Chem. Eur. J. **2022**, e202201038, 1-10.

DOI: 10.1002/chem.202201038

7. *Cooperativity-Driven Reactivity of a Dinuclear Copper Dimethylglyoxime Complex*

Raphael I. Petrikat, **Sophie T. Steiger**, Elham Barani, Pit J. Boden, Maximilian E. Huber, Mark R. Ringenberg, Gereon Niedner-Schatteburg, Karin Fink, and Sabine Becker

Chem. Eur. J. **2023**, e202203438, 1-8.

DOI : 10.1002/chem.202203438

Tagungsteilnahmen

- **SFB 3MET/TRR88 Conference in Heidelberg, 12.10. – 14.10.2022**
“Time-resolved step-scan FTIR and luminescence spectroscopy on transition metal complexes”, Poster
- **Bunsentagung in Gießen, 07.09. – 09.09.2022**
“Reversible (photo)chemistry of Cr(0), Mo(0) and W(0) carbonyl complexes”, Vortrag
- **SPP 2102 – Symposium in Jena, 11.05. – 13.05.2022**
“Photochemical and photophysical studies on transition metal complexes based on earth-abundant metals”, Poster
- **DPG-Frühjahrstagung SAMOP in Erlangen (virtuell), 14.03. – 18.03.2022**
“Reversible (photo)chemistry of Cr(0), Mo(0) and W(0) carbonyl complexes”, Vortrag
- **SFB 3MET/TRR88 Conference in Heidelberg, 13.10. – 15.10.2021**
“Time-resolved step-scan FTIR and luminescence spectroscopy on transition metal complexes”, Poster
- **DPG-Tagung SAMOP in Kaiserslautern (virtuell), 20.09. – 24.09.2021**
“Influence of metal and halide substitution on the photophysics of dinuclear copper(I) and silver(I) complexes”, Vortrag
- **Bunsentagung in Regensburg (virtuell), 10.05. – 12.05.2021**
“Multi-spectroscopic investigations of dinuclear copper(I) and silver(I) complexes”,
Poster
- **SPP 2102 – Workshop in Leipzig (virtuell), 30.11. – 01.12.2020**
- **SFB 3MET/TRR88 Conference in Kaiserslautern (virtuell), 21.09. – 23.09.2020**
- **27. Lecture Conference on Photochemistry in Kiel (virtuell), 14.09. – 15.09.2020**
- **SFB 3MET/TRR88 Conference in Heidelberg, 09.10. – 11.10.2019**
“Multi-spectroscopic investigations of structures and electronic states of transition metal containing complexes”, Poster

Lebenslauf

Sophie Theres Steiger

Studium:

11/2019 – 03/2023: Promotion in der physikalischen Chemie an der RPTU in Kaiserslautern (ehemals TU Kaiserslautern)

10/2017 - 09/2019: Masterstudium in Chemie an der TU Kaiserslautern
Masterarbeit in der physikalischen Chemie zum Thema: „Zeitaufgelöste IR- und Fluoreszenzspektroskopie an fluorierten OLED-Systemen“

10/2014 - 09/2017: Bachelorstudium in Chemie an der TU Kaiserslautern
Bachelorarbeit in der physikalischen Chemie zum Thema: „Einfluss von Dispersionswechselwirkungen auf die Anlagerung von Alkoholen an Dibenzosuberenon“

Schulische Laufbahn:

08/2006 - 03/2014: Gymnasium Nieder-Olm
Abschluss Abitur

04/2011: Schülerpraktikum im Landesuntersuchungsamt Rheinland-Pfalz,
Institut für Lebensmittelchemie und Arzneimittelprüfung Mainz

08/2002 - 07/2006: Burgschule Nieder-Olm